NEW FRONTIERS IN THE REGENERATION OF THE NERVOUS SYSTEM CONNECTIVITY

EDITED BY: Juan Pablo Henríquez, Francisca C. Bronfman and Eran Perlson
PUBLISHED IN: Frontiers in Cellular Neuroscience

frontiers Research Topics

ISSN 1664-8714
ISBN 978-2-88974-335-3
DOI 10.3389/978-2-88974-335-3

About Frontiers

Frontiers is more than just an open-access publisher of scholarly articles: it is a pioneering approach to the world of academia, radically improving the way scholarly research is managed. The grand vision of Frontiers is a world where all people have an equal opportunity to seek, share and generate knowledge. Frontiers provides immediate and permanent online open access to all its publications, but this alone is not enough to realize our grand goals.

Frontiers Journal Series

The Frontiers Journal Series is a multi-tier and interdisciplinary set of open-access, online journals, promising a paradigm shift from the current review, selection and dissemination processes in academic publishing. All Frontiers journals are driven by researchers for researchers; therefore, they constitute a service to the scholarly community. At the same time, the Frontiers Journal Series operates on a revolutionary invention, the tiered publishing system, initially addressing specific communities of scholars, and gradually climbing up to broader public understanding, thus serving the interests of the lay society, too.

Dedication to Quality

Each Frontiers article is a landmark of the highest quality, thanks to genuinely collaborative interactions between authors and review editors, who include some of the world's best academicians. Research must be certified by peers before entering a stream of knowledge that may eventually reach the public - and shape society; therefore, Frontiers only applies the most rigorous and unbiased reviews.
Frontiers revolutionizes research publishing by freely delivering the most outstanding research, evaluated with no bias from both the academic and social point of view. By applying the most advanced information technologies, Frontiers is catapulting scholarly publishing into a new generation.

What are Frontiers Research Topics?

Frontiers Research Topics are very popular trademarks of the Frontiers Journals Series: they are collections of at least ten articles, all centered on a particular subject. With their unique mix of varied contributions from Original Research to Review Articles, Frontiers Research Topics unify the most influential researchers, the latest key findings and historical advances in a hot research area! Find out more on how to host your own Frontiers Research Topic or contribute to one as an author by contacting the Frontiers Editorial Office: frontiersin.org/about/contact

NEW FRONTIERS IN THE REGENERATION OF THE NERVOUS SYSTEM CONNECTIVITY

Topic Editors:
Juan Pablo Henríquez, University of Concepcion, Chile
Francisca C. Bronfman, Andres Bello University, Chile
Eran Perlson, Tel Aviv University, Israel

Citation: Henríquez, J. P., Bronfman, F. C., Perlson, E., eds. (2022). New Frontiers in the Regeneration of the Nervous System Connectivity.
Lausanne: Frontiers Media SA. doi: 10.3389/978-2-88974-335-3

Table of Contents

frontiers in Cellular Neuroscience

ORIGINAL RESEARCH
published: 11 February 2019
doi: 10.3389/fncel.2019.00016

Quantitative and Qualitative Evaluation of Photoreceptor Synapses in Developing, Degenerating and Regenerating Retinas

Ryutaro Akiba[1,2], *Take Matsuyama*[1]*, *Hung-Ya Tu*[1], *Tomoyo Hashiguchi*[1], *Junki Sho*[1], *Shuichi Yamamoto*[2], *Masayo Takahashi*[1] *and Michiko Mandai*[1]

[1] *Laboratory for Retinal Regeneration, RIKEN Center for Biosystems Dynamics Research, Kobe, Japan,* [2] *Department of Ophthalmology and Visual Science, Chiba University Graduate School of Medicine, Chiba, Japan*

Quantitative and qualitative evaluation of synapses is crucial to understand neural connectivity. This is particularly relevant now, in view of the recent advances in regenerative biology and medicine. There is an urgent need to evaluate synapses to access the extent and functionality of reconstructed neural network. Most of the currently used synapse evaluation methods provide only all-or-none assessments. However, very often synapses appear in a wide spectrum of transient states such as during synaptogenesis or neural degeneration. Robust evaluation of synapse quantity and quality is therefore highly sought after. In this paper we introduce QUANTOS, a new method that can evaluate the number, likelihood, and maturity of photoreceptor ribbon synapses based on graphical properties of immunohistochemistry images. QUANTOS is composed of ImageJ Fiji macros, and R scripts which are both open-source and free software. We used QUANTOS to evaluate synaptogenesis in developing and degenerating retinas, as well as *de novo* synaptogenesis of mouse iPSC-retinas after transplantation to a retinal degeneration mouse model. Our analysis shows that while mouse iPSC-retinas are largely incapable of forming synapses *in vitro*, they can form extensive synapses following transplantation. The *de novo* synapses detected after transplantation seem to be in an intermediate state between mature and immature compared to wildtype retina. Furthermore, using QUANTOS we tested whether environmental light can affect photoreceptor synaptogenesis. We found that the onset of synaptogenesis was earlier under cyclic light (LD) condition when compared to constant dark (DD), resulting in more synapses at earlier developmental stages. The effect of light was also supported by micro electroretinography showing larger responses under LD condition. The number of synapses was also increased after transplantation of mouse iPSC-retinas to *rd1* mice under LD condition. Our new probabilistic assessment of synapses may prove to be a valuable tool to gain critical insights into neural-network reconstruction and help develop treatments for neurodegenerative disorders.

Keywords: photoreceptor synapse, stem cell therapy, circuit reconstruction, retinal degeneration, synapse quantification, ribbon synapse, synaptogenesis

OPEN ACCESS

Edited by:
Francisca C. Bronfman, Pontificia Universidad Católica de Chile, Chile

Reviewed by:
Elva Diaz, University of California, Davis, United States
Michel Joseph Roux, INSERM U964 Institut de Génétique et de Biologie Moléculaire et Cellulaire (IGBMC), France

***Correspondence:**
Take Matsuyama
matsutakehoyo@gmail.com

Received: *25 October 2018*
Accepted: *16 January 2019*
Published: *11 February 2019*

Citation:
Akiba R, Matsuyama T, Tu H-Y, Hashiguchi T, Sho J, Yamamoto S, Takahashi M and Mandai M (2019) Quantitative and Qualitative Evaluation of Photoreceptor Synapses in Developing, Degenerating and Regenerating Retinas. Front. Cell. Neurosci. 13:16. doi: 10.3389/fncel.2019.00016

INTRODUCTION

Recent advances in stem cell biology have overturned the long-held belief that neurons do not regenerate. It has now been established beyond doubt that neural networks can be reconstructed after injury or degeneration either by endogenous regeneration (Jorstad et al., 2017; Yao et al., 2018) or by cell or tissue transplantation (Singh et al., 2013; Barnea-Cramer et al., 2016; Mandai et al., 2017). A critical step for neural reconstruction is the requirement for these newly formed or reintroduced neurons to form new chemical synapses. Current methods are however, insufficient to evaluate the extent of neural integration, and more sophisticated methods to evaluate neural integration are in demand.

A chemical synapse is a subcellular structure specialized for communication between neurons through neurotransmitter molecules. As a key parameter to evaluate the functional state of neural networks, various methods have been developed to quantify and assess synapses over the years. The gold standard to assess the state of a synapse is by electron microscopy (EM), where subcellular pre- and post-synaptic components can be directly observed (Geinisman et al., 1996). While EM can provide valuable qualitative information about the state of a particular synapse, it is currently unpractical to survey a large number of synapses, especially if their rough locations are not known. On the other hand, visualization of pre- and post-synaptic markers by immunohistochemistry (IHC) allows for a robust and high throughput analysis, while simultaneously obtaining some qualitative information.

One of the most common approaches to quantifying synapses by IHC is to manually count pre- and post-synaptic marker pairs (Silver and Stryker, 2000; Ribic et al., 2014). Although laborious, a trained expert may be able to reliably count synapses, but different observers may naturally focus on different features and have different thresholds of acceptance. The use of automated software for quantification is another alternative, for example by counting the number of co-localized pre- and post-synaptic markers (Dominic and Eroglu, 2010). These automatic counting programs apparently seem free of human bias, but certain choices are inevitably made by the software developers with or without the user's knowledge. For example, colocalization-based classifiers require binary images where pixels are assigned as stained or unstained for a marker. Binary images are constructed by thresholding the original images by manually adjusting a threshold level (Glynn and McAllister, 2006) or by selecting one of many thresholding algorithms, which calculates a threshold level. In either case, only slight differences in the threshold level can result in drastically different output counts. Different conditions in recording and staining also cause diverse estimates when the same threshold level is applied. A third and more modern approach is machine learning-guided automatic classification methods, which enabled more reproducible analysis (Fantuzzo et al., 2017). However, it is usually unclear what the machine is "learning," and the factors involved in the decision making of the algorithm are typically unknown.

Above all and most unfortunately, all these synapse quantification methods typically assign a binary value to the marker pairs, either as synapses or not, without accounting for any immature or intermediate properties which however do exist, as exemplified in retinal synaptogenesis, where photoreceptors and bipolar cells form synapses through retinal development (Regus-Leidig et al., 2009). A trained expert can discern these immature or transient states from the morphological, geometrical, and signal intensity properties of an IHC image, allowing for a more nuanced interpretation than the mere number of synapses. Furthermore, there is an increasing need in assessing synapse formation in the field of neural regeneration and cell therapies that involves reconstruction of neural networks by neural cells from endogenous regeneration or transplantation, where the quantitative and qualitative synapse evaluation is considered most relevant to *de novo* neural function. We previously showed that transplantation of mouse ES or iPS derived retinas (mESC/miPSC-retinas) could restore light response in the end-stage retinal degeneration mouse models with some evidence of host-graft synaptic connection (Assawachananont et al., 2014; Mandai et al., 2017; Iraha et al., 2018). A quantitative and qualitative evaluation of synapses would therefore provide a strong clue for estimating the functional potency of grafted tissues, and would further help optimize and develop better conditions for this therapeutic approach.

We thus propose a probabilistic evaluation of synapses from IHC images, which would allow us not only to quantify the number of synapses but also to estimate the likelihood of "synapse-ness" based on multi-synaptic factors on a continuous scale. We named this approach QUANTOS (QUalitative and quantitative ANalysis using Bayes Theorem Optimized for Synapse evaluation). The QUANTOS analysis specializes in the distinctive synapse structure called "ribbon synapse" located between photoreceptors and bipolar cells, namely the first and the second order neurons in the retina. RIBEYE is an essential component of synaptic ribbons found in photoreceptor cells and auditory hair cells of the inner ear. Its molecular structure consists of two domains, one of which is identical to Ctbp2 and is homologous to phosphoglycerate dehydrogenases (Schmitz et al., 2000). RIBEYE is the main component of the synaptic ribbon, which exhibits characteristic horseshoe shape at the photoreceptor axon terminal, and acts as a molecular machinery for efficiently storing and releasing glutamate to the synaptic cleft (tom Dieck et al., 2005; Matthews and Fuchs, 2010). Metabotropic glutamate receptor type 6 (mGluR6) is expressed on dendritic tips of ON-bipolar cells to receive the glutamate released from the photoreceptors (Sterling and Matthews, 2005). We used IHC images of presynaptic RIBEYE and postsynaptic mGluR6 to train QUANTOS and thereby analyzed photoreceptor-bipolar ribbon synapses.

In order to showcase QUANTOS, we first studied the impact of light, i.e., photoreceptor activity on the ribbon synapse formation during development. Electrophysiology was tested in parallel to see the physiological relevance of our synapse assessment. We then used QUANTOS to quantify and assess synaptogenesis of miPSC-retinas after transplantation in the *rd1* mice with end stage retinal degeneration. Here again we tested whether light influences regenerative synapse formation.

RESULTS

General Design of the QUANTOS

The general design of the method is described in **Figure 1** and **Figures S1–S5**. Samples obtained at different developmental stages of B6J, *rd1*, and *rd1* after miPSC-retina transplantation were co-stained for pre- and post-synaptic markers, Ctbp2 (RIBEYE) and mGluR6 (**Figure 1A**). Images were segmented and thresholded to isolate regions of interest (ROIs) using macros in ImageJ Fiji (**Figure 1B**). Image processing protocols were customized for DAPI (**Figure S1**), RIBEYE (**Figure S2**), and mGluR6 (**Figure S3**), respectively, for better detection of ROIs. From each ROI, 34 graphical parameters were extracted using the "Measure" function of ImageJ Fiji (**Figure 1B**). These parameters can be categorized into 6 *Geometry* parameters, 14 *Signal* parameters, and 14 *Morphology* parameters.

The training data for synapse and noise was generated from IHC images of 3 to 4 replicate slices each from three P28 B6J mice, assuming most of the photoreceptor synapses at this developmental stage would be mature. The outer plexiform layer (OPL), where photoreceptor synapses are formed, was manually cropped to train the *Ideal Synapse* data, and area outside the OPL was used to train the *Ideal Noise* data (**Figure 1A**). These images were processed as mentioned above, and graphical parameters were extracted to generate probability density functions (PDFs) of *Ideal Synapse* and *Ideal Noise* for each of the parameters. These PDFs were automatically generated by using either Kernel Density Estimation (KDE) or Bounded Density Estimation (BDE). Data were fitted with BDE where there were clear boundaries, and with KDE otherwise. Representative PDFs from each category are presented in the upper panel of **Figure 1C** (Details of parameters are described in Methods section).

Once PDFs of training data were generated, samples were processed for QUANTOS evaluation. IHC Images were processed to extract pre- and post-synaptic markers ROIs, and their graphical parameters were evaluated against PDFs of *Ideal Synapse* and *Ideal Noise* for estimating likelihoods. Marker spatial density was used for estimating the prior probability of synapse, as higher density of markers results in higher chance of markers being randomly proximal to each other (**Figure S4**). Pre- and post- synaptic marker pairs within 1.2 μm were considered as "Synapse Candidates", and their posterior probability was estimated by multiplying the prior probabilities and likelihoods of both pre- and post- synaptic markers altogether (**Figure 1C** lower panel). This allows QUANTOS to identify the pairs that are more likely to be synapses based on the training data and estimate the total amount of synapses as well as their individual synapse likelihood (**Figure 1D**). All of these steps were built into ImageJ Fiji Macros and R scripts and uploaded in public repository (https://github.com/matsutakehoyo/QUANTOS).

Graphical Properties of the Ribbon Synapse

PDFs generated from the training data revealed the properties of noise and synapse staining. The distribution of synapse distances between pre- and post-synaptic markers indicate that synapse distances have a Gaussian distribution with a mean distance of 0.51 μm and a standard deviation of 0.17 μm (**Figure S5**, upper light panel). From our simulation of random markers, the noise distribution was approximated with a polynomial function of second order; however, noise distances were not necessarily distributed randomly, as noise signals tended to be clustered. The noise angle distribution had a uniform distribution as expected from a random distribution, whereas the synapse angle distribution indicated that the major population of synapses were aligned vertically. Interestingly, the synapse angle distribution had a wide tail indicating synapses at various angles, even horizontally aligned or vertically aligned but in opposite directions (**Figure S5**, upper light panel). **Figure S5** shows the PDFs for *Geometry*, *Morphology*, and *Signal* features. The synapse *area* distributions had distinctive acute peaks, whereas noise *area* distributions had more larger values for both markers. On the other hand, the *integrated density* was larger in the synapse distribution for both pre- and post-synaptic markers, indicating that noise is either relatively small and bright or large but weakly stained. Many of the *Morphology* parameters, such as *perimeter*, *width*, *height*, *major*, and *minor*, had a broad distribution for noise and a more defined distribution for synapse indicating that noise features are more randomly distributed whereas synapse features do have characteristic staining patterns. Noise distributions for *mean*, *mode*, *median*, *min*, *max*, and *stdev* parameters tended to have a large peak around small values with a long tail extending to large values. Synapse distributions, on the other hand, were more symmetric and centered around larger values.

Evaluation of QUANTOS

We evaluated the sensitivity and specificity of QUANTOS, using a data set of synapses on postnatal day (P) 28 and P14, which represent emerging and mature synapses, respectively. These samples were manually evaluated by an expert observer to create a *Ground Truth* to evaluate the performance of QUANTOS.

Several receiver operating characteristics (ROC) curves using combinations of *Signal*, *Morphology*, and *Geometry* parameter categories were generated to better understand the features contributing information to the classifier (**Figure 2A**). Ground truths for P28 and P14 samples were generated by careful evaluation by an expert observer. For the P28 sample, the ROC curve for the distance parameter alone performed very poorly with an area under that curve (AUC) of 0.55 (95% confidence interval (CI): 0.51–0.58), indicating that the distance-based classifier performance is close to random chance (**Figure 2B**). Adding *Morphology* and *Geometry* parameters increased the AUC to 0.89 (CI: 0.87–0.92) and 0.95 (CI: 0.93–0.97), respectively. While both parameter categories increased classifier performance substantially, inclusion of *Morphology* seemed to favor sensitivity, whereas *Geometry* enhanced specificity. Among the three categories of parameters, *Signal* parameters showed the largest AUC value of 0.98 (CI: 0.98–0.99), suggesting that *Signal* parameters contained the most information. The best AUC (0.99, CI: 0.98–0.99) was obtained when all the parameters were used (**Figure 2C**). A similar trend was observed in the P14 sample (**Figures 2C,D**), where the largest AUC value was 0.97 (CI:0.96–0.98) for the classifier utilizing all the parameters, indicating that

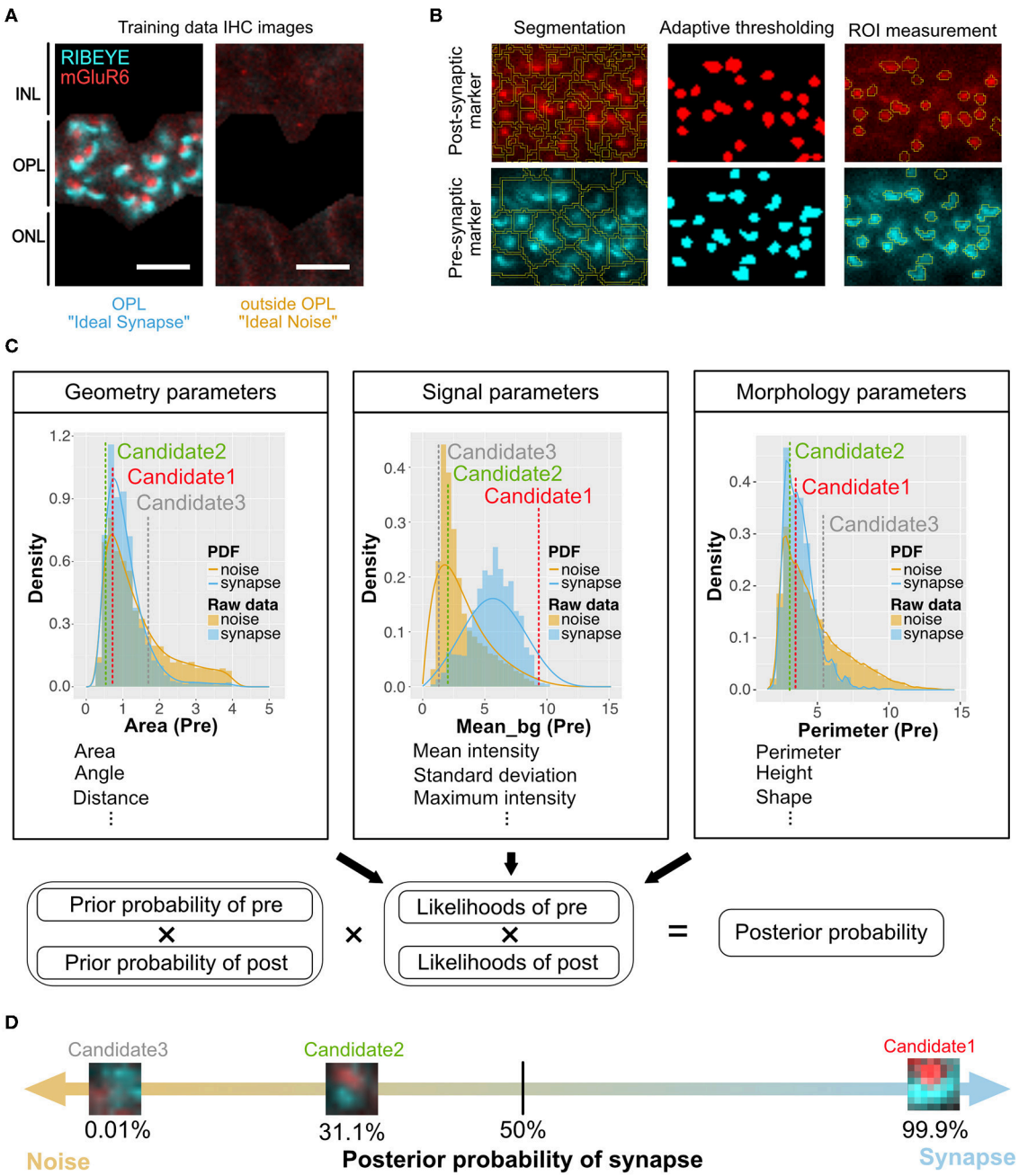

FIGURE 1 | Overview of QUANTOS, a synapse evaluation method using a Naïve Bayes classifier. **(A)** Photoreceptor synapses are visualized by immune-staining of pre-synaptic marker: RIBEYE, and post-synaptic marker: mGluR6. Three to four replicate IHC Images from three P28 B6J mice each were used as training data for *Ideal Synapse* and *Ideal Noise*. The OPL area was manually isolated to train the *Ideal Synapse*, and the area outside the OPL was used to train the *Ideal Noise*. Scale bar = 4 μm. **(B)** IHC images were processed by custom made ImageJ Fiji macros. IHC images were segmented, and thresholded using the background intensity of each segment. The thresholded areas were then overlaid on the original IHC image to extract graphical parameters from ROIs. Details of image processing steps for DAPI, RIBEYE, and mGluR6 are described in **Figures S1–S3**. **(C)** Upper panel: The distribution of extracted parameters was estimated with either Kernel Density Estimation or Bounded Density Estimation to generate PDFs for *Ideal Synapse* and *Ideal Noise*. These PDFs were used to estimate likelihoods of each synaptic marker. Marker spatial density is used to calculate prior probability. Pre- and post-synaptic markers within 1.2 μm of each other (distance from center of mass) were considered as synapse candidates. Lower panel: Posterior probability of synapse candidates being either synapse or noise is estimated by multiplying prior probabilities and likelihoods of both pre- and post-synaptic markers. **(D)** Posterior probability of being synapses are estimated for each individual synapse candidates. Synapse candidates with more than 50% of posterior probability were classified as synapse. IHC, immunohistochemistry; IPL, inner plexiform layer; OPL, outer plexiform layer; ONL, outer nuclear layer; ROIs, regions of interest; PDFs, probability density functions.

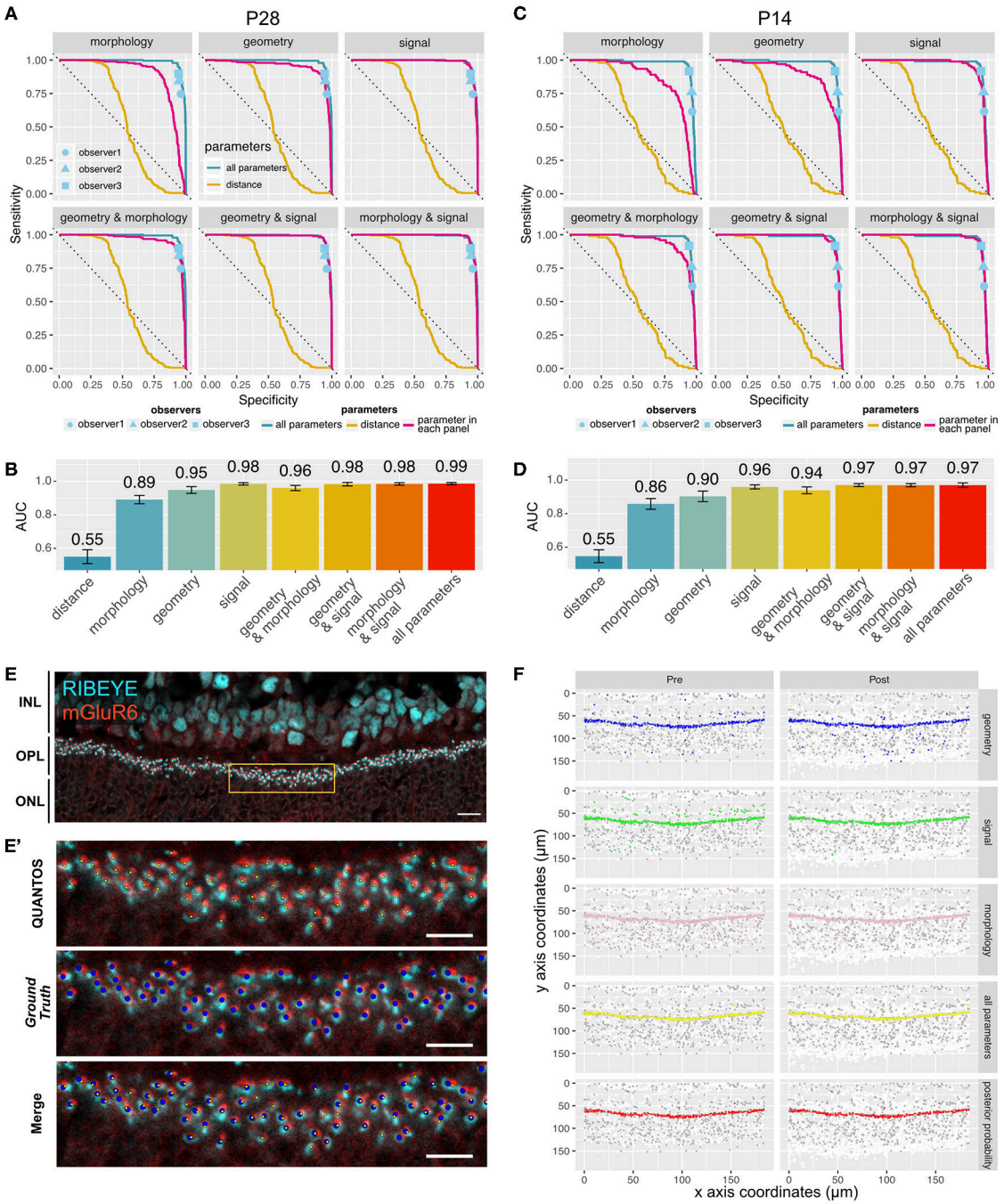

FIGURE 2 | Sensitivity and specificity of QUANTOS. **(A)** ROC curves of classifiers using different combinations of parameters on a P28 sample. ROC curves for each parameter are indicated with a magenta line. The ROC curve of distance and all parameters are shown in all panels for comparison. Dots indicate the results of manual counts by different observers (IHC image: $n = 1$). **(B)** Comparison of AUC between different combination of parameters on P28 sample. Whiskers indicate 95% confidence intervals. **(C)** ROC curves of classifiers using different combinations of parameters on P14 sample (IHC image: $n = 1$). **(D)** Comparison of AUC between different combination of parameters on P14 sample. Whiskers indicate 95% confidence intervals. **(E)** Example of an IHC image of B6J P28 mouse. Yellow box area is shown magnified in **(E')**. Scale bar = 10 µm. **(E')** upper panel: Yellow small dots indicate synapses detected by QUANTOS., middle panel: blue large dots indicate the *Ground Truth* (manually evaluated by an expert), lower panel: overlay image of both QUANTOS results and *Ground Truth*. Scale bar = 5 µm. **(F)** Pre- (left column) and post-synaptic marker (right column) coordinates detected by QUANTOS. Each row shows the synapse candidates, i.e., candidates with high synapse likelihood given different parameters. White dots represent all the markers detected in the Image Processing, and gray dots represents all the synapse candidates (pre- and post-synaptic markers within 1.2 µm), and colored dots represent the synapse candidates with higher likelihood of synapse than noise for different parameters. "all parameters" represents the combined likelihoods of all parameters and pre- and post-synaptic markers. "posterior probability" shows the marker pairs identified as synapses by QUANTOS, which are obtained from "all parameters" by taking into account the prior probability of synapse. ROC, receiver operation characteristics; AUC, area under the curve.

QUANTOS was able to reliably evaluate immature synapses in developing retinas.

We also compared QUANTOS against manual counting. Three observers manually counted synapses, and their results were matched with the ground truth for estimating the specificity and sensitivity. QUANTOS outperformed manual counts with a small margin, consistently in both P28 (**Figure 2A**) and P14 (**Figure 2C**) images. Manual counting varied in the specificity and sensitivity properties, and the difference was more pronounced on P14, suggesting that human assessment is less stable when encountering immature developmental synapse data. On the other hand, QUANTOS showed robust performance both for immature and mature developmental stages.

The IHC image of P28 C57BL/6J (B6J) (**Figure 2E**) with the *Ground Truth* (**Figure 2E'** middle panel) and synapses detected by QUANTOS (**Figure 2E'** upper panel) are shown for comparison. Also, synapse candidates as evaluated by each parameter category are visualized (**Figure 2F**). As visualized by the large number of white dots in **Figure 2F**, the approach of QUANTOS is to pick up as many signals as possible regardless of their intensity, and subsequently filter out candidates based on their likelihoods. This allow us to detect very dim signals and evaluate them accordingly, rather than setting an arbitrary threshold level for markers. Notice that although individual parameter groups may identify markers outside the OPL as synapse candidates, the final synapse evaluation is mostly constrained to the OPL, showing the power of the Naïve Bayes classifier to exclude noise signals by evaluating multiple parameters.

Quantification of the Photoreceptor Ribbon Synapse During Postnatal Development of B6J Mice Under Different Light Conditions

We first used QUANTOS to quantify synapse formation in wildtype B6J mice reared under cyclic light (LD) and constant dark (DD). IHC images of B6J mice on different postnatal days showed that immunoreactivities of RIBEYE and mGluR6 were weak and diffuse on P7 but became stronger on P10. The characteristic horseshoe shape of RIBEYE could be observed after P14, and mGluR6 expression pattern also became punctate on P14. By P21, the shape of the synapse was defined, and the same expression pattern was maintained through P28 and P35 (**Figure 3A**). QUANTOS detected almost no or very few synapses on P7 and P10 either under LD or DD conditions. From P14 to P21, the number of synapses rapidly increased and remained largely constant through P28 and P35 (**Figure 3B**). Notably, samples acquired from mice reared in LD condition tended to have more synapses on P10 and P14. We thus modeled the process of synaptogenesis with a growth curve to analyze the effect of light (**Figure 3E**) using Bayesian parameter estimation. The model shows that while the maximum rate of synaptogenesis (μ_M) and the maximum number of synapses (A) were not significantly different between LD and DD conditions, the onset of synaptogenesis (λ), on the other hand, was faster in LD condition by about one day (**Figures 3C,D**), indicating that light influences synaptogenesis.

Quality Changes of the Photoreceptor Ribbon Synapse During Postnatal Development of B6J Mice Under Different Light Conditions

We then inspected the distributions of the likelihoods of synapses determined by QUANTOS in all synapse candidates (**Figure 3F**). The horizontal axis shows the log synapse likelihood and the vertical axis represents log noise likelihood. The diagonal line represents the boundary where the probability of synapse and noise are equal. On P7, synapse candidates clearly had a peak toward the noise, but from P14 onwards, a second peak with high synapse probability appeared. The synapse peak kept increasing after P21, becoming more prominent on P28 (**Figure 3F**). Similar trends were observed under both LD and DD conditions.

Lastly, we visualized different states of developmental ribbon synapses by creating average images from all the detected synapses (**Figure 3G**). RIBEYE and mGluR6 showed diffuse expression patterns on P7 and P10, which became more focused on P14 and later postnatal stages under both LD and DD conditions. The intensity plot against distance from center coordinates of pre- and post-synaptic markers showed that signal intensity became higher at later postnatal stages under both conditions (**Figure 3H**).

Effect of Light Assessed by Micro Electroretinography (mERG)

In order to determine if the difference in synapse numbers suggested by QUANTOS was physiologically relevant, we recorded the mERG response of P14 retinas, as the difference in synapse numbers was most prominent between LD and DD at this stage. The b-wave, an upward peak between 150 ms after the onset of light pulse stimulation is derived from the ON-bipolar cells that receive signal inputs from photoreceptors through ribbon synapses (**Figure 4A**). We compared the amplitude of b-waves across mice reared in DD, LD, or constant light (LL) conditions. The histograms of b-wave amplitudes showed a skewed distribution toward smaller values (**Figure 4B**, upper), with LD and LL having longer tails toward larger b-wave amplitudes. We modeled the data with a hierarchical generalized linear Gamma model (**Figure 4B**, lower), showing a reasonable summary of b-wave amplitudes. Our model indicates that both the mean value of the b-wave amplitude (**Figure 4C**), and its standard deviation (**Figure 4E**) were significantly higher in LD and LL when compared to DD condition (**Figures 4D,F**). This is consistent with the quantitative evaluation of photoreceptor ribbon synapses in P14 retinas by QUANTOS, suggesting that the presence of light may accelerate development of photoreceptor ribbon synapses.

Evaluation of Photoreceptor Ribbon Synapses in the Progressive Retinal Degeneration Model (*rd1*) During Development and Degeneration

One potential application of QUANTOS is to evaluate the synapse formation after transplantation of ES/iPS derived

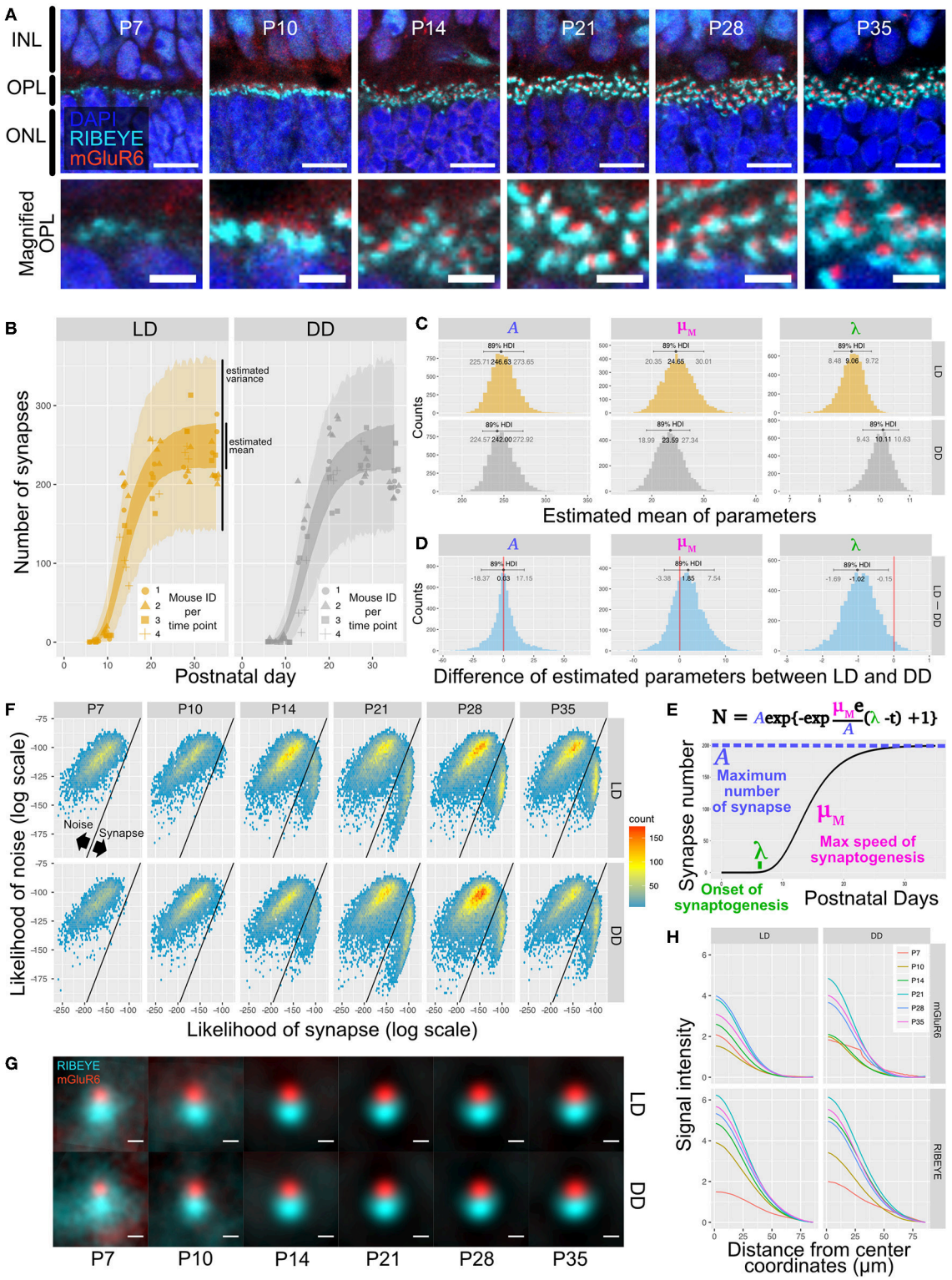

FIGURE 3 | Qualitative and quantitative evaluation of developmental synaptogenesis by QUANTOS in mice reared in DD and LD conditions. **(A)** IHC images of B6J mice on different postnatal days. RIBEYE is the pre-synaptic marker expressed in photoreceptors and mGluR6 is the post-synaptic maker expressed in bipolar cells. Images in upper row show the overview morphology of OPL, and lower row show the magnification of OPL. Scale bar = 10 μm for upper row, 2.5 μm for lower row. **(B)** Result of synapse quantification of postnatal B6J reared under LD and DD conditions. Dots indicate the number of synapses detected in each IHC image. Shape of dots represents the mouse ID for each time point. Dots of each time point were horizontally jittered for better visualization. The dark color-filled area shows the

(Continued)

FIGURE 3 | estimated range of mean number of synapses, and the pale color-filled area represents the estimated range of synapse numbers from each IHC image. ($n = 3$ for P7, P10, P35, and $n = 4$ for P14, 21, 28 samples. 3–4 replicates were taken from each mouse as indicated by the shape of markers). **(C)** Posterior distributions of modified Gompertz model parameters with 89% confidence interval. **(D)** Difference of posterior distributions of parameters between LD and DD conditions. **(E)** Developmental synaptogenesis was parameterized with the modified Gompertz's growth curve which has three parameters; the maximum number of synapses **(A)**, maximum rate of synaptogenesis (μ_M), and the onset of synaptogenesis (λ). **(F)** 2D histograms of all synapse candidates on different postnatal days, with log synapse likelihood on the x axis, and log noise likelihood on the y axis. Synapse candidates on the left-upper side are more likely to be noise, and the ones on the right-lower side are more likely to be synapses. **(G)** All synapses detected by QUANTOS were averaged to visualize the characteristics of synapses on different postnatal days and different rearing conditions. **(H)** Radial profile plots of averaged synapses. The plots show the signal intensity in relation to the center coordinates of pre- and post-synaptic markers. Colors indicate different postnatal days. IHC, immunohistochemistry; INL, inner nuclear layer; OPL, outer plexiform layer, ONL; outer nuclear layer; LD, cyclic light; DD, constant dark; P, postnatal day; HDI, high density interval.

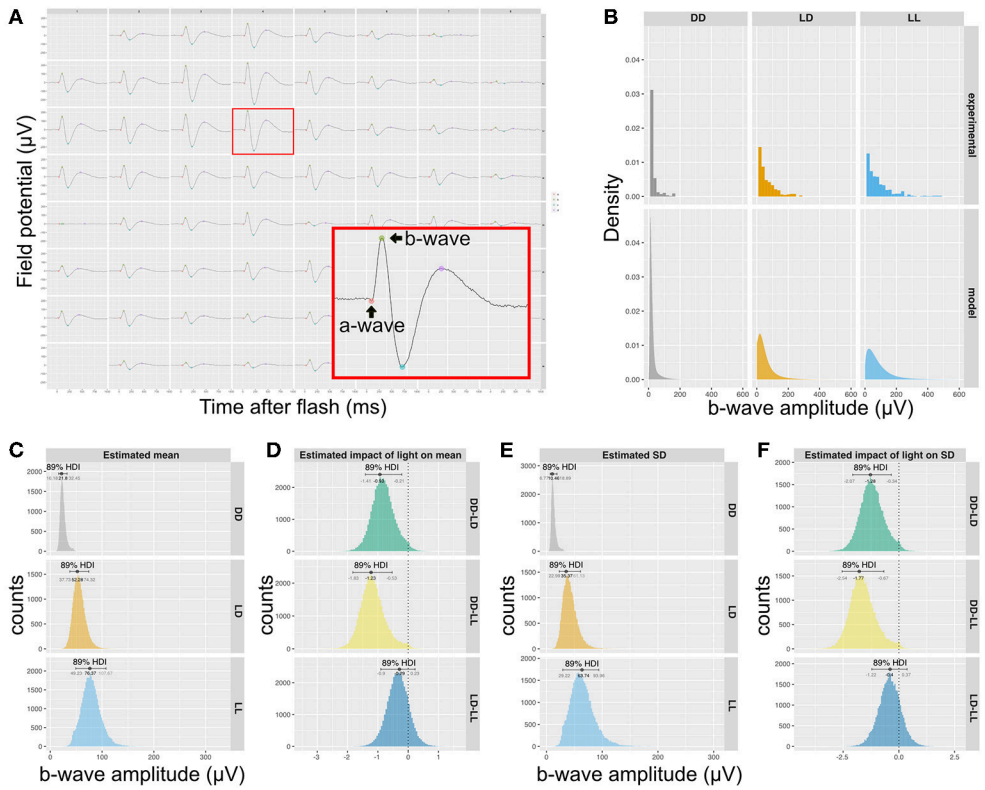

FIGURE 4 | Rearing light conditions alter developmental synaptic function. **(A)** An example of mERG recording. Retinas flat-mounted on the 60-channel probe were stimulated with a mesopic light pulse. The red box is a magnified view of a single channel recording trace, showing a typical waveform with an a-wave and a b-wave. **(B)** Upper panels show histograms of b-wave amplitudes of wildtype P14 mice reared under different light conditions ($n = 5$ for DD and $n = 4$ for LD and LL) and the posterior predictive check of the statistical model used to analyze the data is shown in the lower panels. **(C)** Posterior distributions of mean b-wave amplitude. **(D)** Estimated impact of light on mean b-wave amplitudes. **(E)** Posterior distributions b-wave amplitude SD. **(F)** Estimated impact of light on SD of mean b-wave amplitudes. mERG, micro electroretinography; HDI, high density interval; SD, standard deviation.

retinas in retinal degeneration models. We first quantified photoreceptor ribbon synapses in *rd1* mouse retinas, in which rod photoreceptors are mostly lost in the first 4 postnatal weeks. IHC images of *rd1* retinas on P7 showed weak expression of RIBEYE, which became prominent on P10, showing some horseshoe shape patterns (**Figure 5A**). However, the RIBEYE expression decreased from P14, leaving almost no signals by P28. On the other hand, the expression of mGluR6 was constantly weak throughout all postnatal stages. The number of synapses quantified by QUANTOS are shown in **Figure 5B** together with the B6J data (LD condition) for comparison. Results of *rd1* retinas quantification showed a slight increase of synapses from P7 to P14, followed by a gradual decrease thereafter. The number of synapses in *rd1* was dramatically reduced by P28 compared to B6J. The number of ONL cells started decreasing on P14 and continued to decrease through P21 and P28 (**Figure 5C**). ONL cells did not completely disappear even on P28, as cone photoreceptors survive longer than rods (Lin et al., 2009).

Next, we generated 2D histograms of synapse and noise log likelihoods for all the synapse candidates. While synapses seemed to increase toward P14 in *rd1*, no distinctive synapse group was observed as in the wildtype, suggesting that

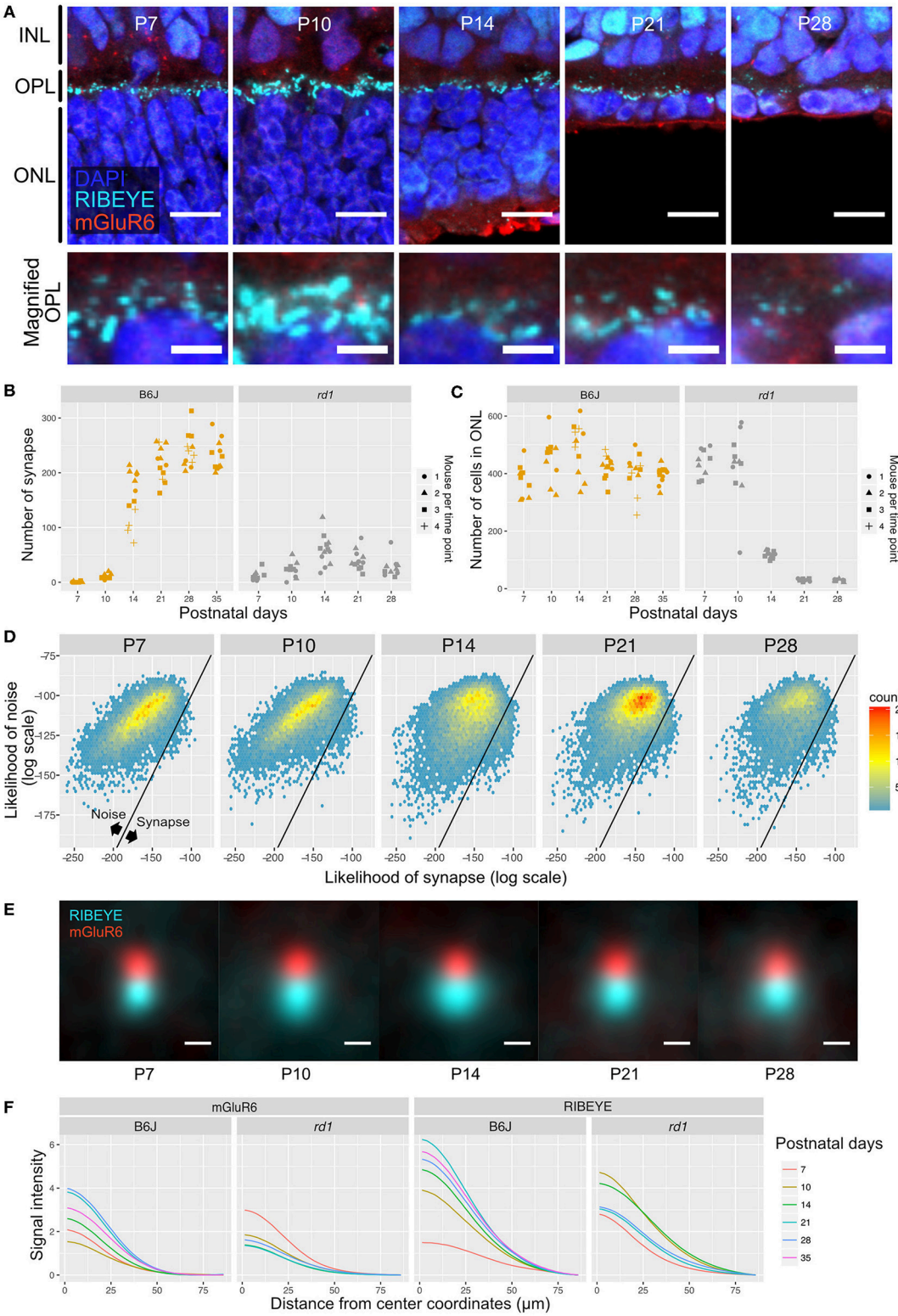

FIGURE 5 | QUANTOS evaluation of synapses during photoreceptor degeneration. **(A)** IHC images of *rd1* mice retinas on different postnatal days. Images in upper row show the overview morphology of OPL, and lower row show the magnification of OPL. Scale bar = 10 μm for upper row, 2.5 μm for lower row. **(B)** The number of synapses detected on different postnatal days in *rd1* mice, accompanied by B6J LD data for comparison ($n = 3$ for each postnatal day of *rd1*. 3–4 replicates were taken from each mouse as indicated by the shape of markers). **(C)** Number of photoreceptor cells estimated form IHC images on different postnatal days of *rd1* mice retinas,

(Continued)

FIGURE 5 | accompanied by B6J data for comparison. **(D)** 2D histograms of all synapse candidates on different postnatal days, with log synapse likelihood on the x axis, and log noise likelihood on the y axis. **(E)** Averaged images of all synapses detected by QUANTOS show the characteristics of synapses on different postnatal days and different rearing conditions. Scale bar = 0.5 μm. **(F)** Radial profile plot of averaged synapses. This plot shows the intensity of signals in relation to the center coordinates of pre- and post-synaptic markers. Colors indicate different postnatal days. IHC, immunohistochemistry; INL, inner nuclear layer; OPL, outer plexiform layer, ONL; outer nuclear layer; SD, standard deviation.

synapses formed in *rd1* are incomplete and small in number compared to B6J (**Figure 5D**). We again visualized synapses from different postnatal days by averaging all the synapses detected by QUANTOS (**Figure 5E**). The signal of RIBEYE transiently increased in size on P14, but then continuously decreased through P21 and P28. mGluR6 expression did not noticeably change from P7 to P21, but slightly decreased on P28. Signal intensity of averaged synapses were plotted against the distance from the center of synaptic markers (**Figure 5F**). These plots show that the intensity peak became higher on later postnatal days in B6J, but the opposite trend was found in *rd1* mice, showing lower intensity on later postnatal days for both synaptic markers.

Quantity and Quality Change of Ribbon Synapses After Subretinal Transplantation of miPSC-Retinas Into *rd1* and the Effect of Light on Regenerative Synaptogenesis

We transplanted miPSC-retinas of differentiation day (dd) 12–13 into 9 to 12-week-old *rd1* mice. We then investigated synaptogenesis by IHC on post-transplantation days (PT) 14, 30, and 60 (approximately equivalent to dd26, 42, and 72). IHC images from PT14 retinas showed immature expression of RIBEYE and almost no expression of mGluR6 (**Figure 6A**). On PT30 and PT60, typical horseshoe shaped RIBEYE and punctate mGluR6 immunoreactivities were observed surrounding the transplants, suggesting the formation of synapses (**Figures 6B,C**). We first examined dd25 and dd36 samples by QUANTOS to test if miPSC-retinas could form synapses *in vitro*, and found that there was almost no synapse formation *in vitro* regardless of differentiation day (**Figure 6D**, left). In contrast, a substantial number of synapses was formed in the post-transplantation *rd1* retinas (**Figure 6D**, middle). The number of synapses per graft photoreceptor increased substantially from PT14 to PT30 and then to PT60, indicating that transplanted photoreceptors form new synapses as miPSC-retinas integrate and mature in the host *rd1* retinas. We also tested the effect of light on post-transplantation synaptogenesis and found that the number of synapses per photoreceptor was higher in LD condition on PT60, indicating that that similarly to developmental B6J retina, light resulted in an increased number of synapses (**Figures 6D–F**). 2D histograms of noise and synapse likelihoods of *in vitro* miPSC-retinas showed sparse synapse candidates distributed in the noise region, and almost no candidates toward synapse were observed on dd25 and dd36 samples (**Figure 6G**). After transplantation, synapse candidates were observed mostly toward noise on P14, with LD-conditioned mice having more candidates toward synapse. On P30, a small peak was observed toward higher synapse likelihood in both LD and DD. The small synapse peak remained in the LD samples on PT60 but was less prominent in the DD condition.

For visualization of the expression pattern, all synapses detected by QUANTOS were averaged (**Figure 6H**). Before transplantation, the expression pattern of RIBEYE from *in vitro mi*PSC-retinas was diffuse on dd25 but became more focused on dd36. mGluR6 expression was quite weak both on dd25 and on dd36. After transplantation, the expression pattern of RIBEYE became larger and brighter, but mGluR6 expression was relatively weak on all post-transplantation days. This trend was confirmed by intensity plots (**Figure 6I**). The intensity of RIBEYE became higher on later post-transplantation days, but the intensity of mGluR6 was low throughout all time points, when compared to the B6J LD condition.

Mature/Immature Likelihoods of Synapses

We built a synapse classifier using synapse and noise training data. Similarly, we attempted to further discriminate synapses by training a new classifier with P10 (DD) and P28 (LD) synapses, representing relatively immature and mature synapses, respectively. Sample images of B6J P14 and P21 synapses are shown (**Figures S6A,C**), along with the results of QUANTOS evaluation (**Figures S6B,D**), showing examples of mature and immature synapses.

Samples of B6J during development under DD/LD conditions and *rd1* after transplantation of miPSC-retina were tested for maturity. 2D histograms of mature and immature synapse likelihoods of the B6J mice show an immature small population dominantly on P10 which starts to shift toward the mature region in the LD condition on P14, but it is delayed in the DD condition (**Figure 7A**). This suggests that LD synapses acquire mature properties earlier than DD synapses. The majority of the synapses were classified on the mature side by P21 in both LD and DD conditions. Synapses in postnatal *rd1* mice exhibited a mixture of mature and immature properties (**Figure 7B**). Synapses in *rd1* mice after miPSC-transplantation were more diverse in mature/immature likelihoods, but some showed higher mature likelihood (**Figure 7C**). When the log likelihoods of mature and immature synapse were plotted separately for pre- and post-synaptic markers, the pre-synaptic marker population is shifted toward mature from PT14 to PT30, suggesting expression of more mature RIBEYE in iPSC-retina after transplantation (**Figure 7D**).

DISCUSSION

In the present study, we introduced our new synapse evaluation method using a Naïve Bayes classifier, "QUANTOS," which offers a transparent evaluation of multiple parameters, thereby achieving a reproducible and robust counting of retinal ribbon

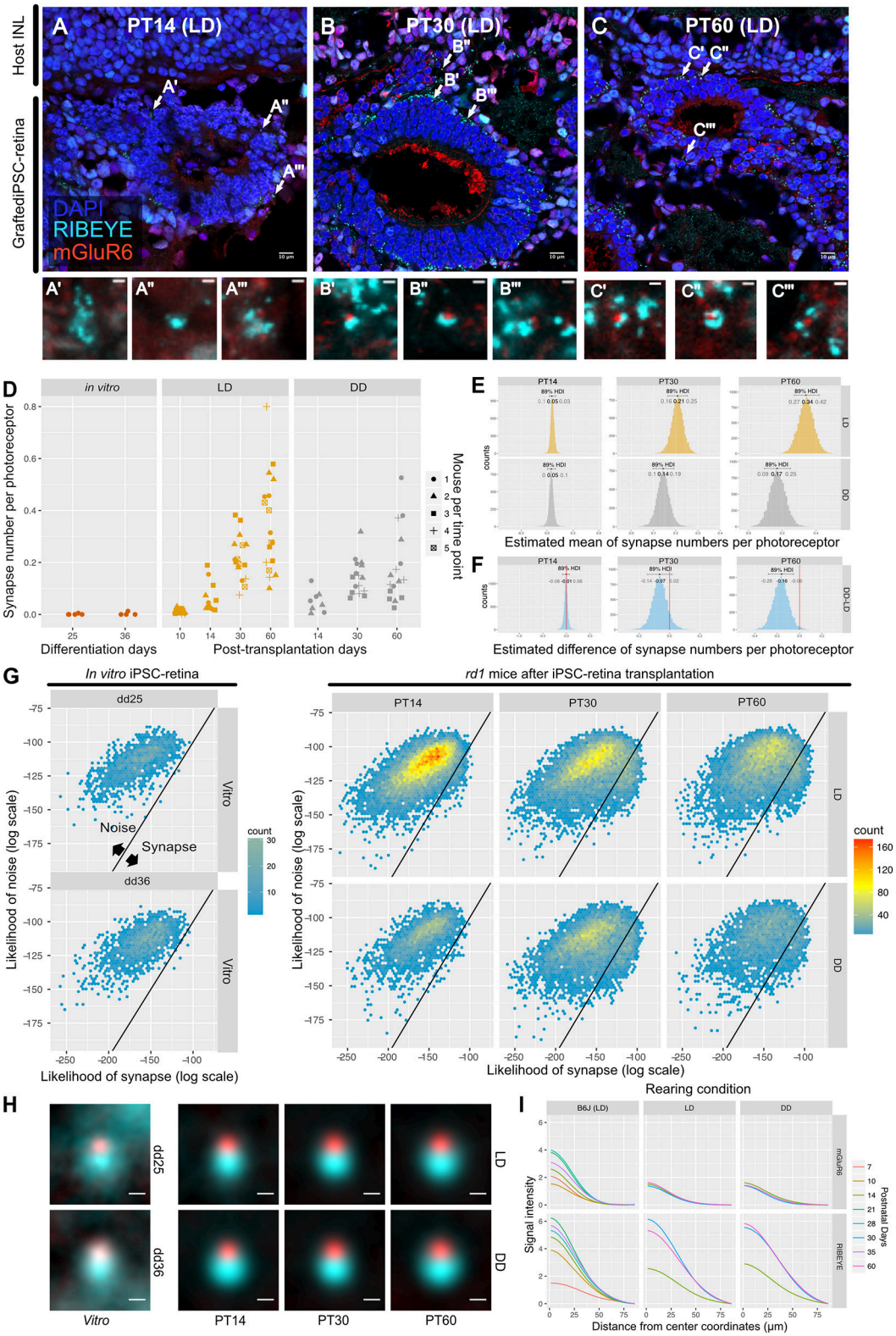

FIGURE 6 | QUANTOS detects *de novo* synapses after miPSC-retina transplantation and shows that light enhances synaptogenesis. **(A–C)** Example IHC images of *rd1* mice after miPSC-retina transplantation on PT 14, 30, 60. Bottom panels show magnified images of some synapse candidates. Scale bar = 10 μm **(D)** Number of synapses of *rd1* mice before and after transplantation of miPSC-retina under different rearing light conditions. (5 and 4 retinal organoids were sampled for *in vitro* dd25

(Continued)

FIGURE 6 | and dd36, respectively. $n = 4$ for PT10 LD, $n = 3$ for PT14 LD, $n = 2$ for PT14 DD, $n = 5$ for PT30 LD, $n = 4$ for PT30 DD, $n = 5$ for PT60 LD, $n = 4$ for PT60 DD. 3–4 replicates were taken from each mouse as indicated by the shape of markers). **(E)** Estimated mean number of synapses per photoreceptor on PT 14, 30, and 60. **(F)** Difference of estimated mean number of synapses per photoreceptor between DD and LD. **(G)** 2D histograms of all synapse candidates on different postnatal days, with log synapse likelihood on the x axis, and log noise likelihood on the y axis. **(H)** Average synapse of *rd1* mice before and after miPSC-retina transplantation. All synapses detected by QUANTOS were averaged from different time points, respectively. Scale bar = 0.5 μm. **(I)** Radial profile plot of averaged synapses. This plot shows the intensity of signals in relation to the center coordinates of pre- and post-synaptic markers. Colors indicate different postnatal days. Data of B6J is presented together for comparison. IHC, immunohistochemistry; PT, post-transplantation day; LD, cyclic light; DD, constant dark; dd, differentiation day; INL, inner nuclear layer; OPL, outer plexiform layer, ONL; outer nuclear layer.

synapses. Many synapse classifiers are simply colocalization-based, however spatial information alone is not enough to reliably evaluate synapses. Our data indicate that the mean distance between pre- and post-synaptic markers in the photoreceptor ribbon synapse is 0.51 μm, which is consistent with a previously reported distance of 400 to 800 nm for mGluR6 and presynaptic active zone in an EM study (Vardi et al., 2000). The identification of overlapping markers depends largely on the adjustment of the threshold which is arbitrary and unstable as evidenced by the ROC curve of the distance-based classifier, which showed near random chance performance. In manual counting, the counter is evaluating multiple parameters simultaneously and setting thresholds of acceptance for those features based on the present image and prior experience. These assessment criteria are often difficult to articulate, and different observers may place importance on different features. Our present approach is more transparent as all the parameter PDFs are defined, and the user may trace back the features that contribute to a particular synapse assessment. QUANTOS allows users to see which parameters and how those parameters are changing during synaptogenesis, and what is causing the difference between synapse and noise, or mature and immature synapses.

We originally intended to only use parameters that had large differences in their synapse and noise PDFs. However, ROC analysis revealed that the largest AUC is obtained when all the parameters are employed. In fact, while the *Signal* parameters alone have an excellent AUC, the *Morphology* and *Geometry* parameters combined also have a considerable AUC, indicating that features other than the signal parameters also contain valuable information. Even when the difference between synapse and noise PDFs is small for individual parameters, they may contain significant information when combined. Another advantage of using a large number of parameters is that QUANTOS is more robust as it is less reliant on a particular trait. This robustness is well-illustrated by the selection process of the synapse, where many parameters detect different synapse candidates, but only the ones in the OPL were selected in the end (**Figure 2F**). In practical comparison, it is interesting that manual counts fall very near along the ROC curve, indicating that QUANTOS is making a very similar trade-off between sensitivity and selectivity to a human observer; however, as its parameters are well-defined, it is highly reproducible, unlike manual counts.

QUANTOS detects synapses based on the *Ideal Synapse* training data which was obtained from the OPL. An important caveat to this is that both rod and cone synapses are contained in the training data. Cones also form ribbon synapses and express RIBEYE and mGluR6, similarly to rod ribbon synapses. Therefore, QUANTOS cannot currently distinguish between rod and cone synapses. Rod photoreceptors account for about 97% of all photoreceptors (Jeon et al., 1998), and therefore the training data of QUANTOS should consist mostly of rod synapses with a small fraction of cone synapses. PDFs of *Ideal Synapse* data did not show any discrete peaks for cone synapses, indicating that either they largely overlap with rod characteristics or the fraction of cone synapses is too low to contribute. We plan to use cone pedicle specific markers to overcome this limitation in future studies.

The noise/synapse classification revealed two separate populations (**Figure 3F**); the mature/immature classifier, on the other hand, did not reveal such discrete groups (**Figure 7**). This indicates that immature and mature synapses exist on a continuum with no clear boundaries, at least regarding their IHC properties. While our definition of mature and immature synapses is completely arbitrary, we were still able to observe a shift from more immature to more mature synapses along retinal development, which would have been impossible to observe with traditional synapse classifiers. Furthermore, the characterization of mature/immature synapse properties by QUANTOS was also consistent with the reported developmental features of the photoreceptor ribbon synapse. An EM study reported that development of the photoreceptor ribbon synapse starts around P4, but the photoreceptors only form dyads with horizontal cells at this stage. Later, around P7–P14, dendrites of bipolar cells invaginate into the dyad and make triads, which makes the photoreceptor ribbon synapse complete. The number of triads starts increasing from P7 to P14, and shows a gradual decrease afterwards (Blanks et al., 1974). Another IHC study showed that the number of mGluR6 puncta rapidly increases in the first two postnatal weeks, and plateaus around P21 (Anastassov et al., 2017). Consistent with these reports, we found that the majority of the synapses were classified as mature by P21.

Furthermore, we used QUANTOS to quantify the photoreceptor ribbon synapses formed under different light conditions in relevance to the physiological function of photoreceptors. There are conflicting reports on the effect of light on photoreceptor synapses. In adult mice, photoreceptor ribbon synapses increase with continuous illumination when observed by EM, but this is thought to be illumination-dependent detachment of ribbons from the active zone, and not an increase of synapse numbers (Spiwoks-Becker et al., 2004). Another study using ERG reported that on P30 and P60 a- and b-wave amplitudes decrease in DD reared mice when compared with LD reared mice (Tian, 2004). Another mERG study reported that dark rearing does not affect rod-driven b-wave amplitude (Dunn

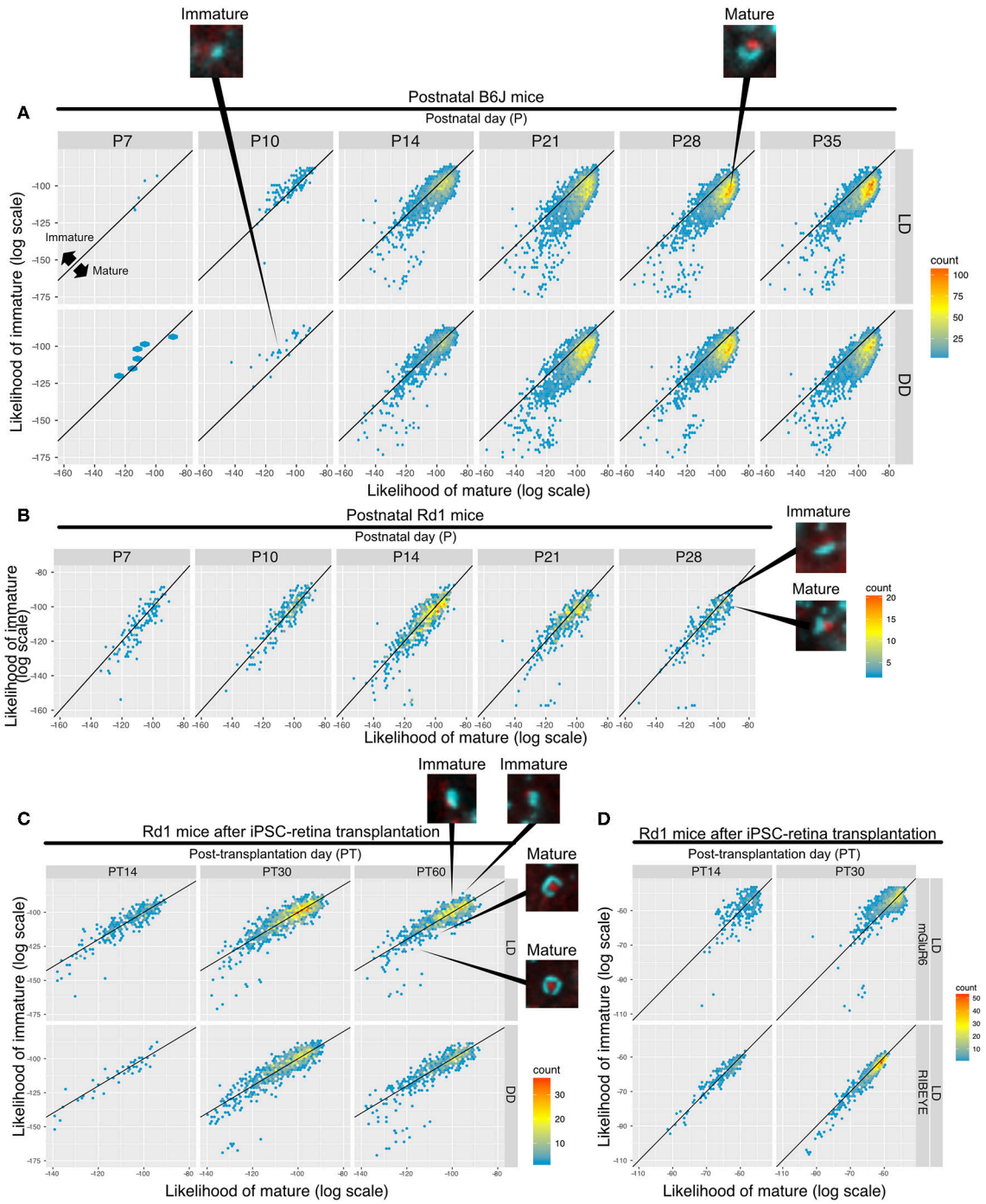

FIGURE 7 | QUANTOS can compare the relative maturation of synapses formed during development, degeneration, and regeneration of the retina. **(A–C)** 2D histograms showing the log likelihood of mature synapse on the x axis, and the log likelihood of immature synapse on the y axis. **(A)** Synapse maturation of B6J mice reared under LD or DD conditions with representative IHC images of synapses from P10 DD and P28 LD. **(B)** Synapse maturation of *rd1* mice with representative IHC images of mature and immature synapses are presented as examples. **(C)** Synapse maturation of *rd1* mice after miPSC-retina transplantation with representative IHC images of mature and immature synapses. **(D)** Synapses of *rd1* mice after miPSC-retina transplantation with pre- and post-synaptic maker log mature/immature likelihoods displayed separately. IHC, immunohistochemistry; LD, cyclic light; DD, constant dark.

et al., 2013). Our analysis of the effect of light throughout the synaptogenesis period suggests that light is accelerating synapse formation itself. Our mERG recordings support the QUANTOS synapse analysis. These findings suggest that the number and/or function of photoreceptor synapses is enhanced by light. This could be in part due to the delayed maturation of the retinal cells,

since it was previously reported that morphological maturation of bipolar cells is delayed by dark rearing (Wu and Chiao, 2007). This highlights the sensitivity of QUANTOS, as raw images do not appear noticeably different at first glance. Despite the fact that there is quite a lot of variance between mice, we were able to identify the differences using QUANTOS.

Lastly, we assessed synapse degeneration in the retinal degeneration model *rd1* and regenerative synaptic formation/maturation of transplanted miPSC-retinal tissues. Previous EM studies indicate that early development of *rd1* is normal up to about P10, but later bipolar cell dendrites fail to invaginate photoreceptors (Blanks et al., 1974). The number of synapses on P28 was dramatically reduced when compared with B6J mice, and the remaining synapses had low likelihood of synapse and low likelihood of being mature as determined by QUANTOS, suggesting incomplete synapse formation, consistent with past EM studies.

Although miPSC-retina formed no substantial synapses *in vitro*, the number of synapses seemed to increase in a time dependent manner after transplantation, suggesting that these synapses are not the remaining *rd1* host synapses, but newly-introduced synapses formed in transplanted cells. This result indicates that synaptogenesis requires intra-ocular factors that are not present in the *in vitro* environment. This was consistent with a recent study reporting that *in vitro* miPSC-retinas can mature up to an equivalent stage of P6 wildtype retina, but do not show apparent synaptogenesis (DiStefano et al., 2018). Here again, the number of synapses formed after transplantation was enhanced by light, suggesting a positive effect of some visual stimuli after transplantation to boost synapse formation.

Finally, a major limitation of the current implementation of QUANTOS is that it is based on thin sliced section samples, with virtually no information on the z-axis. In addition to compromising z-axis information, section preparation inevitably results in some synapses sliced at various angles resulting in an incomplete representation. We are currently expanding QUANTOS to process stacks of 2D confocal images in 3D to analyze whole-mount images. This would also allow a more complete evaluation of complex tissue, such as transplanted retinas.

CONCLUSION

We have established an innovative method, that we have named QUANTOS, to robustly and transparently evaluate the quality and quantity of the photoreceptor ribbon synapse from IHC images. Using this method, we have successfully evaluated developmental synaptogenesis of the wildtype B6J mouse retina, the degenerative process of the *rd1* mouse retina, and regenerative synaptogenesis of the miPSC-retina after transplantation. We showed that miPSC-retina cannot form substantial *de novo* synapses *in vitro* but it is capable of extensive synaptogenesis after transplantation. We also showed that light has a positive effect both on the quantity and quality of synapses formed during developmental and regenerative synaptogenesis of photoreceptors. Although QUANTOS was optimized for the photoreceptor ribbon synapse in this study, this method can be easily adapted to observe synaptogenesis of other neurons.

METHODS

Animals

All animal experiments were conducted in accordance with local guidelines and the ARVO statement on the use of animals in ophthalmic and vision research. All the experimental protocols were approved by the animal care committee of the RIKEN Center for Biosystems Dynamics Research (BDR).

C57BL/6J (B6J) mice were used for developmental analysis, and C57BL/6J-Pde6b^{rd1-2J}/J (*rd1*) mice were used for the retinal degeneration model. Enucleation was carried out immediately after sacrificing the animals.

Animals were reared under different illumination conditions to investigate the effect of light on synaptogenesis. In the LD condition, animals were kept under the standard 12 h light (from 8 a.m. to 8 p.m.) and 12 h dark cyclic light environment. The light source was a fluorescent light bulb with an irradiance, measured vertically upward from the bottom of the rearing cage, of 67.4 μW/cm^2 (233l ux). For the DD condition, B6J mice were kept in constant darkness from before birth. For the retinal transplantation experiments, *rd1* mice were maintained in LD condition and then moved to DD condition immediately after transplantation. For the DD condition, all the animal care was carried out using LED lights with peak wavelength of 690 nm, which had a minimal effect on mouse photoreceptors.

Additionally, animals were reared in constant light (LL) condition for micro electroretinography (mERG) analysis. The irradiance was the same as the LD condition, but the light was always kept on in this condition.

Differentiation and Subretinal Transplantation of iPSC-Retinas

The *Nrl*-GFP miPSC line was generated from transgenic *Nrl*-eGFP mice (Akimoto et al., 2006; Homma et al., 2013). The Ctbp2:tdTomato fusion protein was expressed under Nrl promoter by introducing the gene on the ROSA 26 locus of these lines as previously described and characterized (Mandai et al., 2017). Maintenance, differentiation and optic vesicle structure preparation for transplantation was as previously described (Assawachananont et al., 2014). Briefly, optic vesicle structures (dd 12–13) were cut to small pieces (around 0.5 mm × 2 mm), on the day of transplantation, and inserted sub-retinally into the eye of the 9-12-week-old *rd1* mice using a glass micropipette with a tip diameter of ∼ 500 μm. Indomethacin (10 mg/L) was added to the drinking water of all transplanted mice starting on the day of transplantation.

Immunohistochemistry (IHC)

Animals were sacrificed by cervical dislocation and the eyes were enucleated. The eyes were perforated using a 22G needle, and fixed with 4% paraformaldehyde (PFA) for an hour and then hemisected followed by cryo-protection with 30% sucrose in phosphate buffered saline (PBS) over night at 4°C. The fixed eyes were embedded in OCT compound (4583, Sakura Finetek Japan, Tokyo) and stored at −30°C. Cryo-sections of

12-μm thickness were made with a Cryostat CM3050S (Leica). Heat induced antigen retrieval was carried out at 100°C for 20 min using citrate buffer (10 mM sodium citrate, pH 6.0). The antigen retrieval process removes fluorescence of all fluorescent proteins. Samples were then blocked with Blocking One (nacalai tesque) with 3% Triton X-100 at room temperature for 1 h. Samples were next incubated with primary antibodies in 3% Triton X-100/Dako REAL Antibody Diluent (S2022, Dako, Denmark) over 3 nights at 4°C, followed by washing with PBS 5 times. For the primary antibody of the pre-synaptic marker, we used mouse anti-CtBP2 (612044, BD biosciences, Franklin Lakes, NJ, USA). For the primary antibody of the post-synaptic marker, rabbit anti-mGluR6 antibody (AGC-026, Alomone labs, Jerusalem, Israel) was used. Altogether, expressions of RIBEYE and mGluR6 in proximal area were highly indicative of a functional photoreceptor-ON bipolar cell ribbon synapse.

Samples were incubated with secondary antibodies in 3% Triton X-100/Dako REAL Antibody Diluent (S2022, Dako, Denmark) overnight at 4°C, washed with PBS 5 times, and then mounted with FluorSave Reagent (Millipore). Goat anti-mouse IgG Alexa Fluor 546 (Thermo Fisher, Waltham, MA, USA) and goat anti-rabbit IgG Alexa Fluor 647 (Thermo Fisher, Waltham, MA, USA) were used for pre- and post-synaptic marker visualization, respectively. Images were acquired on an inverted confocal microscope Leica-TCS SP8, with oil-immersion 63x objective magnification lens. Resolution of the image was 1024 pixels by 1024 pixels, and 5 sequential z-stacks with 0.3-μm intervals. The z-stack image was acquired by averaging 4 images on each z-plane with frame sequential method. For postnatal samples of B6J and *rd1* mice, the slices containing optic disc were used, and the area 500 μm away from the optic disc was imaged. We fixed the imaging area because retinal development proceeds from the central area to the periphery, and the timing of synaptogenesis might differ depending on the location. For post-transplantation samples of *rd1*, two randomly selected areas from slices containing transplanted graft were imaged.

For IHC of host-graft synapse evaluation, mouse anti-CACNA1s antibody (MAB427, Millipore, CA, USA) was used as the first antibody of the post-synaptic marker. Antigen retrieval was omitted in these samples in order to image GFP and tdTomato from the host bipolar cells and graft synaptic terminal CtBP2, respectively.

Image Processing

Fiji (version 2.0.0-rc-65), an open source distribution of ImageJ (version 1.51s, NIH, USA) was used for image processing. IHC images were imported to Fiji, and 5 consecutive z-stack images from the upper edge of the sample were z-projected by averaging, to improve image quality and reduce noise. Protocols for DAPI, pre-synaptic and post-synaptic staining were optimized respectively as described below. More details including parameters of each functions are described in depth in **Figures S1–S3**.

[DAPI] (Figure S1)

For processing of the DAPI channel, the "Subtract background" function was used to reduce the background signal, and a bandpass filter was applied for reducing small particle noises. To select the area with signal, "Robust Automatic Threshold Selection" was applied followed by the "Dilate" function to slightly enlarge the selection. Next, "Adjustable watershed" was applied to the image to separate nuclei that have been merged together. Then, "Analyze particle" function was used to select the threshold area and generate regions of interest (ROIs), which were later used on the original image to extract graphical information from the unaltered image.

[Pre-synaptic Marker] (Figure S2)

First, the "Subtract background" function was used to reduce the background signal, then a bandpass filter was applied to the images for reducing small particle noises. The image was then smoothed by applying the "Smoothing" function, to make the signal within each region more homogeneous. Next, images were roughly segmented using the "Find Maxima" function with the "Segmented Particle" option. This separates the entire image into smaller segments based on local maxima, allowing us to extract all the regions regardless of signal intensity. Then, we performed a second "Find Maxima" function on each of the segments, but this time we used the "Maxima Within Tolerance" option for thresholding. The threshold area was then selected by the "Analyze Particle" function for later use as ROI. This sequential approach allowed us to have an adaptive threshold value based on the background intensity around each ROI.

[Post-synaptic Marker] (Figure S3)

A bandpass filter was applied to the images for reducing small particle noises. The post-synaptic marker mGluR6 has a punctate expression pattern in the ribbon synapse, and therefore we used the "Maximum filter" function to enhance the punctate signal. Then, images were processed the same way they were for the pre-synaptic marker. Briefly, images were segmented by the "Find Maxima" function with the "Segmented Particle" option, and adaptively thresholded in each segment, and ROIs were generated by the "Analyze Particle" function.

All generated ROIs were overlaid on the original z-projected image of each channel to extract 34 graphical parameters from each ROI of the unaltered image. Acquired ROI parameters were exported as a csv file for later use in the Naïve Bayes classifier.

All the processes described above were built into an ImageJ macro, so that images can be processed automatically, and multiple images can be processed in batch.

Training Data of Synapse and Noise

The adult retina is organized into distinct layers, with photoreceptor/bipolar synapses located in the outer plexiform layer (OPL), an area that is clearly delineated by photoreceptor cell and bipolar cell nuclei. We prepared images from postnatal day (P) 28 B6J mouse retina containing only the OPL or excluding the OPL as training data for *Ideal Synapse* and *Ideal Noise*. Three to four replicate sections from three different mice were immune-stained and used as training data. The OPL area was manually cropped assuming that signals from this area originate mostly from synapses. The complement of OPL was used as noise teacher data, on the assumption that there are

almost no photoreceptor/bipolar synapses outside the OPL. Note that although we call it noise, we do not necessarily mean or assume that these are non-specific staining or artifacts. In fact, both pre- and post-synaptic markers are known to be present outside the OPL. For example, RIBEYE is present in the inner plexiform layer (IPL) on the axonal terminal of bipolar cells as well as in the OPL (tom Dieck and Brandstätter, 2006); however, as its morphology and molecular component differs from that of the photoreceptor ribbon synapse (Heidelberger et al., 2005), its staining pattern also differs. Thus, although both IPL and OPL synapses are visualized by RIBEYE immunostaining, a careful examination of their signal can distinguish them. Furthermore, the ribbon synapse of IPL and OPL can be distinguished by its post-synaptic marker, because the retinal ganglion cell does not express mGluR6 in IPL. We therefore called staining patterns that resemble the adult photoreceptor ribbon synapse *Ideal Synapse*, and any other signals *Ideal Noise*, regardless of whether those noise signals represent a physiological or functional signal or not.

Ideal Synapse and *Ideal Noise* data were segmented and thresholded, and graphical information of ROIs was extracted as described in **Figure 1** and **Figures S1–S3**. We categorized the extracted parameters into three categories: *Signal*, *Morphology*, and *Geometry*. *Signal* parameters include a series of measurements that represent the characteristics of staining signal including: *mean*, *median*, *mode*, *minimum*, *maximum*, *standard deviation*, *skewness*, and *kurtosis*. In addition to the raw value of these parameters, all the *Signal* parameters, except for *skewness* and *kurtosis*, were divided by a global background intensity to compensate for variance of IHC background intensity. The global background intensity was calculated from the pixel intensity of the entire image. The background was summarized as the peak value of the signal intensity distribution estimated using Kernel Density Estimation (KDE). Signals below the intensity of 8 were ignored in the peak estimation assuming they represent areas where there was no tissue. *Morphology* parameters include *perimeter*, *width*, *height*, *shape*, *major*, *minor*, *angle*, *AR*, *round*, *circularity*, *solidity*, *ferret*, *minferet*, *angle*, and *feret angle*. Perimeter represents the length of outer edge of the ROI. *Width* and *height* represent horizontal and vertical length of bounding box that can fit ROI. *Shape* parameter is our original parameter which is represented by $shape = \sqrt{\{XM - \left(BX - \frac{width}{2}\right)\}^2} + \sqrt{\{YM - \left(BY - \frac{height}{2}\right)\}^2}$ where XM and YM represents coordinates of brightness-weighted center of mass, and BX and BY represents coordinates of upper-left corner of rectangle. *Major* and *Minor* are the longer and shorter axis when the ROI was fitted with ellipsoid. *Angle* is the angle between the longer axis of the ROI and the horizontal line. *AR* is the aspect ratio of width and height of bounding box. *Feret* angle represents the angle of *ferret*. *minferet* represents the longest and shortest diameter of the ROI. Geometrical parameters include the distance between pre- and post-synaptic markers, the angle of the pair, the area of each synaptic marker, and the raw integrated density which represents area and intensity simultaneously.

Using the training data, we generated the Probability Density Functions (PDFs) of *Ideal Synapse* and *Ideal Noise* for each of the parameters (**Figure S5**). PDFs were estimated for each parameter from their histograms, either by Kernel Density Estimation (KDE), or by Bounded Density Estimation (BDE) for parameters that had a clear boundary.

Naïve Bayes Classifier

The Naïve Bayes classifier is a simple but robust classifier algorithm, which employs the Bayes theorem to estimate the posterior probability using the prior probability and likelihood based on training data.

Naïve Bayes classifier used in QUANTOS can be represented as follows:

$$p(C_i|x_1 \ldots x_n) = \frac{p\,(C_i)\,p\,(x_1 \ldots x_n|C_i)}{p\,(x)}$$
$$(\text{where } i = \textit{synapse or noise})$$

$p(C_i|x_1 \ldots x_n)$ represents posterior probability of being either synapse or noise, given n different parameters (x). $p\,(C_i)$ represents prior probability of synapse or noise, $p\,(x_1 \ldots x_n|C_i)$ represents likelihood of synapse or noise under condition of parameters x, and $p\,(x)$ represents evidence.

[Prior Probability]

Prior probability was estimated from marker density, on the assumption that the presence of more markers decreases the probability of correctly identifying synapses. We generated two sets of points randomly within a square area at different densities to simulate the behavior of non-specific pre- and post-synaptic markers. This simulation shows that the number of randomly generated pairs within a certain distance is proportional to the density of the markers (**Figure S4A**). This can clearly be visualized in **Figure S4A**, where the number of random pairs increases with marker density. The slope of the regression line, which we termed "random factor", is in a quadratic relationship with the maximum distance of pairs (**Figure S4C**). Thus, the number of pairs formed by chance (i.e., random pairs) can be estimated from the marker density and the random factor with the following equation:

$$\textit{random pairs} = (\textit{random factor}) \times (\textit{density of pre}) \times (\textit{density of post})$$

(Figure S4D)

A 5 μm × 5 μm square area around each of the center coordinates markers was used for estimating pre- and post-synaptic marker density.

Having estimated the number of random pairs, the prior synapse probability is estimated as:

$$\textit{prior synapse probability} = 0.5 \qquad (\text{if } \textit{random pairs} < 2)$$
$$\textit{prior synapse probability} = \frac{1}{\textit{random pairs}}$$
$$(\text{if } \textit{random pairs} \geq 2)$$

The prior probability for noise is simply

$$\textit{prior noise probability} = 1 - \textit{prior synapse probability}$$

Thus, the priors for synapse and noise are equal if the number of markers is low, but the synapse prior decreases as the number or markers increases.

[Likelihood]

The likelihood is given by the Probability Density Function (PDF) of the *Ideal Synapse* and the *Ideal Noise* data. Pre- and post-synaptic markers are evaluated separately, and the total likelihood of synapse candidate pair is estimated by multiplying their individual likelihoods. Pre- and post-synaptic markers whose centroid coordinates were within 1.2 μm were assigned as possible synapse candidates. The distance threshold was decided based on the *Ideal Synapse* data set, where synapses were most often observed around 0.51 μm with a standard deviation of 0.17 μm. After selecting the synapse candidates, the Naïve Bayes classifier was used to estimate the likeliness of each synapse candidate being synapse or noise. Evidence is likewise calculated from the joint synapse and noise likelihoods, by the following:

$$(\textit{prior synapse probability} \times \textit{likelihood of synapse}) + (\textit{prior noise probability} \times \textit{likelihood of noise})$$

Analysis of *rd1* Mice After miPSC-Retina Transplantation

Host cells and transplanted cells were distinguished by identifying the remaining retinal ganglion cell layer (GCL) and INL of the host by morphology. The area encompassing the transplanted cells was manually traced to evaluate synapse formation in transplanted cells.

Unlike postnatal development of the B6J mouse, the number of transplanted photoreceptors is not homogenous among samples. Therefore, the numbers of photoreceptors were quantified in transplanted samples to estimate the number of synapses per photoreceptor. Transplanted photoreceptors can be identified by their nuclei shape, characteristic of photoreceptor cells, and by the formation of dome-like structures called rosettes. For quantification of photoreceptors, the area of rosette forming cells was manually selected in each image, then the number of DAPI ROIs contained in that area was analyzed using the protocol for DAPI analysis described above in the "Image Processing" section.

Average Synapse

All detected synapses were individually cropped to a 4.34 by 4.34 μm square, with the center coordinates of the synapse in the center of the square. Ribbon synapses can be formed at various angles (**Figure 2D**) and thus images were rotated to align the center coordinates of pre- and post-synaptic markers, using the angle of the line connecting the pre- and post-synaptic markers. Then all synapses from each postnatal day and each rearing condition were averaged. For analysis of average synapse data, we used "Radial Profile" of ImageJ Fiji, which exports the intensity along the distance from the center coordinates. The center coordinates of averaged images were estimated using the "Find Maxima" function for both pre- and post-synaptic markers.

Micro-Electroretinography (mERG)

The mERG was conducted using the multi-electrode array (MEA) recording system (USB-MEA60-Up-System, MultiChannel Systems, Germany) with the standard 8x8 probe (60MEA200/30iR-Ti-gr) as previously described (Iraha et al., 2018). In order to distinguish the effects of prolonged dark adaptation from dark rearing, mice reared under LD and LL conditions were dark adapted for 24 h prior to the recording, as long dark adaptation (6 to 24 h) can significantly reduce the b-wave amplitude (Li et al., 2016). P14 B6J mice were deeply anesthetized with sevoflurane inhalation, followed immediately by decerebration and harvest of retinas. After removal of the vitreous body, retinas were mounted on electrodes with the ganglion cell side down and constantly supplied with warmed ($35 \pm 0.5^{\circ}$C), carbonated (95% O_2 and 5% CO_2) Ames' medium (A1420, Sigma-Aldrich) perfused at 3–3.5 mL/min. Opsinamide (10 μM; AA92593, Sigma-Aldrich) was added in the perfusion medium to suppress the melanopsin-driven RGC light responses during recording. Retinas were allowed to recover in the MEA chamber for at least 20 min before recording. Field potentials to full-field white light stimuli were recorded at 20 kHz. The 10 ms full-field light stimulus was generated using a white LED source with an irradiance of 10.56 log photons/cm^2/s at the focal plane of the electrodes, which approximated the low mesopic range of mature wildtype mouse vision. All of the above procedures were conducted under dim LED light with a peak wavelength at 690 nm.

mERG traces were processed and analyzed in R (R. C. Team - Austria: R Foundation for Statistical Computing Google, 2017). A band-pass Butterworth filter (1–50 Hz) was applied to traces to remove low frequency fluctuations and high frequency jitter. Local minima within 55 ms from light stimulation were flagged as a-wave, and local maxima within 150 ms from light stimulation were flagged as b-wave. The a-wave amplitude was calculated from the baseline, and the b-wave amplitude was calculated from the a-wave, or from the baseline when the a-wave was not detected. Replicates from three repeated stimulations were averaged.

Statistical Analysis

We used full Bayesian statistical inference with MCMC sampling for statistical modeling. Bayesian inference was implemented in Rstan (Stan Development Team, 2017). We estimated population effects, such as the effect of light, individual differences, as well as experimental variation.

Posterior distribution of parameters of interest, which show the most likely values given the data, are shown with 89% confidence intervals. When the difference between conditions is of interest, we show the difference of posterior distributions expressly, as posterior distributions may be correlated or anticorrelated. When the 89% confidence interval of difference of posterior distributions does not cross over zero, estimated parameters are considered different.

[Developmental B6J Mouse Analysis]

We parameterized developmental synaptogenesis with a modified (Gompertz) growth curve (Zwietering et al., 1990),

which is defined by three parameters describing the onset of synaptogenesis (λ), the maximum rate of synaptogenesis (μ) and the maximum capacity of synapse (A). Acquired data was analyzed with the following multilevel model:

$$y_i \sim Poisson(\Lambda_{mouse})$$
$$\Lambda_{mouse} \sim Gamma(\Lambda_{condition,\ day}\ ,\ \beta)$$
$$\Lambda_{condition,\ day} \sim Gompertz(A_{condition,}\ \mu_{condition},\ \lambda_{condition},\ day)$$

Each observation y_i is a count data, so we assumed a Poisson distribution with a mean Λ_{mouse}, representing the average number of synapses for the sampled mouse. We assumed a Gamma distribution for mice sampled on the same postnatal days, as the average number of synapses should be a positive number. The expected number of synapses is given by the Gompertz growth curve given the rearing condition (DD or LD) and postnatal day.

[mERG Analysis]

B-wave amplitude was analyzed with a multilevel generalized linear model using the Gamma distribution as likelihood, as b-wave amplitude is always a positive value and data was spread with a long tail toward larger values.

$$A_n \sim Gamma\,(\mu_n\ ,\sigma_n) \qquad n = 1, \ldots,\ N$$

where A_n is the b-wave amplitude of the n-th observation, μ is the mean, and σ represents the standard deviation. We parameterized with the mean and standard deviation rather than the shape and rate parameters, in order to place informative priors and to make the interpretation more intuitive. The different rearing conditions and the animals from which samples were obtained were used as predictors with the exponential link function.

$$\mu = \exp(a_0 + a_{condition} + a_{mouse})$$
$$\sigma = \exp(b_0 + b_{condition} + b_{mouse})$$

[Synapse Number After Transplantation]

The number of synapses per photoreceptor cell on post-transplantation samples was compared using the Student-t distribution for robust Bayesian estimation assuming equal variance between conditions. Thus each observation (number of synapses per photoreceptor cells) y_i is distributed as

$$y_i \sim Student\_t(\upsilon,\ \mu_i,\ \sigma)$$

where υ is the normality parameter, μ is the mean, and σ is the standard deviation. The different rearing conditions and the animals from which samples were obtained were used as predictors.

$$\mu_i = a_o + a_{condition} + a_{mouse}$$

[ROC analysis]

Ground Truth for P14 and P28 samples were generated by careful classification by an expert observer. Coordinates of QUANTOS result and *Ground Truth* were considered as "matched" when they were within 1 μm. ROC curve analysis was conducted using the "pROC" package in R (Robin et al., 2011). The ROC curve was drawn in reference to the *Ground Truth* to evaluate the sensitivity and specificity of QUANTOS.

Macros and Scripts

ImageJ Fiji macro and R scripts used in this manuscript are available at: https://github.com/matsutakehoyo/QUANTOS

AUTHOR CONTRIBUTIONS

RA, TM, MT, and MM conceptualized the study. RA and TM developed QUANTOS and conducted the statistical analysis. RA conducted immunohistochemistry. RA, MM performed subretinal transplantation. H-YT conducted electrophysiology. TH maintained and differentiated iPSC retina. JS cared for animals and assisted on transplantation. MT and SY oversaw the study. RA, TM, H-YT, and MM wrote the manuscript with input from all authors.

FUNDING

This study was supported by AMED under grant number 18bm0204002h0006 awarded to MT and 2018 JRPS grant awarded to TM.

ACKNOWLEDGMENTS

We would like to thank Genshiro A. Sunagawa for his valuable comments and discussion on the statistical analysis and development of QUANTOS; Jutaro Nakamura for his advice and insight on ERG recordings; and Suguru Yamasaki for advice on retinal organoid culture and immunostaining.

SUPPLEMENTARY MATERIAL

The Supplementary Material for this article can be found online at: https://www.frontiersin.org/articles/10.3389/fncel.2019.00016/full#supplementary-material

Figure S1 | describe image processing protocols for DAPI, RIBEYE, and mGluR6 channel, respectively. Immunostaining samples were imaged with a confocal microscope and 5 sequential z-stack images were projected on the z axis, and processed as described in the Figure. After generating ROIs, the following graphical parameters were exported using the "Measure" function of ImageJ Fiji: *Area*, *Mean*, *StdDev*, *Mode*, *Min*, *Max*, *X*, *Y*, *XM*, *YM*, *Perim*, *BX*, *BY*, *Width*, *Height*, *Major*, *Minor*, *Angle*, *Circ*, *Feret*, *IntDen*, *Median*, *Skew*, *Kurt*, *RawIntDen*, *FeretX*, *FeretY*, *FeretAngle*, *MinFeret*, *AR*, *Round*, *Solidity*.

Figure S2 | Same as **Figure S1**.

Figure S3 | Same as **Figure S1**.

Figure S4 | Estimation of marker density. **(A)** Relationship between pre-synaptic marker density, post-synaptic marker density and the number of pairs when the maximum distance of pairs is 1 μm. **(B)** Modified Figure of **(A)** with the y axis divided by post-synaptic density. **(C,B)** With different maximum distance of pairs. **(D)** As distance of pairs increase, the chance of random pairs increase. Therefore, we used density of markers as prior probability to lower the prior probability when marker densities are high as described in [Prior probability] of Methods section.

Figure S5 | Probability density functions of parameters. PDFs were generated by *Ideal Synapse* and *Ideal Noise* training data. Likelihoods based on each PDF were used upon estimating the posterior probability of synapse for each synapse candidate. Angle and distance histograms of all the detected synapses are also shown here in the right upper panel. Insets show IHC images of detected synapses at various angles. Left upper panel show PDFs of *Geometry* parameters, middle panel show PDFs of *Morphology* parameters, and lower panel show PDFs of *Signal* parameters. PDF, probability density function.

Figure S6 | Example of QUANTOS maturity evaluation Sample IHC image of B6J P14 **(A)** and P21 **(C)** mouse. On P14, both mature and immature synapses can be found. Scale bar = 10 μm Yellow box area of **(A)** and **(C)** were magnified and QUANTOS results are overlaid in **(B)** and **(D)** respectively. Upper panels show all synapses detected by QUANTOS with yellow dots, including immature and mature synapses. Middle panels show mature synapses detected by QUANTOS with magenta circles. Lower panels show both all synapses and mature synapses detected by QUANTOS. Scale bar = 5 μm.

REFERENCES

Akimoto, M., Cheng, H., Zhu, D., Brzezinski, J. A., Khanna, R., Filippova, E., et al. (2006). Targeting of GFP to newborn rods by Nrl promoter and temporal expression profiling of flow-sorted photoreceptors. *Proc. Natl. Acad. Sci. U.S.A.* 103, 3890–95. doi: 10.1073/pnas.0508214103

Anastassov, I. A., Wang, W., and Dunn, F. A. (2017). Synaptogenesis and synaptic protein localization in the postnatal development of rod bipolar cell dendrites in mouse retina. *J. Comp. Neurol.* 289:27019. doi: 10.1002/cne.24251

Assawachananont, J., Mandai, M., Okamoto, S., Yamada, C., Eiraku, M., Yonemura, S., et al. (2014). Transplantation of embryonic and induced pluripotent stem cell-derived 3D retinal sheets into retinal degenerative mice. *Stem Cell Rep.* 2, 662–74. doi: 10.1016/j.stemcr.2014.03.011

Barnea-Cramer, A. O., Wang, W., Lu, S. J., Singh, M. S., Luo, C., Huo, H., et al. (2016). Function of human pluripotent stem cell-derived photoreceptor progenitors in blind mice. *Sci. Rep.* 6:29784. doi: 10.1038/srep29784

Blanks, J. C., Adinolfi, A. M., and Lolley, R. N. (1974). Photoreceptor degeneration and synaptogenesis in retinal-degenerative (Rd) mice. *J. Comp. Neurol.* 156, 95–106. doi: 10.1002/cne.901560108

DiStefano, T., Chen, H. Y., Panebianco, C., Kaya, K. D., Brooks, M. J., Gieser, L., et al. (2018). Accelerated and improved differentiation of retinal organoids from pluripotent stem cells in rotating-wall vessel bioreactors. *Stem Cell Rep.* 10, 300–313. doi: 10.1016/j.stemcr.2017.11.001

Dominic, M. I., and Eroglu, C. (2010). Quantifying synapses: an immunocytochemistry-based assay to quantify synapse number. *J. Vis. Exp*. 45:2270. doi: 10.3791/2270

Dunn, F. A., Della Santina, L., Parker, E. D., Wong R. O. (2013). Sensory Experience shapes the development of the visual system's first synapse. *Neuron* 80, 1159–66. doi: 10.1016/j.neuron.2013.09.024

Fantuzzo, J. A., Mirabella, V. R., Hamod, A. H., Hart, R. P., Zahn, J. D., and Pang, Z. P. (2017). Intellicount: high-throughput quantification of fluorescent synaptic protein puncta by machine learning. *eNeuro* 4:ENEURO.0219-17.2017. doi: 10.1523/ENEURO.0219-17.2017

Geinisman, Y., Gundersen, H. J., Van Der Zee, E., and West, M. J. (1996). Unbiased stereological estimation of the total number of synapses in a brain region. *J. Neurocytol.* 25, 805–19. doi: 10.1007/BF02284843

Glynn, M. W., and McAllister, A. K. (2006). Immunocytochemistry and quantification of protein colocalization in cultured neurons. *Nat. Protocols* 1, 1287–96. doi: 10.1038/nprot.2006.220

Heidelberger, R., Thoreson, W. B., and Witkovsky, P. (2005). Synaptic transmission at retinal ribbon synapses. *Prog. Retin Eye Res.* 24, 682–720. doi: 10.1016/j.preteyeres.2005.04.002

Homma, K., Okamoto, S., Mandai, M., Gotoh, N., Rajasimha, H. K., Chang, Y. S., et al. (2013). Developing rods transplanted into the degenerating retina of Crx-knockout mice exhibit neural activity similar to native photoreceptors. *Stem Cells* 31, 1149–1159. doi: 10.1002/stem.1372

Iraha, S., Tu, H.-Y., Yamasaki, S., Kagawa, T., Goto, M., Takahashi, R., et al. (2018). Establishment of immunodeficient retinal degeneration model mice and functional maturation of human ESC-derived retinal sheets after transplantation. *Stem Cell Rep.* 10, 1059–1074. doi: 10.1016/j.stemcr.2018.01.032

Jeon, C.-J., Strettoi, E., and Masland, R. H. (1998). The major cell populations of the mouse retina. *J. Neurosci.* 18, 8936–8946. doi: 10.1523/JNEUROSCI.18-21-08936.1998

Jorstad, N. L., Wilken, M. S., Grimes, W. N., Wohl, S. G., VandenBosch, L. S., Yoshimatsu, T., et al. (2017). Stimulation of functional neuronal regeneration from muller glia in adult mice. *Nature* 548, 103–107. doi: 10.1038/nature23283

Li, D., Fang, Q., and Yu, H. (2016). The shift of ERG B-wave induced by hours' dark exposure in rodents. *PLoS ONE* 11:e0161010. doi: 10.1371/journal.pone.0161010

Lin, B., Masland, R. H., and Strettoi, E. (2009). Remodeling of cone photoreceptor cells after rod degeneration in rd mice. *Exp. Eye Res.* 88, 589–599. doi: 10.1016/j.exer.2008.11.022

Mandai, M., Fujii, M., Hashiguchi, T., Sunagawa, G. A., Ito, S., Sun, J., et al. (2017). iPSC-derived retina transplants improve vision in Rd1 end-stage retinal-degeneration mice. *Stem Cell Rep.* 8, 69–83. doi: 10.1016/j.stemcr.2016.12.008

Matthews, G., and Fuchs, P. (2010). The Diverse Roles of Ribbon Synapses in Sensory Neurotransmission. *Nat. Rev. Neurosci.* 11, 812–822. doi: 10.1038/nrn2924

R. C. Team - Austria: R Foundation for Statistical Computing Google (2017). *R: A Language and Environment for Statistical Computing*. Vienna.

Regus-Leidig, H., tom Dieck, S., Specht, D., Meyer, L., and Brandstätter, J. H. (2009). Early steps in the assembly of photoreceptor ribbon synapses in the mouse retina: the involvement of precursor. *Spheres* 512, 814–824. doi: 10.1002/cne.21915

Ribic, A., Liu, X., Crair, M. C., and Biederer, T. (2014). Structural organization and function of mouse photoreceptor ribbon synapses involve the immunoglobulin protein synaptic cell adhesion molecule 1. *J. Comp. Neurol.* 522, 900–920. doi: 10.1002/cne.23452

Robin, X., Turck, N., Hainard, A., Tiberti, N., Lisacek, F., Sanchez, J.-C., et al. (2011). pROC: an open-source package for R and S+ to analyze and compare ROC curves. *BMC Bioinform.* 12:77. doi: 10.1186/1471-2105-12-77

Schmitz, F., Königstorfer, A., and Südhof, T. C. (2000). RIBEYE, a component of synaptic ribbons: a protein's journey through evolution provides insight into synaptic ribbon function. *Neuron* 28, 857–872. doi: 10.1016/S0896-6273(00)00159-8

Silver, M. A., and Stryker, M. P. (2000). A Method for measuring colocalization of presynaptic markers with anatomically labeled axons using double label immunofluorescence and confocal microscopy. *J. Neurosci. Methods* 94, 205–215. doi: 10.1016/S0165-0270(99)00145-4

Singh, M. S., Charbel Issa, P., Butler, R., Martin, C., Lipinski, D. M., Sekaran, S., et al. (2013). Reversal of end-stage retinal degeneration and restoration of visual function by photoreceptor transplantation. *Proc. Natl. Acad. Sci. U.S.A.* 110, 1101–1106. doi: 10.1073/pnas.1119416110

Spiwoks-Becker, I., Glas, M., Lasarzik, I., and Vollrath, L. (2004). Mouse photoreceptor synaptic ribbons lose and regain material in response to illumination changes. *Eur. J. Neurosci.* 19, 1559–1571. doi: 10.1111/j.1460-9568.2004.03198.x

Stan Development Team, (2017). *RStan: The R Interface to Stan. R Package Version* 2.16.2. Available online at: http://mc-stan.org).

Sterling, P., and Matthews, G. (2005). Structure and function of ribbon synapses. *Trends Neurosci.* 28, 20–29. doi: 10.1016/j.tins.2004.11.009

Tian, N. (2004). Visual experience and maturation of retinal synaptic pathways. *Vision Res.* 44, 3307–3316. doi: 10.1016/j.visres.2004.07.041

tom Dieck, S., Altrock, W. D., Kessels, M. M., Qualmann, B., Regus, H., Brauner, D., et al. (2005). Molecular dissection of the photoreceptor ribbon synapse: physical interaction of bassoon and RIBEYE is essential for the assembly of the ribbon complex. *J. Cell Biol.* 168, 825–836. doi: 10.1083/jcb.200408157

tom Dieck, S., and Brandstätter, J. H. (2006). Ribbon synapses of the retina. *Cell Tissue Res.* 326, 339–346. doi: 10.1007/s00441-006-0234-0

Vardi, N., Duvoisin, R., Wu, G., and Sterling, P. (2000). Localization of mGluR6 to dendrites of on bipolar cells in primate retina. *J. Comp. Neurol.* 423, 402–412. doi: 10.1002/1096-9861(20000731)423:33.0.CO;2-E

Wu, M. L., and Chiao, C. C. (2007). Light deprivation delays morphological differentiation of bipolar cells in the rabbit retina. *Brain Res.* 1170, 13–19. doi: 10.1016/j.brainres.2007.06.091

Yao, K., Qiu, S., Wang, Y. V., Park, S. J. H., Mohns, E. J., Mehta, B., et al. (2018). Restoration of vision after de novo genesis of rod photoreceptors in mammalian retinas. *Nature* 560, 484–488. doi: 10.1038/s41586-018-0425-3

Zwietering, M. H., Jongenburger, I., Rombouts, F. M., and van 't Riet, K. (1990). Modeling of the bacterial growth curve. *Appl. Environ. Microbiol.* 56, 1875–1881.

Conflict of Interest Statement: The authors declare that the research was conducted in the absence of any commercial or financial relationships that could be construed as a potential conflict of interest.

frontiers in Cellular Neuroscience

REVIEW
published: 06 June 2019
doi: 10.3389/fncel.2019.00248

Regeneration of Spinal Cord Connectivity Through Stem Cell Transplantation and Biomaterial Scaffolds

Hiroyuki Katoh[1,2†], *Kazuya Yokota*[1,3†] *and Michael G. Fehlings*[1,4,5,6*]

[1] Division of Genetics and Development, Krembil Research Institute, Toronto, ON, Canada, [2] Department of Orthopaedic Surgery – Surgical Sciences, School of Medicine, Tokai University, Tokyo, Japan, [3] Department of Orthopaedic Surgery, Graduate School of Medical Sciences, Kyushu University, Fukuoka, Japan, [4] Institute of Medical Science, University of Toronto, Toronto, ON, Canada, [5] Division of Neurosurgery, University of Toronto, Toronto, ON, Canada, [6] Spine Program, Toronto Western Hospital, University Health Network, Toronto, ON, Canada

OPEN ACCESS

Edited by:
Eran Perlson,
Tel Aviv University, Israel

Reviewed by:
Paul Lu,
University of California, San Diego, United States
Tuan Vu Bui,
University of Ottawa, Canada

***Correspondence:**
Michael G. Fehlings
Michael.Fehlings@uhn.ca

[†]*These authors have contributed equally to this work as co-first authors*

Specialty section:
This article was submitted to Cellular Neuropathology, a section of the journal Frontiers in Cellular Neuroscience

Received: *18 March 2019*
Accepted: *17 May 2019*
Published: *06 June 2019*

Citation:
Katoh H, Yokota K and Fehlings MG (2019) Regeneration of Spinal Cord Connectivity Through Stem Cell Transplantation and Biomaterial Scaffolds. Front. Cell. Neurosci. 13:248. doi: 10.3389/fncel.2019.00248

Significant progress has been made in the treatment of spinal cord injury (SCI). Advances in post-trauma management and intensive rehabilitation have significantly improved the prognosis of SCI and converted what was once an "ailment not to be treated" into a survivable injury, but the cold hard fact is that we still do not have a validated method to improve the paralysis of SCI. The irreversible functional impairment of the injured spinal cord is caused by the disruption of neuronal transduction across the injury lesion, which is brought about by demyelination, axonal degeneration, and loss of synapses. Furthermore, refractory substrates generated in the injured spinal cord inhibit spontaneous recovery. The discovery of the regenerative capability of central nervous system neurons in the proper environment and the verification of neural stem cells in the spinal cord once incited hope that a cure for SCI was on the horizon. That hope was gradually replaced with mounting frustration when neuroprotective drugs, cell transplantation, and strategies to enhance remyelination, axonal regeneration, and neuronal plasticity demonstrated significant improvement in animal models of SCI but did not translate into a cure in human patients. However, recent advances in SCI research have greatly increased our understanding of the fundamental processes underlying SCI and fostered increasing optimism that these multiple treatment strategies are finally coming together to bring about a new era in which we will be able to propose encouraging therapies that will lead to appreciable improvements in SCI patients. In this review, we outline the pathophysiology of SCI that makes the spinal cord refractory to regeneration and discuss the research that has been done with cell replacement and biomaterial implantation strategies, both by itself and as a combined treatment. We will focus on the capacity of these strategies to facilitate the regeneration of neural connectivity necessary to achieve meaningful functional recovery after SCI.

Keywords: traumatic spinal cord injury, central nervous system, regeneration, stem cell transplantation, biomaterials

INTRODUCTION

Spinal cord injury (SCI) is a severely debilitating condition leading to neurological dysfunction, loss of independence, respiratory failure, psychological morbidities, and an increased lifelong mortality rate (Marion et al., 2017; Satkunendrarajah et al., 2018; Shibahashi et al., 2018; Wang et al., 2018b). In the United States, approximately 288,000 individuals are estimated to suffer from symptoms caused by SCI, and a recent survey showed the annual incidence of SCI is approximately 54 cases per one million people (Fehlings et al., 2018). Worldwide, the estimated incidence of SCI ranges from 250,000–500,000 individuals per year (Singh et al., 2014). The main causes of SCI are motor vehicle accidents, falls, and violent acts, but with the aging of the population in many industrialized countries, the SCI patient profile is slowly evolving toward more elderly SCI patients injured through falls (Sekhon and Fehlings, 2001). SCI has a tremendous impact on the personal, professional, and social life of patients, imposing enormous psychological and financial burdens on the patients and their caregivers (Munce et al., 2016; Backx et al., 2018). The overall lifetime economic costs with complete SCI can exceed $3 million per person, and the estimated economic burden associated with SCI in Canada is approximately $2.67 billion annually (Krueger et al., 2013). This recognition of the personal and social costs of SCI has fostered extensive basic research into the pathology of the injured spinal cord and treatment strategies for SCI. Despite decades of research and numerous regenerative approaches that demonstrated promising results in animal models, the global scientific community has yet to provide SCI patients with a viable option to prevent the devastating outcome of traumatic SCI or to reverse the neurological impairment brought about by the condition. While SCI patients may be frustrated by the lack of an apparent "cure," there is a palpable anticipation within the circle of SCI researchers that we will soon begin to observe significant functional improvements from clinical trials in the very near future.

Animal studies up until a decade ago had often demonstrated a significant functional improvement with various interventions, citing significantly lower inflammation, smaller cavity size, higher axonal growth, or increased myelination as possible explanations for the observed recovery, but the true reason for the improvement was often left within a black box (Badhiwala et al., 2018). With the accumulating basic knowledge on the fundamental pathophysiology underlying SCI, along with the improvements in techniques and technology to perform increasingly precise analyses on the changes brought about by treatment strategies, we are finally shedding light into this black box. So while the "cure" may still be out of reach, our enhanced understanding of the obstacles and the hurdles in the path to regenerating connectivity of the neural circuits will hopefully greatly improve the accuracy of our endeavors to improve the function and quality of life of patients with SCI. In this review, we outline the pathophysiology of SCI that makes the spinal cord refractory to regeneration and spontaneous recovery following injury and discuss strategies being explored to reestablish connectivity within the injured spinal cord, focusing on stem cell-based therapy and biomaterial engineering.

PATHOPHYSIOLOGY OF SCI

Traumatic injury to the spinal cord can be caused by compressions, lacerations, and contusions, which lead to a spectrum of neurological symptoms depending on the level and the severity of the injury such as motor/sensory dysfunction, autonomic deficits, neuropathic pain, autonomic dysreflexia, and bowel/bladder dysfunction (Furlan et al., 2016; Moonen et al., 2016; Stroman et al., 2016). The processes occurring within the injured spinal cord can be divided according to the elapsed time from the precipitating injury into acute (<48 h), subacute (48 h to 14 days), intermediate (14 days to 3 months), and chronic phases (>3 months) (Aimone et al., 2004; Shechter et al., 2009; Chamankhah et al., 2013; Moghaddam et al., 2015). In order to understand the pathophysiology, cellular composition, inflammatory reaction, and expression of trophic and other factors within the spinal cord after traumatic SCI, it is also helpful to divide the process into primary and secondary injuries.

The initial traumatic event, which may or may not accompany fractures and/or a dislocation of the vertebral column, results in the primary injury through mechanical compression, contusion, stretching, or kinking of the spinal cord (Sekhon and Fehlings, 2001). Neurons, oligodendrocytes, and other components essential for neuronal transmission are physically insulted (Wilcox et al., 2017), and the disrupted vascular components, including the blood-spinal cord barrier (BSCB), induce infiltration of inflammatory cells (Kunis et al., 2013; Shechter et al., 2013; Li et al., 2017). The initial injury triggers a subsequent secondary injury cascade which leads to further chemical and physical damage to the spinal cord and resultant neurological deficits. Increased glutamate results in neuronal excitotoxicity due to the accumulation of intracellular Ca^{2+}, leading to an increase in reactive oxygen species (ROS) (Ouardouz et al., 2009; Yin et al., 2012; Breckwoldt et al., 2014) that damage cellular components such as nucleic acids, proteins, and phospholipids, and cause cellular loss and subsequent neurological dysfunction (Khayrullina et al., 2015; von Leden et al., 2017; **Figure 1A**).

Secondary injury refers to the multifaceted pathological process that begins after primary injury and can last for several weeks, in which increased permeabilization of cells, pro-apoptotic signaling, ischemia, and breakdown of the BSCB further exacerbates insult to the injured spinal cord (Casha et al., 2005; Yu et al., 2009; Yu and Fehlings, 2011; Robins-Steele et al., 2012; Wu et al., 2014). Disrupted blood vessels cause severe hemorrhage (Saiwai et al., 2010; Yokota et al., 2016) and allow infiltration of inflammatory cells including neutrophils, monocytes/macrophages, T cells, and B cells into the spinal cord tissue (Ankeny et al., 2009; Beck et al., 2010; Saiwai et al., 2013; Raposo et al., 2014) that release inflammatory cytokines such as tumor necrosis factor (TNF)-α, interleukin (IL)-1α, IL-1β, and IL-6 (Kumamaru et al., 2012; Nguyen et al., 2012). These cytokines, often reaching their peak 6–12 h after injury, further

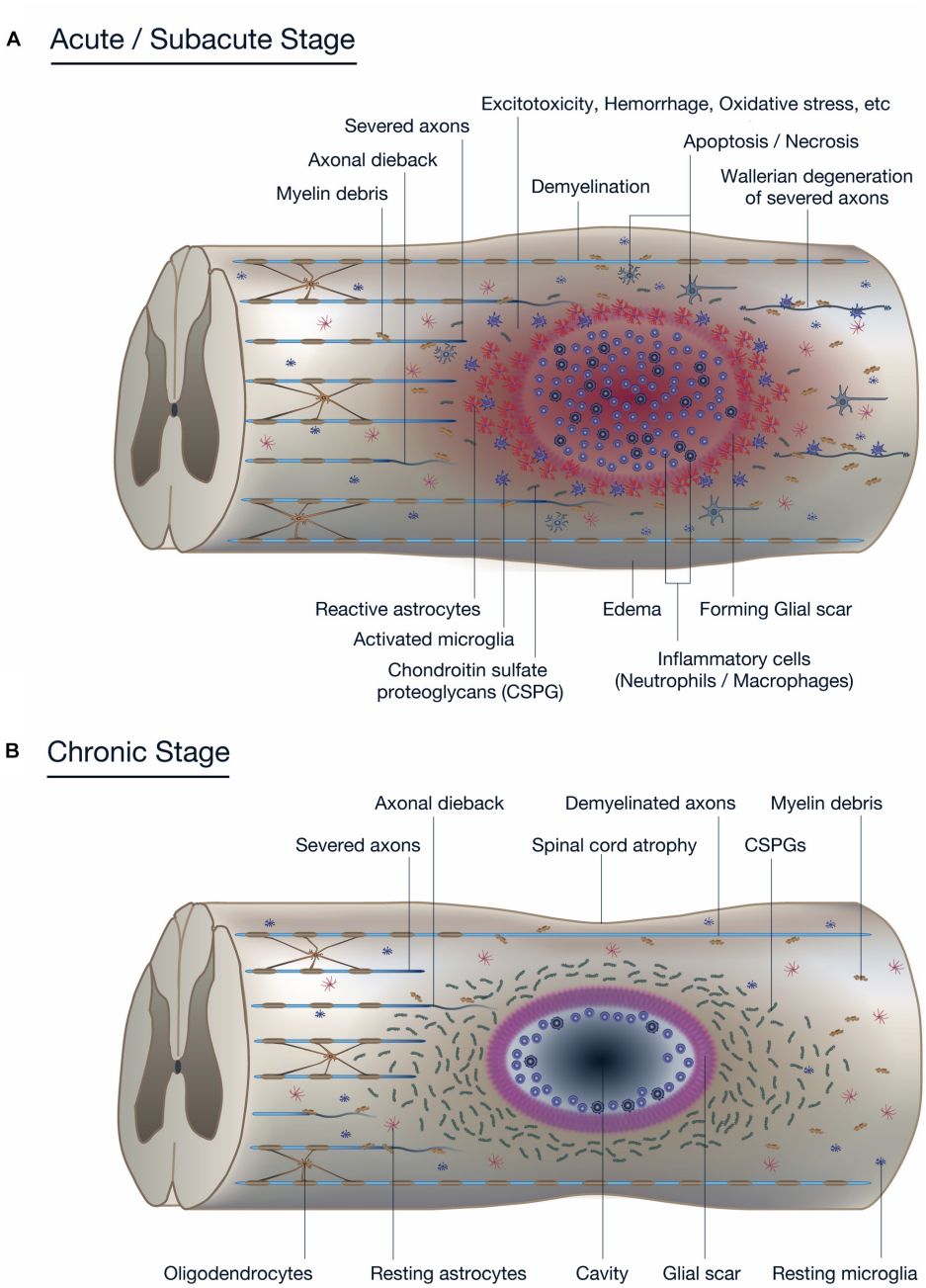

FIGURE 1 | Pathophysiology of spinal cord injury (SCI). **(A)** The diagram shows the pathophysiological events occurring around the lesion site during the acute to subacute phase of SCI. The primary and secondary injury mechanisms lead to inflammation, hemorrhage, apoptosis, and necrosis. Resident neurons, oligodendrocytes, and astrocytes near the lesion are forced into apoptosis or necrosis, resulting in anterograde (Wallerian degeneration) and retrograde (axonal dieback) axonal degeneration. Reactive astrocytes and other glial cells secrete chondroitin sulfate proteoglycans (CSPGs), which acts as a physical and chemical barrier that impedes endogenous tissue repair processes such as axonal sprouting and synaptic reorganization. **(B)** The diagram shows the pathophysiological events in the chronic phase of SCI. In the epicenter of the lesion, a cavitation has occurred that is surrounded by connective scar tissues and contains cerebrospinal fluid (CSF). The phenotype of reactive astrocytes has changed into scar-forming astrocytes that impede regenerating axons from crossing the lesion. Some inflammatory immune cells remain around the lesion even in the chronic phase of SCI.

induce an overwhelming inflammatory response during the acute to subacute phase that expands the lesion in a rostral and caudal direction (Min et al., 2012). Activated microglia and infiltrated macrophages have been shown to be responsible for the necrosis and apoptosis of neurons, astrocytes, and oligodendrocytes residing in the vicinity of the lesion (Chu et al., 2007), further deteriorating the neurological outcome (**Figure 1B**; Horn et al., 2008; Floriddia et al., 2012). Early measures to decrease inflammation and prevent apoptosis have long been a target intervention for SCI, but the increasing knowledge of the beneficial aspects of the inflammation process following SCI has made it necessary to carefully monitor the effects of inflammation-modulating strategies (Rust and Kaiser, 2017).

CELL DEATH IN THE INJURED SPINAL CORD

At the lesion site of the injured spinal cord, the death of the constituent cells that make up the neural circuitry, along with the loss of cells tasked with its maintenance, is a fundamental cause of functional impairment. Traditionally, the mechanism of cell death after SCI was characterized as an initial wave of necrosis at the lesion epicenter followed by a delayed phase of cell death in neighboring tissue through necrotic and apoptotic mechanisms (Baptiste and Fehlings, 2006). Necrosis is a passive non-programmed cell death triggered by SCI trauma that causes lethal disruption of cell structure and activity. It involves failure of membrane integrity, mitochondrial damage, rapid loss of ATP, sudden loss of ionic homeostasis, and induction of ROS that leads to organelle as well as cell swelling and terminates with the disposal of cell corpses in the absence of obvious phagocytic and lysosomal involvement. Apoptosis, on the other hand, is an active programmed cell death sequence in which neurochemical changes occur in an orderly fashion and is often dependent on caspase activation. It is characterized by the activation of cell signals directly involved in mitochondrial function, and leads to cytoplasmic shrinkage, chromatin condensation, and nuclear fragmentation, culminating with the formation of apoptotic bodies that are phagocytosed by neighboring cells and degraded within lysosomes (Galluzzi et al., 2018). A key player in apoptosis is caspase-3, a member of the caspase family of cysteine proteases that regulate programmed cell death, which cleaves essential downstream substrates involved in apoptosis. The initiation of the apoptotic pathway following SCI can be mediated by death receptors FAS (CD95) and p75, which activate caspases and initiate the apoptotic pathway in oligodendrocytes, astrocytes, and microglia (Casha et al., 2001, 2005). The caspase-3 apoptotic pathway triggers apoptosis in neurons in the early phase of injury and in oligodendrocytes adjacent to and distant from the lesion hours to days later. Combined with the limited proliferative potential of OPCs, the susceptibility of oligodendrocytes to apoptosis even when they are distant from the lesion leads to a wide area of demyelination, which greatly impairs the function of preserved axons.

The scientific field regarding cell death is evolving, with novel mechanisms that orchestrate multiple cell-death pathways continually being unveiled. The differentiation of the various processes can be difficult, and the Nomenclature Committee on Cell Death has recently published an updated classification of cell death subroutines focusing on mechanistic and essential aspects of the processes (Galluzzi et al., 2018). Multiple processes of cell death have also been reported in SCI, and the traditional understanding of cell death in the injured spinal cord as either necrosis or apoptosis is no longer accurate. One of the additional major players implicated in mediating cell death in SCI is autophagy, which under normal conditions plays an important role in the maintenance of homeostasis by recycling toxic agents, unnecessary proteins, and damaged organelles through an autophagosomal and lysosomal process. When this processing of components through the autophagy system, or autophagy flux, is blocked or overrun by components awaiting processing, the accumulation of dysfunctional autophagosomes damages cells and triggers death (Lipinski et al., 2015). The autophagy pathway is closely linked to endoplasmic reticulum stress, which also plays a role in maintaining cellular homeostasis and triggers apoptosis if endoplasmic reticulum stress exceeds the capacity of its processing mechanism (Kuroiwa et al., 2014). There are still other pathways of cell death that lay outside of the traditionally acknowledged cell death processes in SCI: a type of programmed cell death termed necroptis (Liu et al., 2015), a regulated cell death called parthanatos that is driven by the hyperactivation of the DNA damage response machinery (Kuzhandaivel et al., 2010), and numerous caspase-independent cell death pathways often involving the apoptosis inducing factor (AIF) (Wu et al., 2007).

Many of the pathways involved in cell death after SCI have been studied as possible targets of therapeutic intervention, but the results have been mixed. The inhibition of caspase-3 was examined exhaustively considering its significance in the apoptotic pathway, with some studies showing improvement (Kaptanoglu et al., 2005), while some studies reported no apparent improvement (Ozawa et al., 2002). In fact, the processes that induce cell death seem to be interconnected and complementary, with the minor pathway becoming dominant when the primary pathway is inhibited (Proskuryakov et al., 2003). Therefore, although the cell-death pathway remains an attractive target to reduce loss of neural cells in SCI, it may be more productive to intervene in the processes that trigger cell death rather than the cell death pathway itself.

WALLERIAN DEGENERATION AND AXONAL DIEBACK

After SCI, axons and dendrites that lose connection to their original neural pathways degenerate from the site of injury in a direction away from the injury epicenter: (Bareyre et al., 2005; Kerschensteiner et al., 2005) the anterograde degenerative process is called Wallerian degeneration, while the retrograde degeneration of axons is referred to as axonal dieback. The spinal cord mass decreases both rostral and caudal to the lesion following SCI, suggesting that the anterograde and retrograde degeneration of neural fibers may be a major factor in the reduction of tissue mass in the

injured spinal cord (Seif et al., 2007; Yokota et al., 2019). Long-distance retraction of injured axons coincides with the infiltration of monocytes/macrophages, whose phenotypes transition from anti-inflammatory to pro-inflammatory in response to myelin debris (Wang et al., 2015). Direct contact of monocytes/macrophages with the dystrophic endings of insulted axons is considered to be essential to this process (Busch et al., 2009), since the depletion of infiltrating macrophages reduces axonal dieback after SCI (Evans et al., 2014).

DEFINITION OF REGENERATION IN THE INJURED SPINAL CORD

The term "regeneration" has been used for decades in the field of central nervous system research (Worcester, 1898), but it may be helpful to review what regeneration entails in the recovery process from SCI. The aim in SCI research has been to repair the disrupted neural network to as close to its former status as possible by supporting and enhancing the endogenous potential of sprouting axons and remyelination, which would hopefully lead to the reconnection of descending neural fibers with their original targets such as spinal interneurons and motor neurons in the caudal spinal cord. In cases of severe and complete SCI, in which there is an absence of neuronal substrates for axonal sprouting and spared axons for re-myelination, stem cell transplantation strategies have been employed to replace the cells that have been lost and restore the neural circuitry. Multiple therapeutic approaches focusing on axonal growth, remyelination, cell replacement, and synaptic reorganization have led to functional improvement in SCI animal models, but the majority of studies have not convincingly verified reestablishment of neural circuits. Without confirmation of the changes brought about to the neural pathways governing motor and sensory function, histological regenerative changes to the spinal cord that lead to decreased cavity size, superior axonal growth, or improved myelination, for example, may be peripheral improvements that contribute to functional improvement but may not directly be responsible for it. This black box laying between the histological changes and functional improvement has been the conundrum in the field of SCI research. With technological limits and technical difficulties in convincingly demonstrating changes in neural circuitry, most studies have not attempted its examination and the peer-review process has not required this analysis. However, this may be part of the reason that many treatment strategies demonstrating significant recovery in rodents have failed to reproduce the benefits in human clinical trials. Furthermore, the inherent differences between rodents and humans in regards to spontaneous recovery and anatomical differences concerning the neural pathways increase the complexity of translating the promising effects observed in animal models to the treatment of human SCI patients (Geisler et al., 1991; Casha et al., 2012; Inada et al., 2014).

The recent advances in neuronal tracers have bestowed researchers with the means to investigate the reorganization of neural networks after SCI and to better appreciate the underlying mechanisms that govern the regeneration of injured spinal cords (Kerschensteiner et al., 2005). To reestablish connectivity of neural circuits, neurons need to be reorganized into existing or newly formed neural pathways and oligodendrocytes must myelinate the axons to facilitate electrical transmission (Nashmi and Fehlings, 2001). The pyramidal tract from the brain cortex projecting to the secondary motor neurons in the spinal cord is the main conduct for motor signals, but the propriospinal circuits in the spinal cord have been shown to be crucial for recovery from SCI (Satkunendrarajah et al., 2018), especially in cases of severe and chronic SCI. Considering that treatment strategies for SCI are shifting toward more combinatorial approaches, it is even more important that not only histological changes, but also regeneration of neural connectivity, be examined to explain any improvement of function.

COMPONENTS OF SPINAL CORD CONNECTIVITY

The basic unit that allows for the signals governing motion to travel from the brain to the muscles is comprised of a supraspinal neuron that extends a long axon to form a synapse with a motor neuron, whose axon connects to muscle fibers at neuromuscular junctions. The axons are surrounded by myelin sheaths, which allow for the rapid conduction of the electrical signal though the axons (**Figure 2**; Bellardita and Kiehn, 2015). In the mammalian motor system, the upper motor neurons are located in the brain motor cortex and brainstem while the lower motor neurons are found in the brain stem (cranial motor neurons) and the spinal cord (Le Ray et al., 2011; Roseberry et al., 2016). The actual process of voluntary limb movement and posture control is complex, involving a coordinated synchronous activation of multiple units that are modulated by sensory feedback loops from muscles, tendons, and skin (Bikoff et al., 2016). Furthermore, it is becoming increasingly apparent that propriospinal interneurons that act as bridges between supraspinal neurons and motor neurons play an important role in the plastic reorganization of spinal circuits, contributing an important substrate for recovery from SCI (Courtine et al., 2008). The complicated neuronal networks and the reorganization that takes place in the recovery process from SCI has been partially determined (Shah et al., 2013; Filli et al., 2014), but there is still much that is unknown regarding the interactions between neurons and the surrounding environment that regulate plasticity.

Another important component in neuronal connectivity is the establishment and maintenance of synaptic connections (Williams et al., 2010; Sudhof, 2018). Synapse assembly is a multiple-step process in which immature axons grow and form a physical contact with their target neurons (Kohl et al., 2015). The immature synaptic contacts, both presynaptic and postsynaptic components, undergo a process of stabilization in order to generate and maintain expression levels of neurotransmitters and their receptors to become functional (Kneussel et al., 1999; Easley-Neal et al., 2013). With the growing knowledge that synapses are dynamic structures that are formed and pruned according to multiple factors (Wu et al., 2012; Jacobi et al., 2015; Filipello et al., 2018; Lehrman et al., 2018), they are gaining

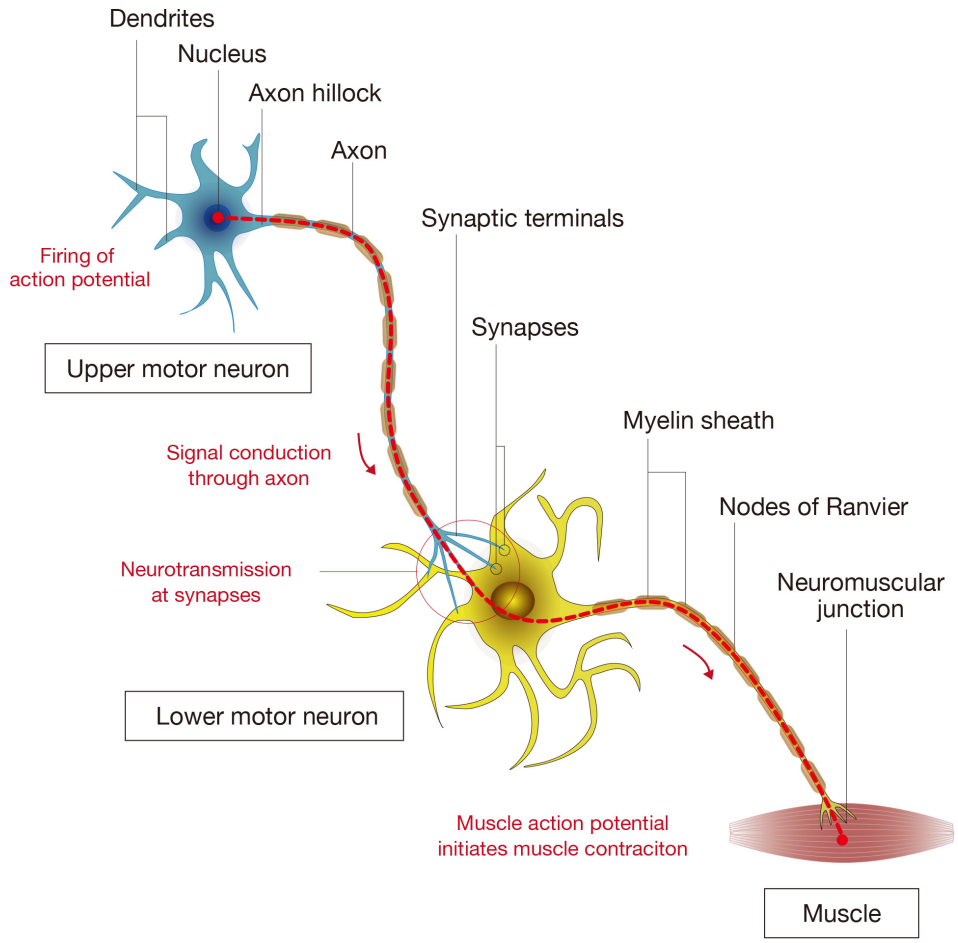

FIGURE 2 | Components of spinal cord connectivity. The diagram shows the simplified components of spinal connectivity composed of an upper motor neuron, a lower motor neuron, and targeted muscle fibers. Neurons have cell bodies, dendrites that receive signals, and axons that transmit signals. At the base of the axon is the axon hillock where the signal transmission is initiated, and the axon divides at its end into several branches, each of which ends in synaptic terminals. The site of interactive communication between a transmitting cell (a presynaptic upper motor neuron) and a receiving one (a postsynaptic lower motor neuron) is called the synapse. The axons of most neurons are covered with a lipid layer knows as the myelin sheath, which insulates axons and speeds up transmission of action potentials through the axon. The axon terminals at a synapse contain tiny vesicles filled with chemicals called neurotransmitters. The lower motor neurons take the impulse to the effector (muscle fibers) and control the coordination of muscle contraction.

attention as a subject for intervention. The myelin sheaths formed by oligodendrocytes are another essential component of the neural network and function to enhance transmission of electrical impulses and secrete neurotrophic supports to maintain axonal integrity (Powers et al., 2013; Ishii et al., 2014; Saab and Nave, 2017). Therefore, in order to acquire the neural connectivity necessary for integrated motor and sensory function, upper motor neurons need to be connected to lower motor neurons, possibly mediated by interneurons, through functional synapses and proper myelination.

CONFIRMING CHANGES IN SPINAL CORD CONNECTIVITY

The means to evaluate the neural networks of the spinal cord have been available for decades in the form of neural tracers, and it remains the only method to map the fine neural circuits and confirm connectivity. Biotinylated dextran amine (BDA), cholera toxin beta subunit, fluorogold, fast blue, fluorescent microspheres, horseradish peroxidase (HRP), wheat germ agglutinin (WGA), and phaseolus vulgaris-leucoagglutinin (PHA-L) are examples of chemical neural tracers that provide a distinct labeling of neuronal morphology including the neuronal body, dendrites, and axonal terminals (Kuang and Kalil, 1990; Hou et al., 2008; Steencken et al., 2009; Tillakaratne et al., 2010; Sharp et al., 2014; Mondello et al., 2016). With the aid of a stereotaxic apparatus to guide the exact site of the injection, the tracer is injected into selected areas of the brain for anterograde transport and into peripheral organs or spinal segments for retrograde transport, and analyzed in histological sections after a specific period (Chen et al., 2009; Mondello et al., 2016). These tracing methods allow us to visualize the morphology and axonal tract of a specific group of neurons and examine different neurons

depending on the amount, sensitivity, and diffusion extent of the tracer. Neurotropic viruses such as herpes simplex virus, lentivirus, and pseudorabies virus were developed to investigate the structural organization of multisynaptic pathways among several neurons (Wickersham et al., 2007; Lo and Anderson, 2011; McGovern et al., 2012; Sheikh et al., 2018). The advantage of this tracing technique is based on the ability of the viruses to transsynaptically enter into connected neuronal cells and self-replicate, providing a means to map multisynaptic neural circuits without signal loss. The disadvantage of viral tracing is the toxicity of the virus to the host neurons, thus limiting studies to approximately 2 weeks. While neural tracers have been available for some time, the technique has been utilized in only a small fraction of researchers examining SCI due to the difficulty in analyzing and interpreting the results. With the growth in knowledge concerning spinal cord neural pathways along with the recent advances in virus engineering to modulate its toxicity, computer technology to create three-dimensional reconstructive images, and software improvements to better trace neuronal tracts, researchers will hopefully be better equipped to analyze the changes that their treatment strategies bring about to spinal cord connectivity. Another recent technique that has been gaining interest is CLARITY (Chung et al., 2013; Tomer et al., 2014), which is a method to chemically transform biological tissue into a transparent hydrogel-tissue hybrid (Yang et al., 2014; Treweek et al., 2015), allowing researchers to perform high-resolution mapping of neuronal networks in combination with viral tracing (Lerner et al., 2015). Neural tracing is a field that is rapidly evolving, and we anticipate that the improved techniques and advances in technology will reveal how our interventions induce plastic reorganizations of neural pathways in SCI, and how the pathways are associated with functional improvements.

While tracing is a well-established method to histologically confirm neural connectivity, electromyograms (EMGs) have been established as a means to non-invasively investigate the functional connectivity of the spinal cord and monitor any longitudinal changes in the same group of animals (Moonen et al., 2016). Motor evoked potentials (MEPs) and somato-sensory evoked potentials (SEPs), which are analyzed in terms of amplitude and latency of the first positive and first negative peaks, provide objective data on spinal cord conductivity with quantitative values and have been shown to predict functional outcomes such as ambulatory capacity and upper limb dexterity. However, it should be noted that reliable MEP and SEP monitoring cannot be obtained in the acute phase of SCI (Feng et al., 2012; Lewis et al., 2017; Dhall et al., 2018). In an evoked EMG, the elicited response includes the H-wave, the M-wave, and the F-wave. The M-wave is the result of direct activation of the motor axons and does not involve the spinal circuits. The later H-wave, or H-reflex, is a compound EMG response in the muscle elicited by synaptic activation of motor neurons through muscle afferents and is regarded as a surrogate for spasticity after SCI. The F-wave is the second voltage change observed after the M-wave, and is the muscle response to the backfire of motor neurons that were stimulated by the antidromic (proximally transmitted) impulses. F waves are often used to measure nerve conduction velocity, and any changes recorded in conduction velocity can reflect the remyelination of neural tracts (Moonen et al., 2016). Longitudinal MEPs, but not SEPs, have been shown to correlate with neurological impairment after SCI (Huang et al., 2018), but their changes may not necessarily be linked with actual phenotypical functional recovery. EMG signals may be useful to verify synaptic connectivity by examining the conduction of electrical impulses through the lesion, but currently cannot be used to examine the regeneration of specific pathways in spinal cord circuits.

Magnetic resonance imaging (MRI) is clinically performed for most SCI patients to diagnose the injury to the cord and vertebral components, plan treatment, and predict prognosis for recovery (Miyanji et al., 2007). With the capability to conduct non-invasive longitudinal studies of an individual subject, MRI is an attractive option to evaluate spinal connectivity (Fehlings et al., 2017). However, since conventional MRI depicts the white matter as uniform tissue and does not have the sensitivity or resolution to depict the complex array of directionally oriented nerve fibers in the spinal cord (Stroman et al., 2012), it becomes necessary to enhance the signals from neural tracts. One such method with a long history is manganese-enhanced MRI, which utilizes manganese ions that are paramagnetic, thus shortening the spin lattice relaxation time constant (T1) of tissue (Martin et al., 2017). Manganese ions are calcium analogs that can enter neurons through voltage-gated calcium channels, be transported along axons by microtubule-dependent axonal transport, and cross synapses to neighboring neurons (Bedenk et al., 2018). Neuronal uptake of manganese ions is activity-dependent, and a study that injected manganese into the cerebrospinal fluid demonstrated that manganese-enhancement was reduced after SCI and that the uptake of manganese ions correlated with functional recovery. Direct injection of manganese ions into the lumbar spinal cord demonstrated enhancement of a wide rostral-caudal area of the thoracic gray matter, demonstrating its possible use to visualize the connectivity of the spinal cord (Stieltjes et al., 2006).

Another more recent innovative use of MRI to visualize neural tracts is diffusion tensor imaging (DTI), which takes advantage of the anisotropic nature of water diffusion in biological tissue to follow the orientation of nerve fibers and trace specific neural pathways, such as the corticospinal tract (CST) (Cheran et al., 2011). DTI has been able to visualize both the intact and injured neural networks of the spinal cord, and the quantitative data from the DTI images was associated with histological findings (Fujiyoshi et al., 2007). When considering the capability of DTI to delineate neural tracts, several limitations of the method need to be understood. The current voxel resolution of 1 to 3 mm in each dimension means that each voxel represents the total anisotropic character of millions of cells, so the images need to be interpreted with the knowledge of this limited resolution (Wheeler-Kingshott et al., 2002). Another factor that affects the results are the effect of free water diffusivity from the cerebral spinal fluid and edema, which contaminates the neuroimaging measurements within a voxel (Maier, 2007; Hoy et al., 2015). However, even with these limitations, the capability to longitudinally visualize changes in spinal cord connectivity make DTI a promising tool, and the advances in imaging

scanner technology and diffusion tensor imaging techniques will hopefully increase the value of this method to evaluate the connectivity of the injured spinal cord.

KEY FACTORS AFFECTING REGENERATIVE FAILURE OF SPINAL CORD CONNECTIVITY

Astrocytic and Fibrotic Scar

After SCI, astrocytes, the most abundant resident cells in the CNS, play a crucial role in SCI pathology through a phenotypic change known as reactive gliosis (Hara et al., 2017). In this process, naive astrocytes undergo a change in phenotype, first as reactive astrocytes and then as scar-forming astrocytes. Immediately after injury, astrocytes proliferate and organize around the edges of the lesion to wall off the damaged area from the surrounding healthy tissue. In the subacute phase (from 1 to 2 weeks after injury), reactive astrocytes migrate to the lesion epicenter and seclude inflammatory cells, leading to tissue repair and functional improvement (Okada et al., 2006; Herrmann et al., 2008; Wanner et al., 2013). Later on, the elongated reactive astrocytes near the lesion perimeter begin to entangle with fibroblast-like pericytes (Goritz et al., 2011; Yokota et al., 2017; Dias et al., 2018), leading to the formation of the astrocytic scar, the main impediment to CNS axonal regeneration (Hara et al., 2017). Although the glial scar was long viewed only as a barrier to CNS regeneration, increasing evidence suggest that the glial scar is necessary to prevent the spread of injury and actually supports CNS repair (Faulkner et al., 2004; Anderson et al., 2016). Indeed, the protective nature of astrocytes were confirmed when complete ablation of astrocytes led to worse outcome after mild to moderate SCI (Bush et al., 1999; Sofroniew, 2009; Burda and Sofroniew, 2014; Anderson et al., 2016). Much has been uncovered concerning the function of reactive astrocytes in SCI, and research is ongoing on how to enhance their beneficial roles while minimizing their deleterious effects.

Although reactive astrocytes have been implicated with most of the inhibitive effects of scarring after SCI, studies have demonstrated the inhibitive effects of a fibrotic scar comprised of a dense extracellular matrix made up of fibronectin, collagen, and fibroblasts. Fibrotic scarring was originally reported to originate from meningeal cells following CNS injury, but recent research has shifted the focus to PDGFRβ-positive pericytes and CD13-positive endothelial cells as an active source of the cellular composition of the fibrotic scar in SCI (Soderblom et al., 2013). Furthermore, a recent study suggested an active role of microvascular endothelial cells in the engulfment of myelin debris through the autophagy-lysosome pathway, which promotes inflammation, angiogenesis, and fibrotic scar formation (Zhou et al., 2019). Although the presence of stromal cells in the scar tissue has been recognized following SCI, their precise origin and role are still not sufficiently elucidated. Further investigation into the origin of the fibrotic scar and the molecular signals leading to its formation may provide potential therapeutic implications for promoting axonal regeneration after SCI.

Chondroitin Sulfate Proteoglycans (CSPGs)

Chondroitin sulfate proteoglycans (CSPGs), which are growth-inhibitory extracellular matrix glycoproteins that include neurocan, versican, brevican, phosphacan, and NG2 (Jones et al., 2003; Andrews et al., 2012, Anderson et al., 2016), are widely expressed in the CNS and serve as guidance cues during development and modulate synaptic connections in the adult. CSPGs have been shown to repel regenerating axons and also prevent oligodendrocyte maturation and remyelination (Karus et al., 2016). After trauma to the CNS, the inflammatory response upregulates the secretion of CSPGs from astrocytes and non-astrocyte cells, and the accumulated CSPGs become a chemophysical barrier to axonal regrowth, which is regarded as the principle cause for regeneration failure after SCI (Tran et al., 2018b). Degradation of CSPGs by chondroitinase ABC (ChABC) has been shown to be a potential therapeutic strategy to break down the inhibitive barrier and promote endogenous pathological repair, leading to synapse reorganization and functional improvement from SCI (Bradbury et al., 2002). In fact, ChABC in combination with neural stem/progenitor cells (NSPCs) was shown to promote functional recovery even in the chronic phase of SCI (Karimi-Abdolrezaee et al., 2010; Suzuki et al., 2017). CSPG inhibition has been shown to be mediated by two members of the Leukocyte Common Antigen Related (LAR) phosphatase subfamily, protein tyrosine phosphatase σ (PTPσ) and LAR, and PTPσ receptors have been shown to mediate the regulation of oligodendrocyte differentiation and apoptosis by CSPGs in the injured spinal cord (Fisher et al., 2011; Dyck et al., 2018). Recent studies have demonstrated that administration of a blocking peptide for the CSPG receptor PTPσ restored neuronal innervation of the pyramidal tract projecting to secondary motor neurons and led to functional recovery (Lang et al., 2015; Tran et al., 2018a). The evidence showing that ChABC is beneficial to functional recovery from SCI is growing, but there remain many obstacles that need to be overcome before ChABC treatment can be clinically applied to SCI. The low thermal stability and the short half-life of ChABC make it necessary to repeatedly or continually administer the drug through invasive channels (Lee et al., 2010), and its bacterial origin raises concerns about its safety and immunogenicity (Prabhakar et al., 2009). Animal studies performed so far have not shown adverse effects of ChABC treatment, but the long-term effects of ChABC administration need to be investigated before clinical application can be considered. In order to sidestep some of the disadvantages of ChABC, recent studies are looking into gene therapies to engineer ChABC expression in the injured spinal cord (James et al., 2015; Burnside et al., 2018). Although gene therapy is still an evolving process and methods to control transgene expression require further refinement, progress in this field may 1 day make this option favorable to administration of ChABC.

Inflammatory Reaction

After SCI, the intensive local inflammatory response leads to the activation of resident microglia and facilitates the infiltration of macrophages into the lesion (Shechter et al., 2009). The CNS

has been traditionally considered an immune-privileged site and the inflammatory storm that occurs in the early phases of SCI was considered detrimental to spinal cord function, but the contribution of immune cells to the healing process has also been revealed. One of the main players in the inflammation process is macrophages, and they have been described as having pro- (M1) or anti-inflammatory (M2) functions (Donnelly et al., 2011; Shechter et al., 2013). This grouping of macrophages into M1 and M2 groups may be an oversimplification with macrophages actually being somewhere on this spectrum of polarization, but this bimodal characteristic of infiltrating macrophages has improved our understanding of their function in the injured spinal cord (Kroner et al., 2014; Wang et al., 2015). With systemic and localized inflammatory reactions persisting from the acute to chronic phase of SCI (Ulndreaj et al., 2017; Badner et al., 2018; Hong et al., 2018), interventions that modify inflammation hold promise as a means to reduce secondary damage after SCI (Nguyen et al., 2012; Badner et al., 2016), and modulating the phenotypes of the infiltrating macrophages may be a therapeutic strategy to promote functional recovery after SCI.

Syringomyelia

The overwhelming cell death and tissue degeneration from the acute to chronic phases after SCI promotes the loss of parenchymal tissue at the lesion epicenter and leads to the formation of cystic cavities referred to as syringomyelia (Seki and Fehlings, 2008). Although the pathological mechanisms underlying syringomyelia progression in CNS trauma is not completely understood, the process of posttraumatic cavitation is found in both humans and mammals. The cystic cavities that form following SCI contain extracellular fluid, bands of connective tissue, and infiltrated monocytes/macrophages (Austin et al., 2012a), and the increasing cerebral spinal fluid (CSF) pressure within the cavity is detrimental for regeneration and acts to enlarge its size. The cavity is a formidable obstacle that regenerating axons need to overcome in order to reconnect with their severed networks, prompting researchers to consider strategies that would modify this gap in the spinal cord into a growth-enhancing medium that would nurture regenerating axons and encourage reinstatement of spinal cord connectivity.

THERAPEUTIC APPROACHES TO OVERCOME OBSTACLES IN THE LESION CORE AND PROMOTE REGENERATION

Cell-Based Therapies

Considering the extensive loss of neural cells after SCI, transplantation of various types of cells into the injured spinal cord to repopulate cells that are not replenished by the endogenous regenerative process is an obvious strategy to treat SCI. We now know that engrafted cells work not only by repopulating cells, but by modulating the transplantation site into a more hospitable environment that prevents demyelination and apoptosis of neural cells (**Figure 3**). Of the numerous candidates for transplantation, NSPCs, which are multipotent CNS cells capable of differentiating into neurons, astrocytes, and oligodendrocytes, have been the most attractive and well-studied cell source for the treatment of SCI (Wilcox et al., 2014). While we recognize that neural stem cells, neural progenitor cells, and neural precursor cells are, strictly speaking, different cell populations, we also believe that most cell transplants are a mix of these cells. Therefore, in the interest of clarity, we have elected to unify the designation of these cells as NSPCs. Following transplantation, engrafted NSPCs differentiate into neural cells that replace damaged cells and provide local neurotrophic factors that support neuroprotection, immunomodulation, axonal sprouting, axonal regeneration, and remyelination. Embryonic stem cells (ESCs) were once considered to be a promising candidate for transplantation due to their unlimited developmental potential, but safety concerns associated with their tumorigenicity have greatly deflated the enthusiasm surrounding ESCs and research has shifted more to ESC-derived NSPCs, which have demonstrated therapeutic potential as a treatment for SCI (Salewski et al., 2015b).

Recent advances in stem cell engineering have led to the development of directly reprogrammed NSPCs from human fibroblasts, blood cells, and mesenchymal cells, and they have demonstrated their potential to promote axonal remyelination and tissue sparing in mammal SCI models (Nagoshi et al., 2018). With the possibility for autologous transplantations that would eliminate the risk of an immune response against the transplanted cells, directly reprogrammed NSPCs are an attractive cell source for transplantation treatments. Induced pluripotent stem (iPS) cells and iPS cell-derived neural stem cells (iPS-NSCs) are currently at the forefront of stem cell transplantation strategies, and recent studies show that iPS-NSCs transplanted into the injured spinal cord contribute to remyelination of axons, secretion of regenerative neurotrophic factors, and synaptic reorganization (Salewski et al., 2015a). However, one of the issues that needs to be addressed is tumorigenicity, which is a potential problem with all stem cell transplantations, but it has been most closely studied in iPS cell lines due to its imminent clinical application. The tumorigenicity of iPS cells was reviewed in a recent report (Deng et al., 2018), and methods to eliminate iPS cell-derived tumors are being refined (Kojima et al., 2019).

HOW ENGRAFTED STEM CELLS CONTRIBUTE TO SPINAL CORD CONNECTIVITY

Remyelination

Remyelination in the CNS is a dynamic process that begins with the proliferation of OPCs and their differentiation into oligodendrocytes, which then ensheath axons. A portion of the NSPCs transplanted in the acute or subacute phases of SCI differentiate into oligodendrocytes, increase the number of myelinated axons around the lesion, and lead to functional improvements (Karimi-Abdolrezaee et al., 2006;

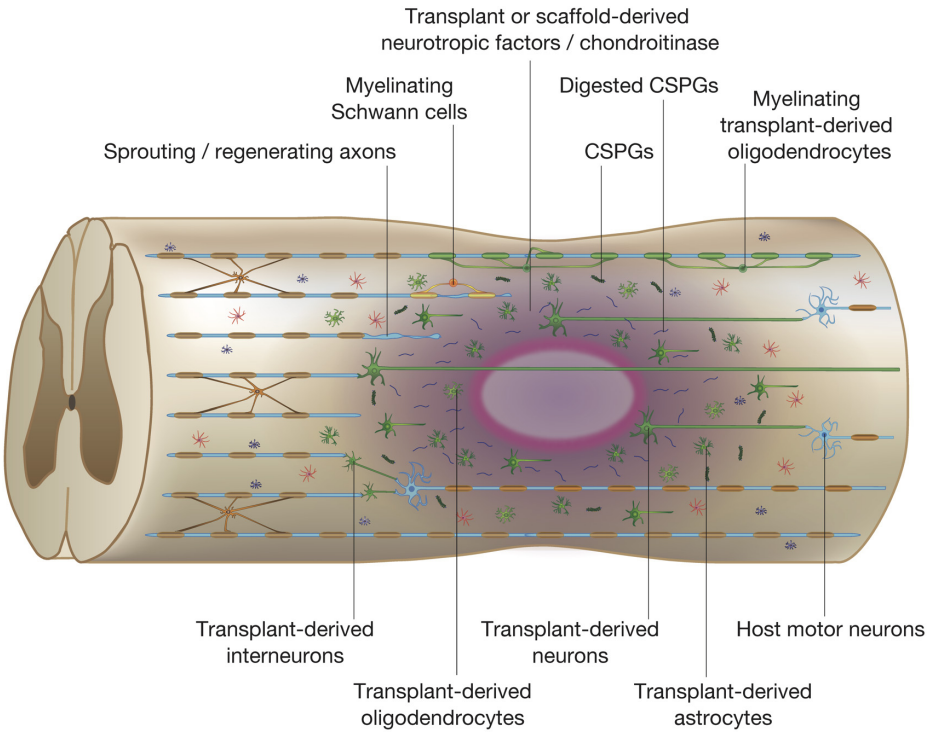

FIGURE 3 | Potential mechanisms of spinal cord repair by stem cell transplantation. The diagram shows potential mechanisms of regeneration brought about by stem cell transplantation. The transplanted stem cells differentiate into neural cells of the three lineages: neurons, astrocytes, and oligodendrocytes (shown in green). The transplanted stem cells and differentiated cells secrete neurotrophic factors that reduce inflammation, degrade CSPGs, and promote endogenous tissue repair. Differentiated oligodendrocytes remyelinate denuded axons. The grafted neurons form synapses with propriospinal neurons and lumbar motor neurons, which reorganize the neuronal circuits by forming *de novo* synaptic connectivity between host and grafted neurons. The regenerated neuronal circuits bridge the lesion by creating a detour route that passes through areas more favorable to regenerating axons. Transplant-derived interneurons indirectly connect the host injured neural tracts through the propriospinal circuits, whereas transplant-derived neurons participate in the regeneration of the injured corticospinal tract (CST) and directly activate muscle contraction.

Eftekharpour et al., 2007). A previous report showed that NSPCs harvested from shiverer rodents, which have severe myelin deficiency throughout the CNS, were less effective than those harvested from wild mice-derived NSPCs when transplanted into the injured spinal cord of wild-type rodents (Yasuda et al., 2011; Hawryluk et al., 2014). These studies reveal that NSPC-derived myelin is essential to the remyelination process after SCI, and demonstrate the important role that remyelination plays in the functional recovery brought about by stem cell transplantation strategies to treat SCI.

With demyelination playing a large role in functional impairment after SCI (Nashmi and Fehlings, 2001; Sinha et al., 2006; Ouyang et al., 2010; Papastefanaki and Matsas, 2015), replacing lost oligodendrocytes through oligodendrocyte precursor cell (OPC) transplantation is another strategy that is being studied (Keirstead et al., 2005). OPCs are predominantly quiescent in the healthy CNS, but in response to injury they proliferate and differentiate into mature oligodendrocytes, which contribute to remyelination (Assinck et al., 2017). Transplanted OPCs not only complement the insufficient remyelination process of endogenous OPCs, but also secrete neurotrophic factors that ameliorate inflammation and promote axonal regeneration (Zhang et al., 2006; Sharp et al., 2010). Schwann cells (SCs), which myelinate peripheral nerve fibers, have also been shown to migrate into the injured spinal cord and support remyelination after SCI (Pearse et al., 2004; Hill et al., 2006). Being more accessible for harvest and easier to culture compared to OPCs, SCs are another attractive cell source to promote remyelination (Anderson et al., 2017). Transplanted SCs have been shown to remyelinate axons and improve neural conduction similar to OPCs, and are reported to produce growth factors, extracellular components, and adhesion molecules that promote functional recovery after SCI (Golden et al., 2007; Papastefanaki et al., 2007; Cao et al., 2010; Lavdas et al., 2010; Deng et al., 2013).

Axonal Sprouting

The dysfunction after SCI is caused mainly by the disruption of functional connections around the lesion site. The cavity that forms in the injured spinal cord lacks the substrate necessary for axonal sprouting and is an impediment for endogenous tissue repair, but the lesion cavity as well as the tissue around the lesion are reasonable engraftment sites for transplanted cells. Stem cells transplanted into the cavity and/or surrounding tissue engraft and secrete neurotropic factors that promote the growth of axons, both endogenous and graft-derived, across the lesion to form synapses and restore spinal cord

connectivity (Lu et al., 2014). Even after decades of research into stem cell transplantation therapies, however, it is still a challenge to induce robust axonal growth that spans the lesion cavity and forms functional connections with the remaining neural network, mainly due to the low regenerative capacity of the injured spinal cord and its refractory environment. Therefore, it is becoming increasingly more frequent to combine stem cell transplantation with other strategies that would enhance the effect of the transplanted cells (Ruff et al., 2012). Biomaterial scaffolds, which provide a growth-permissive substrate for axons to grow, are a logical option to accompany stem cells and will be described later. The scaffolds are often bioengineered to secrete growth-enhancing neurotropic factors, and stem cells are often genetically manipulated to secrete factors that break down growth-inhibitive barriers or promote axonal growth.

Promotion of Neural Pathway Plasticity

One of the mechanisms through which functional improvements occur in subjects with SCI is through neural plasticity, or the ability of the CNS to reorganize its circuits over time (Adler et al., 2017; Wang et al., 2018a). These adaptive changes may occur at any level within the spared neuronal circuitry: the motor cortex, brainstem, or spinal cord level, both above and below the lesion (Bareyre et al., 2004; Courtine et al., 2008). The neurons that differentiate from engrafted NSPCs extend axons and form new synapses with host neurons; the established connections are generally not exact reconnections of the lost neural circuits, but rather *de novo* circuits (Bonner et al., 2011). This reorganization is a very dynamic and variable process, and its degree is believed to depend on the age of the subject and the rehabilitative therapy. Utilizing retrograde neuronal tracing and drug-induced ablation of host neurons, it was demonstrated that the reorganized propriospinal circuits generated through synaptic formation between graft-derived neurons and host-derived neurons directly contributed to functional recovery after NSPC transplantation (Yokota et al., 2015). However, the neural plasticity brought about by NSPC transplantation and its specific role in reestablishing spinal cord connectivity remain ambiguous due to the lack of information regarding the spatial and temporal integration of transplanted stem cells into the host neural circuitry.

While the plasticity of neural circuits in the injured spinal cord has long been proposed to be one of the mechanisms leading to functional recovery from SCI, many studies have only presented fragmentary circumstantial evidence of plasticity. Indeed, the burden of proving plasticity is high because, ideally, one would need to present tracing results to show the pathways before and after SCI and demonstrate functional transference of the microcircuitry from one pathway to another through functional and/or electrophysiological studies. A recent study from our group convincingly demonstrated the plasticity of cervical neural circuits involved in the control of respiration in SCI. In both traumatic (C2 hemisection) and non-traumatic (cervical myelopathy) SCI models, respiratory control shifted from phrenic motor neurons that normally control diaphragm motion to mid-cervical excitatory interneurons, which are normally not essential for the maintenance of breathing in healthy animals. The selective silencing of these excitatory interneurons led to severe disruption of the animals' ability to maintain breathing, indicating their crucial role in respiratory plasticity after SCI (Satkunendrarajah et al., 2018). With increasing attention being paid to the vital role that plasticity plays in maintaining or reestablishing connectivity of the injured spinal cord, the future use of precise neuronal tracing, sophisticated image reconstruction technology, and genetic techniques that manipulate functionality will hopefully elucidate the contribution of plasticity to recovery from SCI.

Stimulation of Endogenous Stem Cells

Ependymal cells, which are the ciliated cells lining the central canal of the spinal cord, are responsible for the propulsion of cerebrospinal fluid and function as a barrier to the spinal cord parenchyma. The normally quiescent ependymal cells self-renew in response to SCI and differentiate into oligodendrocytes and astrocytes (Ke et al., 2006; Barnabe-Heider et al., 2010). The significance of the ependymal cell-derived cell population was confirmed when inhibition of ependymal cell proliferation after SCI severely compromised glial scar formation and led to increased neuron loss (Sabelstrom et al., 2013). Furthermore, harvested and cultured ependymal cells are capable of differentiating into astrocytes, oligodendrocyte, and neurons. Altogether, the characteristics of ependymal cells demonstrate that they are the endogenous stem cells in the adult spinal cord and therefore constitute an attractive cell population to target in the treatment of SCI (Johansson et al., 1999; Yamamoto et al., 2001; Meletis et al., 2008). Indeed, infusion of the growth factors EGF and FGF2 into the central canal was shown to increase the proliferation of ependymal cells and improve functional recovery after SCI, demonstrating the potential of ependymal cell manipulation as an alternative to exogenous stem cell transplantation (Kojima and Tator, 2002).

Additionally, there is experimental data showing that exogenous stem cell transplantation induces proliferation of the endogenous stem cell pool in ependymal cells. Neural stem cells transplanted into the lumbar ventral horn migrated to the central canal and have been shown to stimulate proliferation of ependymal cells and their differentiation into neural precursors and neurons (Xu et al., 2012). The results of this study suggest that transplanted exogenous neural stem cells may induce neurogenesis in the spinal cord ependymal niche and also promote survival of the newly generated host neurons, which is similar to the neurogenesis induced in the brain subventricular zone by NSPC and mesenchymal stem cell grafts (Bao et al., 2011; Jin et al., 2011). If stem cell transplants could be engineered to further stimulate the proliferation of ependymal cells, the synergistic effect between the transplanted exogenous stem cells and endogenous stem cells may bring about greater recovery compared to either stem cell population alone. However, research into the endogenous stem cells of the spinal cord is insufficient to reliably understand and harness this stem cell population, and we await further studies to deepen our knowledge on the potential of ependymal cells.

BIOMATERIAL SCAFFOLDS

Overview of Biomaterials

With the large cavity forming after SCI being an obstacle for regenerating axons, there have been many attempts to implant constructs into the cavity to provide axons with a substrate on which to grow and to restore tissue continuity across the trauma zone. These attempts started as oriented structures to act as bridges for growing axons, but have since evolved to secrete factors that enhance tissue growth and vascularization, deliver drugs, and act as a vehicle to deliver cells into the lesion (Elliott Donaghue et al., 2014). Scaffolds can be designed as devices for controlled release of therapeutic drugs, which would replace the need for multiple and high-dose drug administration (Pakulska et al., 2016b). Many different types of scaffolds have been developed for the treatment of SCI (Liu et al., 2013), but based on composition they can be classified as natural polymers, synthetic biodegradable polymers, or synthetic non-degradable polymers. Being derived and purified from biological sources, natural polymers are biodegradable, have natural biding sites for cells, and generally elicit lower inflammatory reaction and immune response (Tam et al., 2014). Being the product of chemical bioengineering, synthetic biomaterials allow for greater product consistency and tunable properties compared to natural ones (Pakulska et al., 2015, 2016a). Many biomaterial substrates have been studied as candidate scaffolds for the treatment of SCI: collagen, laminin, fibrin matrices, fibronectin, hyaluronan-methylcellulose, chitosan, agarose, alginate, methylcellulose, poly(2-hydroxyethyl methacrylate) or pHEMA, poly(N-(2-hydroxypropyl) methacrylamide) or pHPMA, and poly(lactic-co-glycolic) acid or PLGA. Each substrate has its advantages and disadvantages, and there is currently no consensus on the substrate of choice (Haggerty and Oudega, 2013). The ideal scaffold would have a simple design that allows for smooth manufacturing, have good biocompatibility with low immunogenicity, be biodegradable, have mechanical properties ideal for cell adhesion and axonal regeneration, and would be easy to transplant into the injured spinal cord. Focusing on the ease of transplantation into the SCI cavity, form-filling injectable hydrogel polymers have been receiving attention, and studies have shown that hydrogels decrease cavitation, improve engraftment of transplanted cells, and provide sustained delivery of neurotrophic agents (Austin et al., 2012b). The treatment strategies for SCI have been shifting toward a combinatorial approach, and with the many beneficial characteristics provided by biomaterial scaffolds (Pawar et al., 2015; Chedly et al., 2017; Ropper et al., 2017; Santhosh et al., 2017; Ghosh et al., 2018; Oudega et al., 2018), it is not surprising that many studies have incorporated scaffolds into their treatment paradigms.

How Biomaterial Scaffolds Contribute to Spinal Cord Connectivity

The microenvironment of the SCI lesion is inhibitive to regeneration, and biomaterial scaffolds are implanted in the hopes of improving the lesion into a more growth-supportive environment that would support endogenous neurogenesis, axonal sprouting, and neural plasticity. Scaffolds provide contact-mediated guidance for aligned axon growth across the lesion site and act as a vehicle to deliver drugs and biomolecules that favorably modify the environment as well as stem cells that repopulate the lost neural cells.

A recent study reported on the positive effects of transplanting chitosan, a porous hydrogel scaffold, loaded with neutrotrophin-3 (NT-3) into the SCI lesion of adult rats or rhesus monkeys. The chitosan scaffold effectively prevented infiltration of inflammatory cells, attracted endogenous neural stem cells to proliferate, migrate, and differentiate into neurons, and facilitated the reorganization of neural relay networks to transmit ascending and descending neural signals (Yang et al., 2015). Diffusion tensor imaging, functional MRI, electrophysiology, and kinematics-based quantitative walking behavioral analyses were employed to confirm the robust neural regeneration that led to significant motor and sensory functional recovery (Rao et al., 2018). Diffusion tensor imaging, functional MRI, electrophysiology, and kinematics-based quantitative walking behavioral analyses were employed to confirm the robust neural regeneration that led to significant motor and sensory functional recovery. Anterograde neuronal tracing revealed that axons of the corticospinal tract (CST) regenerated through the grafted scaffold into the caudal part of the spinal cord, and electrophysiology confirmed restoration of MEP signals by the regenerated neural tissue, demonstrating partial restoration of spinal connectivity.

Another recent study performed by Sofroniew's group strategically used injected hydrogels, termed biomaterial depots, to achieve sustained delivery of growth factors. These biomaterial depots were prepared using diblock copolypeptide hydrogels that are biocompatible with the CNS, biodegrade over several weeks, and provide delivery of bioactive growth factors for at least 2 weeks (Yang et al., 2009; Song et al., 2012). Adeno-associated viral vectors (AAV) were injected 2 weeks before injury to reactivate intrinsic propriospinal neuronal growth capacity through phosphatase and tensin homologue (PTEN) knockdown or by expressing osteopontin, insulin-like growth factor 1 (IGF1) and ciliary-derived neurotrophic factor (CNTF). After inducing a severe crush SCI, biomaterial depots delivering fibroblast growth factor 2 (FGF2) and epidermal growth factor (EGF), in combination with and without glial-derived neurotrophic factor (GDNF) or an integrin-function-blocking antibody, were injected into the spinal cord. The authors demonstrated that by sequentially reinstating several developmentally essential mechanisms that facilitate axon growth, it is possible to induce robust growth of propriospinal axons across anatomically complete SCI lesions in adult rodents (Anderson et al., 2018). BDA tract-tracing of propriospinal neurons demonstrated that axons regenerated across the lesion and formed synapses that conveyed a significant return of electrophysiological conduction capacity across the lesion. Although the intervention did not elicit supraspinal serotonergic axonal regeneration or result in observable functional recovery, possibly due to the severity of

the injury and the lack of rehabilitation that promotes neural pathway plasticity, this study demonstrates how biomaterials can be utilized to restore spinal connectivity.

COMBINATORIAL THERAPIES INCLUDING NEURAL STEM/PROGENITOR CELL TRANSPLANTATION AND BIOMATERIAL SCAFFOLDS

While the transplantation of stem cells and scaffolds have each demonstrated beneficial effects as sole treatments, there are numerous studies reporting the synergistic enhancements elicited by combining these two methods (Li et al., 2013). Some selected studies using combinatorial treatment strategies are outlined in **Table 1**. Our group has been studying the benefits of combining NSPCs and K2(QL)6K2 (QL6), which is an aqueous self-assembling peptide (SAP) that aggregates into a stable nanofiber gel due to multiple non-covalent interactions. When injected by itself into the injured spinal cord, QL6 reduced neural cell apoptosis, inflammation, and astrogliosis and brought about electrophysiological and behavioral improvements (Liu et al., 2013). The combination of SAP injection and NSPC transplantation improved NSPC engraftment, reduced astrogliosis and CSPG deposition, increased synaptic connectivity, and improved behavioral outcomes compared to sole treatments (Zweckberger et al., 2016).

Current treatment strategies now often combine scaffolds and stem cells with enhancements bioengineered into the scaffolds, cells, or both. In a study that explored the modification of a scaffold with platelet-derived growth factor-A (PDGF-A) to induce oligodendrocyte differentiation, NSPCs cultured in a hydrogel blend of hyaluronan and methylcellulose (HAMC) modified with PDGF-A had improved survival and a higher percentage of cells differentiating into oligodendrocytes. SCI rats transplanted with NSPCs in HAMC-PDGF-A showed reduced cavitation, improved graft survival with increased oligodendrocytes differentiation, and improved behavioral recovery compared to rats transplanted with NSPCs in media (Mothe et al., 2013). The authors further modified the HAMC-PDGF-A scaffold with arginine-glycine-aspartic acid (RGD) peptide to improve the survival and engraftment of human iPS cell-derived OPCs. Compared to iPS cell-derived OPCs transplanted with media, iPS cell-derived OPCs transplanted in HAMC-RGD/PDGF-A had higher rates of survival and engraftment. Interestingly, while all animals that received cells in media formed teratomas, cells injected in HAMC-RGD/ PDGF-A only formed teratomas in half of the animals, demonstrating that the modified hydrogel promoted cell differentiation and attenuated tumor formation (Fuhrmann et al., 2016). These studies demonstrate the large effects that scaffold modifications can have on the survivability of transplanted cells and its characteristics after engraftment into the injured spinal cord.

Some of the most dramatic synergistic effects of scaffolds, stem cells, and growth factors have been reported by Tuszynski's group. In a report examining the effects of transplanting spinal cord-derived NSPCs into a rat thoracic cord transection model, NSPCs transplanted alone engrafted only on the lesion margin. When the same cells were transplanted in fibrin matrix containing a cocktail of growth factors (brain-derived neurotrophic factor, neurotrophin-3, glial-cell-line-derived neurotrophic factor, epidermal growth factor, basic fibroblast growth factor, acidic fibroblast growth factor, hepatocyte growth factor, insulin-like growth factor, platelet-derived growth factor, vascular endothelial growth factor, and a calpain inhibitor), the transplanted NSPCs filled the lesion gap and demonstrated robust axonal growth caudally into the host spinal cord. The axons from the engrafted NSPCs formed synapses that led to improved electrophysiological and functional improvements (Lu et al., 2012). A following study that examined the regeneration of the corticospinal tract (CST) by transplanting NSPCs and the growth cocktail-enhanced fibrin matrix into a similar rat transection model demonstrated robust CST axon regeneration across the lesion that formed functional synapses and led to improved forelimb function. However, this regeneration was observed only when the grafts were caudalized NSPCs or primary spinal cord–derived NSPCs, demonstrating that the characteristics of the graft were a vital ingredient for CST regeneration (Kadoya et al., 2016). With the aim of generating translational data, the group then studied the effects of transplanting human spinal cord–derived NSPCs and the growth cocktail-enhanced fibrin matrix into sites of cervical SCI in rhesus monkeys. Although modifications of the grafting technique and immunosuppression were required, the human NSPCs grafted into the monkey spinal cord extended long axons through the host white matter that formed synapses in the caudal lumbar gray matter, and led to improved forelimb function (Rosenzweig et al., 2018). In the group's most recent report, the authors created complex 3D biomimetic CNS scaffolds composed of polyethylene glycol-gelatin-methacrylate (PEG-GelMa) based on images of the rat spinal cord (Koffler et al., 2019). Spinal cord-derived NSPCs suspended in a fibrin matrix containing brain-derived neurotrophic factor, basic fibroblast growth factor, vascular endothelial growth factor, and a calpain inhibitor were loaded into the scaffolds and inserted into a rat thoracic cord transection lesion. The transplanted NSPCs survived and filled the scaffold channels at 1 month, and the scaffolds maintained their 3D architecture 6 months after implantation. Host axons regenerated into the scaffolds and formed synapses with NSPCs in the scaffold, while engrafted NSPCs extended axons into the host spinal cord and restored synaptic transmission, leading to electrophysiological and functional improvements. These studies show that with the appropriate combination of optimally engineered stem cells, scaffolds, and growth factors, the hostile environment of the SCI lesion can be improved and neural cells of the spinal cord can be coaxed into a state of regeneration.

Especially for the treatment of chronic SCI, a combinatorial approach is believed to be the only possible avenue to reactivate the regenerative processes and gain functional improvements. Previous reports showed that a combinatorial treatment strategy

TABLE 1 | Selected studies using a combinatorial therapy comprised of neural stem cell transplantation with a biomaterial containing neuroprotective agents.

Author	Year	Cell source	Biomaterial	Neurotrophic agents	SCI model, species	Results
Koffler	2019	Rat spinal cord-derived NSPCs	3D biomimetic hydrogel scaffolds including GelMa, PEGDA, and LAP	Growth factor cocktail (BDNF, VEGF, bFGF, calpain inhibitor)	T3 complete transection, Fischer rats	The injured host axons regenerated into 3D biomimetic scaffolds and synapsed onto NSPCs implanted into the device, and implanted NSPCs extended axons out of the scaffold and into the host spinal cord below the injury to restore synaptic transmission and significantly improve functional outcomes.
Rosenzweig	2018	Human spinal cord-derived NSPCs	Fibrin matrix	Growth factor cocktail (BDNF, NT-3, GDNF, EGF, bFGF, aFGF, HGF, IGF-1, VEGF, PDGF-AA, calpain inhibitor)	C7 right lateral hemisection, rhesus macaques (Macaca mulatta)	Grafted axons extended through host white matter and synapsed in distal gray matter. Grafts gradually matured over 9 months and improved forelimb function beginning several months after grafting.
Nori	2018	Human directly reprogrammed drOPCs	Thiolated methylcellulose modified with SH3 domain binding peptides	Recombinant ChABC-SH3 fusion protein	T7 clip injury, RNU (athymic nude) rats	This combinatorial therapy increased long-term survival of drOPCs around lesion epicenter and facilitated greater oligodendrocyte differentiation, which led to remyelination of the spared axons by engrafted drOPCs and enhanced synaptic connectivity with anterior horn cells, leading to neurobehavioral recovery.
Kadoya	2016	Rat spinal cord-derived NSPCs	Fibrin matrix	Growth factor cocktail (BDNF, NT-3, PDGF-AA, IGF-1, EGF, bFDF, aFGF, GDNF, HGF, calpain inhibitor)	T3 complete transection and C4 (CST) lesion, Fischer rats	Grafted cells showed robust corticospinal axon regeneration that formed functional synapses and led to improvement in skilled forelimb function.
Führmann	2016	Human iPSC-derived OPCs	Hydrogel blend of hyaluronan and methylcellulose (HAMC)	RGD (arginine-glycine-aspartic acid) peptide, PDGF-A	T2 clip injury, Sprague Dawley rats	HAMC hydrogel, modified with a RGD peptide and PDGF-A, promoted early survival and integration of grafted cells. Teratoma formation was attenuated when cells were transplanted in the hydrogel, where most cells differentiated to a glial phenotype.
Mothe	2013	Rat brain-derived NSPCs	Hydrogel blend of hyaluronan and methylcellulose (HAMC)	Recombinant PDGF-A (rPDGF-A)	T2 clip injury, Wistar rats	SCI rats transplanted with NSPCs in HAMC-rPDGF-A showed improved behavioral recovery compared to rats transplanted with NSPCs in media. NSPC/HAMC-rPDGF-A group had significantly reduced cavitation, improved graft survival, increased oligodendrocytic differentiation, and increased sparing of perilesional host oligodendrocytes and neurons.
Li	2013	Rat brain-derived NSPCs	Collagen scaffolds	EGFR neutralizing antibody	T13-L2 lateral hemisection, Sprague Dawley rats	The scaffold loaded with the EGFR antibody neutralized the negative effects of myelin proteins and directed the differentiation of transplanted NSPCs to a neuronal lineage, which promoted functional recovery after SCI.

NSPCs, neural stem/progenitor cells; GelMa, gelatin methacrylate; PEGDA: poly(ethylene glycol) diacrylate; LAP, lithium phenyl-2,4,6-trimethylbenzoylphosphinate; BDNF, brain derived neurotrophic factor; NT-3, neurotrophin-3; GDNF: glial cell-derived neurotrophic factor; EGF, epidermal growth factor; bFGF, basic fibroblast growth factor; aFGF, acidic fibroblast growth factor; HGF, hepatocyte growth factor; IGF-1, insulin-like growth factor-1; PDGF, platelet-derived growth factor; VEGF, vascular endothelial growth factor; drOPCs, directly reprogrammed oligodendrogenic progenitor cells; ChABC, chondrotinase ABC; SH3, Src homology 3; CST, corticospinal tract; SCI, spinal cord injury; iPSCs, induced pluripotent stem cells; HAMC, hyaluronan methylcellulose; RGD, arginine-glycine-aspartic acid; EGFR, epidermal growth factor receptor.

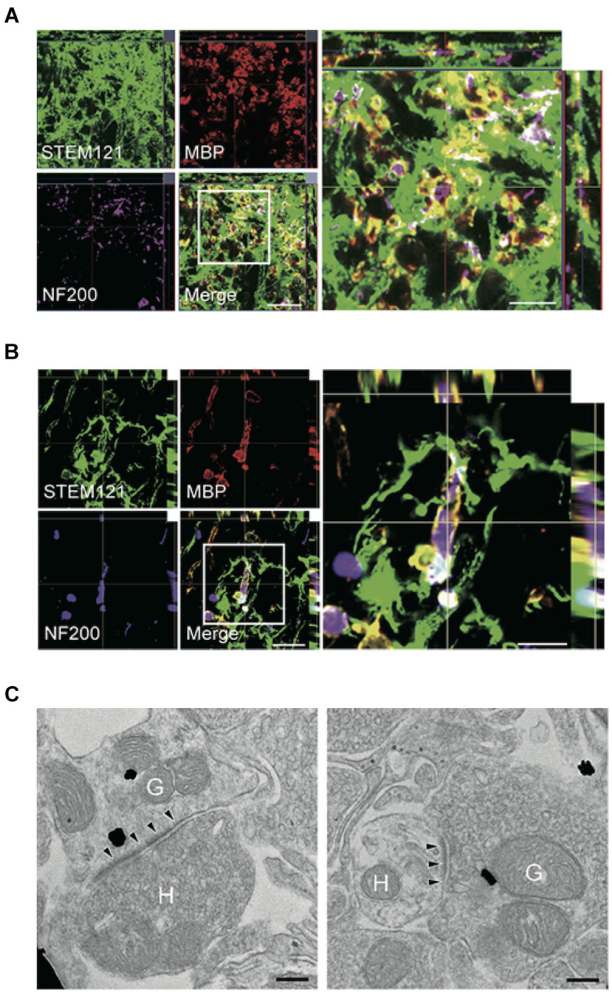

FIGURE 4 | Combinatorial treatment of stem cells and biomaterials containing ChABC elicits remyelination and synaptic reorganization. **(A,B)** Representative images of axial **(A)** and sagittal **(B)** sections stained for STEM121 (a specific marker for human cytoplasmic protein; green), MBP (red), and NF200 (magenta). Many STEM121-positive/MBP-positive graft-derived myelin sheathes were observed around NF200-positive host axons.
(C) Immunoelectron microscopy images show synapses formed between host and graft-derived neurons after the combinatorial treatment. Presynaptic and postsynaptic structures indicate transmission from host neurons to graft-derived neuron (left image), and from graft-derived neurons to host neurons (right image). Annotated (H) indicates host neurons, and (G) indicates graft-derived neurons. Arrowheads indicate postsynaptic density. Figure altered with permission from Nori et al. (2018). Human oligodendrogenic neural progenitor cells delivered with chondroitinase ABC facilitate functional repair of chronic spinal cord injury (2018).

using stem cells and ChABC promoted functional recovery in the chronic phase of SCI (Karimi-Abdolrezaee et al., 2010; Suzuki et al., 2017; Nori et al., 2018), demonstrating that ChABC treatment can modify the chronically injured spinal cord into a microenvironment conducive to regenerative cell-based therapy. After ChABC was administered by intrathecal injection of a methylcellulose hydrogel containing ChABC, human-derived directly reprogrammed oligodendrocyte progenitor cells (drOPCs) were transplanted into the injured spinal cord of rats. ChABC was administered with the intent to degrade CSPGs and also to maintain the oligodendrocytes profile of the drOPCs (Karimi-Abdolrezaee et al., 2012). The transplanted drOPCs enhanced synapse formation, promoted remyelination of host axons, and improved functional recovery (Nori et al., 2018). They found that graft-derived cells formed a MBP-positive myelin sheath and enwrapped host spared axons in the chronically injured spinal cord (**Figures 4A,B**). Using immunoelectron microscopy, they also revealed that immunogold-labeled differentiated graft-derived neurons formed synaptic connectivity with host neurons (**Figure 4C**). This study demonstrated that with an appropriate combinatorial therapy including ChABC and stem cell transplantation, regeneration in the chronically injured spinal cord is also possible.

CONCLUSION AND FUTURE PERSPECTIVES

As we have outlined in this review, significant progress has been made in the recent decades to elucidate the pathophysiology of SCI and to uncover the mechanisms that make the injured spinal cord refractory to regeneration. By modulating inflammation, repopulating lost neural cells through transplantation, improving the local environment by implanting biomaterial scaffolds with growth factors, and implementing strategies to break down the inhibitory barriers, impressive recovery has been demonstrated in animal models of SCI. Yet it is important to keep in mind that all interventions must bring about an improvement in neural connectivity for any meaningful improvement to occur. The ongoing progress seen in neural tracing procedures, electrophysiological techniques, as well as imaging hardware and software has improved our understanding of the plasticity of neural circuits following SCI and the importance of propriospinal circuits in the restoration of neural connectivity, but at the same time, the increasing knowledge emphasizes our lack of control on the processes that govern the rewiring of pathways. Since aberrant rewiring has been implicated in mechanical allodynia, we must learn how to establish control of plasticity and not just blindly promote it. As more SCI studies begin to examine changes in spinal cord connectivity and the mechanisms underlying the rewiring of circuits and synapses, therapies that harness and enhance plasticity to promote the recovery from SCI will hopefully be developed in the near future.

AUTHOR CONTRIBUTIONS

HK and KY reviewed the literature, wrote and edited the manuscript, and finalized and approved the manuscript. MF conceived the frame and reviewed, edited, finalized, and approved the manuscript.

FUNDING

This study was supported by the Canadian Institutes of Health Research (CIHR to MF). MF was supported by the Halbert Chair in Neural Repair and Regeneration and the DeZwirek Foundation. Additional grant support was from the Krembil Foundation (to MF and KY). KY was supported by the Japan Society for the Promotion of Science Overseas Research Fellowships.

ACKNOWLEDGMENTS

We would like to thank Dr. Tim Worden for copyediting the manuscript. We would also like to thank all the investigators who contributed to the establishment of therapeutic strategies for spinal cord injury utilizing biomaterials or stem cell transplantation over the years and apologize to those investigators whose work is not cited here due to the space limitations.

REFERENCES

Adler, A. F., Lee-Kubli, C., Kumamaru, H., Kadoya, K., and Tuszynski, M. H. (2017). Comprehensive monosynaptic rabies virus mapping of host connectivity with neural progenitor grafts after spinal cord injury. *Stem Cell Reports* 8, 1525–1533. doi: 10.1016/j.stemcr.2017.04.004

Aimone, J. B., Leasure, J. L., Perreau, V. M., and Thallmair, M. (2004). Spatial and temporal gene expression profiling of the contused rat spinal cord. *Exp. Neurol.* 189, 204–221. doi: 10.1016/j.expneurol.2004.05.042

Anderson, K. D., Guest, J. D., Dietrich, W. D., Bartlett Bunge, M., Curiel, R., Dididze, M., et al. (2017). Safety of Autologous human Schwann cell transplantation in subacute thoracic spinal cord injury. *J. Neurotrauma* 34, 2950–2963. doi: 10.1089/neu.2016.4895

Anderson, M. A., Burda, J. E., Ren, Y., Ao, Y., O'Shea, T. M., Kawaguchi, R., et al. (2016). Astrocyte scar formation aids central nervous system axon regeneration. *Nature* 532, 195–200. doi: 10.1038/nature17623

Anderson, M. A., O'Shea, T. M., Burda, J. E., Ao, Y., Barlatey, S. L., Bernstein, A. M., et al. (2018). Required growth facilitators propel axon regeneration across complete spinal cord injury. *Nature* 561, 396–400. doi: 10.1038/s41586-018-0467-6

Andrews, E. M., Richards, R. J., Yin, F. Q., Viapiano, M. S., and Jakeman, L. B. (2012). Alterations in chondroitin sulfate proteoglycan expression occur both at and far from the site of spinal contusion injury. *Exp. Neurol.* 235, 174–187. doi: 10.1016/j.expneurol.2011.09.008

Ankeny, D. P., Guan, Z., and Popovich, P. G. (2009). B cells produce pathogenic antibodies and impair recovery after spinal cord injury in mice. *J. Clin. Invest.* 119, 2990–2999. doi: 10.1172/jci39780

Assinck, P., Duncan, G. J., Plemel, J. R., Lee, M. J., Stratton, J. A., Manesh, S. B., et al. (2017). Myelinogenic plasticity of oligodendrocyte precursor cells following spinal cord contusion injury. *J. Neurosci.* 37, 8635–8654. doi: 10.1523/jneurosci.2409-16.2017

Austin, J. W., Afshar, M., and Fehlings, M. G. (2012a). The relationship between localized subarachnoid inflammation and parenchymal pathophysiology after spinal cord injury. *J. Neurotrauma* 29, 1838–1849. doi: 10.1089/neu.2012.2354

Austin, J. W., Kang, C. E., Baumann, M. D., DiDiodato, L., Satkunendrarajah, K., Wilson, J. R., et al. (2012b). The effects of intrathecal injection of a hyaluronan-based hydrogel on inflammation, scarring and neurobehavioural outcomes in a rat model of severe spinal cord injury associated with arachnoiditis. *Biomaterials* 33, 4555–4564. doi: 10.1016/j.biomaterials.2012.03.022

Backx, A. P. M., Spooren, A. I. F., Bongers-Janssen, H. M. H., and Bouwsema, H. (2018). Quality of life, burden and satisfaction with care in caregivers of patients with a spinal cord injury during and after rehabilitation. *Spinal Cord* 56, 890–899. doi: 10.1038/s41393-018-0098-7

Badhiwala, J. H., Ahuja, C. S., and Fehlings, M. G. (2018). Time is spine: a review of translational advances in spinal cord injury. *J. Neurosurg. Spine* 30, 1–18. doi: 10.3171/2018.9.spine18682

Badner, A., Hacker, J., Hong, J., Mikhail, M., Vawda, R., and Fehlings, M. G. (2018). Splenic involvement in umbilical cord matrix-derived mesenchymal stromal cell-mediated effects following traumatic spinal cord injury. *J. Neuroinflammation* 15:219. doi: 10.1186/s12974-018-1243-0

Badner, A., Vawda, R., Laliberte, A., Hong, J., Mikhail, M., Jose, A., et al. (2016). Early intravenous delivery of human brain stromal cells modulates systemic inflammation and leads to vasoprotection in traumatic spinal cord injury. *Stem Cells Transl. Med.* 5, 991–1003. doi: 10.5966/sctm.2015-0295

Bao, X., Wei, J., Feng, M., Lu, S., Li, G., Dou, W., et al. (2011). Transplantation of human bone marrow-derived mesenchymal stem cells promotes behavioral recovery and endogenous neurogenesis after cerebral ischemia in rats. *Brain Res.* 1367, 103–113. doi: 10.1016/j.brainres.2010.10.063

Baptiste, D. C., and Fehlings, M. G. (2006). Pharmacological approaches to repair the injured spinal cord. *J. Neurotrauma* 23, 318–334. doi: 10.1089/neu.2006.23.318

Bareyre, F. M., Kerschensteiner, M., Misgeld, T., and Sanes, J. R. (2005). Transgenic labeling of the corticospinal tract for monitoring axonal responses to spinal cord injury. *Nat. Med.* 11, 1355–1360. doi: 10.1038/nm1331

Bareyre, F. M., Kerschensteiner, M., Raineteau, O., Mettenleiter, T. C., Weinmann, O., and Schwab, M. E. (2004). The injured spinal cord spontaneously forms a new intraspinal circuit in adult rats. *Nat. Neurosci.* 7, 269–277. doi: 10.1038/nn1195

Barnabe-Heider, F., Goritz, C., Sabelstrom, H., Takebayashi, H., Pfrieger, F. W., Meletis, K., et al. (2010). Origin of new glial cells in intact and injured adult spinal cord. *Cell Stem Cell* 7, 470–482. doi: 10.1016/j.stem.2010.07.014

Beck, K. D., Nguyen, H. X., Galvan, M. D., Salazar, D. L., Woodruff, T. M., and Anderson, A. J. (2010). Quantitative analysis of cellular inflammation after traumatic spinal cord injury: evidence for a multiphasic inflammatory response in the acute to chronic environment. *Brain* 133(Pt. 2), 433–447. doi: 10.1093/brain/awp322

Bedenk, B. T., Almeida-Correa, S., Jurik, A., Dedic, N., Grunecker, B., Genewsky, A. J., et al. (2018). Mn(2+) dynamics in manganese-enhanced MRI (MEMRI): Cav1.2 channel-mediated uptake and preferential accumulation in projection terminals. *Neuroimage* 169, 374–382. doi: 10.1016/j.neuroimage.2017.12.054

Bellardita, C., and Kiehn, O. (2015). Phenotypic characterization of speed-associated gait changes in mice reveals modular organization of locomotor networks. *Curr. Biol.* 25, 1426–1436. doi: 10.1016/j.cub.2015.04.005

Bikoff, J. B., Gabitto, M. I., Rivard, A. F., Drobac, E., Machado, T. A., Miri, A., et al. (2016). Spinal inhibitory interneuron diversity delineates variant motor microcircuits. *Cell* 165, 207–219. doi: 10.1016/j.cell.2016.01.027

Bonner, J. F., Connors, T. M., Silverman, W. F., Kowalski, D. P., Lemay, M. A., and Fischer, I. (2011). Grafted neural progenitors integrate and restore synaptic connectivity across the injured spinal cord. *J. Neurosci.* 31, 4675–4686. doi: 10.1523/jneurosci.4130-10.2011

Bradbury, E. J., Moon, L. D., Popat, R. J., King, V. R., Bennett, G. S., Patel, P. N., et al. (2002). Chondroitinase ABC promotes functional recovery after spinal cord injury. *Nature* 416, 636–640. doi: 10.1038/416636a

Breckwoldt, M. O., Pfister, F. M., Bradley, P. M., Marinkovic, P., Williams, P. R., Brill, M. S., et al. (2014). Multiparametric optical analysis of mitochondrial redox signals during neuronal physiology and pathology *in vivo*. *Nat. Med.* 20, 555–560. doi: 10.1038/nm.3520

Burda, J. E., and Sofroniew, M. V. (2014). Reactive gliosis and the multicellular response to CNS damage and disease. *Neuron* 81, 229–248. doi: 10.1016/j.neuron.2013.12.034

Burnside, E. R., De Winter, F., Didangelos, A., James, N. D., Andreica, E. C., Layard-Horsfall, H., et al. (2018). Immune-evasive gene switch enables regulated delivery of chondroitinase after spinal cord injury. *Brain* 141, 2362–2381. doi: 10.1093/brain/awy158

Busch, S. A., Horn, K. P., Silver, D. J., and Silver, J. (2009). Overcoming macrophage-mediated axonal dieback following CNS injury. *J. Neurosci.* 29, 9967–9976. doi: 10.1523/jneurosci.1151-09.2009

Bush, T. G., Puvanachandra, N., Horner, C. H., Polito, A., Ostenfeld, T., Svendsen, C. N., et al. (1999). Leukocyte infiltration, neuronal degeneration, and neurite

outgrowth after ablation of scar-forming, reactive astrocytes in adult transgenic mice. *Neuron* 23, 297–308. doi: 10.1016/s0896-6273(00)80781-3

Cao, Q., He, Q., Wang, Y., Cheng, X., Howard, R. M., Zhang, Y., et al. (2010). Transplantation of ciliary neurotrophic factor-expressing adult oligodendrocyte precursor cells promotes remyelination and functional recovery after spinal cord injury. *J. Neurosci.* 30, 2989–3001. doi: 10.1523/jneurosci.3174-09.2010

Casha, S., Yu, W. R., and Fehlings, M. G. (2001). Oligodendroglial apoptosis occurs along degenerating axons and is associated with FAS and p75 expression following spinal cord injury in the rat. *Neuroscience* 103, 203–218. doi: 10.1016/s0306-4522(00)00538-8

Casha, S., Yu, W. R., and Fehlings, M. G. (2005). FAS deficiency reduces apoptosis, spares axons and improves function after spinal cord injury. *Exp. Neurol.* 196, 390–400. doi: 10.1016/j.expneurol.2005.08.020

Casha, S., Zygun, D., McGowan, M. D., Bains, I., Yong, V. W., and Hurlbert, R. J. (2012). Results of a phase II placebo-controlled randomized trial of minocycline in acute spinal cord injury. *Brain* 135(Pt. 4), 1224–1236. doi: 10.1093/brain/aws072

Chamankhah, M., Eftekharpour, E., Karimi-Abdolrezaee, S., Boutros, P. C., San-Marina, S., and Fehlings, M. G. (2013). Genome-wide gene expression profiling of stress response in a spinal cord clip compression injury model. *BMC Genomics* 14:583. doi: 10.1186/1471-2164-14-583

Chedly, J., Soares, S., Montembault, A., von Boxberg, Y., Veron-Ravaille, M., Mouffle, C., et al. (2017). Physical chitosan microhydrogels as scaffolds for spinal cord injury restoration and axon regeneration. *Biomaterials* 138, 91–107. doi: 10.1016/j.biomaterials.2017.05.024

Chen, B. K., Knight, A. M., de Ruiter, G. C., Spinner, R. J., Yaszemski, M. J., Currier, B. L., et al. (2009). Axon regeneration through scaffold into distal spinal cord after transection. *J. Neurotrauma* 26, 1759–1771. doi: 10.1089/neu.2008-0610

Cheran, S., Shanmuganathan, K., Zhuo, J., Mirvis, S. E., Aarabi, B., Alexander, M. T., et al. (2011). Correlation of MR diffusion tensor imaging parameters with ASIA motor scores in hemorrhagic and nonhemorrhagic acute spinal cord injury. *J. Neurotrauma* 28, 1881–1892. doi: 10.1089/neu.2010.1741

Chu, G. K., Yu, W., and Fehlings, M. G. (2007). The p75 neurotrophin receptor is essential for neuronal cell survival and improvement of functional recovery after spinal cord injury. *Neuroscience* 148, 668–682. doi: 10.1016/j.neuroscience.2007.05.028

Chung, K., Wallace, J., Kim, S. Y., Kalyanasundaram, S., Andalman, A. S., Davidson, T. J., et al. (2013). Structural and molecular interrogation of intact biological systems. *Nature* 497, 332–337. doi: 10.1038/nature12107

Courtine, G., Song, B., Roy, R. R., Zhong, H., Herrmann, J. E., Ao, Y., et al. (2008). Recovery of supraspinal control of stepping via indirect propriospinal relay connections after spinal cord injury. *Nat. Med.* 14, 69–74. doi: 10.1038/nm1682

Deng, J., Zhang, Y., Xie, Y., Zhang, L., and Tang, P. (2018). Cell transplantation for spinal cord injury: tumorigenicity of induced pluripotent stem cell-derived neural stem/progenitor cells. *Stem Cells Int.* 2018:5653787. doi: 10.1155/2018/5653787

Deng, L. X., Deng, P., Ruan, Y., Xu, Z. C., Liu, N. K., Wen, X., et al. (2013). A novel growth-promoting pathway formed by GDNF-overexpressing Schwann cells promotes propriospinal axonal regeneration, synapse formation, and partial recovery of function after spinal cord injury. *J. Neurosci.* 33, 5655–5667. doi: 10.1523/jneurosci.2973-12.2013

Dhall, S. S., Haefeli, J., Talbott, J. F., Ferguson, A. R., Readdy, W. J., Bresnahan, J. C., et al. (2018). Motor evoked potentials correlate with magnetic resonance imaging and early recovery after acute spinal cord injury. *Neurosurgery* 82, 870–876. doi: 10.1093/neuros/nyx320

Dias, D. O., Kim, H., Holl, D., Werne Solnestam, B., Lundeberg, J., Carlen, M., et al. (2018). Reducing pericyte-derived scarring promotes recovery after spinal cord injury. *Cell* 173, 153–165.e22. doi: 10.1016/j.cell.2018.02.004

Donnelly, D. J., Longbrake, E. E., Shawler, T. M., Kigerl, K. A., Lai, W., Tovar, C. A., et al. (2011). Deficient CX3CR1 signaling promotes recovery after mouse spinal cord injury by limiting the recruitment and activation of Ly6Clo/iNOS+ macrophages. *J. Neurosci.* 31, 9910–9922. doi: 10.1523/jneurosci.2114-11.2011

Dyck, S., Kataria, H., Akbari-Kelachayeh, K., Silver, J., and Karimi-Abdolrezaee, S. (2018). LAR and PTPsigma receptors are negative regulators of oligodendrogenesis and oligodendrocyte integrity in spinal cord injury. *Glia* 67, 125–145. doi: 10.1002/glia.23533

Easley-Neal, C., Fierro, J. Jr., Buchanan, J., and Washbourne, P. (2013). Late recruitment of synapsin to nascent synapses is regulated by Cdk5. *Cell Rep.* 3, 1199–1212. doi: 10.1016/j.celrep.2013.03.031

Eftekharpour, E., Karimi-Abdolrezaee, S., Wang, J., El Beheiry, H., Morshead, C., and Fehlings, M. G. (2007). Myelination of congenitally dysmyelinated spinal cord axons by adult neural precursor cells results in formation of nodes of Ranvier and improved axonal conduction. *J. Neurosci.* 27, 3416–3428. doi: 10.1523/jneurosci.0273-07.2007

Elliott Donaghue, I., Tam, R., Sefton, M. V., and Shoichet, M. S. (2014). Cell and biomolecule delivery for tissue repair and regeneration in the central nervous system. *J. Control. Release* 190, 219–227. doi: 10.1016/j.jconrel.2014.05.040

Evans, T. A., Barkauskas, D. S., Myers, J. T., Hare, E. G., You, J. Q., Ransohoff, R. M., et al. (2014). High-resolution intravital imaging reveals that blood-derived macrophages but not resident microglia facilitate secondary axonal dieback in traumatic spinal cord injury. *Exp. Neurol.* 254, 109–120. doi: 10.1016/j.expneurol.2014.01.013

Faulkner, J. R., Herrmann, J. E., Woo, M. J., Tansey, K. E., Doan, N. B., and Sofroniew, M. V. (2004). Reactive astrocytes protect tissue and preserve function after spinal cord injury. *J. Neurosci.* 24, 2143–2155. doi: 10.1523/jneurosci.3547-03.2004

Fehlings, M. G., Kim, K. D., Aarabi, B., Rizzo, M., Bond, L. M., McKerracher, L., et al. (2018). Rho inhibitor VX-210 in acute traumatic subaxial cervical spinal cord injury: design of the spinal cord injury rho inhibition investigation (SPRING) clinical trial. *J. Neurotrauma* 35, 1049–1056. doi: 10.1089/neu.2017.5434

Fehlings, M. G., Martin, A. R., Tetreault, L. A., Aarabi, B., Anderson, P., Arnold, P. M., et al. (2017). A clinical practice guideline for the management of patients with acute spinal cord injury: recommendations on the role of baseline magnetic resonance imaging in clinical decision making and outcome prediction. *Global Spine J.* 7(3 Suppl.), 221s–230s. doi: 10.1177/2192568217703089

Feng, B., Qiu, G., Shen, J., Zhang, J., Tian, Y., Li, S., et al. (2012). Impact of multimodal intraoperative monitoring during surgery for spine deformity and potential risk factors for neurological monitoring changes. *J. Spinal Disord. Tech.* 25, E108–E114. doi: 10.1097/BSD.0b013e31824d2a2f

Filipello, F., Morini, R., Corradini, I., Zerbi, V., Canzi, A., Michalski, B., et al. (2018). The microglial innate immune receptor TREM2 is required for synapse elimination and normal brain connectivity. *Immunity* 48, 979–991.e8. doi: 10.1016/j.immuni.2018.04.016

Filli, L., Engmann, A. K., Zorner, B., Weinmann, O., Moraitis, T., Gullo, M., et al. (2014). Bridging the gap: a reticulo-propriospinal detour bypassing an incomplete spinal cord injury. *J. Neurosci.* 34, 13399–13410. doi: 10.1523/jneurosci.0701-14.2014

Fisher, D., Xing, B., Dill, J., Li, H., Hoang, H. H., Zhao, Z., et al. (2011). Leukocyte common antigen-related phosphatase is a functional receptor for chondroitin sulfate proteoglycan axon growth inhibitors. *J. Neurosci.* 31, 14051–14066. doi: 10.1523/jneurosci.1737-11.2011

Floriddia, E. M., Rathore, K. I., Tedeschi, A., Quadrato, G., Wuttke, A., Lueckmann, J. M., et al. (2012). p53 Regulates the neuronal intrinsic and extrinsic responses affecting the recovery of motor function following spinal cord injury. *J. Neurosci.* 32, 13956–13970. doi: 10.1523/jneurosci.1925-12.2012

Fuhrmann, T., Tam, R. Y., Ballarin, B., Coles, B., Elliott Donaghue, I., van der Kooy, D., et al. (2016). Injectable hydrogel promotes early survival of induced pluripotent stem cell-derived oligodendrocytes and attenuates longterm teratoma formation in a spinal cord injury model. *Biomaterials* 83, 23–36. doi: 10.1016/j.biomaterials.2015.12.032

Fujiyoshi, K., Yamada, M., Nakamura, M., Yamane, J., Katoh, H., Kitamura, K., et al. (2007). In vivo tracing of neural tracts in the intact and injured spinal cord of marmosets by diffusion tensor tractography. *J. Neurosci.* 27, 11991–11998. doi: 10.1523/jneurosci.3354-07.2007

Furlan, J. C., Verocai, F., Palmares, X., and Fehlings, M. G. (2016). Electrocardiographic abnormalities in the early stage following traumatic spinal cord injury. *Spinal Cord* 54, 872–877. doi: 10.1038/sc.2016.11

Galluzzi, L., Vitale, I., Aaronson, S. A., Abrams, J. M., Adam, D., Agostinis, P., et al. (2018). Molecular mechanisms of cell death: recommendations of the nomenclature committee on cell death 2018. *Cell Death Differ.* 25, 486–541. doi: 10.1038/s41418-017-0012-4

Geisler, F. H., Dorsey, F. C., and Coleman, W. P. (1991). Recovery of motor function after spinal-cord injury–a randomized, placebo-controlled trial with GM-1 ganglioside. *N. Engl. J. Med.* 324, 1829–1838. doi: 10.1056/nejm199106273242601

Ghosh, B., Wang, Z., Nong, J., Urban, M. W., Zhang, Z., Trovillion, V. A., et al. (2018). Local BDNF delivery to the injured cervical spinal cord using an engineered hydrogel enhances diaphragmatic respiratory function. *J. Neurosci.* 38, 5982–5995. doi: 10.1523/jneurosci.3084-17.2018

Golden, K. L., Pearse, D. D., Blits, B., Garg, M. S., Oudega, M., Wood, P. M., et al. (2007). Transduced Schwann cells promote axon growth and myelination after spinal cord injury. *Exp. Neurol.* 207, 203–217. doi: 10.1016/j.expneurol.2007.06.023

Goritz, C., Dias, D. O., Tomilin, N., Barbacid, M., Shupliakov, O., and Frisen, J. (2011). A pericyte origin of spinal cord scar tissue. *Science* 333, 238–242. doi: 10.1126/science.1203165

Haggerty, A. E., and Oudega, M. (2013). Biomaterials for spinal cord repair. *Neurosci. Bull.* 29, 445–459. doi: 10.1007/s12264-013-1362-7

Hara, M., Kobayakawa, K., Ohkawa, Y., Kumamaru, H., Yokota, K., Saito, T., et al. (2017). Interaction of reactive astrocytes with type I collagen induces astrocytic scar formation through the integrin-N-cadherin pathway after spinal cord injury. *Nat. Med.* 23, 818–828. doi: 10.1038/nm.4354

Hawryluk, G. W., Spano, S., Chew, D., Wang, S., Erwin, M., Chamankhah, M., et al. (2014). An examination of the mechanisms by which neural precursors augment recovery following spinal cord injury: a key role for remyelination. *Cell Transplant.* 23, 365–380. doi: 10.3727/096368912x662408

Herrmann, J. E., Imura, T., Song, B., Qi, J., Ao, Y., Nguyen, T. K., et al. (2008). STAT3 is a critical regulator of astrogliosis and scar formation after spinal cord injury. *J. Neurosci.* 28, 7231–7243. doi: 10.1523/jneurosci.1709-08.2008

Hill, C. E., Moon, L. D., Wood, P. M., and Bunge, M. B. (2006). Labeled Schwann cell transplantation: cell loss, host Schwann cell replacement, and strategies to enhance survival. *Glia* 53, 338–343. doi: 10.1002/glia.20287

Hong, J., Chang, A., Zavvarian, M. M., Wang, J., Liu, Y., and Fehlings, M. G. (2018). Level-specific differences in systemic expression of pro- and anti-inflammatory cytokines and chemokines after spinal cord injury. *Int. J. Mol. Sci.* 19:E2167. doi: 10.3390/ijms19082167

Horn, K. P., Busch, S. A., Hawthorne, A. L., van Rooijen, N., and Silver, J. (2008). Another barrier to regeneration in the CNS: activated macrophages induce extensive retraction of dystrophic axons through direct physical interactions. *J. Neurosci.* 28, 9330–9341. doi: 10.1523/jneurosci.2488-08.2008

Hou, S., Duale, H., Cameron, A. A., Abshire, S. M., Lyttle, T. S., and Rabchevsky, A. G. (2008). Plasticity of lumbosacral propriospinal neurons is associated with the development of autonomic dysreflexia after thoracic spinal cord transection. *J. Comp. Neurol.* 509, 382–399. doi: 10.1002/cne.21771

Hoy, A. R., Kecskemeti, S. R., and Alexander, A. L. (2015). Free water elimination diffusion tractography: a comparison with conventional and fluid-attenuated inversion recovery, diffusion tensor imaging acquisitions. *J. Magn. Reson. Imaging* 42, 1572–1581. doi: 10.1002/jmri.24925

Huang, Z., Li, R., Liu, J., Huang, Z., Hu, Y., Wu, X., et al. (2018). Longitudinal electrophysiological changes after cervical hemi-contusion spinal cord injury in rats. *Neurosci. Lett.* 664, 116–122. doi: 10.1016/j.neulet.2017.11.019

Inada, T., Takahashi, H., Yamazaki, M., Okawa, A., Sakuma, T., Kato, K., et al. (2014). Multicenter prospective nonrandomized controlled clinical trial to prove neurotherapeutic effects of granulocyte colony-stimulating factor for acute spinal cord injury: analyses of follow-up cases after at least 1 year. *Spine* 39, 213–219. doi: 10.1097/brs.0000000000000121

Ishii, A., Furusho, M., Dupree, J. L., and Bansal, R. (2014). Role of ERK1/2 MAPK signaling in the maintenance of myelin and axonal integrity in the adult CNS. *J. Neurosci.* 34, 16031–16045. doi: 10.1523/jneurosci.3360-14.2014

Jacobi, A., Loy, K., Schmalz, A. M., Hellsten, M., Umemori, H., Kerschensteiner, M., et al. (2015). FGF22 signaling regulates synapse formation during post-injury remodeling of the spinal cord. *EMBO J.* 34, 1231–1243. doi: 10.15252/embj.201490578

James, N. D., Shea, J., Muir, E. M., Verhaagen, J., Schneider, B. L., and Bradbury, E. J. (2015). Chondroitinase gene therapy improves upper limb function following cervical contusion injury. *Exp. Neurol.* 271, 131–135. doi: 10.1016/j.expneurol.2015.05.022

Jin, K., Xie, L., Mao, X., Greenberg, M. B., Moore, A., Peng, B., et al. (2011). Effect of human neural precursor cell transplantation on endogenous neurogenesis after focal cerebral ischemia in the rat. *Brain Res.* 1374, 56–62. doi: 10.1016/j.brainres.2010.12.037

Johansson, C. B., Momma, S., Clarke, D. L., Risling, M., Lendahl, U., and Frisen, J. (1999). Identification of a neural stem cell in the adult mammalian central nervous system. *Cell* 96, 25–34. doi: 10.1016/s0092-8674(00)80956-3

Jones, L. L., Margolis, R. U., and Tuszynski, M. H. (2003). The chondroitin sulfate proteoglycans neurocan, brevican, phosphacan, and versican are differentially regulated following spinal cord injury. *Exp. Neurol.* 182, 399–411. doi: 10.1016/s0014-4886(03)00087-6

Kadoya, K., Lu, P., Nguyen, K., Lee-Kubli, C., Kumamaru, H., Yao, L., et al. (2016). Spinal cord reconstitution with homologous neural grafts enables robust corticospinal regeneration. *Nat. Med.* 22, 479–487. doi: 10.1038/nm.4066

Kaptanoglu, E., Caner, H., Solaroglu, I., and Kilinc, K. (2005). Mexiletine treatment-induced inhibition of caspase-3 activation and improvement of behavioral recovery after spinal cord injury. *J. Neurosurg. Spine* 3, 53–56. doi: 10.3171/spi.2005.3.1.0053

Karimi-Abdolrezaee, S., Eftekharpour, E., Wang, J., Morshead, C. M., and Fehlings, M. G. (2006). Delayed transplantation of adult neural precursor cells promotes remyelination and functional neurological recovery after spinal cord injury. *J. Neurosci.* 26, 3377–3389. doi: 10.1523/jneurosci.4184-05.2006

Karimi-Abdolrezaee, S., Eftekharpour, E., Wang, J., Schut, D., and Fehlings, M. G. (2010). Synergistic effects of transplanted adult neural stem/progenitor cells, chondroitinase, and growth factors promote functional repair and plasticity of the chronically injured spinal cord. *J. Neurosci.* 30, 1657–1676. doi: 10.1523/jneurosci.3111-09.2010

Karimi-Abdolrezaee, S., Schut, D., Wang, J., and Fehlings, M. G. (2012). Chondroitinase and growth factors enhance activation and oligodendrocyte differentiation of endogenous neural precursor cells after spinal cord injury. *PLoS One* 7:e37589. doi: 10.1371/journal.pone.0037589

Karus, M., Ulc, A., Ehrlich, M., Czopka, T., Hennen, E., Fischer, J., et al. (2016). Regulation of oligodendrocyte precursor maintenance by chondroitin sulphate glycosaminoglycans. *Glia* 64, 270–286. doi: 10.1002/glia.22928

Ke, Y., Chi, L., Xu, R., Luo, C., Gozal, D., and Liu, R. (2006). Early response of endogenous adult neural progenitor cells to acute spinal cord injury in mice. *Stem Cells* 24, 1011–1019. doi: 10.1634/stemcells.2005-0249

Keirstead, H. S., Nistor, G., Bernal, G., Totoiu, M., Cloutier, F., Sharp, K., et al. (2005). Human embryonic stem cell-derived oligodendrocyte progenitor cell transplants remyelinate and restore locomotion after spinal cord injury. *J. Neurosci.* 25, 4694–4705. doi: 10.1523/jneurosci.0311-05.2005

Kerschensteiner, M., Schwab, M. E., Lichtman, J. W., and Misgeld, T. (2005). In vivo imaging of axonal degeneration and regeneration in the injured spinal cord. *Nat. Med.* 11, 572–577. doi: 10.1038/nm1229

Khayrullina, G., Bermudez, S., and Byrnes, K. R. (2015). Inhibition of NOX2 reduces locomotor impairment, inflammation, and oxidative stress after spinal cord injury. *J. Neuroinflammation* 12:172. doi: 10.1186/s12974-015-0391-8

Kneussel, M., Brandstatter, J. H., Laube, B., Stahl, S., Muller, U., and Betz, H. (1999). Loss of postsynaptic GABA(A) receptor clustering in gephyrin-deficient mice. *J. Neurosci.* 19, 9289–9297. doi: 10.1523/jneurosci.19-21-09289.1999

Koffler, J., Zhu, W., Qu, X., Platoshyn, O., Dulin, J. N., Brock, J., et al. (2019). Biomimetic 3D-printed scaffolds for spinal cord injury repair. *Nat. Med.* 25, 263–269. doi: 10.1038/s41591-018-0296-z

Kohl, A., Marquardt, T., Klar, A., and Sela-Donenfeld, D. (2015). Control of axon guidance and neurotransmitter phenotype of dB1 hindbrain interneurons by Lim-HD code. *J. Neurosci.* 35, 2596–2611. doi: 10.1523/jneurosci.2699-14.2015

Kojima, A., and Tator, C. H. (2002). Intrathecal administration of epidermal growth factor and fibroblast growth factor 2 promotes ependymal proliferation and functional recovery after spinal cord injury in adult rats. *J. Neurotrauma* 19, 223–238. doi: 10.1089/08977150252806974

Kojima, K., Miyoshi, H., Nagoshi, N., Kohyama, J., Itakura, G., Kawabata, S., et al. (2019). Selective ablation of tumorigenic cells following human induced pluripotent stem cell-derived neural stem/progenitor cell transplantation in spinal cord injury. *Stem Cells Transl. Med.* 8, 260–270. doi: 10.1002/sctm.18-0096

Kroner, A., Greenhalgh, A. D., Zarruk, J. G., Passos Dos Santos, R., Gaestel, M., and David, S. (2014). TNF and increased intracellular iron alter macrophage polarization to a detrimental M1 phenotype in the injured spinal cord. *Neuron* 83, 1098–1116. doi: 10.1016/j.neuron.2014.07.027

Krueger, H., Noonan, V. K., Trenaman, L. M., Joshi, P., and Rivers, C. S. (2013). The economic burden of traumatic spinal cord injury in Canada. *Chronic Dis. Inj. Can.* 33, 113–122.

Kuang, R. Z., and Kalil, K. (1990). Specificity of corticospinal axon arbors sprouting into denervated contralateral spinal cord. *J. Comp. Neurol.* 302, 461–472. doi: 10.1002/cne.903020304

Kumamaru, H., Saiwai, H., Ohkawa, Y., Yamada, H., Iwamoto, Y., and Okada, S. (2012). Age-related differences in cellular and molecular profiles of inflammatory responses after spinal cord injury. *J. Cell. Physiol.* 227, 1335–1346. doi: 10.1002/jcp.22845

Kunis, G., Baruch, K., Rosenzweig, N., Kertser, A., Miller, O., Berkutzki, T., et al. (2013). IFN-gamma-dependent activation of the brain's choroid plexus for CNS immune surveillance and repair. *Brain* 136(Pt. 11), 3427–3440. doi: 10.1093/brain/awt259

Kuroiwa, M., Watanabe, M., Katoh, H., Suyama, K., Matsuyama, D., Imai, T., et al. (2014). Effect of amiloride on endoplasmic reticulum stress response in the injured spinal cord of rats. *Eur. J. Neurosci.* 40, 3120–3127. doi: 10.1111/ejn.12647

Kuzhandaivel, A., Nistri, A., and Mladinic, M. (2010). Kainate-mediated excitotoxicity induces neuronal death in the rat spinal cord *in vitro* via a PARP-1 dependent cell death pathway (Parthanatos). *Cell. Mol. Neurobiol.* 30, 1001–1012. doi: 10.1007/s10571-010-9531-y

Lang, B. T., Cregg, J. M., DePaul, M. A., Tran, A. P., Xu, K., Dyck, S. M., et al. (2015). Modulation of the proteoglycan receptor PTPsigma promotes recovery after spinal cord injury. *Nature* 518, 404–408. doi: 10.1038/nature13974

Lavdas, A. A., Chen, J., Papastefanaki, F., Chen, S., Schachner, M., Matsas, R., et al. (2010). Schwann cells engineered to express the cell adhesion molecule L1 accelerate myelination and motor recovery after spinal cord injury. *Exp. Neurol.* 221, 206–216. doi: 10.1016/j.expneurol.2009.10.024

Le Ray, D., Juvin, L., Ryczko, D., and Dubuc, R. (2011). Chapter 4 – supraspinal control of locomotion: the mesencephalic locomotor region. *Prog. Brain Res.* 188, 51–70. doi: 10.1016/b978-0-444-53825-3.00009-7

Lee, H., McKeon, R. J., and Bellamkonda, R. V. (2010). Sustained delivery of thermostabilized chABC enhances axonal sprouting and functional recovery after spinal cord injury. *Proc. Natl. Acad. Sci. U.S.A.* 107, 3340–3345. doi: 10.1073/pnas.0905437106

Lehrman, E. K., Wilton, D. K., Litvina, E. Y., Welsh, C. A., Chang, S. T., Frouin, A., et al. (2018). CD47 protects synapses from excess microglia-mediated pruning during development. *Neuron* 100, 120–134.e6. doi: 10.1016/j.neuron.2018.09.017

Lerner, T. N., Shilyansky, C., Davidson, T. J., Evans, K. E., Beier, K. T., Zalocusky, K. A., et al. (2015). Intact-brain analyses reveal distinct information carried by SNc dopamine subcircuits. *Cell* 162, 635–647. doi: 10.1016/j.cell.2015.07.014

Lewis, M. J., Howard, J. F. Jr., and Olby, N. J. (2017). The relationship between trans-lesional conduction, motor neuron pool excitability, and motor function in dogs with incomplete recovery from severe spinal cord injury. *J. Neurotrauma* 34, 2994–3002. doi: 10.1089/neu.2017.5012

Li, X., Xiao, Z., Han, J., Chen, L., Xiao, H., Ma, F., et al. (2013). Promotion of neuronal differentiation of neural progenitor cells by using EGFR antibody functionalized collagen scaffolds for spinal cord injury repair. *Biomaterials* 34, 5107–5116. doi: 10.1016/j.biomaterials.2013.03.062

Li, Y., Lucas-Osma, A. M., Black, S., Bandet, M. V., Stephens, M. J., Vavrek, R., et al. (2017). Pericytes impair capillary blood flow and motor function after chronic spinal cord injury. *Nat. Med.* 23, 733–741. doi: 10.1038/nm.4331

Lipinski, M. M., Wu, J., Faden, A. I., and Sarkar, C. (2015). Function and mechanisms of autophagy in brain and spinal cord trauma. *Antioxid. Redox Signal.* 23, 565–577. doi: 10.1089/ars.2015.6306

Liu, M., Wu, W., Li, H., Li, S., Huang, L. T., Yang, Y. Q., et al. (2015). Necroptosis, a novel type of programmed cell death, contributes to early neural cells damage after spinal cord injury in adult mice. *J. Spinal Cord Med.* 38, 745–753. doi: 10.1179/2045772314y.0000000224

Liu, Y., Ye, H., Satkunendrarajah, K., Yao, G. S., Bayon, Y., and Fehlings, M. G. (2013). A self-assembling peptide reduces glial scarring, attenuates post-traumatic inflammation and promotes neurological recovery following spinal cord injury. *Acta Biomater.* 9, 8075–8088. doi: 10.1016/j.actbio.2013.06.001

Lo, L., and Anderson, D. J. (2011). A Cre-dependent, anterograde transsynaptic viral tracer for mapping output pathways of genetically marked neurons. *Neuron* 72, 938–950. doi: 10.1016/j.neuron.2011.12.002

Lu, P., Kadoya, K., and Tuszynski, M. H. (2014). Axonal growth and connectivity from neural stem cell grafts in models of spinal cord injury. *Curr. Opin. Neurobiol.* 27, 103–109. doi: 10.1016/j.conb.2014.03.010

Lu, P., Wang, Y., Graham, L., McHale, K., Gao, M., Wu, D., et al. (2012). Long-distance growth and connectivity of neural stem cells after severe spinal cord injury. *Cell* 150, 1264–1273. doi: 10.1016/j.cell.2012.08.020

Maier, S. E. (2007). Examination of spinal cord tissue architecture with magnetic resonance diffusion tensor imaging. *Neurotherapeutics* 4, 453–459. doi: 10.1016/j.nurt.2007.05.003

Marion, T. E., Rivers, C. S., Kurban, D., Cheng, C. L., Fallah, N., Batke, J., et al. (2017). Previously identified common post-injury adverse events in traumatic spinal cord injury-validation of existing literature and relation to selected potentially modifiable comorbidities: a prospective canadian cohort study. *J. Neurotrauma* 34, 2883–2891. doi: 10.1089/neu.2016.4933

Martin, A. R., De Leener, B., Cohen-Adad, J., Cadotte, D. W., Kalsi-Ryan, S., Lange, S. F., et al. (2017). Clinically feasible microstructural MRI to quantify cervical spinal cord tissue injury using DTI, MT, and T2*-weighted imaging: assessment of normative data and reliability. *AJNR Am. J. Neuroradiol.* 38, 1257–1265. doi: 10.3174/ajnr.A5163

McGovern, A. E., Davis-Poynter, N., Rakoczy, J., Phipps, S., Simmons, D. G., and Mazzone, S. B. (2012). Anterograde neuronal circuit tracing using a genetically modified herpes simplex virus expressing EGFP. *J. Neurosci. Methods* 209, 158–167. doi: 10.1016/j.jneumeth.2012.05.035

Meletis, K., Barnabe-Heider, F., Carlen, M., Evergren, E., Tomilin, N., Shupliakov, O., et al. (2008). Spinal cord injury reveals multilineage differentiation of ependymal cells. *PLoS Biol.* 6:e182. doi: 10.1371/journal.pbio.0060182

Min, K. J., Jeong, H. K., Kim, B., Hwang, D. H., Shin, H. Y., Nguyen, A. T., et al. (2012). Spatial and temporal correlation in progressive degeneration of neurons and astrocytes in contusion-induced spinal cord injury. *J. Neuroinflammation* 9:100. doi: 10.1186/1742-2094-9-100

Miyanji, F., Furlan, J. C., Aarabi, B., Arnold, P. M., and Fehlings, M. G. (2007). Acute cervical traumatic spinal cord injury: MR imaging findings correlated with neurologic outcome–prospective study with 100 consecutive patients. *Radiology* 243, 820–827. doi: 10.1148/radiol.2433060583

Moghaddam, A., Child, C., Bruckner, T., Gerner, H. J., Daniel, V., and Biglari, B. (2015). Posttraumatic inflammation as a key to neuroregeneration after traumatic spinal cord injury. *Int. J. Mol. Sci.* 16, 7900–7916. doi: 10.3390/ijms16047900

Mondello, S. E., Jefferson, S. C., O'Steen, W. A., and Howland, D. R. (2016). Enhancing Fluorogold-based neural tract tracing. *J. Neurosci. Methods* 270, 85–91. doi: 10.1016/j.jneumeth.2016.06.004

Moonen, G., Satkunendrarajah, K., Wilcox, J. T., Badner, A., Mothe, A., Foltz, W., et al. (2016). A new acute impact-compression lumbar spinal cord injury model in the rodent. *J. Neurotrauma* 33, 278–289. doi: 10.1089/neu.2015.3937

Mothe, A. J., Tam, R. Y., Zahir, T., Tator, C. H., and Shoichet, M. S. (2013). Repair of the injured spinal cord by transplantation of neural stem cells in a hyaluronan-based hydrogel. *Biomaterials* 34, 3775–3783. doi: 10.1016/j.biomaterials.2013.02.002

Munce, S. E. P., Webster, F., Fehlings, M. G., Straus, S. E., Jang, E., and Jaglal, S. B. (2016). Meaning of self-management from the perspective of individuals with traumatic spinal cord injury, their caregivers, and acute care and rehabilitation managers: an opportunity for improved care delivery. *BMC Neurol.* 16:11. doi: 10.1186/s12883-016-0534-2

Nagoshi, N., Khazaei, M., Ahlfors, J. E., Ahuja, C. S., Nori, S., Wang, J., et al. (2018). Human spinal oligodendrogenic neural progenitor cells promote functional recovery after spinal cord injury by axonal remyelination and tissue sparing. *Stem Cells Transl. Med.* 7, 806–818. doi: 10.1002/sctm.17-0269

Nashmi, R., and Fehlings, M. G. (2001). Changes in axonal physiology and morphology after chronic compressive injury of the rat thoracic spinal cord. *Neuroscience* 104, 235–251. doi: 10.1016/s0306-4522(01)00009-4

Nguyen, D. H., Cho, N., Satkunendrarajah, K., Austin, J. W., Wang, J., and Fehlings, M. G. (2012). Immunoglobulin G (IgG) attenuates neuroinflammation and improves neurobehavioral recovery after cervical spinal cord injury. *J. Neuroinflammation* 9:224. doi: 10.1186/1742-2094-9-224

Nori, S., Khazaei, M., Ahuja, C. S., Yokota, K., Ahlfors, J. E., Liu, Y., et al. (2018). Human oligodendrogenic neural progenitor cells delivered with chondroitinase ABC facilitate functional repair of chronic spinal cord injury. *Stem Cell Rep.* 11, 1433–1448. doi: 10.1016/j.stemcr.2018.10.017

Okada, S., Nakamura, M., Katoh, H., Miyao, T., Shimazaki, T., Ishii, K., et al. (2006). Conditional ablation of Stat3 or Socs3 discloses a dual role for reactive astrocytes after spinal cord injury. *Nat. Med.* 12, 829–834. doi: 10.1038/nm1425

Ouardouz, M., Coderre, E., Basak, A., Chen, A., Zamponi, G. W., Hameed, S., et al. (2009). Glutamate receptors on myelinated spinal cord axons: I, GluR6 kainate receptors. *Ann. Neurol.* 65, 151–159. doi: 10.1002/ana.21533

Oudega, M., Hao, P., Shang, J., Haggerty, A. E., Wang, Z., Sun, J., et al. (2018). Validation study of neurotrophin-3-releasing chitosan facilitation of neural tissue generation in the severely injured adult rat spinal cord. *Exp. Neurol.* 312, 51–62. doi: 10.1016/j.expneurol.2018.11.003

Ouyang, H., Sun, W., Fu, Y., Li, J., Cheng, J. X., Nauman, E., et al. (2010). Compression induces acute demyelination and potassium channel exposure in spinal cord. *J. Neurotrauma* 27, 1109–1120. doi: 10.1089/neu.2010.1271

Ozawa, H., Keane, R. W., Marcillo, A. E., Diaz, P. H., and Dietrich, W. D. (2002). Therapeutic strategies targeting caspase inhibition following spinal cord injury in rats. *Exp. Neurol.* 177, 306–313. doi: 10.1006/exnr.2002.7998

Pakulska, M. M., Elliott Donaghue, I., Obermeyer, J. M., Tuladhar, A., McLaughlin, C. K., Shendruk, T. N., et al. (2016a). Encapsulation-free controlled release: electrostatic adsorption eliminates the need for protein encapsulation in PLGA nanoparticles. *Sci. Adv.* 2:e1600519. doi: 10.1126/sciadv.1600519

Pakulska, M. M., Miersch, S., and Shoichet, M. S. (2016b). Designer protein delivery: from natural to engineered affinity-controlled release systems. *Science* 351:aac4750. doi: 10.1126/science.aac4750

Pakulska, M. M., Vulic, K., Tam, R. Y., and Shoichet, M. S. (2015). Hybrid crosslinked methylcellulose hydrogel: a predictable and tunable platform for local drug delivery. *Adv. Mater.* 27, 5002–5008. doi: 10.1002/adma.201502767

Papastefanaki, F., Chen, J., Lavdas, A. A., Thomaidou, D., Schachner, M., and Matsas, R. (2007). Grafts of Schwann cells engineered to express PSA-NCAM promote functional recovery after spinal cord injury. *Brain* 130(Pt. 8), 2159–2174. doi: 10.1093/brain/awm155

Papastefanaki, F., and Matsas, R. (2015). From demyelination to remyelination: the road toward therapies for spinal cord injury. *Glia* 63, 1101–1125. doi: 10.1002/glia.22809

Pawar, K., Cummings, B. J., Thomas, A., Shea, L. D., Levine, A., Pfaff, S., et al. (2015). Biomaterial bridges enable regeneration and re-entry of corticospinal tract axons into the caudal spinal cord after SCI: association with recovery of forelimb function. *Biomaterials* 65, 1–12. doi: 10.1016/j.biomaterials.2015.05.032

Pearse, D. D., Pereira, F. C., Marcillo, A. E., Bates, M. L., Berrocal, Y. A., Filbin, M. T., et al. (2004). cAMP and Schwann cells promote axonal growth and functional recovery after spinal cord injury. *Nat. Med.* 10, 610–616. doi: 10.1038/nm1056

Powers, B. E., Sellers, D. L., Lovelett, E. A., Cheung, W., Aalami, S. P., Zapertov, N., et al. (2013). Remyelination reporter reveals prolonged refinement of spontaneously regenerated myelin. *Proc. Natl. Acad. Sci. U.S.A.* 110, 4075–4080. doi: 10.1073/pnas.1210293110

Prabhakar, V., Capila, I., Soundararajan, V., Raman, R., and Sasisekharan, R. (2009). Recombinant expression, purification, and biochemical characterization of chondroitinase ABC II from Proteus vulgaris. *J. Biol. Chem.* 284, 974–982. doi: 10.1074/jbc.M806630200

Proskuryakov, S. Y., Konoplyannikov, A. G., and Gabai, V. L. (2003). Necrosis: a specific form of programmed cell death? *Exp. Cell Res.* 283, 1–16. doi: 10.1016/s0014-4827(02)00027-7

Rao, J. S., Zhao, C., Zhang, A., Duan, H., Hao, P., Wei, R. H., et al. (2018). NT3-chitosan enables de novo regeneration and functional recovery in monkeys after spinal cord injury. *Proc. Natl. Acad. Sci. U.S.A.* 115, E5595–E5604. doi: 10.1073/pnas.1804735115

Raposo, C., Graubardt, N., Cohen, M., Eitan, C., London, A., Berkutzki, T., et al. (2014). CNS repair requires both effector and regulatory T cells with distinct temporal and spatial profiles. *J. Neurosci.* 34, 10141–10155. doi: 10.1523/jneurosci.0076-14.2014

Robins-Steele, S., Nguyen, D. H., and Fehlings, M. G. (2012). The delayed post-injury administration of soluble fas receptor attenuates post-traumatic neural degeneration and enhances functional recovery after traumatic cervical spinal cord injury. *J. Neurotrauma* 29, 1586–1599. doi: 10.1089/neu.2011.2005

Ropper, A. E., Thakor, D. K., Han, I., Yu, D., Zeng, X., Anderson, J. E., et al. (2017). Defining recovery neurobiology of injured spinal cord by synthetic matrix-assisted hMSC implantation. *Proc. Natl. Acad. Sci. U.S.A.* 114, E820–E829. doi: 10.1073/pnas.1616340114

Roseberry, T. K., Lee, A. M., Lalive, A. L., Wilbrecht, L., Bonci, A., and Kreitzer, A. C. (2016). Cell-type-specific control of brainstem locomotor circuits by basal ganglia. *Cell* 164, P526–P537. doi: 10.1016/j.cell.2015.12.037

Rosenzweig, E. S., Brock, J. H., Lu, P., Kumamaru, H., Salegio, E. A., Kadoya, K., et al. (2018). Restorative effects of human neural stem cell grafts on the primate spinal cord. *Nat. Med.* 24, 484–490. doi: 10.1038/nm.4502

Ruff, C. A., Wilcox, J. T., and Fehlings, M. G. (2012). Cell-based transplantation strategies to promote plasticity following spinal cord injury. *Exp. Neurol.* 235, 78–90. doi: 10.1016/j.expneurol.2011.02.010

Rust, R., and Kaiser, J. (2017). Insights into the dual role of inflammation after spinal cord injury. *J. Neurosci.* 37, 4658–4660. doi: 10.1523/jneurosci.0498-17.2017

Saab, A. S., and Nave, K. A. (2017). Myelin dynamics: protecting and shaping neuronal functions. *Curr. Opin. Neurobiol.* 47, 104–112. doi: 10.1016/j.conb.2017.09.013

Sabelstrom, H., Stenudd, M., Reu, P., Dias, D. O., Elfineh, M., Zdunek, S., et al. (2013). Resident neural stem cells restrict tissue damage and neuronal loss after spinal cord injury in mice. *Science* 342, 637–640. doi: 10.1126/science.1242576

Saiwai, H., Kumamaru, H., Ohkawa, Y., Kubota, K., Kobayakawa, K., Yamada, H., et al. (2013). Ly6C+ Ly6G- Myeloid-derived suppressor cells play a critical role in the resolution of acute inflammation and the subsequent tissue repair process after spinal cord injury. *J. Neurochem.* 125, 74–88. doi: 10.1111/jnc.12135

Saiwai, H., Ohkawa, Y., Yamada, H., Kumamaru, H., Harada, A., Okano, H., et al. (2010). The LTB4-BLT1 axis mediates neutrophil infiltration and secondary injury in experimental spinal cord injury. *Am. J. Pathol.* 176, 2352–2366. doi: 10.2353/ajpath.2010.090839

Salewski, R. P., Mitchell, R. A., Li, L., Shen, C., Milekovskaia, M., Nagy, A., et al. (2015a). Transplantation of induced pluripotent stem cell-derived neural stem cells mediate functional recovery following thoracic spinal cord injury through remyelination of axons. *Stem Cells Transl. Med.* 4, 743–754. doi: 10.5966/sctm.2014-0236

Salewski, R. P., Mitchell, R. A., Shen, C., and Fehlings, M. G. (2015b). Transplantation of neural stem cells clonally derived from embryonic stem cells promotes recovery after murine spinal cord injury. *Stem Cells Dev.* 24, 36–50. doi: 10.1089/scd.2014.0096

Santhosh, K. T., Alizadeh, A., and Karimi-Abdolrezaee, S. (2017). Design and optimization of PLGA microparticles for controlled and local delivery of Neuregulin-1 in traumatic spinal cord injury. *J. Control. Release* 261, 147–162. doi: 10.1016/j.jconrel.2017.06.030

Satkunendrarajah, K., Karadimas, S. K., Laliberte, A. M., Montandon, G., and Fehlings, M. G. (2018). Cervical excitatory neurons sustain breathing after spinal cord injury. *Nature* 562, 419–422. doi: 10.1038/s41586-018-0595-z

Seif, G. I., Nomura, H., and Tator, C. H. (2007). Retrograde axonal degeneration "dieback" in the corticospinal tract after transection injury of the rat spinal cord: a confocal microscopy study. *J. Neurotrauma* 24, 1513–1528. doi: 10.1089/neu.2007.0323

Sekhon, L. H., and Fehlings, M. G. (2001). Epidemiology, demographics, and pathophysiology of acute spinal cord injury. *Spine* 26, (24 Suppl), S2–S12.

Seki, T., and Fehlings, M. G. (2008). Mechanistic insights into posttraumatic syringomyelia based on a novel *in vivo* animal model. Laboratory investigation. *J. Neurosurg. Spine* 8, 365–375. doi: 10.3171/spi/2008/8/4/365

Shah, P. K., Garcia-Alias, G., Choe, J., Gad, P., Gerasimenko, Y., Tillakaratne, N., et al. (2013). Use of quadrupedal step training to re-engage spinal interneuronal networks and improve locomotor function after spinal cord injury. *Brain* 136(Pt. 11), 3362–3377. doi: 10.1093/brain/awt265

Sharp, J., Frame, J., Siegenthaler, M., Nistor, G., and Keirstead, H. S. (2010). Human embryonic stem cell-derived oligodendrocyte progenitor cell transplants improve recovery after cervical spinal cord injury. *Stem Cells* 28, 152–163. doi: 10.1002/stem.245

Sharp, K. G., Yee, K. M., and Steward, O. (2014). A re-assessment of long distance growth and connectivity of neural stem cells after severe spinal cord injury. *Exp. Neurol.* 257, 186–204. doi: 10.1016/j.expneurol.2014.04.008

Shechter, R., London, A., Varol, C., Raposo, C., Cusimano, M., Yovel, G., et al. (2009). Infiltrating blood-derived macrophages are vital cells playing an anti-inflammatory role in recovery from spinal cord injury in mice. *PLoS Med.* 6:e1000113. doi: 10.1371/journal.pmed.1000113

Shechter, R., Miller, O., Yovel, G., Rosenzweig, N., London, A., Ruckh, J., et al. (2013). Recruitment of beneficial M2 macrophages to injured spinal cord is orchestrated by remote brain choroid plexus. *Immunity* 38, 555–569. doi: 10.1016/j.immuni.2013.02.012

Sheikh, I. S., Keefe, K. M., Sterling, N. A., Junker, I. P., Eneanya, C. I., Liu, Y., et al. (2018). Retrogradely transportable lentivirus tracers for mapping spinal cord locomotor circuits. *Front. Neural Circuits* 12:60. doi: 10.3389/fncir.2018.00060

Shibahashi, K., Nishida, M., Okura, Y., and Hamabe, Y. (2018). Epidemiological state, predictors of early mortality, and predictive models for traumatic spinal cord injury: a multicenter nationwide cohort study. *Spine* 44, 479–487. doi: 10.1097/brs.0000000000002871

Singh, A., Tetreault, L., Kalsi-Ryan, S., Nouri, A., and Fehlings, M. G. (2014). Global prevalence and incidence of traumatic spinal cord injury. *Clin. Epidemiol.* 6, 309–331. doi: 10.2147/clep.s68889

Sinha, K., Karimi-Abdolrezaee, S., Velumian, A. A., and Fehlings, M. G. (2006). Functional changes in genetically dysmyelinated spinal cord axons of shiverer mice: role of juxtaparanodal Kv1 family K+ channels. *J. Neurophysiol.* 95, 1683–1695. doi: 10.1152/jn.00899.2005

Soderblom, C., Luo, X., Blumenthal, E., Bray, E., Lyapichev, K., Ramos, J., et al. (2013). Perivascular fibroblasts form the fibrotic scar after contusive spinal cord injury. *J. Neurosci.* 33, 13882–13887. doi: 10.1523/jneurosci.2524-13.2013

Sofroniew, M. V. (2009). Molecular dissection of reactive astrogliosis and glial scar formation. *Trends Neurosci.* 32, 638–647. doi: 10.1016/j.tins.2009.08.002

Song, B., Song, J., Zhang, S., Anderson, M. A., Ao, Y., Yang, C. Y., et al. (2012). Sustained local delivery of bioactive nerve growth factor in the central nervous system via tunable diblock copolypeptide hydrogel depots. *Biomaterials* 33, 9105–9116. doi: 10.1016/j.biomaterials.2012.08.060

Steencken, A. C., Siebert, J. R., and Stelzner, D. J. (2009). Lack of axonal sprouting of spared propriospinal fibers caudal to spinal contusion injury is attributed to chronic axonopathy. *J. Neurotrauma* 26, 2279–2297. doi: 10.1089/neu.2009.0934

Stieltjes, B., Klussmann, S., Bock, M., Umathum, R., Mangalathu, J., Letellier, E., et al. (2006). Manganese-enhanced magnetic resonance imaging for in vivo assessment of damage and functional improvement following spinal cord injury in mice. *Magn. Reson. Med.* 55, 1124–1131. doi: 10.1002/mrm.20888

Stroman, P. W., Bosma, R. L., Kornelsen, J., Lawrence-Dewar, J., Wheeler-Kingshott, C., Cadotte, D., et al. (2012). Advanced MR imaging techniques and characterization of residual anatomy. *Clin. Neurol. Neurosurg.* 114, 460–470. doi: 10.1016/j.clineuro.2012.01.003

Stroman, P. W., Khan, H. S., Bosma, R. L., Cotoi, A. I., Leung, R., Cadotte, D. W., et al. (2016). Changes in pain processing in the spinal cord and brainstem after spinal cord injury characterized by functional magnetic resonance imaging. *J. Neurotrauma* 33, 1450–1460. doi: 10.1089/neu.2015.4257

Sudhof, T. C. (2018). Towards an understanding of synapse formation. *Neuron* 100, 276–293. doi: 10.1016/j.neuron.2018.09.040

Suzuki, H., Ahuja, C. S., Salewski, R. P., Li, L., Satkunendrarajah, K., Nagoshi, N., et al. (2017). Neural stem cell mediated recovery is enhanced by Chondroitinase ABC pretreatment in chronic cervical spinal cord injury. *PLoS One* 12:e0182339. doi: 10.1371/journal.pone.0182339

Tam, R. Y., Fuehrmann, T., Mitrousis, N., and Shoichet, M. S. (2014). Regenerative therapies for central nervous system diseases: a biomaterials approach. *Neuropsychopharmacology* 39, 169–188. doi: 10.1038/npp.2013.237

Tillakaratne, N. J., Guu, J. J., de Leon, R. D., Bigbee, A. J., London, N. J., Zhong, H., et al. (2010). Functional recovery of stepping in rats after a complete neonatal spinal cord transection is not due to regrowth across the lesion site. *Neuroscience* 166, 23–33. doi: 10.1016/j.neuroscience.2009.12.010

Tomer, R., Ye, L., Hsueh, B., and Deisseroth, K. (2014). Advanced CLARITY for rapid and high-resolution imaging of intact tissues. *Nat. Protoc.* 9, 1682–1697. doi: 10.1038/nprot.2014.123

Tran, A. P., Sundar, S., Yu, M., Lang, B. T., and Silver, J. (2018a). Modulation of receptor protein tyrosine phosphatase sigma increases chondroitin sulfate proteoglycan degradation through cathepsin B secretion to enhance axon outgrowth. *J. Neurosci.* 38, 5399–5414. doi: 10.1523/jneurosci.3214-17.2018

Tran, A. P., Warren, P. M., and Silver, J. (2018b). The biology of regeneration failure and success after spinal cord injury. *Physiol. Rev.* 98, 881–917. doi: 10.1152/physrev.00017.2017

Treweek, J. B., Chan, K. Y., Flytzanis, N. C., Yang, B., Deverman, B. E., Greenbaum, A., et al. (2015). Whole-body tissue stabilization and selective extractions via tissue-hydrogel hybrids for high-resolution intact circuit mapping and phenotyping. *Nat. Protoc.* 10, 1860–1896. doi: 10.1038/nprot.2015.122

Ulndreaj, A., Tzekou, A., Mothe, A. J., Siddiqui, A. M., Dragas, R., Tator, C. H., et al. (2017). Characterization of the antibody response after cervical spinal cord injury. *J. Neurotrauma* 34, 1209–1226. doi: 10.1089/neu.2016.4498

von Leden, R. E., Khayrullina, G., Moritz, K. E., and Byrnes, K. R. (2017). Age exacerbates microglial activation, oxidative stress, inflammatory and NOX2 gene expression, and delays functional recovery in a middle-aged rodent model of spinal cord injury. *J. Neuroinflammation* 14:161. doi: 10.1186/s12974-017-0933-3

Wang, X., Cao, K., Sun, X., Chen, Y., Duan, Z., Sun, L., et al. (2015). Macrophages in spinal cord injury: phenotypic and functional change from exposure to myelin debris. *Glia* 63, 635–651. doi: 10.1002/glia.22774

Wang, Y., Wu, W., Wu, X., Sun, Y., Zhang, Y. P., Deng, L. X., et al. (2018a). Remodeling of lumbar motor circuitry remote to a thoracic spinal cord injury promotes locomotor recovery. *eLife* 7:e39016. doi: 10.7554/eLife.39016

Wang, Y., Xie, H., and Zhao, X. (2018b). Psychological morbidities and positive psychological outcomes in people with traumatic spinal cord injury in Mainland China. *Spinal Cord* 56, 704–711. doi: 10.1038/s41393-017-0044-0

Wanner, I. B., Anderson, M. A., Song, B., Levine, J., Fernandez, A., Gray-Thompson, Z., et al. (2013). Glial scar borders are formed by newly proliferated, elongated astrocytes that interact to corral inflammatory and fibrotic cells via STAT3-dependent mechanisms after spinal cord injury. *J. Neurosci.* 33, 12870–12886. doi: 10.1523/jneurosci.2121-13.2013

Wheeler-Kingshott, C. A., Hickman, S. J., Parker, G. J., Ciccarelli, O., Symms, M. R., Miller, D. H., et al. (2002). Investigating cervical spinal cord structure using axial diffusion tensor imaging. *Neuroimage* 16, 93–102. doi: 10.1006/nimg.2001.1022

Wickersham, I. R., Finke, S., Conzelmann, K. K., and Callaway, E. M. (2007). Retrograde neuronal tracing with a deletion-mutant rabies virus. *Nat. Methods* 4, 47–49. doi: 10.1038/nmeth999

Wilcox, J. T., Satkunendrarajah, K., Nasirzadeh, Y., Laliberte, A. M., Lip, A., Cadotte, D. W., et al. (2017). Generating level-dependent models of cervical and thoracic spinal cord injury: exploring the interplay of neuroanatomy, physiology, and function. *Neurobiol. Dis.* 105, 194–212. doi: 10.1016/j.nbd.2017.05.009

Wilcox, J. T., Satkunendrarajah, K., Zuccato, J. A., Nassiri, F., and Fehlings, M. G. (2014). Neural precursor cell transplantation enhances functional recovery and reduces astrogliosis in bilateral compressive/contusive cervical spinal cord injury. *Stem Cells Transl. Med.* 3, 1148–1159. doi: 10.5966/sctm.2014-0029

Williams, M. E., de Wit, J., and Ghosh, A. (2010). Molecular mechanisms of synaptic specificity in developing neural circuits. *Neuron* 68, 9–18. doi: 10.1016/j.neuron.2010.09.007

Worcester, W. L. (1898). Regeneration of nerve fibres in the central nervous system. *J. Exp. Med.* 3, 579–583. doi: 10.1084/jem.3.6.579

Wu, K. L., Hsu, C., and Chan, J. Y. (2007). Impairment of the mitochondrial respiratory enzyme activity triggers sequential activation of apoptosis-inducing factor-dependent and caspase-dependent signaling pathways to induce apoptosis after spinal cord injury. *J. Neurochem.* 101, 1552–1566. doi: 10.1111/j.1471-4159.2006.04445.x

Wu, X., Fu, Y., Knott, G., Lu, J., Di Cristo, G., and Huang, Z. J. (2012). GABA signaling promotes synapse elimination and axon pruning in developing cortical inhibitory interneurons. *J. Neurosci.* 32, 331–343. doi: 10.1523/jneurosci.3189-11.2012

Wu, Y., Satkunendrarajah, K., and Fehlings, M. G. (2014). Riluzole improves outcome following ischemia-reperfusion injury to the spinal cord by preventing delayed paraplegia. *Neuroscience* 265, 302–312. doi: 10.1016/j.neuroscience.2014.01.059

Xu, L., Mahairaki, V., and Koliatsos, V. E. (2012). Host induction by transplanted neural stem cells in the spinal cord: further evidence for an

adult spinal cord neurogenic niche. *Regen. Med.* 7, 785–797. doi: 10.2217/rme.12.76

Yamamoto, S., Nagao, M., Sugimori, M., Kosako, H., Nakatomi, H., Yamamoto, N., et al. (2001). Transcription factor expression and Notch-dependent regulation of neural progenitors in the adult rat spinal cord. *J. Neurosci.* 21, 9814–9823. doi: 10.1523/jneurosci.21-24-09814.2001

Yang, B., Treweek, J. B., Kulkarni, R. P., Deverman, B. E., Chen, C. K., Lubeck, E., et al. (2014). Single-cell phenotyping within transparent intact tissue through whole-body clearing. *Cell* 158, 945–958. doi: 10.1016/j.cell.2014.07.017

Yang, C. Y., Song, B., Ao, Y., Nowak, A. P., Abelowitz, R. B., Korsak, R. A., et al. (2009). Biocompatibility of amphiphilic diblock copolypeptide hydrogels in the central nervous system. *Biomaterials* 30, 2881–2898. doi: 10.1016/j.biomaterials.2009.01.056

Yang, Z., Zhang, A., Duan, H., Zhang, S., Hao, P., Ye, K., et al. (2015). NT3-chitosan elicits robust endogenous neurogenesis to enable functional recovery after spinal cord injury. *Proc. Natl. Acad. Sci. U.S.A.* 112, 13354–13359. doi: 10.1073/pnas.1510194112

Yasuda, A., Tsuji, O., Shibata, S., Nori, S., Takano, M., Kobayashi, Y., et al. (2011). Significance of remyelination by neural stem/progenitor cells transplanted into the injured spinal cord. *Stem Cells* 29, 1983–1994. doi: 10.1002/stem.767

Yin, H. Z., Hsu, C. I., Yu, S., Rao, S. D., Sorkin, L. S., and Weiss, J. H. (2012). TNF-alpha triggers rapid membrane insertion of Ca^{2+} permeable AMPA receptors into adult motor neurons and enhances their susceptibility to slow excitotoxic injury. *Exp. Neurol.* 238, 93–102. doi: 10.1016/j.expneurol.2012.08.004

Yokota, K., Kobayakawa, K., Kubota, K., Miyawaki, A., Okano, H., Ohkawa, Y., et al. (2015). Engrafted neural stem/progenitor cells promote functional recovery through synapse reorganization with spared host neurons after spinal cord injury. *Stem Cell Reports* 5, 264–277. doi: 10.1016/j.stemcr.2015.06.004

Yokota, K., Kobayakawa, K., Saito, T., Hara, M., Kijima, K., Ohkawa, Y., et al. (2017). Periostin promotes scar formation through the interaction between pericytes and infiltrating monocytes/macrophages after spinal cord injury. *Am. J. Pathol.* 187, 639–653. doi: 10.1016/j.ajpath.2016.11.010

Yokota, K., Kubota, K., Kobayakawa, K., Saito, T., Hara, M., Kijima, K., et al. (2019). Pathological changes of distal motor neurons after complete spinal cord injury. *Mol. Brain* 12:4. doi: 10.1186/s13041-018-0422-3

Yokota, K., Saito, T., Kobayakawa, K., Kubota, K., Hara, M., Murata, M., et al. (2016). The feasibility of *in vivo* imaging of infiltrating blood cells for predicting the functional prognosis after spinal cord injury. *Sci. Rep.* 6:25673. doi: 10.1038/srep25673

Yu, W. R., and Fehlings, M. G. (2011). Fas/FasL-mediated apoptosis and inflammation are key features of acute human spinal cord injury: implications for translational, clinical application. *Acta Neuropathol.* 122, 747–761. doi: 10.1007/s00401-011-0882-3

Yu, W. R., Liu, T., Fehlings, T. K., and Fehlings, M. G. (2009). Involvement of mitochondrial signaling pathways in the mechanism of Fas-mediated apoptosis after spinal cord injury. *Eur. J. Neurosci.* 29, 114–131. doi: 10.1111/j.1460-9568.2008.06555.x

Zhang, Y. W., Denham, J., and Thies, R. S. (2006). Oligodendrocyte progenitor cells derived from human embryonic stem cells express neurotrophic factors. *Stem Cells Dev.* 15, 943–952. doi: 10.1089/scd.2006.15.943

Zhou, T., Zheng, Y., Sun, L., Badea, S. R., Jin, Y., Liu, Y., et al. (2019). Microvascular endothelial cells engulf myelin debris and promote macrophage recruitment and fibrosis after neural injury. *Nat. Neurosci.* 22, 421–435. doi: 10.1038/s41593-018-0324-9

Zweckberger, K., Ahuja, C. S., Liu, Y., Wang, J., and Fehlings, M. G. (2016). Self-assembling peptides optimize the post-traumatic milieu and synergistically enhance the effects of neural stem cell therapy after cervical spinal cord injury. *Acta Biomater.* 42, 77–89. doi: 10.1016/j.actbio.2016.06.016

Conflict of Interest Statement: The authors declare that the research was conducted in the absence of any commercial or financial relationships that could be construed as a potential conflict of interest.

frontiers in Cellular Neuroscience

ORIGINAL RESEARCH
published: 24 July 2019
doi: 10.3389/fncel.2019.00338

Bone Marrow Stromal Cells Alleviate Secondary Damage in the Substantia Nigra After Focal Cerebral Infarction in Rats

Jizi Jin[1,2†], Yanyan Tang[1,2†], Kongping Li[1,2†], Xialin Zuo[1,2], Lixuan Zhan[1,2], Weiwen Sun[1,2] and En Xu[1,2]*

[1] Department of Neurology, Institute of Neurosciences, The Second Affiliated Hospital of Guangzhou Medical University, Guangzhou, China, [2] Key Laboratory of Neurogenetics and Channelopathies of Guangdong Province, Ministry of Education of China, Collaborative Innovation Center for Neurogenetics and Channelopathies, Guangzhou, China

Transplantation of bone marrow stromal cells (BMSCs) is a promising therapy for ischemic stroke. Previously, we had reported that the secondary degeneration occurred in the ipsilateral substantia nigra (SN) after permanent distal branch of middle cerebral artery occlusion (dMCAO) in Sprague-Dawley rats. However, whether BMSCs have neurorestorative effects on the secondary damage in the SN after focal cerebral infarction has not known. In this study, rats were subjected to dMCAO followed by intravenous administration of BMSCs 1 day later. We found that transplanted BMSCs survived and migrated to cortical infarct areas and ipsilateral SN. Furthermore, BMSCs promoted neurogenesis through proliferation and differentiation in the SN after dMCAO. Rats implanted with BMSCs showed significant improvement in their performance of modified neurological severity scores and adhesive-removal test. Engrafted BMSCs enhanced survival of dopaminergic neuron, reduced gliosis in the ipsilateral SN, and increased contents of dopamine (DA) and its metabolites in the ipsilateral striatum after dMCAO. With pseudorabies virus-152 as a retrograde tracer, we also demonstrated that BMSCs could effectively enhance the cortico-striatum-nigral connections. These results suggest that BMSCs transplantation exerts neurorestorative effects after cortical infarction through promoting endogenous neurogenesis, increasing contents of DA and its metabolites, alleviating the secondary neuronal damage in the SN, enhancing the cortico-striatum-nigral projections pathway, and finally improving the neurological functional outcome.

Keywords: cerebral infarction, substantia nigra, bone marrow stromal cells, secondary degeneration, neurorestoration

OPEN ACCESS

Edited by:
Francisca C. Bronfman, Pontifical Catholic University of Chile, Chile

Reviewed by:
Jiro Kasahara, Tokushima University, Japan
Francisco Javier Nualart, Universidad de Concepción, Chile

***Correspondence:**
En Xu
enxu@163.net

† These authors have contributed equally to this work

Specialty section:
This article was submitted to Cellular Neuropathology, a section of the journal Frontiers in Cellular Neuroscience

Received: *23 January 2019*
Accepted: *10 July 2019*
Published: *24 July 2019*

Citation:
Jin J, Tang Y, Li K, Zuo X, Zhan L, Sun W and Xu E (2019) Bone Marrow Stromal Cells Alleviate Secondary Damage in the Substantia Nigra After Focal Cerebral Infarction in Rats. Front. Cell. Neurosci. 13:338. doi: 10.3389/fncel.2019.00338

Abbreviations: BMSCs, bone marrow stromal cells; con, contralateral; Cor, cotrex; d, day; DA, dopamine; DAPI, 4′,6-diamidino-2-phenylindole; DCX, doublecortin; DiR^+, DiR-labeled; DiR, 1,1-dioctadecyltetramethyl indotricarbocyanine iodide; DiR^-, DiR-nonlabeled; dMCAO, distal middle cerebral artery occlusion; DOPAC, 3,4-dihydroxyphenylacetic acid; ESI, electrospray ionization; GFAP, glial fibrillary acidic protein; HPLC-MS/MS: high performance liquid chromatography-tandem mass spectrometric; HVA, homovanillic acid; ip, ipsilateral; Ki-67, nuclear-associated antigen Ki-67; MRM: multiple reaction monitoring; NeuN, neuron-specific nuclear-binding protein; NSS, neurological severity score; PRV, pseudorabies virus; Sham, sham-operated; SN, substantia nigra; SNc, substantia nigra compact par; SNr, substantia nigra pars reticulata; Str, striatum; TH, tyrosine hydroxylase; w, week.

INTRODUCTION

Stroke has been the leading cause of mortality and disability in China, the current mortality rate in China is 157 per 100,000, constituting almost 1/3 of the total number of deaths from stroke worldwide (Liu et al., 2011; Wang et al., 2017). Among the survivors about 15–30% left with permanent disability (Go et al., 2014). It has been accepted that cortical cerebral infarction leads to neuropathologic damages not only at primary lesion site, but also in nonischemic remote regions such as hippocampus, thalamus, substantia nigra (SN), distal pyramidal tract, peripheral nerves and muscles (Forno, 1983; Zhang et al., 2012; Dang et al., 2016; Zuo et al., 2016, 2018). This phenomenon is termed as post-stroke secondary degeneration. Focal cerebral infarction leads to dynamic trans-neuronal degeneration in non-ischemic remote brain regions, with the disruption of connections to synapsed neurons sustaining ischemic insults (Zuo et al., 2018). Owing to SN has extensive efferent and afferent fibers connecting with globus pallidus, ventrolateral nucleus and motor cortex, SN is a very common brain structure that is subjected to secondary degeneration after distal middle cerebral artery occlusion (dMCAO). On the other hand, SN is composed of dopaminergic neurons. It has been reported that the secondary damage in the SN after focal cerebral infarction was associated with the development of vascular Parkinson's syndrome, sustained dementia, and poor neurofunctional outcomes (Kirton et al., 2007; Jellinger, 2008; Domi et al., 2009; DeVetten et al., 2010; Rodriguez-Grande et al., 2013). Secondary degeneration of SN and the corticospinal tract in patients was demonstrated as a hyperintensity lesion within 1–4 weeks after MCA infarction on diffusion-weighted imaging or fluid-attenuated inversion recovery and T2-weighted MRI (Nakajima et al., 2010; Ohe et al., 2013). Also, the observation in monkeys from Chen et al. (2015) revealed an area of high signal in the ipsilateral SN on T2-weighted MRI at 1 week after occlusion in the distal M1 branch of MCA by electrocoagulation. Previously, we have demonstrated that secondary damage occurred in the SN after focal cortical infarction (Zuo et al., 2018). Although some acute phase therapies such as intravenous recombinant tissue plasminogen activator (rt-PA) and endovascular treatment have been shown to improve ischemic stroke outcome, these treatments are only available for a limited number of patients because of the short time window (Campbell et al., 2018; Grossberg et al., 2018). Hence, alleviating secondary neurodegeneration can be a promising target of neuroprotection and neurorestoration beyond the therapeutic time window for acute stroke.

Over the past two decades, bone marrow stromal cells (BMSCs) based neurorepair has emerged as a promising therapeutic strategy for ischemic stroke. As a class of unique, self-renewing cells, BMSCs give rise to differentiated progeny when implanted into appropriate tissues (Maria Ferri et al., 2016). The experimental studies in animal stroke models have shown that the transplantation of BMSCs improved neurofunctional outcome through cellular replacement, stimulating endogenous neurogenesis and angiogenesis, modulating inflammatory environment and reducing the formation of glial scar (Panepucci et al., 2004; Shen et al., 2006; Gutiérrez-Fernández et al., 2013; Fukuda et al., 2015).

It is well known that BMSCs can proliferate and migrate in the brain (Yano et al., 2005; Feng et al., 2017). However, there is no information on the roles of BMSCs affecting neurorestoration in the secondary nigral degeneration after cortical ischemic stroke. Thus, the present study aims to investigate whether BMSCs injected from tail vein enters the brain, migrates to the SN, and attenuates the secondary nigral degeneration following dMCAO. We also sought to examine the possible mechanism of BMSCs on the secondary nigral degeneration after focal cerebral infarction in adult rats.

MATERIALS AND METHODS

Adult, male Sprague-Dawley (SD) rats, weighing 280–320 g (10–12 weeks old) were obtained from Southern Medical University (Guangzhou, China). Rats used in the experiment were housed in a controlled environment under standard temperature (22 ± 1°C) and a 12 h light/dark cycle with free access to food and water. Weight gain and health condition of rats are comparable between different groups. All animal procedures were performed in accordance with Animal Research: Reporting *in vivo* Experiments guidelines and were approved and monitored by the Animal Care and Use Committee of Guangzhou Medical University (Guangzhou, China). All efforts had been made to minimize the suffering of animals and the number of animals used.

In this study, 189 rats were used for the experiments. One rat during the surgical procedure and 2 after surgery died in the dMCAO groups. Three rats in the vehicle groups and 1 in the BMSCs groups died during the surgical procedure. In addition, 2 rats died after injection of pseudorabies virus (PRV)-152 in the ipsilateral SNr, and 5 were excluded because neither neurologic deficit nor cortical infarction after dMCAO was observed.

Animal Model

Permanent occlusion of distal branch of middle cerebral artery was performed using an electrocoagulation methodology described previously (Tamura et al., 1981; Xing et al., 2012). In brief, rats were placed in the anesthesia induction box supplied with 3–4% isoflurane at 3 L/min in 100% oxygen. Anesthesia was maintained with 1.5–2.5% isoflurane at 800 mL/min in 100% oxygen, delivered through a nose mask (SurgiVet, Waukesha, WI, United States) during the surgical procedure. The distal striatal branch of MCA was exposed and occluded by unipolar electrocoagulation under an operating microscope. Rectal temperature of the animals was monitored and maintained at approximately 37°C throughout the procedure. Sham-operated animals were performed with the same surgical procedures except for the electrocoagulation of dMCAO. After surgery, the rats were allowed to wake up and evaluated the neurological status as described by previously (Rodriguez-Grande et al., 2013). Rats neither

with neurologic deficit nor cortical infarction were excluded from this study.

Histology

Animals were intracardially perfused with normal saline, followed by 4% paraformaldehyde (PFA) in phosphate buffer saline (PBS) (0.01 M, pH 7.4) under anesthesia with 10% chloral hydrated administered intraperitoneally (350 mg/Kg). The brains were pos-fixed for 12 h in 4% PFA and then cryoprotected with 10, 20, 30% sucrose in the same fixative overnight. Coronal tissue blocks (bregma 1.7 mm to −5.8 mm) were cut on a freezing microtome (Leica CM1950, Heidelberg, Germany) into 30 μm-thick sections. According to the standard procedure, Nissl staining was performed with 0.1% cresyl violet (MilliporeSigma, Burlington, MA, United States), and then sections were dehydrated with 90 and 100% ethanol and immersed into dimethylbenzene.

Nissl staining was used for infarct volume evaluation. Relative infarct volume was expressed as the percentage of the contralateral hemisphere (Swanson et al., 1990). Briefly, the coronal brain sections from bregma level of 1.0 mm to −1.0 mm were analyzed. Relative infarct volumes at 28 days after dMCAO were evaluated from the contralateral hemisphere volume (Vc) and ipsilateral nonischemic hemisphere volume (Vi) according to the equation (Vc-Vi)/Vc × 100%.

Immunohistochemistry

The rats were divided into four groups, sham-operated, dMCAO, vehicle and BMSCs groups for immunohistochemical experiments. Rats were euthanized at 7, 14, and 28 days after dMCAO, respectively (n = 7 in each group). Single-label immunohistochemistry was conducted by the avidin-biotin complex (ABC) peroxidase method (Zhan et al., 2010). Briefly, sections from bregma −4.52 to −6.3 mm were rinsed with 0.01 M PBS, treated with 3% H_2O_2 for 30 min, followed by 5% normal serum for 1 h at room temperature, and then incubated overnight at 4°C with primary antibodies, including rabbit polyclonal anti-nuclear-associated antigen Ki-67 (Ki-67) (1:2000, Abcam, Cat# ab15580, RRID:AB_443209), rabbit polyclonal anti-doublecortin (DCX) (1:9000, Abcam, Cat# ab18723, RRID:AB_732011), rabbit polyclonal anti-tyrosine hydroxylase (TH) (1:3000, MilliporeSigma, Cat# AB152, RRID:AB_390204), mouse monoclonal antibody anti-neuron-specific nuclear-binding protein (NeuN) (1:2000; MilliporeSigma, Cat# MAB377, RRID:AB_2298772) and rabbit polyclonal anti-glial fibrillary acidic protein (GFAP) (1:2000, MilliporeSigma, Cat# AB5804, RRID:AB_11212369). After washing three times with 0.01 M PBS, the sections were incubated with biotinylated secondary IgG antibody for 2 h at room temperature. Following washing with PBS, the sections were incubated with the ABC peroxidase for 30 min at room temperature. The peroxidase reaction was visualized with 0.05% diaminobenzidine and 0.01% hydrogen peroxide. Immunopositive cells in ipsilateral and contralateral substantia nigra compact (SNc) part were quantified in three sections of each animal. The number of immunoreactive cells for TH, NeuN, GFAP, Ki-67, and DCX was counted, respectively. Only cells with reaction products that presented within a clear border were quantified from three non-overlapping fields under a light microscope with ×200 magnification and presented as the average cell number per field on each section using ImageJ software (NIH, Bethesda, MD, United States). Data were assessed in a double-blind procedure.

Isolation and Culture of BMSCs

BMSCs were isolated and cultured as previously described (Shen et al., 2006). Healthy specific pathogen free (SPF) grade, 3 weeks old male SD rats weighing 50–100 g were soaked in 70% ethanol for 3 min, sacrificed by cervical dislocation. Fresh bone marrow was harvested aseptically from femurs and tibias by inserting a syringe fitted with 18-gauge needle into the shaft of the bone and flushing bone marrow out with a low glucose Dulbecco's Modified Eagle's Medium [LG-DMEM (Gibco, Carlsbad, CA, United States)]. Then the bone marrow was mechanically dissociated by pipetting repeatedly. Next, the cells were separated from the bone marrow by a centrifuge with 1300 rpm for 3 min and incubated with complete growth medium [LG-DMEM (Gibco) containing 10% FBS (Gibco) and 1% penicillin/streptomycin (HyClone)] at 37°C in 5% CO_2 in a sterile petri dish. After 3 days, nonadherent cells were removed by replacing the medium every three days. The adherent cells after 3–5 passages were prepared for transplantation.

Flow Cytometry Analysis

BMSCs were analyzed for the expression of a panel of antigens. Flow cytometry analysis was performed with BMSCs at five passage of culture. Cells were incubated with fluorescent isothiocyanate (FITC)-conjugated mice anti-human CD29, CD45, and phycoerythrin (PE)-conjugated mice anti-human CD34, CD44, and CD90 (1×10^6 cells/100 μL + 20 μL antibody, Becton Dickinson, Pharmingen) for phenotypic characterization. As negative controls, cells were stained with an isotype control antibody. After incubation with the antibody for 25 min, cells were washed with PBS twice and re-suspended in PBS and analyzed using flow cytometer (MoFlo XDP, Beckman Coulter, United States).

The surface antigen expression of BMSCs was identified as $CD29^+$, $CD44^+$, and $CD90^+$, $CD34^-$ and $CD45^-$ (**Supplementary Figure 1**). The lack of CD34 and CD45 expression suggested that the cell population was depleted of hematopoietic stem cells during sub cultivation by plastic adherence. Thus, the cells used in this investigation were regarded as BMSCs.

Transplantation of BMSCs

At 24 h after dMCAO, rats were randomly selected for BMSCs transplantation. After anesthetizing with 3–4% isoflurane in 100% oxygen, rats were injected slowly with approximately 4×10^6 BMSCs in 1 mL of PBS (0.01 M, pH 7.4) or PBS only as control *via* the tail vein over a 5 min period.

Labeling BMSCs With DiR and *in vivo*/*ex vivo* Cell Imaging

BMSCs were incubated with 10 μM DiR-PBS (PH7.4) for 30 min at 37°C according to the protocol of Xeno-Light 1, 1-dioctadecyltetramethyl indotricarbocyanine iodide (DiR) (Caliper Lifesciences). At 1 day after dMCAO, rats were injected slowly with approximately 4×10^6 BMSCs-DiR$^+$ (DiR-labeled) or BMSCs-DiR$^-$ (DiR-nonlabeled) in 1 mL of PBS *via* the tail vein under anesthesia with 3–4% isoflurane in 100% oxygen. At 2 h, and 1, 7, 14 days after transplantation, the rats were completely anesthetized with chloral hydrate, *in vivo* their fluorescence imaging were monitored to assess bio-distribution of DiR$^+$ or DiR$^-$ labeled BMSCs by Xenogen IVIS Spectrum imaging system (PerkinElmer, MA, United States) under 745 nm of excitation and 800 nm of emission. Coronal brain slices, 2 mm thick, were obtained using a brain slicer for *ex vivo* imaging. Fluorescent images of each sample including cortex (−0.4 mm from bregma) and SN (−5.3 mm from bregma) were analyzed and overlaid using Living Image software (Xenogen, Alameda, CA, United States). DiR fluorescence intensity which was presented as an average radiant efficiency was plotted in units of the maximum number of photons per second per centimeter square per steradian (p/s/cm^2/sr) (Ruan et al., 2012).

Behavioral Testing

The behavioral tests were performed at 1, 4, 8, 12, 16, 20, 24, and 28 days after dMCAO by an investigator who was blinded to the experimental groups. All rats were familiarized with the testing environment before surgery. In the adhesive removal test, a piece of adhesive paper sized 200 mm^2 was placed onto the contralesional forepaw (Schallert and Whishaw, 1984; Bouet et al., 2009). The rat performance was assessed by measuring the time needed sense and to remove the adhesives. The time to remove each stimulus from forelimbs was recorded on 3 trials/day. Individual trial was separated by at least 3 min. Before surgical procedure, the animals were trained 1 trial/d for 5 days. Once the rats were able to remove the tape within 2 min, they were subjected to dMCAO. In addition, neurological function was assessed by modified neurological severity scores (NSS) which is a composite of motor, sensory, reflex, and balance tests graded on a scale of 0–18 (normal score, 0; maximal deficit score, 18) (Chen et al., 2001).

Retrograde Pseudorabies Virus Tracing

In this study, retrograde tracing were employed to label the neurons between the infarct cortex and the ipsilateral SN. The attenuated (Bartha) strain of PRV-152, which was constructed to express EGFP (a gift from Enquist L. W., Princeton University), was used. PRV-152 viruses were grown in pig kidney (PK15) cells and stored at -80°C. The final titers deters determined in PK15 cells were $1 \times 10^{8-9}$ PFU for PRV-152 (Xu et al., 2006). Under anesthesia with 3–4% isoflurane, 3 μL PRV-152 was injected to the ipsilateral SNr of rats (5.4 mm posterior to the bregma, 2.1 mm lateral to the midline, and 8.3 mm below the dura) stereotactically at 7 days of dMCAO. The needle was left in place for an additional 30 min before it was removed. A fresh stock of virus was thawed for each injection.

Immunofluorescence

Triple-fluorescent immunohistochemistry was performed as previously described (Zuo et al., 2018). Sections were pre-incubated with 5% normal goat serum (containing 0.2% Triton X-100) for 1 h at room temperature, and then incubated overnight at 4°C with mixtures of primary antibodies: rabbit anti-GFP (1:800, MilliporeSigma, Cat# MAB3580, RRID:AB_2313783), rabbit polyclonal anti-Ki-67 (1:1000, Abcam, Cat# ab15580, RRID:AB_443209), rabbit polyclonal anti-DCX (1:5000, Abcam, Cat# ab18723, RRID:AB_732011) and mouse monoclonal antibody anti-NeuN (1:1000; MilliporeSigma, Cat# MAB377, RRID:AB_2298772). After rinsing in 0.01 M PBS, the sections were incubated for 1 h at room temperature with the following secondary antibodies: Cy3-conjugated goat anti-mouse IgG antibody (1:100; MilliporeSigma, Cat# AP124C, RRID:AB_11213281) and FITC-conjugated goat anti-rabbit antibody (1:100; MilliporeSigma, Cat# AP307F, RRID:AB_92652). Then, sections were PBS-washed and mounted with mounting medium containing 4′, 6-diamidino-2-phenylindole (DAPI). Slides were analyzed with a confocal laser microscope (Leica Microsystems, Wetzlar, Hessen, Germany).

Determination of Dopamine, 3, 4-Dihydroxyphenylacetic Acid, and Homovanillic Acid Concentrations in the Striata

Rats were anesthetized with 10% chloral hydrate (3.5 mg/kg, i.p.) and perfused transcardially with normal saline. According to previous study (Jackson-Lewis and Przedborski, 2007), the striata were removed quickly (within 30 s) from rats after dMCAO with or without BMSCs transplantation and placed immediately into ice-cold saline before being stored at -80°C for high performance liquid chromatography-tandem mass spectrometric (HPLC-MS/MS) analysis.

According to the protocol described by Man et al. (2019), the concentrations of dopamine (DA), 3, 4-dihydroxyphenylacetic acid (DOPAC), and homovanillic acid (HVA) in the striata were analyzed by HPLC-MS/MS (1290-6460C, Agilent Technologies, CA, United States) in National Analytical Center of China (NACC), Guangzhou. Briefly, the striata were extracted in 2 mL of 100% methanol by homogenizer and centrifuged at 4500 *g* for 5 min at 4°C. This process was repeated for 3 times. The supernatant was transferred to clean vials and evaporated to dryness under thermostat water bath at 80°C, and then reconstituted in 500 μL of 20% methanol, followed by thoroughly filtered through microporous membrane filters (0.22 μm) prior to analysis. Reference samples of DA, DOPAC and HVA were obtained from Sigma-Alorich (St. Louis, MO, United States). The samples were placed in an Agilent G1367A well plate autosampler and were chilled to 4°C. A 5 μL aliquot of sample was injected an InfinityLab Poroshell 120 Phenyl Hexyl column (4.6 × 50 mm, 2.7 μm column (Agilent Technologies, CA, United States) with a C18 Security Guard Cartridges (2.0 mm × 4.0 mm, Phenomenex,

CA, United States). The mobile phase A was acetonitrile, and B was 0.1% formic acid aqueous solution. For DA, the initial mobile phase was consisted of mobile phase A and B (3:97, *v/v*), increased to 90% mobile phase A at 2.1 min and kept for 1.4 min. Then the mixture was reversed back to 3% mobile phase A at 3.6 min and kept for 1.4 min. For DOPAC and HVA, the initial mobile phase was consisted of mobile phase A and B (5:95, *v/v*), increased to 95% mobile phase A at 3.5 min and kept for 1.5 min. Then the mixture was reversed back to 5% mobile phase A at 5.1 min and kept for 0.9 min. Mass spectrometric analysis for DA was operated in the positive electrospray ionization (ESI) mode, while the analysis for DOPAC and HVA was in the negative ESI mode (Agilent Technologies, CA, United States). Quantification of the analyte was achieved by multiple reaction monitoring (MRM) with the transitions of *m/z* 153.9–136.9, 167–123, and 181–137 for DA, DOPAC and HVA, respectively. Data were analyzed using Agilent Mass Hunter (Agilent Technologies, CA, United States) with results in tissue expressed in ng/mg.

Data Analyses

All compared data are expressed as mean ± SD. and analyzed using SPSS 13.0 (SPSS, Inc., Chicago, IL, United States). Statistical significance was determined by two-tailed Student's *t*-test or one-way ANOVA, followed by LSD or Tamhane's T2 *post hoc* test. $p < 0.05$ was considered statistically significant.

RESULTS

Secondary Degeneration Was Observed in the Ipsilateral Substantia Nigra After Focal Cortical Infarction

Progressive neuronal damage in the ipsilateral SNc was characterized by the reduced numbers of TH^+ and $NeuN^+$ cells after dMCAO (**Figure 1**). Compared with the sham-operated group, the numbers of TH^+ cells at 1, 2, and 4 weeks were significantly decreased in the ipsilateral and contralateral SNc after dMCAO (**Figures 1AVI,X,XIV,BI**), but this decrease in the ipsilateral SNc was more obvious. Compared to the contralateral and sham-operated groups, the number of $NeuN^+$ cells in the ipsilateral SNc displayed a significant reduction after dMCAO (**Figures 1AVII,IX,XV,BII**). On the contrary, the number of $GFAP^+$ cells in the ipsilateral SNc was increased as early as in the first week, peaking at 4 weeks after dMCAO compared with the contralateral and sham-operated groups. These astrocytes cells were characterized by their typical hypertrophic shape with thickened process (**Figures 1AVIII,XII,XVI,BIII**).

Transplanted Bone Marrow Stromal Cells Migrated to the Ipsilateral Cortex and Substantia Nigra After Focal Cortical Infarction

Biodistribution of BMSCs-DiR^+ was monitored within 14 days by IVIS imaging system. The *in vivo* fluorescence imaging showed that the transplanted BMSCs-DiR^+ could migrate from peripheral blood to the ipsilateral brain after dMCAO (**Figure 2A**). The *ex vivo* fluorescence imaging demonstrated that BMSCs-DiR^+ mainly existed in the ipsilateral cortex and SN (**Figure 2B**). Within the BMSCs-DiR^+ transplanted dMCAO groups, there were no significant differences in the fluorescence intensities in the ipsilateral cortex and SN across all time points except the first day post-transplantation intravenously. No fluorescent signals were detected in the brain region of BMSCs-DiR^- groups both *in vivo* and *ex vivo* (**Figure 2C**). These results illustrated that intravenous transplanted BMSCs can migrate to the ipsilateral cortex and SN after focal cortical infarction.

Transplanted Bone Marrow Stromal Cells Enhanced Neurogenesis in the Ipsilateral Substantia Nigra After Focal Cortical Infarction

Immunohistochemical study showed that the Ki-67^+ and DCX^+ cells in sham-operated group were expressed in SNc (**Figures 3AI–III**), and these cells in the ipsilateral SNc stained deeply both in vehicle and BMSCs groups at 2 days after dMCAO (**Figures 3AV–IX**). In contrast to the sham-operated group, the number of Ki-67^+ cell was significantly increased in the ipsilateral SNc at 2 days, and 1, 2, and 4 weeks after dMCAO with or without BMSCs transplantation, and it also increased in the contralateral SNc at 1, 2, and 4 weeks after dMCAO with or without BMSCs transplantation. Notably, BMSCs transplantation increased obviously the number of Ki-67^+ cells in the ipsilateral SNc at 2 days, 1, 2, and 4 weeks after dMCAO when compared with vehicle groups (**Figure 3B**). Similarly, in comparison with the sham-operated group, the number of DCX^+ cells in the ipsilateral SNc was increased at 2 days, 1, 2, and 4 weeks post-dMCAO. Furthermore, transplantation with BMSCs apparently increased the number of DCX^+ cells in the ipsilateral SNc at 2 days, 2 and 4 weeks when compared with vehicle groups (**Figure 3C**). In comparison to the contralateral SNc, the number of ipsilateral BMSCs-DiR^+ cells was significantly increased, with a peak at 2 days after dMCAO (**Figure 3D**). In addition, in the BMSCs group, the triple-labeled immunofluorescence assay showed that BMSCs-DiR^+ cells colocalized with Ki-67^+, DCX^+, and TH^+ cells in the ipsilateral SN at 1 week after dMCAO (**Figures 3EI–XII**). These results indicated that transplanted BMSCs could proliferate and differentiate into mature neurons in the SN after dMCAO and stimulate endogenous neurogenesis.

Transplanted Bone Marrow Stromal Cells Improved the Neurological Functional Outcome After Focal Cortical Infarction

The schematic diagram in **Figure 4A** represented that cortical infarction marked with arrowhead was induced by dMCAO and the secondary damage of ipsilateral SN marked with asterisk occurs after dMCAO. Nissl-staining assay in **Figure 4B** clearly showed that ischemic foci were confined within the cortex at 4 weeks after dMCAO. The relative infarction volumes at 4 weeks after dMCAO were evaluated in **Figure 4C**. There was no significant difference in the relative infarct volume between BMSCs and vehicle treatment groups after dMCAO. To assess

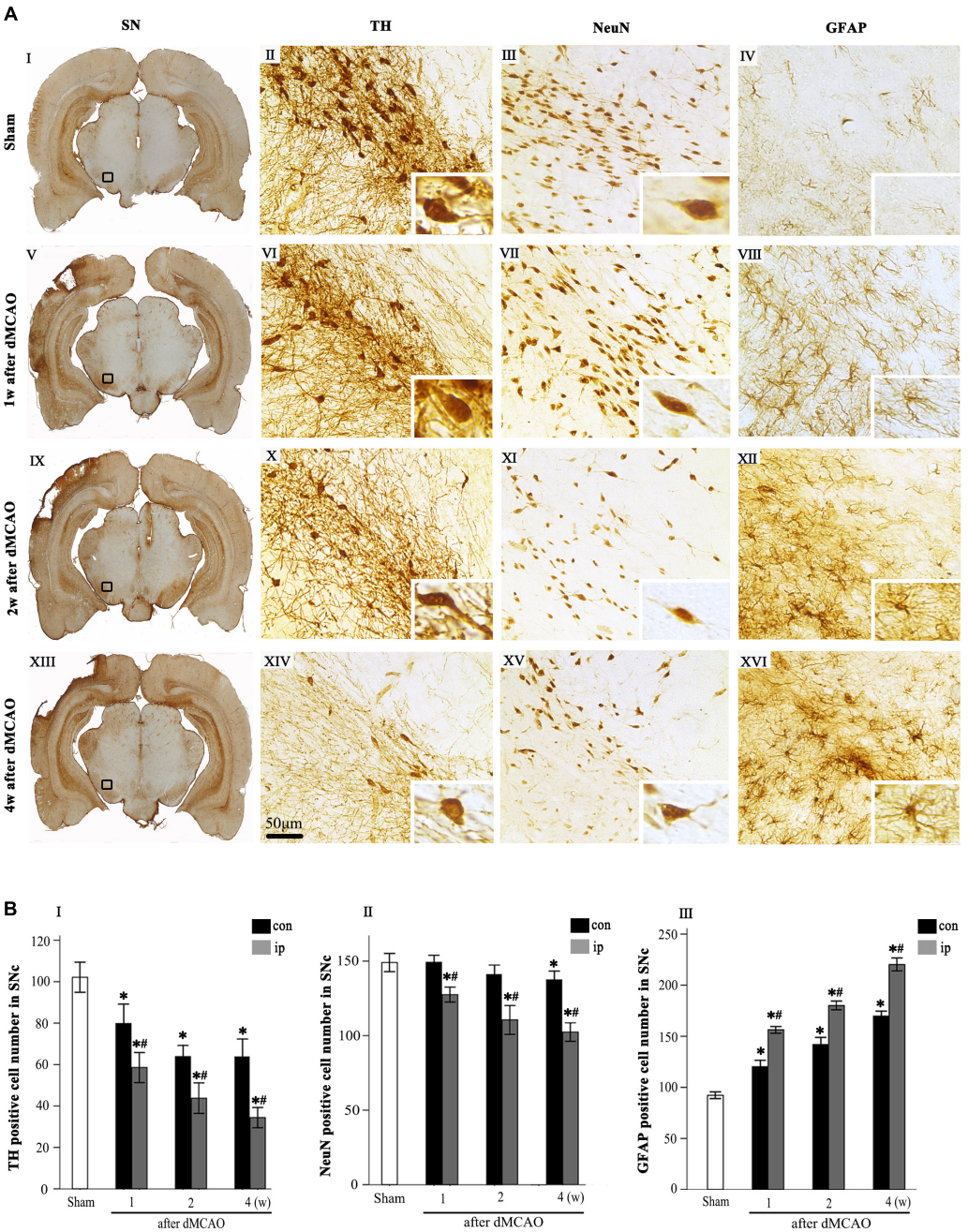

FIGURE 1 | Secondary degeneration in the ipsilateral SN after dMCAO in rats. **(A)** Representative microphotographs of immunohistochemistry for TH **(II,VI,X,XIV)**, NeuN **(III,VII,XI,XV)** and GFAP **(IV,VIII,XII,XVI)** in SNc at 1 week **(V–VIII)**, 2 weeks **(IX–XII)**, and 4 weeks **(XIII–XVI)** after dMCAO and sham-operated groups **(I–IV)**. The pictures on the right are magnified from the square area on the left. Scale bar, 50 μm. **(B)** Quantitative analyses of TH^+ **(I)**, $NeuN^+$ **(II)**, and $GFAP^+$ **(III)** cells in the SNc at 1, 2, and 4 weeks after dMCAO. Quantitative analyses showed that dMCAO decreased the number of TH^+ cells in the ipsilateral [$F_{(3,101)} = 94.59$, $p < 0.01$] and contralateral SNc [$F_{(3,101)} = 25.78$, $p < 0.01$], and $NeuN^+$ cells in the ipsilateral SNc [$F_{(3,83)} = 38.19$, $p < 0.01$], and increased the number of $GFAP^+$ cells in the ipsilateral SNc [$F_{(3,122)} = 638.85$, $p < 0.01$] at 1, 2, and 4 weeks. Each bar represents the mean ± SD ($n = 6$ in each group). $^*p < 0.05$ vs. sham-operated group; $^\#p < 0.05$ vs. contralateral groups at the same time point. SN, substantia nigra; SNc, substantia nigra compact part; TH, tyrosine hydroxylase; NeuN, neuron-specific nuclear-binding protein; GFAP, glial fibrillary acidic protein; Sham, sham-operated; w, week; dMCAO, distal middle cerebral artery occlusion.

the long-term functional deficits and possible recovery with or without transplanted BMSCs treatment after dMCAO, the adhesive-removal test and NSS were carried out. The mean time to remove the adhesive from the forepaws was significantly shorter in the BMSCs group than that in the vehicle group after 16 days of dMCAO (**Figure 4D**). Furthermore, compared with

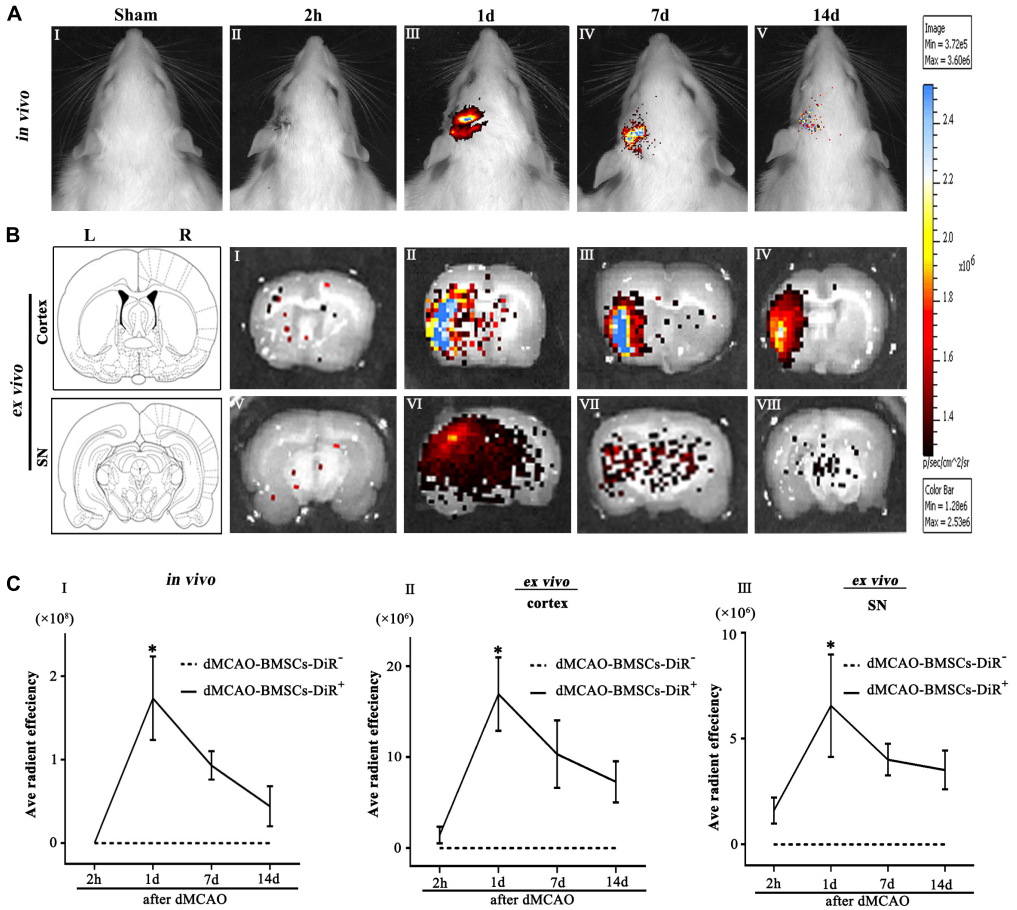

FIGURE 2 | Transplanted BMSCs migrate to the ipsilateral SN after dMCAO in rats. **(A)** The *in vivo* fluorescence images of migrated BMSCs-DiR$^+$ in the brain at 2 h and 1, 7, 14 days post-intravenous transplantation following focal cortical infarction. **(B)** The *ex vivo* fluorescence images of migrated BMSCs-DiR$^+$ in the cortex **(I–IV)** and SN **(V–VIII)** at 2 h and 1, 7, 14 days post-intravenous transplantation following focal cortical infarction. **(C)** Quantitative analyses (*in vivo* and *ex vivo*) of migrated BMSCs-DiR$^+$ in the brain **(I)**, cortex **(II)**, and SN **(III)** at 2 h and 1, 7, 14 days post-intravenous transplantation following focal cortical infarction. Compared with the sham-operated group, the fluorescence intensities of BMSCs-DiR$^+$ groups both *in vivo* [$F_{(4,25)} = 7.67$, $p < 0.01$] and *ex vivo* [cortex: $F_{(4,25)} = 6.58$, $p < 0.01$, SN: $F_{(4,25)} = 4.09$, $p < 0.05$] were significantly increased. *$p < 0.05$ vs. BMSCs-DiR$^-$ group ($n = 7$ in each group). Sham, sham-operated; h, hour; d, day; w, week; L, left; R, right; SN, substantia nigra; dMCAO, distal middle cerebral artery occlusion; BMSCs, bone marrow stromal cells; DiR (1,1-dioctadecyltetramethyl indotricarbocyanine iodide); DiR$^+$, DiR-labeled; DiR$^-$, DiR-nonlabeled.

the vehicle group, rats in the BMSCs group exhibited higher NSS after 16 days of dMCAO (**Figure 4E**). These data suggest that BMSCs treatment could improve the neurological functional outcome after dMCAO.

Transplanted Bone Marrow Stromal Cells Reduced Secondary Neuronal Damage in the Ipsilateral Substantia Nigra After Focal Cortical Infarction

To determine whether transplanted BMSCs offer neuroprotection in the ipsilateral SN after focal cortical infarction, neuronal damage and astrocytic activation were evaluated in the SNc at 1 and 4 weeks after dMCAO, respectively. Compared with sham-operated and contralateral groups, the numbers of TH$^+$ and NeuN$^+$ cells were significantly decreased, while GFAP$^+$ cells were increased in the ipsilateral SNc at 1 and 4 weeks after dMCAO. As expected, after BMSCs treatment, the numbers of TH$^+$ cell at 4 weeks and NeuN$^+$ cell at 1 and 4 weeks were evidently increased in the ipsilateral SNc and GFAP$^+$ cell were decreased at 1 and 4 weeks after dMCAO when compared to vehicle groups (**Figures 5A,B**). Furthermore, we detected the concentrations of DA and its metabolites, DOPAC and HVA, in the striata at 1 and 4 weeks after dMCAO with or without BMSCs treatment. Compared with sham-operated and contralateral groups, the concentration of DA was significantly decreased in the ipsilateral striatum at 1 week after dMCAO. Transplantation of BMSCs apparently increased the concentration of DA in the ipsilateral striata at 1 and 4 weeks after dMCAO (**Figure 5CI**). Similarly, the concentrations of DOAPC and HVA were significantly decreased in the ipsilateral striatum at 1 week after dMCAO when compared with sham-operated and contralateral groups. As expected, transplantation of BMSCs prevented the decline

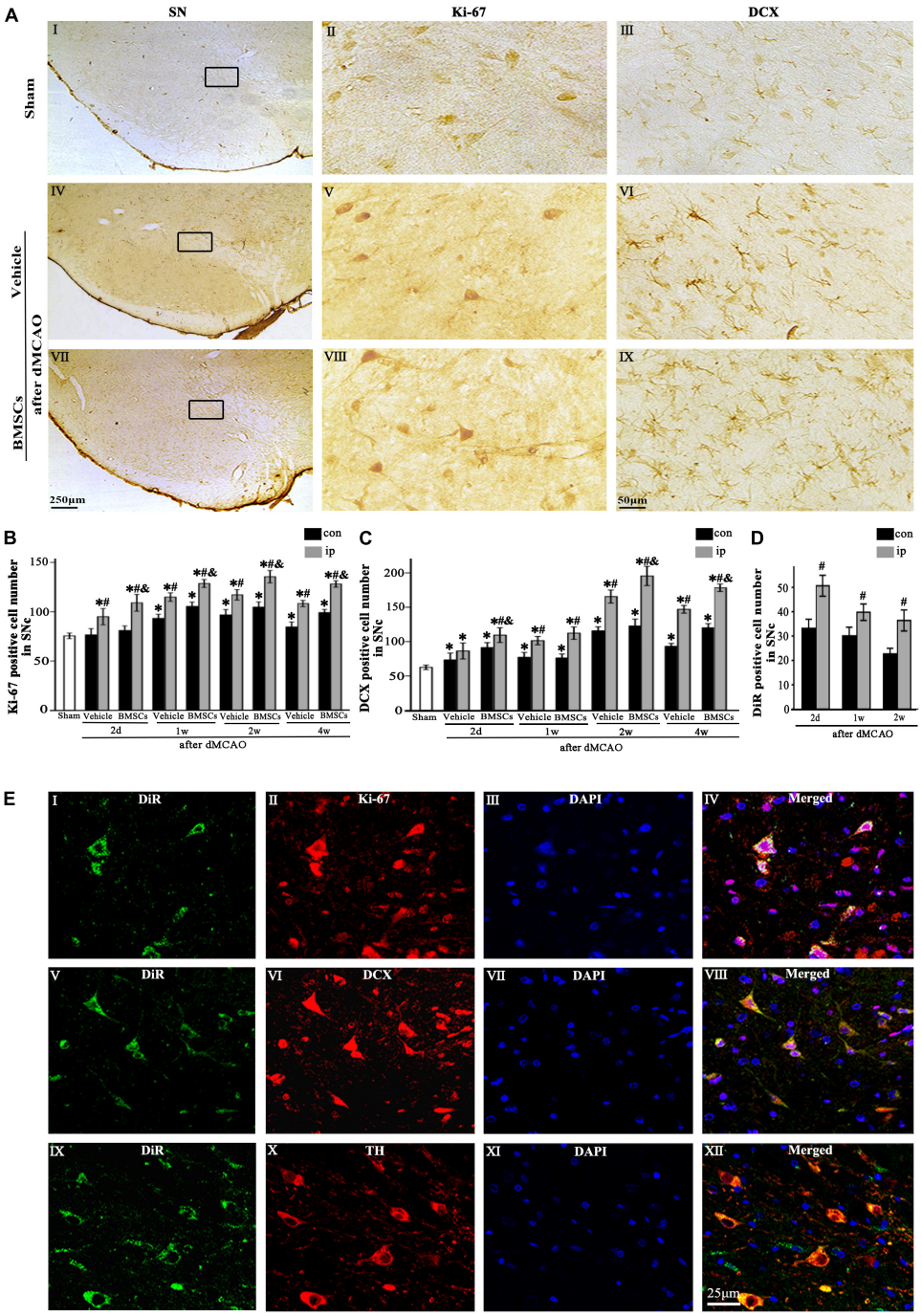

FIGURE 3 | The proliferation and differentiation of BMSCs in SNc after dMCAO. **(A)** Representative microphotographs of immunohistochemistry for Ki-67 and DCX in SN after dMCAO with or without BMSCs transplantation. **(I–III)** Sham group; **(IV–VI)** vehicle group at 2 days after dMCAO; **(VII–IX)** BMSCs group at 2 days after dMCAO; **(B,C)** Quantitative analyses of Ki-67$^+$ and DCX$^+$ cells in SNc at 2 days, 1, 2, and 4 weeks after dMCAO. BMSCs transplantation increased the numbers of Ki-67$^+$ cell [$F_{(4,106)} = 90.12$, $p < 0.01$] and DCX$^+$ cell [$F_{(4,106)} = 154.17$, $p < 0.01$] in the ipsilateral SNc after dMCAO). **(D)** Quantitative analyses of DiR$^+$ cells in SNc at 2 days, 1 and 2 weeks after dMCAO. The number of ipsilateral BMSCs-DiR$^+$ cells was significantly increased after dMCAO [$F_{(2,57)} = 13.93$, $p < 0.01$]. **(E)** Representative images of fluorescent staining of BMSCs-DiR$^+$ (**I,V,IX,** green) and Ki-67 (**II**, red), DCX (**VI**, red), TH (**X**, red) and DAPI (**III,VII,XI**, blue) in SNc with BMSCs transplantation at 1 week after dMCAO. The overlapped images showed that DiR$^+$ BMSCs were colocalized with Ki-67$^+$, DCX$^+$, and TH$^+$ cells, respectively at 1 week after dMCAO **(IV,VIII,XII)**. Scale bar: A, **I, IV, VII,** 250 μm; **II, III, V, VI, VIII, IX**, 50 μm; **(E)**, 25 μm. Data are represented with mean ± S.D. $^*p < 0.05$ vs. sham-operated group, $^\#p < 0.05$ vs. contralateral groups at the same time point and $^\&p < 0.05$ vs. ipsilateral vehicle groups ($n = 6$ in each group). SN, substantia nigra; SNc, substantia nigra compact part; DCX, doublecortin; Sham, sham-operated; BMSCs, bone marrow stromal cells; con, contralateral; ip, ipsilateral; d, day; w, week; dMCAO, distal middle cerebral artery occlusion, DiR (1,1-dioctadecyltetramethyl indotricarbocyanine iodide), Ki-67, nuclear-associated antigen Ki-67; DAPI, 4',6- diamidino-2-phenylindole; TH, tyrosine hydroxylase.

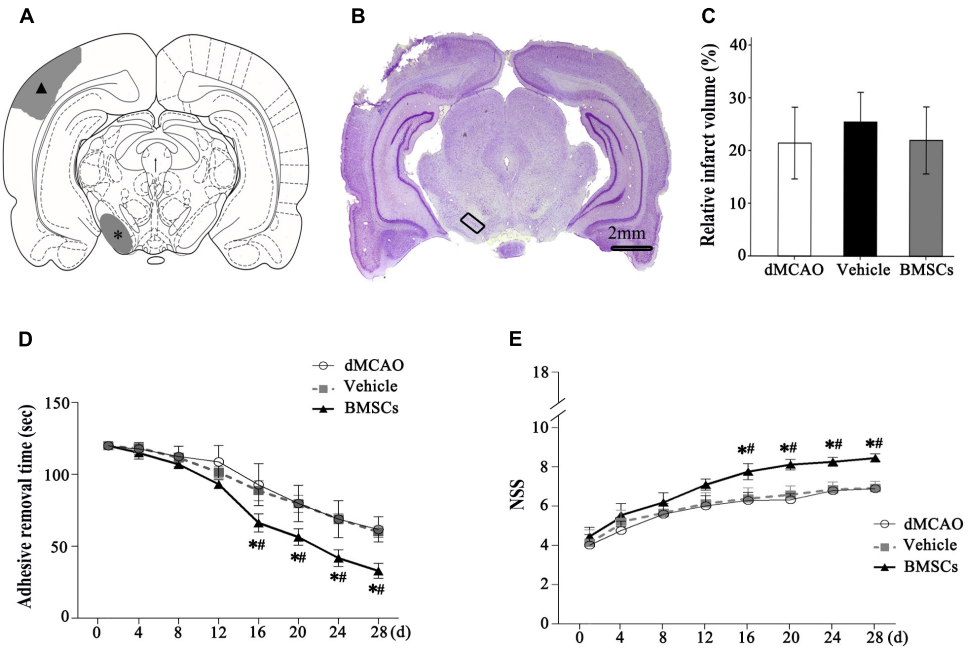

FIGURE 4 | Relative infarct volume and neurological functional evaluations with or without BMSCs transplantation after dMCAO in rats. **(A)** Schematic diagram of cortical infarction (marked with arrowhead) and ipsilateral SN (marked with asterisk). **(B)** Nissl-stained coronal brain sections of focal cortical infarction at 4 weeks after dMCAO. The infarcted tissue appeared white, while the intact tissue is colored. The ipsilateral SN was marked with quadrangle. **(C)** Quantitative analyses of relative infarct volume at 4 weeks after dMCAO. There was no significant difference in the relative infarct volume among dMCAO, vehicle and BMSCs groups [$F_{(2,18)} = 0.478$, $p > 0.05$]. **(D)** Adhesive removal test at 1–4 weeks after cortical infarction. Quantitative analyses showed that transplantation of BMSCs reduced the mean time to remove the adhesive from the forepaws after dMCAO [$F_{(2,\ 19)16\ d} = 16.87$, $p < 0.01$; $F_{(2,19)20\ d} = 19.76$, $p < 0.01$; $F_{(2,19)24\ d} = 30.14$, $p < 0.01$; $F_{(2,22)\ 28\ d} = 52.75$, $p < 0.01$]. **(E)** NSS at 1–4 weeks after dMCAO. Quantitative analyses showed that transplantation of BMSCs raised NSS after dMCAO [$F_{(2,19)\ 16\ d} = 22.08$, $p < 0.01$; $F_{(2,19)20\ d} = 54.54$, $p < 0.01$; $F_{(2,19)24\ d} = 60.91$, $p < 0.01$; $F_{(2,18)\ 28\ d} = 79.67$, $p < 0.01$]. $^{*}p < 0.05$ vs. dMCAO groups, $^{\#}p < 0.05$ vs. vehicle groups ($n = 7$ in each group). dMCAO, distal middle cerebral artery occlusion; BMSCs, bone marrow stromal cells; NSS, neurological severity score; d, day.

of the concentration of DOAPC and HVA in the ipsilateral striatum at 1 week after dMCAO (**Figures 5CII,III**). These data showed that BMSCs transplantation could mitigate the secondary damage through promoting dopaminergic neuronal survival and alleviating astrocytic activation, thereby increasing contents of DA and its metabolites, in the ipsilateral SN after dMCAO.

Transplanted Bone Marrow Stromal Cells Enhanced the Cortico-Striatum-Nigral Connections After Focal Cortical Infarction

To investigate whether BMSCs transplantation enhanced cortico-striatum-nigral connection after dMCAO, PRV-152 for retrograde tracing was injected stereotaxically to the ipsilateral SN with or without BMSCs transplantation at 7 days of dMCAO (**Figure 6**). **Figure 6A** is the schematic diagram showed that PRV-152 was injected to the ipsilateral SNr of rats, and the regions of interest of cortex, striatum and SNr. After PRV-152 was injected into the ipsilateral SNr, PRV-152 would reach to the regions of interest aforementioned by the way of retrograde axoplasmic transport in sham-operated and dMCAO groups (**Figure 6B**). PRV-152^{+} staining in the ipsilateral cortex, striatum and SNr were detected by immunofluorescence assay. **Figures 6C–E** showed that PRV-152^{+} cells were characterized by PRV-152^{+} staining around the nucleus (**Figures 6C–E**). In sham-operated rats, few PRV-152^{+} cells were visible in the ipsilateral cortex, striatum and SNr (**Figures 6CI–XII**). In the vehicle group, PRV-152^{+} cells mainly distributed in the ipsilateral cortex, at 4 weeks after focal cortical infarction (**Figures 6DI–XII**). Importantly, compared with sham-operated and vehicle groups, the number of PRV-152^{+} cells in BMSCs treatment group was obviously increased in the ipsilateral cortex, striatum and SNr at 4 weeks after focal cortical infarction (**Figures 6EI–XII,F**). These results suggested that the intravenous transplantation of BMSCs potentially enhanced cortico-striatum-nigral connections after dMCAO.

DISCUSSION

In this study, we confirmed that transplanted BMSCs intravenously could migrate to the ipsilateral SN in adult SD rats after dMCAO. BMSCs transplantation significantly improved neurological functional outcome and attenuated the secondary nigral degeneration following focal cerebral ischemia. In addition, BMSCs enhanced neurogenesis in the ipsilateral SN and cortico-striatum-nigral connections after focal cortical infarction. To our knowledge, this is the first

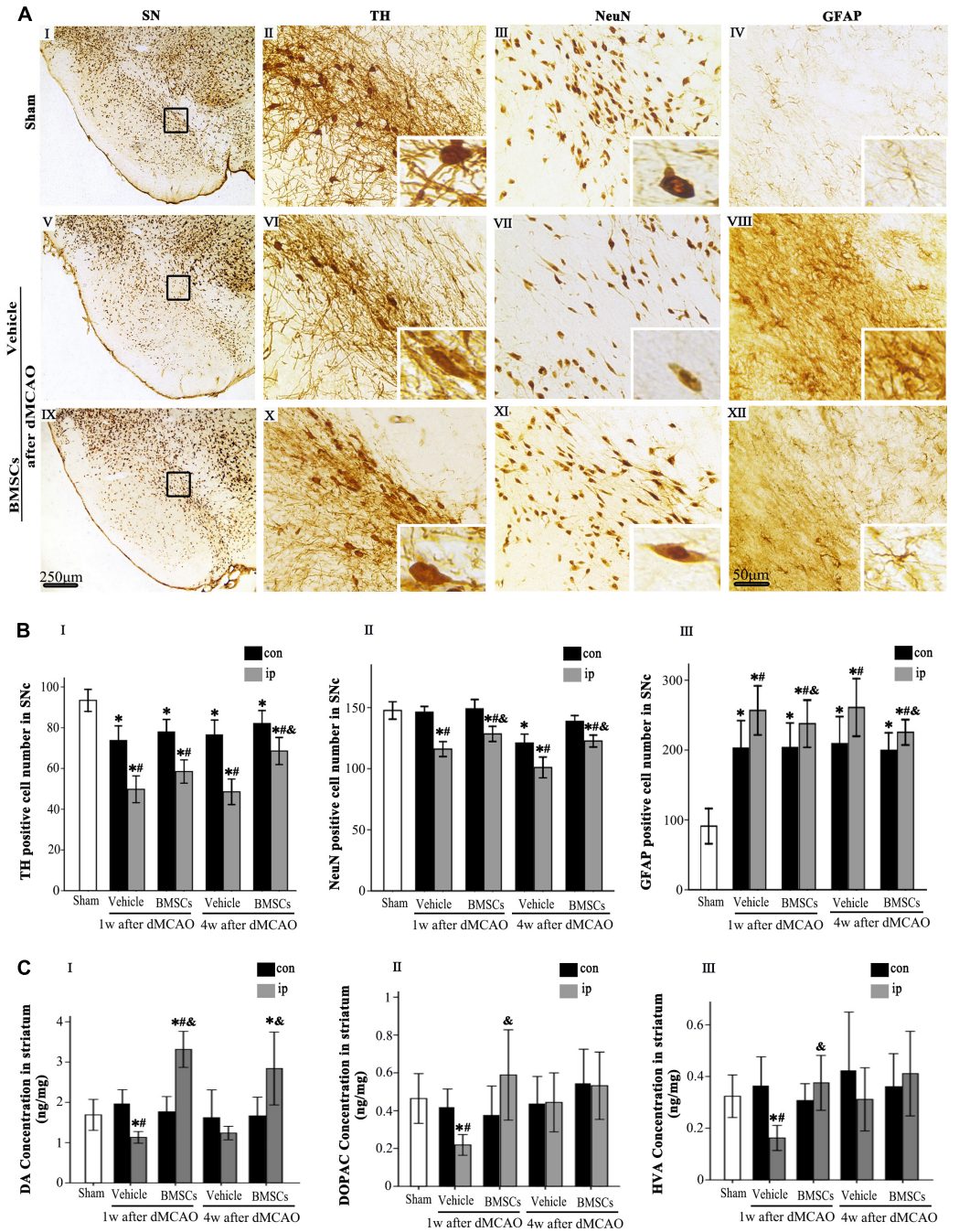

FIGURE 5 | Effects of BMSCs treatment on the number of TH, NeuN, and GFAP positive cells in SN, and DA and its metabolites in striatum at 4 weeks after dMCAO. **(A)** Representative microphotographs of immunohistochemistry for TH **(II,VI,X)**, NeuN **(III,VII,XI)**, and GFAP **(IV,VIII,XII)** in SN. The pictures on the right are magnified from the square area on the left. Scale bar: **I, V, IX,** 250 μm; **II–IV, VI–VIII, X–XII,** 50 μm. **(B)** Quantitative analyses of TH, NeuN, GFAP-positive cells in the SNc at 1 and 4 weeks after dMCAO. Transplantation of BMSCs increased the numbers of TH^+ [$F_{(2,60)} = 31.51$, $p < 0.01$] and $NeuN^+$ cells [$F_{(2,78)} = 17.20$, $p < 0.01$], and decreased the number of $GFAP^+$ cells [$F_{(2,78)} = 1848.10$, $p < 0.01$] in the ipsilateral SNc after dMCAO. Each bar represents the mean ± S.D. $^*p < 0.05$ vs. sham-operated group, $^\#p < 0.05$ vs. contralateral groups at the same time point and $^\&p < 0.05$ vs. ipsilateral vehicle groups ($n = 6$ in each group). **(C)** The DA **(I)**, DOPAC **(II)**, and HVA **(III)** concentrations in striata at 1 and 4 weeks after dMCAO with or without BMSCs transplantation. Transplantation with BMSCs increased the concentration of DA [$F_{(2,8)} = 6.33$, $p < 0.05$] in the ipsilateral striatum after dMCAO, maintained the concentration of DOPAC [$F_{(2,11)} = 0.53$, $p > 0.05$] and HVA [$F_{(2,\ 11)} = 0.67$, $p > 0.05$] in the ipsilateral striatum after dMCAO. Each bar represents the mean ± SD $^*p < 0.05$ vs. sham-operated group and $^\#p < 0.05$ vs. contralateral groups at the same time point and $^\&p < 0.05$ vs. ipsilateral vehicle groups ($n = 4$ in each group). SN, substantia nigra; SNc, substantia nigra compact part; TH, tyrosine hydroxylase; NeuN, neuron-specific nuclear-binding protein; GFAP, Glial fibrillary acidic protein; Sham, sham-operated; BMSCs, bone marrow stromal cells; DA, dopamine; DOPAC, 3,4-dihydroxyphenylacetic acid; HVA, homovanillic acid; con, contralateral; ip, ipsilateral; w, week; dMCAO, distal middle cerebral artery occlusion.

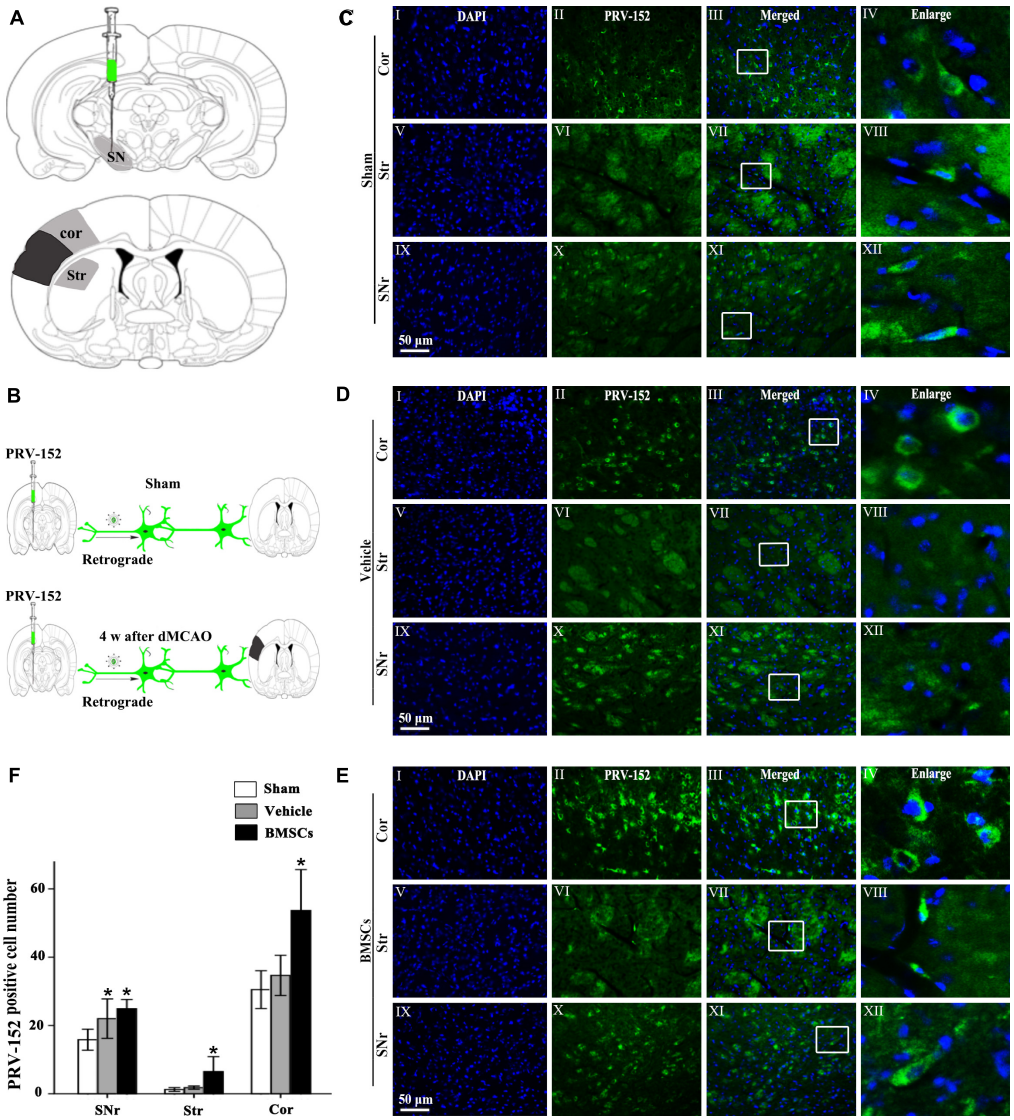

FIGURE 6 | Cortico-striatum-nigral tract retrograde tracing with PRV-152. **(A)** PRV-152 was injected into the ipsilateral SNr. Regions of interest (ROI) of PRV-152 positive cell counting were shown. Dark shaded area represents ischemic region after dMCAO; lighter shaded area represents ROI. **(B)** Schematic illustration of the fluorescent signal of PRV-152 in sham-operated and dMCAO groups with or without BMSCs transplantation after PRV-152 was injected into the ipsilateral SNr. **(C)** Representative photographs of fluorescent double staining of PRV-152 (green) and DAPI (blue) in the ipsilateral cortex **(I–IV)**, striatum **(V–VIII)** and SNr **(IX-XII)** at 4 days after PRV-152 injection in sham-operated group. **(D)** Representative photographs of fluorescent double staining of PRV-152 (green) and DAPI (blue) in the ipsilateral cortex **(I–IV)**, striatum **(V–VIII)**, and SNr **(IX–XII)** at 4 weeks after PRV-152 injection in vehicle group. **(E)** Representative photographs of fluorescent double staining of PRV-152 (green) and DAPI (blue) in the ipsilateral cortex **(I–IV)**, striatum **(V–VIII)** and SNr **(IX–XII)** at 4 weeks after PRV-152 injection in BMSCs group. Scale bar, 50 μm. **(F)** Quantitative analyses of PRV-152$^+$ cell number in the ipsilateral cortex, striatum and SNr after dMCAO. Transplantation with BMSCs increased PRV-152$^+$ cells in the ipsilateral cortex [$F_{(2,19)} = 9.85$, $p < 0.01$], striatum [$F_{(2,\ 41)} = 10.67$, $p < 0.01$] and SNr [$F_{(2,\ 19)} = 6.05$, $p < 0.01$] after dMCAO. Each bar represents the mean ± SD $^*p < 0.05$ vs. sham-operated group and $^{\#}p < 0.05$ vs. vehicle group ($n = 7$ in each group). SNr, substantia nigra pars reticulata; Cor, cortex; Str, striatum; PRV, pseudorabies virus; Sham, sham-operated; w, week; dMCAO, distal middle cerebral artery occlusion; BMSCs, bone marrow stromal cells; DAPI, 4', 6- diamidino-2-phenylindole.

report that BMSCs transplantation exerts neuroprotective effects against the secondary damage in the SN after focal cerebral infarction.

After focal cerebral infarction in the dMCAO territory, neuronal death, axonal degeneration, gliosis and marked atrophy have been found in the ipsilateral thalamus, SN, distal pyramidal tract and so on (Tamura et al., 1990; Zhang et al., 2012). Being not directly affected by primary ischemic lesion, the midbrain SN has been a suitable site to study remote lesion after cortical ischemic stroke. SN is densely composed of dopaminergic neurons. As a marker of dopaminergic neurons, TH was employed to investigate neuronal loss within the region in this study. We found the obvious losses of nigral TH$^+$ and NeuN$^+$ neuron and gliosis in the ipsilateral SNc after dMCAO. Accordingly, the

concentration of DA and its metabolites (DOPAC and HVA) in the ipsilateral striatal tissue was decreased at 1 week after dMCAO. It is known that the nigrostriatal pathway arises from SNc DA neurons that primarily project their axons to the striatum and release DA to control motor activity (Gower and Tiberi, 2018). Our results could be interpreted as retrograde, anterograde and transsynaptic reactions in the ipsilateral SN to partial deafferentation after stroke (Tamura et al., 1990; Uchida et al., 2010; Yang et al., 2014). Owing to progressive secondary degeneration will occur at several days or weeks after focal cerebral infarction, it is possible to be a therapeutic target beyond the narrow time window for acute stroke (Prinz et al., 2015).

The advances in BMSCs biology have offered a number of enticing potential avenues for the treatment of multiple diseases including ischemic stroke. In the present study, BMSCs were uniformly negative for the hematopoietic lineage marker CD34 and the leukocyte common antigen CD45 but positive for CD29, CD44, and CD90, which are routinely used to characterize the MSCs (Zhao et al., 2016). These $CD29^+$, $CD44^+$, and $CD90^+$ BMSCs displayed highly proliferative potential as reported previously (Hou et al., 2007; Xue et al., 2015). Therefore, they could be easily expanded to a sufficient amount for transplantation. As evidenced by biodistrubution imaging analyses *in vivo* and *ex vivo*, BMSCs-DiR^+ can selectively migrate from peripheral blood to the ipsilateral cortex and SN within 14 days after dMCAO. It represents that BMSC migrated to brain. Over time, the number of BMSCs-DiR^+ were gradually decreased, which may due to the effect of fluorescent quenching of DiR (Cho et al., 2012), but Ki-67^+ (as a marker of proliferation) and DCX^+ (as a marker of differentiation) cells were significantly increased from second to 28th day after dMCAO, suggesting that transplanted BMSCs stimulated endogenous nigral neurogenesis, and then exerted neurorestorative effects. Multiline age differentiation potential of BMSCs can differentiate into ectodermal-lineage cells, neurons and neuroglia (Jiang et al., 2002; Bosnakovski et al., 2005). Interestingly, BMSCs can spontaneously indicate some neuronal markers, such as DCX and TH in the SN at 7 days after dMCAO with immunofluorescent staining of DiR^+/DCX^+ and DiR^+/TH^+ cells. It is evident that after transplantation of BMSCs, the number of TH^+ cell was increased at 28 days post-ischemia, suggesting that the transplanted BMSCs can differentiate into dopaminergic neurons or promote the survival of the remaining dopaminergic neurons in the SN, thereby increasing concentration of DA and preventing the decline of DOAPC and HVA in the ipsilateral striatum at 1 week after dMCAO.

It is accepted that progenitor cells with neurogenic potential reside in the adult SN and can give rise to new neurons when exposed to appropriate environmental signals (Lie et al., 2002). On the other hand, transplanted BMSCs reduce neuronal apoptosis and promote neuronal proliferation through releasing of neurotrophins, growth factors and other supportive substances (Kinnaird et al., 2004; Qu et al., 2007; Deng et al., 2010; Wakabayashi et al., 2010; Shichinohe et al., 2015), increasing axonal sprouting and promoting axonal plasticity (van Velthoven et al., 2012) after stroke. In addition, the immunomodulatory function is also considered to account for the beneficial effects of BMSCs in stroke rats (Ohtaki et al., 2008; Pavlichenko et al., 2008; Tsai et al., 2014; Tan et al., 2018). Therefore, engrafted BMSCs may provide an appropriate environment to reduce neuronal damage and promote neurogenesis in the SN after cerebral ischemia. Our current study showed, although the relative infarct volume in the BMSCs transplanted rats at 28 days post-ischemic stroke did not significantly differ from the vehicle group, that the increase of neuron, decrease of astrocyte and improvement of behavioral functional outcome implied that intravenous transplantation of BMSC exerts neuroprotective role through alleviating secondary injuries in the SN after cortical infarction.

To date, the underlying mechanisms of secondary degeneration in remote sites after ischemic stroke have not been completely clarified. Previously, we have demonstrated the occurrence of secondary degeneration in the ipsilateral thalamus and SN, and the impairment of cortical-striatum-nigral connections after cortical infarction (Zuo et al., 2016, 2018), suggesting the anterograde degeneration, retrograde degeneration, and transneuronal degeneration might be the major mechanism. It is possible that BMSCs transplantation improves neurofunctional restoration through increasing axonal sprouting, upregulating the expression of synaptophysin in corticospinal and corticorubral tracts and neural/glial antigen 2 in white matter after focal cerebral ischemia (Liu et al., 2007; Yu et al., 2018). BMSCs can promote axonal plasticity and remyelination after stroke, which conduce to preserve interhemispheric cortical connections (Nagahama et al., 2018), reinforce inter- and intracortical axonal connections (Liu et al., 2010) and restore thalamocortical circuits (Song et al., 2013). In current study, transplanted BMSCs enhanced the cortico-striatum-nigral connections after focal cortical infarction might be related to the induction of axon and myelin remodeling.

In summary, our study provides the compelling evidence that intravenous transplanted BMSCs could migrate to the ipsilateral SN and cortex after focal cortical infarction. The proliferation and differentiation of BMSCs stimulates endogenous neurogenesis. In addition, we demonstrated that BMSCs transplantation exerts neurorestorative effects through alleviating the secondary damage of dopaminergic neuron, enhancing cortico-striatum-nigral connections, increasing contents of DA and its metabolites, reducing gliosis, and improving the neurological functional outcome after focal cortical infarction. These evidences provide a promising therapeutic strategy for repairing post-dMCAO secondary damage in the ipsilateral SN.

ETHICS STATEMENT

This study was carried out in accordance with the recommendations of Animal Research: Reporting *in vivo* Experiments guidelines. The protocol was approved by the Animal Care and Use Committee of Guangzhou Medical University (Guangzhou, China).

AUTHOR CONTRIBUTIONS

EX and JJ designed the experiments. JJ and YT collected the data. JJ performed the experiments with assistance from YT and XZ. WS performed the experiments related to the fluorescent staining of immunohistochemistry. The manuscript was prepared by EX with assistance from JJ, YT, KL, and LZ. All authors read and commented on the manuscript, and approved the final version of the manuscript.

FUNDING

This study was supported by the Natural Science Foundation of Guangdong Province, China (Grant No. 2016A030310284), National Natural Science Foundation of China (Grant No. 81501952), and the Science and Technology Planning Project of Guangdong Province, China (Grant No. 2015B020228003).

ACKNOWLEDGMENTS

We thank Professor L. W. Enquist, Princeton University, for providing us with recombinant pseudorabies virus (PRV)-152 and PRV-BaBlu.

SUPPLEMENTARY MATERIAL

The Supplementary Material for this article can be found online at: https://www.frontiersin.org/articles/10.3389/fncel.2019.00338/full#supplementary-material

REFERENCES

Bosnakovski, D., Mizuno, M., Kim, G., Takagi, S., Okumura, M., and Fujinaga, T. (2005). Isolation and multilineage differentiation of bovine bone marrow mesenchymal stem cells. *Cell Tissue Res.* 319, 243–253. doi: 10.1007/s00441-004-1012-5

Bouet, V., Boulouard, M., Toutain, J., Divoux, D., Bernaudin, M., Schumann-Bard, P., et al. (2009). The adhesive removal test: a sensitive method to assess sensorimotor deficits in mice. *Nat. Protoc.* 4, 1560–1564. doi: 10.1038/nprot.2009.12

Campbell, B. C. V., Mitchell, P. J., Churilov, L., Yassi, N., Kleinig, T. J., Dowling, R. J., et al. (2018). Tenecteplase versus alteplase before thrombectomy for ischemic stroke. *N. Engl. J. Med.* 378, 1573–1582. doi: 10.1056/NEJMoa1716405

Chen, J., Li, Y., Wang, L., Zhang, Z., Lu, D., Lu, M., et al. (2001). Therapeutic benefit of intravenous administration of bone marrow stromal cells after cerebral ischemia in rats. *Stroke* 32, 1005–1011. doi: 10.1161/01.STR.32.4.1005

Chen, X., Dang, G., Dang, C., Liu, G., Xing, S., Chen, Y., et al. (2015). An ischemic stroke model of nonhuman primates for remote lesion studies: a behavioral and neuroimaging investigation. *Restor. Neurol. Neurosci.* 33, 131–142. doi: 10.3233/RNN-140440

Cho, H., Indig, G. L., Weichert, J., Shin, H., and Kwon, G. S. (2012). In vivo cancer imaging by poly(ethylene glycol)-b-poly(ε-caprolactone) micelles containing a near-infrared probe. *Nanomedicine* 8, 228–236. doi: 10.1016/j.nano.2011.06.009

Dang, G., Chen, X., Chen, Y., Zhao, Y., Ouyang, F., and Zeng, J. (2016). Dynamic secondary degeneration in the spinal cord and ventral root after a focal cerebral infarction among hypertensive rats. *Sci. Rep.* 6, 22655–22664. doi: 10.1038/srep22655

Deng, Y. B., Ye, W. B., Hu, Z. Z., Yan, Y., Wang, Y., Takon, B. F., et al. (2010). Intravenously administered BMSCs reduce neuronal apoptosis and promote neuronal proliferation through the release of VEGF after stroke in rats. *Neurol. Res.* 32, 148–156. doi: 10.1179/174313209X414434

DeVetten, G., Coutts, S. B., Hill, M. D., Goyal, M., Eesa, M., O'Brien, B., et al. (2010). Acute corticospinal tract wallerian degeneration is associated with stroke outcome. *Stroke* 41, 751–756. doi: 10.1161/STROKEAHA.109.573287

Domi, T., DeVeber, G., Shroff, M., Kouzmitcheva, E., MacGregor, D. L., and Kirton, A. (2009). Corticospinal tract pre-wallerian degeneration: a novel outcome predictor for pediatric stroke on acute. *Stroke* 40, 780–787. doi: 10.1161/STROKEAHA.108.529958

Feng, Y., Ju, Y., Cui, J., and Wang, L. (2017). Bone marrow stromal cells promote neuromotor functional recovery, via upregulation of neurotrophic factors and synapse proteins following traumatic brain injury in rats. *Mol. Med. Rep.* 16, 654–660. doi: 10.3892/mmr.2017.6619

Forno, L. S. (1983). Reaction of the substantia nigra to massive basal ganglia infarction. *Acta Neuropathol.* 62, 96–102. doi: 10.1007/BF00684925

Fukuda, Y., Horie, N., Satoh, K., Yamaguchi, S., Morofuji, Y., Hiu, T., et al. (2015). Intra-Arterial transplantation of low-dose stem cells provides functional recovery without adverse effects after stroke. *Cell Mol. Neurobiol.* 35, 399–406. doi: 10.1007/s10571-014-0135-9

Go, A. S., Mozaffarian, D., Roger, V. L., Benjamin, E. J., Berry, J. D., Blaha, M. J., et al. (2014). Heart disease and stroke statistics—2014 update. *Circulation* 129, 399–410. doi: 10.1161/01.cir.0000441139.02102.80

Gower, A., and Tiberi, M. (2018). The intersection of central dopamine system and stroke: potential avenues aiming at enhancement of motor recovery. *Front. Synaptic Neurosci.* 10:18. doi: 10.3389/fnsyn.2018.00018

Grossberg, J. A., Rebello, L. C., Haussen, D. C., Bouslama, M., Bowen, M., Barreira, C. M., et al. (2018). Beyond large vessel occlusion strokes: distal occlusion thrombectomy. *Stroke* 49, 1662–1668. doi: 10.1161/STROKEAHA.118.020567

Gutiérrez-Fernández, M., Rodríguez-Frutos, B., Ramos-Cejudo, J., Teresa Vallejo-Cremades, M., Fuentes, B., Cerdán, S., et al. (2013). Effects of intravenous administration of allogenic bone marrow- and adipose tissue-derived mesenchymal stem cells on functional recovery and brain repair markers in experimental ischemic stroke. *Stem Cell Res. Ther.* 4, 11–23. doi: 10.1186/scrt159

Hou, M., Yang, K., Zhang, H., Zhu, W., Duan, F., Wang, H., et al. (2007). Transplantation of mesenchymal stem cells from human bone marrow improves damaged heart function in rats. *Int. J. Cardiol.* 115, 220–228. doi: 10.1016/j.ijcard.2006.03.028

Jackson-Lewis, V., and Przedborski, S. (2007). Protocol for the MPTP mouse model of Parkinson's disease. *Nat. Protoc.* 2, 141–151. doi: 10.1038/nprot.2006.342

Jellinger, K. A. (2008). Vascular Parkinsonism. *Therapy* 5, 237–255. doi: 10.2217/14750708.5.2.237

Jiang, Y., Jahagirdar, B. N., Reinhardt, R. L., Schwartz, R. E., Keene, C. D., Ortiz-Gonzalez, X. R., et al. (2002). Pluripotency of mesenchymal stem cells derived from adult marrow. *Nature* 418, 41–49. doi: 10.1038/nature00870

Kinnaird, T., Stabile, E., Burnett, M. S., Lee, C. W., Barr, S., Fuchs, S., et al. (2004). marrow-derived stromal cells express genes encoding a broad spectrum of arteriogenic cytokines and promote in vitro and in vivo arteriogenesis through paracrine mechanisms. *Circ. Res.* 94, 678–685. doi: 10.1161/01.RES.0000118601.37875.AC

Kirton, A., Shroff, M., Visvanathan, T., and DeVeber, G. (2007). Quantified corticospinal tract diffusion restriction predicts neonatal stroke outcome. *Stroke* 38, 974–980. doi: 10.1161/01.STR.0000258101.67119.72

Lie, D. C., Dziewczapolski, G., Willhoite, A. R., Kaspar, B. K., Shults, C. W., and Gage, F. H. (2002). The adult substantia nigra contains progenitor cells with neurogenic potential. *J. Neurosci.* 22, 6639–6649. doi: 10.1523/JNEUROSCI.22-15-06639.2002

Liu, L., Wang, D., Wong, S. L., and Wang, Y. (2011). Stroke and stroke care in China: huge burden, significant workload, and a national priority. *Stroke* 42, 3651–3654. doi: 10.1161/STROKEAHA.111.635755

Liu, Z., Li, Y., Qu, R., Shen, L., Gao, Q., Zhang, X., et al. (2007). Axonal sprouting into the denervated spinal cord and synaptic and postsynaptic protein

expression in the spinal cord after transplantation of bone marrow stromal cell in stroke rats. *Brain Res.* 1149, 172–180. doi: 10.1016/j.brainres.2007.02.047

Liu, Z., Li, Y., Zhang, Z. G., Cui, X., Cui, Y., Lu, M., et al. (2010). Bone marrow stromal cells enhance inter- and intracortical axonal connections after ischemic stroke in adult rats. *J. Cereb. Blood Flow Metab.* 30, 1288–1295. doi: 10.1038/jcbfm.2010.8

Man, J., Jiao, F., Wang, Y., Gu, Y., Ding, L., Shu, C., et al. (2019). Determination of benzonatate and its metabolite in human plasma by HPLC–MS/MS: a preliminary pharmacokinetic study in healthy Chinese volunteers after oral administration of benzonatate soft capsule. *J. Pharm. Biomed. Anal.* 173, 134–143. doi: 10.1016/j.jpba.2019.05.030

Maria Ferri, A. L., Bersano, A., Lisini, D., Boncoraglio, G., Frigerio, S., and Parati, E. (2016). Mesenchymal stem cells for ischemic stroke: progress and possibilities. *Curr. Med. Chem.* 23, 1598–1608. doi: 10.2174/0929867323666160222113702

Nagahama, H., Nakazaki, M., Sasaki, M., Kataoka-Sasaki, Y., Namioka, T., Namioka, A., et al. (2018). Preservation of interhemispheric cortical connections through corpus callosum following intravenous infusion of mesenchymal stem cells in a rat model of cerebral infarction. *Brain Res.* 1695, 37–44. doi: 10.1016/j.brainres.2018.05.033

Nakajima, M., Hirano, T., Terasaki, T., and Uchino, M. (2010). Signal change of the substantia nigra on diffusion-weighted imaging following striatal infarction. *Intern. Med.* 49, 65–68. doi: 10.2169/internalmedicine.49.2694

Ohe, Y., Uchino, A., Horiuchi, Y., Maruyama, H., Deguchi, I., Fukuoka, T., et al. (2013). Magnetic resonance imaging investigation of secondary degeneration of the mesencephalic substantia nigra after cerebral infarction. *J. Stroke Cerebrovasc. Dis.* 22, 58–65. doi: 10.1016/j.jstrokecerebrovasdis.2011.06.006

Ohtaki, H., Ylostalo, J. H., Foraker, J. E., Robinson, A. P., Reger, R. L., Shioda, S., et al. (2008). Stem/progenitor cells from bone marrow decrease neuronal death in global ischemia by modulation of inflammatory/immune responses. *Proc. Natl. Acad. Sci. U.S.A.* 105, 14638–14643. doi: 10.1073/pnas.0803670105

Panepucci, R. A., Siufi, J. L., Silva, W. A. Jr., Proto-Siquiera, R., Neder, L., Orellana, M., et al. (2004). Comparison of gene expression of umbilical cord vein and bone Marrow-Derived mesenchymal stem cells. *Stem Cells* 22, 1263–1278. doi: 10.1634/stemcells.2004-0024

Pavlichenko, N., Sokolova, I., Vijde, S., Shvedova, E., Alexandrov, G., Krouglyakov, P., et al. (2008). Mesenchymal stem cells transplantation could be beneficial for treatment of experimental ischemic stroke in rats. *Brain Res.* 1233, 203–213. doi: 10.1016/j.brainres.2008.06.123

Prinz, V., Hetzer, A. M., Müller, S., Balkaya, M., Leithner, C., Kronenberg, G., et al. (2015). MRI heralds secondary nigral lesion after brain ischemia in mice: a secondary time window for neuroprotection. *J. Cereb. Blood Flow Metab.* 35, 1903–1909. doi: 10.1038/jcbfm.2015.153

Qu, R., Li, Y., Gao, Q., Shen, L., Zhang, J., Liu, Z., et al. (2007). Neurotrophic and growth factor gene expression profiling of mouse bone marrow stromal cells induced by ischemic brain extracts. *Neuropathology* 27, 355–363. doi: 10.1111/j.1440-1789.2007.00792.x

Rodriguez-Grande, B., Blackabey, V., Gittens, B., Pinteaux, E., and Denes, A. (2013). Loss of substance P and inflammation precede delayed neurodegeneration in the substantia nigra after cerebral ischemia. *Brain Behav. Immun.* 29, 51–61. doi: 10.1016/j.bbi.2012.11.017

Ruan, J., Song, H., Li, C., Bao, C., Fu, H., Wang, K., et al. (2012). DiR-labeled embryonic stem cells for targeted imaging ofin vivo gastric cancer cells. *Theranostics* 2, 618–628. doi: 10.7150/thno.4561

Schallert, T., and Whishaw, I. Q. (1984). Bilateral cutaneous stimulation of the somatosensory system in hemidecorticate rats. *Behav. Neurosci.* 98, 518–540. doi: 10.1037/0735-7044.98.3.518

Shen, L. H., Li, Y., Chen, J., Zhang, J., Vanguri, P., Borneman, J., et al. (2006). Intracarotid transplantation of bone marrow stromal cells increases axon-myelin remodeling after stroke. *Neuroscience* 137, 393–399. doi: 10.1016/j.neuroscience.2005.08.092

Shichinohe, H., Ishihara, T., Takahashi, K., Tanaka, Y., Miyamoto, M., Yamauchi, T., et al. (2015). Bone marrow stromal cell rescue ischemic brain by trophic effects and phenotypic change toward neural cells. *Neurorehabil. Neural Res.* 29, 80–89. doi: 10.1177/1545968314525856

Song, M., Mohamad, O., Gu, X., Wei, L., and Yu, S. P. (2013). Restoration of intracortical and thalamocortical circuits after transplantation of bone marrow mesenchymal stem cells into the ischemic brain of mice. *Cell Transplant.* 22, 2001–2015. doi: 10.3727/096368912X657909

Swanson, R. A., Morton, M. T., Tsao-Wu, G., Savalos, R. A., Davidson, C., and Sharp, F. R. (1990). A semiautomated method for measuring brain infarct volume. *J. Cereb. Blood Flow Metab.* 10, 290–293. doi: 10.1038/jcbfm.1990.47

Tamura, A., Graham, D. I., McCulloch, J., and Teasdale, G. M. (1981). Focal cerebral ischaemia in the rat: 1. description of technique and early neuropathological consequences following middle cerebral artery occlusion. *J. Cereb. Blood Flow Metab.* 1, 53–60. doi: 10.1038/jcbfm.1981.6

Tamura, A., Kirino, T., Sano, K., Takagi, K., and Oka, H. (1990). Atrophy of the ipsilateral substantia nigra following middle cerebral artery occlusion in the rat. *Brain Res.* 510, 154–157. doi: 10.1016/0006-8993(90)90744-V

Tan, C., Zhao, S., Higashikawa, K., Wang, Z., Kawabori, M., Abumiya, T., et al. (2018). [18F]DPA-714 PET imaging shows immunomodulatory effect of intravenous administration of bone marrow stromal cells after transient focal ischemia. *EJNMMI Res.* 8, 35–45. doi: 10.1186/s13550-018-0392-6

Tsai, M. J., Tsai, S. K., Hu, B. R., Liou, D. Y., Huang, S. L., Huang, M. C., et al. (2014). Recovery of neurological function of ischemic stroke by application of conditioned medium of bone marrow mesenchymal stem cells derived from normal and cerebral ischemia rats. *J. Biomed. Sci.* 21, 5–17. doi: 10.1186/1423-0127-21-5

Uchida, H., Yokoyama, H., Kimoto, H., Kato, H., and Araki, T. (2010). Long-term changes in the ipsilateral substantia nigra after transient focal cerebral ischaemia in rats. *Int. J. Exp. Pathol.* 91, 256–266. doi: 10.1111/j.1365-2613.2010.00712.x

van Velthoven, C. T., van de Looij, Y., Kavelaars, A., Zijlstra, J., van Bel, F., Huppi, P. S., et al. (2012). Mesenchymal stem cells restore cortical rewiring after neonatal ischemia in mice. *Ann. Neurol.* 71, 785–796. doi: 10.1002/ana.23543

Wakabayashi, K., Nagai, A., Sheikh, A. M., Shiota, Y., Narantuya, D., Watanabe, T., et al. (2010). Transplantation of human mesenchymal stem cells promotes functional improvement and increased expression of neurotrophic factors in a rat focal cerebral ischemia model. *J. Neurosci. Res.* 88, 1017–1025. doi: 10.1002/jnr.22279

Wang, W., Jiang, B., Sun, H., Ru, X., Sun, D., Wang, L., et al. (2017). Prevalence, incidence, and mortality of stroke in china. *Circulation* 135, 759–771. doi: 10.1161/CIRCULATIONAHA.116.025250

Xing, S., Zhang, Y., Li, J., Zhang, J., Li, Y., Dang, C., et al. (2012). Beclin 1 knockdown inhibits autophagic activation and prevents the secondary neurodegenerative damage in the ipsilateral thalamus following focal cerebral infarction. *Autophagy* 8, 63–76. doi: 10.4161/auto.8.1.18217

Xu, C., Giuliano, F., Yaici, E. D., Conrath, M., Trassard, O., Benoit, G., et al. (2006). Identification of lumbar spinal neurons controlling simultaneously the prostate and the bulbospongiosus muscles in the rat. *Neuroscience* 138, 561–573. doi: 10.1016/j.neuroscience.2005.11.016

Xue, K., Xia, W., Zhang, X., Qi, L., Zhou, J., Xu, P., et al. (2015). Isolation and identification of stem cells in different subtype of cartilage tissue. *Expert Opin. Biol. Ther.* 15, 623–632. doi: 10.1517/14712598.2015.989207

Yang, Y. M., Li, C. C., Yin, L. K., and Feng, X. (2014). Normalization of T2 relaxation time and apparent diffusion coefficient in relation to the inflammatory changes in the substantia nigra of rats with focal cerebral ischemia. *Acta Radiol.* 56, 837–843. doi: 10.1177/0284185114549496

Yano, S., Kuroda, S., Shichinohe, H., Hida, K., and Iwasaki, Y. (2005). Do bone marrow stromal cells proliferate after transplantation into mice cerebral infarct?–a double labeling study. *Brain Res.* 1065, 60–67. doi: 10.1016/j.brainres.2005.10.031

Yu, X., Wu, H., Zhao, Y., Guo, Y., Chen, Y., Dong, P., et al. (2018). Bone marrow mesenchymal stromal cells alleviate brain white matter injury via the enhanced proliferation of oligodendrocyte progenitor cells in focal cerebral ischemic rats. *Brain Res.* 1680, 127–136. doi: 10.1016/j.brainres.2017.12.019

Zhan, L., Wang, T., Li, W., Xu, Z. C., Sun, W., and Xu, E. (2010). Activation of Akt/FoxO signaling pathway contributes to induction of neuroprotection against transient global cerebral ischemia by hypoxic pre-conditioning in adult rats. *J. Neurochem.* 14, 897–908. doi: 10.1111/j.1471-4159.2010.06949816.x

Zhang, J., Zhang, Y., Xing, S., Liang, Z., and Zeng, J. (2012). Secondary neurodegeneration in remote regions after focal cerebral infarction. *Stroke* 43, 1700–1705. doi: 10.1161/STROKEAHA.111.632448

Zhao, Y., Wang, X., Dong, P., Xu, Q., Ma, Z., Mu, Q., et al. (2016). Bone marrow derived mesenchymal stem cells alleviated brain injury via down-regulation of interleukin-1β in focal cerebral ischemic rats. *Am. J. Transl. Res.* 8, 1541–1550.

Zuo, X., Hou, Q., Jin, J., Chen, X., Zhan, L., Tang, Y., et al. (2018). Inhibition of cathepsins B induces neuroprotection against secondary degeneration in ipsilateral substantia nigra after focal cortical infarction in adult male rats. *Front. Aging. Neurosci.* 10:125. doi: 10.3389/fnagi.2018.00125

Zuo, X., Hou, Q., Jin, J., Zhan, L., Li, X., Sun, W., et al. (2016). Inhibition of cathepsin B alleviates secondary degeneration in ipsilateral thalamus after focal cerebral infarction in adult rats. *J. Neuropathol. Exp. Neurol.* 75, 816–826. doi: 10.1093/jnen/nlw054

Conflict of Interest Statement: The authors declare that the research was conducted in the absence of any commercial or financial relationships that could be construed as a potential conflict of interest.

frontiers in Cellular Neuroscience

ORIGINAL RESEARCH
published: 24 July 2019
doi: 10.3389/fncel.2019.00332

The Prenylflavonoid ENDF1 Overrules Central Nervous System Growth Inhibitors and Facilitates Regeneration of DRG Neurons

*Lara Bieler[1,2], Michael Vogl[1,2], Michael Kirchinger[3,4], Corinna Urmann[3,4], Herbert Riepl[3,4], Christine Bandtlow[5], Lars Klimaschewski[6], Ludwig Aigner[2,7,8] and Sebastien Couillard-Despres[1,2,8]**

[1] Institute of Experimental Neuroregeneration, Paracelsus Medical University, Salzburg, Austria, [2] Spinal Cord Injury and Tissue Regeneration Center Salzburg (SCI-TReCS), Salzburg, Austria, [3] Organic-Analytical Chemistry, Weihenstephan-Triesdorf University of Applied Sciences, Straubing, Germany, [4] TUM Campus Straubing, Straubing, Germany, [5] Division of Neurobiochemistry, Innsbruck Medical University, Innsbruck, Austria, [6] Department of Anatomy, Histology and Embryology, Division of Neuroanatomy, Medical University of Innsbruck, Innsbruck, Austria, [7] Institute of Molecular Regenerative Medicine, Paracelsus Medical University, Salzburg, Austria, [8] Austrian Cluster for Tissue Regeneration, Vienna, Austria

OPEN ACCESS

Edited by:
Francisca C. Bronfman, Pontifical Catholic University of Chile, Chile

Reviewed by:
Yen-Chung Chang, National Tsing Hua University, Taiwan
Melissa R. Andrews, University of Southampton, United Kingdom

***Correspondence:**
Sebastien Couillard-Despres
s.couillard-despres@pmu.ac.at

Specialty section:
This article was submitted to Cellular Neurophysiology, a section of the journal Frontiers in Cellular Neuroscience

Received: *07 February 2019*
Accepted: *04 July 2019*
Published: *24 July 2019*

Citation:
Bieler L, Vogl M, Kirchinger M, Urmann C, Riepl H, Bandtlow C, Klimaschewski L, Aigner L and Couillard-Despres S (2019) The Prenylflavonoid ENDF1 Overrules Central Nervous System Growth Inhibitors and Facilitates Regeneration of DRG Neurons. Front. Cell. Neurosci. 13:332. doi: 10.3389/fncel.2019.00332

Restoration of neuronal connectivity after lesion of the central nervous system, such as spinal cord injury, is one of the biggest challenges in modern medicine. In particular, the accumulation of axon growth inhibitory factors at the site of injury constitutes a major obstacle to structural and thus functional repair. We previously investigated a group of prenylflavonoids derived from hops for their capacity to promote neuroregeneration. We identified a molecule called ENDF1 that was very potent to enhance regrowth and branching of neurites from dorsal root ganglion neurons in culture on growth promoting substrates. In the present study, we investigated ENDF1's capacity to promote regeneration of rat dorsal root ganglion neurons *in vitro* in the presence of three main components of the extracellular matrix acting as axon growth inhibitors: Semaphorin 3A, Ephrin A4 and mixed chondroitin sulfate proteoglycans. We report that ENDF1 application significantly promoted the percentages of sensory neurons able to regrow their neurites regardless of the presence of those inhibitors, and this to an extent similar to the one obtained after NGF treatment. Moreover, ENDF1 strongly enhanced the total neurite length and the complexity of neurites extending from neurons challenged with axon growth inhibitors. Although the impact of NGF and ENDF1 on the regeneration of neurons was similar, the activity of ENDF1 was not mediated by signaling through the TrkA receptor, indicating that each molecule act through different signaling pathways. In addition, ENDF1 did not decrease the phosphorylation of cofilin, a downstream effector of the regeneration-associated RhoA/ROCK signaling pathway. Hence, ENDF1 is a potent pro-neuroregenerative factors that could help in identifying new efficient targets for regenerative therapies of the nervous system.

Keywords: flavonoids, dorsal root ganglions, DRG neurons, axonal outgrowth, semaphorin, ephrin, CSPGs, neuroregeneration

INTRODUCTION

Many therapeutic interventions currently applied following spinal cord injury aim for a stabilization of the lesion and for a limitation of exacerbating secondary damages. These interventions, however, cannot re-establish lost neuronal connectivity which would be crucial for functional regeneration. Unfortunately, in the injured central nervous system (CNS), the accumulation of axon growth inhibitors at the lesion site severely hinders regeneration. Hence, strategies supporting axonal regeneration in the lesioned CNS are strongly needed.

The extracellular matrix (ECM) is the most abundant structure found in the microenvironment of the CNS. It is mainly composed of proteins (e.g., collagens, laminins) and carbohydrate-enriched molecules named proteoglycans (Kwok et al., 2014). The chondroitin sulfate proteoglycans (CSPGs) constitute the main proteoglycans subclass occurring in the CNS. CSPGs can be subdivided into lecticans (namely aggrecan, brevican, neurocan and versican), phosphacan, small leucine-rich proteoglycans (decorin and biglycan), NG2 and neuroglycan-C (Ruoslahti, 1996; Iozzo, 1998; Kwok et al., 2014). CSPGs are synthesized by neurons, as well as glia (Crespo et al., 2007). After traumatic injury, astrocytes, microglia and various NG2 expressing cells migrate to the lesion site and contribute to the glial scar by upregulating the secretion of ECM components such as CSPGs (Galtrey and Fawcett, 2007; Goritz et al., 2011). The scar formation is on the one hand considered to be beneficial to circumscribe and prevent spreading of the lesion in the acute phase after injury. However, it is thereafter thought to hinder the axonal regeneration in the chronic phase after CNS injury (Quraishe et al., 2018).

Proteins of the semaphorin and ephrin families play crucial roles in the development of the nervous system and have system-stabilizing properties in adult organisms under physiological conditions (Dick et al., 2013; Boyd et al., 2014). However, following CNS injury, semaphorin 3A expression is elevated in the vicinity of the lesion, especially within scarred tissue (Pasterkamp et al., 2001). Additionally, ephrin A4 receptors (ephA4) also become rapidly upregulated at the lesion site, promoting astrogliosis and loss of neurite regrowth (Fabes et al., 2006; Frugier et al., 2012). Both semaphorins and ephrins are major chemorepellent axon guidance molecules present in the ECM and their accumulation at the lesion site provokes the collapse of growth cone from regenerating axons (Rohm et al., 2000; Lisabeth et al., 2013).

The anti-regenerative impact of the ECM growth inhibitors following spinal cord injury has been substantiated by studies attempting to remove or neutralize their signaling. Hence, the local application of chondroitinase ABC, degrading the CSPGs at the injury site, allowed axons to better regrow and enhanced functional recovery in animal models of spinal cord injury and stroke (Bradbury et al., 2002; Sorg et al., 2016; Wiersma et al., 2017). Kaneko et al. (2006) also reported that inhibition of semaphorin 3A by selective inhibitors considerably increased functional recovery in a rat model of spinal cord transection. Furthermore, mice deficient in ephA4 or mice treated with ephA4 inhibitors showed a remarkable reduction of astrogliosis after spinal cord injury, concomitant with a stronger axonal regrowth across the lesion site (Goldshmit et al., 2004, 2011). Therefore, the neutralization of the axon growth inhibitory activities of ECM components appears more and more as a promising strategy to improve regeneration of the injured CNS.

The flavonoid family comprises a large variety of molecules, some of which have been investigated for their therapeutic activities in disorders of the nervous system. For example, a flavonoid-rich food uptake has been suggested to prevent age-dependent cognitive decline (Gildawie et al., 2018). Moreover, flavonoids have been reported to reduce oxidative stress and amyloid-β-protein production in animal models of Alzheimer's disease and to reduce neuronal death in models of Parkinson's disease (reviewed in de Andrade Teles et al., 2018). We previously reported on the neuroregenerative activities of a prenylflavonoid, named ENDF1 (Enhancement of Neuronal Differentiation Factor 1) isolated from hops. ENDF1 was found to promote neurite regrowth of dorsal root ganglion (DRG) neurons *in vitro*, and in addition to promote neuronal differentiation and neuroprotection (Oberbauer et al., 2013). In the present study, we investigated the capacity of ENDF1 to promote regeneration of rat DRG neurons in the presence of ECM axonal growth inhibitors known to accumulate at the CNS lesion sites.

MATERIALS AND METHODS

Primary Sensory Neuron Cultures

Experiments were performed in accordance to the guidelines of the "Directive 2010/63/EU of the European Parliament and of the Council of 22 September 2010 on the protection of animals used for scientific purposes." According to the European Directive 2010/63/EU Article 3 and the Austrian legislation for experiments on living animals Tierversuchsgesetz 2012 §2c, no additional approval was required for the killing of animals with the aim of collecting tissues. DRGs for this study were isolated from postnatal day 2 (P2) Fisher-344 rats. Preparation of dorsal root ganglion neurons was done according to a protocol previously published (Haller et al., 2007). In short, pups were decapitated and DRGs were harvested along the complete spinal cord. Dissected DRGs were maintained in ice-cold DMEM medium containing 4.5 g/L D-glucose (Biochrom, Berlin, Germany) until all DRGs were harvested. Thereafter, DRGs were triturated and incubated in 5000 U/mL collagenase Type I (Life Technologies, Carlsbad, Germany) dissolved in HBSS solution containing 1.4 mM calcium chloride (Gibco, Thermo fisher Scientific, Austria) for 15 min at 37°C. DRGs were further digested at 37°C for 15 min with Accutase (Pan-Biotech, Aidenbach, Germany). Following three washes in DMEM supplemented with 4.5 g/L D-glucose, DRG neurons were resuspended in DMEM containing 4.5 g/L D-glucose, 100 U/mL penicillin, 100 µg/mL streptomycin (Pan-Biotech, Aidenbach, Germany), B27 supplement (Life Technologies, Karlsbad, Germany) and further triturated twice with fire-polished glass pipettes. Approximately 500 neurons contained in 50 µL of culture medium were seeded on the coated coverslips (see below) placed in 24 wells/plates and allowed

to adhere for 30 min before adjusting the final volume of culture medium to 1 mL per well. After 16 h cells of culture, DRG neurons were fixed with 0.1 M phosphate-buffered 4% paraformaldehyde pH 7.4 for 10 min at room temperature and the regeneration of DRG neurons in the various culture conditions was analyzed.

Determination of Inhibitor and ENDF1 Concentrations for *in vitro* Assays

Coverslips were coated using various concentrations of each inhibitors to determine the concentrations of inhibitors lowering to approximately 30% the proportion of rat DRG neurons capable of regrowing their processes within 16 h. To this end, HCl-etched glass coverslips (12 mm) were first coated with 100 μg/mL poly-L-ornithine hydrobromide (Sigma-Aldrich, MO, United States) overnight at 37°C. Afterward, coverslips were washed three times with distilled water and allowed to air dry. Human semaphorin 3A-Fc (Biomedica, Vienna, Austria) and human ephrin A4-Fc (Biomedica, Vienna, Austria) were pre-clustered 1:1 with anti-hFc-antibody (Biomedica, Vienna, Austria) for 1 h on ice. Coverslips were then coated with semaphorin 3A and ephrin A4 at concentrations of 1, 5, and 10 μg/mL, whereas chicken CSPGs (Millipore, Darmstadt, Germany) were applied at concentrations of 1, 5, and 50 μg/mL and incubated overnight at 4°C. Finally, inhibitors were removed and the coverslips were coated with 5 μg/mL laminin (Sigma-Aldrich, MO, United States) for 2 h at 37°C. Coverslips coated with 100 μg/mL poly-L-ornithine directly followed by 5 μg/mL laminin served as no-inhibitor control (Baumer et al., 2014).

The most effective ENDF1 concentration for regeneration was determined with a dose response assay. Rat DRG neurons were seeded on 5 μg/mL CSPGs-coated coverslips and treated with 1 μM ENDF1, 5 μM ENDF1, 10 μM ENDF1, 20 μM ENDF1, or 50 μM ENDF1 prepared from a 100 mM ENDF1 stock solution in DMSO. The final concentration of DMSO was adjusted to 0.05% in every well. Culture medium and medium containing 0.05% DMSO (vehicle) served as negative controls. NGF has been extensively studied for its axonal growth promoting activity on DRG neurons in culture and therefore 20 ng/mL NGF (Life Technologies, Carlsbad, Germany) in 0.05% DMSO was used as positive control for regeneration.

Further assays were performed with 10 μM ENDF1 prepared from a stock solution of 100 mM ENDF1 in DMSO. The standard vehicle control conditions corresponded to 0.01% DMSO in the culture medium and NGF 20 ng/mL (Life Technologies, Carlsbad, Germany) was used as positive control for regeneration of DRG neurons.

For the inhibition of TrkA signaling, 1 μM of the selective TrkA-receptor inhibitor (GW441756, stock solution 50 mM in DMSO, Selleck Chemicals, Munich, Germany) was added to the cultures 30 min before adding ENDF1 or NGF.

Immunocytochemistry

Immunocytochemistry was conducted as described previously (Couillard-Despres et al., 2008). Labeling of the DRG neurons was performed using a rabbit anti-β-III-tubulin primary antibody (Abcam, #ab18207, dilution 1:1000) followed by a donkey anti-rabbit Alexa 568 secondary antibody (Invitrogen, Dilution 1:1000). Nuclear counterstaining was obtained using 1 μg/mL 2-Diamidinphenylindol (DAPI). Micrographs were acquired using a microscope for epifluorescence (Olympus IX81) and the cellSens Dimension Software (Olympus).

PC-12 Cell Culture

PC-12 cell line (ATCC CRL-1721) was cultured in RPMI 1640 medium containing L-glutamine (Gibco, Thermofisher, Austria), 5% fetal bovine serum (Gibco, Thermo fisher scientific, Austria), 10% horse serum (Gibco, Thermo fisher scientific, Austria), 100 U/mL penicillin, 100 μg/mL streptomycin (Pan-Biotech, Aidenbach, Germany) at 37°C and 5% CO_2 in a humidified incubator. Culture flasks were coated with 250 μg/mL poly-L-ornithine hydrobromide (Sigma-Aldrich, MO, United States). Cultures were passaged using Accutase (Pan-Biotech, Aidenbach, Germany).

For the analysis of TrkA phosphorylation and RhoA/ROCK signaling, PC-12 cells were seeded in 6-well plates (3×10^6 cells/well) for 24 h. To investigate TrkA phosphorylation, PC-12 cells were treated with 10 μM ENDF1 for 5, 15, and 30 min. Treatment with 100 ng/mL NGF (Life Technologies, Carlsbad, Germany) served as positive control to induce TrkA phosphorylation (Kaplan et al., 1991). Culture medium and 0.01% DMSO were used as negative controls. To investigate impact of ENDF1 on the RhoA/ROCK signaling, PC12 cells were treated with 10 μM ENDF1 for 30 and 120 min. The selective Rho kinase inhibitor Y27632 (stock solution 50 mM in DMSO; Selleck Chemicals, Munich, Germany) was applied at 25 μM for 30 and 120 min as positive control of RhoA/ROCK signaling inhibition. Culture medium and 0.05% DMSO served as negative controls.

Protein Extraction and Western Blotting

For the analysis of TrkA and cofilin phosphorylation, PC-12 cells were detached using a cell scraper and collected in ice-cold PBS (Biochrom GmbH, Berlin, Germany). After centrifugation at 300 × *g* and 4°C, pellets were resuspended and homogenized in 200 μL of ice-cold RIPA-buffer (Abcam, Cambridge, United Kingdom) supplemented with protease inhibitors (cOmplete, Roche, Switzerland) and phosphatase inhibitors (PhosSTOP, Roche, Switzerland). Suspensions were centrifuged at 14 000 × *g* for 20 min at 4°C and supernatants were stored at −80°C until further use. Protein concentration was determined using the Pierce BCA Protein Assay Kit (Thermo fisher scientific, Austria).

For western blotting, 10 μg of proteins per well were loaded on 4–20% TGX stain-free gels (Bio-Rad Laboratories, Austria). After electrophoresis, gels were UV-irradiated for 2.5 min using a ChemiDoc Imaging system (Bio-Rad Laboratories, Austria) according to manufacturers' manual. Thereby, trihalo compounds in the gel react with the proteins and generated fluorophores allow for total protein loading normalization. Proteins were transferred on a 0.2 μm PVDF membrane (Bio-Rad Laboratories, Austria) using a *Trans*-blot turbo transfer system (Bio-Rad Laboratories, Austria). Membranes were incubated in blocking solution containing 0.1 M Tris

(pH 7.5), 0.15 M NaCl, 5% bovine serum albumin (Sigma-Aldrich, Germany) and 0.1% Tween-20 for 1 h at room temperature. Afterward, membranes were incubated overnight at 4°C with primary antibodies diluted in blocking solution: rabbit anti-p-TrkA (#9141; 1:1000; Cell Signaling Technologies, Germany), rabbit anti-cofilin (D3F9; 1:1000; Cell Signaling Technologies, Germany), rabbit anti p-cofilin (77G2; 1:1000; Cells Signaling Technologies, Germany). Membrane were washed 3 × 10 min in TBST (Tris-buffered saline containing 0.1 M Tris (pH 7.5), 0.15 M NaCl and 0.1% Tween-20) and incubated with secondary antibody diluted in blocking solution for 1 h at room temperature: goat anti-rabbit–HRP (1:50000; Bio-Rad Laboratories, Austria). Afterward, membranes were washed 3 × 10 min with TBST and chemiluminescent signal was obtained using Clarity Western ECL Substrate (Bio-Rad laboratories, Austria) and detected with the ChemiDoc Imaging system.

Documentation and Statistical Analyses

Experiments were performed in three independent biological replicates. Immunodetection of β-III-tubulin was used to label DRG neurons for analysis. The frequency of neurite outgrowth was assessed in a minimum of 200 β-III-tubulin-labeled DRG neurons for each condition in three biological replicates. A neurite of at least one soma size length was used as criterion to define regenerating DRG neurons. Total neurite length of neurons examined was determined by manual tracing of all β-III-tubulin-labeled neurites and branching points using Fiji (Schindelin et al., 2012). Total neurite length and the number of branching points were calculated in at least 50 neurons per condition and biological replicate. Western blots were analyzed using the Image Lab 5.2 software (Bio-Rad Laboratories, Austria). Band intensities were normalized to the total protein in the lane and to the medium controls.

Data are presented as mean value ± standard deviation. Statistical analysis was performed by one-way analysis of variance (ANOVA) with a Bonferroni Multiple Comparison *post hoc* test or student's *t*-test using Prism7 (GraphPad, San Diego, United States). A *p*-value of ≤ 0.05 was considered statistically significant.

RESULTS

Dose-Dependent Regeneration of DRG Neurons Seeded on ECM Inhibitors

Dose-response curves for three preparations of ECM inhibitors, namely mixed CSPGs, ephrin A4, and semaphorin 3A, were established to determine the concentrations inhibiting neuronal outgrowth to the extent that only approximately 30% of the DRG neurons can spontaneously regrow neurites. This inhibition level is optimal to study neurite growth promoting substances as it allows a certain degree of spontaneous neurite regrowth and can accommodate for batch-to-batch fluctuation in inhibitory activity of the commercial inhibitor preparations. We evaluated the ability of DRG neurons to regrow their neurites on coverslips coated with 1 to 50 μg/mL CSPGs, or coated with ephrin A4 or semaphorin 3A in concentrations ranging from 1 to 10 μg/mL. The percentage of process-bearing DRG neurons was determined for each condition. As shown in **Figure 1A**, 28.9 ± 6.9% of DRG neurons displayed neurites 16 h after seeding on 5 μg/mL CSPGs. Similarly, 10 μg/mL ephrin A4 (**Figure 1B**) or 5 μg/mL semaphorin 3A (**Figure 1C**) limited the percentages of seeded DRG neurons growing their neurites to 31.4 ± 5.8% and 33.5 ± 5.3%, respectively. These concentrations of inhibitors were further used for this study. Neurons seeded on laminin without inhibitor displayed spontaneous neurites regrowth in a frequency of 84.2 ± 6.7%.

A dose response experiment was performed to define the most effective concentration of ENDF1 for the regeneration of DRG neurons seeded on 5 μg/mL CSPGs (**Figure 1D**). The highest level of DRG neurons regeneration was observed using 10 μM ENDF1 which lead to a significantly increased of the percentage of neurons with neurites (43.1 ± 2.4%), compared to cultures with 0.05% DMSO vehicle (31.3 ± 3.3%; $p = 0.02$). Higher concentrations of ENDF1 did not provide stronger regenerative activity, or even decrease the frequency of DRG neurons regenerating their neurites. Regeneration of DRG neurons exposed to 0.05% DMSO did not significantly differ from the regeneration observed in culture medium control ($p = 0.90$).

ENDF1 Enables Neurite Regrowth Despite ECM Inhibitors

We previously reported that application of 10 μM ENDF1 in the culture medium promotes neurite regeneration of embryonic chicken DRG neurons seeded on laminin, which is a growth-supporting substrate (Oberbauer et al., 2013). In this study, we further addressed the potency of ENDF1 to promote regeneration of DRG neurons seeded on ECM inhibitors-coated coverslips (i.e., 5 μg/mL CSPGs, 10 μg/mL ephrin A4, or 5 μg/mL semaphorin 3A). The pro-regenerative activity of ENDF1 in the presence of each inhibitor was assessed by comparison to the vehicle conditions, and was in addition compared to the regenerative activity of NGF, a growth factor promoting regeneration of neurons in culture (Nusser et al., 2002).

When DRG neurons were seeded on CSPGs in the presence of vehicle (DMSO 0.01%), only 17.3 ± 5.2% of the neurons displayed neurites. In the presence of 10 μM ENDF1, 37.1 ± 5.4% of the DRG neurons regrow their neurites, which was a highly significant increase compared to the vehicle condition ($p = 0.0024$). Similarly, 20 ng/mL NGF highly significantly increased the percentage of neurons displaying neurites (40.6 ± 8.3%; $p = 0.0013$). The combination of both treatments, ENDF1 and NGF, was also successful to highly significantly raise the percentage of neurons developing neurites (47.0 ± 7.9%; $p = 0.0002$) as compared to the vehicle, however, the treatment with NGF and ENDF1 in combination had no additional benefit compared to the NGF treatment alone ($p = 0.7454$) (**Figures 2A,B**).

Furthermore, ENDF1 also counteracted the inhibitory effect of ephrin A4 in the culture. When only the vehicle was applied, 17.1 ± 1.8% of the neurons showed neurites. A treatment with ENDF1 highly significantly raised the percentage of regrowing neurons to 43.0 ± 2.7% ($p < 0.0001$). Similarly, NGF highly

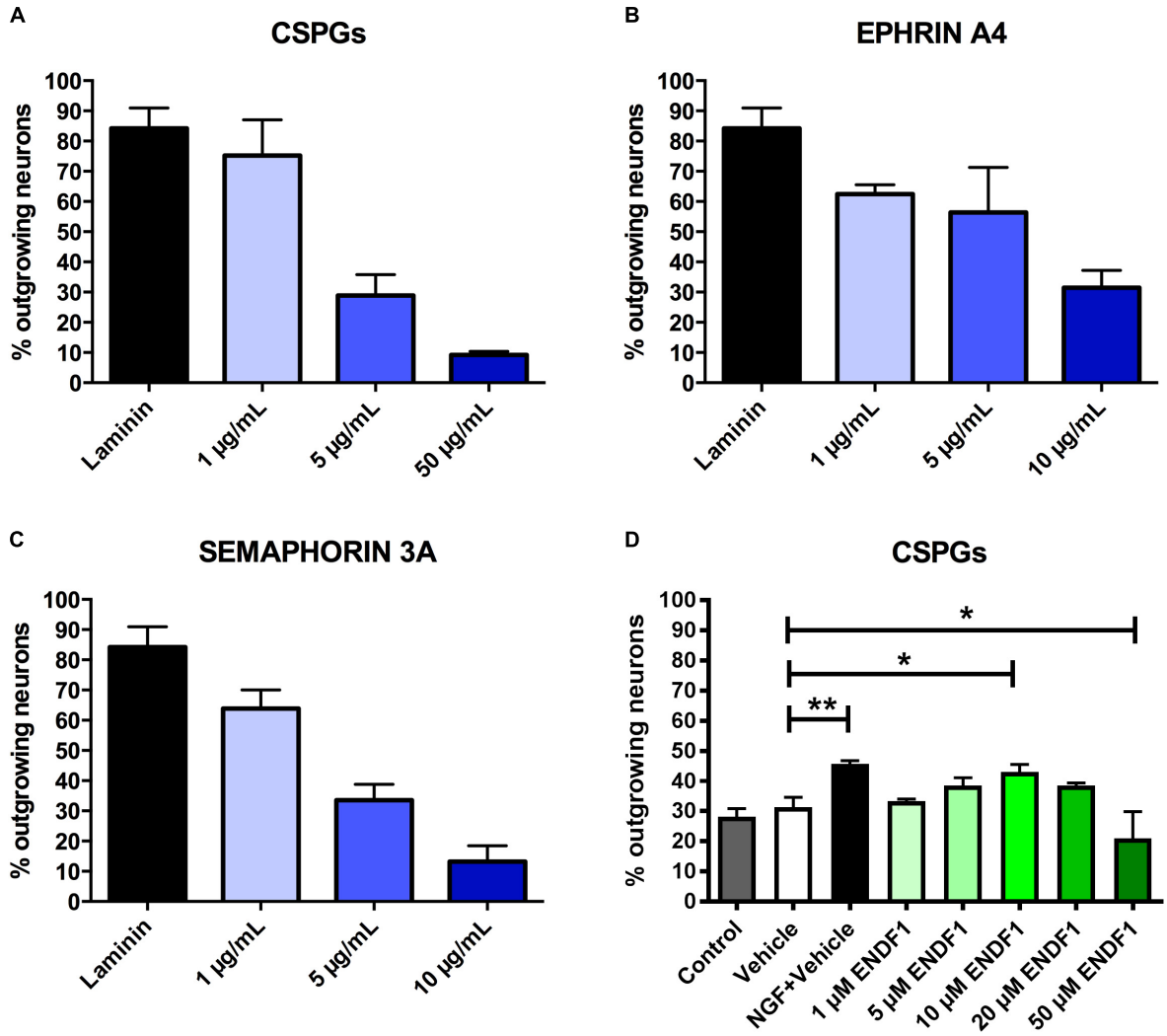

FIGURE 1 | Determination of effective ECM inhibitor and ENDF1 concentrations. Different concentrations of CSPGs **(A)**, ephrin A4 **(B)** and semaphorin 3A **(C)** were coated on the coverslips to determine the optimal inhibitor concentration for the analysis of DRG neurons neurite regrowth. **(D)** ENDF1 dose-response curve for DRG neurons neurite regrowth on 5 µg/mL CSPGs. Values are shown as mean ± SD. *$p \leq 0.05$ and **$p \leq 0.01$.

significantly increased the percentage of process-bearing neurons to 42.8 ± 1.8% ($p < 0.0001$). The combination of ENDF1 and NGF treatments significantly raised the percentage of DRG neurons regrowing neurites to 56.7 ± 2.9% compared to NGF solely treated neurons ($p = 0.0003$) (**Figures 2A,C**).

Finally, in the presence of semaphorin 3A on the coverslips, treatment with 10 µM ENDF1 raised the number of regrowing neurons from 24.2 ± 7.2% (vehicle) to 47.0 ± 9.4% (ENDF1; $p = 0.0021$). A comparable regeneration was seen upon treatment with NGF, resulting in 46.7 ± 7.3% of the neurons regrowing their neurites ($p = 0.0013$). A combined treatment with ENDF1 and NGF also significantly increased the percentage of neurons regrowing their neurites to 54.3 ± 3.0% ($p = 0.0002$). The combination of both treatments, however, had no additional benefits when compared to the application of NGF alone ($p = 0.4003$) (**Figures 2A,D**).

ENDF1 Enhances Neurite Length Despite ECM Inhibitors

The extent of neurite elongation was determined by measuring the total length of neurites per neuron for each condition investigated. In the presence of CSPGs, neurites reached an average total length of 392.3 ± 58.2 µm in vehicle conditions. A treatment with ENDF1 more than doubled the neurite length, for a total length of 872.3 ± 145.7 µm ($p = 0.0158$). NGF also significantly increased the neurite length of DRG neurons regrowing on CSPGs to 840.3 ± 87.1 µm ($p = 0.0026$). A combination of ENDF1 and NGF further increased the neurite length to 1232.0 ± 132.1 µm ($p < 0.0001$ as compared to vehicle). Furthermore, the treatment with both substances together was significantly more effective on DRG neurons as compared to treatment with NGF only ($p = 0.0060$) (**Figure 2E**).

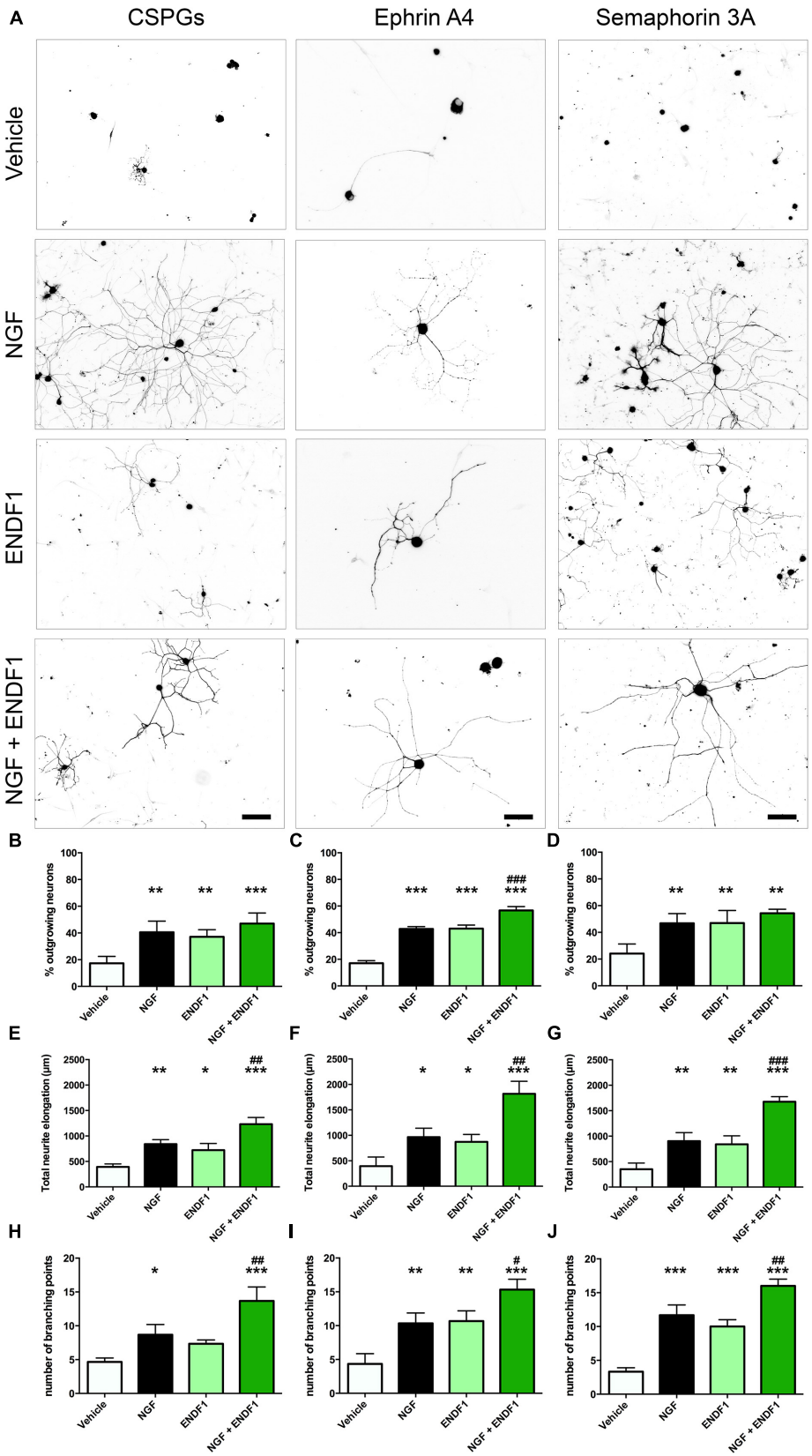

FIGURE 2 | Continued

FIGURE 2 | Neurite outgrowth, length and complexity in inhibitory conditions and ENDF1 treatment. **(A)** Representative micrographs showing sensory DRG neurons seeded over CSPGs, ephrin A4 and semaphorin 3A. The various cultures were treated with either vehicle, 20 ng/mL NGF, 10 μM ENDF1 or combined 20 ng/mL NGF/10 μM ENDF1. Panels **(B–D)** shows the percentage of neurons displaying neurites regrowth in the different inhibitory conditions. The total neurite length of DRG neurons regrowing their neurites in the various inhibitory conditions is displayed in panels **(E–G)**. The complexity of the regrowing neurites was evaluated by determination of the number of branching points present in the neurite arborization in the various inhibitory conditions **(H–J)**. All values are displayed as mean ± SD. $^{*}p \leq 0.05$, $^{**}p \leq 0.01$, and $^{***}p \leq 0.001$ compared to vehicle control. $^{\#}p \leq 0.05$, $^{\#\#}p \leq 0.01$, and $^{\#\#\#}p \leq 0.001$ compared to NGF treatment.

Under the inhibitory influence of ephrin A4, the application of ENDF1 enhanced the total neurite length (ENDF1: 872.3 ± 145.7 μm; vehicle: 393.9 ± 180.5 μm; $p = 0.0457$). A treatment with NGF also generated a significant augmentation of the neurite elongation (NGF: 965.3 ± 175.5 μm; $p = 0.0188$) and the combination of the two substances increased even more the total neurite length to 1815.0 ± 246.2 μm ($p < 0.0001$). Additionally, the treatment with NGF and ENDF1 in combination significantly enhanced neurite growth compared to NGF treatment alone ($p = 0.0018$) (**Figure 2F**).

In the presence of semaphorin 3A, ENDF1 treatment doubled the elongation of the neurites to a total length of 722.7 ± 130.6 μm compared to the vehicle controls (352.0 ± 119.1 μm; $p = 0.0089$). Similarly, NGF enhanced the total neurite length of DRG neurons seeded on semaphorin 3A to 902.3 ± 167.0 μm ($p = 0.0044$). The combination of ENDF1 and NGF caused a further significant increase in total neurite length to 1675.0 ± 101.4 μm ($p < 0.0001$) compared to the vehicle control. In addition, the combination of ENDF1 and NGF significantly induced more regrowth compared to the NGF alone in semaphorin 3A inhibitory condition ($p = 0.0005$) (**Figure 2G**).

ENDF1 Increases Complexity of the Neurite Arborization of DRG Neurons Seeded on ECM-Inhibitors

In addition to the total neurite length, the number of branching points of the neurite arborization was quantified as an indicator of complexity for the DRG neurons regrowing their neurite in the three inhibitory conditions. When DRG neurons were seeded on CSPGs (**Figure 2H**), ENDF1 treatment did not significantly influence the complexity of the arborization (vehicle: 4.7 ± 0.6; ENDF1: 7.3 ± 0.6; $p = 0.1271$). In contrast, NGF treatment enhanced the number of branching points to a mean of 8.7 ± 1.5 branching points per neuron ($p = 0.0204$). The combined treatment with ENDF1 and NGF resulted in a significant increase of branching points (13.7 ± 2.1; $p > 0.0001$). Furthermore, the treatment with both substances significantly increased the number of branching points of DRG neurons seeded on CSPGs in comparison to NGF treatment alone ($p = 0.0058$).

In ephrin A4 containing cultures (**Figure 2I**), ENDF1 significantly increased the number of branching points to a total of 10.7 ± 1.5 per neuron compared to neurons in vehicle conditions having 4.3 ± 1.5 branching points per cell ($p = 0.0029$). NGF also significantly increased the complexity of the neurons (10.3 ± 1.5 branching points; $p = 0.0040$). A combination of ENDF1 and NGF further increased the number of branching points to 15.3 ± 1.5 ($p < 0.0001$), which is significantly higher than the average obtained with NGF treatment alone ($p = 0.0117$). Similarly, when neurite regrowth was inhibited by semaphorin 3A in the culture (**Figure 2J**), ENDF1 treatment significantly increased complexity of the regrowing neurites (vehicle: 3.3 ± 0.6 branching points, ENDF1: 10.0 ± 1.0 branching points, $p = 0.0002$). NGF treatment also resulted in a more complex morphology compared to vehicle conditions (NGF: 11.7 ± 1.5 branching points, $p < 0.0001$). Treatment with ENDF1 and NGF in combination further increased the number of branching points (16.0 ± 1.0) compared to NGF treatment alone ($p = 0.0035$).

ENDF1 Signaling Does Not Require TrkA-Receptor

Considering the similarity between the regenerative activities of ENDF1 and NGF on DRG neurons, we investigated the possibility that these two factors share a common signaling pathway. NGF mediates its pro-regenerative activities via signaling through its receptor TrkA (Zhang et al., 2000; Nusser et al., 2002). To gain insight information about a possible involvement of this NGF receptor in ENDF1 signaling, DRG neurons seeded on CSPGs were incubated with a specific TrkA inhibitor (GW441756) prior to the application of ENDF1 in the cultures. The percentage of DRG neurons regrowing their neurites in the presence or absence of TrkA inhibitor was determined after 16 h of treatment with ENDF1 or NGF. Significantly less NGF-treated DRG neurons regrew their neurites following inhibition of the NGF receptor TrkA (37.5 ± 8.2%) compared to neuron treated with NGF only (52.2 ± 1.4%; $p = 0.0381$) (**Figure 3C**). In contrast, the addition TrkA inhibitor only slightly decreased the percentage of ENDF1-treated DRG neurons regrowing their neurites (ENDF1 + TrkA inhibitor: 32.1 ± 5.5%; ENDF1: 35.8 ± 7.5%; $p = 0.5198$). The capacity of ENDF1 to induce TrkA phosphorylation by direct or indirect mechanisms was further investigated in PC-12 cells. Application of 100 ng/mL NGF led to a robust phosphorylation of the TrkA receptor within 5 min. On the other hand, no increase in the level of TrkA phosphorylation was detected following addition of 10 μM ENDF1 (**Figures 3A,B**).

Impact of ENDF1 on RhoA/ROCK Signaling Pathway

RhoA/ROCK signaling pathway is involved in neurite outgrowth and is directly upregulated by ECM inhibitors and inhibited by pro-regenerative substances (Tonges et al., 2011). Inhibition of RhoA/ROCK signaling leads to a downregulation of LIMK-1 activity and thereby to a lower level of cofilin phosphorylation, enabling the reorganization of the actin cytoskeleton and neurite growth in PC-12 cells (Zhang et al., 2006). Application of 10 μM

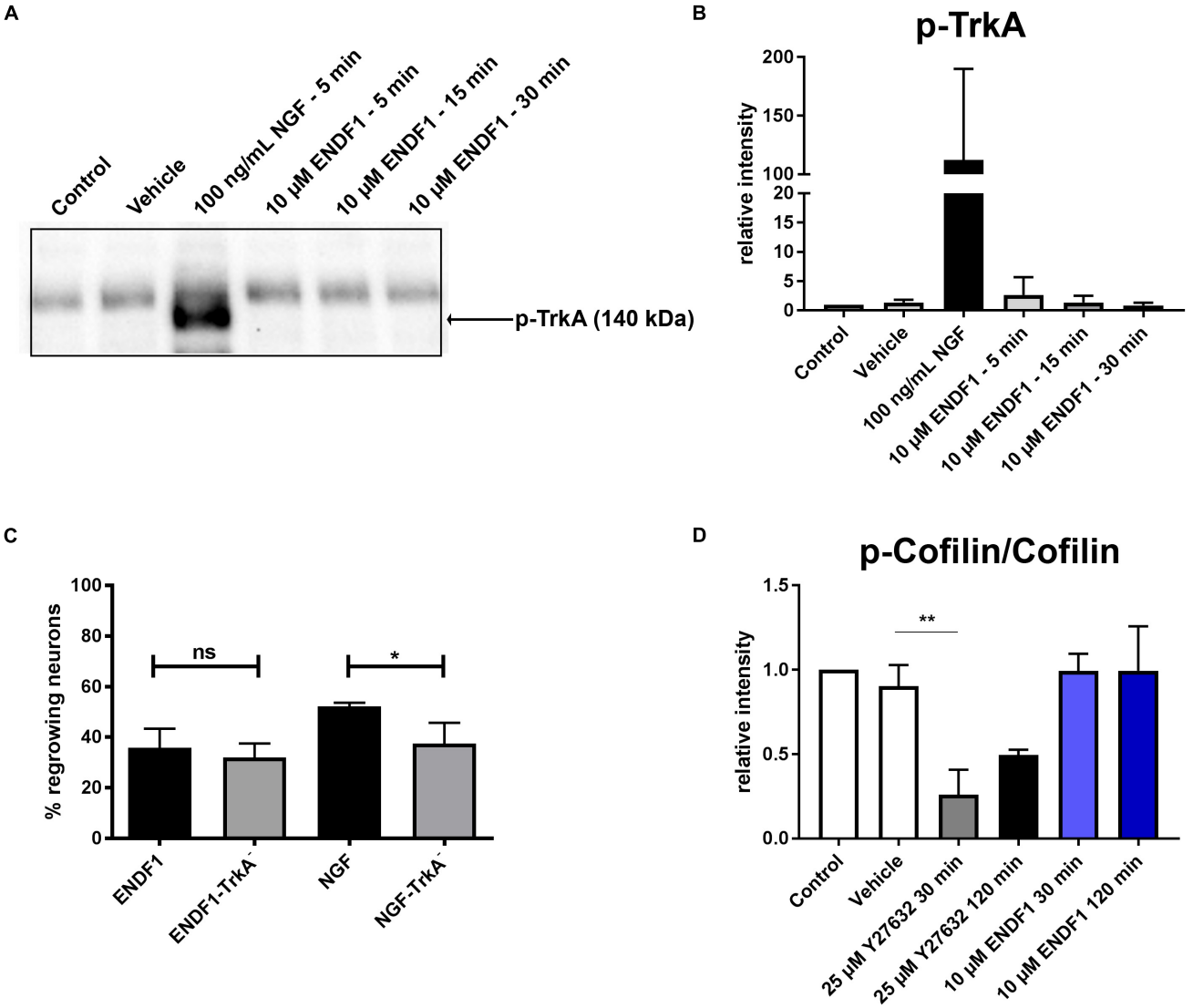

FIGURE 3 | ENDF1 signaling pathways. **(A)** Western blot revealing levels of phospho-TrkA following application of 10 µM ENDF1 or 20 ng/mL NGF in PC-12 cell cultures. **(B)** Quantification of the levels of phospho-TrkA detected on the western blot shown in **(A)**. **(C)** Percentages of DRG neurons seeded on CSPGs displaying neurites after application of ENDF1 or NGF, in the presence or absence of TrkA inhibitor. **(D)** Relative levels of cofilin phosphorylation in PC-12 cell following application of ENDF1 or ROCK inhibitor (Y-27632). Values are displayed as mean ± SD. $^{*}p \leq 0.05$ and $^{**}p \leq 0.01$.

ENDF1 on PC-12 cells for up to 120 min did not reduce the level of cofilin phosphorylation (**Figure 3D**). In contrast, the addition of 25 µM Y27632, a ROCK inhibitor, reduced the level of phosphorylation of cofilin by 73.9 ± 14.7% at 30 min, as compared to the vehicle condition ($p = 0.0028$), and to a lesser extent at 120 min.

DISCUSSION

Restoration of neuronal connectivity rather than compensatory recovery constitutes a goal following CNS injuries, such as spinal cord injury or traumatic brain injury. Based on its pro-regenerative activity on neurite outgrowth observed *in vitro*, ENDF1 constitutes an attractive candidate to address neuronal injury *in vivo*. In the CNS, however, the accumulation of ECM components at the lesion site leads to the inhibition of axonal regrowth and currently represents a main obstacle for functional recovery after injuries. In this study, we demonstrated that ENDF1 is potent to induce neurite regrowth of DRG neurons despite the presence of inhibitory ECM molecules. Using a widespread DRG neuron culture model, we showed that ENDF1 enhanced the percentages of neurons capable of neurite regrowth, as well as the total length and complexity of their arborization despite the presence of three major ECM axon growth inhibitors, namely CSPGs, semaphorin 3A or ephrin A4. Additionally, we showed that ENDF1 is not acting via direct or indirect TrkA signaling.

The ECM-inhibitors used in this study act via their specific receptors to induce growth cone collapse. An interaction of ENDF1 with plexin-neuropilin1 complexes, Eph4A as well as PTPσ, i.e., the respective receptors of the ECM inhibitors used for this study, is very unlikely. Hence, a common downstream signaling component shared by the different inhibitors is a more plausible target for ENDF1. The RhoA/ROCK pathway is such a component relevant for neurite elongation that gets activated by the three inhibitors used in this study (Tonges et al., 2011). RhoA/ROCK inhibition induces a downregulation of LIMK-1 activity, which is leading to cofilin dephosphorylation and onset of neurite growth (Zhang et al., 2006). Previous studies have reported the modulation of Rho GTPases' through the flavonoids isoquercetin and luteolin (Hendriks et al., 2004; Palazzolo et al., 2012). In our study, the level of cofilin phosphorylation was not decreased following incubation with ENDF1, arguing against an inhibitory activity of the later on the RhoA/ROCK signaling pathway.

Thus, the signaling pathway(s) and molecular interaction(s) conveying the regenerative activity of ENDF1 needs to be further elucidated and gives space for speculations. Among potential mechanisms, a regulation of NF-κB signaling could be involved. Several members of flavonoids subgroup named chalcones, which contained also xanthohumol and ENDF1, have been shown to inhibit NF-κB activation and signaling (Yadav et al., 2011). Lowering the activity of NF-κB has been previously proposed to improve CNS regeneration after injury (Engelmann et al., 2014). The stabilization of cytoskeletal elements could also be part of ENDF1 activity supporting neurite regeneration. For example, the microtubule stabilizing agent taxol can significantly increase axonal regeneration after optic nerve injury (Sengottuvel et al., 2011). Similarly, the application of another microtubule-stabilizing compound named epothilone B augmented the length and number of axons showing regenerative growth at the lesion site and accelerated the locomotor recovery in rodent models of spinal cord injury (Ruschel et al., 2015). Since the capacity of some flavonoids to stabilize microtubules has been previously reported in the context of anti-cancer drug development, the same mechanisms could apply in ENDF1 regenerative modes of action on neurites (Touil et al., 2009; Mukhtar et al., 2015).

Stabilization of the microtubule network by ENDF1 could also be indirect. We reported that the application of ENDF1 on mouse embryonic forebrain cells strongly induced the expression of DCX, a microtubule-stabilizing protein expressed in immature neurons (Oberbauer et al., 2013). DCX belongs to a family of microtubule-binding proteins that includes DCLK1 and DCLK2 which, in contrast to DCX, are also expressed in mature neurons of the CNS. In 2015, Nawabi et al. reported that following injury of retinal ganglion neurons, DCLK1 and DCLK2 are among the most dramatically downregulated proteins. Introducing an over-expression of DCLK2 through AAV vector following optic nerve crush resulted in a significantly better regeneration of the axons from retinal ganglion neurons (Nawabi et al., 2015). Therefore, ENDF1 could modulate the expression of genes involved in axonal regeneration, such as the member of the DCX family.

Finally, modulation of calcium channels further represents a possible mode of action of ENDF1 on axonal regeneration. Dysregulation of axonal calcium influx and storage is very detrimental in the acute phase following CNS injury (reviewed in Couillard-Despres et al., 2017). Moreover, Tedeschi et al. (2016) demonstrated that calcium channel subunits expressed in the adult CNS, such as alpha2delta2a subunit of voltage-gated calcium channels (VGCCs), are strong inhibitors of axonal regeneration. Targeted inhibition of this VGCC subunit using Pregabalin improved axonal regeneration following spinal cord injury in a mouse model. A recent study demonstrated that flavonoids can also regulate calcium channels and the hops-derived flavonoids 6-prenylnaringenin and 8-prenylnaringenin were shown to block calcium T-channels, alleviating thereby neuropathic pain after sciatic nerve ligation (Sekiguchi et al., 2018). Hence, modulation of calcium channels activity by ENDF1 should be further scrutinized as a potential target leading to improved regeneration.

In summary, the lack of axonal regrowth is currently one of the major obstacles in functional recovery after injury of the CNS. With this study, we substantiated the pro-neuroregenerative activity of the prenylated flavonoid ENDF1 for the structural repair. We demonstrated that ENDF1 strongly induced neurite regrowth and branching in DRG neurons despite the presence of axon growth inhibitors of the ECM accumulating in the lesioned CNS. Although ENDF1's modes of action are still fairly unknown and need to be further investigated, ENDF1 constitutes a promising small molecule for regenerative therapy of the injured CNS.

ETHICS STATEMENT

Experiments were performed in accordance with the guidelines of the "Directive 2010/63/EU of the European Parliament and of the Council of 22 September 2010 on the protection of animals used for scientific purposes." No experiments were performed on living animals. According to the European and Autrian directives, no additional authorizations are required for the sampling of tissues on freshly sacrificed animals.

AUTHOR CONTRIBUTIONS

LB, MV, LA, LK, CB, HR, and SC-D contributed to the conception and design of the study. LB, MV, MK, and CU conducted and analyzed the experiments. LB and MV performed the statistical analysis. LB and SC-D wrote the manuscript. All authors contributed to manuscript revision, and read and approved the submitted version.

FUNDING

This project was supported by the Paracelsus Medical University Research Fund (R-14/03/060-BIE, E-15/21/109-COU, and S-15/05/008-VOG).

REFERENCES

Baumer, B. E., Kurz, A., Borrie, S. C., Sickinger, S., Dours-Zimmermann, M. T., Zimmermann, D. R., et al. (2014). Nogo receptor homolog NgR2 expressed in sensory DRG neurons controls epidermal innervation by interaction with Versican. *J. Neurosci.* 34, 1633–1646. doi: 10.1523/JNEUROSCI.3094-13.2014

Boyd, A. W., Bartlett, P. F., and Lackmann, M. (2014). Therapeutic targeting of EPH receptors and their ligands. *Nat. Rev. Drug. Discov.* 13, 39–62. doi: 10.1038/nrd4175

Bradbury, E. J., Moon, L. D., Popat, R. J., King, V. R., Bennett, G. S., Patel, P. N., et al. (2002). Chondroitinase ABC promotes functional recovery after spinal cord injury. *Nature* 416, 636–640.

Couillard-Despres, S., Bieler, L., and Vogl, M. (2017). "Pathophysiology of traumatic spinal cord injury," in *Neurological Aspects of Spinal Cord Injury*, eds N. Weidner, R. Rupp, and K. Tansey (Berlin, BE: Springer), 503–528. doi: 10.1007/978-3-319-46293-6_19

Couillard-Despres, S., Quehl, E., Altendorfer, K., Karl, C., Ploetz, S., Bogdahn, U., et al. (2008). Human in vitro reporter model of neuronal development and early differentiation processes. *BMC Neurosci.* 9:31. doi: 10.1186/1471-2202-9-31

Crespo, D., Asher, R. A., Lin, R., Rhodes, K. E., and Fawcett, J. W. (2007). How does chondroitinase promote functional recovery in the damaged CNS? *Exp. Neurol.* 206, 159–171. doi: 10.1016/j.expneurol.2007.05.001

de Andrade Teles, R. B., Diniz, T. C., Costa Pinto, T. C., De Oliveira Junior, R. G., Gama, E. S. M., De Lavor, E. M., et al. (2018). Flavonoids as therapeutic agents in alzheimer's and parkinson's diseases: a systematic review of preclinical evidences. *Oxid. Med. Cell. Longev.* 2018:7043213. doi: 10.1155/2018/7043213

Dick, G., Tan, C. L., Alves, J. N., Ehlert, E. M., Miller, G. M., Hsieh-Wilson, L. C., et al. (2013). Semaphorin 3A binds to the perineuronal nets via chondroitin sulfate type E motifs in rodent brains. *J. Biol. Chem.* 288, 27384–27395. doi: 10.1074/jbc.M111.310029

Engelmann, C., Weih, F., and Haenold, R. (2014). Role of nuclear factor kappa B in central nervous system regeneration. *Neural Regen. Res.* 9, 707–711. doi: 10.4103/1673-5374.131572

Fabes, J., Anderson, P., Yanez-Munoz, R. J., Thrasher, A., Brennan, C., and Bolsover, S. (2006). Accumulation of the inhibitory receptor EphA4 may prevent regeneration of corticospinal tract axons following lesion. *Eur. J. Neurosci.* 23, 1721–1730. doi: 10.1111/j.1460-9568.2006.04704.x

Frugier, T., Conquest, A., Mclean, C., Currie, P., Moses, D., and Goldshmit, Y. (2012). Expression and activation of EphA4 in the human brain after traumatic injury. *J. Neuropathol. Exp. Neurol.* 71, 242–250. doi: 10.1097/NEN.0b013e3182496149

Galtrey, C. M., and Fawcett, J. W. (2007). The role of chondroitin sulfate proteoglycans in regeneration and plasticity in the central nervous system. *Brain Res. Rev.* 54, 1–18. doi: 10.1016/j.brainresrev.2006.09.006

Gildawie, K. R., Galli, R. L., Shukitt-Hale, B., and Carey, A. N. (2018). Protective effects of foods containing flavonoids on age-related cognitive decline. *Curr. Nutr. Rep.* 7, 39–48. doi: 10.1007/s13668-018-0227-0

Goldshmit, Y., Galea, M. P., Wise, G., Bartlett, P. F., and Turnley, A. M. (2004). Axonal regeneration and lack of astrocytic gliosis in EphA4-deficient mice. *J. Neurosci.* 24, 10064–10073. doi: 10.1523/jneurosci.2981-04.2004

Goldshmit, Y., Spanevello, M. D., Tajouri, S., Li, L., Rogers, F., Pearse, M., et al. (2011). EphA4 blockers promote axonal regeneration and functional recovery following spinal cord injury in mice. *PLoS One* 6:e24636. doi: 10.1371/journal.pone.0024636

Goritz, C., Dias, D. O., Tomilin, N., Barbacid, M., Shupliakov, O., and Frisen, J. (2011). A pericyte origin of spinal cord scar tissue. *Science* 333, 238–242. doi: 10.1126/science.1203165

Haller, I., Lirk, P., Keller, C., Wang, G. K., Gerner, P., and Klimaschewski, L. (2007). Differential neurotoxicity of tricyclic antidepressants and novel derivatives in vitro in a dorsal root ganglion cell culture model. *Eur. J. Anaesthesiol.* 24, 702–708. doi: 10.1017/s0265021507000154

Hendriks, J. J., Alblas, J., Van Der Pol, S. M., Van Tol, E. A., Dijkstra, C. D., and De Vries, H. E. (2004). Flavonoids influence monocytic GTPase activity and are protective in experimental allergic encephalitis. *J. Exp. Med.* 200, 1667–1672. doi: 10.1084/jem.20040819

Iozzo, R. V. (1998). Matrix proteoglycans: from molecular design to cellular function. *Annu. Rev. Biochem.* 67, 609–652. doi: 10.1146/annurev.biochem.67.1.609

Kaneko, S., Iwanami, A., Nakamura, M., Kishino, A., Kikuchi, K., Shibata, S., et al. (2006). A selective Sema3A inhibitor enhances regenerative responses and functional recovery of the injured spinal cord. *Nat. Med.* 12, 1380–1389. doi: 10.1038/nm1505

Kaplan, D. R., Martin-Zanca, D., and Parada, L. F. (1991). Tyrosine phosphorylation and tyrosine kinase activity of the trk proto-oncogene product induced by NGF. *Nature* 350, 158–160. doi: 10.1038/350158a0

Kwok, J. C., Yang, S., and Fawcett, J. W. (2014). Neural ECM in regeneration and rehabilitation. *Prog. Brain. Res.* 214, 179–192. doi: 10.1016/b978-0-444-63486-3.00008-6

Lisabeth, E. M., Falivelli, G., and Pasquale, E. B. (2013). Eph receptor signaling and ephrins. *Cold Spring Harb. Perspect. Biol.* 5:a009159. doi: 10.1101/cshperspect.a009159

Mukhtar, E., Adhami, V. M., Sechi, M., and Mukhtar, H. (2015). Dietary flavonoid fisetin binds to beta-tubulin and disrupts microtubule dynamics in prostate cancer cells. *Cancer Lett.* 367, 173–183. doi: 10.1016/j.canlet.2015.07.030

Nawabi, H., Belin, S., Cartoni, R., Williams, P. R., Wang, C., Latremoliere, A., et al. (2015). Doublecortin-like kinases promote neuronal survival and induce growth cone reformation via distinct mechanisms. *Neuron* 88, 704–719. doi: 10.1016/j.neuron.2015.10.005

Nusser, N., Gosmanova, E., Zheng, Y., and Tigyi, G. (2002). Nerve growth factor signals through TrkA, phosphatidylinositol 3-kinase, and Rac1 to inactivate RhoA during the initiation of neuronal differentiation of PC12 cells. *J. Biol. Chem.* 277, 35840–35846. doi: 10.1074/jbc.m203617200

Oberbauer, E., Urmann, C., Steffenhagen, C., Bieler, L., Brunner, D., Furtner, T., et al. (2013). Chroman-like cyclic prenylflavonoids promote neuronal differentiation and neurite outgrowth and are neuroprotective. *J. Nutr. Biochem.* 24, 1953–1962. doi: 10.1016/j.jnutbio.2013.06.005

Palazzolo, G., Horvath, P., and Zenobi-Wong, M. (2012). The flavonoid isoquercitrin promotes neurite elongation by reducing RhoA activity. *PLoS One* 7:e49979. doi: 10.1371/journal.pone.0049979

Pasterkamp, R. J., Anderson, P. N., and Verhaagen, J. (2001). Peripheral nerve injury fails to induce growth of lesioned ascending dorsal column axons into spinal cord scar tissue expressing the axon repellent semaphorin3A. *Eur. J. Neurosci.* 13, 457–471. doi: 10.1046/j.0953-816x.2000.01398.x

Quraishe, S., Forbes, L. H., and Andrews, M. R. (2018). The extracellular environment of the cns: influence on plasticity, sprouting, and axonal regeneration after spinal cord injury. *Neural Plast.* 2018:2952386. doi: 10.1155/2018/2952386

Rohm, B., Ottemeyer, A., Lohrum, M., and Puschel, A. W. (2000). Plexin/neuropilin complexes mediate repulsion by the axonal guidance signal semaphorin 3A. *Mech. Dev.* 93, 95–104. doi: 10.1016/s0925-4773(00)00269-0

Ruoslahti, E. (1996). Brain extracellular matrix. *Glycobiology* 6, 489–492.

Ruschel, J., Hellal, F., Flynn, K. C., Dupraz, S., Elliott, D. A., Tedeschi, A., et al. (2015). Axonal regeneration. systemic administration of epothilone B promotes axon regeneration after spinal cord injury. *Science* 348, 347–352. doi: 10.1126/science.aaa2958

Schindelin, J., Arganda-Carreras, I., Frise, E., Kaynig, V., Longair, M., Pietzsch, T., et al. (2012). Fiji: an open-source platform for biological-image analysis. *Nat. Methods* 9, 676–682. doi: 10.1038/nmeth.2019

Sekiguchi, F., Fujita, T., Deguchi, T., Yamaoka, S., Tomochika, K., Tsubota, M., et al. (2018). Blockade of T-type calcium channels by 6-prenylnaringenin, a hop component, alleviates neuropathic and visceral pain in mice. *Neuropharmacology* 138, 232–244. doi: 10.1016/j.neuropharm.2018.06.020

Sengottuvel, V., Leibinger, M., Pfreimer, M., Andreadaki, A., and Fischer, D. (2011). Taxol facilitates axon regeneration in the mature CNS. *J. Neurosci.* 31, 2688–2699. doi: 10.1523/JNEUROSCI.4885-10.2011

Sorg, B. A., Berretta, S., Blacktop, J. M., Fawcett, J. W., Kitagawa, H., Kwok, J. C., et al. (2016). Casting a wide net: role of perineuronal nets in neural plasticity. *J. Neurosci.* 36, 11459–11468. doi: 10.1523/jneurosci.2351-16.2016

Tedeschi, A., Dupraz, S., Laskowski, C. J., Xue, J., Ulas, T., Beyer, M., et al. (2016). The Calcium channel subunit alpha2delta2 suppresses axon regeneration in the adult CNS. *Neuron* 92, 419–434. doi: 10.1016/j.neuron.2016.09.026

Tonges, L., Koch, J. C., Bahr, M., and Lingor, P. (2011). ROCKing regeneration: rho kinase inhibition as molecular target for neurorestoration. *Front. Mol. Neurosci.* 4:39. doi: 10.3389/fnmol.2011.00039

Touil, Y. S., Fellous, A., Scherman, D., and Chabot, G. G. (2009). Flavonoid-induced morphological modifications of endothelial cells through microtubule stabilization. *Nutr. Cancer* 61, 310–321. doi: 10.1080/01635580802521346

Wiersma, A. M., Fouad, K., and Winship, I. R. (2017). Enhancing spinal plasticity amplifies the benefits of rehabilitative training and improves recovery from stroke. *J. Neurosci.* 37, 10983–10997. doi: 10.1523/JNEUROSCI.0770-17.2017

Yadav, V. R., Prasad, S., Sung, B., and Aggarwal, B. B. (2011). The role of chalcones in suppression of NF-kappaB-mediated inflammation and cancer. *Int. Immunopharmacol.* 11, 295–309. doi: 10.1016/j.intimp.2010.12.006

Zhang, Y., Moheban, D. B., Conway, B. R., Bhattacharyya, A., and Segal, R. A. (2000). Cell surface trk receptors mediate NGF-induced survival while internalized receptors regulate NGF-induced differentiation. *J. Neurosci.* 20, 5671–5678. doi: 10.1523/jneurosci.20-15-05671.2000

Zhang, Z., Ottens, A. K., Larner, S. F., Kobeissy, F. H., Williams, M. L., Hayes, R. L., et al. (2006). Direct Rho-associated kinase inhibition [correction of inhibiton] induces cofilin dephosphorylation and neurite outgrowth in PC-12 cells. *Cell. Mol. Biol. Lett.* 11, 12–29.

Conflict of Interest Statement: LA and SC-D own a patent on the use of chroman-like cyclic prenylflavonoids for the medical intervention in neurological disorders.

The remaining authors declare that the research was conducted in the absence of any commercial or financial relationships that could be construed as a potential conflict of interest.

frontiers in Cellular Neuroscience

ORIGINAL RESEARCH
published: 14 August 2019
doi: 10.3389/fncel.2019.00346

A VDAC1-Derived N-Terminal Peptide Inhibits Mutant SOD1-VDAC1 Interactions and Toxicity in the SOD1 Model of ALS

Anna Shteinfer-Kuzmine[1†], Shirel Argueti[2†], Rajeev Gupta[1†], Neta Shvil[2], Salah Abu-Hamad[2], Yael Gropper[2], Jan Hoeber[3], Andrea Magrì[4], Angela Messina[4], Elena N. Kozlova[3], Varda Shoshan-Barmatz[1] and Adrian Israelson[2]**

[1] Department of Life Sciences, The National Institute for Biotechnology in the Negev, Ben-Gurion University of the Negev, Beersheba, Israel, [2] Department of Physiology and Cell Biology, Faculty of Health Sciences, The Zlotowski Center for Neuroscience, Ben-Gurion University of the Negev, Beersheba, Israel, [3] Department of Neuroscience, Uppsala University, Uppsala, Sweden, [4] Department of Biological, Geological and Environmental Sciences, University of Catania, Catania, Italy

Mutations in superoxide dismutase (SOD1) are the second most common cause of familial amyotrophic lateral sclerosis (ALS), a fatal neurodegenerative disease caused by the death of motor neurons in the brain and spinal cord. SOD1 neurotoxicity has been attributed to aberrant accumulation of misfolded SOD1, which in its soluble form binds to intracellular organelles, such as mitochondria and ER, disrupting their functions. Here, we demonstrate that mutant SOD1 binds specifically to the N-terminal domain of the voltage-dependent anion channel (VDAC1), an outer mitochondrial membrane protein controlling cell energy, metabolic and survival pathways. Mutant SOD1^{G93A} and SOD1^{G85R}, but not wild type SOD1, directly interact with VDAC1 and reduce its channel conductance. No such interaction with N-terminal-truncated VDAC1 occurs. Moreover, a VDAC1-derived N-terminal peptide inhibited mutant SOD1-induced toxicity. Incubation of motor neuron-like NSC-34 cells expressing mutant SOD1 or mouse embryonic stem cell-derived motor neurons with different VDAC1 N-terminal peptides resulted in enhanced cell survival. Taken together, our results establish a direct link between mutant SOD1 toxicity and the VDAC1 N-terminal domain and suggest that VDAC1 N-terminal peptides targeting mutant SOD1 provide potential new therapeutic strategies for ALS.

Keywords: ALS, misfolded SOD1, mutant SOD1, N-terminal peptide, VDAC1

OPEN ACCESS

Edited by:
Francisca C. Bronfman, Pontifical Catholic University of Chile, Chile

Reviewed by:
Kim A. Staats, University of Southern California, United States
Mauro Cozzolino, Institute of Translational Pharmacology (CNR), Italy
Koji Yamanaka, Nagoya University, Japan

***Correspondence:**
Varda Shoshan-Barmatz
vardasb@bgu.ac.il
Adrian Israelson
adriani@bgu.ac.il

† These authors have contributed equally to this work

Specialty section:
This article was submitted to Cellular Neuropathology, a section of the journal Frontiers in Cellular Neuroscience

Received: *20 January 2019*
Accepted: *15 July 2019*
Published: *14 August 2019*

Citation:
Shteinfer-Kuzmine A, Argueti S, Gupta R, Shvil N, Abu-Hamad S, Gropper Y, Hoeber J, Magrì A, Messina A, Kozlova EN, Shoshan-Barmatz V and Israelson A (2019) A VDAC1-Derived N-Terminal Peptide Inhibits Mutant SOD1-VDAC1 Interactions and Toxicity in the SOD1 Model of ALS. Front. Cell. Neurosci. 13:346. doi: 10.3389/fncel.2019.00346

INTRODUCTION

Amyotrophic lateral sclerosis (ALS) is a progressive and fatal neurodegenerative disease caused by the death of upper and lower motor neurons in the brain and spinal cord (Cleveland and Rothstein, 2001). The age of onset is typically between 50 and 60 years, followed by progressive paralysis and death 2–5 years after diagnosis (Mulder et al., 1986; Dorst et al., 2019). Most cases of ALS are sporadic and lack any apparent genetic linkage, although in 10% of cases, the disease is inherited in a dominant manner. About a fifth of these familial cases have been attributed to mutations in the gene encoding cytoplasmic Cu/Zn superoxide dismutase (SOD1) (Rosen et al., 1993).

To date, more than 180 different human SOD1 mutations have been identified throughout the length of the SOD1 protein that are directly linked to familial ALS (fALS),[1] including active dismutase mutants, such as $SOD1^{G93A}$ and $SOD1^{G37R}$, and inactive dismutase mutants in which the mutation affects the metal-binding region, such as $SOD1^{G85R}$ and $SOD1^{H46R}$ (Abu-Hamad et al., 2017). The latter group of mutants are more unstable than are the former. Moreover, wild type human SOD1 ($SOD1^{WT}$) can become misfolded and toxic, thus sharing an aberrant conformation with SOD1 mutants, when oxidatively modified (Tiwari et al., 2009; Bosco et al., 2010; Guareschi et al., 2012; Lim and Song, 2016; Medinas et al., 2018; Xu et al., 2018). The exact mechanism which drives motor neuron degeneration and disease progression remains unknown, although multiple hypotheses have been proposed to explain mutant SOD1-dependent toxic effects (Ilieva et al., 2009). These include ER stress, oxidative stress, glutamate-mediated excitotoxicity and mutant SOD1 misfolding and aggregation-induced pathology. Indeed, aggregation of misfolded SOD1 proteins is a common pathological observation among subjects with different SOD1 mutations and is, therefore, believed to be central to ALS pathogenesis (Bruijn et al., 1998; Wang et al., 2005; Prudencio et al., 2009; Abu-Hamad et al., 2017; Shvil et al., 2018).

Mitochondrial dysfunction has also been proposed as a major factor contributing to ALS pathology. SOD1 mutants affect various aspects of mitochondrial normal function, including fission and fusion, energy metabolism and transport (Ferri et al., 2006; Shi et al., 2010; Carri and Cozzolino, 2011; Magrane et al., 2012). Aberrant mitochondrial structures have been reported in both familial and sporadic ALS patients (Hirano et al., 1984a,b; Sasaki and Iwata, 1996, 2007), as well as in mutant SOD1 mouse models (Dal Canto and Gurney, 1994; Wong et al., 1995; Kong and Xu, 1998; Higgins et al., 2003). In addition, mitochondrial dysfunction and Ca^{2+} dysregulation has been reported in spinal cord and skeletal muscles of familial and sporadic ALS patients (Vielhaber et al., 1999; Echaniz-Laguna et al., 2002; Wiedemann et al., 2002; Dupuis et al., 2003), as well as in different ALS mouse models (Mattiazzi et al., 2002; Damiano et al., 2006; Nguyen et al., 2009).

Although predominantly a cytosolic protein, SOD1 is also found localized in other cellular compartments, including mitochondria. Both in mouse and rat models of ALS and post-mortem tissue samples from ALS patients, mutant SOD1 was found in fractions enriched for mitochondria derived only from affected but not unaffected tissues (Mattiazzi et al., 2002; Liu et al., 2004; Vijayvergiya et al., 2005; Bergemalm et al., 2006; Deng et al., 2006; Vande Velde et al., 2008). Moreover, a clear temporal correlation between disease progression and mitochondrial association was shown for different SOD1 mutants in rodent models (Liu et al., 2004). In addition, we have recently reported a clear inverse correlation between mutant SOD1 mitochondrial association in motor neuron-like NSC-34 cells and disease duration in patients carrying mutations in SOD1 (Abu-Hamad et al., 2017). Highly purified floated mitochondria coupled with protease accessibility has demonstrated deposition of mutant SOD1 on the cytoplasmic-facing surface of spinal cord mitochondria (Liu et al., 2004; Vande Velde et al., 2008). Sensitivity to proteolysis and immunoprecipitation with specific antibodies for misfolded SOD1 further demonstrated that misfolded species of SOD1 are associated with the outer mitochondrial membrane of the spinal cord (Vande Velde et al., 2008). In addition, mutant SOD1 was proposed to interact with other components of the outer mitochondrial membrane, including Bcl-2 (Pedrini et al., 2010) and the protein import machinery (Li et al., 2010), thus affecting the corresponding functions. Importantly, this was seen only for spinal cord mitochondria but not for mitochondria isolated from unaffected tissues (Israelson et al., 2010; Li et al., 2010). More specifically, direct binding of misfolded SOD1 to the voltage-dependent anion channel-1 (VDAC1) was previously shown, causing reduction of VDAC1 conductance and channel instability, leading to inhibition of VDAC1 transport of adenine nucleotides across the outer mitochondrial membrane (Israelson et al., 2010; Magri et al., 2016).

VDAC1, also known as the mitochondrial porin, is located at the outer mitochondrial membrane, where it assumes a crucial position controlling the metabolic cross-talk between the mitochondria and the rest of the cell, thus regulating the metabolic and energetic functions of mitochondria. VDAC1 is also a central player in mitochondria-mediated apoptosis and has been implicated in apoptotic-related functions, given its role as the target for pro- and anti-apoptotic Bcl2-family of proteins (Shimizu et al., 1999; Arbel and Shoshan-Barmatz, 2010) and due to its function in the release of apoptotic proteins from the mitochondrial inter membrane space (Tajeddine et al., 2008; Abu-Hamad et al., 2009). VDAC1, the main VDAC isoform, is composed of 19 transmembrane β-strands forming a membrane-embedded β-barrel and a flexible amphipathic 26-residue-long N-terminal domain lying inside the pore but able to translocate from within the pore to the channel surface (Geula et al., 2012). This mobility is important for controlling channel gating but also for interactions with pro- and anti-apoptotic proteins (Abu-Hamad et al., 2009; Arbel and Shoshan-Barmatz, 2010; Shoshan-Barmatz et al., 2010, 2015; Arbel et al., 2012; Geula et al., 2012). Importantly, cells expressing an N-terminally truncated form of VDAC1 are resistant to apoptosis (Abu-Hamad et al., 2009). These findings suggest that the VDAC1 N-terminal domain is required for interaction with VDAC1-associated proteins and apoptosis.

Here, we demonstrate the direct interaction of VDAC1 with mutant SOD1 and show that this interaction requires the VDAC1 N-terminal domain. Moreover, SOD1-mediated toxicity was prevented by synthetic VDAC1-N-terminal peptides. Finally, we show that a VDAC1 N-terminal peptide enhanced the survival of mutant $SOD1^{G93A}$ motor neuron-like NSC-34 cells and mutant $SOD1^{G93A}$ mouse embryonic stem cell-derived motor neurons. These findings point to VDAC1 N-terminal peptides as offering possible novel therapeutic strategies for ALS.

[1] http://alsod.iop.kcl.ac.uk/als/

MATERIALS AND METHODS

Materials

Bovine serum albumin (BSA), dithiothreitol (DTT), HEPES, leupeptin, phenylmethylsulfonyl fluoride (PMSF), propidium iodide (PI), sucrose and Tris were purchased from Sigma (St. Louis, MO, United States). Dulbecco's modified Eagle's medium (DMEM) was purchased from Gibco (Grand Island, NY, United States). The CellTiter 96 AQueous one-solution cell proliferation assay was purchased from Promega (Madison, WI).

Peptides

The peptides used in this study (listed in **Table 1**) were synthesized by GL Biochem (Shanghai, China). The peptides were first dissolved in DMSO as a 40 mM solution and then diluted 20-fold in the appropriate buffer. Peptide concentrations were determined as described previously (Shteinfer-Kuzmine et al., 2018). The final concentration of DMSO in control and peptide-containing samples was $\leq$0.5%.

Protein Purification

Recombinant hSOD1^{wt}, hSOD1^{G93A}, and hSOD1^{G85R} were expressed in sf-9 cells and purified by hydrophobic interaction chromatography using phenyl-Sepharose 6 Fast Flow high sub (Amersham Biosciences), followed by ion exchange chromatography using a HiTrap Q-Sepharose anion exchange column (Amersham Biosciences), as described previously (Hayward et al., 2002).

VDAC1 Purification

VDAC1 was purified from rat liver mitochondria using celite:hydroxyapatite and CMC chromatography, as previously described (Gincel et al., 2001). DNA sequences encoding full-length murine VDAC1 and N-terminally truncated VDAC1 (ΔN-VDAC1) lacking residues 1–26 were cloned into the pET21a vector (Novagen) using the *Nhe*I/*Xho*I sites. *Escherichia coli* BL21(DE3) cells were transformed with plasmid pET21a harboring the VDAC1 or ΔN-VDAC1 genes. Protein expression was induced for 3 h using 1 mM isopropyl-β-D-thiogalactopyranoside (IPTG; Sigma). Proteins were purified on agarose-packed nickel-nitrilotriacetic acid resin (Ni-NTA; Qiagen) in the presence of 8 M urea. Refolding of the eluted protein was performed essentially as described previously (Hiller et al., 2008). The refolded protein was further purified as above for mitochondrial VDAC1.

Microscale Thermophoresis (MST)

Microscale thermophoresis analysis was performed using a NanoTemper Monolith NT.115 apparatus, as recently described (Wienken et al., 2010; Zillner et al., 2012). Briefly, purified wild type or mutant SOD1 proteins or mitochondria-purified VDAC1 were fluorescently labeled using the NanoTemper BLUE protein-labeling kit (NanoTemper Technologies, Munich, Germany). SOD1 was incubated for 20 min at 20°C in the dark with different concentrations of VDAC1-derived peptides (0.4–100 μM) in 10 mM HEPES buffer (pH 7.4) and then thermophoresis analysis was performed (light-emitting diode 20%, IR laser 20%). The results are presented as the bound fraction, calculated as follows: fraction bound $100 \times (F - F\text{min})/(F\text{max} - F\text{min})$.

VDAC1 Channel Reconstitution, Recording and Analysis

The reconstitution of recombinant WT or ΔN-VDAC1 into a planar lipid bilayer (PLB) prepared from soybean asolectin, and subsequent single channel current recordings and data analysis were carried out as described previously (Gincel et al., 2001). Currents were recorded under voltage-clamp conditions before and 5 min after the addition of 40 μg of recombinant hSOD1^{wt}, hSOD1^{G93A}, or hSOD1^{G85R} to the *cis* compartment

TABLE 1 | Peptides used in this study.

Peptide	Sequence	No. of AA	Molecular Mass, kDa	Calculated molar extinction coefficient, M^{-1}	Purity, %
1-26 N-Terminal	1-MAVPPTYADLGKSA-RDVFTKGYGFGL-26	26	2762	2980	>95
1-26 N-Ter-Antp	1-MAVPPTYADLGKSARDVFTKG YGFGL-26- RQIKIWFQNRRMKWKK	42	4991	13,980	97.72
1-20 N-Ter-Antp	1-MAVPPTYADLGKSARDVFTK-20-RQIKIWFQNRRMKWKK	36	4396	12,490	87.92
5-20 N-Ter-Antp	5-PTYADLGKSARDVFTK-20-RQIKIWFQNRRMKWKK	32	3997	12,490	87.39
10-20 N-Ter-Antp	10-LGKSARDVFTK-20-RQIKIWFQNRRMKWKK	27	3450	11,000	85.18
D-Δ(1-14) N-Ter-Antp	14-RDVFTKGYGFGL-26-RQIKIWFQNRRMKWKK	28	3558	12,490	95.79
LP3	159-ETAKSRVTQSNFAVGYKT-177	18	1987	1490	>85

The VDAC1-based peptides used in this study with the amino acid sequence number, molecular mass, calculated molar extinction coefficient and purity are presented. The cell-penetrating sequence is underlined. The molar extinction coefficient was calculated based on amino acid composition using the following link: http://www.biomol.net/en/tools/proteinextinction.htm.

using a Bilayer Clamp BC-535B amplifier (Warner Instrument, Hamden, CT, United States). Current amplitude histograms were prepared using AxoGraph X software. Relative conductance was determined as the average steady-state conductance at a given voltage normalized to the conductance at 10 mV, the maximal conductance. Relative conductance-voltage plots were prepared using Microsoft Excel software.

Cell Treatment With VDAC1-Based Peptides, Cell Death and XTT Analyses

NSC-34 cells, a mouse motor neuron-like hybrid cell line, the A549 human lung adenocarcinoma and U-87MG human glioblastoma cell lines were incubated with the (1-26)N-Ter-Antp, D-(15-26)N-Ter-Antp, (1-20)N-Ter-Antp, (5-20)N-Ter-Antp, or (10-20)N-Ter-Antp peptides in the appropriate serum-free growth medium for 5 h at 37°C. Cells were harvested, and analyzed for cell death using propidium iodide (PI) staining and flow cytometry. For XTT, the CellTiter 96 AQueous one-solution cell proliferation assay was used to follow cell viability as described previously (Leyton-Jaimes et al., 2016).

Apoptotic cell death was also analyzed using Acridine Orange (AcOr)/ethidium bromide (EtBr) staining (McGahon et al., 1995). Cells in 24-well plates were washed with 200 μl PBS and 10 μl of a solution containing 100 mg/ml AcOr and 100 mg/ml EtBr in PBS was added. The cells were then visualized by fluorescence microscopy (ZOE fluorescence cell imager, Bio-Rad), images were recorded and cells at early and late apoptotic stages were counted.

Immunostaining

For immunostaining, SH-SY5Y cells (4.5×10^4) were grown on sterilized coverslips in 24-well plates. 30 h post-transfection, cells were fixed using 4% paraformaldehyde (PFA; diluted in PBS) for 15 min, and then washed 3 times with PBS (5 min each wash). Cells were then permeabilized with 0.3% Triton X-100 in PBS for 5 min followed by washing with PBS. Cells were then blocked for 1 h with blocking buffer (1% BSA free fatty acids diluted in PBS). Anti-VDAC1 polyclonal antibody (ab15895) and mouse anti misfolded SOD1 (B8H10, Medimabs) were incubated at room temperature for 1–2 h in a buffer of 1% BSA free fatty acids and 0.3% Triton-X100 in PBS. Following incubation with primary antibodies, cells were washed with PBS and incubated with fluorescent conjugated secondary Alexa Flour 488 anti-rabbit and Alexa flour 647 anti-mouse antibodies. The coverslips were carefully dried and mounted on slides using Immumount (Immumount^{TM}, Thermo). After overnight drying, images were acquired on an Olympus IX81 confocal microscope.

Mouse Embryonic Stem Cell (mESC) Cultures

Mouse embryonic stem cell lines harboring human mutant SOD1 (SOD1^{G93A}) were a kind gift from Dr. Kevin Eggan (Harvard Stem Cell Institute). This cell line carries green fluorescent protein (GFP) under the control of the promoter for the motor neuron (MN)-specific transcription factor HB9 (*HB9*:GFP cells) (Di Giorgio et al., 2007). We used the SOD1^{G93A} mESC line to derive GFP$^+$ MNs.

Motor neuron differentiation was induced as described previously with some modifications (Wichterle et al., 2002). Cells were cultured in ADFNB medium composed of advanced D-MEM/F12:Neurobasal (1:1), 0.1 mM 2-mercaptoethanol, and GlutaMAX supplement, B27 supplement, and N2 supplement all from Invitrogen, to form embryoid bodies (EBs), and supplemented with 0.1 μM of retinoic acid (RA, Sigma), as well as 0.5 μM of sonic hedgehog (Shh) agonist Ag1.3 (Curis) every second day.

For an *in vitro* differentiation assay, EBs were enzymatically dissociated after 7 days in culture with TrypLE Express (Gibco) and seeded on 0.01% poly-l-ornithine (Sigma) pre-coated coverslips followed by laminin (10 μg/ml, Sigma). Cells (5×10^4) were seeded on coverslip in 24-well plates with ADFNB cell medium supplemented with of Ciliary neurotrophic factor (10 ng/ml, CNTF) and Glial cell-derived neurotrophic factor (GDNF; Miltenyi Biotec). During plating, 1-20N-Ter-Antp VDAC1-peptide was added to the cultures. Half of the medium was replaced with fresh medium every second day and at the indicated time points. The cultures were fixed in 4% paraformaldehyde in PBS.

Determination of Neurite Outgrowth, Intersections Between Neurites and Survival

Stereological estimation of neurite lengths to evaluate neurite outgrowth in cultured cells was carried out as described previously (Ronn et al., 2000). The total neuritic length per cell was estimated by counting the number of GFP$^+$ soma and neurite intersections with test lines of an unbiased counting frame superimposed on images of cell cultures obtained using a 20× objective (NA 0.75) of a Nikon Eclipse E800 epifluorescence microscope equipped with a Nikon DXM1200F CCD camera. The absolute length, L, of neurites per cell was subsequently estimated from the number of neurite intersections, I, per cell by means of the equation $L = (\pi d/2)I$ describing the relationship between the number of neurite intersections and the vertical distance, d, between the test lines used.

Statistical Analyses

Statistical comparisons between groups were performed by a two-tailed unpaired Student's t-test. The mean ± SEM of results obtained from at least three independent experiments are presented. The significance of differences was calculated by a two-tailed Student's t-test and is reported as $^{**}p < 0.01$. Statistical comparisons between conditions in the mESC MN assays was performed by one-way ANOVA followed by Dunnett's Multiple Comparison test against the control condition (**Figure 6B**) or Tukey's Multiple Comparison test (**Figures 6C,E**). The confidence interval was stated at the 95% confidence level, placing statistical significance at $p < 0.05$. GraphPad Prism 6 was used for plotting data and statistical analysis.

RESULTS

VDAC1 N-Terminal Domain and a VDAC1-Derived Peptide Specifically Interact With Mutant but Not Wild Type SOD1

The interaction of purified WT and the SOD1 mutants SOD1^{G93A} and SOD^{G85R} with purified VDAC1 (**Figure 1A**) was assayed by MST (**Figures 1B–E**). MST measures any variation in the thermal movement of a fluorescently labeled binding partner. The subsequent fluorescence depletion in a heated spot of the protein solution is measured as a function of increasing interacting partner concentration, with dissociation constants (K_D) values being derived from the depletion curves (Wienken et al., 2010; **Figure 1D**). Fluorescently labeled VDAC1 incubated with increasing concentrations of WT or mutant SOD1 (0–100 μM) showed that mutant SOD1^{G93A} and SOD1^{G85R} but not SOD1^{WT} bound to VDAC1 (**Figure 1B**).

Next, to identify the binding site for mutant SOD1 in VDAC1, we took advantage of different VDAC1-based peptides which we have developed and previously tested (Arzoine et al., 2008; Arbel and Shoshan-Barmatz, 2010). As the N-terminal domain of VDAC1 has been the shown to interact with several proteins, such as hexokinase, Bcl-2 and Bcl-xL (Arzoine et al., 2008; Arbel and Shoshan-Barmatz, 2010; Arbel et al., 2012), we tested whether a synthetic N-terminal peptide interacts with SOD1. Accordingly, fluorescently labeled mutant SOD1^{G93A} or SOD1^{G85R} protein was incubated with increasing concentrations of the synthetic VDAC1 N-terminal peptide and changes in fluorescence were monitored (**Figure 1C**). By plotting the percentage change of normalized fluorescence (ΔF Norm %) as a function of peptide concentration, a fitted curve yielded dissociation constants (K_D) for the three versions of SOD1 (**Figure 1D**). The results showed that the VDAC1 N-terminal peptide bound both mutant SOD1^{G93A} and SOD1^{G85R}, but not to SOD1^{WT} (**Figures 1C,D**), indicating that these mutants interact specifically with the N-terminal region.

The specificity of the N-terminal peptide to mutant SOD1 was demonstrated by testing the binding of another VDAC1-derived peptide, LP3. This peptide, representing the sequence of a VDAC1 loop facing the cytosol (Arzoine et al., 2008), showed significantly lower binding to mutant SOD1 than did the (1-26)-N-terminal peptide (**Figure 1E**). These results show that VDAC1 and the N-terminal VDAC1 peptide specifically interact with mutant SOD1^{G93A} and SOD1^{G85R}.

Mutant but Not Wild Type SOD1 Interacts With VDAC1 and Reduces Its Channel Activity

To test whether mutant hSOD1^{G93A} and hSOD1^{G85R} binding to VDAC1 affects VDAC1 function, as well as the requirement of the N-terminal domain for such binding, full length and N-terminally truncated VDAC1 were expressed in *E. coli*, purified (**Figure 2M**) and reconstituted into a PLB as described previously (Gincel et al., 2001).

Single-channel conductance under voltage-clamp conditions was measured as a function of time, reflecting ions passing through the channel in response to an applied voltage gradient. Current-time traces recorded at −10 or 10 mV from purified recombinant full length VDAC1 showed a stable full open state that was maintained for extended periods. Addition of hSOD1^{WT}, even at the highest concentration (60 μg/ml), had no effect on the current (**Figures 2A,B**). VDAC1 showed a bell-shaped relative conductance curve as function of the voltage, with hSOD1^{WT} having no effect on VDAC1 channel conductance at all tested voltages, i.e., −60 to +60 mV (**Figure 2C**). This was also revealed in the current amplitude histograms (**Figure 2D**), which showed a single channel conductance of 32 pA, at 10 mV.

In contrast to hSOD1^{WT}, both mutant hSOD1^{G93A} and hSOD1^{G85R} reduced the channel conductance of bilayer-reconstituted VDAC1 at all tested voltages and decreased the current amplitude histograms (**Figures 2E–L**). hSOD1^{G93A} was found to be more effective in reducing VDAC1 conductance than was hSOD1^{G85R} when added at the same concentration, resulting in 57 and 40% inhibition of channel conductance, respectively (**Table 2**).

As reported previously (Prezma et al., 2013; Shteinfer-Kuzmine et al., 2018), VDAC1 lacking the N-terminal 26 residues (ΔN-VDAC1) showed no voltage-dependent gating, with hSOD1^{WT} having no effect on channel conductance at all voltages tested or on the channel current amplitude histograms (**Figures 3A–D**). Moreover, and in contrast to what was observed upon SOD1 mutants interaction with VDAC1 (see **Figures 2E–L**), hSOD1^{G93A} or hSOD1^{G85R} had no effect on ΔN-VDAC1 conductance at all tested voltages (**Figures 3E–L**). These results thus suggest that VDAC1 N-terminal is important for binding of hSOD1^{G93A} and hSOD1^{G85R} to VDAC1.

The summary of the effects of SOD1^{WT}, hSOD1^{G93A}, and hSOD1^{G85R} on the channel conductance of VDAC1 and ΔN-VDAC1 is presented in **Table 2**.

Cell-Penetrating VDAC1 N-Terminal Peptides Inhibit Cell Death of NSC-34 Cells as Induced by Mutant SOD1^{G93A}

In our previous study (Shteinfer-Kuzmine et al., 2018), several novel VDAC1 N-terminal-derived peptides were designed and tested for their ability to induce cell death in cancer cells. Here, we sought to determine whether any of these peptides does not induce cell death yet can interact with misfolded mutated SOD1 and protect against SOD1^{G93A}-mediated cell death in neuronal cultures. Accordingly, we assessed the effects of synthetic cell-penetrating VDAC1-N-terminal-derived peptides in inducing cell death in NSC-34 cells, a mouse motor neuron-like hybrid cell line, and in the U-87MG and A549 cancer cell lines (**Figures 4A–C**). We considered five cell-penetrating peptides derived from the VDAC1-N-terminal domain in these studies: (1) (1-26)-N-Ter-Antp peptide composed of the first 26 residues of the VDAC1 sequence fused to the cell-penetrating Antp (penetrating) sequence, a 16 residue long sequence from the *Drosophila* antennapedia-homeodomain; (2) D-(15-26)-N-Ter-Antp, a peptide like (1-26)-N-Ter-Antp but shortened by 13

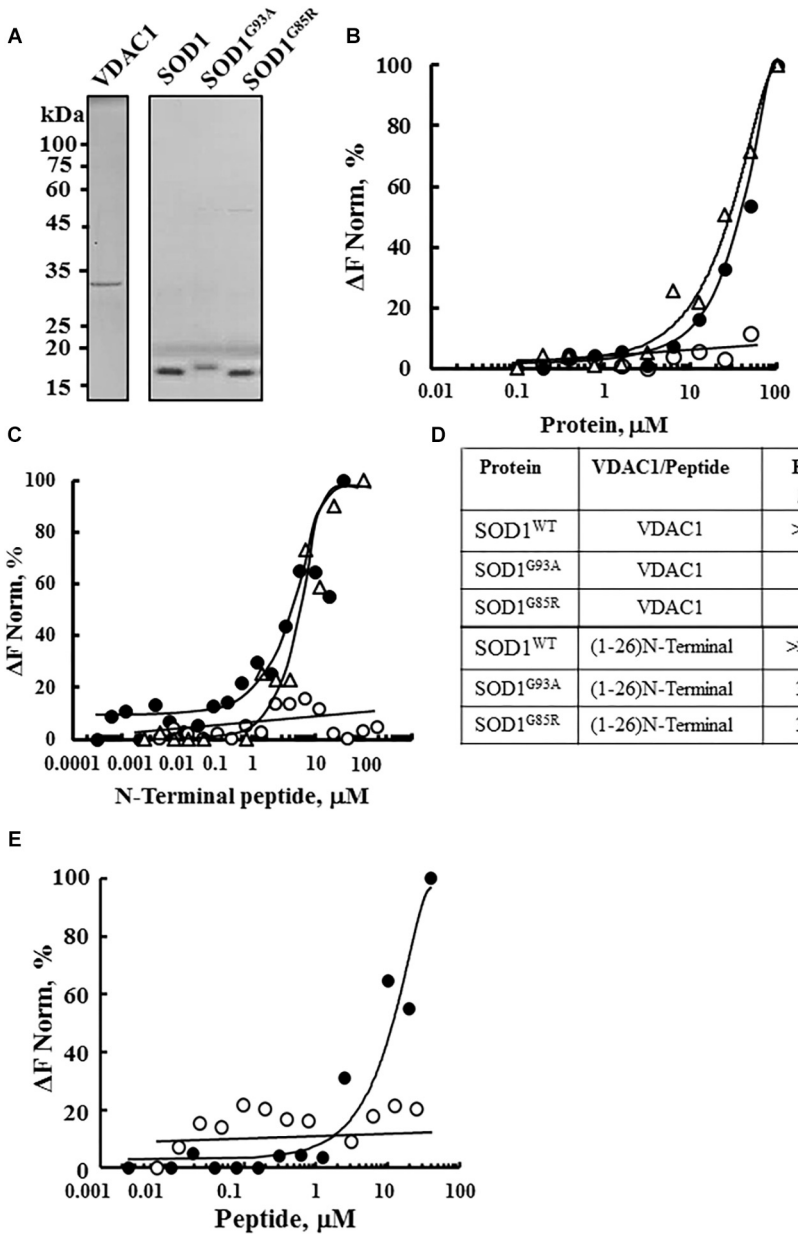

Protein	VDAC1/Peptide	EC_{50} μM
$SOD1^{WT}$	VDAC1	>>50
$SOD1^{G93A}$	VDAC1	40
$SOD1^{G85R}$	VDAC1	30
$SOD1^{WT}$	(1-26)N-Terminal	>>200
$SOD1^{G93A}$	(1-26)N-Terminal	3.75
$SOD1^{G85R}$	(1-26)N-Terminal	3.75

FIGURE 1 | Interaction of wild type and mutant SOD1 with VDAC1 and VDAC1-N-terminal derived peptides. **(A)** Coomassie blue staining of mitochondrial VDAC1, and recombinant $SOD1^{WT}$, $SOD1^{G93A}$, and $SOD1^{G85R}$ expressed in sf-9 cells, purified as described in the Methods section. Molecular weight standards are presented. **(B)** Purified VDAC1 was fluorescently labeled using a NanoTemper blue protein-labeling kit and incubated with $SOD1^{WT}$ (○), $SOD1^{G93A}$ (●), or $SOD1^{G85R}$ (Δ; 0.1–100 μM). After 20 min of incubation, 3–5 μl aliquots were loaded into MST-grade glass capillaries (NanoTemper Technologies) and thermophoresis was measured with a NanoTemper Monolith-NT115 system. The percentage change in normalized fluorescence (ΔF Norm %) is plotted as a function of protein concentration. **(C)** Fluorescently labeled $SOD1^{WT}$ (○, 165 nM), $SOD1^{G85R}$ (Δ, 230 nM) or $SOD1^{G93A}$ (●, 56 nM), was incubated with different concentrations of the VDAC1 N-terminal peptide (0.001–50 μM) in 10 mM HEPES buffer, pH 7.4 and analyzed for binding as in **(B)**. **(D)** Summary of the binding affinity (dissociation constants) of the peptide to $SOD1^{WT}$, $SOD1^{G93A}$ and $SOD1^{G85R}$, as derived from a fitted curve of the percentage change in normalized fluorescence (ΔF Norm %) as a function of peptide and purified VDAC1 concentration. **(E)** Fluorescently labeled $SOD1^{G93A}$ (675 nM) was incubated with the indicated concentrations of N-terminal (●, 0.01–40 μM) or LP3 (○, 6–40 μM) peptides in HEPES buffer, and binding was assayed as in **(B)**. K_D values were calculated using the mass action equation in the NanoTemper software from duplicate reads of triplicate experiments.

amino acids from the N-terminus, and presenting all residues in the D configuration; (3) (1-20)-N-Ter-Antp peptide, again a peptide like (1-26)-N-Ter-Antp but shortened by six amino acids at the C-terminus; (4) (5-20)-N-Ter-Antp peptide, a peptide like (1-20)-N-Ter-Antp peptide but shortened by four amino acids at the N-terminus; and (5) (10-20)-N-Ter-Antp peptide, a peptide like (1-20)-N-Ter-Antp peptide but shortened by nine amino acids at the N-terminus of the peptide (**Table 1**).

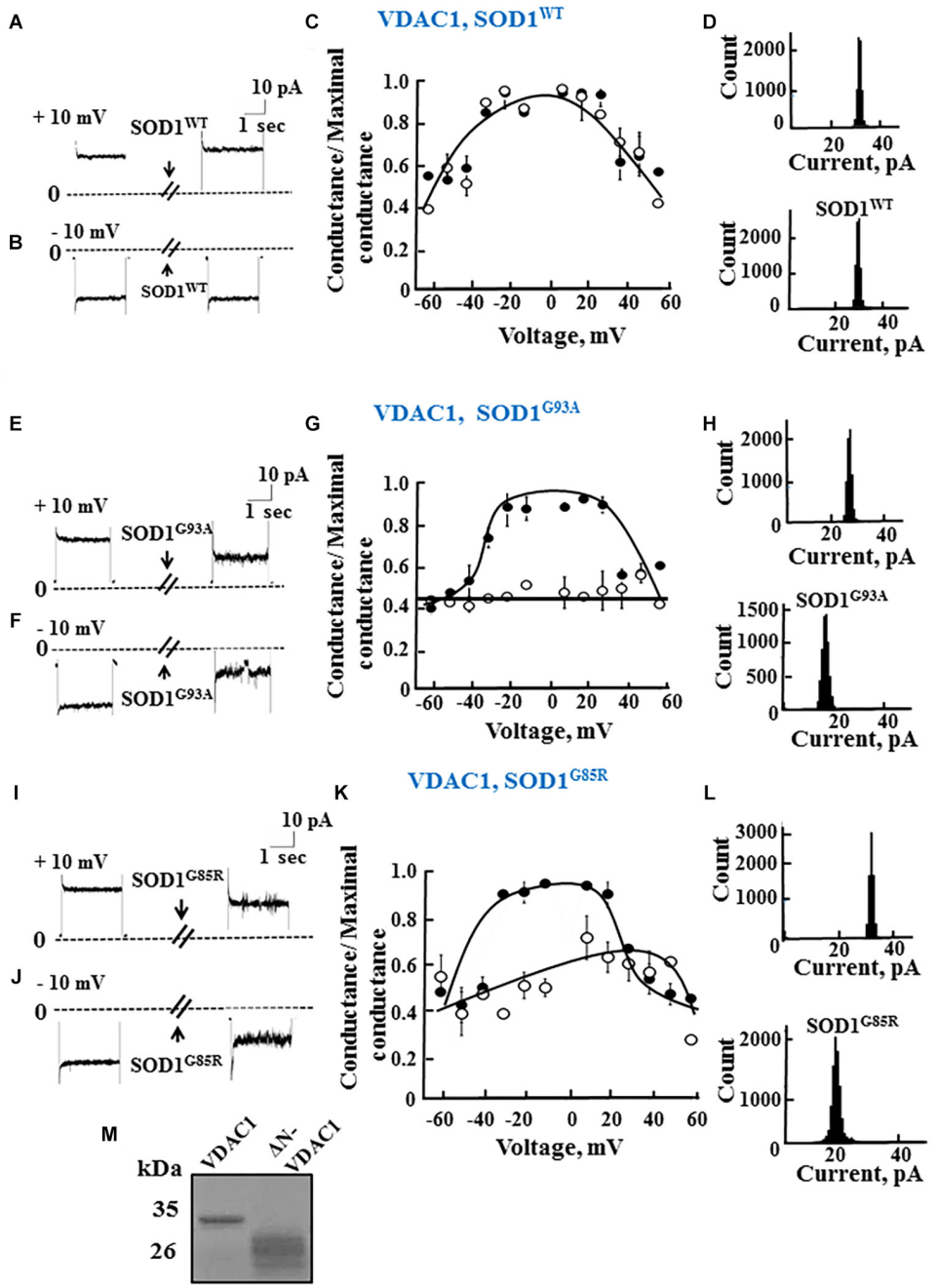

FIGURE 2 | Mutant SOD1 but not wild type SOD1 interacts with VDAC1 and inhibits channel conductance. **(A,B)** Recombinant full length VDAC1 purified from *E. coli* was reconstituted into a PLB and channel currents through VDAC1, in response to a voltage step from 0 to 10 mV **(A)** or to –10 mV **(B)**, before and 15–20 min after addition of 40 μg/ml (final concentration) of SOD1 were recorded. **(C)** VDAC1 relative conductance as a function of voltage in a 60 to –60 mV step before (•) and after addition of $SOD1^{WT}$ (○). Relative conductance (conductance/maximal conductance) was determined as the average steady-state conductance at a given voltage normalized to the conductance at 10 mV, considered the maximal conductance. **(D)** Histogram of VDAC1 current amplitudes at 10 mV before and after addition of $SOD1^{WT}$. **(E–H)** Similar experiments as in **(A–D)**, except that mutant $SOD1^{G93A}$ was used. **(I–L)** Similar experiments as in **(A–D)**, except that mutant $SOD1^{G85R}$ was used. **(M)** Coomassie blue staining of recombinant full length and residue 1-26-truncated VDAC1 (ΔN-VDAC1).

The results showed that (1-26)-N-Ter-Antp and D-(15-26)-N-Ter-Antp peptides induced massive cell death in NSC-34 (**Figure 4A**), U-87MG (**Figure 4B**), and A549 (**Figure 4C**) cells, as analyzed using PI and flow cytometry analysis. However, shortening the (1–26)-N-Ter-Antp by deleting six residues from the C-terminus of the peptide, including the GXXXG motif, to generate the (1-20)-N-Ter-Antp, (5-20)-N-Ter-Antp and (10-20)-N-Ter-Antp

TABLE 2 | Summary of the effects of $SOD1^{WT}$ and mutant SOD1 on the conductance of VDAC1 and ΔN-VDAC1 reconstituted in planar lipid bilayer.

Protein	Conductance, nS	
	VDAC1	**VDAC1 + SOD1**
$SOD1^{WT}$	3.79 ± 0.11	3.84 ± 0.1
$SOD1^{G93A}$	3.51 ± 0.005	1.65 ± 0.33
$SOD1^{G85R}$	3.65 ± 0.14	2.3 ± 0.35
	ΔN-VDAC1	**ΔN-VDAC1 + SOD1**
$SOD1^{WT}$	3.88 ± 0.11	3.69 ± 0.13
$SOD1^{G93A}$	3.39 ± 0.19	3.45 ± 0.01
$SOD1^{G85R}$	3.65 ± 0.14	3.92 ± 0.08

*Results are the conductance (1 M NaCl, pH 7.4, at 10 mV), calculated from experiments as in **Figures 2**, **3** presented as mean ± SE (n = 3).*

peptides, yielded peptides that could not induce cell death (**Figures 4A–C**).

To test *in vitro* whether the different shortened versions of the VDAC1 N-terminal peptide could prevent mutant SOD1 toxicity in neurons, NSC-34 cells were transfected to express $SOD1^{WT}$ or mutant $SOD1^{G93A}$ protein and then treated with or without the above indicated VDAC1 N-terminal peptides. Cell viability was quantified using the XTT assay and apoptosis using acridine orange and ethidium bromide staining. Whereas $SOD1^{WT}$ had not effect on cell viability, expressing $SOD1^{G93A}$ reduced cell viability by 25–30%. The presence of VDAC1 N-terminal peptides reduced the toxic effect of $SOD1^{G93A}$ in a concentration-dependent manner (**Figures 4D–G**). Importantly, this effect was observed using the three non-cell death-inducing VDAC1-derived N-terminal peptides, i.e., the (1-20)-N-Ter-Antp, (5-20)-N-Ter-Antp and (10-20)-N-Ter-Antp peptides.

In order to show that the rescue effect of the N-terminal peptide is not specific for mutant $SOD1^{G93A}$, but a general effect, we have expressed two different dismutase active mutants $SOD1^{G93A}$ or $SOD1^{G37R}$ to induce cell death, increasing it from 17% in the control plasmid-transfected cells to 67 and 70%, in cells expressing mutant $SOD1^{G93A}$ or $SOD1^{G37R}$, respectively. Incubation with the (10-20)-N-Ter-Antp peptide, decreased $SOD1^{G93A}$ and $SOD1^{G37R}$-mediated cell death by 68 and 81%, respectively (**Figure 4H**).

In addition, to test whether the N-terminal VDAC1-based peptide could promote misfolded SOD1 detachment from the mitochondria and more specifically from VDAC1, SH-SY5Y neuronal cells were transfected to express two different mutated $SOD1^{G93A}$ or $SOD1^{G37R}$ proteins and then treated with or without the VDAC1 (10-20)-N-Ter-Antp peptide. Co-localization of misfolded SOD1 with VDAC1 was determined by immunostaining analysis using an anti-VDAC1 antibody that does not target the N-terminus region of the protein, and the B8H10 antibody specifically recognizing misfolded SOD1. In cells transfected with $SOD1^{G93A}$ or $SOD1^{G37R}$, VDAC1 staining is punctuated as expected for mitochondrial localization, while misfolded SOD1 shows both punctuated staining but mostly diffused, indicating that part of the misfolded SOD1 protein is mitochondria bound (**Figures 5A,C**). Yet, a clear co-localization of misfolded SOD1 with VDAC1 can be observed (**Figures 5A,C**). However, this co-localization was greatly eliminated in cells subjected to treatment with (10-20)-N-Ter-Antp peptide (**Figures 5B,D**).

A VDAC1 N-Terminal Peptide Enhances the Survival of Mouse Embryonic Stem Cell-Derived Motor Neurons Expressing $SOD1^{G93A}$

The effects of increasing concentrations of the VDAC1-based (1-20)-N-Ter-Antp peptide on three characteristics of $SOD1^{G93A}$-expressing ESC-derived motor neurons were analyzed *in vitro*. Specifically, we assessed neurite outgrowth, MN survival shortly after induction of final differentiation and survival of maturing $SOD1^{G93A}$-expressing MNs. To follow neuronal development and remodeling of neuronal extensions, we determined neurite outgrowth in cell cultures by tracing neurites and their branches using the stereological procedure, as described previously (Ronn et al., 2000). $SOD1^{G93A}$-expressing MNs grown in relatively pure cultures die rapidly over the 1st week (Aggarwal et al., 2017). Therefore, the first two assays were performed over the first 2 days of culture. This period is characterized by small to minimal loss of MNs, with the exception of those cells that fail to attach or which die immediately. The third assay was performed after the onset of cell death, when around 50% of cells had died.

Images showing the effects of the N-terminal peptide on neurite outgrowth of mESC-derived $SOD1^{G93A}$-expressing MNs (**Figures 6A,D**), as well as quantification of neurite outgrowth (**Figure 6B**), are presented. Cells were incubated with the indicated concentrations of the peptide and analyzed 24 h later. The results showed that adding the peptide at a 10 μM concentration significantly ($p < 0.05$) improved neurite outgrowth of $SOD1^{G93A}$-expressing MNs (**Figures 6A,B**). The effect of the peptide on the survival of mESC-derived $SOD1^{G93A}$-expressing MNs was analyzed 24 h after plating. The results showed that when added at concentrations of 5 or 10 μM, the peptide significantly ($p < 0.05$) improved MN density (**Figures 6A,C**). The reduced effect of the peptide at higher concentrations (25 μM) may result from other non-specific interactions. Moreover, the VDAC1 N-terminal peptide extended survival of the mESC-derived $SOD1^{G93A}$-expressing mature MNs (**Figures 6D,E**). When five cultures were incubated with the indicated peptide concentration for 96 h, it was seen that the peptide significantly ($p < 0.05$) improved MN survival when administered at a 10 μM concentration (**Figures 6D,E**). Thus, the peptide improved survival of $SOD1^{G93A}$-expressing MNs by twofold.

DISCUSSION

The results of the present study contribute to the better understanding of mutant SOD1-mediated mitochondrial dysfunction and cellular toxicity with relevance to ALS pathogenesis. Our results demonstrate that SOD1 mutants bind

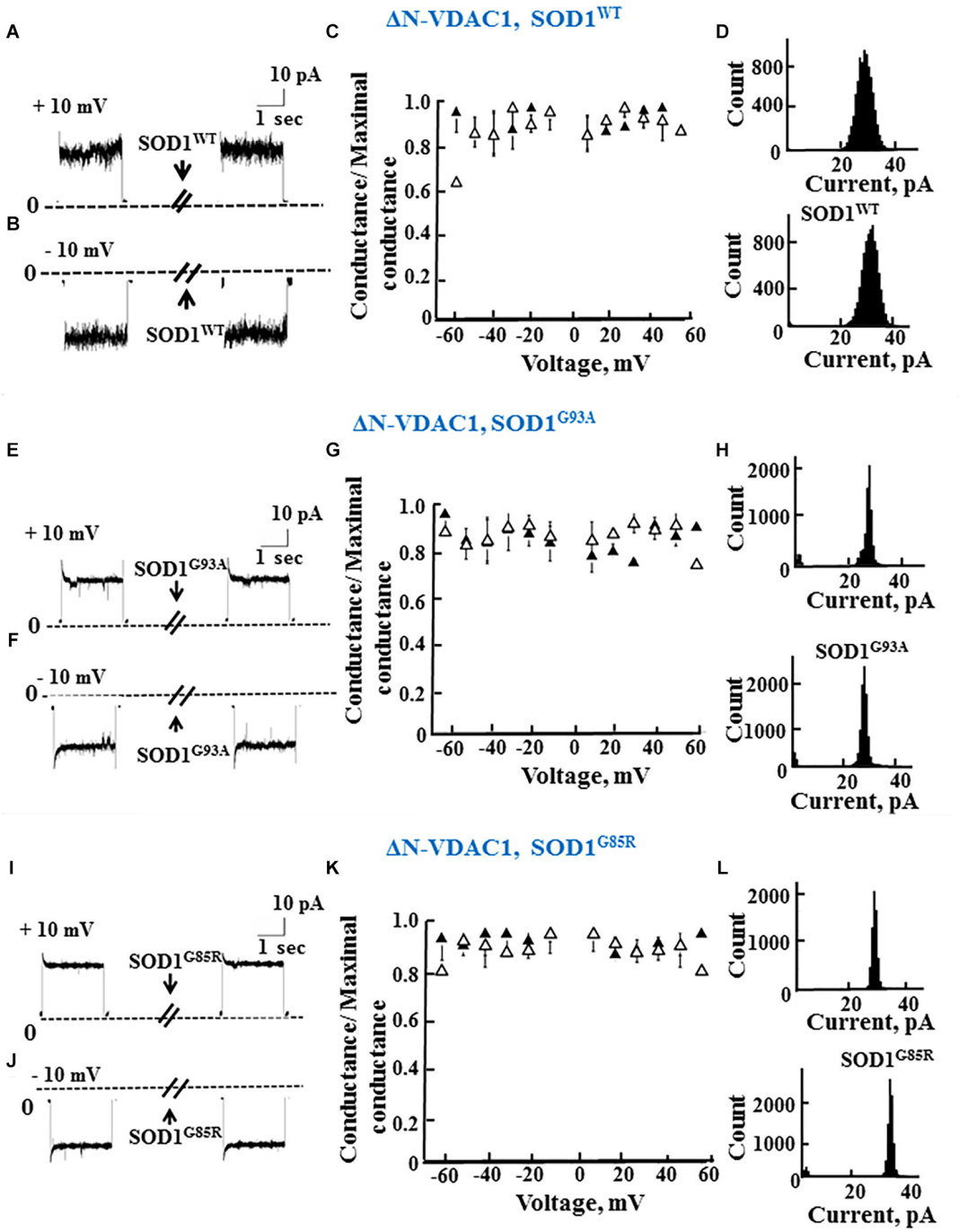

FIGURE 3 | The N-terminal domain of VDAC1 is required for mutant SOD1 interaction with VDAC1 and inhibition of channel conductance. **(A,B)** Currents passing through bilayer-reconstituted recombinant N-terminally truncated VDAC1 (ΔN-VDAC1) were recorded in response to voltage step from 0 to 10 mV **(A)** or –10 mV **(B)** before and 15–20 min after the addition of 40 μg/ml (final concentration) of $SOD1^{WT}$. **(C)** Relative conductance of ΔN-VDAC1 as a function of voltage in a step from 60 to –60 mV before (▲) and after addition of $SOD1^{WT}$ (Δ). Relative conductance (conductance/maximal conductance) was determined as the average steady-state conductance at a given voltage normalized to the conductance at 10 mV, taken as the maximal conductance. **(D)** Histogram of VDAC1 current amplitudes at 10 mV before and after addition of $SOD1^{WT}$. **(E–H)** Similar experiments as in **(A–D)**, except that mutant $SOD1^{G93A}$ was used. **(I–L)** Similar experiments as in **(A–D)**, except that mutant $SOD1^{G85R}$ was used.

directly and selectively to the N-terminal domain of VDAC1. Both dismutase-active $SOD1^{G93A}$ and dismutase-inactive SOD^{G85R} mutants, but not wild type SOD1, bind to the VDAC1 N-terminal region. Moreover, we demonstrated that different versions of an N-terminal peptide suppressed mutant SOD1 toxicity in motor neuron-like NSC-34 cells expressing mutant

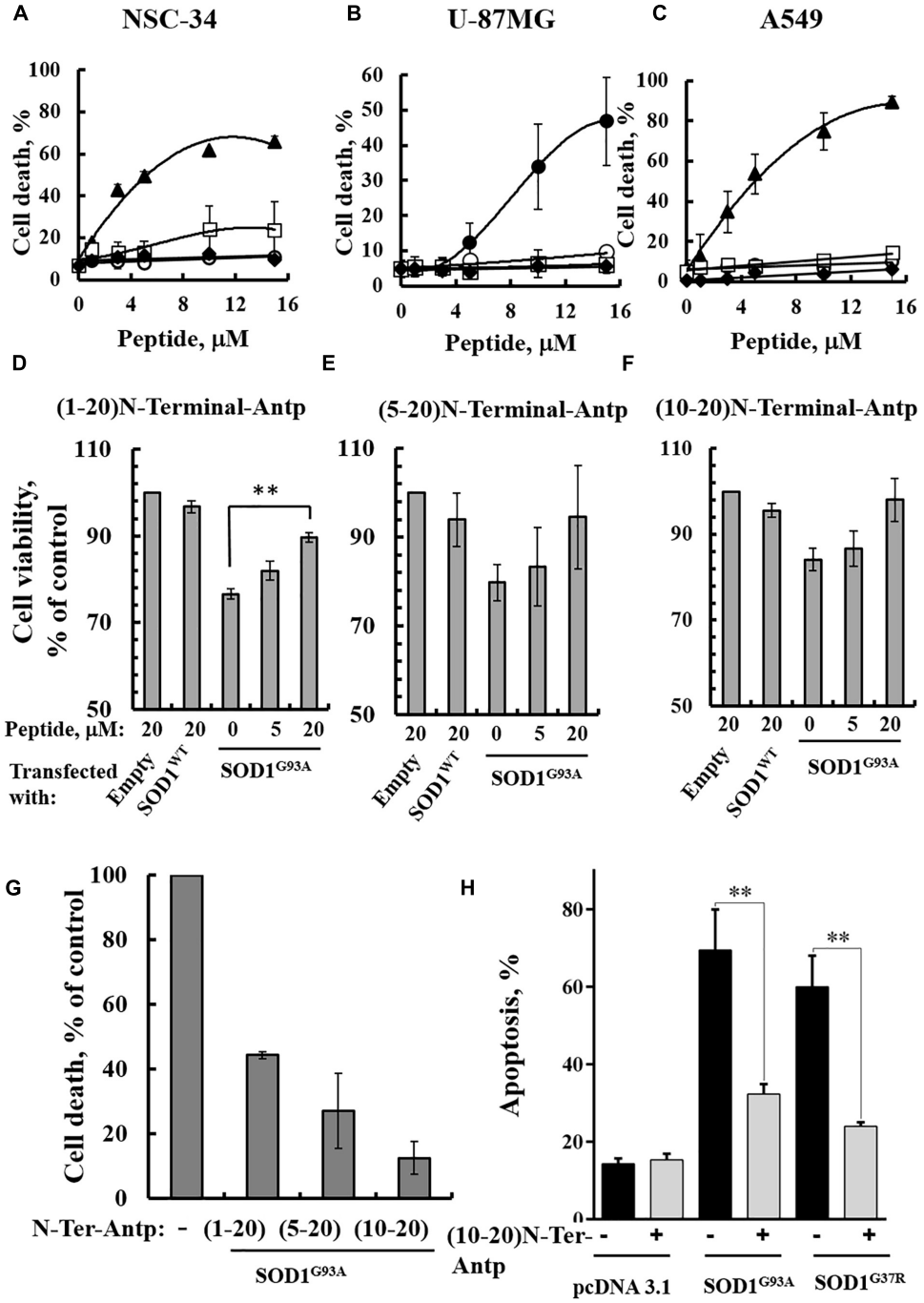

FIGURE 4 | VDAC1 N-terminal peptides inhibit the cell death of NSC-34 cells mediated by mutant SOD1^{G93A}. NSC-34 **(A)**, U-87MG **(B)**, or A549 **(C)** cells were incubated with the indicated concentrations of (1-26)N-Ter-Antp (●), D-(15-26) (19-26)N-Ter-Antp (▲), (1-20)N-Ter-Antp (○), (5-20)N-Ter-Antp (□) or (10-20)N-Ter-Antp (♦) peptide for 5 h. Cell death was analyzed using PI staining and flow cytometry. **(D–F)** NSC-34 cells were transfected to express human SOD1^{WT}, the human mutant SOD1^{G93A}, or neither (empty), in each case either without or with addition of increasing concentrations of the indicated VDAC1 N-terminal-derived peptide for 5 h. Cell viability analysis was performed with the CellTiter 96 AQueous one-solution cell proliferation assay with ELISA at 490 nm. **(G)** The rescuing effects of the VDAC1 N-terminal-derived peptides are shown as a percentage of cell death. The significance of quantitative analysis of triplicates of different biological repeats (n = 3) was performed by Student's t-test; $^{**}P < 0.01$. **(H)** SH-SY5Y cells (4.5×10^4 cells/well in 24-well plates) were transfected with an empty plasmid or a plasmid encoding for mutant SOD1^{G93A} or SOD1^{G37R}. Twenty-four hours post-transfection, the cells were incubated for 5 h with (10-20)N-Ter-Antp peptide (20 μM) and then analyzed for apoptosis using acridine orange and ethidium bromide staining, as described previously (McGahon et al., 1995). Fluorescence microscopy images were analyzed and about 100 to 300 cells were counted for each treatment in representative microscopic fields. The significance of quantitative analysis of triplicates of different biological repeats (n = 3) was performed by one-way Anova; $^{**}P < 0.01$.

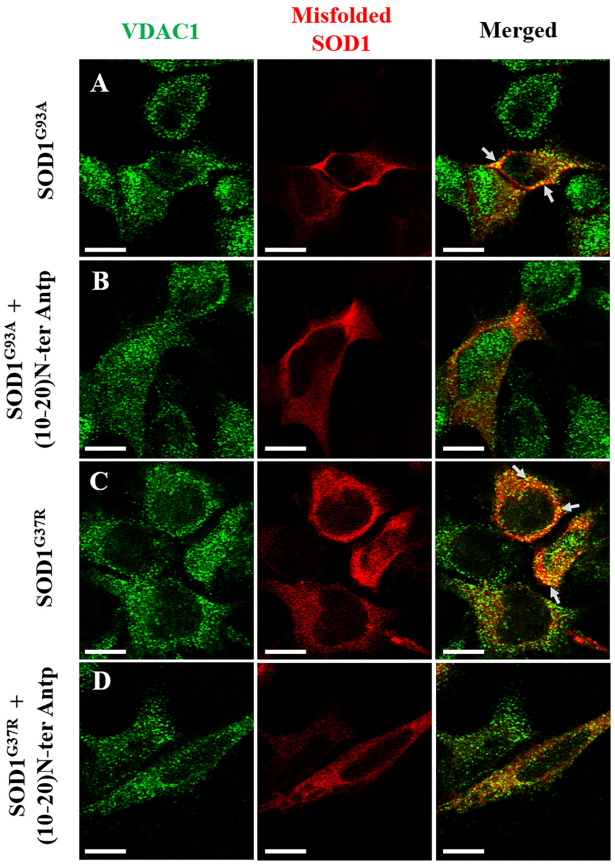

FIGURE 5 | The VDAC1 N-terminal peptide induces detachment of misfolded SOD1 from its mitochondrial binding site. Co-localization of VDAC1 and misfolded SOD1 in SH-SY5Y cells was assayed by indirect immunofluorescence with antibodies for VDAC1 along with simultaneous identification of misfolded SOD1 (with the B8H10 antibody). Twenty-four hours post-transfection, the cells were incubated for 5 h with (10-20)N-Ter-Antp peptide (20 μM) and then analyzed for co-localization using a confocal microscope. Representative images of SH-SY5Y cells transfected to express human mutant $SOD1^{G93A}$ **(A)** or $SOD1^{G37R}$ **(C)** in each case either without **(A,C)** or with **(B,D)** addition of the (10-20)N-Ter-Antp peptide are shown. Scale bar, 10 μm.

SOD1 in a concentration-dependent manner and enhanced the survival of $SOD1^{G93A}$-expressing mESC-derived motor neurons.

Mutant SOD1 Interacts With VDAC1 to Mediate Mitochondrial Dysfunction

The direct interaction of mutant SOD1 with VDAC1 was previously determined by immunoprecipitation using anti-SOD1, anti-VDAC1 and anti-misfolded SOD1 antibodies together with mutant SOD1 from rat spinal cord tissues or using purified proteins in a lipid bilayer system (Israelson et al., 2010; Magri et al., 2016). Now, we extended these findings and showed using both MST and VDAC1 channel conductance that the dismutase-active $SOD1^{G93A}$ mutant or the dismutase-inactive $SOD1^{G85R}$ mutant but not $SOD1^{wt}$ specifically interact with VDAC1.

Binding of misfolded SOD1 species to mitochondrial membranes was shown to disrupt transport of metabolites required for oxidative phosphorylation, reduce membrane potential, and the activity of electron transport chain complexes (Liu et al., 2004), and to the generation of reactive oxygen (ROS) or nitrogen species with damaging effects on respiratory chain complexes (Martin et al., 2007). All these effects can be produced by interactions of mutant SOD1 with VDAC1, which mediates the transport of metabolites, ions (including Ca^{2+}) and ROS (Shoshan-Barmatz et al., 2010).

VDAC1 Interacts With Mutant SOD1 Through the VDAC1 N-Terminal Domain

We identified the binding sites mediating VDAC1-mutant SOD1 interactions by showing that $SOD1^{G93A}$ and $SOD1^{G85R}$ do not bind the VDAC1 N-terminally truncated protein, but interact with the VDAC1-derived N-terminal peptide, suggesting that mutant SOD1 interacts with the VDAC1 N-terminal domain to mediate its cell toxic effects. This finding is not surprising as the N-terminal domain of VDAC1 was shown to be the interaction site for many proteins (Arzoine et al., 2008; Abu-Hamad et al., 2009; Arbel and Shoshan-Barmatz, 2010; Arbel et al., 2012; Geula et al., 2012) and to possess an ATP-binding site (Yehezkel et al., 2007). The first eight amino acids of the VDAC1-N-terminal domain are hydrophobic in nature, thus providing a natural possible site of contact with misfolded SOD1. Wild type recombinant SOD1 remains soluble, whereas mutations in the SOD1 protein leads to exposure of certain hydrophobic residues normally buried with the protein core. These structural changes lead to misfolding and aggregation of mutant SOD1 proteins via exposure of hydrophobic residues, such that they interact with intracellular membranes, such as mitochondria, ER and others (Israelson et al., 2015).

The interaction of misfolded SOD1 with VDAC1 is further suggested by the co-localization of two different SOD1 mutants with VDAC1 at the mitochondria (**Figure 5**). Furthermore, the N-terminal-derived peptide decreasing the extent of this co-localization, points to VDAC1-N-terminus as the misfolded SOD1 interaction site. Surprisingly, we have noticed a tendency for a nuclear localization of VDAC1 in cells accumulating misfolded SOD1. This phenomenon is not clear and should be further investigated.

The VDAC1 N-terminal region is proposed to move within the channel pore (Hiller and Wagner, 2009) and to translocate from the internal pore to the channel surface (Geula et al., 2012), allowing it to interact with cytosolic proteins. The multiple glycine residues (^{21}GlyTyrGlyPheGly^{25}) following this domain represent a GXXXG motif that connects the N-terminal domain to β-strand 1, and confer the flexibility required for N-terminal domain translocation out of the channel pore (Geula et al., 2012). The GXXXG motif has been shown to be involved in dimerization in proteins such as glycophorin A (Gerber and Shai, 2001), human carbonic anhydrase (Whittington et al., 2001), yeast ATP synthase (Saddar and Stuart, 2005), carnitine palmitoyltransferase (Jenei et al., 2009), and others. In VDAC1, this motif is not required for VDAC1 dimerization

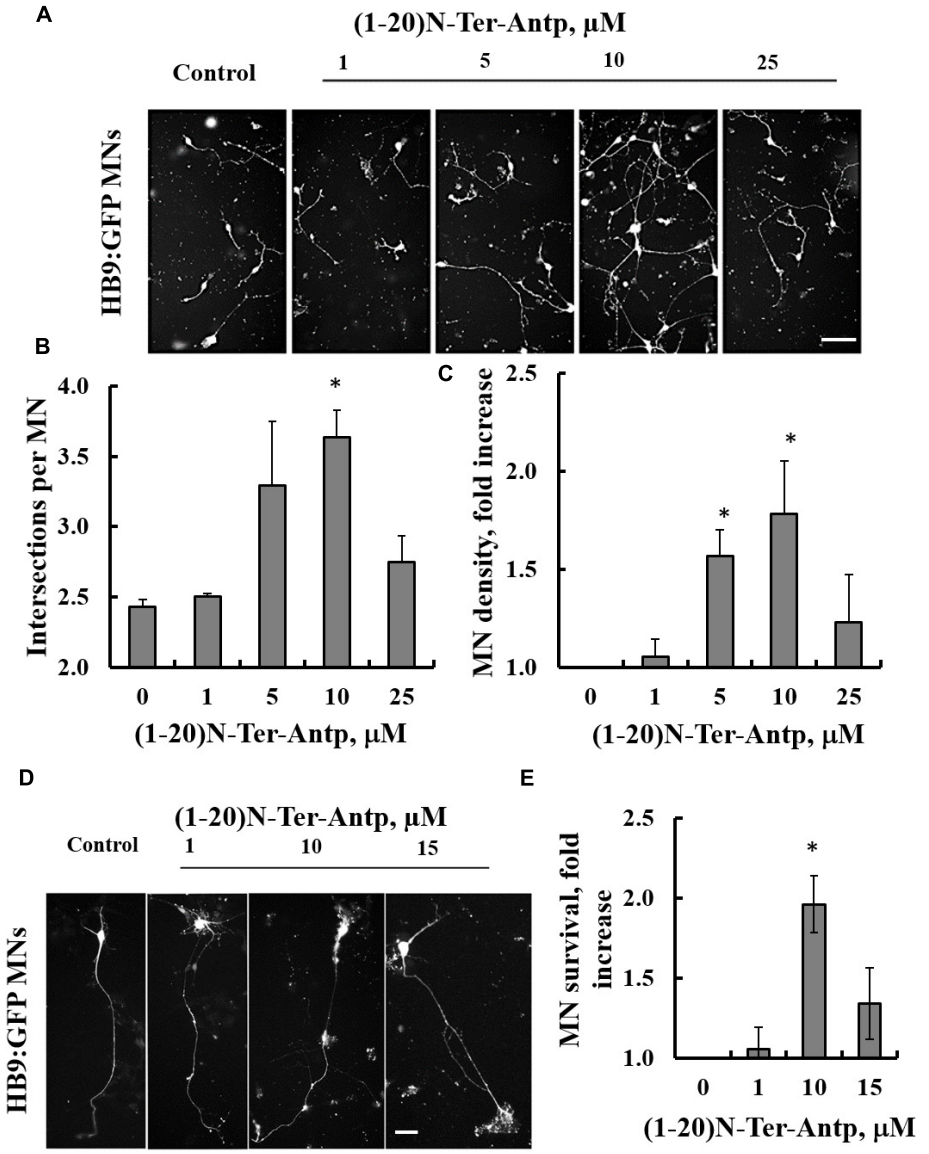

FIGURE 6 | The VDAC1 N-terminal peptide ameliorates SOD1^{G93A}-mediated motor neuron toxicity. SOD1^{G93A}-expressing mESC-derived MNs were incubated with the indicated concentrations of (1-20)N-Ter-Antp peptide for 1–4 days following initiation of final differentiation. **(A,B)** (1-20)N-Ter-Antp at a concentration of 10 μM significantly increased MN neurite outgrowth over the first 24 h. Scale bar, 100 μm. **(C)** Twenty-four hours after the initiation of differentiation, 5 and 10 μM of (1-20)N-Ter-Antp peptide significantly increased the number of MNs present in the culture. **(D)** (1-20)N-Ter-Antp at a concentration of 10 μM significantly increased the number of surviving MNs over the course of final differentiation. After 96 h, MNs showed the typical cellular morphology of maturing neurons with extension of a singular long process and branching resembling a dendritic tree. GFP fluorescence indicates the expression of the motor neuron-specific transcription factor HB9. Gross cellular morphology of surviving MNs remained unaffected by the (1-20)N-Ter-Antp peptide. Scale bar, 25 μm. **(E)** Quantification of MNs survival. For all assays, results are expressed as the mean ± SEM ($n = 3$). *$P < 0.05$.

but it might be involved in interaction with VDAC1-associated proteins (Geula et al., 2012). Interestingly, SOD1 contains three GXXXG (residues 11–16, 32–36, and 36–41) and two GXXXXG motifs (residues 51–56 and 56–61), but their importance for the interaction of VDAC1 with mutant SOD1 proteins is unknown.

In a PLB, reconstituted VDAC1 but not the N-terminally truncated protein bound a misfolded SOD1 mutant but not wild type SOD1, leading to reduced VDAC1 conductance. It is very likely that the exposure of residues in mutant SOD1 proteins that are normally hidden leads to increased interactions between SOD1 mutants and the VDAC1 N-terminal domain. Such association would reduce the overall transit of ions through the VDAC1 pore, thereby leading to the observed reduction in VDAC1 conductance. This interaction is expected to also reduce ATP, ADP, metabolite and ROS transport, in turn leading to an inhibition of cell growth and induction of mitochondrial dysfunction and cell toxicity (**Figure 7**).

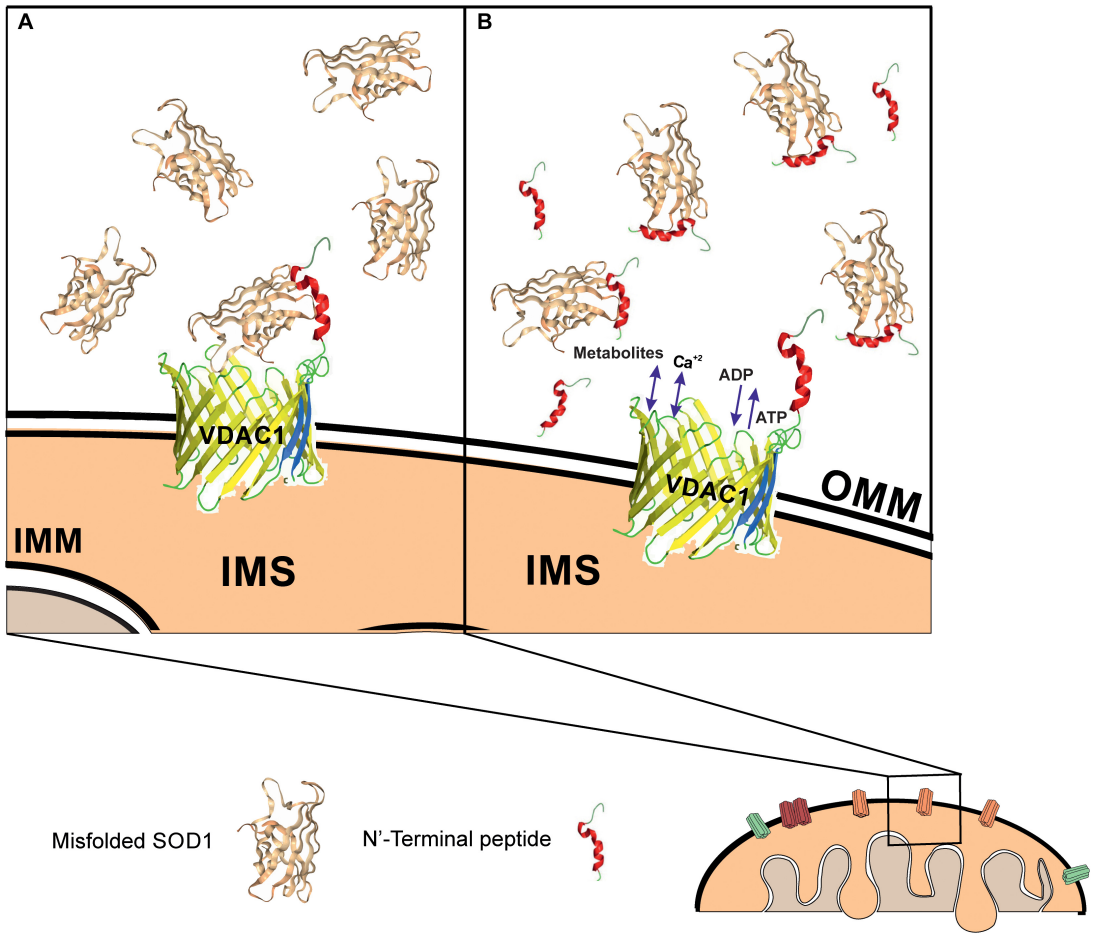

FIGURE 7 | Mutant SOD1 binds to VDAC1 and inhibits VDAC1 activities, with addition of a VDAC1 N-terminal peptide preventing such inhibition. Schematic model showing mutant SOD1 binding to VDAC1, with the N-terminal peptide serving as a decoy. **(A)** Mutant SOD1 is proposed to bind to the VDAC1 N-terminal domain and inhibit VDAC1 conductance, thereby suppressing both influx and efflux of different mitochondrial metabolites and ions, including Ca^{2+}, and ROS. This reduction in metabolite flux results in reduced energy production and increased oxidative stress, leading to mitochondrial dysfunction and cell death. **(B)** VDAC1 N-terminal-derived peptides bind mutant SOD1 and prevent its association with VDAC1, thereby preventing mitochondria dysfunction. The N-terminal peptide thus provides a new therapeutic approach for inhibiting mutant SOD1 toxicity in ALS. OMM and IMM indicate outer and inner mitochondrial membrane, respectively while IMS indicates, the intermembrane space.

VDAC1 N-Terminal Peptides Inhibit Cell Death of NSC-34 Cells Expressing Mutant SOD1^{G93A} and Enhance Survival of Mouse SOD1^{G93A}-Expressing mESC-Derived Motor Neurons

We have shown here that different versions of the N-terminal peptide are able to suppress the toxicity of motor neuron-like NSC-34 cells expressing mutant SOD1^{G93A} in a concentration-dependent manner. For these experiments, we used short versions of the VDAC1 N-terminal domain peptide which lack the GXXXG motif, as this domain is required for N-terminal peptide-induced cell death (**Figures 4A–C**) but not for the interaction with mutant SOD1 (**Figures 4D–F**).

In contrast to mutant SOD1 that by binding to VDAC1 N-terminus induces apoptosis, the binding of apoptosis regulatory proteins such as Bcl-2, Bcl-xL and hexokinase to VDAC1 protects against apoptosis (Arzoine et al., 2008; Abu-Hamad et al., 2009; Arbel and Shoshan-Barmatz, 2010; Arbel et al., 2012; Prezma et al., 2013; Shteinfer-Kuzmine et al., 2018). This protection is mediated via their binding to the N-terminus (Arzoine et al., 2008; Arbel and Shoshan-Barmatz, 2010; Arbel et al., 2012), with Δ(1-24)hVDAC1 showing decreased binding to Bax or Bcl-xL relative to VDAC1 or Δ(1-12) VDAC1 (Shi et al., 2003). Accordingly, interfering with their binding to VDAC1 resulted in apoptosis induction. In addition, the N-terminal peptide lacking 21–26 amino acids, used in the current study, lost its ability to induce apoptosis (Prezma et al., 2013; Shteinfer-Kuzmine et al., 2018). Thus, these results suggest that the peptides serve as decoy to compete with VDAC1 for misfolded SOD1 binding, thereby protecting against its cytotoxicity.

Finally, experiments with mESC-derived SOD1^{G93A}-expressing MNs showed that the (1-20)-N-Ter-Antp VDAC1-based peptide significantly improved neurite

outgrowth and the survival of $SOD1^{G93A}$-expressing MNs in a concentration-dependent manner (with an optimal peptide concentration of 10 μM). This not only corroborates the insight gained from studies on NSC-34 cells but also demonstrates that the VDAC1-based peptide acts as a neuroprotectant against misfolded SOD1-mediated MN toxicity. Further, these results underline the importance of a direct misfolded SOD1-VDAC1 interaction for the appearance of misfolded SOD1 toxicity. It remains to be shown whether the VDAC1-based (1-20)-N-Ter-Antp peptide also has the same effect on fully mature human motor neurons. Indeed, the results justify more thorough *in vitro* and *in vivo* analysis of the therapeutic potential of the VDAC1-based (1-20)-N-Ter-Antp peptide in treating ALS. These include improving peptide stability, such as by introducing amino acids in the D-conformation and carrying out toxicological studies, as performed with another VDAC1-based peptide specifically inducing cell death of cancer cells (Shteinfer-Kuzmine et al., 2018).

In summary, we have shown here that SOD1 mutants interact with VDAC1 through the VDAC1 N-terminal domain to exert their inhibitory effect on VDAC1 channel conductance. Moreover, we have shown that VDAC1 N-terminal-derived peptides specifically bind mutant SOD1 and inhibit mutant SOD1-induced toxicity in motor neuron-like NSC-34 cells expressing mutant SOD1 or in mouse embryonic stem cell-derived motor neurons. Thus, we suggest that this VDAC1-based peptide represents a new strategy for interfering with mutant SOD1-mediated cell toxicity.

AUTHOR CONTRIBUTIONS

AMe, EK, VS-B, and AI designed the research. SA, RG, AS-K, NS, SA-H, YG, JH, and AMa conducted the experiments. SA, RG, AS-K, SA-H, NS, JH, AMa, AMe, EK, VS-B, and AI analyzed the data. VS-B and AI wrote the manuscript.

FUNDING

This research was supported by a grant from the Chief Scientist's Office, Israel Ministry of Health (CSO-MOH) as part of EURONANOMEDII to VS-B and AI.

ACKNOWLEDGMENTS

We thank Dr. Srinivas Pittala for helping with the confocal microscope experiments.

REFERENCES

Abu-Hamad, S., Arbel, N., Calo, D., Arzoine, L., Israelson, A., Keinan, N., et al. (2009). The VDAC1 N-terminus is essential both for apoptosis and the protective effect of anti-apoptotic proteins. *J. Cell Sci.* 122, 1906–1916. doi: 10.1242/jcs.040188

Abu-Hamad, S., Kahn, J., Leyton-Jaimes, M. F., Rosenblatt, J., and Israelson, A. (2017). Misfolded SOD1 accumulation and mitochondrial association contribute to the selective vulnerability of motor neurons in familial als: correlation to human disease. *ACS Chem. Neurosci.* 8, 2225–2234. doi: 10.1021/acschemneuro.7b00140

Aggarwal, T., Hoeber, J., Ivert, P., Vasylovska, S., and Kozlova, E. N. (2017). Boundary cap neural crest stem cells promote survival of mutant sod1 motor neurons. *Neurotherapeutics.* 14, 773–783. doi: 10.1007/s13311-016-0505-8

Arbel, N., Ben-Hail, D., and Shoshan-Barmatz, V. (2012). Mediation of the antiapoptotic activity of Bcl-xL protein upon interaction with VDAC1 protein. *J. Biol. Chem.* 287, 23152–23161. doi: 10.1074/jbc.M112.345918

Arbel, N., and Shoshan-Barmatz, V. (2010). Voltage-dependent anion channel 1-based peptides interact with Bcl-2 to prevent antiapoptotic activity. *J. Biol. Chem.* 285, 6053–6062. doi: 10.1074/jbc.M109.082990

Arzoine, L., Zilberberg, N., Ben-Romano, R., and Shoshan-Barmatz, V. (2008). Voltage-dependent anion channel-1-based peptides interact with hexokinase to prevent its anti-apoptotic activity. *J. Biol. Chem.* 284, 3946–3955. doi: 10.1074/jbc.M803614200

Bergemalm, D., Jonsson, P. A., Graffmo, K. S., Andersen, P. M., Brannstrom, T., Rehnmark, A., et al. (2006). Overloading of stable and exclusion of unstable human superoxide dismutase-1 variants in mitochondria of murine amyotrophic lateral sclerosis models. *J. Neurosci.* 26, 4147–4154. doi: 10.1523/jneurosci.5461-05.2006

Bosco, D. A., Morfini, G., Karabacak, N. M., Song, Y., Gros-Louis, F., Pasinelli, P., et al. (2010). Wild-type and mutant SOD1 share an aberrant conformation and a common pathogenic pathway in ALS. *Nat. Neurosci.* 13, 1396–1403. doi: 10.1038/nn.2660

Bruijn, L. I., Houseweart, M. K., Kato, S., Anderson, K. L., Anderson, S. D., Ohama, E., et al. (1998). Aggregation and motor neuron toxicity of an ALS-linked SOD1 mutant independent from wild-type SOD1. *Science* 281, 1851–1854. doi: 10.1126/science.281.5384.1851

Carri, M. T., and Cozzolino, M. (2011). SOD1 and mitochondria in ALS: a dangerous liaison. *J. Bioenerg. Biomembr.* 43, 593–599. doi: 10.1007/s10863-011-9394-z

Cleveland, D. W., and Rothstein, J. D. (2001). From charcot to lou gehrig: deciphering selective motor neuron death in ALS. *Nat. Rev. Neurosci.* 2, 806–819. doi: 10.1038/35097565

Dal Canto, M. C., and Gurney, M. E. (1994). Development of central nervous system pathology in a murine transgenic model of human amyotrophic lateral sclerosis. *Am. J. Pathol.* 145, 1271–1279.

Damiano, M., Starkov, A. A., Petri, S., Kipiani, K., Kiaei, M., Mattiazzi, M., et al. (2006). Neural mitochondrial Ca2+ capacity impairment precedes the onset of motor symptoms in G93A Cu/Zn-superoxide dismutase mutant mice. *J. Neurochem.* 96, 1349–1361. doi: 10.1111/j.1471-4159.2006.03619.x

Deng, H. X., Shi, Y., Furukawa, Y., Zhai, H., Fu, R., Liu, E., et al. (2006). Conversion to the amyotrophic lateral sclerosis phenotype is associated with intermolecular linked insoluble aggregates of SOD1 in mitochondria. *Proc. Natl. Acad. Sci. U.S.A.* 103, 7142–7147. doi: 10.1073/pnas.0602046103

Di Giorgio, F. P., Carrasco, M. A., Siao, M. C., Maniatis, T., and Eggan, K. (2007). Non-cell autonomous effect of glia on motor neurons in an embryonic stem cell-based ALS model. *Nat. Neurosci.* 10, 608–614. doi: 10.1038/nn1885

Dorst, J., Chen, L., Rosenbohm, A., Dreyhaupt, J., Hubers, A., Schuster, J., et al. (2019). Prognostic factors in ALS: a comparison between germany and china. *J. Neurol.* 266, 1516–1525. doi: 10.1007/s00415-019-09290-4

Dupuis, L., di Scala, F., Rene, F., de Tapia, M., Oudart, H., Pradat, P. F., et al. (2003). Up-regulation of mitochondrial uncoupling protein 3 reveals an early muscular metabolic defect in amyotrophic lateral sclerosis. *Faseb J.* 17, 2091–2093. doi: 10.1096/fj.02-1182fje

Echaniz-Laguna, A., Zoll, J., Ribera, F., Tranchant, C., Warter, J. M., Lonsdorfer, J., et al. (2002). Mitochondrial respiratory chain function in skeletal muscle of ALS patients. *Ann. Neurol.* 52, 623–627. doi: 10.1002/ana.10357

Ferri, A., Cozzolino, M., Crosio, C., Nencini, M., Casciati, A., Gralla, E. B., et al. (2006). Familial ALS-superoxide dismutases associate with mitochondria and shift their redox potentials. *Proc. Natl. Acad. Sci. U.S.A.* 103, 13860–13865. doi: 10.1073/pnas.0605814103

Gerber, D., and Shai, Y. (2001). In vivo detection of hetero-association of glycophorin-A and its mutants within the membrane. *J. Biol. Chem.* 276, 31229–31232. doi: 10.1074/jbc.m101889200

Geula, S., Ben-Hail, D., and Shoshan-Barmatz, V. (2012). Structure-based analysis of VDAC1: N-terminus location, translocation, channel gating and association with anti-apoptotic proteins. *Biochem. J.* 444, 475–485. doi: 10.1042/BJ20112079

Gincel, D., Zaid, H., and Shoshan-Barmatz, V. (2001). Calcium binding and translocation by the voltage-dependent anion channel: a possible regulatory mechanism in mitochondrial function. *Biochem. J.* 358, 147–155. doi: 10.1042/bj3580147

Guareschi, S., Cova, E., Cereda, C., Ceroni, M., Donetti, E., Bosco, D. A., et al. (2012). An over-oxidized form of superoxide dismutase found in sporadic amyotrophic lateral sclerosis with bulbar onset shares a toxic mechanism with mutant SOD1. *Proc. Natl. Acad. Sci. U.S.A.* 109, 5074–5079. doi: 10.1073/pnas.1115402109

Hayward, L. J., Rodriguez, J. A., Kim, J. W., Tiwari, A., Goto, J. J., Cabelli, D. E., et al. (2002). Decreased metallation and activity in subsets of mutant superoxide dismutases associated with familial amyotrophic lateral sclerosis. *J. Biol. Chem.* 277, 15923–15931. doi: 10.1074/jbc.m112087200

Higgins, C. M., Jung, C., and Xu, Z. (2003). ALS-associated mutant SOD1G93A causes mitochondrial vacuolation by expansion of the intermembrane space and by involvement of SOD1 aggregation and peroxisomes. *BMC Neurosci* 4:16. doi: 10.1186/1471-2202-4-16

Hiller, S., Garces, R. G., Malia, T. J., Orekhov, V. Y., Colombini, M., and Wagner, G. (2008). Solution structure of the integral human membrane protein VDAC-1 in detergent micelles. *Science* 321, 1206–1210. doi: 10.1126/science.1161302

Hiller, S., and Wagner, G. (2009). The role of solution NMR in the structure determinations of VDAC-1 and other membrane proteins. *Curr. Opin. Struct. Biol.* 19, 396–401. doi: 10.1016/j.sbi.2009.07.013

Hirano, A., Donnenfeld, H., Sasaki, S., and Nakano, I. (1984a). Fine structural observations of neurofilamentous changes in amyotrophic lateral sclerosis. *J. Neuropathol. Exp. Neurol.* 43, 461–470. doi: 10.1097/00005072-198409000-00001

Hirano, A., Nakano, I., Kurland, L. T., Mulder, D. W., Holley, P. W., and Saccomanno, G. (1984b). Fine structural study of neurofibrillary changes in a family with amyotrophic lateral sclerosis. *J. Neuropathol. Exp. Neurol.* 43, 471–480. doi: 10.1097/00005072-198409000-00002

Ilieva, H., Polymenidou, M., and Cleveland, D. W. (2009). Non-cell autonomous toxicity in neurodegenerative disorders: ALS and beyond. *J. Cell Biol.* 187, 761–772. doi: 10.1083/jcb.200908164

Israelson, A., Arbel, N., Da Cruz, S., Ilieva, H., Yamanaka, K., Shoshan-Barmatz, V., et al. (2010). Misfolded mutant SOD1 directly inhibits VDAC1 conductance in a mouse model of inherited ALS. *Neuron* 67, 575–587. doi: 10.1016/j.neuron.2010.07.019

Israelson, A., Ditsworth, D., Sun, S., Song, S., Liang, J., Hruska-Plochan, M., et al. (2015). Macrophage migration inhibitory factor as a chaperone inhibiting accumulation of misfolded SOD1. *Neuron* 86, 218–232. doi: 10.1016/j.neuron.2015.02.034

Jenei, Z. A., Borthwick, K., Zammit, V. A., and Dixon, A. M. (2009). Self-association of transmembrane domain 2 (TM2), but not TM1, in carnitine palmitoyltransferase 1A: role of GXXXG(A) motifs. *J. Biol. Chem.* 284, 6988–6997. doi: 10.1074/jbc.M808487200

Kong, J., and Xu, Z. (1998). Massive mitochondrial degeneration in motor neurons triggers the onset of amyotrophic lateral sclerosis in mice expressing a mutant SOD1. *J. Neurosci.* 18, 3241–3250. doi: 10.1523/jneurosci.18-09-03241.1998

Leyton-Jaimes, M. F., Benaim, C., Abu-Hamad, S., Kahn, J., Guetta, A., Bucala, R., et al. (2016). Endogenous macrophage migration inhibitory factor reduces the accumulation and toxicity of misfolded SOD1 in a mouse model of ALS. *Proc. Natl. Acad. Sci. U.S.A.* 113, 10198–10203. doi: 10.1073/pnas.1604600113

Li, Q., Vande Velde, C., Israelson, A., Xie, J., Bailey, A. O., Dong, M. Q., et al. (2010). ALS-linked mutant superoxide dismutase 1 (SOD1) alters mitochondrial protein composition and decreases protein import. *Proc. Natl. Acad. Sci. U.S.A.* 107, 21146–21151. doi: 10.1073/pnas.1014862107

Lim, L., and Song, J. (2016). SALS-linked WT-SOD1 adopts a highly similar helical conformation as FALS-causing L126Z-SOD1 in a membrane environment. *Biochim. Biophys. Acta* 1858, 2223–2230. doi: 10.1016/j.bbamem.2016.06.027

Liu, J., Lillo, C., Jonsson, P. A., Vande Velde, C., Ward, C. M., Miller, T. M., et al. (2004). Toxicity of familial ALS-linked SOD1 mutants from selective recruitment to spinal mitochondria. *Neuron* 43, 5–17. doi: 10.1016/j.neuron.2004.06.016

Magrane, J., Sahawneh, M. A., Przedborski, S., Estevez, A. G., and Manfredi, G. (2012). Mitochondrial dynamics and bioenergetic dysfunction is associated with synaptic alterations in mutant SOD1 motor neurons. *J. Neurosci.* 32, 229–242. doi: 10.1523/JNEUROSCI.1233-11.2012

Magri, A., Belfiore, R., Reina, S., Tomasello, M. F., Di Rosa, M. C., Guarino, F., et al. (2016). Hexokinase I N-terminal based peptide prevents the VDAC1-SOD1 G93A interaction and re-establishes ALS cell viability. *Sci. Rep.* 6:34802. doi: 10.1038/srep34802

Martin, L. J., Liu, Z., Chen, K., Price, A. C., Pan, Y., Swaby, J. A., et al. (2007). Motor neuron degeneration in amyotrophic lateral sclerosis mutant superoxide dismutase-1 transgenic mice: mechanisms of mitochondriopathy and cell death. *J. Comp. Neurol.* 500, 20–46. doi: 10.1002/cne.21160

Mattiazzi, M., D'Aurelio, M., Gajewski, C. D., Martushova, K., Kiaei, M., Beal, M. F., et al. (2002). Mutated human SOD1 causes dysfunction of oxidative phosphorylation in mitochondria of transgenic mice. *J. Biol. Chem.* 277, 29626–29633. doi: 10.1074/jbc.m203065200

McGahon, A. J., Martin, S. J., Bissonnette, R. P., Mahboubi, A., Shi, Y., Mogil, R. J., et al. (1995). The end of the (cell) line: methods for the study of apoptosis in vitro. *Methods Cell Biol.* 46, 153–185. doi: 10.1016/s0091-679x(08)61929-9

Medinas, D. B., Rozas, P., Martinez Traub, F., Woehlbier, U., Brown, R. H., Bosco, D. A., et al. (2018). Endoplasmic reticulum stress leads to accumulation of wild-type SOD1 aggregates associated with sporadic amyotrophic lateral sclerosis. *Proc. Natl. Acad. Sci. U.S.A.* 115, 8209–8214. doi: 10.1073/pnas.1801109115

Mulder, D. W., Kurland, L. T., Offord, K. P., and Beard, C. M. (1986). Familial adult motor neuron disease: amyotrophic lateral sclerosis. *Neurology* 36, 511–517. doi: 10.1212/wnl.36.4.511

Nguyen, K. T., Garcia-Chacon, L. E., Barrett, J. N., Barrett, E. F., and David, G. (2009). The Psi(m) depolarization that accompanies mitochondrial Ca2+ uptake is greater in mutant SOD1 than in wild-type mouse motor terminals. *Proc. Natl. Acad. Sci. U.S.A.* 106, 2007–2011. doi: 10.1073/pnas.0810934106

Pedrini, S., Sau, D., Guareschi, S., Bogush, M., Brown, R. H. Jr., Naniche, N., et al. (2010). ALS-linked mutant SOD1 damages mitochondria by promoting conformational changes in Bcl-2. *Hum. Mol. Genet.* 19, 2974–2986. doi: 10.1093/hmg/ddq202

Prezma, T., Shteinfer, A., Admoni, L., Raviv, Z., Sela, I., Levi, I., et al. (2013). VDAC1-based peptides: novel pro-apoptotic agents and potential therapeutics for B-cell chronic lymphocytic leukemia. *Cell Death Dis.* 4:e809. doi: 10.1038/cddis.2013.316

Prudencio, M., Hart, P. J., Borchelt, D. R., and Andersen, P. M. (2009). Variation in aggregation propensities among ALS-associated variants of SOD1: correlation to human disease. *Hum. Mol. Genet.* 18, 3217–3226. doi: 10.1093/hmg/ddp260

Ronn, L. C., Ralets, I., Hartz, B. P., Bech, M., Berezin, A., Berezin, V., et al. (2000). A simple procedure for quantification of neurite outgrowth based on stereological principles. *J. Neurosci. Methods* 100, 25–32. doi: 10.1016/s0165-0270(00)00228-4

Rosen, D. R., Siddique, T., Patterson, D., Figlewicz, D. A., Sapp, P., Hentati, A., et al. (1993). Mutations in Cu/Zn superoxide dismutase gene are associated with familial amyotrophic lateral sclerosis. *Nature* 362, 59–62.

Saddar, S., and Stuart, R. A. (2005). The yeast F(1)F(0)-ATP synthase: analysis of the molecular organization of subunit g and the importance of a conserved GXXXG motif. *J. Biol. Chem.* 280, 24435–24442. doi: 10.1074/jbc.m502804200

Sasaki, S., and Iwata, M. (1996). Dendritic synapses of anterior horn neurons in amyotrophic lateral sclerosis: an ultrastructural study. *Acta Neuropathol.* 91, 278–283. doi: 10.1007/s004010050426

Sasaki, S., and Iwata, M. (2007). Mitochondrial alterations in the spinal cord of patients with sporadic amyotrophic lateral sclerosis. *J. Neuropathol. Exp. Neurol.* 66, 10–16. doi: 10.1097/nen.0b013e31802c396b

Shi, P., Wei, Y., Zhang, J., Gal, J., and Zhu, H. (2010). Mitochondrial dysfunction is a converging point of multiple pathological pathways in amyotrophic lateral sclerosis. *J. Alzheimers Dis.* 20(Suppl. 2), S311–S324. doi: 10.3233/JAD-2010-100366

Shi, Y., Chen, J., Weng, C., Chen, R., Zheng, Y., Chen, Q., et al. (2003). Identification of the protein-protein contact site and interaction mode of human VDAC1 with Bcl-2 family proteins. *Biochem. Biophys. Res. Commun.* 305, 989–996. doi: 10.1016/s0006-291x(03)00871-4

Shimizu, S., Narita, M., and Tsujimoto, Y. (1999). Bcl-2 family proteins regulate the release of apoptogenic cytochrome c by the mitochondrial channel VDAC. *Nature* 399, 483–487. doi: 10.1038/20959

Shoshan-Barmatz, V., Ben-Hail, D., Admoni, L., Krelin, Y., and Tripathi, S. S. (2015). The mitochondrial voltage-dependent anion channel 1 in tumor cells. *Biochim. Biophys. Acta* 1848, 2547–2575. doi: 10.1016/j.bbamem.2014.10.040

Shoshan-Barmatz, V., De Pinto, V., Zweckstetter, M., Raviv, Z., Keinan, N., and Arbel, N. (2010). VDAC, a multi-functional mitochondrial protein regulating cell life and death. *Mol. Aspects Med.* 31, 227–285. doi: 10.1016/j.mam.2010.03.002

Shteinfer-Kuzmine, A., Amsalem, Z., Arif, T., Zooravlov, A., and Shoshan-Barmatz, V. (2018). Selective induction of cancer cell death by VDAC1-based peptides and their potential use in cancer therapy. *Mol. Oncol.* 12, 1077–1103. doi: 10.1002/1878-0261.12313

Shvil, N., Banerjee, V., Zoltsman, G., Shani, T., Kahn, J., Abu-Hamad, S., et al. (2018). MIF inhibits the formation and toxicity of misfolded SOD1 amyloid aggregates: implications for familial ALS. *Cell Death Dis.* 9:107. doi: 10.1038/s41419-017-0130-4

Tajeddine, N., Galluzzi, L., Kepp, O., Hangen, E., Morselli, E., Senovilla, L., et al. (2008). Hierarchical involvement of Bak, VDAC1 and Bax in cisplatin-induced cell death. *Oncogene* 27, 4221–4232. doi: 10.1038/onc.2008.63

Tiwari, A., Liba, A., Sohn, S. H., Seetharaman, S. V., Bilsel, O., Matthews, C. R., et al. (2009). Metal deficiency increases aberrant hydrophobicity of mutant superoxide dismutases that cause amyotrophic lateral sclerosis. *J. Biol. Chem.* 284, 27746–27758. doi: 10.1074/jbc.M109.043729

Vande Velde, C., Miller, T. M., Cashman, N. R., and Cleveland, D. W. (2008). Selective association of misfolded ALS-linked mutant SOD1 with the cytoplasmic face of mitochondria. *Proc. Natl. Acad. Sci. U.S.A.* 105, 4022–4027. doi: 10.1073/pnas.0712209105

Vielhaber, S., Winkler, K., Kirches, E., Kunz, D., Buchner, M., Feistner, H., et al. (1999). Visualization of defective mitochondrial function in skeletal muscle fibers of patients with sporadic amyotrophic lateral sclerosis. *J. Neurol. Sci.* 169, 133–139. doi: 10.1016/s0022-510x(99)00236-1

Vijayvergiya, C., Beal, M. F., Buck, J., and Manfredi, G. (2005). Mutant superoxide dismutase 1 forms aggregates in the brain mitochondrial matrix of amyotrophic lateral sclerosis mice. *J. Neurosci.* 25, 2463–2470. doi: 10.1523/jneurosci.4385-04.2005

Wang, J., Xu, G., Slunt, H. H., Gonzales, V., Coonfield, M., Fromholt, D., et al. (2005). Coincident thresholds of mutant protein for paralytic disease and protein aggregation caused by restrictively expressed superoxide dismutase cDNA. *Neurobiol. Dis.* 20, 943–952. doi: 10.1016/j.nbd.2005.06.005

Whittington, D. A., Waheed, A., Ulmasov, B., Shah, G. N., Grubb, J. H., Sly, W. S., et al. (2001). Crystal structure of the dimeric extracellular domain of human carbonic anhydrase XII, a bitopic membrane protein overexpressed in certain cancer tumor cells. *Proc. Natl. Acad. Sci. U.S.A.* 98, 9545–9550. doi: 10.1073/pnas.161301298

Wichterle, H., Lieberam, I., Porter, J. A., and Jessell, T. M. (2002). Directed differentiation of embryonic stem cells into motor neurons. *Cell* 110, 385–397.

Wiedemann, F. R., Manfredi, G., Mawrin, C., Beal, M. F., and Schon, E. A. (2002). Mitochondrial DNA and respiratory chain function in spinal cords of ALS patients. *J. Neurochem.* 80, 616–625. doi: 10.1046/j.0022-3042.2001.00731.x

Wienken, C. J., Baaske, P., Rothbauer, U., Braun, D., and Duhr, S. (2010). Protein-binding assays in biological liquids using microscale thermophoresis. *Nat. Commun.* 1:100. doi: 10.1038/ncomms1093

Wong, P. C., Pardo, C. A., Borchelt, D. R., Lee, M. K., Copeland, N. G., Jenkins, N. A., et al. (1995). An adverse property of a familial ALS-linked SOD1 mutation causes motor neuron disease characterized by vacuolar degeneration of mitochondria. *Neuron* 14, 1105–1116. doi: 10.1016/0896-6273(95)90259-7

Xu, W. C., Liang, J. Z., Li, C., He, Z. X., Yuan, H. Y., Huang, B. Y., et al. (2018). Pathological hydrogen peroxide triggers the fibrillization of wild-type SOD1 via sulfenic acid modification of Cys-111. *Cell Death Dis.* 9:67. doi: 10.1038/s41419-017-0106-4

Yehezkel, G., Abu-Hamad, S., and Shoshan-Barmatz, V. (2007). An N-terminal nucleotide-binding site in VDAC1: involvement in regulating mitochondrial function. *J. Cell Physiol.* 212, 551–561. doi: 10.1002/jcp.21048

Zillner, K., Jerabek-Willemsen, M., Duhr, S., Braun, D., Langst, G., and Baaske, P. (2012). Microscale thermophoresis as a sensitive method to quantify protein: nucleic acid interactions in solution. *Methods Mol. Biol.* 815, 241–252. doi: 10.1007/978-1-61779-424-7_18

Conflict of Interest Statement: The authors declare that the research was conducted in the absence of any commercial or financial relationships that could be construed as a potential conflict of interest.

frontiers in Cellular Neuroscience

ORIGINAL RESEARCH
published: 29 October 2019
doi: 10.3389/fncel.2019.00485

The p75 Neurotrophin Receptor Facilitates TrkB Signaling and Function in Rat Hippocampal Neurons

*Juan P. Zanin†, Laura E. Montroull†, Marta Volosin and Wilma J. Friedman**

Department of Biological Sciences, Rutgers University, Newark, NJ, United States

Neurotrophins activate Trk receptor signaling to support neuronal survival and many aspects of neuronal function. Early studies demonstrated that TrkA formed a complex with the p75 neurotrophin receptor ($p75^{NTR}$), which increased the affinity and selectivity of NGF binding, however, whether interaction of $p75^{NTR}$ with other Trk receptors performs a similar function to enhance ligand binding has not been demonstrated. We investigated the interaction of TrkB with full length $p75^{NTR}$ in hippocampal neurons in response to BDNF and found that the association of these receptors occurs after ligand binding and requires phosphorylation of TrkB, indicating that formation of this receptor complex was not necessary for ligand binding. Moreover, the interaction of these receptors required internalization and localization to early endosomes. We found that association of TrkB with $p75^{NTR}$ was necessary for optimal downstream signaling of the PI_3K-Akt pathway, but not the Erk pathway, in hippocampal neurons. The absence of $p75^{NTR}$ impaired the ability of BDNF to rescue hippocampal neurons in a trophic deprivation model, suggesting that $p75^{NTR}$ facilitates the ability of TrkB to activate specific pathways to promote neuronal survival.

Keywords: TrkB, p75 neurotrophin receptor, brain derived neurotrophic factor, Akt, Erk

OPEN ACCESS

Edited by:
Francisca C. Bronfman, Universidad Andrés Bello, Chile

Reviewed by:
Christopher Deppmann, The University of Virginia, United States
Bruce Douglas Carter, Vanderbilt University, United States
Elizabeth J. Coulson, The University of Queensland, Australia

***Correspondence:**
Wilma J. Friedman
wilmaf@newark.rutgers.edu

†These authors have contributed equally to this work

Specialty section:
This article was submitted to Cellular Neurophysiology, a section of the journal Frontiers in Cellular Neuroscience

Received: *29 July 2019*
Accepted: *14 October 2019*
Published: *29 October 2019*

Citation:
Zanin JP, Montroull LE, Volosin M and Friedman WJ (2019) The p75 Neurotrophin Receptor Facilitates TrkB Signaling and Function in Rat Hippocampal Neurons. Front. Cell. Neurosci. 13:485. doi: 10.3389/fncel.2019.00485

INTRODUCTION

The neurotrophin family of trophic factors, which includes NGF, BDNF, NT3, and NT4, regulate multiple aspects of neuronal survival and function by interacting with distinct receptor complexes. These factors promote survival, axonal growth, and synaptic activity by signaling via Trk receptors, and can induce apoptosis by signaling via the p75 neurotrophin receptor ($p75^{NTR}$). The $p75^{NTR}$ has been shown to associate with a variety of co-receptors, such as TrkA or sortilin, to facilitate binding to NGF (Hempstead et al., 1991) or proNGF (Nykjaer et al., 2004), respectively. Previous studies demonstrated that the association of $p75^{NTR}$ with TrkA increased the affinity and selectivity of NGF binding, promoting TrkA signaling and supporting survival and differentiation of sympathetic neurons (Hempstead et al., 1991). In contrast, the association of $p75^{NTR}$ with a member of the sortilin family allows the binding of proneurotrophins and apoptotic signaling by $p75^{NTR}$ (Lee et al., 2001; Volosin et al., 2006). Once receptors bind their ligands, receptor internalization and trafficking are important aspects of their signaling. Several studies have focused on retrograde trafficking of neurotrophin receptors from the axon terminal to the soma (Ginty and Segal, 2002; Schmieg et al., 2014), however, the route of endosomal trafficking within the soma can determine

which signaling pathways are activated and the duration of signaling. Moreover, localization of neurotrophin receptors may be different depending on cell type (Yano and Chao, 2005), and Trk receptors localized to different intracellular locations have distinct functions. TrkB receptors at the synapse can promote glutamatergic signaling and modulate synaptic activity (Schinder and Poo, 2000) while TrkB receptors in dendrites can promote BDNF-induced branching (Lazo et al., 2013).

Several studies have evaluated the trafficking of Trk receptors and p75^{NTR} independently in a variety of neuronal cell types (Bronfman et al., 2003; Chen et al., 2005; Hibbert et al., 2006; Lazo et al., 2013; Escudero et al., 2014). Previous studies on the trafficking of p75^{NTR} in PC12 cells and sympathetic neurons demonstrated that BDNF, a ligand that binds only to p75^{NTR} in these cells, elicited internalization and retrograde transport in compartments independent of Trk signaling (Hibbert et al., 2006). Additionally, p75^{NTR} can be internalized in Rab5-positive early endosomes, trafficked to multivesicular bodies, and released from the cells in exosomes (Bronfman et al., 2003; Escudero et al., 2014).

Studies investigating trafficking of Trk receptors in PC12 cells showed that TrkA and TrkB were trafficked differently in response to their respective ligands, NGF, or BDNF. NGF induced TrkA to be recycled to the plasma membrane, while BDNF elicited TrkB trafficking to the lysosome for degradation (Chen et al., 2005). This difference was reported to be due to a specific sequence in the TrkA juxtamembrane domain that was absent from TrkB. However, in hippocampal neurons, BDNF was shown to induce the localization of TrkB to rab11-positive recycling endosomes to promote dendritic branching (Lazo et al., 2013) rather than to the lysosome, indicating that ligand-induced trafficking may differ in distinct cell types.

In hippocampal neurons, treatment with BDNF elicits an association between TrkB and full length p75^{NTR}. Whether these receptors form a complex that is maintained during internalization and trafficking, and whether subcellular localization and signaling is altered by the association of the two receptors, is unknown. Since specific subcellular localization of signaling proteins is critical for their function, we have analyzed whether BDNF-induced trafficking and signaling of TrkB is altered in the absence of p75^{NTR}.

MATERIALS AND METHODS

Neuronal Cultures

All animal studies were conducted using the National Institutes of Health guidelines for the ethical treatment of animals with approval of the Rutgers IACUC. Pregnant rats were sacrificed by exposure to CO2 and soaked in 70% ethanol for 5 min. Rats lacking p75^{NTR} were obtained from SAGE/Horizon Laboratories and confirmed by us using PCR, Western blot, and immunostaining to be lacking p75^{NTR}. Rat fetuses were removed at embryonic day 18 (E18) under sterile conditions and kept in PBS on ice. The hippocampus was dissected, dissociated by trituration in serum-free medium, plated on polylysine (0.1 mg/ml) coated tissue culture wells or glass coverslips, and maintained in a serum-free environment (Friedman et al., 1993; Farinelli et al., 1998). Medium consists of a 1:1 mixture of Eagle's MEM and Ham's F12 supplemented with glucose (6 mg/ml), putrescine (60 μM), progesterone (20 nM), transferrin (100 μg/ml), selenium (30 nM), penicillin (0.5 U/ml), and streptomycin (0.5 μg/ml). In all experiments, neurons were cultured for 4–5 days before treatment. Cultures maintained under these conditions contained <2% glial cells, confirmed by staining for glial markers.

Immunoprecipitation and Western Blot Analysis

Cultured hippocampal neurons were treated with BDNF (25 ng/ml) for different time points and compared with untreated control neurons. Cells were lysed in a buffer consisting of Tris–buffered saline with 10% Triton, 0.6 M octylglucoside, and protease inhibitor cocktail (Roche, 11836153001) and phosphatase inhibitor cocktail (Roche, 04906845001). Total protein was quantified by the Bradford assay (Bio-Rad, Hercules, CA, United States). Samples were equilibrated to have the same total protein quantity and the same final volume. Lysates were subjected to Western Blot analysis with antibodies to pAkt (Ser473, Cell Signaling, 587F11) and pErk1/2 (Thr202/Tyr 204, Cell Signaling, 9106). Blots were re-probed for total Akt (Cell Signaling, 9272) and Erk1/2 (Cell Signaling, 9102). For the immunoprecipitation analysis, lysates were precleared with 5 μl of protein G-magnetic beads (New England Bio Labs S1430S) at 4°C for 60 min. For p75 immunoprecipitation, 150–200 μg total protein from hippocampal neuron cleared lysates was incubated with anti-p75 (Millipore, MAB365, RRID: AB_2152788) overnight on a rocking platform at 4°C. Protein G-magnetic beads (10 μl per 100 μg of total protein) was then added to the lysates and kept for an additional 2 h at 4°C. Immunoprecipitates were collected using a magnetic rack (New England Bio Labs S1506S) and washed 3X with lysis buffer and eluted by adding 30 μl of loading buffer and subjected to Western blot analysis with antibodies to TrkB (Millipore, 07-225, RRID: AB 310445). Blots were stripped and re-probed with anti-p75 (Millipore, MAB365, RRID: AB_2152788). All Western blot analyses were performed at least four times with samples from independent experiments. Membranes were visualized using either ECL (Pierce) or scanned with the Odyssey infrared imaging system (LI-COR Bioscience). To ensure equal protein levels in Western blots, membranes were stained with Ponceau and re-probed with anti-actin (Sigma, A5316, RRID: AB 476743).

Immunocytochemistry

Cultured cells were treated with BDNF for the indicated times, washed with PBS and fixed in 4% paraformaldehyde for 15 min at room temperature. Cells were permeabilized with PBS/0.5%Triton X-100 and then blocked for 1 hr with PBS/1% BSA/5% normal goat serum and exposed to primary antibodies overnight at 4°C. Cells were washed 3X with PBS, and exposed to secondary antibodies coupled to different fluorophores for

1 hr at room temp. Cells were washed three times in PBS and then mounted using Prolong Gold containing 4′,6′-diamidino-2-phenylindole (DAPI) (Life Technologies P36934). Cells were analyzed by epifluorescence (Nikon Eclipse TE200), confocal (Zeiss 510 Meta), or enhanced resolution (Leica SP8, 63X, 1.4 NA, Lightning Mode) microscopy. No immunostaining was seen in controls with omission of the primary antibodies.

FRET Analysis

The interaction of TrkB with p75^{NTR} was analyzed by acceptor photobleaching FRET. Briefly, FRET occurs because the acceptor receives parts of the energy emitted by the donor molecule. Therefore, when the acceptor is bleached, the donor emission will increase. This is only possible when the two molecules analyzed are close enough to induce the energy transfer. We used Alexa 488 (Life Technologies, A-11039, A32790 or A-11015) as the energy donor and Alexa 555 (Life Technologies, A-31570 or A-21432) as the acceptor. Images were acquired before and after the acceptor was bleached. The fluorophore was bleached using the laser 549 at 100% power for 200 iterations with the 63X oil objective of a Zeiss LSM 510 Meta microscope. Only the cells with a reduction of at least 80% in the intensity of the acceptor channel were used for the analysis. The donor fluorescence intensity was quantified before and after bleaching the acceptor fluorophore. The ΔF/F formula (Fluorescence after – Fluorescence Before/Fluorescence Before) was used to measure the change in the intensity. The average of the ΔF/F was used for statistical analysis. In the experiments for early endosome marker, the analysis of fluorescence intensity was done in vesicle positives for Rab 5 that contain p75NTR and TrkB.

Receptor Biotinylation

Hippocampal neurons were maintained for 5 d before treatment. To identify proteins internalized after treatment, cells were rinsed twice with PBS containing 1 mM $CaCl_2$ and 0.5 mM $MgCl_2$ (PBS-Ca-Mg) and then incubated with 1mg/ml Sulfo-NHS-SS-Biotin dissolved in biotinylation buffer (0.01 m TEA, pH 7.4, 2 mm $CaCl_2$, 150 mm NaCl) for 1 h at 4°C. Remaining biotin was then quenched with PBS-Ca-Mg containing 0.1M glycine for 20 min at 4°C. After warming to 37°C, cells were treated with 25 ng/ml BDNF, NGF, or vehicle for the indicated times. As a control for internalization, cells treated with BDNF were maintained at 4°C. After treatment, biotin from the proteins that remained in the cell surface was cleaved using glutathione buffer (5M NaCl, 0.5M EDTA, 1% BSA, 1.5% Glutathione, 5N NaOH). Cells were then lysed in RIPA buffer 1% NP-40, 0.1% SDS, 0.1% deoxycholate, 150 mM NaCl, 1 mM EDTA, 10 mM Tris, pH 8.0, protease inhibitor cocktail (Roche, 11836153001) and phosphatase inhibitor cocktail (Roche, 04906845001) and incubated on ice for 30 min. Internalized biotinylated proteins were isolated using streptavidin-conjugated sepharose beads (Pierce), eluted from the beads, separated by SDS-PAGE, and immunoblotted with the corresponding antibodies.

To determine interactions of internalized receptors, hippocampal neurons were incubated with or without BDNF for 15 or 30 min to induce receptor internalization prior to biotinylation. The remaining cell-surface proteins were biotinylated with 1mg/ml Sulfo-NHS-SS-Biotin for 30 min at 4^{o}C. After quenching the excess biotin with 0.1 M glycine, cells were harvested with RIPA lysis buffer. Lysates were incubated with Streptavidin-beads overnight at 4°C to remove proteins remaining on the cell surface. The supernatants of the streptavidin-beads, representing the internalized proteins from control and BDNF treated neurons, were immunoprecipitated with rabbit anti-p75^{NTR} (Millipore, MAB365, RRID: AB_2152788) or mouse anti-p75^{NTR} (Millipore, MAB365, RRID: AB 2152788) antibodies overnight at 4°C, separated by SDS-PAGE, and immunoblotted for TrkB (Millipore, 07-225, RRID: AB 310445) and p75NTR (Millipore, MAB365, RRID: AB_2152788).

Survival Assay

On the fourth day in culture, fifty percent of the SFM was replaced by a media lacking insulin ("insulin deprivation" media), with or without BDNF (25 ng/ml). Control cultures did not have media change. One day later, hippocampal neurons from WT or KO rats were lysed and intact nuclei were counted using a hemocytometer to assess cell viability as described before (Friedman, 2010; Greenwood et al., 2018). Cell counts were performed in 3 to 5 independent experiments with triplicate cultures per experiment.

Statistical Analysis

Quantitative data are presented as mean ± SEM. The results represent the average of at least three independent experiments, unless specifically indicated. Statistical significance was determined by ANOVA followed by Tukey's test or ANOVA repeated measurements with Sidak's test with $p < 0.05$ considered significant.

RESULTS

BDNF Induces Association Between TrkB and p75NTR That Depends on TrkB Activation

The p75^{NTR} can interact with different co-receptors, with distinct consequences for activation of signaling pathways and effects on cellular function. In cultured embryonic hippocampal neurons, BDNF induced an increased association between TrkB and full length p75^{NTR}. Immunostaining for TrkB and p75^{NTR} showed an increase in intracellular colocalization after 30 min of BDNF treatment, shown using enhanced resolution microscopy (**Figure 1A**). Additionally, co-immunoprecipitation of BDNF-treated neurons showed increased association of p75^{NTR} with TrkB after 15 and 30 min (**Figure 1B**), and FRET analysis after acceptor photobleaching showed increased fluorescence of the donor fluorophore (**Figure 1C**). The interaction of p75^{NTR} with TrkB was seen with BDNF treatment, but not NGF or NT3 treatment, indicating the specificity of the response (**Figure 1D**). Interestingly, although BDNF is known to rapidly activate TrkB phosphorylation within 5 min (Marsh et al., 1993), the interaction between TrkB and p75^{NTR} was minimal after

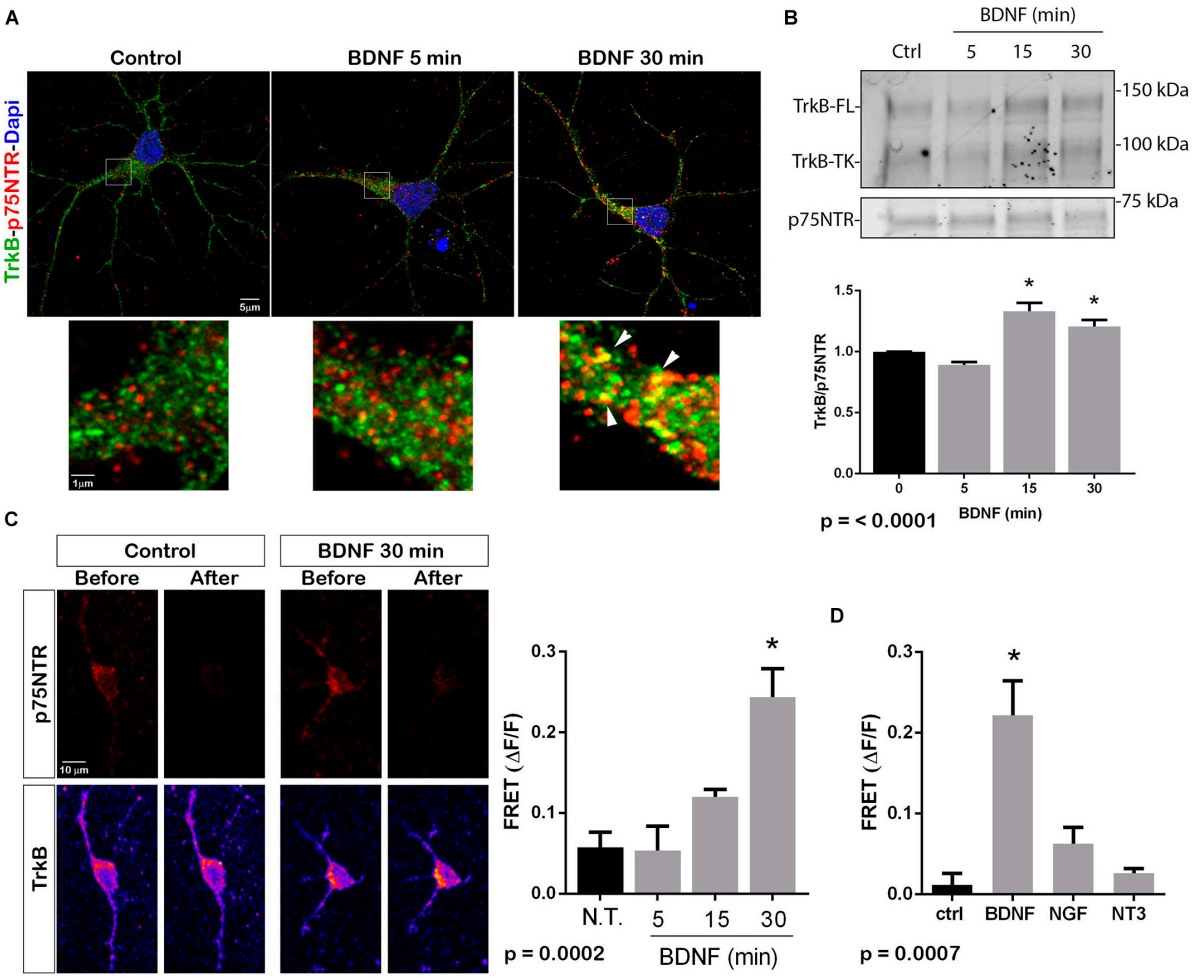

FIGURE 1 | BDNF elicits association between TrkB and p75NTR. **(A)** Cultured hippocampal neurons were treated with BDNF (25 ng/ml) at 37°C for 5 or 30 min. Cells were immunostained with goat anti-p75^{NTR} (red) and rabbit anti-trkB (green). Top images show an entire neuron with each treatment, and boxes indicate the areas analyzed by superresolution microscopy (Leica SP8, 63X, and 1.4 NA), which demonstrated the increase in double-labeled puncta indicative of association of p75^{NTR} and TrkB. Arrows denote areas of colocalization (yellow puncta). **(B)** Lysates stimulated with BDNF for the indicated times, were immunoprecipitated (IP) with anti-p75^{NTR}, probed with anti-TrkB, and reprobed with anti-p75^{NTR}. BDNF stimulation increased the amount of TrkB that coimmunoprecipitated with p75^{NTR} in time-dependent manner. Graph shows quantification of 4 independent experiments. * indicates $p < 0.001$ by ANOVA with Tukey's *post hoc* analysis. **(C)** Receptor photobleaching FRET was used to analyze interaction of p75^{NTR} and TrkB after BDNF treatment of hippocampal neurons. Cultured neurons were treated with 50 ng/ml BDNF for 5, 15, or 30 min. Cells were immunostained with mouse anti-p75^{NTR} (red) and chicken anti-TrkB (green). The acceptor fluorophore was photobleached and the increased fluorescence of the donor fluorophore is indicated in the graph. Images show p75^{NTR} (top) and TrkB (bottom) immunostaining before and after photobleaching with and without 30 min BDNF treatment. The graph shows quantification of fluorescence intensity at all time points. * indicates $p = 0.0002$ by ANOVA with Tukey's *post hoc* analysis. **(D)** The specificity of ligand-induced TrkB-p75^{NTR} interactions was analyzed by FRET. Hippocampal neurons were treated as indicated for 30 min, and the level of fluorescence was measured after acceptor photobleaching. BDNF, but not NGF or NT3, increased the association of TrkB with p75^{NTR}. * indicates $p = 0.0007$ by ANOVA with Tukey's *post hoc* analysis.

5 min of BDNF treatment, and was only increased after 15 and 30 min of treatment, indicating that association of TrkB with p75^{NTR} occurred after TrkB was activated by the ligand, and suggesting that formation of a TrkB/p75^{NTR} complex was not required for BDNF to bind and activate TrkB. Early studies had indicated that p75^{NTR} interacted primarily with the phosphorylated form of TrkB (Bibel et al., 1999). To confirm whether TrkB phosphorylation was required for association with p75^{NTR}, neurons were treated with K252a to prevent BDNF-induced TrkB phosphorylation (**Figure 2A**). K252a prevented the interaction of TrkB with p75^{NTR} assessed by FRET analysis (**Figure 2B**) and co-immunoprecipitation (**Figures 2C,D**).

BDNF Induces TrkB-p75^{NTR} Interaction in the Endosomal Pathway

To determine whether internalization of TrkB and p75^{NTR} was necessary for the receptors to associate, hippocampal neurons were treated with dynasore, an inhibitor of dynamin GTPase, to prevent dynamin-mediated endocytosis. Dynasore treatment prevented the interaction of TrkB with p75^{NTR},

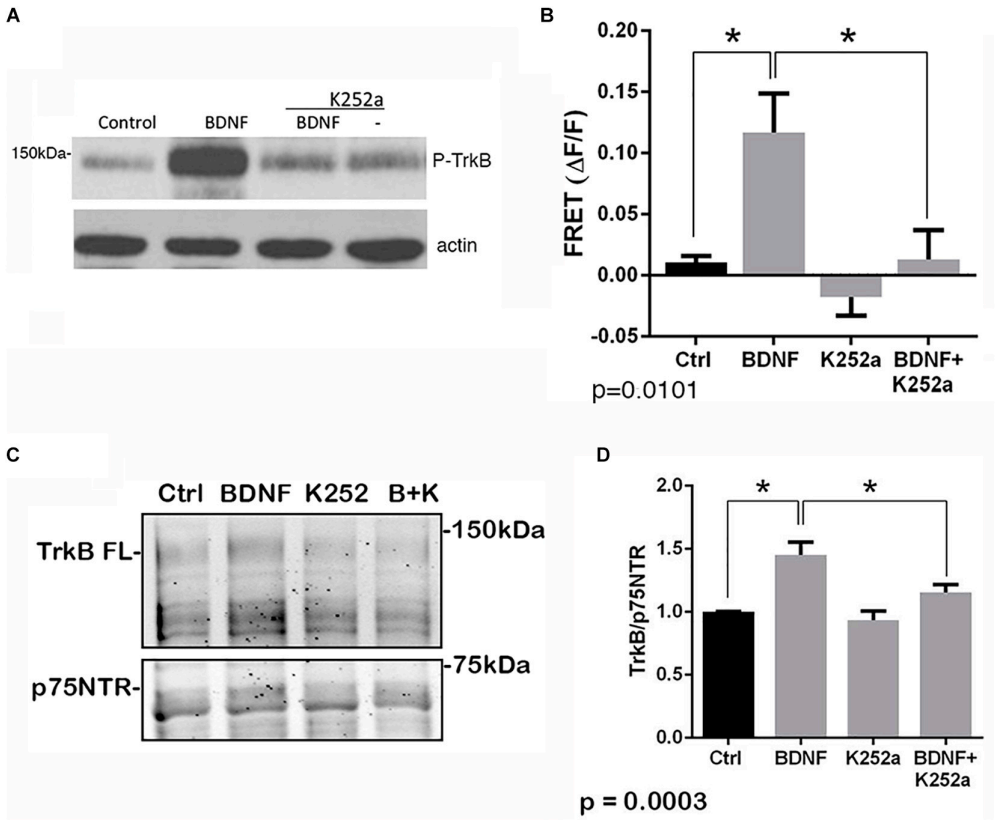

FIGURE 2 | Interaction of TrkB with p75^{NTR} requires kinase activation. Hippocampal neurons were incubated with 25 ng/ml BDNF for 30 min with or without pretreatment with 200 nM K252a for 30 min. **(A)** Phosphorylation of TrkB by BDNF was prevented by preincubation with K252a. Total lysates were analyzed by Western blot, using an anti-phospho-Trk antibody. The membrane was reprobed with an anti-actin antibody. **(B)** K252a pretreatment inhibited BDNF-induced p75^{NTR}-TrkB association. Acceptor photobleaching FRET analysis demonstrated that K252a pretreatment prevented association of p75^{NTR} and TrkB. Quantification of 3 independent experiments, $^*p = 0.0101$ by ANOVA with Tukey's *post hoc* comparison. **(C)** Lysates were immunoprecipitated with anti-p75^{NTR} antibody, probed with anti-TrkB, and reprobed with anti-p75^{NTR} antibody. **(D)** Quantification of 6 independent experiments, $^*p = 0.0003$ by ANOVA with Tukey's *post hoc* analysis.

analyzed by co-IP (**Figure 3A**) and FRET (**Figure 3B**), indicating that internalization was necessary for association of the receptors. Additionally, surface biotinylation experiments were performed. Hippocampal neurons were biotinylated and then treated with BDNF to promote internalization. After 15 min, TrkB was detected following streptavidin pulldown, indicating internalization of the receptor (**Figure 3C**). An increase in internalized truncated as well as full length TrkB was detected. Cells maintained at 4°C showed no increased receptor internalization with BDNF treatment.

To confirm that the internalized TrkB and p75^{NTR} receptors were interacting, hippocampal neurons were first treated with BDNF to promote receptor internalization, then the proteins remaining on the cell surface were biotinylated. Then, cells were lysed and the cell surface proteins were removed by streptavidin pulldown. The remaining supernatants of these pulldowns, representing the internalized proteins, were analyzed by immunoprecipitation with anti-p75^{NTR} followed by Western blot for TrkB and p75NTR, and showed increased TrkB association with p75^{NTR} at 15 and 30 min after BDNF treatment (**Figure 3D**). Treatment with NGF as a control did not show interaction of internalized TrkB and p75^{NTR}.

To determine in which intracellular compartments TrkB and p75^{NTR} were interacting, triple labeling was performed to assess the localization of the receptors to early endosomes, and labeling was analyzed by enhanced resolution microscopy. The number of triple labeled puncta, representing colocalization of TrkB, p75^{NTR} with the early endosome marker EEA1, was quantified with or without BDNF treatment, and showed that BDNF treatment increased localization of both TrkB and p75^{NTR} to the early endosomes over time (**Figures 4A,B**). Analysis of the individual receptors in the EEA1-positive endosome did not show any change with BDNF treatment (**Figures 4C,D**). Additionally, FRET analysis confirmed an increase in TrkB-p75^{NTR} association in the Rab 5-labeled early endosomes following BDNF treatment (**Figure 4E**).

p75^{NTR} Is Necessary for Optimal TrkB Signaling and Function

We investigated whether the absence of p75^{NTR} affected the ability of TrkB to signal in response to BDNF. Hippocampal neurons were cultured from WT or p75$^{NTR-/-}$ rats. We found that the absence of p75^{NTR} attenuated the ability of BDNF

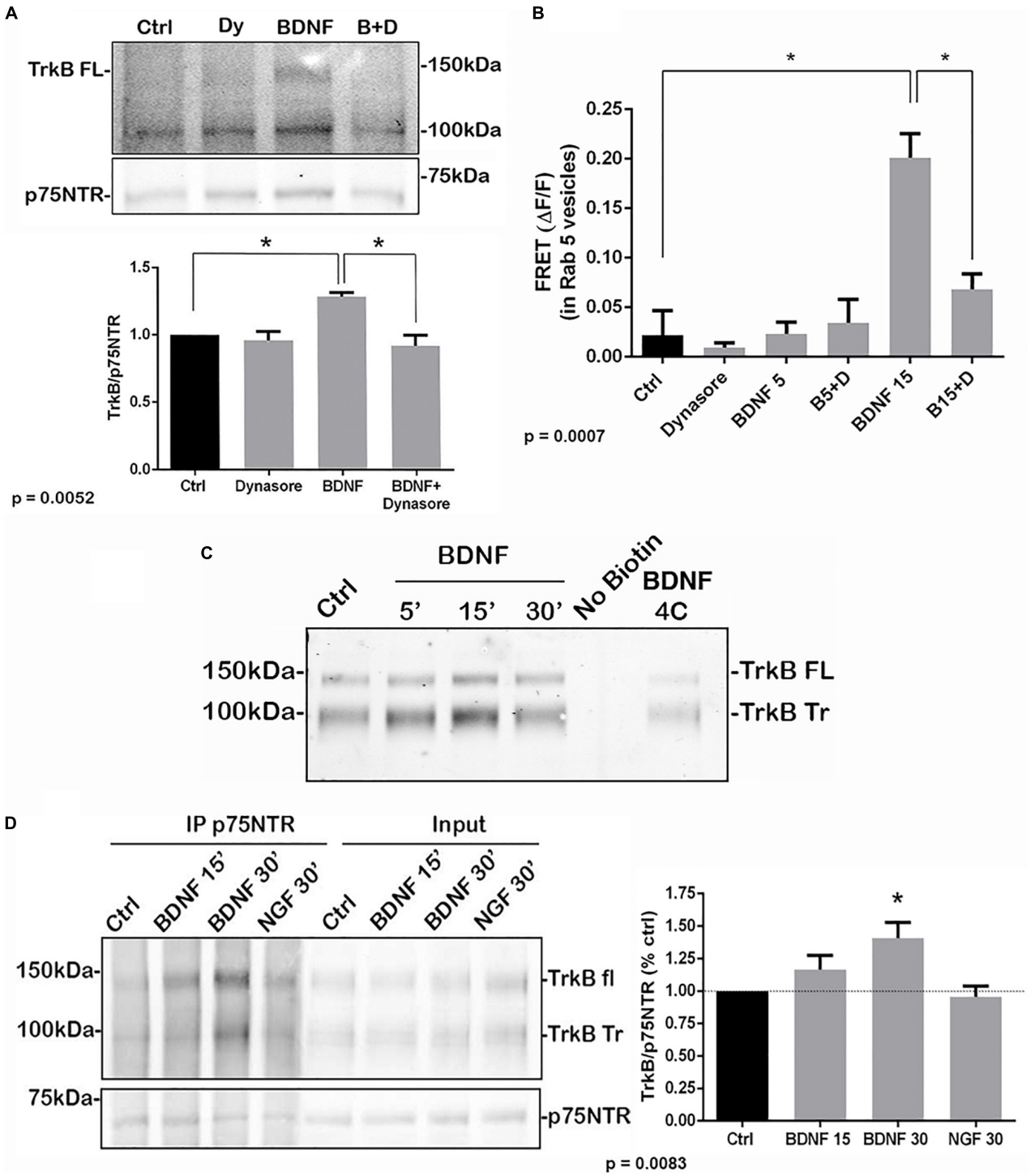

FIGURE 3 | Association of TrkB with p75^{NTR} requires internalization. **(A)** Hippocampal neurons were treated with Dynasore for 30 min to prevent internalization prior to treatment with BDNF. Co-IP analysis demonstrated that Dynasore treatment prevented BDNF-induced association of TrkB with p75^{NTR}. Lysates of hippocampal neurons treated as indicated were immunoprecipitated with anti-p75^{NTR} and probed with anti-TrkB. Quantification of 3 independent experiments is shown below. * indicates significance at $p = 0.0052$ by ANOVA with Tukey's *post hoc* analysis. **(B)** FRET analysis also demonstrates that association of TrkB with p75^{NTR} induced by 15 min of BDNF treatment was inhibited by Dynasore (B15 + D), quantification of 3 independent experiments, *$p = 0.0007$ by ANOVA. **(C)** Hippocampal neurons were biotinylated and then treated with BDNF as indicated to induce receptor internalization. BDNF treatment elicited internalization of TrkB after 15 min which was prevented by incubation at 4°C. **(D)** Hippocampal neurons were first treated with BDNF or NGF as indicated to induce receptor internalization. The cells were then biotinylated and streptavidin used to remove the proteins remaining on the cell surface. The internalized proteins were then immunoprecipitated with anti-p75^{NTR} and probed for TrkB. The graph shows the increased association of internalized TrkB with p75^{NTR} after 30 min of BDNF treatment. *$p = 0.0083$.

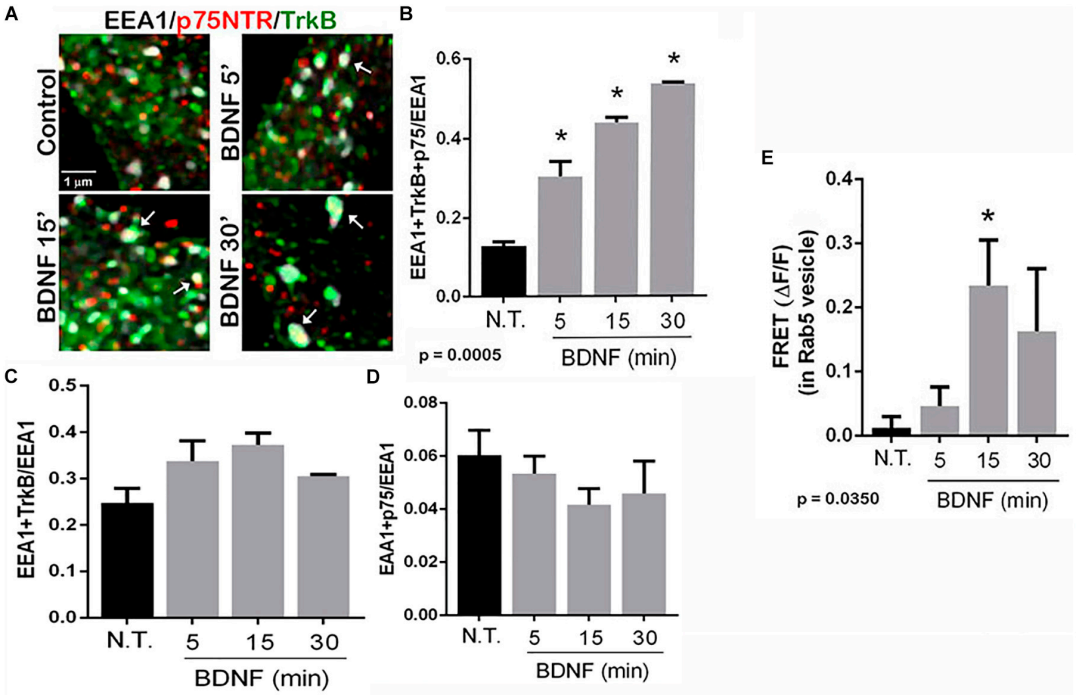

FIGURE 4 | TrkB and p75^{NTR} associate in early endosomes. **(A)** Hippocampal neurons were triple-labeled with antibodies to p75^{NTR}, TrkB, and EEA1 to label early endosomes. Enhanced resolution microscopy analysis shows the increase in triple labeling (arrows) over time with BDNF treatment. **(B)** Quantification of triple labeled puncta, indicating that p75^{NTR} and TrkB are colocalized in the early endosomes, $p = 0.0005$ by ANOVA with Tukey's *post hoc* analysis. **(C)** Quantification of double-labeled puncta for EEA1 and TrkB. **(D)** Quantification of puncta double-labeled for EEA1 and p75NTR. **(E)** Acceptor photobleaching FRET analysis of p75^{NTR} and TrkB in early endosomes, quantification of 3 independent experiments, $^{*}p \leq 0.0001$ by ANOVA with Tukey's *post hoc* analysis.

to induce and maintain phosphorylation of Akt (**Figure 5A**). However, phosphorylation of Erk was unaffected by the absence of p75^{NTR} (**Figure 5B**).

The PI$_3$K-Akt pathway is critical for signaling neuronal survival, therefore we tested whether survival of hippocampal neurons from the p75$^{NTR-/-}$ rats was compromised. Although basal survival of cultured hippocampal neurons from the p75$^{NTR-/-}$ rats was not different from WT, we used a trophic withdrawal model of reducing insulin in the media to test the ability of BDNF to rescue the neurons. BDNF (25 ng/ml) was able to rescue WT neurons from insulin depletion, however, BDNF was unable to rescue neurons lacking p75^{NTR} (**Figure 6**), suggesting that p75^{NTR} facilitates the ability of TrkB to activate the PI$_3$K pathway and promote neuronal survival.

DISCUSSION

Each of the neurotrophin receptors, the Trk family and p75^{NTR}, can signal in response to its neurotrophin or proneurotrophin ligand. Trk receptors have been well-established to promote neuronal survival and differentiation when activated by mature neurotrophins. The p75^{NTR}, not having any kinase activity, recruits different intracellular binding proteins to activate signaling pathways that can have multiple different functions depending on the cellular context. These actions of p75^{NTR} depend on the particular ligand and co-receptor that associate with the receptor (Barker, 2004). Interaction of p75^{NTR} with a member of the sortilin family can promote apoptosis in response to proneurotrophins (Lee et al., 2001; Ibanez and Simi, 2012). In contrast, early studies demonstrated that association between TrkA and p75^{NTR} was required to generate a high affinity binding site for NGF (Hempstead et al., 1991) and that p75^{NTR} conferred greater selectivity for Trk receptors to bind their specific ligands (Bibel et al., 1999; Patapoutian and Reichardt, 2001). Moreover, the localization of TrkA was shown to influence the cellular response to NGF, with internalization being required for a differentiation, but not a survival, response in PC12 cells (Zhang et al., 2000). However, the nature and association of p75^{NTR} with other Trk receptors has not been thoroughly investigated. Previous studies had shown that p75^{NTR} interacts preferentially with the phosphorylated form of TrkB (Bibel et al., 1999), which we confirmed, suggesting that the association of the two receptors occurs after TrkB is activated and thus not required for binding of the ligand. Moreover, a previous study also showed that endocytosis was necessary for TrkA or TrkB-induced activation of Akt, but not Erk (Zheng et al., 2008). We therefore investigated whether association of TrkB with p75^{NTR} was required for proper trafficking and signaling.

Localization and Signaling

It has become clear that localization of receptors and signaling molecules to specific intracellular compartments can regulate

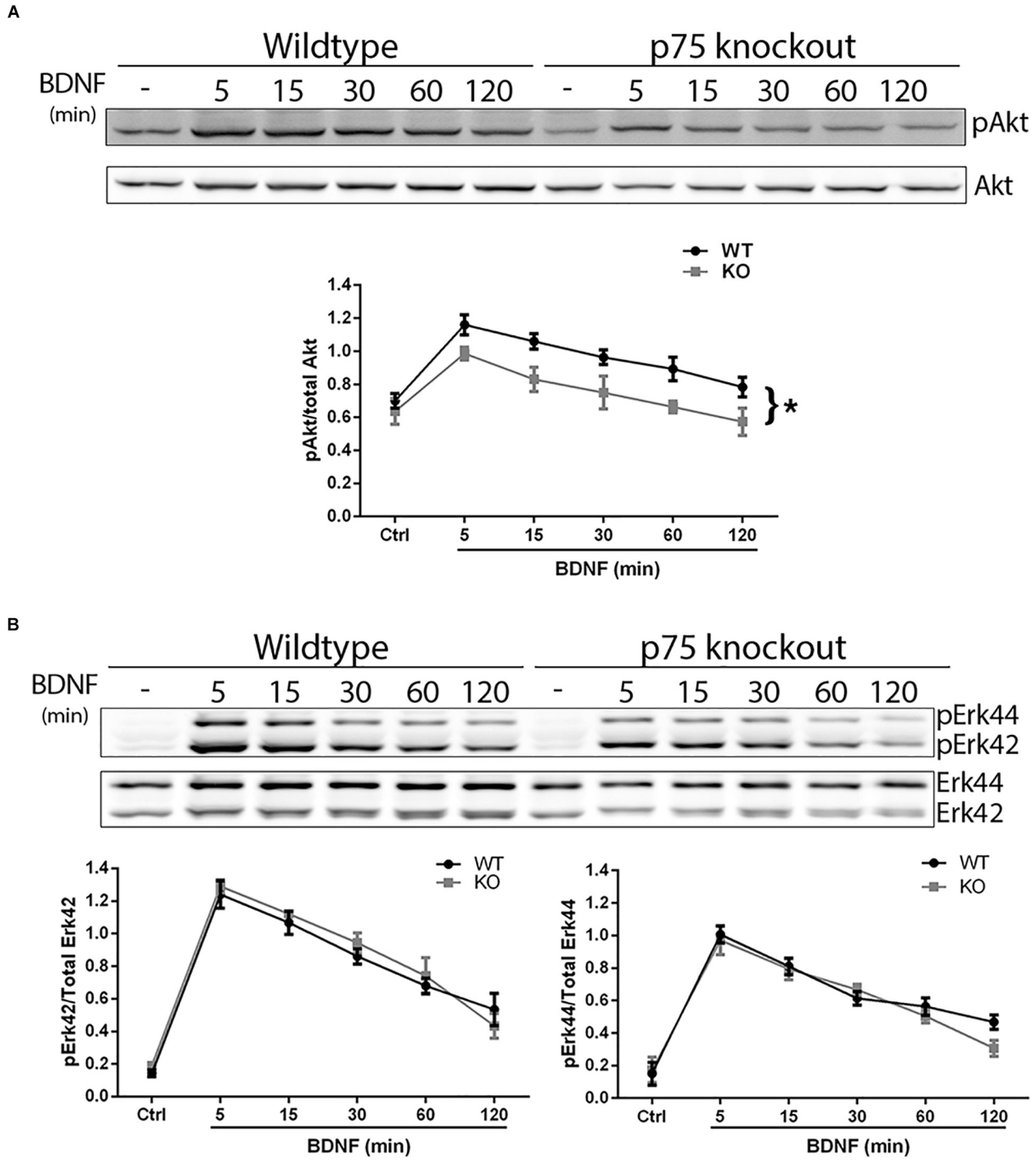

FIGURE 5 | Lack of p75^{NTR} attenuates Akt, but not Erk, activation. Hippocampal neurons from WT or p75$^{NTR-/-}$ rats were cultured for 5 days and treated with BDNF (25 ng/ml) for the indicated times. **(A)** Lysates were probed for P-Akt and total Akt. Graph indicates the ratio of P-Akt to total Akt, $n = 3$ independent experiments, $^{*}p = 0.0405$ comparing WT vs. KO by ANOVA repeated measurement. **(B)** Lysates were probed for P-Erk and total Erk. Graph indicates the ratio of P-Erk42 to total Erk42 and P-Erk44 to total Erk44, $n = 3$ independent experiments, $p = 0.63$ for P-Erk42 and $p = 0.62$ for P-Erk44 by ANOVA repeated measurement with Sidak's *post hoc* analysis.

the specific pathways activated and modulate the cellular response (Bucci et al., 2014). Previous studies have investigated neurotrophin-induced trafficking of Trk receptors and p75^{NTR} independently in a variety of cell types. BDNF treatment of PC12 cells induced trafficking of TrkB to lysosomes (Chen et al., 2005), however, in hippocampal neurons BDNF elicited TrkB

localization to Rab5-positive early endosomes (Moya-Alvarado et al., 2018) and Rab11-positive recycling endosomes (Lazo et al., 2013) to modulate dendritic branching, suggesting that the trafficking and signaling may be dependent on the particular cell context. In contrast to TrkB, p75^{NTR} did not traffic to lysosomes in PC12 cells and sympathetic neurons, but instead could be found in Rab11-positive endosomes and multivesicular bodies (Escudero et al., 2014). This group also found little p75^{NTR} in RAB5+ early endosomes. Our observations indicate that in hippocampal neurons, BDNF induced trafficking of both p75^{NTR} and TrkB to Rab5 and EEA1-positive early endosomes, and that localization of TrkB to the early endosomes was reduced in the absence of p75^{NTR}. BDNF did not elicit any change in the number of EEA1-positive endosomes with either TrkB or p75^{NTR} alone. A previous study had indicated that p75^{NTR} can interact with Rab5 to regulate glucose uptake in adipocytes (Baeza-Raja et al., 2012), suggesting that p75^{NTR} may facilitate internalization of other signaling proteins, such as TrkB, into early endosomes by interacting with Rab5.

TrkB is known to activate both the PI$_3$K-Akt and Ras-ERK pathways to regulate and coordinate numerous cellular functions. Localization of these signaling proteins within the cell can impact activation of specific downstream pathways. PI$_3$K can phosphorylate phosphoinositides at the plasma membrane or in internal membrane compartments such as early endosomes, and activate Akt locally at those sites (Jethwa et al., 2015). Since our studies demonstrate that TrkB and p75^{NTR} interact at the early endosome, it is possible that this localization is required for optimal activation of the Akt pathway. Indeed, our results demonstrate that the absence of p75^{NTR} specifically attenuated activation of Akt, but not Erk. Previous studies have suggested that Akt activation by BDNF requires internalization and endosomal localization, and may occur at the early endosome (Zahavi et al., 2018), and this is supported by our current study.

The p75^{NTR} can interact with numerous co-receptors in response to different ligands, and can influence a variety of cellular processes (Barker, 2004). In specific circumstances, p75^{NTR} has been shown to undergo intramembrane proteolysis by alpha secretase to shed the extracellular domain, generating a C-terminal fragment (CTF), which then can be cleaved to generate the intracellular domain (ICD). The cleavage of p75^{NTR} is essential for its role in promoting neuronal apoptosis (Coulson et al., 2000; Volosin et al., 2008), however, whether p75^{NTR} cleavage is necessary for other receptor associations and functions is unclear. Studies investigating the interaction of p75^{NTR} with TrkA have yielded conflicting results, with one study demonstrating that TrkA interacts with either the full-length p75NTR or the CTF, but that generation of the ICD abrogates that interaction (Jung et al., 2003), while other studies suggested that the p75^{NTR} ICD interacts with TrkA and potentiates NGF binding (Ceni et al., 2010; Kommaddi et al., 2011; Matusica et al., 2013). It is also unclear whether TrkA and TrkB show the same interactions with p75^{NTR}. There are differences in the intracellular domains of TrkA and TrkB that influence their intracellular signaling and trafficking in different ways (Sommerfeld et al., 2000; Chen et al., 2005), which may also impact how these receptors interact with p75^{NTR}.

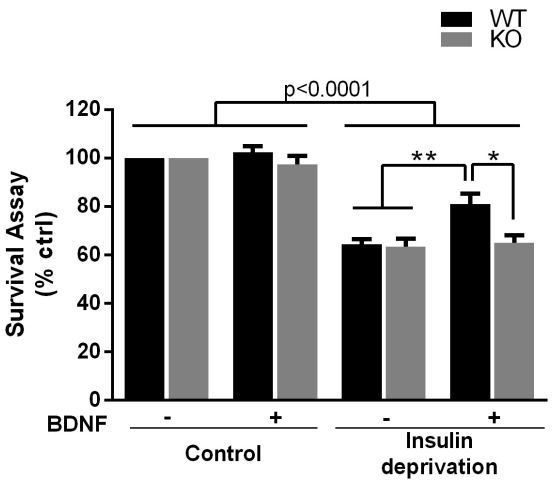

FIGURE 6 | Absence of p75^{NTR} impairs rescue of hippocampal neurons by BDNF in a trophic deprivation model with reduced insulin, decreasing survival of the hippocampal neurons by 40%. BDNF (25 ng/ml) provided significant protection to the WT neurons but was unable to rescue the p75$^{NTR-/-}$ neurons. $^{**}p < 0.006$; $^{*}p = 0.013$ by ANOVA repeated measurement with Sidak's *post hoc* analysis.

In this study, we have demonstrated that full-length p75^{NTR} interacts with TrkB, and that they are internalized together into early endosomes.

Regulation of Neuronal Survival

The cellular consequences of p75^{NTR} actions are strongly dependent on the cell context and may be determined by which co-receptors are engaged as well as which intracellular adapter proteins can be recruited to signal (Nykjaer et al., 2005). Many studies in the literature have investigated the role of p75^{NTR} with respect to neuronal survival, with some studies showing pro-survival effects and some showing apoptotic induction, especially after injury. We have demonstrated that some pro-survival effects of p75^{NTR} may be due to facilitation of TrkB trafficking and signaling in response to BDNF, apart from direct activation of survival signaling by p75^{NTR}. In this study we showed that phosphorylation of Akt by BDNF, which is induced by TrkB signaling, was attenuated in the absence of p75^{NTR}. Since the PI$_3$K-Akt signaling pathway mediates neuronal survival in many paradigms, we investigated whether the lack of p75^{NTR} compromised neuronal survival. Although basal survival of hippocampal neurons was not impaired in the absence of p75^{NTR}, a trophic deprivation assay with the depletion of insulin from the media elicited neuronal death, which was rescued by BDNF in WT neurons but not p75$^{NTR-/-}$ neurons.

In sum, we have demonstrated that BDNF induces the association of TrkB with p75^{NTR} following TrkB phosphorylation and internalization of the receptors to early endosomes. The absence of p75^{NTR} attenuated activation of Akt, but not Erk, and prevented the ability of BDNF to rescue hippocampal neurons

from trophic deprivation, suggesting that p75^{NTR} may facilitate the ability of TrkB to activate specific downstream signaling pathways to regulate neuronal survival and function.

DATA AVAILABILITY STATEMENT

The datasets generated for this study are available on request to the corresponding author.

ETHICS STATEMENT

The animal study was reviewed and approved by the Rutgers IACUC.

AUTHOR CONTRIBUTIONS

JZ, LM, and MV performed the experiments. JZ, LM, and WF analyzed the data. WF wrote the manuscript.

FUNDING

This work was supported by the NIH Grant NS045556.

ACKNOWLEDGMENTS

The authors would like to thank Dipti Kelkar for technical assistance.

REFERENCES

Baeza-Raja, B., Li, P., Le Moan, N., Sachs, B. D., Schachtrup, C., Davalos, D., et al. (2012). p75 neurotrophin receptor regulates glucose homeostasis and insulin sensitivity. *Proc. Natl. Acad. Sci. U.S.A.* 109, 5838–5843. doi: 10.1073/pnas.1103638109

Barker, P. A. (2004). p75NTR is positively promiscuous: novel partners and new insights. *Neuron* 42, 529–533. doi: 10.1016/j.neuron.2004.04.001

Bibel, M., Hoppe, E., and Barde, Y. A. (1999). Biochemical and functional interactions between the neurotrophin receptors trk and p75NTR. *EMBO J.* 18, 616–622. doi: 10.1093/emboj/18.3.616

Bronfman, F. C., Tcherpakov, M., Jovin, T. M., and Fainzilber, M. (2003). Ligand-induced internalization of the p75 neurotrophin receptor: a slow route to the signaling endosome. *J. Neurosci.* 23, 3209–3220. doi: 10.1523/jneurosci.23-08-03209.2003

Bucci, C., Alifano, P., and Cogli, L. (2014). The role of rab proteins in neuronal cells and in the trafficking of neurotrophin receptors. *Membranes* 4, 642–677. doi: 10.3390/membranes4040642

Ceni, C., Kommaddi, R. P., Thomas, R., Vereker, E., Liu, X., McPherson, P. S., et al. (2010). The p75NTR intracellular domain generated by neurotrophin-induced receptor cleavage potentiates trk signaling. *J. Cell Sci.* 123, 2299–2307. doi: 10.1242/jcs.062612

Chen, Z.-Y., Ieraci, A., Tanowitz, M., and Lee, F. S. (2005). A novel endocytic recycling signal distinguishes biological responses of Trk neurotrophin receptors. *Mol. Biol. Cell* 16, 5761–5772. doi: 10.1091/mbc.e05-07-0651

Coulson, E. J., Reid, K., Baca, M., Shipham, K. A., Hulett, S. M., Kilpatrick, T. J., et al. (2000). Chopper, a new death domain of the p75 neurotrophin receptor that mediates rapid neuronal cell death [in process citation]. *J. Biol. Chem.* 275, 30537–30545. doi: 10.1074/jbc.m005214200

Escudero, C., Lazo, O., Galleguillos, C., Parraguez, J., Lopez-Verrilli, M., Cabeza, C., et al. (2014). p75 neurotrophin receptor evades the endolysosomal route, favouring multivesicular bodies specialised for exosomal release in neuronal cells. *J. Cell Sci.* 127, 1966–1979. doi: 10.1242/jcs.141754

Farinelli, S. E., Greene, L. A., and Friedman, W. J. (1998). Neuroprotective actions of dipyridamole on cultured CNS neurons. *J. Neurosci.* 18, 5112–5123. doi: 10.1523/jneurosci.18-14-05112.1998

Friedman, W. J. (2010). Proneurotrophins, seizures, and neuronal apoptosis. *Neuroscientist* 16, 244–252. doi: 10.1177/1073858409349903

Friedman, W. J., Ibanez, C. F., Hallbook, F., Persson, H., Cain, L. D., Dreyfus, C. F., et al. (1993). Differential actions of neurotrophins in the locus coeruleus and basal forebrain. *Exp. Neurol.* 119, 72–78. doi: 10.1006/exnr.1993.1007

Ginty, D. D., and Segal, R. A. (2002). Retrograde neurotrophin signaling: Trk-ing along the axon. *Curr. Opin. Neurobiol.* 12, 268–274. doi: 10.1016/s0959-4388(02)00326-4

Greenwood, S. G., Montroull, L., Volosin, M., Scharfman, H. E., Teng, K. K., Light, M., et al. (2018). A novel neuroprotective mechanism for lithium that prevents association of the p75^{NTR}-sortilin receptor complex and attenuates proNGF-induced neuronal death *in vitro* and *in vivo*. *eNeuro* 5. doi: 10.1523/ENEURO.0257-17.2017

Hempstead, B. L., Martin-Zanca, D., Kaplan, D. R., and Chao, M. V. (1991). High affinity NGF binding requires co-expression of the trk proto-oncogene and the low affinity NGF receptor. *Nature* 350, 678–683. doi: 10.1038/350678a0

Hibbert, A. P., Kramer, B. M., Miller, F. D., and Kaplan, D. R. (2006). The localization, trafficking and retrograde transport of BDNF bound to p75NTR in sympathetic neurons. *Mol. Cell. Neurosci.* 32, 387–402. doi: 10.1016/j.mcn.2006.06.001

Ibanez, C. F., and Simi, A. (2012). p75 neurotrophin receptor signaling in nervous system injury and degeneration: paradox and opportunity. *Trends Neurosci.* 35, 431–440. doi: 10.1016/j.tins.2012.03.007

Jethwa, N., Chung, G. H., Lete, M. G., Alonso, A., Byrne, R. D., Calleja, V., et al. (2015). Endomembrane PtdIns(3,4,5)P3 activates the PI3K-akt pathway. *J. Cell Sci.* 128, 3456–3465. doi: 10.1242/jcs.172775

Jung, K. M., Tan, S., Landman, N., Petrova, K., Murray, S., Lewis, R., et al. (2003). Regulated intramembrane proteolysis of the p75 neurotrophin receptor modulates its association with the TrkA receptor. *J. Biol. Chem.* 278, 42161–42169. doi: 10.1074/jbc.m306028200

Kommaddi, R. P., Thomas, R., Ceni, C., Daigneault, K., and Barker, P. A. (2011). Trk-dependent ADAM17 activation facilitates neurotrophin survival signaling. *FASEB J.* 25, 2061–2070. doi: 10.1096/fj.10-173740

Lazo, O. M., Gonzalez, A., Ascano, M., Kuruvilla, R., Couve, A., and Bronfman, F. C. (2013). BDNF regulates rab11-mediated recycling endosome dynamics to induce dendritic branching. *J. Neurosci.* 33, 6112–6122. doi: 10.1523/JNEUROSCI.4630-12.2013

Lee, R., Kermani, P., Teng, K. K., and Hempstead, B. L. (2001). Regulation of cell survival by secreted proneurotrophins. *Science* 294, 1945–1948. doi: 10.1126/science.1065057

Marsh, H. N., Scholz, W. K., Lamballe, F., Klein, R., Nanduri, V., Barbacid, M., et al. (1993). Signal transduction events mediated by the BDNF receptor gp 145TrkB in primary hippocampal pyramidal cell culture. *J. Neurosci.* 13, 4281–4292. doi: 10.1523/jneurosci.13-10-04281.1993

Matusica, D., Skeldal, S., Sykes, A. M., Palstra, N., Sharma, A., and Coulson, E. J. (2013). An intracellular domain fragment of the p75 neurotrophin receptor (p75(NTR)) enhances tropomyosin receptor kinase a (TrkA) receptor function. *J. Biol. Chem.* 288, 11144–11154. doi: 10.1074/jbc.M112.436469

Moya-Alvarado, G., Gonzalez, A., Stuardo, N., and Bronfman, F. C. (2018). Brain-derived neurotrophic factor (BDNF) regulates rab5-positive early endosomes in hippocampal neurons to induce dendritic branching. *Front. Cell Neurosci.* 12:493. doi: 10.3389/fncel.2018.00493

Nykjaer, A., Lee, R., Teng, K., Jansen, P., Madsen, P., Nielsen, M., et al. (2004). Sortilin is essential for proNGF-induced neuronal cell death. *Nature* 427, 843–848. doi: 10.1038/nature02319

Nykjaer, A., Willnow, T. E., and Petersen, C. M. (2005). p75NTR–live or let die. *Curr. Opin. Neurobiol.* 15, 49–57. doi: 10.1016/j.conb.2005.01.004

Patapoutian, A., and Reichardt, L. F. (2001). Trk receptors: mediators of neurotrophin action. *Curr. Opin. Neurobiol.* 11, 272–280. doi: 10.1016/s0959-4388(00)00208-7

Schinder, A. F., and Poo, M. (2000). The neurotrophin hypothesis for synaptic plasticity. *Trends Neurosci.* 23, 639–645. doi: 10.1016/s0166-2236(00)01672-6

Schmieg, N., Menendez, G., Schiavo, G., and Terenzio, M. (2014). Signalling endosomes in axonal transport: travel updates on the molecular highway. *Semin. Cell Dev. Biol.* 27, 32–43. doi: 10.1016/j.semcdb.2013.10.004

Sommerfeld, M. T., Schweigreiter, R., Barde, Y. A., and Hoppe, E. (2000).). Down-regulation of the neurotrophin receptor TrkB following ligand binding. Evidence for an involvement of the proteasome and differential regulation of TrkA and TrkB. *J. Biol. Chem.* 275, 8982–8990. doi: 10.1074/jbc.275.12.8982

Volosin, M., Song, W., Almeida, R. D., Kaplan, D. R., Hempstead, B. L., and Friedman, W. J. (2006). Interaction of survival and death signaling in basal forebrain neurons: roles of neurotrophins and proneurotrophins. *J. Neurosci.* 26, 7756–7766. doi: 10.1523/jneurosci.1560-06.2006

Volosin, M., Trotter, C., Cragnolini, A., Kenchappa, R. S., Light, M., Hempstead, B. L., et al. (2008). Induction of proneurotrophins and activation of p75NTR-mediated apoptosis via neurotrophin receptor-interacting factor in hippocampal neurons after seizures. *J. Neurosci.* 28, 9870–9879. doi: 10.1523/JNEUROSCI.2841-08.2008

Yano, H., and Chao, M. V. (2005). Biochemical characterization of intracellular membranes bearing Trk neurotrophin receptors. *Neurochem. Res.* 30, 767–777. doi: 10.1007/s11064-005-6870-z

Zahavi, E. E., Steinberg, N., Altman, T., Chein, M., Joshi, Y., Gradus-Pery, T., et al. (2018). The receptor tyrosine kinase TrkB signals without dimerization at the plasma membrane. *Sci. Signal.* 11:eaao4006. doi: 10.1126/scisignal.aao4006

Zhang, Y., Moheban, D. B., Conway, B. R., Bhattacharyya, A., and Segal, R. A. (2000). Cell surface trk receptors mediate NGF-induced survival while internalized receptors regulate NGF-induced differentiation. *J. Neurosci.* 20, 5671–5678. doi: 10.1523/jneurosci.20-15-05671.2000

Zheng, J., Shen, W. H., Lu, T. J., Zhou, Y., Chen, Q., Wang, Z., et al. (2008). Clathrin-dependent endocytosis is required for TrkB-dependent Akt-mediated neuronal protection and dendritic growth. *J. Biol. Chem.* 283, 13280–13288. doi: 10.1074/jbc.M709930200

Conflict of Interest: The authors declare that the research was conducted in the absence of any commercial or financial relationships that could be construed as a potential conflict of interest.

frontiers in Cellular Neuroscience

ORIGINAL RESEARCH
published: 26 November 2019
doi: 10.3389/fncel.2019.00526

c-Abl Deficiency Provides Synaptic Resiliency Against Aβ-Oligomers

*Daniela A. Gutierrez, Lina M. Vargas, América Chandia-Cristi, Catalina de la Fuente, Nancy Leal and Alejandra R. Alvarez**

Cell Signaling Laboratory, Faculty of Biological Science, Department of Cell and Molecular Biology, Center for Aging and Regeneration (CARE), Pontificia Universidad Católica de Chile, Santiago, Chile

Spine pathology has been implicated in the early onset of Alzheimer's disease (AD), where Aβ-Oligomers (AβOs) cause synaptic dysfunction and loss. Previously, we described that pharmacological inhibition of c-Abl prevents AβOs-induced synaptic alterations. Hence, this kinase seems to be a key element in AD progression. Here, we studied the role of c-Abl on dendritic spine morphological changes induced by AβOs using c-Abl null neurons (c-Abl-KO). First, we characterized the effect of c-Abl deficiency on dendritic spine density and found that its absence increases dendritic spine density. While AβOs-treatment reduces the spine number in both wild-type (WT) and c-Abl-KO neurons, AβOs-driven spine density loss was not affected by c-Abl. We then characterized AβOs-induced morphological changes in dendritic spines of c-Abl-KO neurons. AβOs induced a decrease in the number of mushroom spines in c-Abl-KO neurons while preserving the populations of immature stubby, thin, and filopodia spines. Furthermore, synaptic contacts evaluated by PSD95/Piccolo clustering and cell viability were preserved in AβOs-exposed c-Abl-KO neurons. In conclusion, our results indicate that in the presence of AβOs c-Abl participates in synaptic contact removal, increasing susceptibility to AβOs damage. Its deficiency increases the immature spine population reducing AβOs-induced synapse elimination. Therefore, c-Abl signaling could be a relevant actor in the early stages of AD.

Keywords: Alzheimer's disease, c-Abl tyrosine kinase, synapse, Aβ-oligomers, dendritic spines

OPEN ACCESS

Edited by:
Juan Pablo Henríquez, Universidad de Concepción, Chile

Reviewed by:
Rodrigo A. Cunha, University of Coimbra, Portugal
Valentina Echeverria Moran, Bay Pines VA Healthcare System, United States

****Correspondence:***
Alejandra R. Alvarez
aalvarez@bio.puc.cl

Received: *08 April 2019*
Accepted: *11 November 2019*
Published: *26 November 2019*

Citation:
Gutierrez DA, Vargas LM, Chandia-Cristi A, de la Fuente C, Leal N and Alvarez AR (2019) c-Abl Deficiency Provides Synaptic Resiliency Against Aβ-Oligomers. Front. Cell. Neurosci. 13:526. doi: 10.3389/fncel.2019.00526

INTRODUCTION

In the adult central nervous system, synaptic connections are highly dynamic, allowing the brain to reorganize and integrate new information. The formation, stabilization, weakening and elimination of synapses play a key role in neuronal transmission and wiring (Fernandes and Carvalho, 2016). Excitatory synaptic contacts have actin-enriched structures known as dendritic spines, which are constantly modified. Dendritic spines arise from the dendritic shaft and have immature forms known as filopodia and thin spines. The mature forms known as mushroom spines have post-synaptic densities enriched in scaffolding proteins and glutamate receptors (Harris, 1999; Hayashi and Majwska, 2005). The formation, maturation, shape-changing and pruning of

dendritic spines have been associated with learning and memory (Riccomagno and Kolodkin, 2015; Piochon et al., 2016). Interestingly, processes that alter the size, shape and density of dendritic spines such as the remodeling of synaptic complexes, and changes in actin cytoskeleton, have been implicated in synaptic plasticity, synaptic dysfunction and neuronal death (Kommaddi et al., 2018). In fact, synaptic dysfunction has been associated with the genesis and progression of different neurodegenerative diseases (Hardy and Selkoe, 2002; Clare et al., 2010; Henstridge et al., 2018).

Alzheimer's disease (AD) is characterized by synaptic and neuronal loss in brain regions related with memory and cognition (Gomez-Isla et al., 2008; Viola and Klein, 2015). Cognitive decline strongly correlates with the loss of pre- and post-synaptic markers in AD brains (Sze et al., 1997; Masliah et al., 2001; Reddy et al., 2005; Calabrese et al., 2007). And it also correlates with early changes in glutamatergic function (Kirvell et al., 2006). Neuronal cultures are mostly excitatory, and $A\beta_{1-42}$ oligomers (AβOs) bind mainly to synapses that use glutamate as a neurotransmitter (Lacor et al., 2007). Synaptic binding of AβOs in hippocampal neurons decreases surface N-Methyl-D-aspartate (NMDA) receptors and EphB2 protein levels (Calabrese et al., 2007; Lacor et al., 2007); it also reduces levels of PSD95 and the GluR1 subunit of the AMPA receptor (Almeida et al., 2005). Furthermore, there is dendritic spine loss in the brains of AD patients and in mice models of AD that express the mutant human Amyloid Precursor Protein (APP; Davies et al., 1987; Moolman et al., 2004; Jacobsen et al., 2006). Neuronal degeneration begins with early neuronal dysfunction mediated by AβOs, which disrupts the synapse and inhibits long-term potentiation (LTP; Lambert et al., 1998; Selkoe, 2008; Ferreira and Klein, 2011; Tu et al., 2014). AβOs bind to dendritic spines, significantly decreasing the number of synaptic terminals, reducing dendritic spine density in neurons and changing their morphology to more elongated shapes (filopodia spines; Spires et al., 2005; Jacobsen et al., 2006; Lacor et al., 2007). Altogether, these data suggest that early synaptic dysfunction and synaptic loss induced by AβOs are involved in the cognitive decline in AD patients.

Previously, we identified c-Abl as a key signaling molecule involved in AD pathology (Alvarez et al., 2004; Cancino et al., 2008; Vargas et al., 2014; Gonzalez-Zuñiga et al., 2014). The ABL family of non-receptor tyrosine kinases, includes c-Abl and the Abl-related gene (Arg). Deletion of c-Abl or Arg in mice causes hematopoietic or behavioral defects, respectively (Tybulewicz et al., 1991). The complete deletion of both kinases causes lethal neurulation defects due to actin accumulation in the neuroepithelium and defective closure of the neural tube. Therefore, animals die from hemorrhaging at embryonic day E11 (Koleske et al., 1998). On the other hand, the knockout conditional mice model (c-Abl-KO) used here, is under the promoter of neuronal and glial progenitor cells Nestin-CRE; and does not present neurulation defects or embryonic lethality (Qiu et al., 2010).

c-Abl is a key signal transducer for growth factors, adhesion and axon-guidance receptors as well as for DNA damage, oxidative stress and others (Wang, 2014). Since it has G- and F-actin binding domains, c-Abl can interact with cytoskeletal related proteins. It phosphorylates Abi and WAVE2 and therefore activates Arp2/3 to regulate actin polymerization (Mendoza, 2013). c-Abl is expressed at high levels in neurons, especially in pre- and post-synaptic terminals and its activity inactivates RhoA promoting dendrogenesis and synaptic plasticity (Moresco and Koleske, 2003; Jones et al., 2004; Lin et al., 2013). Furthermore, unlike Arg, c-Abl has the ability to shuttle between the cytoplasm and the nucleus regulating chromatin (Tip60), gene expression and apoptosis (p73/p53; Jiang et al., 2011; Wang, 2014).

Interestingly, the c-Abl activation pathway has also been involved in neuronal apoptosis linked to the pathology of different neurodegenerative diseases (Schlatterer et al., 2011). In the case of AD, we described that Aβ fibrils-induced c-Abl-activation triggers apoptosis in neuronal cultures (Alvarez et al., 2004; Jing et al., 2009). Also, c-Abl stabilizes HDAC2 repressing neuronal gene expression, contributing to memory impairment in AD (Gonzalez-Zuñiga et al., 2014). We have also demonstrated that c-Abl plays a key role in synaptic structural changes induced by AβOs. In this pathway, AβOs bind to the EphA4 receptor causing downstream activation of c-Abl, synaptic loss and LTP blockade (Vargas et al., 2014). Moreover, EphA4/c-Abl signaling is inherently activated in APPswe/PSEN1ΔE9 transgenic mice, and thus, c-Abl inhibition resulted in decreased AβOs accumulation in the brain (Cancino et al., 2008; Fu et al., 2014; Yáñez et al., 2016). On the other hand, c-Abl inhibition by Imatinib (ATP binding site c-Abl inhibitor), improves behavioral impairments in Aβ-fibrils injected animals, and also reduces AβOs-mediated spine density loss (Cancino et al., 2008). However, Imatinib does not only inhibits c-Abl, but also Arg, c-kit, PDGFR and Src (Greuber et al., 2013; Lin and Roux, 2013).

Here, we show that c-Abl is present at synapses and co-localizes with the post-synaptic protein PSD95. To further dissect the role of c-Abl on synaptic changes induced by AβOs, we used c-Abl null hippocampal neurons. In the absence of c-Abl, these neurons showed increased spine density and enrichment of immature spines. Even though AβOs disrupt the synapse, c-Abl null neurons remodel dendritic spines, decreasing the number of mature spines and increasing the number of immature spines; but maintaining their synaptic contacts as a way to overcome the synaptic damage induced by AβOs.

MATERIALS AND METHODS

Animals

c-Abl null mice were bred from c-Abl^{loxp}/c-Abl^{loxp} and Nestin-Cre^{+} mice, kindly donated by Dr. AJ Koleske (Yale School of Medicine, New Haven, CT, USA). Genotyping was performed using a polymerase chain reaction (PCR)-based screening (Bradley and Koleske, 2009). Primers: Abl1-floxA: 5′-GATGTCTCTACAGGGTTTAAGATTAAGAGCA-3′; and Abl1-floxB: 5′-AGTTAACACACCTCCAGAGTGAGTGCCCT-3′; Cre: B: 5′-GCAATTTCGGCTATACGTAACAGGG-3′; and A: 5′-GCAAGAACCTGATGGACATGTTCAG-3′.

All protocols were approved and followed local guidance documents generated by the *ad hoc* Chilean committee (CONICYT), and were approved by the Bioethics and Care of Laboratory Animals Committee of the Pontificia Universidad Católica de Chile (Protocol #150721002). We followed the recommendations of the Guide for Care and Use of Laboratory Animals from US Public Health Service.

Primary Hippocampal Cell Culture

Hippocampi from c-Abl knockout (c-Abl^{loxp}/c-Abl^{loxp}; Nestin-Cre^{+}; c-Abl-KO) and their WT siblings (c-Abl$^{floxo/floxo}$; WT) mice embryos at day 18 (E18) were dissected, and primary hippocampal cultures were prepared as previously described (Kaech and Banker, 2006). This conditional c-Abl-KO mice model does not present the c-Abl protein in the brain, unlike their WT littermates, although it is present in other tissues (see **Supplementary Figure S1**). Pregnant mice were anesthetized with CO_2 and subsequently euthanized by cervical dislocation. Cultures were maintained at 37°C in 5% CO_2 with neurobasal growth medium (Invitrogen, Carlsbad, CA, USA), supplemented with B27, 2 mM L-glutamine, 100 U/ml penicillin, and 100 μg/ml streptomycin (Invitrogen, Carlsbad, CA, USA). On the next day, cultured neurons were treated with 1 μM AraC to prevent glial cell proliferation. Hippocampal neurons were treated with AβOs at 5 μM final concentration for 5 h.

Aβ Oligomers Preparation

Human synthetic $A\beta_{1-42}$ peptide (Genemed Biotechnologies Inc, San Francisco, CA, USA) was suspended in 1, 1, 1, 3, 3, 3 hexafluoro-2-propanol 0.5 mg/ml (Sigma-Aldrich, St. Louis, MO, USA). Peptide samples were vortexed to obtain a homogenous solution, aliquoted into microfuge tubes and lyophilized. The $A\beta_{1-42}$ peptide aliquots were resuspended in nanopure water at 200 μM concentration and vortexed briefly. Aggregation was allowed to proceed for 12 h at 4°C following the protocols by Arimon et al. (2005) and Sokolov et al. (2006). To form fluorescent AβOs (AβOs-FITC), synthetic $A\beta_{1-42}$ coupled to FITC (Bachem, Torrance, CA, USA) was used. Gel electrophoresis was performed at 4°C in Tris-tricine gels (4% stacking, 10% spacer and 16% resolutive gel) at 50 V to 80 V. $A\beta_{1-42}$ species were transferred onto nitrocellulose membrane (0.22 μm pore) for 1 h and 350 mA. Blocking was performed in TBS-3% non-fat milk, and incubated with the primary antibody WO2 raised against Amyloid-β-peptide (MABN10, Millipore, Burlington, MA, USA 1:1,000; **Supplementary Figure S2**).

Neuronal Dendritic Spine Labeling and Quantification

Hippocampal neurons from WT and c-Abl-KO embryos (E18) were seeded onto poly-L-lysine-coated coverslips in 24-well culture plates at a density of 10^4 cells per well. For transfection of pcDNA 3.0 GFP-plasmids, we used the Magnetofection^{TM} technology with the reagent Neuromag (OZ Biosciences, NM50200) in 18 DIV neurons. After 24 h, these neurons were treated with 5 μM AβOs for 5 h. For dendritic spine quantification, we analyzed GFP-expressing neurons and the co-localization with PSD95 or TRITC-phalloidin (ECM Biosciences, Versailles, KY, USA) to label actin cytoskeleton and examine spine morphology. Coverslips were mounted with mounting medium (DAKO) and then observed using an Olympus IX81 LSM Fluoview or a Nikon Eclipse C2 Ti-E confocal microscope. Images were processed with ImageJ (NIH). Antibodies used for immunofluorescence were anti-Piccolo [epitope 44aII antibody (Cases-Langhoff et al., 1996; Gundelfinger et al., 2016) produced by Viviana I. Torres and Craig C. Garner]; anti-PSD95 (75–028) from NeuroMab, Davis, CA, USA. Dendrite and spine morphology classification was performed according to the method described by Tyler and Pozzo-Miller (2003).

Immunoblot Analysis

Hippocampal neurons from WT and c-Abl-KO embryos were plated at a density of 10^6 cells/cm^2. At different DIV, they were washed and lysed in radioimmunoprecipitation assay (RIPA) buffer (50 mM Tris, 150 mM NaCl, 1 mM EGTA, 1 mM EDTA, 0.5% deoxycholate, 1% NP-40, and 0.1% SDS) supplemented with protease inhibitors. Cell lysates were centrifuged at 14,000 rpm for 15 min at 4°C. Protein quantification was performed using the Pierce® BCA Protein Assay Kit (Thermo Fisher Scientific, Waltham, MA, USA). The fractions were subjected to SDS-PAGE and transferred onto nitrocellulose membranes (Thermo Fisher Scientific, Waltham, MA, USA). The antibodies used were: anti-βIII-tubulin (AA10 sc80016, Santa Cruz Biotechnology, Dallas, TX, USA), anti-c-Abl (A5844, Sigma-Aldrich, St. Louis, MO, USA); anti-PSD95 (75–028) and anti-SAP102 (75–058), from NeuroMAb Antibodies Inc.

Apoptotic Nuclei Quantification

Hippocampal neurons from WT and c-Abl-KO embryos were seeded onto poly-L-lysine-coated coverslips in 24-well culture plates at a density of 5×10^4 cells per well and treated with 5 μM AβOs for 5 h. Cells were fixated and immunostained with active caspase-3 (AB3623, Millipore, Burlington, MA, USA) and Hoechst (33342, Thermo Fisher Scientific, Waltham, MA, USA), to visualize apoptotic nuclei.

RT-PCR

Total RNA from 10 DIV WT and c-Abl-KO hippocampal neurons was extracted using TRIzol (Life Technologies, Carlsbad, CA, USA, 15596). Neurons were treated with 5 μM AβOs for 1, 3, 5 and 12 h. Fibrillary forms of the Aβ-peptide (Aβf) were used as control at 5 μM. Total RNA was reverse-transcribed into cDNA using the High Capacity cDNA Reverse Transcription kit (Applied Biosystems). Primers: c-Abl Forward: 5′ AGCATCACTAAAGGCGAGAA 3′; c-Abl Reverse: 5′ CACC CTCCCTTCATACCG 3′; GAPDH Forward: 5′ GGGTGTGA ACCACGAGAAATA 3′; GAPDH Reverse: 5′ CTGTGGTCA TGAGCCCTTC 3′.

Statistical Analyses

We use ImageJ for dendritic spine quantification every 10 μm of each secondary dendrite. We performed three independent experiments (mice cultures) with a total of four to five embryos

per condition, and two to five dendrites per neuron analyzed for a total of 13–17 neurons per condition. The total number of spines is indicated in each figure. For spine profile analyses, we used quantifications for each type (Mushroom, Stubby, Thin, Filopodium and Branched) and normalized with the total number of dendritic spines per dendrite analyzed per neuron. All data are presented as Mean ± Mean Standard Error (SEM). Mean, SEM and SE values and the number of experiments are indicated in each figure. Spine quantification statistical analyses were performed using Mann–Whitney unpaired *t*-test for dendritic spine type analyses and two-way ANOVA, followed by Tukey's *post hoc* multiple comparison test using GraphPad Prism 6 software for genotype/treatment comparisons. Pearson's and Mander's colocalization were performed using the ImageJ

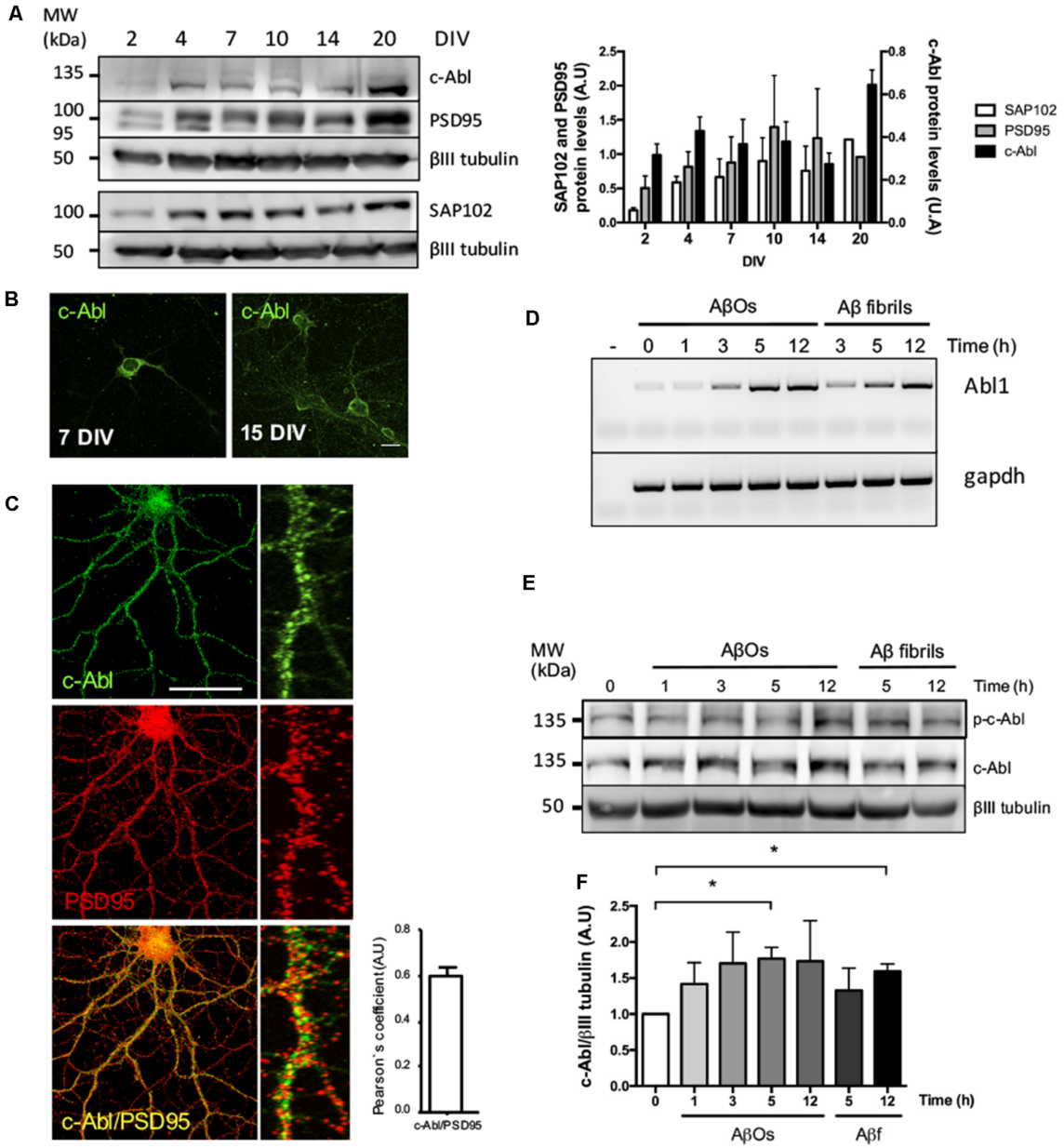

FIGURE 1 | c-Abl is located at the synapse and its mRNA and protein levels increase after Aβ oligomers (AβOs) treatment. **(A)** c-Abl, PSD95 and SAP102 protein levels increase as the neuronal culture ages (from 7 to 20 DIV). The graph shows quantification of protein levels. $n = 3$ **(B)** Immunofluorescence of hippocampal neurons showing c-Abl (in green) from soma to dendrites at 15 DIV. **(C)** Immunofluorescence showing c-Abl (in green) and PSD95 (in red) in hippocampal neurons at 19 DIV. The graph shows protein colocalization by Pearson's correlation. Scale bar = 20 μm and 2 μm for magnifications. **(D)** Hippocampal cultured neurons were treated with 5 μM AβOs at indicated times. mRNA expression for *Abl1* gene was assayed by RT-PCR using *gapdh* as loading control (water negative control). **(E)** Western-blot of c-Al total protein levels normalized to βIII tubulin, as the graph shows **(F)**. Neurons incubated with 5 μM fibrillary forms of the Aβ-peptide (Aβf) were used as control. Unpaired *t*-test, $*p < 0.5$.

plugin COLOC2. The significance level was $P < 0.05$ for all treatments.

RESULTS

c-Abl Is Located in Neurites and Its Absence Increases Spine Density

First, in order to examine the role of c-Abl in the synapse, we analyzed its protein levels over time. During culture maturation, the post-synaptic scaffold protein SAP102 and the post-synaptic density protein-95 (PSD95), continuously increase their protein levels. Meanwhile, c-Abl displays the highest protein levels during neurite extension at 4 DIV and at full culture maturation at 20 DIV (**Figure 1A**). At 7 DIV c-Abl is found mainly located at the soma, while at 15 DIV c-Abl is broadly distributed, not only in the soma, but it also has a punctate shape in all neuronal processes (**Figure 1B**). As shown by Pearson's correlation (**Figure 1C**), c-Abl localizes in the post-synaptic compartment, where it co-localizes with PSD95.

To investigate whether c-Abl could be regulating dendritic spine density, we studied spine morphology in cultured c-Abl knock-out (c-Abl-KO) hippocampal neurons transfected with GFP expression plasmids at 18 DIV to label whole single neurons (**Figure 2A**). One day later, we counted their dendritic spine population in secondary branches. Interestingly, we found that c-Abl deficiency increases dendritic spine density. c-Abl-KO neurons showed an enriched spine density with 4.22 ± 0.25 spines/10 μm dendrite (**Figure 2B**), in comparison with WT neurons that showed 3.36 ± 0.20 spines/10 μm dendrite. Therefore, c-Abl-KO neurons display a 25.6% dendritic spine increase in their spine density (**Figure 2B**).

Dendritic Spine Loss Induced by AβOs Is Independent of c-Abl

Exposure to AβOs significantly decreases dendritic spine density in neurons. Using a synthetic $A\beta_{1-42}$ human peptide (see "Materials and Methods" section), we prepared an overnight solution of AβOs characterized by the presence of dimers and trimers (**Supplementary Figure S2**). These soluble species of the peptide have been previously described as the most toxic species of AβOs that bind to the synapse of hippocampal neurons (Tu et al., 2014; Mi et al., 2017). Previously, we described that AβOs induce c-Abl activation participating in the loss of synapses (Vargas et al., 2014). Moreover, the binding of FITC-labeled AβOs to dendrites activates c-Abl (p-c-Abl; **Figure 1E**, **Supplementary Figure S3**). Thus, we treated hippocampal neurons with AβOs and observed a quick increase (at 1 h) in c-Abl phosphorylation that remains active 5 h after treatment with AβOs. This increase in active c-Abl was also associated with a later increase in both Abl1 mRNA and c-Abl protein levels from 3 h post-AβOs incubation (**Figures 1D–F**). Fibrillary forms of the Aβ-peptide (Aβf) also increased c-Abl protein levels by 3 h incubation and were used as a control.

Then, we asked whether c-Abl ablation modulates AβOs-induced synapsis loss. GFP-expressing WT and c-Abl-KO hippocampal neurons were exposed to AβOs and after 5 h treatment, the number of dendritic spines was evaluated. Primary dendrites were the least affected by the AβOs treatment, while tertiary and far-away branches were the most affected, and even disrupted by AβOs. Therefore, we quantified dendritic spines in secondary branches. WT neurons showed reduced spine density after AβOs treatment (3.36 ± 0.20 vs. 2.45 ± 0.15 spines/10 μm dendrite), representing 27% spine loss. As well as WT neurons, c-Abl-KO neurons displayed a significant reduction over spine density (4.22 ± 0.22 vs. 3.19 ± 0.15 spines/10 μm dendrite), representing a 24.3% spine loss (**Figure 2B**, **Supplementary Figure S4C**). Thus, AβOs treatment induced a decrease in the number of dendritic spines in both, WT and c-Abl-KO neurons. Since we found only a 3% difference in dendritic spine density between c-Abl-KO and WT neurons treated with AβOs, suggesting that AβOs-driven spine loss seems to be independent of c-Abl.

AβOs-Induced Immature Spines Are Influenced by the Presence of c-Abl

Then, we evaluated spine morphology by analyzing the dendritic spines shape profile following five major categories: mushroom, stubby, branched, thin and filopodia spines. Mature spines are mushroom, big spines in which the head is wider than the neck. Intermediate states are stubby, smaller and neckless spines. Branched spines are two-headed spines. Finally, immature spines are thin protrusions shorter than 2 μm length; and filopodium, in which protrusions are longer than 2 μm length (Tyler and Pozzo-Miller, 2003).

To distinguish between different types of spine morphology, we measure head, length, and neck of dendritic spines in GFP-expressing neurons (**Figures 3A–D**), and quantified the number of each spine type in a 10 μm dendrite section. We found a tendency for c-Abl-KO neurons to display more mushroom, branched and filopodia spines than WT neurons per 10 μm dendrite, however non-significant (**Figure 3B**). This trend towards increasing some spine types correlated with the augmented spine density observed before (**Figure 2B**). Since both, the neuron genotype and the binding of AβOs alter the number of dendritic spines, we normalized to the total population of dendritic spines within each dendrite analyzed. Then, we found that c-Abl deficiency alters the distribution of the spine population.

When we analyzed the head diameter of dendritic spines, we found that c-Abl-KO spines had wider heads compared to WT (0.46 ± 0.01 μm vs. 0.42 ± 0.01 μm in average head diameter, respectively; **Supplementary Figure S4A**), which correlates with an increased number of mushroom spines. Interestingly, we also found that c-Abl-KO spines were slender than WT spines, with a total length increase for longer filopodia and thin spines (**Figure 3D**) and an increment of the overall spine length (WT: 0.79 ± 0.04 and KO: 0.98 ± 0.05 μm spine length; **Supplementary Figure S4B**), probably due to the increase in thin population.

As expected, when AβOs were added to the medium, the most mature, mushroom spines were significantly affected by AβOs treatment. As the spine profile shows, mushroom decreased 42% by AβOs in WT, but also decreased 37% in c-Abl-KO

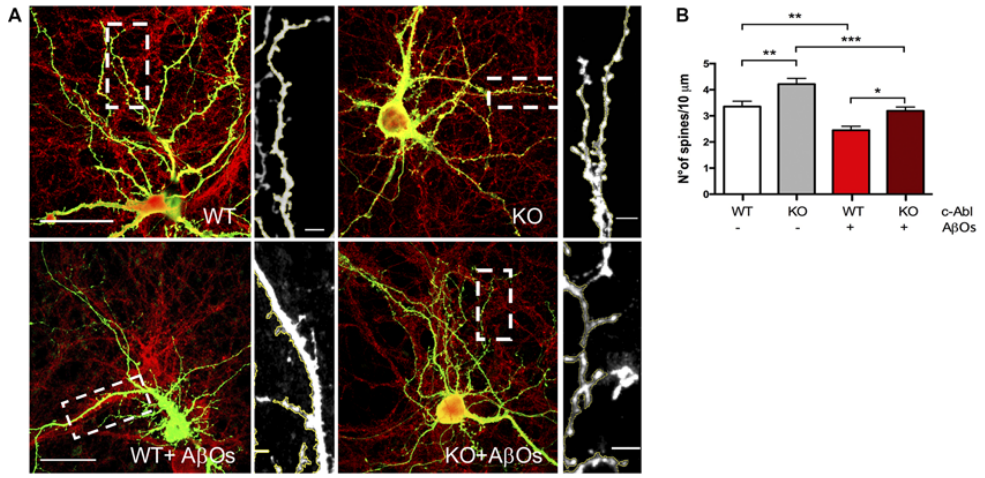

FIGURE 2 | Aβ oligomer-induced dendritic spine density decrease is independent of c-Abl. **(A)** GFP-transfected wild-type (WT) and c-Abl-KO neurons were treated with Aβ oligomers (AβOs) for 5 h, and dendritic spines were counted (PSD95 is shown in red). The sections of secondary dendrites (rectangle) were delimited to show dendritic spine morphology. Complete image scale bar = 20 μm, magnifications scale bar = 2 μm. **(B)** Quantification of spine density (number of spines/10 μm dendrite) shows that c-Abl-KO neurons show higher spine density (4.22 ± 0.22 spines/10 mm dendrite) than WT neurons (3.36 ± 0.20 spines/10 mm dendrite). On the other hand, AβOs treatment significantly reduces spine density in both, WT and c-Abl-KO neurons (2.45 ± 0.15 and 3.19 ± 0.15 spines/10 mm, respectively; $n = 47$ WT; $n = 49$ WT+AβOs; $n = 49$ KO, and $n = 53$ dendrites for KO+AβOs). Two-way ANOVA and Tukey's multiple comparisons. $^{*}p < 0.5$; $^{**}p < 0.01$; $^{***}p < 0.001$. $n = 3$ independent cultures, 4–5 mice embryos per condition.

neurons. Stubby spines were also significantly affected by AβOs treatment with a 7.2% less in WT neurons, while they tend to 6.5% augment in KO neurons (**Figure 3C**). Interestingly, the histogram of dendritic spines changed mushroom, stubby, thin and filopodia in WT vs. WT-treated neurons, while the overall pattern was similar for KO vs. KO-treated neurons. Interestingly, c-Abl deficiency increased the relative abundance of immature spines and maintained the mushroom and stubby population (**Figure 3C**). We observed a slight increase in the relative abundance of thin and filopodia spines in c-Abl-KO neurons when they were treated with AβOs (thin: 41% vs. 43.4%, and filopodium: 13.3% vs. 11.6% WT+AβOs vs. KO+AβOs, respectively; **Figure 3C**). Interestingly, the spine profile of WT-treated neurons displays a significant increase for filopodia spines (54.9% increase) as they are usually found within 10 μm dendrite (WT: 0.04 ± 0.01 vs. WT+ AβOs: 0.07 ± 0.02 spines/10 μm dendrite), in correlation with the lengthening of dendritic spines (WT: 0.79 ± 0.04 μm vs. WT+AβOs: 1.03 ± 0.07 μm length; **Supplementary Figure S4B**). Finally, branched spines were non-significantly affected by AβOs in both WT and c-Abl-KO neurons. These results suggest that AβOs-induced an overall decrease in the dendritic spine population of WT and c-Abl-KO neurons, but the effect becomes attenuated in the immature spine population of c-Abl-KO neurons. Whereas these immature spines, thin and filopodia together comprise 55% of the total spine population in c-Abl-KO treated neurons, they represent 54% in WT control-treated neurons. In the same line, the abundance of mature mushroom spines represents almost 7% of the overall population for WT, while 8% for c-Abl-KO dendritic spines after AβOs incubation (**Figure 3C**). The same as controls, spine head diameter of WT and c-Abl-KO neurons exposed to AβOs was very similar (WT+AβOs: 0.40 ± 0.02 μm and KO+AβOs: 0.37 ± 0.01 μm average spine head diameter), and no changes were evident between them. However, spine head diameter was significantly reduced in c-Abl-KO neurons exposed to AβOs compared with basal levels (**Supplementary Figure S4A**), in agreement with the significant reduction of mushroom spines.

Therefore, in the absence of c-Abl, treatment with AβOs enriches the immature dendritic spine population and preserves mushroom and stubby population maintaining the overall spine density, which suggests that this may be a possible mechanism for synaptic resiliency against AβOs.

c-Abl Participates in the Reduction of Synaptic Clustering Induced by AβOs

In AD mice models and AD patients, AβOs induce synapse loss, decreasing levels of pre- and post-synaptic proteins and reducing the number of synaptic contacts (Sze et al., 1997; Masliah et al., 2001; Reddy et al., 2005; Calabrese et al., 2007). Therefore, we next evaluated the effect of c-Abl deficiency on AβOs synapse alteration. We examined synaptic contacts in c-Abl null hippocampal neurons after AβOs treatment by following PSD95 and Piccolo clustering (post-synaptic and pre-synaptic proteins, respectively).

c-Abl-KO neurons display increased numbers of Piccolo clusters in basal conditions in comparison to WTs. Interestingly, AβOs significantly reduced Piccolo clustering in WT neurons (3.82 ± 0.17 clusters/10 μm dendrite). While the number of Piccolo clusters in c-Abl-KO-treated neurons was very similar to its controls and significantly different from WT-treated neurons. Therefore, indicating maintenance of the pre-synaptic terminal (6.41 ± 0.19 clusters/10 μm dendrite; **Figures 4A,B**). Opposite

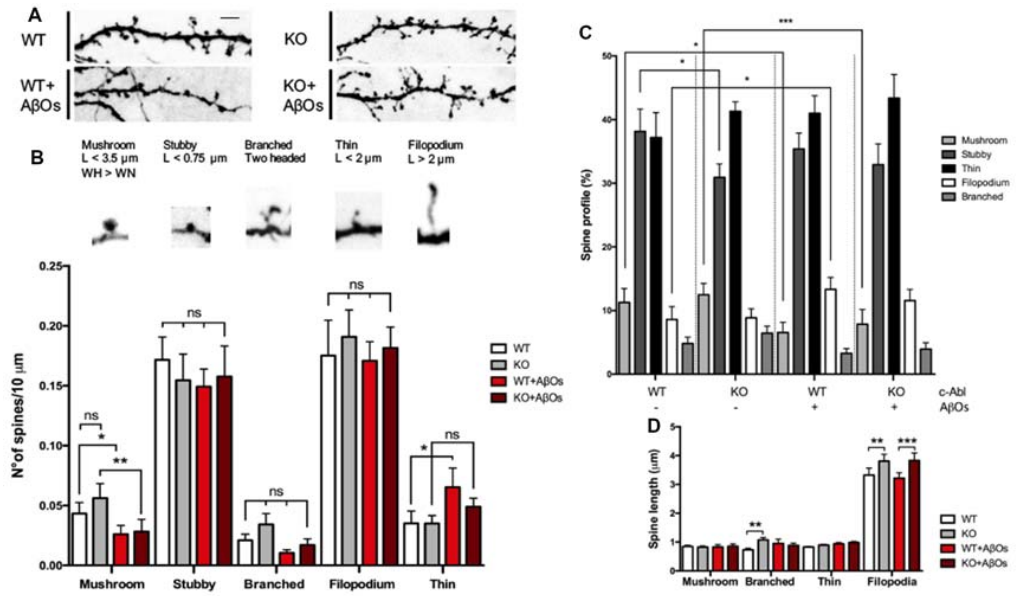

FIGURE 3 | c-Abl modulates dendritic spine morphology: c-Abl deficiency increased formation of immature spines after Aβ oligomers treatment. **(A)** Dendrite sections of WT and c-Abl-KO neurons treated with AβOs present morphological variations on dendritic spines. Scale bar = 2 μm. Dendritic spines were classified into five categories: mushroom when the head (H) is wider (W) than the width of the neck (WN); stubby for neckless protrusions less than 0.75 μm length (L); thin for protrusions shorter than 2 μm; filopodium for protrusions longer than 2 μm. Finally, two-headed spines were classified as branched. **(B)** Analysis of spines suggests their distribution per 10 μm dendrite. Control WT and c-Abl-KO neurons have significantly more mushroom than treated neurons (WT: 0.04 ± 0.01 vs. KO: 0.06 ± 0.01 spines/10 μm dendrite), slightly decreased stubby (WT: 0.17 ± 0.02 vs. KO: 0.15 ± 0.02 spines/10 μm dendrite), slightly increased thin (WT: 0.18 ± 0.03 vs. KO: 0.19 ± 0.02 spines/10 μm dendrite) and filopodium (WT: 0.04 ± 0.01 vs. KO: 0.04 ± 0.01 spines/10 μm dendrite) and slightly increased branched spines per dendrite (WT: 0.02 ± 0.01 vs. KO: 0.03 ± 0.01 spines/10 μm dendrite). After AβOs treatment, both, WT and c-Abl-KO neurons showed a significant reduction in the density of mushroom (WT: 0.03 ± 0.01 and KO: 0.03 ± 0.01 spines/10 μm dendrite) and stubby spines (WT: 0.15 ± 0.01 and KO: 0.16 ± 0.03 spines/10 μm). After AβOs treatment WT neurons presented higher density of filopodia spines than c-Abl-KO neurons (0.07 ± 0.02 vs. 0.05 ± 0.01 spines/10 μm dendrite, respectively) and maintenance of thin spines (0.17 ± 0.02 vs. 0.18 ± 0.02 spines/10 μm dendrite). Branched spines showed no changes after AβOs treatment (WT: 0.01 ± 0.002 vs. KO: 0.02 ± 0.01 spines/10 μm dendrite). **(C)** Spine type relative profile [percentage of each spine type classified in **(B)** counting 2–5 dendrites per neuron]. In WT and c-Abl-KO neurons, the population of thin spines increases (WT: 37.2 ± 2.8% n = 14 neurons; KO: 41.3 ± 1.5% n = 15 neurons; WT+AβOs: 41 ± 3.9% n = 13 neurons; KO+AβOs: 43.4 ± 1.7%, n = 18 neurons) and mushroom spines decreases after AβOs treatment (WT: 11.3 ± 2.2%; KO: 12.5 ± 1.8%; WT+AβOs: 6.6 ± 1.6%; KO+AβOs: 7.9 ± 2.3%); while filopodia spines increased (WT: 8.6 ± 2%; KO: 8.9 ± 1.4%; WT+AβOs: 13.3 ± 1.9%; KO+AβOs: 11.6 ± 1.9%); Stubby (WT: 38.1 ± 3.5%; KO: 30.9 ± 2.1%; WT+AβOs: 35.4 ± 2.5%; KO+AβOs: 32.9 ± 3.3%); and branched (WT: 4.8 ± 1.0%; KO: 6.5 ± 1.1%; WT+AβOs: 3.3 ± 0.8%; KO+AβOs: 3.9 ± 1.0%). **(D)** The graph shows spine length for mushroom, branched, thin and filopodia spines. AβOs induced longer filopodia spines (WT+AβOs: 3.22 ± 0.19 μm, KO: 3.83 ± 0.26 μm). Two-way ANOVA, $^{***}p < 0.001$. n = 3 independent cultures, 4–5 mice embryos per condition. non-significant: ns; $^{*}p < 0.5$; $^{**}p < 0.01$.

results were obtained for PSD95, as c-Abl deficiency did not perturb the basal number of PSD95 synaptic clustering (WT: 5.72 ± 0.18 and KO: 5.27 ± 0.24 clusters/10 μm dendrite; **Figures 4A,C**). However, we observed a strong reduction in PSD95 clusters after WT neurons were treated with AβOs (WT+AβOs: 3.91 ± 0.14 clusters/10 μm dendrite) whereas, c-Abl-KO neurons treated with AβOs display less reduction in PSD95 clusters (KO+AβOs: 4.38 ± 0.15 clusters/10 μm dendrite; **Figures 4A,C**). However, we did not find significant differences between WT and KO-treated neurons.

On the other hand, WT neurons showed a significant reduction in PSD95/Piccolo clusters when incubated with AβOs whereas the c-Abl-KO neurons did not show synaptic loss (2.53 ± 0.2 and 4.15 ± 0.27 clusters/10 μm dendrite, respectively; **Figure 4D**). Colocalization analysis by Mander's and Pearson's correlation also showed decreased correlation for WT-treated neurons while c-Abl-KO neurons were non-significantly affected, which means protection of synaptic clustering in correlation with synaptic contact quantification (**Supplementary Figures S5A,B**). Our results strongly suggest that c-Abl deficiency protects the synapse.

c-Abl Deficiency Protects Against AβOs-Induced Cell Death

Since AβOs-induced synaptotoxicity is linked to neuronal cell death (Yang et al., 2009), and c-Abl inhibition by Imatinib prevents AβOs-induced apoptosis (Cancino et al., 2008), we asked whether c-Abl could be responsible for apoptosis. Therefore, we quantified apoptotic nuclei using Hoechst staining (**Figures 5A,C**) and caspase-3 immuno-labeling (**Figures 5B,D**), in WT and c-Abl-KO neurons after a 5 h treatment with AβOs. As expected, in WT neurons, AβOs induced a significant increase in apoptotic nuclei (18.2 ± 4.8% control vs. 49.7 ± 4.1% AβOs-treated neurons) and in the number of caspase-3 positive cells (30.7 ± 7.2% control vs. 54.7 ± 6.5% AβOs-treated neurons). While c-Abl deficiency significantly decreased

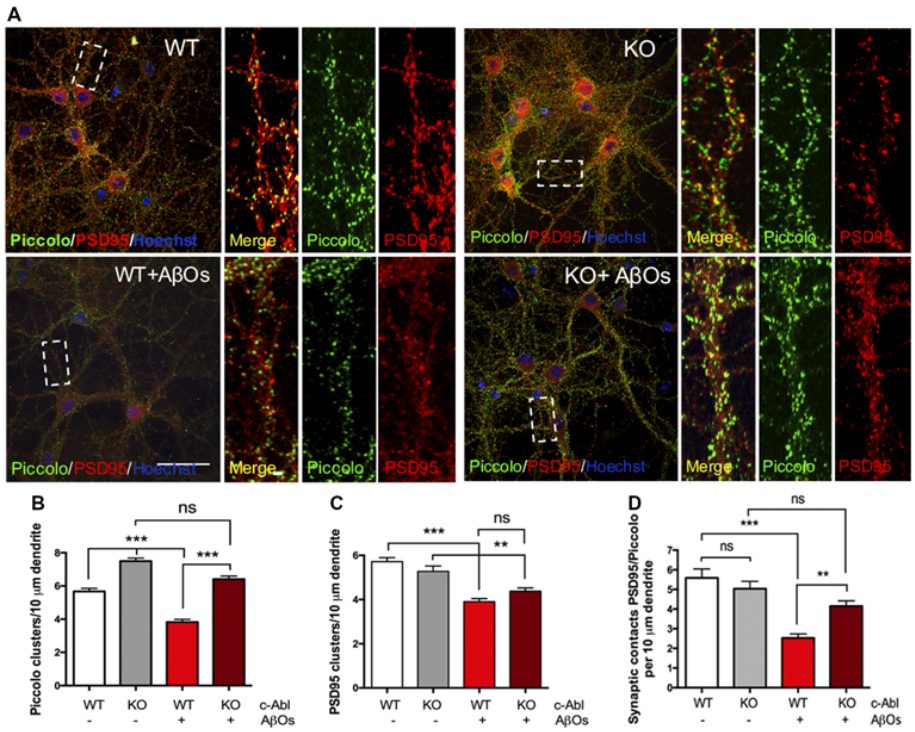

FIGURE 4 | c-Abl deficiency protects Piccolo/PSD95 synaptic clustering against Aβ oligomers. **(A)** Representative example of WT and c-Abl-KO neurons stained for the pre-synaptic marker Piccolo (green) and for the post-synaptic markers PSD95 (red). **(B)** AβOs treatment does not affect the clustering of Piccolo in c-Abl-KO neurons compared with WT-treated neurons (WT: 5.67 ± 0.19 vs. WT+AβOs: 3.82 ± 0.17 clusters/10 μm dendrite, and KO: 7.45 ± 0.18 vs. KO+AβOs: 6.41 ± 0.19 clusters/10 μm dendrite; WT: $n = 75$, WT+AβOs: $n = 81$, KO: $n = 57$ and KO+AβOs: $n = 85$ dendrites; **C**). AβOs induce a significant reduction of PSD95 protein clustering in WT neurons. However, not significant reduction in the number of PSD95 clusters as observed in c-Abl-KO neurons (WT: 5.72 ± 0.18 vs. WT+AβOs: 3.91 ± 0.14 clusters/10 μm dendrite, and KO: 5.27 ± 0.24 vs. KO+AβOs: 4.38 ± 0.15 clusters/10 μm dendrite; WT: $n = 83$, WT+AβOs: $n = 86$, KO: $n = 63$ and KO+AβOs: $n = 85$ dendrites). **(D)** AβOs-induced reduction of synaptic contacts between PSD95 and Piccolo affects WT neurons (WT: 5.59 ± 0.46 vs. WT+AβOs: 2.53 ± 0.2 contacts/10 μm dendrite), while c-Abl-KO neurons maintained intact synaptic contacts (KO: 5.04 ± 0.37 vs. KO+AβOs: 4.15 ± 0.27 contacts/10 μm dendrite; WT: $n = 23$, WT+AβOs: $n = 33$, KO: $n = 33$ and KO+AβOs: $n = 24$ neurons). Two-way ANOVA and Tukey's multiple comparison test, $^{***}p < 0.001$. Scale bar = 20 μm and 2 μm for dendrite magnifications. non-significant: ns; $^{**}p < 0.01$.

AβOs-induced apoptosis followed by apoptotic nuclei (16 ± 3.4% control vs. 31 ± 4.9% AβOs-treated neurons) and active caspase-3 positive cells (12 ± 4.1% control vs. 22.9 ± 7.1% AβOs-treated neurons; **Figures 5C,D**). Therefore, c-Abl deficiency protects against AβOs-induced cell death.

We also analyzed the effect of AβOs over synaptic protein removal by following PSD95 and Piccolo clusters in apoptotic and non-apoptotic WT and c-Abl-KO neurons. As before, we counted the number of clusters per 10 μm dendrite and found a strong and robust reduction of Piccolo clusters in WT neurons under AβOs, both in apoptotic and non-apoptotic neurons (**Figure 5E**; non-apoptotic WT: 6.52 ± 0.18 vs. WT+AβOs: 4.36 ± 0.21 clusters/10 μm dendrite). Interestingly, the number of Piccolo clusters in c-Abl-KO neurons were maintained after AβOs treatment. Regardless of whether we examined apoptotic or non-apoptotic c-Abl-KO neurons, there was no significant difference with their controls (non-apoptotic KO: 8.19 ± 0.19 vs. KO+AβOs: 7.1 ± 0.24 clusters/10 μm dendrite). Although apoptotic neurons showed fewer Piccolo clusters than non-apoptotic neurons, after AβOs treatment all of them display a loss of Piccolo. In spite of AβOs treatment, c-Abl-KO neurons showed significantly more clusters than WT neurons in both apoptotic and non-apoptotic cells.

However, the effects of c-Abl deficiency and apoptosis on PSD95 clusters reduction induced by AβOs are less clear (**Figure 5F**). First, there are fewer PSD95 clusters under basal conditions in apoptotic cells compared to non-apoptotic neurons. Additionally, non-apoptotic c-Abl-KO neurons showed reduced PSD95 cluster numbers in comparison with WT under basal conditions (WT: 6.76 ± 0.17 vs. KO: 5.7 ± 0.33 clusters/10 μm dendrite). However, when treated with AβOs, both WT and c-Abl-KO non-apoptotic neurons showed fewer PSD95 clusters, with no significant differences between them (WT+AβOs: 4.29 ± 0.17 vs. KO+AβOs: 4.66 ± 0.22 clusters/10 μm dendrite). Interestingly, c-Abl-KO apoptotic neurons did not show a further reduction in PSD95 clusters in comparison with WT neurons (apoptotic KO+AβOs: 4.11 ± 0.19 clusters/10 μm dendrite).

Our results suggest that AβOs-induced Piccolo clustering reduction is significantly prevented in c-Abl-KO apoptotic and non-apoptotic neurons in comparison with WTs. On the other

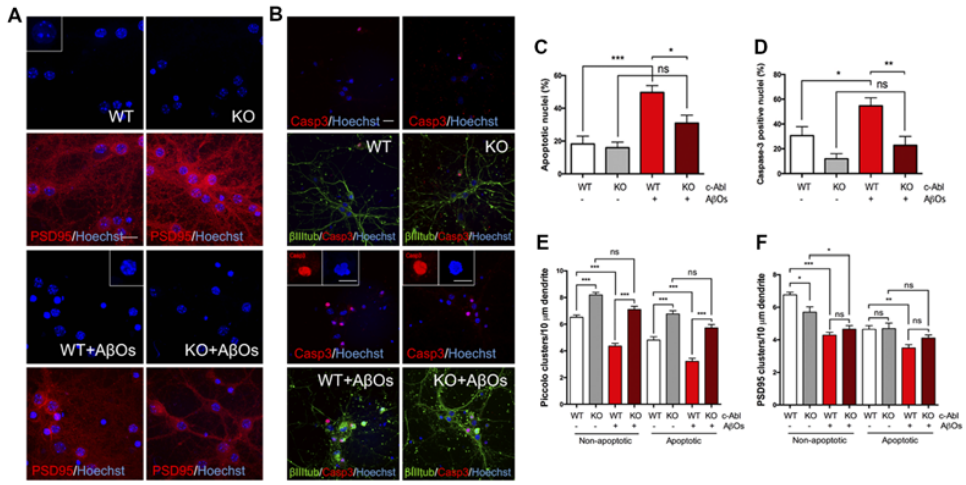

FIGURE 5 | c-Abl ablation protects against Aβ oligomers-induced cell death and preserves Piccolo clusters in apoptotic and non-apoptotic neurons. **(A,B)** WT and c-Abl-KO neurons were treated with 5 μM AβOs for 5 h and Hoechst stained to label apoptotic nuclei (blue; PSD95 in red) **(A)**; and co-stained with active caspase-3 (red) antibody to confirm apoptosis; cytoskeletal protein β-tubulin is shown in green **(B)**. Graphs show the percentage of apoptotic nuclei **(C)** and the percentage of active caspase-3 nuclei **(D)** for each condition. **(E–F)** WT and c-Abl-KO neurons were classified into apoptotic vs. non-apoptotic neurons and analyzed for Piccolo **(E)** and PSD95 **(F)** cluster quantification per 10 μm dendrite. Both were significantly affected in non-apoptotic neurons, especially in WT neurons. While c-Abl-KO neurons display higher number of Piccolo clusters and were significantly preserved after AβOs treatment (WT: 6.52 ± 0.18 vs. WT+AβOs: 4.36 ± 0.21 clusters/10 μm dendrite, and KO: 8.19 ± 0.19 vs. KO+AβOs: 7.1 ± 0.24 clusters/10 μm dendrite; WT: n = 38, WT+AβOs: n = 43, KO: n = 29 and KO+AβOs: n = 42 dendrites). Apoptotic neurons displayed the same tendency for Piccolo clusters (WT: 4.81 ± 0.26 vs. WT+AβOs: 3.22 ± 0.23 clusters/10 μm dendrite, and KO: 6.77 ± 0.23 vs. KO+AβOs: 5.73 ± 0.25 clusters/10 μm dendrite; WT: n = 37, WT+AβOs: n = 38, KO: n = 29 and KO+AβOs: n = 42 dendrites). **(F)** PSD95 clusters strongly decreased in WT compared with c-Abl-KO non-apoptotic neurons while all conditions in apoptosis display significantly less clusters than healthy conditions (Non-apoptotic: WT: 6.76 ± 0.17 vs. WT+AβOs: 4.29 ± 0.17 clusters/10 μm dendrite, and KO: 5.7 ± 0.33 vs. KO+AβOs: 4.66 ± 0.22 clusters/10 μm dendrite; WT: n = 42, WT+AβOs: n = 44, KO: n = 36 and KO+AβOs: n = 42 dendrites; Apoptotic: WT: 4.65 ± 0.22 vs. WT+AβOs: 3.5 ± 0.21 clusters/10 μm dendrite, and KO: 4.69 ± 0.34 vs. KO+AβOs: 4.11 ± 0.19 clusters/10 μm dendrite; WT: n = 41, WT+AβOs: n = 42, KO: n = 27 and KO+AβOs: n = 43 dendrites; non-apoptotic: WT: n = 9, WT+AβOs: n = 10, KO: n = 7 and KO+AβOs: n = 9 neurons; apoptotic: WT: n = 9, WT+AβOs: n = 11, KO: n = 6 and KO+AβOs: n = 9 neurons). Two-way ANOVA and Tukey's multiple comparison test, ***$p < 0.001$. Scale bar = 20 μm and 10 μm for magnifications. n = 2 independent cultures, 3–4 mice embryos per condition. ns: non-significant; *$p < 0.5$; **$p < 0.01$; ***$p < 0.001$.

hand, PSD95 clusters are strongly affected by the apoptotic state of neurons derived from AβOs.

Finally, our results suggest that c-Abl mediates the signaling pathway triggered by AβOs that induces synaptic elimination and neuronal death, and could, therefore, be a relevant player in the early onset of AD.

DISCUSSION

Dendritic spines are specialized structures that protrude from dendrites and are the morphological correlate of excitatory synapses (Rochefort and Konnerth, 2012; Maiti et al., 2015). These structures receive and integrate information. They contain the post-synaptic machinery and signaling molecules for the propagation of signals sent out by pre-synaptic terminals and for the modulation of synaptic plasticity. Alterations in synaptic plasticity are common in neurodegenerative diseases such as the early stages of AD (Knobloch and Mansuy, 2008; Shankar et al., 2008). In AD, the decrease in synaptic density, caused mainly by oligomeric forms of the amyloid β-peptide (AβOs), shows the strongest correlation with the progression of dementia (Hardy and Selkoe, 2002; Almeida et al., 2005; Calabrese et al., 2007; Haass and Selkoe, 2007; Lacor et al., 2007; Selkoe, 2008; Ferreira and Klein, 2011; Tu et al., 2014).

As previously shown, we observed that AβOs bind to dendritic spines and induce c-Abl activation. Also, we found that *Abl1* mRNA and c-Abl protein levels increase when neurons are exposed to AβOs, just like with Aβ fibrils incubation (**Figures 1D–F**). Although pharmacological inhibition of c-Abl with Imatinib prevents the loss of dendritic spines induced by AβOs (Vargas et al., 2014), this inhibitor also has other targets such as Arg, c-kit, PDGFR and Src (Greuber et al., 2013; Lin and Roux, 2013). In order to dissect the contribution of c-Abl to the synaptic damage triggered by AβOs, we analyzed c-Abl null neurons. Here, we found that they exhibit increased dendritic spine density under basal conditions compared with WT neurons (**Figure 2**). This result is probably due to the effect that the absence of c-Abl has on the actin cytoskeleton. The C-terminal region of c-Abl directly interacts with the cytoskeleton through its G- and F-actin binding domains. c-Abl transduces several extracellular signals from tyrosine kinase receptors, promoting cytoskeleton reorganization (Jones et al., 2004; Bradley and Koleske, 2009) through the activation of GTPases like Rac1 and RhoA (Tashiro et al., 2000; Zandy et al., 2007), and the phosphorylation of the members of the WASP and WAVE2 protein families such as Abi (Takenawa and Suetsugu, 2007; Wang, 2014). Additionally, we have to consider compensatory

gene effects in KO models, especially from the Arg protein (Abl1-related protein).

Results on c-Abl chemical inhibition and knockdown experiments indicate that the deficiency of this kinase protects the synapse against AβOs-damage. Indeed, c-Abl-knockdown neurons (transfected with an shRNA against c-Abl), treated with AβOs, display a slightly larger number of spines per micrometer than control neurons (Vargas et al., 2014). However, as we see in **Figure 2**, the dendritic spine density of c-Abl-KO and WT neurons was similarly affected by AβOs damage, even though KO neurons display more dendritic spines at basal levels. c-Abl-KO neurons were highly sensitive to AβOs, showing decreased spine density after exposure to AβOs. However, we have to consider the participation of Arg (Abl2) as a compensatory effect over the dendritic population. Therefore, AβOs-driven spine loss seems to be independent of c-Abl.

We evaluated spine morphology to explore if c-Abl deficiency exerts an effect in the presence of different types of spines driven by AβOs. As we mentioned earlier, c-Abl null neurons have more dendritic spines, including a slight increase in mushroom spines (**Figures 3B,C**), which are considered the most mature state of dendritic spines. This type of spine has a consolidated post-synaptic density, enriched in receptors and scaffolding proteins (Harris and Weinberg, 2012; Colgan and Yasuda, 2014). The increased presence of these proteins correlates with the enlarged spine heads present in the dendritic spines of c-Abl null neurons (**Supplementary Figure S4A**). Different spine shapes are a reflection of their state of maturation from the initial establishment of a dynamic synaptic contact represented by a filopodia type spine, to more mature synapses represented by mushroom spines (Harris and Kater, 1994; Fiala et al., 1998; Harris, 1999; Hayashi and Majwska, 2005; Alvarez and Sabatini, 2007). This categorization might seem rigid, but analyses of live-cell imaging show that spines are highly dynamic and may vary between thin and mushroom morphologies in timeframes that can extend from minutes to hours (Fischer et al., 1998). In response to AβOs treatment, WT neurons showed an overall decrease in the dendritic spine population. As previously described by Klein's group, AβOs treatment induces filopodia formation (Lacor et al., 2007). We observed a significant difference for the remaining dendritic spine population to include more immature thin and filopodia spines and a shift towards these immature spines in WT neurons. Interestingly, this trend was also observed in AβOs-treated c-Abl-KO neurons. The mushroom population was highly compromised, in correspondence with overall decreased spine head widening and increased spine lengthening. However, the mushroom spine population was still higher than in WT neurons. The number of thin and filopodia spines slightly increased while stable stubby shaped spines were preserved (**Figure 3B**). Therefore, we hypothesize that the absence of c-Abl specifically protects the transient and highly dynamic spine population against AβOs, promoting the development of dendritic spines. This might underlie the resilience against AβOs damage showed by c-Abl-KO neurons.

However, some specific roles have been linked to c-Abl in the synapse (Vargas et al., 2018). As shown here and by others, c-Abl is located in the synapse, and its levels increase by 20 DIV neurons (**Figure 1A**). Using immunoelectron microscopy, Koleske and collaborators found Arg and c-Abl in the contact area of pre-synaptic terminals, mostly in dendritic spines, but not in the dendritic shaft (Moresco and Koleske, 2003). c-Abl also modulates the post-synaptic scaffold protein PSD95 through phosphorylation of Y533 (Perez de Arce et al., 2010). Therefore, we were interested in studying synapse maturation in c-Abl-KO mice when neurons are treated with AβOs. As described by Klein's group (Lacor et al., 2007; Ferreira and Klein, 2011; Mi et al., 2017), WT neurons display a substantial reduction of PSD95 clustering when treated with AβOs while c-Abl-KO neurons display less reduction, even though the difference is non-significant between them. Interestingly, when we examined apoptotic and non-apoptotic neurons, the effect of AβOs-induced removal of PSD95 clusters was less clear. First, we found that c-Abl-KO non-apoptotic neurons show reduced PSD95 cluster numbers under basal conditions. Second, there are fewer PSD95 clusters under basal conditions in apoptotic cells compared to non-apoptotic neurons. Third, after AβOS treatment, both WT and c-Abl-KO non-apoptotic neurons show fewer PSD95 clusters. However, the differences are non-significant between these groups; this result is very similar to the one shown in **Figure 4C**. Interestingly, c-Abl-KO neurons showed no further decrease in PSD95 clusters compared to WT neurons after AβOs treatment. Perhaps, the absence of c-Abl prevents the removal of PSD95 associated with neuronal apoptosis, but it also leads to a decrease in basal PSD95 clustering (Perez de Arce et al., 2010), reducing the protective effect of c-Abl deficiency.

We analyzed the clusters of Piccolo, a pre-synaptic marker protein, that together with Bassoon, are scaffolding proteins of the active zone that maintain the clustering of vesicles at the nerve terminals (Gundelfinger et al., 2016). Surprisingly, c-Abl deficiency significantly contributed to the maintenance of the pre-synaptic protein Piccolo under AβOs treatment (**Figure 4B**). When we evaluated if the apoptotic state could affect Piccolo clustering, we found that Piccolo clusters were affected mostly by AβOs treatment in WT but not in c-Abl-KO neurons. Meaning that AβOs could induce the removal of pre-synaptic proteins like Piccolo independently of the apoptotic state of neurons and that apoptosis does not influence the protective effect promoted by c-Abl absence.

Our results on PSD95 clusters, and more clearly on Piccolo clusters, show that c-Abl deficiency prevents the loss of synapses induced by AβOs. Although the absence of c-Abl also prevents or delays apoptosis, it appears that part of the synaptic resilience seen in c-Abl-KO cells is independent of apoptosis.

In conclusion, our experiments suggest that the absence of c-Abl could stabilize Piccolo clusters while its presence could promote the removal of PSD95 clusters driven by AβOs.

We also analyzed the number of synaptic contacts (apposition between Piccolo and PSD95), and as expected, the number of synaptic contacts decreases in response to AβOs in WT neurons. However, the loss of synaptic contacts was prevented in c-Abl null neurons (**Figure 4D**). These results show that the reorganization of spine shapes towards immature populations

induced by AβOs correlates with a smaller decrease of synaptic contacts.

We have shown here two different processes controlled in two different ways by c-Abl. One of these processes is independent of c-Abl as AβOs affect dendritic spine loss in both c-Abl-KO and WT neurons. The other process is dependent on c-Abl presence since PSD95 clustering is maintained in c-Abl-KO neurons. These processes could be differentially regulated in time and space and therefore have an opposite relation with c-Abl. We propose that the local activation of the c-Abl kinase in dendritic spines can be a determinant in the propagation of AβOs-induced damage signaling. Moreover, spine signaling and morphological changes can transduce damage signals to the rest of the cell and finally induce cell death. For this reason, we evaluated cell death induced by AβOs and found that neuronal death induced by AβOs is decreased in c-Abl null neurons (**Figure 5**).

Interestingly, in AD patients, synaptic dysfunction starts early on and is followed by loss of the neuronal population in cognitive regions of the brain (DeKosky and Scheff, 1990). Although it has been observed that there is a significant decrease in the number of dendritic spines in post-mortem samples of AD brains, 30–50% of older individuals have Aβ-plaques and neurofibrillary tangles but do not develop clinical dementia. Such individuals seem to have cognitive resilience that protects them against AD dementia (Mucke et al., 2000; Driscoll and Troncoso, 2011; Boros et al., 2017). Analyses of Golgi-COX stained sections of their prefrontal cortex showed that these individuals display AD pathology without the associated dementia symptoms. Even though they do not present a decrease in dendritic spine density, they do display changes in spine morphology.

Moreover, the asymptomatic women group shows an increase in the density of dendritic spines when compared with non-AD controls. Regarding the predominant spine morphology in these patients, these are mainly thin and mushroom spines, not stubby spines (Driscoll and Troncoso, 2011; Boros et al., 2017). Thus, high spine plasticity could generate synaptic resiliency against Aβ-oligomers, as we see in c-Abl null neurons in this study.

Finally, the pharmacological inhibition and genetic ablation of c-Abl kinase provide neuron resilience against damage induced by AβOs. These findings strengthen the role of c-Abl in AD and suggest that synaptic changes associated with the deficiency of c-Abl contribute to the mechanisms involved in decreasing early AD pathology and the progression of cognitive decline.

DATA AVAILABILITY STATEMENT

The datasets (generated/analyzed) for this study can be found in the Figshare repository: Raw Data c-Abl deficiency provides synaptic resiliency against Abeta oligomers.xlsx; https://figshare.com/s/7f0ddf725ca86709240d.

ETHICS STATEMENT

All protocols were approved and followed local guidance documents generated by the *ad hoc* Chilean committee (CONICYT), and were approved by the Bioethics and Care of Laboratory Animals Committee of the Pontificia Universidad Católica de Chile (Protocol #150721002). We followed the recommendations of the Guide for Care and Use of Laboratory Animals from US Public Health Service.

AUTHOR CONTRIBUTIONS

DG, LV and AA designed all the experiments and DG carried out c-Abl-KO neuron experiments with and without AβOs. CF and AC-C performed western-blot and qPCR analysis. NL and DG prepared neuronal cultures of c-Abl^{floxo} mice. DG, LV and AC-C performed the formal analysis. DG, AC-C and AA participated in results, discussion and preparation of the first and final draft of the manuscript. All authors contributed to manuscript revision, read and approved the submitted version.

FUNDING

This work was supported by FONDECYT 1161065, CARE-Chile-UC AFB170005 and Fondo de Fomento al Desarrollo Científico y Tecnológico (FONDEF) D10E1077 to AA; Comisión Nacional de Ciencia y Tecnología (CONICYT) 21141157 to AC-C and UC Vicerrectoría de Investigación (VRI) to DG. The authors acknowledge the services provided by UC CINBIOT Animal Facility funded by PIA CONICYT ECM-07.

ACKNOWLEDGMENTS

We thank Dr. Viviana Torres for providing us with the Piccolo antibody we used in all experiments and the funding agencies of CONICYT. This work was supported by the Advanced Microscopy Facility UC.

SUPPLEMENTARY MATERIAL

The Supplementary Material for this article can be found online at: https://www.frontiersin.org/articles/10.3389/fncel.2019.00526/full#supplementary-material.

REFERENCES

Almeida, C. G., Tampellini, D., Takahashi, R. H., Greengard, P., Lin, M. T., Snyder, E. M., et al. (2005). β-amyloid accumulation in APP mutant neurons reduces PSD95 and GluR1 in synapses. *Neurobiol. Dis.* 20, 187–198. doi: 10.1016/j.nbd.2005.02.008

Alvarez, A. R., Sandoval, P. C., Leal, N. R., Castro, P. U., and Kosik, K. S. (2004). Activation of the neuronal c-Abl tyrosine kinase by amyloid-β-peptide and reactive oxygen species. *Neurobiol. Dis.* 17, 326–336. doi: 10.1016/j.nbd.2004.06.007

Alvarez, V. A., and Sabatini, B. L. (2007). Anatomical and physiological plasticity of dendritic spines. *Annu. Rev. Neurosci.* 30, 79–97. doi: 10.1146/annurev.neuro.30.051606.094222

Arimon, M., Díez-Pérez, I., Kogan, M., Durany, N., Giralt, E., Sanz, F., et al. (2005). Fine structure study of Aβ1–42 fibrillogenesis with atomic force microscopy. *FASEB J.* 19, 1344–1346. doi: 10.1096/fj.04-3137fje

Boros, B. D., Greathouse, K. M., Gentry, E. G., Curtis, K. A., Birchall, E. L., Gearing, M., et al. (2017). Dendritic spines provide cognitive resilience against Alzheimer's disease. *Ann. Neurol.* 82, 602–614. doi: 10.1002/ana.25049

Bradley, W. D., and Koleske, A. J. (2009). Regulation of cell migration and morphogenesis by Abl-family kinases: emerging mechanisms and physiological contexts. *J. Cell Sci.* 122, 3441–3454. doi: 10.1242/jcs.039859

Calabrese, B., Shankar, G. M., Tabarean, I. V., Braga, J., Koo, E. H., and Holpain, S. (2007). Rapid, concurrent alterations in pre- and post-synaptic structure induced by naturally-secreted amyloid-β protein. *Mol. Cell. Neurosci.* 35, 183–193. doi: 10.1016/j.mcn.2007.02.006

Cancino, G. I., Toledo, E. M., Leal, N. R., Hernandez, D. E., Yévenes, L. F., Inestrosa, N. C., et al. (2008). STI571 prevents apoptosis, tau phosphorylation and behavioural impairments induced by Alzheimer's β-amyloid deposits. *Brain* 131, 2425–2442. doi: 10.1093/brain/awn125

Cases-Langhoff, C., Voss, B., Garner, A. M., Appeltauer, U., Takei, K., Kindler, S., et al. (1996). Piccolo, a novel 420 kDa protein associated with the pre-synaptic cytomatrix. *Eur. J. Cell Biol.* 69, 214–223.

Clare, R., King, V. G., Wirenfeldt, M., and Vinters, H. V. (2010). Synapse loss in dementias. *J. Neurosci. Res.* 88, 2083–2090. doi: 10.1002/jnr.22392

Colgan, L. A., and Yasuda, R. (2014). Plasticity of dendritic spines: subcompartmentalization of signaling. *Annu. Rev. Physiol.* 76, 365–385. doi: 10.1146/annurev-physiol-021113-170400

Davies, C. A., Mann, D. M., Sumpter, P. Q., and Yates, P. O. (1987). A quantitative morphometric analysis of the neuronal and synaptic content of the frontal and temporal cortex in patients with Alzheimer's disease. *J. Neurol. Sci.* 78, 151–164. doi: 10.1016/0022-510x(87)90057-8

DeKosky, S. T., and Scheff, S. W. (1990). Synapse loss in frontal cortex biopsies in Alzheimer's disease: correlation with cognitive severity. *Ann. Neurol.* 27, 457–464. doi: 10.1002/ana.410270502

Driscoll, I., and Troncoso, J. (2011). Asymptomatic Alzheimer's disease: a prodrome or a state of resilience? *Curr. Alzheimer Res.* 8, 330–335. doi: 10.2174/156720511795745348

Fernandes, D., and Carvalho, A. L. (2016). Mechanisms of homeostatic plasticity in the excitatory synapse. *J. Neurochem.* 139, 9733–9996. doi: 10.1111/jnc.13687

Ferreira, S. T., and Klein, W. L. (2011). The Aβ oligomer hypothesis for synapse failure and memory loss in Alzheimer's disease. *Neurobiol. Learn. Mem.* 96, 529–543. doi: 10.1016/j.nlm.2011.08.003

Fiala, J. C., Feinberg, M., Popov, V., and Harris, K. M. (1998). Synaptogenesis *via* dendritic filopodia in developing hippocampal area CA1. *J. Neurosci.* 18, 8900–8911. doi: 10.1523/JNEUROSCI.18-21-08900.1998

Fischer, M., Kaech, S., Knutti, D., and Matus, A. (1998). Rapid actin-based plasticity in dendritic spines. *Neuron* 20, 847–854. doi: 10.1016/s0896-6273(00)80467-5

Fu, A. K., Hung, K. W., Huang, H., Gu, S., Shen, Y., Cheng, E. Y., et al. (2014). Blockade of EphA4 signaling ameliorates hippocampal synaptic dysfunctions in mouse models of Alzheimer's disease. *Proc. Natl. Acad. Sci. U S A* 111, 9959–9964. doi: 10.1073/pnas.1405803111

Gomez-Isla, T., Spires, T., De Calignon, A., and Hyman, B. T. (2008). Neuropathology of Alzheimer's disease. *Handb. Clin. Neurol.* 89, 233–243. doi: 10.1016/S0072-9752(07)01222-5

Gonzalez-Zuñiga, M., Contreras, P. S., Estrada, L. D., Chamorro, D., Villagra, A., Zanlungo, S., et al. (2014). c-Abl stabilizes HDAC2 levels by tyrosine phosphorylation repressing neuronal gene expression in Alzheimer's disease. *Mol. Cell* 56, 163–173. doi: 10.1016/j.molcel.2014.08.013

Greuber, E., Smith-Pearson, P., Wang, J., and Pendergast, A. M. (2013). Role of ABL family kinases in cancer: from leukaemia to solid tumours. *Nat. Rev.* 3, 559–571. doi: 10.1038/nrc3563

Gundelfinger, E. D., Reissner, C., and Garner, C. C. (2016). Role of Basson and Piccolo in assembly and molecular organization of the active zone. *Front. Synaptic Neurosci.* 7:19. doi: 10.3389/fnsyn.2015.00019

Haass, C., and Selkoe, D. J. (2007). Soluble protein oligomers in neurodegeneration: lessons from the Alzheimer's amyloid β-peptide. *Nat. Rev. Mol. Cell Biol.* 8, 101–12133. doi: 10.1038/nrm2101

Hardy, J., and Selkoe, D. J. (2002). The amyloid hypothesis of Alzheimer's disease: progress and problems on the road to therapeutics. *Science* 297, 353–356. doi: 10.1126/science.1072994

Harris, K. M. (1999). Structure, development, and plasticity of dendritic spines. *Curr. Opin. Neurobiol.* 9, 343–348. doi: 10.1016/s0959-4388(99)80050-6

Harris, K. M., and Kater, S. B. (1994). Dendritic spines: cellular specializations imparting both stability and flexibility to synaptic function. *Annu. Rev. Neurosci.* 17, 341–371. doi: 10.1146/annurev.ne.17.030194.002013

Harris, K. M., and Weinberg, R. J. (2012). Ultrastructure of the synapse in the mammalian brain. *Cold Spring Harb. Perspect. Biol.* 5:a005587. doi: 10.1101/cshperspect.a005587

Hayashi, Y., and Majwska, A. K. (2005). Dendritic spine geometry: functional implication and regulation. *Neuron* 46, 529–532. doi: 10.1016/j.neuron.2005.05.006

Henstridge, C. M., Sideris, D. I., Carroll, E., Rotariu, S., Salomonsson, S., Tzioras, M., et al. (2018). Synapse loss in the prefrontal cortex is associated with cognitive decline in amyotrophic lateral sclerosis. *Acta Neuropathol.* 135, 213–226. doi: 10.1007/s00401-017-1797-4

Jacobsen, J. S., Wu, C. C., Redwine, J. M., Comery, T. A., Arias, R., Bowlby, M., et al. (2006). Early-onset behavioural and synaptic deficits in a mouse model of Alzheimer's disease. *Proc. Natl. Acad. Sci. U S A* 103, 5161–5166. doi: 10.1073/pnas.0600948103

Jiang, Z., Kamath, R., Jin, S., Balasubramani, M., Pandita, T. K., and Rajasekaran, B. (2011). Tip60-mediated acetylation activates transcription independent apoptotic activity of Abl. *Mol. Cancer* 10:88. doi: 10.1186/1476-4598-10-88

Jing, Z., Caltagarone, J., and Bowser, R. (2009). Altered subcellular distribution of c-Abl in Alzheimer's disease. *J. Alzheimers Dis.* 17, 409–422. doi: 10.3233/JAD-2009-1062

Jones, S. B., Lu, H. Y., and Lu, Q. (2004). Abl tyrosine kinase promotes dendrogenesis by inducing actin cytoskeletal rearrangements in cooperation with Rho family small GTPases in hippocampal neurons. *J. Neurosci.* 24, 8510–8521. doi: 10.1523/JNEUROSCI.1264-04.2004

Kaech, S., and Banker, G. (2006). Culturing hippocampal neurons. *Nat. Protoc.* 1, 2406–2415. doi: 10.1038/nprot.2006.356

Kirvell, S. L., Esiri, M., and Francis, P. T. (2006). Down-regulation of vesicular glutamate transporters precedes cell loss and pathology in Alzheimer's disease. *J. Neurochem.* 98, 939–950. doi: 10.1111/j.1471-4159.2006.03935.x

Knobloch, M., and Mansuy, I. M. (2008). Dendritic spine loss and synaptic alterations in Alzheimer's disease. *Mol. Neurobiol.* 37, 73–82. doi: 10.1007/s12035-008-8018-z

Koleske, A. J., Gifford, A. M., Scott, M. L., Nee, M., Bronson, R. T., Miczek, K. A., et al. (1998). Essential role for Abl and Arg tyrosine kinases in neurulation. *Neuron* 21, 1259–1272. doi: 10.1016/s0896-6273(00)80646-7

Kommaddi, R. P., Das, D., Karunakaran, S., Nanguneri, S., Bapat, D., Ray, A., et al. (2018). Aβ mediates F-actin disassembly in dendritic spines leading to cognitive deficits in Alzheimer's disease. *Neurobiol. Dis.* 38, 1085–1099. doi: 10.1523/JNEUROSCI.2127-17.2017

Lacor, P. N., Buniel, M. C., Furlow, P. W., Clemente, A. S., Velasco, P. T., Wood, M., et al. (2007). Aβ oligomer-induced aberrations in synapse composition, shape, and density provide a molecular basis for loss of connectivity in Alzheimer's disease. *J. Neurosci.* 27, 796–807. doi: 10.1523/JNEUROSCI.3501-06.2007

Lambert, M. P., Barlow, A. K., Chromy, B. A., Edwards, C., Freed, R., Liosatos, M., et al. (1998). Diffusible, nonfibrillar ligands derived from Aβ1–42 are potent central nervous system neurotoxins. *Proc. Natl. Acad. Sci. U S A* 95, 6448–6453. doi: 10.1073/pnas.95.11.6448

Lin, Y. L., and Roux, B. (2013). Computational analysis of the binding specificity of Gleevec to Abl, c-Kit, Lck, and c-Src tyrosine kinases. *J. Am. Chem. Soc.* 135, 14741–14753. doi: 10.1021/ja405939x

Lin, Y. C., Yeckel, M. F., and Koleske, A. J. (2013). Abl2/Arg controls dendritic spine and dendrite arbor stability *via* distinct cytoskeletal control pathways. *J. Neurosci.* 33, 1846–1857. doi: 10.1523/JNEUROSCI.4284-12.2013

Maiti, P., Manna, J., Ilavazhagan, G., Rossignol, J., and Dunbar, G. (2015). Molecular regulation of dendritic spine dynamics and their potential impact on synaptic plasticity and neurological diseases. *Neurosci. Biobehav. Rev.* 59, 208–237. doi: 10.1016/j.neubiorev.2015.09.020

Masliah, E., Mallory, M., Alford, M., DeTeresa, R., Hansen, L. A., McKeel, D. W. Jr., et al. (2001). Altered expression of synaptic proteins

occurs early during progression of Alzheimer's disease. *Neurology* 56, 127–129. doi: 10.1212/wnl.56.1.127

Mendoza, M. C. (2013). Phosphoregulation of the WAVE regulatory complex and signal integration. *Semin. Cell Dev. Biol.* 24, 272–279. doi: 10.1016/j.semcdb.2013.01.007

Mi, Z., Abrahamson, E. E., Ryu, A. Y., Fish, K. N., Sweet, R. A., Mufson, E. J., et al. (2017). Loss of precuneus dendritic spines immunopositive for spinophilin is related to cognitive impairment in early Alzheimer's disease. *Neurobiol. Aging* 55, 159–166. doi: 10.1016/j.neurobiolaging.2017.01.022

Moolman, D. L., Vitolo, O. V., Vonsattel, J. P., and Shelanski, M. L. (2004). Dendrite and dendritic spine alterations in Alzheimer models. *J. Neurocytol.* 33, 377–387. doi: 10.1023/b:neur.0000044197.83514.64

Moresco, E. M., and Koleske, A. J. (2003). Regulation of neuronal morphogenesis and synaptic function by Abl kinases. *Curr. Opin. Neurobiol.* 13, 535–544. doi: 10.1016/j.conb.2003.08.002

Mucke, L., Masliah, E., Yu, G. Q., Mallory, M., Rockenstein, E., Tatsuno, G., et al. (2000). High-level neuronal expression of Aβ 1–42 in wild-type human amyloid protein precursor transgenic mice: synaptotoxicity without plaque formation. *J. Neurosci.* 20, 4050–4058. doi: 10.1523/JNEUROSCI.20-11-04050.2000

Perez de Arce, K., Varela-Nallar, L., Farias, O., Cifuentes, A., Bull, P., Couch, B. A., et al. (2010). Synaptic clustering of PSD-95 is regulated by c-Abl through tyrosine phosphorylation. *J. Neurosci.* 30, 3728–3738. doi: 10.1523/JNEUROSCI.2024-09.2010

Piochon, C., Kano, M., and Hansel, C. (2016). LTD-like molecular pathways in developmental synaptic pruning. *Nat. Neurosci.* 19, 1299–1310. doi: 10.1038/nn.4389

Qiu, Z., Cang, Y., and Goff, S. P. (2010). Abl family tyrosine kinases are essential for basement membrane integrity and cortical lamination in the cerebellum. *J. Neurosci.* 30, 14430–14439. doi: 10.1523/JNEUROSCI.2861-10.2010

Reddy, P. H., Mani, G., Park, B. S., Jacques, S., Murdoch, G., Whetsell, W. Jr., et al. (2005). Differential loss of synaptic proteins in Alzheimer's disease: implications for synaptic dysfunction. *J. Alzheimers Dis.* 7, 103–117. doi: 10.3233/jad-2005-7203

Riccomagno, M. M., and Kolodkin, A. L. (2015). Sculping neural circuits by axon and dendrite pruning. *Annu. Rev. Cell Dev. Biol.* 31, 779–805. doi: 10.1146/annurev-cellbio-100913-013038

Rochefort, N. L., and Konnerth, A. (2012). Dendritic spines: from structure to *in vivo* function. *EMBO Rep.* 13, 699–708. doi: 10.1038/embor.2012.102

Schlatterer, S. D., Acker, C. M., and Davies, P. (2011). c-Abl in neurodegenerative disease. *J. Mol. Neurosci.* 45, 445–452. doi: 10.1007/s12031-011-9588-1

Selkoe, D. J. (2008). Soluble oligomers of the amyloid β-protein impair synaptic plasticity and behaviour. *Behav. Brain Res.* 192, 106–113. doi: 10.1016/j.bbr.2008.02.016

Shankar, G. M., Li, S., Mehta, T. H., Garcia-Muñoz, A., Shepardson, N. E., Smith, I., et al. (2008). Amyloid-β protein dimers isolated directly from Alzheimer's brains impair synaptic plasticity and memory. *Nat. Med.* 14, 837–842. doi: 10.1038/nm1782

Sokolov, Y., Kozak, J. A., Kayed, R., Chanturiya, A., Glabe, C., and Hall, J. E. (2006). Soluble amyloid oligomers increase bilayer conductance by altering dielectric structure. *J. Gen. Physiol.* 128, 637–647. doi: 10.1085/jgp.200609533

Spires, T. L., Meyer-Luehmann, M., Stern, E. A., McLean, P. J., Skoch, J., Nguyen, P. T., et al. (2005). Dendritic spine abnormalities in amyloid precursor protein transgenic mice demonstrated by gene transfer and intravital multiphoton microscopy. *J. Neurosci.* 25, 7278–7287. doi: 10.1523/JNEUROSCI.1879-05.2005

Sze, C., Troncoso, J. C., Kawas, C., Mouton, P., Price, D. L., and Martin, L. J. (1997). Loss of the pre-synaptic vesicle protein synaptophysin in hippocampus correlates with cognitive decline in Alzheimer disease. *J. Neuropathol. Exp. Neurol.* 56, 933–944. doi: 10.1097/00005072-199708000-00011

Takenawa, T., and Suetsugu, S. (2007). The WASP-WAVE protein network: connecting the membrane to the cytoskeleton. *Nat. Rev. Mol. Cell Biol.* 8, 37–48. doi: 10.1038/nrm2069

Tashiro, A., Minden, A., and Yuste, R. (2000). Regulation of dendritic spine morphology by the Rho family of small GTPases: antagonistic roles of Rac and Rho. *Cereb. Cortex* 10, 927–938. doi: 10.1093/cercor/10.10.927

Tu, S., Okamoto, S., Lipton, S. A., and Xu, H. (2014). Oligomeric Aβ-induced synaptic dysfunction in Alzheimer's disease. *Mol. Neurodeg.* 9:48. doi: 10.1186/1750-1326-9-48

Tybulewicz, V. L. J., Crawford, C. E., Jackson, P. K., Bronson, R. T., and Mulligan, R. C. (1991). Neonatal lethality and lymponemia in mice with a disruption of the c-abl proto-oncogene. *Cell* 65, 1153–1163. doi: 10.1016/0092-8674(91)90011-m

Tyler, W. J., and Pozzo-Miller, L. (2003). Miniature synaptic transmission and BDNF modulate dendritic spine growth and form in rat CA1 neurons. *J. Physiol.* 553, 497–509. doi: 10.1113/jphysiol.2003.052639

Vargas, L. M., Cerpa, W., Muñoz, F. J., Zanlungo, S., and Alvarez, A. R. (2018). Amyloid-β oligomers synaptotoxicity: the emerging role of EphA4/c-Abl signaling in Alzheimer's disease. *Biochim. Biophys. Acta Mol. Basis Dis.* 1864, 1148–1159. doi: 10.1016/j.bbadis.2018.01.023

Vargas, L., Leal, N., Estrada, L., González, A., Serrano, F., Araya, K., et al. (2014). Eph4A activation of c-Abl mediates synaptic loss and LTP blockade caused by amyloid-β oligomers. *PLoS One* 9:e92309. doi: 10.1371/journal.pone.0092309

Viola, K. L., and Klein, W. L. (2015). Amyloid β oligomers in Alzheimer's disease pathogenesis, treatment, and diagnosis. *Acta Neuropathol.* 129, 183–206. doi: 10.1007/s00401-015-1386-3

Wang, J. Y. (2014). The capable ABL: what is its biological function? *ASM* 34, 1188–1197. doi: 10.1128/mcb.01454-13

Yáñez, M. J., Belbin, O., Estrada, L. D., Leal, N., Contreras, P. S., Lleó, A., et al. (2016). c-Abl links APP-BACE1 interaction promoting APP amyloidogenic processing in Niemann-Pick type C disease. *Biochim. Biophys. Acta* 1862, 2158–2167. doi: 10.1016/j.bbadis.2016.08.016

Yang, T. T., Hsu, C. T., and Kuo, Y. M. (2009). Cell-derived soluble oligomers of human amyloid-β peptides disturb cellular homeostasis and induce apoptosis in primary hippocampal neurons. *J. Neural Transm.* 116, 1561–1569. doi: 10.1007/s00702-009-0311-0

Zandy, N. L., Playford, M., and Pendergast, A. M. (2007). Abl tyrosine kinases regulate cell-cell adhesion through Rho GTPases. *Proc. Natl. Acad. Sci. U S A* 104, 17686–17691. doi: 10.1073/pnas.0703077104

Conflict of Interest: The authors declare that the research was conducted in the absence of any commercial or financial relationships that could be construed as a potential conflict of interest.

frontiers in Cellular Neuroscience

REVIEW
published: 23 June 2020
doi: 10.3389/fncel.2020.00188

Collapsin Response Mediator Proteins: Their Biological Functions and Pathophysiology in Neuronal Development and Regeneration

Fumio Nakamura[1†], *Toshio Ohshima*[2†] *and Yoshio Goshima*[3*]

[1]Department of Biochemistry, Tokyo Women's Medical University, Tokyo, Japan, [2]Department of Life Science and Medical Bio-Science, Waseda University, Tokyo, Japan, [3]Department of Molecular Pharmacology and Neurobiology, Yokohama City University Graduate School of Medicine, Yokohama, Japan

OPEN ACCESS

Edited by:
Juan Pablo Henríquez, University of Concepcion, Chile

Reviewed by:
Anne Marie Duchemin, The Ohio State University, United States
Lisette Leyton, University of Chile, Chile

***Correspondence:**
Yoshio Goshima
goshima@med.yokohama-cu.ac.jp

[†]*These authors have contributed equally to this work*

Specialty section:
This article was submitted to Cellular Neurophysiology, a section of the journal Frontiers in Cellular Neuroscience

Received: *01 April 2020*
Accepted: *29 May 2020*
Published: *23 June 2020*

Citation:
Nakamura F, Ohshima T and Goshima Y (2020) Collapsin Response Mediator Proteins: Their Biological Functions and Pathophysiology in Neuronal Development and Regeneration. Front. Cell. Neurosci. 14:188. doi: 10.3389/fncel.2020.00188

Collapsin response mediator proteins (CRMPs), which consist of five homologous cytosolic proteins, are one of the major phosphoproteins in the developing nervous system. The prominent feature of the CRMP family proteins is a new class of microtubule-associated proteins that play important roles in the whole process of developing the nervous system, such as axon guidance, synapse maturation, cell migration, and even in adult brain function. The CRMP C-terminal region is subjected to posttranslational modifications such as phosphorylation, which, in turn, regulates the interaction between the CRMPs and various kinds of proteins including receptors, ion channels, cytoskeletal proteins, and motor proteins. The gene-knockout of the CRMP family proteins produces different phenotypes, thereby showing distinct roles of all CRMP family proteins. Also, the phenotypic analysis of a non-phosphorylated form of CRMP2-knockin mouse model, and studies of pharmacological responses to CRMP-related drugs suggest that the phosphorylation/dephosphorylation process plays a pivotal role in pathophysiology in neuronal development, regeneration, and neurodegenerative disorders, thus showing CRMPs as promising target molecules for therapeutic intervention.

Keywords: CRMP, neuronal development, regeneration, structural biology, posttranslational modifications, phosphorylation, neurological disorders, drug target

INTRODUCTION

Cell to cell interactions mediated by extracellular molecules drives numerous physiological processes and helps enable coordinated functioning in neuronal development and regeneration. Extracellular signals are often integrated into complex regulatory networks in which cytoskeletal rearrangement and membrane reorganization are precisely regulated. The growth cone is a characteristic structure at the distal tip of growing axons during development. Growth cones are composed of an actin-rich peripheral domain and a microtubule-rich central domain. At the distal tip of the growth cone, finger-like filopodia and sheet-like lamellipodia extend and retract rapidly as they sense the environmental axon guidance cues around the growth cone.

The first member of the Collapsin Response Mediator Proteins (CRMPs) family, was originally identified as an intracellular protein mediating the action of semaphorin-3A (Sema3A)-signaling, a repulsive axon guidance molecule (Goshima et al., 1995). The initial name of the protein was CRMP-62 because collapsin is the former name of Sema3A and 62 was the new molecule's molecular weight. As CRMP-62 has significant homology with UNC-33, which is involved in axon guidance in C. elegans through the regulation of tubulin-cytoskeleton, CRMP-62 has been thought to mediate the intracellular signaling involved in axon guidance *via* its modulation of the cytoskeleton at various developmental stages. After the identification of CRMP-62, an additional four members of the CRMP family were identified by several groups, such as TOAD-64, Ulip, DRP, DPYSL (Schmidt and Strittmatter, 2007). Currently, the nomenclature has been unified by calling the family members "CRMP1" through "CRMP5" (**Supplementary Table S1**); CRMP-62 has been renamed as CRMP2. The CRMP family of proteins are now recognized as multifunctional proteins, not only being involved in neuronal development, regeneration and inflammation, but also in various neurological and psychiatric disease states (Tobe et al., 2017; Tsutiya et al., 2017).

In this review, we summarize the molecular aspects of the CRMPs and discuss their possible involvement in pathophysiological conditions of various disease states. Comprehensive reviews on the implication of CRMPs in Alzheimer's disease (AD) and psychiatric disorders have been described elsewhere (Gu and Ihara, 2000; Yamashita and Goshima, 2012; Quach et al., 2015; Hensley and Kursula, 2016; Nagai et al., 2017; Tobe et al., 2017; Nakashima et al., 2018).

STRUCTURE OF THE CRMPs

CRMP1, 2, and 4 have long and short alternate splicing isoforms (Leung et al., 2002). Short isoforms of CRMP1, 2 and 4, CRMP3, and CRMP5 are 565–572 amino acid lengths. The apparent molecular size of these proteins on SDS-PAGE is 62–65 kDa. The long isoforms of CRMP1, 2, and 4 extend approximately 100 amino acids at their N-termini and exhibit 72–75 kDa on SDS-PAGE. We hereafter describe long and short isoforms as "L-CRMP" and "CRMP," respectively. CRMP1 to CRMP4 share 69–76% amino acid identity while these members and CRMP5 share approximately 50% identity. The long isoforms of CRMPs are minor components in most of the cells and organs. The amino acid identity of the N-terminal regions of L-CRMP1, 2, and 4 is 35% to 54%. The N-terminal extended region has several unique functions such as distal localization of L-CRMP2 (CRMP2A) in axons (Balastik et al., 2015), L-CRMP4 (CRMP4b) and RhoA interaction in Nogo signaling (Alabed et al., 2007), and correlation of L-CRMP1 expression and cancer cell migration (Pan et al., 2011).

X-ray crystal structures of the short isoforms of CRMP1, 2, 4, and 5 have been reported (Deo et al., 2004; Stenmark et al., 2007; Ponnusamy and Lohkamp, 2013; Ponnusamy et al., 2014). Central regions of the CRMPs (8–490) forms a tetramer (**Figure 1**). The folded CRMP structure resembles dihydropyrimidinase (DHPase), which hydrolyzes the amide bond of pyrimidine bases (Gojkovic et al., 2003). Each CRMP monomer consists of an N-terminal β-sheet enriched region (15–69) and central α/β barrel domain (70–490). The central domain contains tetramer interfaces. The ternary structure of the entire CRMP C-terminal region (490–572) has not been determined possibly because the region stays flexible and the structure is somewhat random, altering its conformation upon posttranslational modification such as phosphorylation. However, the partial ternary structure of the C-terminal proximal region of CRMP2 has been reported (Niwa et al., 2017). The C-terminal visible residues from the α-helix19 (480–487) further extend in the same direction and several residues in (491–506) interact with the neighboring monomer (**Figure 1**), contributing to stabilizing the tetramer. It has been shown that CRMPs form hetero-oligomerized complexed in the brain (Wang and Strittmatter, 1996). *In vitro* reconstitution revealed that CRMP1, CRMP2, and CRMP3 prefer hetero oligomerization. However, the biological significance of the hetero-complexed CRMPs has not yet been fully addressed (Makihara et al., 2016).

Although the CRMPs have 51–54% amino acid identity with DHPase, they have no enzymatic activity toward dihydropyrimidines (Wang and Strittmatter, 1996), as His69 and His248 residues coordinating Zn ions in the catalytic center of DHPase are not conserved in the CRMPs. Instead, CRMP3 has histone H4 deacetylase activity, which is involved in neuronal cell death after the translocation of CRMP3 to the nucleus (Hou et al., 2013). Other enzymatic activities of the CRMPs are currently unknown.

PHOSPHORYLATION OF CRMPs

Posttranslational modifications play a crucial role in regulating the folding of proteins, their targeting to specific subcellular compartments, their interaction with other proteins, and their functional states, such as activation and inactivation in signal transduction pathways. Protein phosphorylation is the major molecular mechanism through which protein function is regulated in response to extracellular stimuli both inside and outside the nervous system. Many kinases phosphorylate CRMPs (**Figure 2**, **Supplementary Table S2**). Most of the phosphorylation sites are localized in their C-terminal regions. As the primary structures of their C-termini are relatively not conserved compared to their central domains, some kinases specifically phosphorylate one of the CRMPs but not the others. Such phosphorylation may contribute to the unique function of each member of the CRMP family protein. Here we summarize the phosphorylation by kinase-based classification.

Cyclin-dependent kinase 5 (Cdk5) and glycogen kinase 3β (GSK3β)—the phosphorylation of CRMP2 by Cdk5 and GSK3β is the most extensively studied among the CRMP members (**Figure 2**). CRMP2 is primarily phosphorylated at Ser522 by Cdk5 and subsequently phosphorylated at Ser518, Thr514, and Thr509 by GSK3β (Cole et al., 2006; Brittain et al., 2012; Yamashita and Goshima, 2012; Nagai et al., 2017). The latter phosphorylation requires Cdk5-primed phosphorylation of Ser522, therefore, the substitution of Ser522 with Ala

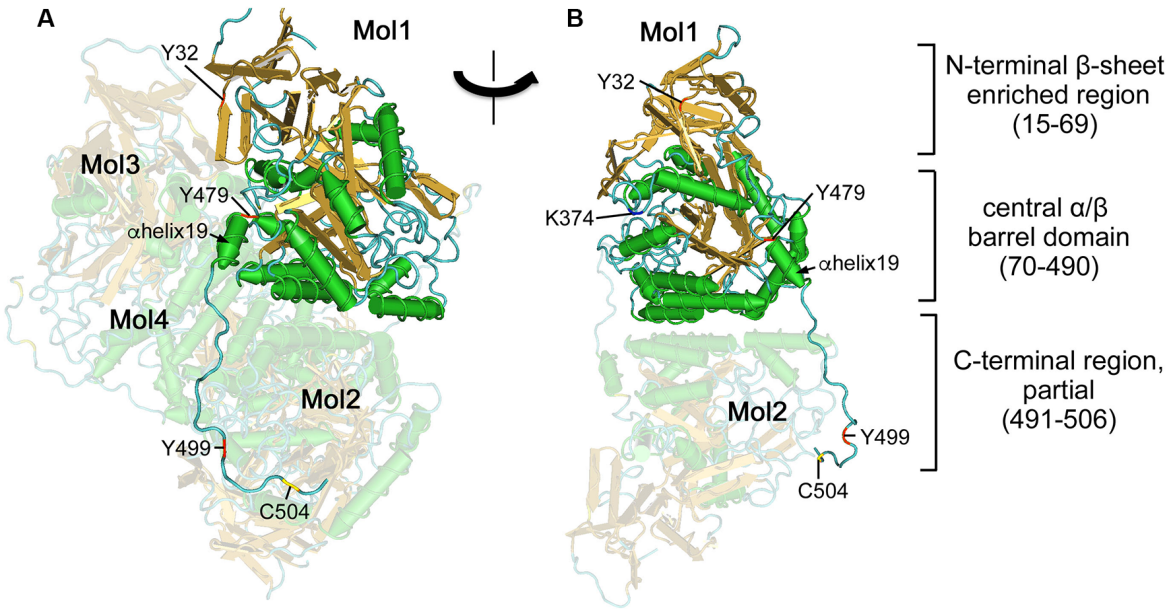

FIGURE 1 | Ternary structure of Collapsin response mediator proteins 2 (CRMP2). **(A)** Crystal structure of human CRMP2 (1–525) homo-tetramer (5X1A; Niwa et al., 2017). A secondary structure-based view was rendered using Cn3D (version 4.3). One monomer (Mol1) is shown in secondary structure-based color (α-helix, green; β-sheet, gold; random coil, cyan). The structure is visible between 14 and 506 residues. Phosphorylation (Tyr32, Tyr479, and Tyr499), SUMOylation (Lys374), and oxidation (Cys504) sites are indicated by red, blue, and yellow, respectively. Other monomers (Mol2–4) are shown in faded colors. The C-terminal domain of Mol1 interacts with Mol2. **(B)** Rotate view. The interface of Mol1 to Mol3 is shown by omitting Mol3 and Mol4. Note that Lys374 and Tyr479 are present on the interface.

eliminates the phosphorylation of Ser518, Thr514, and Thr509 in CRMP2. CRMP's phosphorylation state determines its biological function. Non-phosphorylated CRMP2 binds tubulin dimers to facilitate the axonal elongation; the phosphorylation eliminates that function. Instead, the phosphorylated CRMP2 acts as an intracellular signaling mediator for inhibition of axonal guidance such as *via* Sema3A. Recent crystal structural analysis of CRMP2 revealed that non-phosphorylated CRMP2 monomer forms hetero-trimer between CRMP2 monomer and the GTP-tubulin hetero-dimer (Sumi et al., 2018). Using the phosphorylation-mimicking form of CRMP2, Sumi et al. (2018) revealed that the increased negative charge of the C-terminal region alters CRMP2 homo-tetramer conformation and reduces the interaction of CRMP2 and tubulin-dimers. Ser522 phosphorylation of CRMP2 augments the interaction with CaV2.2 to enhance Ca^{2+} influx (Brittain et al., 2012).

Phosphorylation state is not only regulated by kinase but also by phosphatases that dephosphorylate. PP2A dephosphorylates CRMP2 Thr514 and facilitates the non-phospho CRMP2 effect on neurite outgrowth (Zhu et al., 2010). L-CRMP2 is phosphorylated by Cdk5 at Ser27 in N-terminal extended region as well as at Ser623, an equivalent residue of Ser522 in the short form (Balastik et al., 2015). Prolyl Isomerase Pin1 catalyzes and stabilizes phosho-Ser32-Pro33 in L-CRMP2. This brings distal localization of L-CRMP2 in axons and attenuates Sema3A-repulsive response despite Cdk5-dependent phosphorylation.

The C-terminal phosphorylation sites, Thr509, Thr514, Ser518, and Ser522, are conserved in human CRMP1 and CRMP4. Different priming kinases, Cdk5 and dual-specificity tyrosine phosphorylation-regulated kinase 2 (DYRK2) phosphorylate Ser522 of CRMP1 and CRMP4, respectively (Cole et al., 2006). GSK3β secondarily phosphorylates human CRMP1 and CRMP4 like CRMP2. However, Cdk5 directly phosphorylates Thr509 of mouse/rat CRMP1 because Thr514 is replaced with Ala. CRMP5 is phosphorylated by GSK3β at Thr516 and this phosphorylation is essential for tubulin-binding of CRMP5 but inhibits neurite outgrowth (Brot et al., 2014).

Rho-kinase—Rho-kinase phosphorylation of Thr555 CRMP2 was initially identified by *in vitro* kinase assays (Arimura et al., 2000). As Rho-kinase acts as the downstream molecule of lysophosphatidic acid (LPA), the primary cultured dorsal root ganglion (DRG) neurons stimulated with LPA induced CRMP2-Thr555 phosphorylation (**Figure 2**). Overexpression of CRMP2-Thr555Ala in DRG neurons suppressed the LPA-induced growth cone collapse response but not the Sema3A-response. A similar mechanism is utilized in Ephrin-A5 signaling. Ephrin-A5-stimulation induced growth cone collapse response and the Thr555 phosphorylation in cultured DRG neurons. This response was abrogated by a Rho-kinase inhibitor or by the overexpression of CRMP2 Thr555Ala (Arimura et al., 2005).

Other Ser/Thr kinases—it has been shown that Protein kinase A (PKA), Protein kinase C (PKC), and Calmodulin kinase II (CaMKII) phosphorylate CRMP2 in pathological conditions. PKA-dependent phosphorylation of CRMP2 was observed in the nucleus accumbens neurons of cocaine-sensitized

rats (Boudreau et al., 2009). The PKA-phosphorylation site has not been determined. PKC-βII phosphorylates CRMP2 at the Thr514 residue. This phosphorylation prevents calpain-mediated CRMP2 proteolysis during ischemic injury (Yang et al., 2016). CaMKII phosphorylates CRMP2 at Thr555, which, in turn, attenuates glutamate toxicity in ischemic brains (Hou et al., 2009).

Tyrosine kinases—it has been shown that the constitutive active form of Fyn phosphorylates all members of CRMPs (Uchida et al., 2009). The constitutive active form phosphorylates Tyr32 of CRMP2; this phosphorylation is involved in Sema3A-signaling in mouse DRG neurons (**Figure 2**). In contrast, wild-type Fyn selectively phosphorylates CRMP1 at Tyr504 but not other CRMPs (Buel et al., 2010). The absence of an autoinhibitory mechanism in the constitutive active form may contribute to the non-selective phosphorylation of CRMPs. Fyn-related kinase Fes and Fer phosphorylate CRMP2 and CRMP5. *In vitro* phosphorylation assay and mass spectrometry analysis revealed that Fer phosphorylates CRMP2 at the 32, 251, 275, 431, 479, and 499 Tyr residues (Zheng et al., 2018). Among these sites, Tyr479 and/or Tyr499 phosphorylation prevents the tetramerization of CRMP2, which, in turn, decreases the interaction of CRMP2 and microtubules (**Figures 1**, **2**).

OTHER POSTTRANSLATIONAL MODIFICATIONS

SUMOylation—CRMP2 is post-translationally modulated by a small ubiquitin-like modifier (SUMO) at Lys374, and this modulation alters CRMP2-interaction with Ca^{2+} and Na^{+} channels in a different manner (**Figure 2**). While SUMOylated CRMP2 enhances Na^{+} currents through NaV1.7 surface expression (Dustrude et al., 2013), it reduces Ca^{2+} influx through CaV2.2 (Ju et al., 2013). De-SUMOylation and de-phosphorylation of CRMP2 at Thr514 contribute to the formation and maturation of dendritic spines (Zhang et al., 2018). As the SUMO consensus motif including Lys374 is conserved among CRMPs, SUMOylation may regulate other CRMPs.

Oxidation—genetic dissection of drosophila axon guidance revealed the involvement of flavoprotein oxidoreductase MICAL in semaphorin-signaling (Terman et al., 2002). CRMP2 binds and activates MICAL, by releasing its autoinhibition domain (Schmidt et al., 2008). CRMP2 is subsequently oxidized at Cys504 by MICAL upon Sema3A-stimulation and transiently forms disulfate bonds with thioredoxin (TRX; **Figure 2**). The CRMP2-TRX complex facilitates the phosphorylation of CRMP2 at Thr509 by GSK3β (Morinaka et al., 2011), indicating cross-talk between oxidation and phosphorylation in Sema3A-signaling.

Proteolysis—various brain injuries such as ischemia and glutamate toxicity induce calpain-mediated cleavage of all members of the CRMP family and produce approximately 54 kDa truncated products (Jiang et al., 2007). Calpain cleavage sites have been identified in CRMP3 and CRMP4. CRMP3 is cleaved at N-terminal Arg75-Leu76 bond and CRMP4 is at the C-terminal Arg550-Ser551 bond (Kowara et al., 2005; Hou et al., 2006). Processing of CRMP2 at the C-terminal region exposes nuclear localization signal (NLS) within residues Arg471-Lys472, which brings the truncated CRMP2 to the nucleus (Rogemond et al., 2008). Each truncated CRMP has a unique function. Truncated CRMP2 suppresses neurite outgrowth and reduces surface expression of the NR2B NMDA receptor subunit to protect neurons from glutamate toxicity (Bretin et al., 2006; Rogemond et al., 2008). Cleaved CRMP3 translocates to the nucleus and acts as a histone H4 deacetylase, which, in turn, induces neuronal cell death (Hou et al., 2006; Hou et al., 2013).

CRMP INTERACTING MOLECULES

CRMPs interact with membrane and intracellular proteins (**Supplementary Table S3**). Here, we classify those proteins into several categories including cytoskeletal proteins and ion channels.

Tubulin and microtubules—overexpression CRMP2 in hippocampal neurons switch neurite identity from dendrites to axons (Fukata et al., 2002; Yoshimura et al., 2005). This action is accomplished by two functions (Niwa et al., 2017). First, CRMP2 monomers bind to tubulin dimers and transport them to the distal end of axons to facilitate the neurite outgrowth. Second, CRMP2 tetramer stabilizes microtubules (Lin et al., 2011). These actions are canceled by the C-terminal phosphorylation of CRMP2 by GSK3β because phosphorylated CRMP2 loses its binding ability (**Figure 2**). It has been shown that Fer phosphorylates CRMP2 at Tyr479 and Tyr499. Crystal structures of the CRMP2-Tyr479Glu phospho-mimicking mutant revealed that the phosphorylation of Tyr479 interferes with the tetramerization of CRMP2 by introducing a negative charge in the hydrophobic cavity of the tetramer interface (Zheng et al., 2018). CRMP2 α-helix 19 (476–487) serves as a tubulin-dimer interface (Niwa et al., 2017). As CRMP2-tubulin dimer interaction is abrogated by the C-terminal phosphorylation of CRMP2 (Sumi et al., 2018), this modulation would also alter the higher structure of the C-terminal region and α-helix 19. However, such alteration of full-length CRMPs has not been revealed in a structural basis. CRMP3 inhibits tubulin polymerization and neurite outgrowth in cultured cerebellar granule neurons (Aylsworth et al., 2009). CRMP4 interacts with microtubules in hippocampal neurons to facilitate axon outgrowth (Khazaei et al., 2014). CRMP5 is phosphorylated by GSK3β at Thr516 (Brot et al., 2014). This phosphorylation is essential for tubulin-binding of CRMP5 but inhibits neurite outgrowth.

Actin—CRMP1 indirectly regulates actin-cytoskeleton through the interaction with actin-binding proteins including filamin-A and Ena/VASP proteins (Nakamura et al., 2014; Yu-Kemp et al., 2017). Interestingly, distinct roles were demonstrated for CRMP1 and CRMP2 in steering axonal outgrowth, using microscale-chromophore-assisted local inactivation (micro-CALI) method (Higurashi et al., 2012). CRMP1 and CRMP2 have characteristic distribution in the growth cones. CRMP1 was co-localized with actin in the peripheral domain, while CRMP2 was co-localized

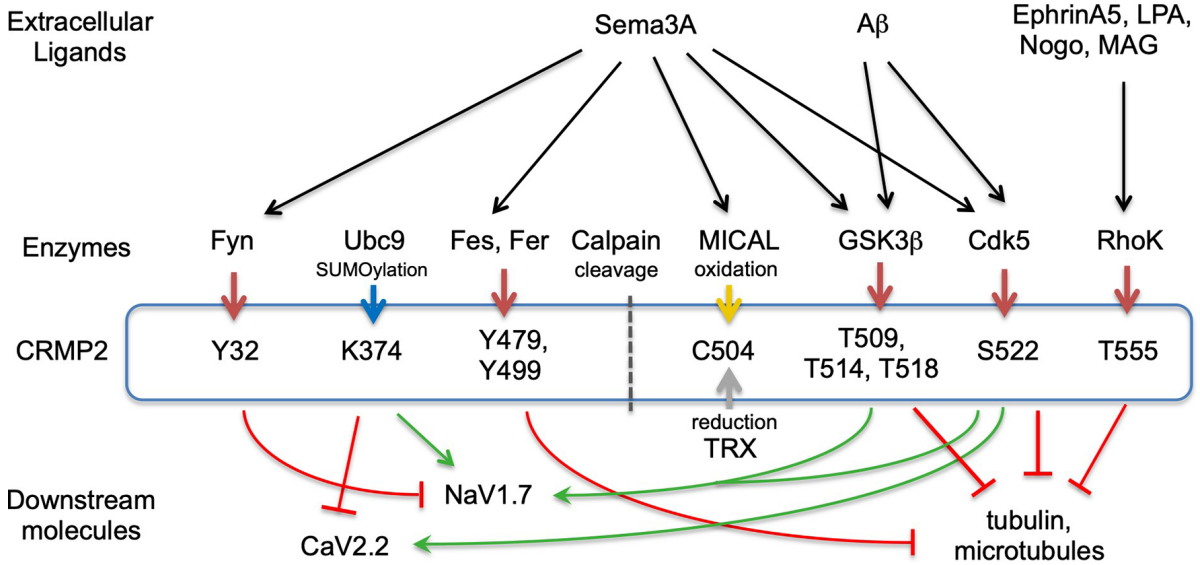

FIGURE 2 | CRMP2-posttranslational modification and signaling. Extracellular ligands, modulating enzymes, posttranslational medication sites in CRMP2, and downstream molecules are represented. Red arrows from enzymes to CRMP2 represent phosphorylation. Blue, yellow, and gray arrows indicate SUMOylation, oxidation, and reduction, respectively. Green and red stop arrows represent facilitation and inhibition, respectively. Not all ligands or downstream molecules are shown.

with tubulin in the central domain. It has been shown that CRMP4 binds F-actin and causes actin bundling (Rosslenbroich et al., 2005). This actin bundling is involved in the filopodia extension of hippocampal growth cones (Khazaei et al., 2014). CRMP5 interacts with actin and tubulin in growth cones (Gong et al., 2016). CRMP5 is localized in filopodia of growth cones and its overexpression promotes filopodial formation (Hotta et al., 2005).

Motor proteins—both Antero- and retro-grade motor proteins bind to CRMP2. Kinesin-1 binds to CRMP2 through the interaction of the kinesin light chain and the C-terminal region of CRMP2 (Kimura et al., 2005). In contrast, the N-terminus of CRMP2 binds to the dynein heavy chain but the interaction interferes with the retrograde transporting activity (Arimura et al., 2009). Combining these actions may facilitate the transport of the CRMP2-tubulin dimer complex to the distal end of the axons. The CRMP2 and Kinesin-1 complex also transports TrkB-containing vesicles to axonal plasma membranes (Arimura et al., 2009).

Na^+ channel—CRMP1 interacts with NaV1.7 and modulates the Na^+ currents by lowering the threshold of the channel (Yamane et al., 2017). This action is probably augmented by C-terminal phosphorylation because the overexpression of phosphomimetic CRMP1-Thr509Asp/Ser522Asp mutant enhanced the current. CRMP2 also interacts with NaV1.7 and phosphorylation of Thr509 and Ser522 of CRMP2 augments the action (Dustrude et al., 2013). This interaction is modulated by SUMOylation and phosphorylation of CRMP2. While Ser522 phosphorylation and Lys374 SUMOylation prevent NaV1.7 internalization, Tyr32-phosphorylation facilitates the endocytosis of NaV1.7 (Dustrude et al., 2016).

Ca^{2+} channel—CRMP2 binds to CaV2.2 and increases Ca^{2+} current by cell surface expression of the channel (Brittain et al., 2009). Cdk5-phosphorylation at Ser522 augments the interaction with and Ca^{2+} influx through CaV2.2 (Brittain et al., 2012). However, in contrast to NaV1.7 modulation, Lys374 SUMOylation of CRMP2 attenuates the Ca^{2+} current (Ju et al., 2013). Three domains in CRMP2, CBD1(94–166), CBD2(212–297), and CBD3(479–500), are involved in CaV2.2-binding (Brittain et al., 2009). The peptide fuses TAT (transduction domain of HIV), and CBD3 interferes with CRMP2 and CaV2.2 coupling to suppress inflammatory and neuropathic pain in model mice (Brittain et al., 2011). This effect is due to the reduction of membrane surface expression of CaV2.2. As the CBD3 sequence partially overlaps with α-helix 19 (476–487), a tubulin-dimer binding domain, TAT-CBD3 may also affect CRMP2-tubulin interaction. Also, CRMP2 interacts with NMDAR and Na/Ca Exchanger 3 to facilitate glutamate-induced Ca^{2+} dysregulation in hippocampal neurons (Brustovetsky et al., 2014). CRMP3 facilitates the depolarization-evoked Ca^{2+} response of L- and N-type Ca channels to promote dendrite morphogenesis of hippocampal neurons (Quach et al., 2013).

Other membrane and intracellular proteins—CRMP1 interacts with actin-binding protein Filamin-A. This interaction is augmented by the Cdk5-phosphorylation of CRMP1 (Nakamura et al., 2014). CRMP1-binding to Filamin-A decreases the F-actin gelation cross-linked by Filamin-A, which, in turn, facilitates remodeling of the actin cytoskeleton. CRMP1 also interacts with EVL, one of Ena/VASP proteins, to facilitate actin filament elongation at the barbed end (Yu-Kemp et al., 2017). CRMP2 interacts with Numb, one of

the endocytosis adaptor proteins, to regulate endocytosis and recycling of axonal growth cone membranes (Nishimura et al., 2003). Long-form CRMP4, but not short-form, interacts with RhoA and suppresses neurite outgrowth (Alabed et al., 2007). GSK3β phosphorylates L-CRMP4 at Thr622 and attenuates RhoA-binding and cancels the suppression (Alabed et al., 2010). Myelin-associated inhibitors (MAIs) bring their inhibitory action through the inactivation of GSK3β and dephosphorylation of L-CRMP4 Thr622. Other known interactions are summarized in **Supplementary Table S3**.

NEURONAL SUBCELLULAR LOCALIZATION OF CRMPs

Each CRMP has a different subcellular localization in a developmental-stage dependent manner. In primary cultured cortical neurons, CRMP1 and CRMP2 are predominantly expressed in axons and, to a lesser extent, in the somatodendritic regions at 7 days *in vitro* (DIV 7; Makihara et al., 2016). By DIV14, while CRMP1 tends to localize to the presynaptic region, CRMP2 distributes to the axons and dendrites.

Alternative splicing also contributes to localization. L-CRMP2 localizes to the distal axons of hippocampal neurons (Balastik et al., 2015). Studies in mice in which CRMP3 has been knocked-out revealed that CRMP3 regulates the dendritic growth of hippocampal neurons (Quach et al., 2013). CRMP4 distributes along axons and dendrites of hippocampal neurons and facilitates their growth through its interaction with actin and tubulin (Khazaei et al., 2014; Cha et al., 2016). CRMP5 is involved in the dendritic growth of hippocampal neurons (Yamashita et al., 2011). The effect of CRMP5 on axon outgrowth is inconsistent i.e., it can both variably promote and inhibit it (Brot et al., 2014; Gong et al., 2016); however, the inhibitory effect may reflect Thr516 phosphorylation of CRMP5 by GSK3β (Brot et al., 2014).

The neuronal growth cone consists of an actin-rich peripheral region and a tubulin-rich central domain. The peripheral region is further divided into filopodia and lamellipodia. CRMP1 localizes to both the peripheral and central domains, while CRMP2 localizes to the central domain in chick DRG growth cones (Higurashi et al., 2012). Focal inactivation of CRMP2 by micro-CALI support the role of CRMP2 in microtubule extension and stabilization. CRMP4 localizes to both the peripheral and central regions of hippocampal growth cones (Khazaei et al., 2014). Peripheral and central CRMP4 participate in filopodial F-actin bundling and microtubule elongation, respectively. CRMP5 predominantly localizes to the peripheral region of hippocampal growth cones to promote filopodial formation (Hotta et al., 2005).

Nuclear-translocation of calpain-digested CRMPs has already been discussed above under the "Proteolysis" section.

THE RELATION OF CRMPs AND AXON GUIDANCE MOLECULES

Sema3A, a prototypical inhibitory axonal guidance molecule, regulates axonal projection of various neurons in the peripheral and central nervous system (CNS; Nakamura et al., 2000). It also participates in the dendritic growth and synapse formation and maturation (Goshima et al., 2016). The role of the CRMPs in Sema3A-signaling has been studied both *in vitro* and *in vivo*. Sema3A binds the NRP1 and Plexin-A receptor complex, which activates at least three distinct downstream signaling pathways; the phosphorylation cascade, the small-G-protein cascade, and MICAL-mediated oxidation. CRMPs are involved in all of these signaling pathways.

Sema3A activates Cdk5 and GSK3β kinases, which sequentially phosphorylates CRMP2 Ser522 and Thr509 residues, respectively. Phosphorylation of CRMP2 at Tyr32 by Fyn or Fes has also been shown to be involved in Sema3A-signaling (Yamashita et al., 2012; **Figure 2**). Phosphorylation makes CRMP2 alter its binding partners from tubulin-dimer to other downstream molecules such as CaV2.2 (Brittain et al., 2012). CRMP1 also acts on molecules downstream of Sema3A by being phosphorylated at Ser522 by Cdk5 (Yamashita et al., 2012). CRMP2 binds and activates α2-chimaerin, a Rac-GTPase activating protein, to downregulate Rac. This action is involved in the Sema3A response in DRG neurons (Brown et al., 2004). CRMP2 binds and activates MICAL by releasing its autoinhibition domain (Schmidt et al., 2008).

Sema3a-knockout mice demonstrate that Sema3A restricts peripheral neuron projections while facilitating the formation of dendrites and synapses in CNS. *Sema3a*$^{-/-}$ mice showed an overshooting and defasciculation of trigeminal branches and DRG neurons (Taniguchi et al., 1997). *Crmp2*$^{-/-}$ mice show CRMP2 to be involved in the peripheral projection of the trigeminal ophthalmic branches (Ziak et al., 2020). However, as the irregular peripheral projection of DRG axons is absent in *Crmp2*$^{-/-}$ mice, CRMP2 may mediate additional guidance cues such as ephrin-A5 and Slit2 in this projection (Jayasena et al., 2005; Kubilus and Linsenmayer, 2010).

The involvement of CRMPs in Sema3A-signaling is more evident in CNS development. Synapse formation of cortical pyramidal neurons is reduced in *Sema3a*$^{-/-}$, *Crmp2*$^{-/-}$, and *Crmp2*$^{-/-}$ mutants compared to wild-type (Makihara et al., 2016). *Sema3a*$^{+/-}$; *Crmp1*$^{+/-}$ and *Sema3a*$^{+/-}$; *Crmp2*$^{+/-}$ double heterozygous mice exhibit a similar phenotype, indicating that both CRMP1 and CRMP2 act as downstream molecules of Sema3A-regulated synapse formation. However, as *Crmp1*$^{+/-}$; *Crmp2*$^{+/-}$ double heterozygous showed normal phenotype, CRMP1 and CRMP2 may mediate different intracellular signaling pathways.

Considering the obvious role of CRMPs in synapse maturation, it is noteworthy that the "lithium-response (LiR) pathway" governs the phosphorylation state of CRMP2, hence yielding insight into the pathogenesis of bipolar disorder (BPD; Tobe et al., 2017). Proteomic and phospho-proteomic analysis of human-induced pluripotent stem cells (hiPSCs) and their neuronal derivatives showed that the "set-point" for the ratio of inactive phosphorylated CRMP2 to active non-phosphorylated CRMP2 is elevated uniquely in LiR BPD patients, but not in patients with other psychiatric (including lithium-nonresponsive BPD)

or neurological disorders. Lithium (and other CRMP2 pathway modulators) lowers pCRMP2, increasing dendritic spine area and density. Actual human BPD brains show similarly elevated CRMP2 ratios and diminished spine densities; lithium therapy normalizes the ratios and spines. Behaviorally, transgenic mice that reproduce lithium's postulated site-of-action in dephosphorylating CRMP2 emulate lithium responsiveness in BPD.

The CRMPs also play roles as downstream target genes of signaling of other axon guidance molecules, morphogens, and cytokines in neuronal development and function. BMP-Smad1 signal suppresses CRMP2 gene expression (Sun et al., 2010). TGF-β signaling regulates neuronal morphogenesis through the suppression of CRMP2 expression during brain development (Nakashima et al., 2018). Nicotine administration causes gene up-regulation of CRMP2 in adult mice during nicotine-induced hippocampal long-term-potentiation (Kadoyama et al., 2015).

Sema3F binds Neuropilin-2 (NRP2)/Plexin-A complex and activates intracellular signaling like Sema3A. *Sema3f* and *Nrp2* knockout mice showed axon guidance defects including disorganized anterior commissure and pruning defect of hippocampal mossy fiber axons in the infrapyramidal bundle (Chen et al., 2000; Sahay et al., 2003). *Crmp2*$^{-/-}$ mice exhibit reduction of the corpus callosum, hypoplastic anterior commissure, and defective pruning of CA3 infrapyramidal bundle and corticospinal visual axons (Ziak et al., 2020). As *Crmp2*$^{-/-}$ mice show normal pruning of the hippocampo-septal bundle, of which projection is regulated by Sema3A, CRMP2 is involved in Sema3F-regulated axon guidance rather than Sema3A-guidance.

Reelin regulates neuronal cell migration including neocortex six-layer formation and hippocampal lamination (Yamamoto et al., 2009). CRMP1 is involved in Reelin signaling (Yamashita et al., 2006). Radial migration of cortical neurons is delayed in *Crmp2*$^{-/-}$ brain. Dab1, an adaptor protein of Reelin signaling, is co-localized with CRMP1 in migrating neurons. Homozygous Dab1 yotari mutant mice, *Dab1*$^{yot/yot}$, exhibit disrupted hippocampal lamination. A similar phenotype is observed in *Crmp2*$^{-/-}$; *Dab1*$^{+/yot}$ mice but not in *Crmp2*$^{-/-}$ or *Dab1*$^{+/yot}$ mutants. This genetic augmentation suggests that CRMP1 is involved in the Reelin-regulated neuronal cell migration.

Nogo, an inhibitory signal for neurite outgrowth after spinal cord injury (SCI), exerts the action through NgR1 and its associated transmembrane proteins. It has been shown that CRMP2 is involved in the downstream of Nogo-signaling by the Rho-kinase phosphorylation at Thr555 (Mimura et al., 2006; Petratos et al., 2012). As Nogo downstream signaling, L-CRMP4 (CRMP4b) binds to RhoA and interferes with neurite outgrowth (Alabed et al., 2007). NgR1 forms a receptor complex with Plexin-A2, which associates with CRMP2 and CRMP4 in Nogo dependent manner (Sekine et al., 2019).

Repulsive guidance molecule-a (RGMa) exerts its inhibition through the phosphorylation of CRMP2 by Rho-kinase and GSK3β (Wang et al., 2013). Chondroitin sulfate proteoglycan (CSPG) is a major inhibitor of axonal regeneration after CNS trauma. Knockout mice studies revealed that CRMP4 mediates the action of CSPG and/or other inhibitory molecules related to SCI (Nagai et al., 2015, 2016). The functional recovery of motor and sensory neurons from SCI is accelerated in *Crmp4*$^{-/-}$ mice. Sema4D binds Plexin-B1 and downregulates R-Ras and PI3K-Akt signaling. This brings the activation of GSK3β and CRMP2 phosphorylation at Thr514 (Ito et al., 2006). Plexin-A also inactivates R-Ras by the same mechanism in Sema3A-signaling. *In vivo* Sema4D-CRMP2 relation has yet to be examined.

CRMPs IN CNS REGENERATION AND DEGENERATION

After nerve injury, peripheral nervous system (PNS) axons form growth cones and regenerate (Ertürk et al., 2007). However, axons in the CNS fail to form tips and instead become dystrophic retraction bulbs (Ertürk et al., 2007; Bradke et al., 2012). Growth cones contain organized microtubules that form tight bundles along with axonal axis, whereas retraction bulbs have disassembled microtubules. The importance of the microtubule state for growth cone structure is supported by the fact that the application of the microtubule-destabilizing agent nocodazole transforms the growth cone into a retraction bulb-like structure *in vitro*, resulting in axonal growth arrest (Ertürk et al., 2007).

Phosphorylation of CRMP2 at its C-terminal domain by serine/threonine (Ser/Thr) kinases causes growth cone collapse *via* microtubule destabilization, while inhibition of C-terminal phosphorylation stabilizes the microtubules (Yamashita and Goshima, 2012; Nagai et al., 2017). CRMP2 phosphorylation is also induced during Wallerian degeneration after optic nerve injury. During Wallerian degradation, zinc/RING finger protein 1 (ZNRF1)-dependent protein kinase B (Akt) degradation increases GSK3β activity and results in an increase in CRMP2 phosphorylation at Thr514 (Wakatsuki et al., 2011). The introduction of the CRMP2-Thr514Ala (CRMP2^{T514A}) virus suppresses the Wallerian degradation of the optic nerve *in vivo* (Wakatsuki et al., 2011). To delineate the *in vivo* role of CRMP2 phosphorylation at Ser522, the CRMP2$^{S522A/S522A}$ (CRMP2$^{KI/KI}$) mouse was generated (Yamashita et al., 2012). Due to the phosphorylation of Ser522 by Cdk5 functions, as priming phosphorylation followed GSK3β phosphorylation of Thr509/Thr514/Ser518, 4 sites of phosphorylation in the C-terminal domain of CRMP2 are eliminated in the CRMP2$^{KI/KI}$ mice (Yamashita et al., 2012). Wallerian degeneration following optic nerve injury was found to be suppressed in CRMP2$^{KI/KI}$ mice (Kinoshita et al., 2019). Axonal damage of the optic nerve induces retinal ganglion cell death in the wild-type mice (Duan et al., 2015). However, suppression of retinal ganglion cell death is observed in CRMP2$^{KI/KI}$ mice (Kondo et al., 2019). Moreover, axonal regeneration was promoted in CRMP2$^{KI/KI}$ mice. CRMP2$^{KI/KI}$ mice showed higher expression of the regenerative axonal marker growth-associated protein 43 (GAP43). Tracing of the axon by injecting an anterograde tracer into the eye showed elongated optic nerves in CRMP2$^{KI/KI}$ mice, while

labeled axons were limited in wild-type mice after optic nerve injury. These results are in agreement with the observation that optic nerve regeneration occurs after the intravitreal administration of the CRMP2^{T514A} virus (Leibinger et al., 2017). Overexpression of wild-type CRMP2 *via* a viral infection promoted regeneration of the hypoglossal nerve in the adult rats (Suzuki et al., 2003). In an SCI model, microtubule-stabilizing agents have been found to promote functional recovery and serotonergic axon regeneration (Hellal et al., 2011). CRMP2$^{KI/KI}$ mice also showed better functional, motor and sensory recovery, and serotonergic axon regeneration (Nagai et al., 2016). CRMP2$^{KI/KI}$ DRG neurons showed an enhanced neurotrophic response to brain-derived neurotrophic factor and a hindered inhibitory response against CSPG. These alternations, which were in response to external factors, may also be linked to the recovery in CRMP2$^{KI/KI}$ mice after SCI.

Recently, the mutant superoxide dismutase (SOD)1^{G93A} mouse model of amyotrophic lateral sclerosis (ALS) was crossed with the CRMP2$^{KI/KI}$ mice to assess the genetic inhibition of CRMP2 phosphorylation. Compared to baseline, CRMP2$^{KI/KI}$ mice x SOD1^{G93A} mice developed a slower degeneration of axons and neuromuscular junctions and a delayed progression of motor symptoms (Numata-Uematsu et al., 2019). The myelin oligodendrocyte glycoprotein-induced experimental autoimmune encephalomyelitis (EAE) mouse model of multiple sclerosis (MS) showed an increase in CRMP2 phosphorylation at Thr555 in a Nogo-dependent manner (Petratos et al., 2012). The anti-Nogo-A antibody prevented the development of EAE and increased CRMP2 phosphorylation at Thr555. A recent study further demonstrated that abrogation of the NgR1/pCRMP2 signaling cascade maintains Kinesin-1-dependent anterograde axonal transport to limit the inflammation-mediated axonopathy and demyelination of the EAE model (Lee et al., 2019).

Methyl-phenyl-tetrahydropyridine (MPTP) readily penetrates the blood-brain barrier and enters the brain where it is converted into 1-methyl-4-phenylpyridinium (MPP^+) by MAO-B in astrocytes. MPP^+ is transported by the dopamine (DA) transporter into DA nerve terminals, and it destroys dopaminergic neurons, thereby causing the symptoms similar to those of Parkinson's disease (PD). MPTP administration in non-human primates and aged rodents are often used to model PD. The elevation of CRMP2 phosphorylation at Thr514 through Akt/GSK3β was reported in an MPP^+-PD model in dopaminergic neurons *in vitro* (Fang et al., 2015). Elevation of CRMP2 phosphorylation at Ser522 was observed in dopaminergic neurons in the substantia nigra compacta (SNc) *in vivo* (Togashi et al., 2019). Production of p25 and elevation of Cdk5 activity have been reported in an MPTP-induced PD mouse model (Smith et al., 2003; Cheung and Ip, 2012). Therefore, increased phosphorylation of CRMP2 at Ser522 is consistent with these studies. CRMP2$^{KI/KI}$ mice showed increased axonal viability in the nigro-striatal pathway in an MPTP-induced PD model (Togashi et al., 2019).

Another member of the CRMPs, CRMP4, is reported to be involved in the signal pathway of myelin-associated inhibitors (MAIs; Alabed et al., 2007, 2010; Nagai et al., 2015). MAIs activate ras homolog family member A (RhoA), which interacts with L-CRMP4 to inhibit axonal growth *in vitro*. CRMP4 also interacts with CSPG through the NgR/GSK3β pathway. After SCI, CRMP4$^{-/-}$ mice showed motor and sensory axonal growth (Nagai et al., 2015, 2016). Furthermore, the deletion of CRMP4 prevents DA neuronal loss in SNc and increases axonal viability in the DA neurons in the striatum (Tonouchi et al., 2016).

THE ROLE OF CRMPs IN INFLAMMATORY CELLS AND GLIA

In SCIs, scar formation occurs at the lesion site where astrocytes are recruited by the pro-inflammatory cytokines secreted from the activated microglia/macrophages. The compaction and seclusion of infiltrating inflammatory cells in the lesion center occur during the sub-acute phase of SCI. It is generally accepted that glial scars inhibit axonal growth, by physically interacting with the distal tip of axons (Filous et al., 2014) or by secreting extracellular matrix molecules such as CSPGs (Tan et al., 2011; Burnside and Bradbury, 2014; Cregg et al., 2014) and inhibitory axon guidance molecules such as Sema3A (Kaneko et al., 2006).

A reduction in scar formation after SCI in CRMP2$^{KI/KI}$ mice has been reported (Nagai et al., 2015). In rat SCI, activation of GSK3β in reactive astrocytes is involved in the infiltration of inflammatory cells and scar formation by Wnt signaling-mediated β1-integrin expression (Renault-Mihara et al., 2011). Compaction of scar formation was observed in the GSK3β inhibitor treatment of SCI. Therefore, one possible explanation for the reduced scar formation in CRMP2$^{KI/KI}$ after SCI is that it is mediated by the inhibition of CRMP2 phosphorylation.

After SCI, CRMP4 expression is reported in activated microglia/macrophages (Nagai et al., 2015). In cultured BV-2 microglial cells, microglia express CRMP4 after lipopolysaccharide stimulation (Manivannan et al., 2013). CRMP4 is involved in the association of F-actin, cytokine release, migration, and phagocytosis in BV-2 cells. Injection of Zymosan, macrophage-activating agent, to the spinal cord of *Crmp4*$^{-/-}$ mice, showed reduced microglial activation (Nagai et al., 2015). In *Crmp4*$^{-/-}$ mice with SCIs, reduction of scar formation promoted axonal growth and significant locomotor recovery was observed.

Inflammatory responses have been implicated in other causes of neuronal degeneration, including PD. Disease progression has been linked to the secretion of inflammatory cytokines that engage neighboring cells, including astrocytes, which, in turn, induce autocrine and paracrine responses that amplify the inflammation, leading to further neurodegeneration (Niranjan, 2014). Reduced inflammatory response and suppressed DA neuron death after MPTP injection have been observed in CRMP4$^{-/-}$ mice (Tonouchi et al., 2016). Since cell death of DA neurons by MPTP injection was suppressed, the reduced inflammatory response may be a secondary consequence of the limited release of factors from

dying neurons. MS is a chronic inflammatory, demyelinating, and neurodegenerative disorder of the CNS. In an EAE mouse model of MS, the importance of CRMP2 Ser522 phosphorylation was demonstrated using $CRMP2^{KI/KI}$ mice (Moutal et al., 2019). CRMP2 is also expressed in the immune system and plays a critical role in T lymphocyte polarization and migration (Vincent et al., 2005). C-X-C motif chemokine 12 (CXCL12)/SDF1 treatment activates T lymphocyte migration by switching the dephosphorylation of the GSK3β site (Thr509/Thr514) of CRMP2 (Varrin-Doyer et al., 2009). CXCL12/SDF1 also induces tyrosine phosphorylation at Tyr479 *via* Yes kinase, and the introduction of CRMP2-Tyr479Phe expression suppresses the migration of Jurkat cells, indicating the importance of tyrosine phosphorylation of CRMP2 (Varrin-Doyer et al., 2009).

CRMP2-INTERACTING DRUGS

Several small molecules that have been shown to bind CRMP2 are lacosamide (Wilson et al., 2012, 2014), lanthionine ketimine (LK; Hensley et al., 2010a, 2013; Hensley and Harris-White, 2015), edonerpic maleate (Abe et al., 2018) and naringenin (Ghofrani et al., 2015; Lawal et al., 2018). These molecules are considered candidates for application in the treatment of some of the CRMP2-related pathological conditions discussed above.

(R)-Lacosamide inhibits CRMP2-mediated neurite outgrowth in cultured cortical neurons. (R)-lacosamide reduces CRMP2-mediated tubulin polymerization *in vitro* (Wilson et al., 2012). It seems to prevent posttraumatic axon sprouting *in vivo*. An *in vitro* study showed that (S)-lacosamide, a stereoisomer of the clinically used antiepileptic drug (R)-lacosamide, impairs the ability of CRMP2 to enhance tubulin polymerization *in vitro* without altering tubulin-binding (Wilson et al., 2014).

Lanthionine ketamine-ethyl ester (LKE) is a synthetic cell-penetrating ester derivative of LK, an endogenous sulfur amino acid metabolite in the mammalian brain (Hensley et al., 2010a). LK and LKE bind directly to CRMP2 and change the binding affinity of CRMP2 to its binding partners such as tubulin dimers and neurofilaments. LKE administration reduces CRMP2-tubulin affinity while enhancing CRMP2-neurofilament binding. The neurite growth-promoting action of LKE has been reported in NSC-34 mouse motor neuron-like cells and primary chick DRG neurons (Hensley et al., 2010a). LKE has also been shown to have a neuroprotective effect on these cells from oxidative stress insults. When applied to the $SOD1^{G93A}$ transgenic mouse model of ALS, LKE was reported to delay progressive neurodegeneration (Hensley et al., 2010b). LKE treatment also substantially diminished cognitive decline and brain amyloid-β (Aβ) peptide deposition and phospho-tau accumulation in the 3 × Tg-AD mouse model of AD, reducing the density of Iba1-positive microglia (Hensley et al., 2013). In this study, LKE normalized CRMP2 phosphorylation at Thr514 and suppressed neuroinflammation in the brains of these mice (Hensley et al., 2013). LKE has also been tested in a mouse model of SCI and was reported to benefit the recovery of motor function and reduce post-traumatic neuroinflammation (Kotaka et al., 2017).

Edonerpic maleate has been shown to bind CRMP2, and facilitate experience-driven synaptic glutamate α-amino-3-hydroxy-5-methyl-4-isoxazole-propionic-acid (AMPA) receptor delivery and accelerate motor function recovery after motor cortex cryoinjury in mice in a training-dependent manner through cortical reorganization (Abe et al., 2018). Edonerpic maleate decreased the amount of phosphorylated form of CRMP2, and activated actin-depolymerizing factor (ADF)/cofilin, thereby leading to the trafficking of AMPA receptors into the spine surface under plasticity-inducing conditions. The drug failed to augment recovery in CRMP2-deficient mice, suggesting a CRMP2-dependent action (Abe et al., 2018).

Naringenin has demonstrated the ability to bind and decrease CRMP2 phosphorylation (Yang et al., 2016; Lawal et al., 2018). This action of changing CRMP2's phosphorylated status and hence the binding of cytoskeletal elements may account for the ability of naringenin to improve AD pathology and cognitive deficits in mouse models of AD. For example, naringenin has been shown to significantly improve the performance of Aβ-injected rats in passive avoidance and radial arm maze tasks (Ghofrani et al., 2015). In a 5xFAD mouse model of AD, naringenin ameliorated memory deficits and decreased amyloid plaques and phosphorylated tau (p-tau; Yang et al., 2016). Some of the beneficial effects of naringenin in rodent models of AD may also be related to its anti-inflammatory actions (Park et al., 2012; Wu et al., 2016).

CONCLUSION

The CRMPs family of proteins appear to coordinately be involved in several coordinated biological events including axon guidance, target recognition, synapse maturation, and dendritic branching. The CRMPs possess the ability to interact with various kinds of molecules, thereby being involved in these many processes. Although the CRMPs themselves are regulated by versatile enzymes having a wide substrate spectrum, successful chemical modulators or therapeutic agents may be developed to act on such protein-protein interaction interfaces.

AUTHOR CONTRIBUTIONS

FN, TO, and YG contributed to the writing and editing of this review.

FUNDING

FN is funded by a Grant-in-Aid for Scientific Research(C); (nos. 2450044, 16K07062). TO is funded by a Grant-in-Aid for Scientific Research(C); (no. 26430043). YG is funded by a Grants-in-Aid for Scientific Research in a priority Area (no. 17082006), Targeted Proteins Research Program (no. 0761890004), and by Global COE Program, Innovative Integration between Medicine and Engineering Based on Information Communication Technology (no. 1542140002), and

Creation of Innovation Centers for Advanced Interdisciplinary Research Areas Program in the Project for Developing Innovation Systems (no. 42890001) from the Ministry of Education, Science, Sports, and Culture.

ACKNOWLEDGMENTS

We sincerely thank Drs. Yukio Sasaki, Naoya Yamashita, Kohtaro Takei, Evan Snyder, Kenneth Hensley, Ritsuko Ohtani-Kaneko, Hiroshi Kiyonari, Go Shioi, Pappachan Kolattukudy and Jerome Honnorat for collaboration. We also thank Dr. EY Snyder for his critical reading of our manuscript.

SUPPLEMENTARY MATERIAL

The Supplementary Material for this article can be found online at: https://www.frontiersin.org/articles/10.3389/fncel.2020.00188/full#supplementary-material.

REFERENCES

Abe, H., Jitsuki, S., Nakajima, W., Murata, Y., Jitsuki-Takahashi, A., Katsuno, Y., et al. (2018). CRMP2-binding compound, edonerpic maleate, accelerates motor function recovery from brain damage. *Science* 360, 50–57. doi: 10.1126/science.aao2300

Alabed, Y. Z., Pool, M., Ong Tone, S., and Fournier, A. E. (2007). Identification of CRMP4 as a convergent regulator of axon outgrowth inhibition. *J. Neurosci.* 27, 1702–1711. doi: 10.1523/jneurosci.5055-06.2007

Alabed, Y. Z., Pool, M., Ong Tone, S., Sutherland, C., and Fournier, A. E. (2010). GSK_3 β regulates myelin-dependent axon outgrowth inhibition through $CRMP_4$. *J. Neurosci.* 30, 5635–5643. doi: 10.1523/jneurosci.6154-09.2010

Arimura, N., Inagaki, N., Chihara, K., Menager, C., Nakamura, N., Amano, M., et al. (2000). Phosphorylation of collapsin response mediator protein-2 by Rho-kinase. Evidence for two separate signaling pathways for growth cone collapse. *J. Biol. Chem.* 275, 23973–23980. doi: 10.1074/jbc.m001032200

Arimura, N., Kimura, T., Nakamuta, S., Taya, S., Funahashi, Y., Hattori, A., et al. (2009). Anterograde transport of TrkB in axons is mediated by direct interaction with Slp1 and Rab27. *Dev. Cell* 16, 675–686. doi: 10.1016/j.devcel.2009.03.005

Arimura, N., Menager, C., Kawano, Y., Yoshimura, T., Kawabata, S., Hattori, A., et al. (2005). Phosphorylation by Rho kinase regulates CRMP-2 activity in growth cones. *Mol. Cell. Biol.* 25, 9973–9984. doi: 10.1128/mcb.25.22.9973-9984.2005

Aylsworth, A., Jiang, S. X., Desbois, A., and Hou, S. T. (2009). Characterization of the role of full-length CRMP3 and its calpain-cleaved product in inhibiting microtubule polymerization and neurite outgrowth. *Exp. Cell Res.* 315, 2856–2868. doi: 10.1016/j.yexcr.2009.06.014

Balastik, M., Zhou, X. Z., Alberich-Jorda, M., Weissova, R., Ziak, J., Pazyra-Murphy, M. F., et al. (2015). Prolyl isomerase pin1 regulates axon guidance by stabilizing CRMP2A selectively in distal axons. *Cell Rep.* 13, 812–828. doi: 10.1016/j.celrep.2015.09.026

Boudreau, A. C., Ferrario, C. R., Glucksman, M. J., and Wolf, M. E. (2009). Signaling pathway adaptations and novel protein kinase A substrates related to behavioral sensitization to cocaine. *J. Neurochem.* 110, 363–377. doi: 10.1111/j.1471-4159.2009.06140.x

Bradke, F., Fawcett, J. W., and Spira, M. E. (2012). Assembly of a new growth cone after axotomy: the precursor to axon regeneration. *Nat. Rev. Neurosci.* 13, 183–193. doi: 10.1038/nrn3176

Bretin, S., Rogemond, V., Marin, P., Maus, M., Torrens, Y., Honnorat, J., et al. (2006). Calpain product of WT-CRMP2 reduces the amount of surface NR2B NMDA receptor subunit. *J. Neurochem.* 98, 1252–1265. doi: 10.1111/j.1471-4159.2006.03969.x

Brittain, J. M., Duarte, D. B., Wilson, S. M., Zhu, W., Ballard, C., Johnson, P. L., et al. (2011). Suppression of inflammatory and neuropathic pain by uncoupling CRMP-2 from the presynaptic Ca^{2+} channel complex. *Nat. Med.* 17, 822–829. doi: 10.1038/nm.2345

Brittain, J. M., Piekarz, A. D., Wang, Y., Kondo, T., Cummins, T. R., and Khanna, R. (2009). An atypical role for collapsin response mediator protein 2 (CRMP-2) in neurotransmitter release *via* interaction with presynaptic voltage-gated calcium channels. *J. Biol. Chem.* 284, 31375–31390. doi: 10.1074/jbc.m109.009951

Brittain, J. M., Wang, Y., Eruvwetere, O., and Khanna, R. (2012). Cdk5-mediated phosphorylation of CRMP-2 enhances its interaction with CaV2.2. *FEBS Lett.* 586, 3813–3818. doi: 10.1016/j.febslet.2012.09.022

Brot, S., Smaoune, H., Youssef-Issa, M., Malleval, C., Benetollo, C., Besancon, R., et al. (2014). Collapsin response-mediator protein 5 (CRMP5) phosphorylation at threonine 516 regulates neurite outgrowth inhibition. *Eur. J. Neurosci.* 40, 3010–3020. doi: 10.1111/ejn.12674

Brown, M., Jacobs, T., Eickholt, B., Ferrari, G., Teo, M., Monfries, C., et al. (2004). α2-chimaerin, cyclin-dependent Kinase 5/p35 and its target collapsin response mediator protein-2 are essential components in semaphorin 3A-induced growth-cone collapse. *J. Neurosci.* 24, 8994–9004. doi: 10.1523/jneurosci.3184-04.2004

Brustovetsky, T., Pellman, J. J., Yang, X. F., Khanna, R., and Brustovetsky, N. (2014). Collapsin response mediator protein 2 (CRMP2) interacts with N-methyl-D-aspartate (NMDA) receptor and Na^{+}/Ca^{2+} exchanger and regulates their functional activity. *J. Biol. Chem.* 289, 7470–7482. doi: 10.1074/jbc.m113.518472

Buel, G. R., Rush, J., and Ballif, B. A. (2010). Fyn promotes phosphorylation of collapsin response mediator protein 1 at tyrosine 504, a novel, isoform-specific regulatory site. *J. Cell. Biochem.* 111, 20–28. doi: 10.1002/jcb.22659

Burnside, E. R., and Bradbury, E. J. (2014). Manipulating the extracellular matrix and its role in brain and spinal cord plasticity and repair. *Neuropathol. Appl. Neurobiol.* 40, 26–59. doi: 10.1111/nan.12114

Cha, C., Zhang, J., Ji, Z., Tan, M., Li, S., Wu, F., et al. (2016). CRMP4 regulates dendritic growth and maturation *via* the interaction with actin cytoskeleton in cultured hippocampal neurons. *Brain Res. Bull.* 124, 286–294. doi: 10.1016/j.brainresbull.2016.06.008

Chen, H., Bagri, A., Zupicich, J. A., Zou, Y., Stoeckli, E., Pleasure, S. J., et al. (2000). Neuropilin-2 regulates the development of selective cranial and sensory nerves and hippocampal mossy fiber projections. *Neuron* 25, 43–56. doi: 10.1016/s0896-6273(00)80870-3

Cheung, Z. H., and Ip, N. Y. (2012). Cdk5: a multifaceted kinase in neurodegenerative diseases. *Trends Cell Biol.* 22, 169–175. doi: 10.1016/j.tcb.2011.11.003

Cole, A. R., Causeret, F., Yadirgi, G., Hastie, C. J., Mclauchlan, H., Mcmanus, E. J., et al. (2006). Distinct priming kinases contribute to differential regulation of collapsin response mediator proteins by glycogen synthase kinase-3 *in vivo*. *J. Biol. Chem.* 281, 16591–16598. doi: 10.1074/jbc.m513344200

Cregg, J. M., Depaul, M. A., Filous, A. R., Lang, B. T., Tran, A., and Silver, J. (2014). Functional regeneration beyond the glial scar. *Exp. Neurol.* 253, 197–207. doi: 10.1016/j.expneurol.2013.12.024

Deo, R. C., Schmidt, E. F., Elhabazi, A., Togashi, H., Burley, S. K., and Strittmatter, S. M. (2004). Structural bases for CRMP function in plexin-dependent semaphorin3A signaling. *EMBO J.* 23, 9–22. doi: 10.1038/sj.emboj.7600021

Duan, X., Qiao, M., Bei, F., Kim, I. J., He, Z., and Sanes, J. R. (2015). Subtype-specific regeneration of retinal ganglion cells following axotomy: effects of osteopontin and mTOR signaling. *Neuron* 85, 1244–1256. doi: 10.1016/j.neuron.2015.02.017

Dustrude, E. T., Moutal, A., Yang, X., Wang, Y., Khanna, M., and Khanna, R. (2016). Hierarchical CRMP2 posttranslational modifications control NaV1.7 function. *Proc. Natl. Acad. Sci. U S A* 113, E8443–E8452. doi: 10.1073/pnas.1610531113

Dustrude, E. T., Wilson, S. M., Ju, W., Xiao, Y., and Khanna, R. (2013). CRMP2 protein SUMOylation modulates NaV1.7 channel trafficking. *J. Biol. Chem.* 288, 24316–24331. doi: 10.1074/jbc.m113.474924

Ertürk, A., Hellal, F., Enes, J., and Bradke, F. (2007). Disorganized microtubules underlie the formation of retraction bulbs and the failure of axonal

regeneration. *J. Neurosci.* 27, 9169–9180. doi: 10.1523/JNEUROSCI.0612-07.2007

Fang, W., Gao, G., Zhao, H., Xia, Y., Guo, X., Li, N., et al. (2015). Role of the Akt/GSK-3β/CRMP-2 pathway in axon degeneration of dopaminergic neurons resulting from MPP+ toxicity. *Brain Res.* 1602, 9–19. doi: 10.1016/j.brainres.2014.08.030

Filous, A. R., Tran, A., Howell, C. J., Busch, S. A., Evans, T. A., Stallcup, W. B., et al. (2014). Entrapment *via* synaptic-like connections between NG2 proteoglycan+ cells and dystrophic axons in the lesion plays a role in regeneration failure after spinal cord injury. *J. Neurosci.* 34, 16369–16384. doi: 10.1523/jneurosci.1309-14.2014

Fukata, Y., Itoh, T. J., Kimura, T., Menager, C., Nishimura, T., Shiromizu, T., et al. (2002). CRMP-2 binds to tubulin heterodimers to promote microtubule assembly. *Nat. Cell Biol.* 4, 583–591. doi: 10.1038/ncb825

Ghofrani, S., Joghataei, M. T., Mohseni, S., Baluchnejadmojarad, T., Bagheri, M., Khamse, S., et al. (2015). Naringenin improves learning and memory in an Alzheimer's disease rat model: insights into the underlying mechanisms. *Eur. J. Pharmacol.* 764, 195–201. doi: 10.1016/j.ejphar.2015.07.001

Gojkovic, Z., Rislund, L., Andersen, B., Sandrini, M. P., Cook, P. F., Schnackerz, K. D., et al. (2003). Dihydropyrimidine amidohydrolases and dihydroorotases share the same origin and several enzymatic properties. *Nucleic Acids Res.* 31, 1683–1692. doi: 10.1093/nar/gkg258

Gong, X., Tan, M., Gao, Y., Chen, K., and Guo, G. (2016). CRMP5 interacts with actin to regulate neurite outgrowth. *Mol. Med. Rep.* 13, 1179–1185. doi: 10.3892/mmr.2015.4662

Goshima, Y., Nakamura, F., Strittmatter, P., and Strittmatter, S. M. (1995). Collapsin-induced growth cone collapse mediated by an intracellular protein related to UNC-33. *Nature* 376, 509–514. doi: 10.1038/376509a0

Goshima, Y., Yamashita, N., Nakamura, F., and Sasaki, Y. (2016). Regulation of dendritic development by semaphorin 3A through novel intracellular remote signaling. *Cell Adh. Migr.* 10, 627–640. doi: 10.1080/19336918.2016.1210758

Gu, Y., and Ihara, Y. (2000). Evidence that collapsin response mediator protein-2 is involved in the dynamics of microtubules. *J. Biol. Chem.* 275, 17917–17920. doi: 10.1074/jbc.c000179200

Hellal, F., Hurtado, A., Ruschel, J., Flynn, K. C., Laskowski, C. J., Umlauf, M., et al. (2011). Microtubule stabilization reduces scarring and causes axon regeneration after spinal cord injury. *Science* 331, 928–931. doi: 10.1126/science.1201148

Hensley, K., Christov, A., Kamat, S., Zhang, X. C., Jackson, K. W., Snow, S., et al. (2010a). Proteomic identification of binding partners for the brain metabolite lanthionine ketimine (LK) and documentation of LK effects on microglia and motoneuron cell cultures. *J. Neurosci.* 30, 2979–2988. doi: 10.1523/JNEUROSCI.5247-09.2010

Hensley, K., Venkova, K., and Christov, A. (2010b). Emerging biological importance of central nervous system lanthionines. *Molecules* 15, 5581–5594. doi: 10.3390/molecules15085581

Hensley, K., Gabbita, S. P., Venkova, K., Hristov, A., Johnson, M. F., Eslami, P., et al. (2013). A derivative of the brain metabolite lanthionine ketimine improves cognition and diminishes pathology in the 3 x Tg-AD mouse model of Alzheimer disease. *J. Neuropathol. Exp. Neurol.* 72, 955–969. doi: 10.1097/nen.0b013e3182a74372

Hensley, K., and Harris-White, M. E. (2015). Redox regulation of autophagy in healthy brain and neurodegeneration. *Neurobiol. Dis.* 84, 50–59. doi: 10.1016/j.nbd.2015.03.002

Hensley, K., and Kursula, P. (2016). Collapsin response mediator protein-2 (CRMP2) is a plausible etiological factor and potential therapeutic target in Alzheimer's disease: comparison and contrast with microtubule-associated protein tau. *J. Alzheimers Dis.* 53, 1–14. doi: 10.3233/jad-160076

Higurashi, M., Iketani, M., Takei, K., Yamashita, N., Aoki, R., Kawahara, N., et al. (2012). Localized role of CRMP1 and CRMP2 in neurite outgrowth and growth cone steering. *Dev. Neurobiol.* 72, 1528–1540. doi: 10.1002/dneu.22017

Hotta, A., Inatome, R., Yuasa-Kawada, J., Qin, Q., Yamamura, H., and Yanagi, S. (2005). Critical role of collapsin response mediator protein-associated molecule CRAM for filopodia and growth cone development in neurons. *Mol. Biol. Cell* 16, 32–39. doi: 10.1091/mbc.e04-08-0679

Hou, S. T., Jiang, S. X., Aylsworth, A., Cooke, M., and Zhou, L. (2013). Collapsin response mediator protein 3 deacetylates histone H4 to mediate nuclear condensation and neuronal death. *Sci. Rep.* 3:1350. doi: 10.1038/srep01350

Hou, S. T., Jiang, S. X., Aylsworth, A., Ferguson, G., Slinn, J., Hu, H., et al. (2009). CaMKII phosphorylates collapsin response mediator protein 2 and modulates axonal damage during glutamate excitotoxicity. *J. Neurochem.* 111, 870–881. doi: 10.1111/j.1471-4159.2009.06375.x

Hou, S. T., Jiang, S. X., Desbois, A., Huang, D., Kelly, J., Tessier, L., et al. (2006). Calpain-cleaved collapsin response mediator protein-3 induces neuronal death after glutamate toxicity and cerebral ischemia. *J. Neurosci.* 26, 2241–2249. doi: 10.1523/JNEUROSCI.4485-05.2006

Ito, Y., Oinuma, I., Katoh, H., Kaibuchi, K., and Negishi, M. (2006). Sema4D/plexin-B1 activates GSK-3β through R-Ras GAP activity, inducing growth cone collapse. *EMBO Rep.* 7, 704–709. doi: 10.1038/sj.embor.7400737

Jayasena, C. S., Flood, W. D., and Koblar, S. A. (2005). High EphA3 expressing ophthalmic trigeminal sensory axons are sensitive to ephrin-A5-Fc: implications for lobe specific axon guidance. *Neuroscience* 135, 97–109. doi: 10.1016/j.neuroscience.2005.05.052

Jiang, S. X., Kappler, J., Zurakowski, B., Desbois, A., Aylsworth, A., and Hou, S. T. (2007). Calpain cleavage of collapsin response mediator proteins in ischemic mouse brain. *Eur. J. Neurosci.* 26, 801–809. doi: 10.1111/j.1460-9568.2007.05715.x

Ju, W., Li, Q., Wilson, S. M., Brittain, J. M., Meroueh, L., and Khanna, R. (2013). SUMOylation alters CRMP2 regulation of calcium influx in sensory neurons. *Channels* 7, 153–159. doi: 10.4161/chan.24224

Kadoyama, K., Matsuura, K., Nakamura-Hirota, T., Takano, M., Otani, M., and Matsuyama, S. (2015). Changes in the expression of collapsin response mediator protein-2 during synaptic plasticity in the mouse hippocampus. *J. Neurosci. Res.* 93, 1684–1692. doi: 10.1002/jnr.23626

Kaneko, S., Iwanami, A., Nakamura, M., Kishino, A., Kikuchi, K., Shibata, S., et al. (2006). A selective Sema3A inhibitor enhances regenerative responses and functional recovery of the injured spinal cord. *Nat. Med.* 12, 1380–1389. doi: 10.1038/nm1505

Khazaei, M. R., Girouard, M. P., Alchini, R., Ong Tone, S., Shimada, T., Bechstedt, S., et al. (2014). Collapsin response mediator protein 4 regulates growth cone dynamics through the actin and microtubule cytoskeleton. *J. Biol. Chem.* 289, 30133–30143. doi: 10.1074/jbc.m114.570440

Kimura, T., Watanabe, H., Iwamatsu, A., and Kaibuchi, K. (2005). Tubulin and CRMP-2 complex is transported *via* Kinesin-1. *J. Neurochem.* 93, 1371–1382. doi: 10.1111/j.1471-4159.2005.03063.x

Kinoshita, Y., Kondo, S., Takahashi, K., Nagai, J., Wakatsuki, S., Araki, T., et al. (2019). Genetic inhibition of CRMP2 phosphorylation delays Wallerian degeneration after optic nerve injury. *Biochem. Biophys. Res. Commun.* 514, 1037–1039. doi: 10.1016/j.bbrc.2019.05.060

Kondo, S., Takahashi, K., Kinoshita, Y., Nagai, J., Wakatsuki, S., Araki, T., et al. (2019). Genetic inhibition of CRMP2 phosphorylation at serine 522 promotes axonal regeneration after optic nerve injury. *Sci. Rep.* 9:7188. doi: 10.1038/s41598-019-43658-w

Kotaka, K., Nagai, J., Hensley, K., and Ohshima, T. (2017). Lanthionine ketimine ester promotes locomotor recovery after spinal cord injury by reducing neuroinflammation and promoting axon growth. *Biochem. Biophys. Res. Commun.* 483, 759–764. doi: 10.1016/j.bbrc.2016.12.069

Kowara, R., Chen, Q., Milliken, M., and Chakravarthy, B. (2005). Calpain-mediated truncation of dihydropyrimidinase-like 3 protein (DPYSL3) in response to NMDA and H2O2 toxicity. *J. Neurochem.* 95, 466–474. doi: 10.1111/j.1471-4159.2005.03383.x

Kubilus, J. K., and Linsenmayer, T. F. (2010). Developmental corneal innervation: interactions between nerves and specialized apical corneal epithelial cells. *Invest. Ophthalmol. Vis. Sci.* 51, 782–789. doi: 10.1167/iovs.09-3942

Lawal, M. F., Olotu, F. A., Agoni, C., and Soliman, M. E. (2018). Exploring the C-terminal tail dynamics: structural and molecular perspectives into the therapeutic activities of novel CRMP-2 inhibitors, naringenin and naringenin-7-O-glucuronide, in the treatment of Alzheimer's disease. *Chem. Biodivers* 15:e1800437. doi: 10.1002/cbdv.201800437

Lee, J. Y., Kim, M. J., Thomas, S., Oorschot, V., Ramm, G., Aui, P. M., et al. (2019). Limiting neuronal nogo receptor 1 signaling during experimental autoimmune encephalomyelitis preserves axonal transport and abrogates inflammatory demyelination. *J. Neurosci.* 39, 5562–5580. doi: 10.1523/JNEUROSCI.1760-18.2019

Leibinger, M., Andreadaki, A., Golla, R., Levin, E., Hilla, A. M., Diekmann, H., et al. (2017). Boosting CNS axon regeneration by harnessing antagonistic

effects of GSK3 activity. *Proc. Natl. Acad. Sci. U S A* 114, E5454–E5463. doi: 10.1073/pnas.1621225114

Leung, T., Ng, Y., Cheong, A., Ng, C. H., Tan, I., Hall, C., et al. (2002). p80 ROKα binding protein is a novel splice variant of CRMP-1 which associates with CRMP-2 and modulates RhoA-induced neuronal morphology. *FEBS Lett.* 532, 445–449. doi: 10.1016/s0014-5793(02)03736-5

Lin, P. C., Chan, P. M., Hall, C., and Manser, E. (2011). Collapsin response mediator proteins (CRMPs) are a new class of microtubule-associated protein (MAP) that selectively interacts with assembled microtubules *via* a taxol-sensitive binding interaction. *J. Biol. Chem.* 286, 41466–41478. doi: 10.1074/jbc.m111.283580

Makihara, H., Nakai, S., Ohkubo, W., Yamashita, N., Nakamura, F., Kiyonari, H., et al. (2016). CRMP1 and CRMP2 have synergistic but distinct roles in dendritic development. *Genes Cells* 21, 994–1005. doi: 10.1111/gtc.12399

Manivannan, J., Tay, S. S., Ling, E. A., and Dheen, S. T. (2013). Dihydropyrimidinase-like 3 regulates the inflammatory response of activated microglia. *Neuroscience* 253, 40–54. doi: 10.1016/j.neuroscience.2013.08.023

Mimura, F., Yamagishi, S., Arimura, N., Fujitani, M., Kubo, T., Kaibuchi, K., et al. (2006). Myelin-associated glycoprotein inhibits microtubule assembly by a Rho-kinase-dependent mechanism. *J. Biol. Chem.* 281, 15970–15979. doi: 10.1074/jbc.m510934200

Morinaka, A., Yamada, M., Itofusa, R., Funato, Y., Yoshimura, Y., Nakamura, F., et al. (2011). Thioredoxin mediates oxidation-dependent phosphorylation of CRMP2 and growth cone collapse. *Sci. Signal.* 4:ra26. doi: 10.1126/scisignal.2001127

Moutal, A., Kalinin, S., Kowal, K., Marangoni, N., Dupree, J., Lin, S. X., et al. (2019). Neuronal conditional knockout of collapsin response mediator protein 2 ameliorates disease severity in a mouse model of multiple sclerosis. *ASN Neuro* 11:1759091419892090. doi: 10.1177/1759091419892090

Nagai, J., Baba, R., and Ohshima, T. (2017). CRMPs function in neurons and glial cells: potential therapeutic targets for neurodegenerative diseases and CNS injury. *Mol. Neurobiol.* 54, 4243–4256. doi: 10.1007/s12035-016-0005-1

Nagai, J., Kitamura, Y., Owada, K., Yamashita, N., Takei, K., Goshima, Y., et al. (2015). Crmp4 deletion promotes recovery from spinal cord injury by neuroprotection and limited scar formation. *Sci. Rep.* 5:8269. doi: 10.1038/srep08269

Nagai, J., Takaya, R., Piao, W., Goshima, Y., and Ohshima, T. (2016). Deletion of Crmp4 attenuates CSPG-induced inhibition of axonal growth and induces nociceptive recovery after spinal cord injury. *Mol. Cell. Neurosci.* 74, 42–48. doi: 10.1016/j.mcn.2016.03.006

Nakamura, F., Kalb, R. G., and Strittmatter, S. M. (2000). Molecular basis of semaphorin-mediated axon guidance. *J. Neurobiol.* 44, 219–229. doi: 10.1002/1097-4695(200008)44:2<219::aid-neu11>3.0.co;2-w

Nakamura, F., Kumeta, K., Hida, T., Isono, T., Nakayama, Y., Kuramata-Matsuoka, E., et al. (2014). Amino- and carboxyl-terminal domains of Filamin-A interact with CRMP1 to mediate Sema3A signalling. *Nat. Commun.* 5:5325. doi: 10.1038/ncomms6325

Nakashima, H., Tsujimura, K., Irie, K., Ishizu, M., Pan, M., Kameda, T., et al. (2018). Canonical TGF-β signaling negatively regulates neuronal morphogenesis through TGIF/smad complex-mediated CRMP2 suppression. *J. Neurosci.* 38, 4791–4810. doi: 10.1523/JNEUROSCI.2423-17.2018

Niranjan, R. (2014). The role of inflammatory and oxidative stress mechanisms in the pathogenesis of Parkinson's disease: focus on astrocytes. *Mol. Neurobiol.* 49, 28–38. doi: 10.1007/s12035-013-8483-x

Nishimura, T., Fukata, Y., Kato, K., Yamaguchi, T., Matsuura, Y., Kamiguchi, H., et al. (2003). CRMP-2 regulates polarized Numb-mediated endocytosis for axon growth. *Nat. Cell Biol.* 5, 819–826. doi: 10.1038/ncb1039

Niwa, S., Nakamura, F., Tomabechi, Y., Aoki, M., Shigematsu, H., Matsumoto, T., et al. (2017). Structural basis for CRMP2-induced axonal microtubule formation. *Sci. Rep.* 7:10681. doi: 10.1038/s41598-017-11031-4

Numata-Uematsu, Y., Wakatsuki, S., Nagano, S., Shibata, M., Sakai, K., Ichinohe, N., et al. (2019). Inhibition of collapsin response mediator protein-2 phosphorylation ameliorates motor phenotype of ALS model mice expressing SOD1G93A. *Neurosci. Res.* 139, 63–68. doi: 10.1016/j.neures.2018.08.016

Pan, S. H., Chao, Y. C., Hung, P. F., Chen, H. Y., Yang, S. C., Chang, Y. L., et al. (2011). The ability of LCRMP-1 to promote cancer invasion by enhancing filopodia formation is antagonized by CRMP-1. *J. Clin. Invest.* 121, 3189–3205. doi: 10.1172/jci42975

Park, H. Y., Kim, G. Y., and Choi, Y. H. (2012). Naringenin attenuates the release of pro-inflammatory mediators from lipopolysaccharide-stimulated BV2 microglia by inactivating nuclear factor-kappaB and inhibiting mitogen-activated protein kinases. *Int. J. Mol. Med.* 30, 204–210. doi: 10.3892/ijmm.2012.979

Petratos, S., Ozturk, E., Azari, M. F., Kenny, R., Lee, J. Y., Magee, K. A., et al. (2012). Limiting multiple sclerosis related axonopathy by blocking Nogo receptor and CRMP-2 phosphorylation. *Brain* 135, 1794–1818. doi: 10.1093/brain/aws100

Ponnusamy, R., Lebedev, A. A., Pahlow, S., and Lohkamp, B. (2014). Crystal structure of human CRMP-4: correction of intensities for lattice-translocation disorder. *Acta Crystallogr. D Biol. Crystallogr.* 70, 1680–1694. doi: 10.1107/S1399004714006634

Ponnusamy, R., and Lohkamp, B. (2013). Insights into the oligomerization of CRMPs: crystal structure of human collapsin response mediator protein 5. *J. Neurochem.* 125, 855–868. doi: 10.1111/jnc.12188

Quach, T. T., Honnorat, J., Kolattukudy, P. E., Khanna, R., and Duchemin, A. M. (2015). CRMPs: critical molecules for neurite morphogenesis and neuropsychiatric diseases. *Mol. Psychiatry* 20, 1037–1045. doi: 10.1038/mp.2015.77

Quach, T. T., Wilson, S. M., Rogemond, V., Chounlamountri, N., Kolattukudy, P. E., Martinez, S., et al. (2013). Mapping CRMP3 domains involved in dendrite morphogenesis and voltage-gated calcium channel regulation. *J. Cell Sci.* 126, 4262–4273. doi: 10.1242/jcs.131409

Renault-Mihara, F., Katoh, H., Ikegami, T., Iwanami, A., Mukaino, M., Yasuda, A., et al. (2011). Beneficial compaction of spinal cord lesion by migrating astrocytes through glycogen synthase kinase-3 inhibition. *EMBO Mol. Med.* 3, 682–696. doi: 10.1002/emmm.201100179

Rogemond, V., Auger, C., Giraudon, P., Becchi, M., Auvergnon, N., Belin, M. F., et al. (2008). Processing and nuclear localization of CRMP2 during brain development induce neurite outgrowth inhibition. *J. Biol. Chem.* 283, 14751–14761. doi: 10.1074/jbc.m708480200

Rosslenbroich, V., Dai, L., Baader, S. L., Noegel, A. A., Gieselmann, V., and Kappler, J. (2005). Collapsin response mediator protein-4 regulates F-actin bundling. *Exp. Cell Res.* 310, 434–444. doi: 10.1016/j.yexcr.2005.08.005

Sahay, A., Molliver, M. E., Ginty, D. D., and Kolodkin, A. L. (2003). Semaphorin 3F is critical for development of limbic system circuitry and is required in neurons for selective CNS axon guidance events. *J. Neurosci.* 23, 6671–6680. doi: 10.1523/JNEUROSCI.23-17-06671.2003

Schmidt, E. F., Shim, S. O., and Strittmatter, S. M. (2008). Release of MICAL autoinhibition by semaphorin-plexin signaling promotes interaction with collapsin response mediator protein. *J. Neurosci.* 28, 2287–2297. doi: 10.1523/JNEUROSCI.5646-07.2008

Schmidt, E. F., and Strittmatter, S. M. (2007). The CRMP family of proteins and their role in Sema3A signaling. *Adv. Exp. Med. Biol.* 600, 1–11. doi: 10.1007/978-0-387-70956-7_1

Sekine, Y., Algarate, P. T., Cafferty, W. B. J., and Strittmatter, S. M. (2019). Plexina2 and CRMP2 signaling complex is activated by Nogo-A-liganded Ngr1 to restrict corticospinal axon sprouting after trauma. *J. Neurosci.* 39, 3204–3216. doi: 10.1523/JNEUROSCI.2996-18.2019

Smith, P. D., Crocker, S. J., Jackson-Lewis, V., Jordan-Sciutto, K. L., Hayley, S., Mount, M. P., et al. (2003). Cyclin-dependent kinase 5 is a mediator of dopaminergic neuron loss in a mouse model of Parkinson's disease. *Proc. Natl. Acad. Sci. U S A* 100, 13650–13655. doi: 10.1073/pnas.2232515100

Stenmark, P., Ogg, D., Flodin, S., Flores, A., Kotenyova, T., Nyman, T., et al. (2007). The structure of human collapsin response mediator protein 2, a regulator of axonal growth. *J. Neurochem.* 101, 906–917. doi: 10.1111/j.1471-4159.2006.04401.x

Sumi, T., Imasaki, T., Aoki, M., Sakai, N., Nitta, E., Shirouzu, M., et al. (2018). Structural insights into the altering function of CRMP2 by phosphorylation. *Cell Struct. Funct.* 43, 15–23. doi: 10.1247/csf.17025

Sun, Y., Fei, T., Yang, T., Zhang, F., Chen, Y. G., Li, H., et al. (2010). The suppression of CRMP2 expression by bone morphogenetic protein (BMP)-SMAD gradient signaling controls multiple stages of neuronal development. *J. Biol. Chem.* 285, 39039–39050. doi: 10.1074/jbc.m110.168351

Suzuki, Y., Nakagomi, S., Namikawa, K., Kiryu-Seo, S., Inagaki, N., Kaibuchi, K., et al. (2003). Collapsin response mediator protein-2 accelerates axon regeneration of nerve-injured motor neurons of rat. *J. Neurochem.* 86, 1042–1050. doi: 10.1046/j.1471-4159.2003.01920.x

Tan, C. L., Kwok, J. C., Patani, R., Ffrench-Constant, C., Chandran, S., and Fawcett, J. W. (2011). Integrin activation promotes axon growth on inhibitory chondroitin sulfate proteoglycans by enhancing integrin signaling. *J. Neurosci.* 31, 6289–6295. doi: 10.1523/JNEUROSCI.0008-11.2011

Taniguchi, M., Yuasa, S., Fujisawa, H., Naruse, I., Saga, S., Mishina, M., et al. (1997). Disruption of semaphorin III/D gene causes severe abnormality in peripheral nerve projection. *Neuron* 19, 519–530. doi: 10.1016/s0896-6273(00)80368-2

Terman, J. R., Mao, T., Pasterkamp, R. J., Yu, H. H., and Kolodkin, A. L. (2002). MICALs, a family of conserved flavoprotein oxidoreductases, function in plexin-mediated axonal repulsion. *Cell* 109, 887–900. doi: 10.1016/s0092-8674(02)00794-8

Tobe, B. T. D., Crain, A. M., Winquist, A. M., Calabrese, B., Makihara, H., Zhao, W. N., et al. (2017). Probing the lithium-response pathway in hiPSCs implicates the phosphoregulatory set-point for a cytoskeletal modulator in bipolar pathogenesis. *Proc. Natl. Acad. Sci. U S A* 114, E4462–E4471. doi: 10.1073/pnas.1700111114

Togashi, K., Hasegawa, M., Nagai, J., Tonouchi, A., Masukawa, D., Hensley, K., et al. (2019). Genetic suppression of collapsin response mediator protein 2 phosphorylation improves outcome in methyl-4-phenyl-1,2,3,6-tetrahydropyridine-induced Parkinson's model mice. *Genes Cells* 24, 31–40. doi: 10.1111/gtc.12651

Tonouchi, A., Nagai, J., Togashi, K., Goshima, Y., and Ohshima, T. (2016). Loss of collapsin response mediator protein 4 suppresses dopaminergic neuron death in an 1-methyl-4-phenyl-1,2,3,6-tetrahydropyridine-induced mouse model of Parkinson's disease. *J. Neurochem.* 137, 795–805. doi: 10.1111/jnc.13617

Tsutiya, A., Nakano, Y., Hansen-Kiss, E., Kelly, B., Nishihara, M., Goshima, Y., et al. (2017). Human CRMP4 mutation and disrupted Crmp4 expression in mice are associated with ASD characteristics and sexual dimorphism. *Sci. Rep.* 7:16812. doi: 10.1038/s41598-017-16782-8

Uchida, Y., Ohshima, T., Yamashita, N., Ogawara, M., Sasaki, Y., Nakamura, F., et al. (2009). Semaphorin3A signaling mediated by Fyn-dependent tyrosine phosphorylation of collapsin response mediator protein 2 at tyrosine 32. *J. Biol. Chem.* 284, 27393–27401. doi: 10.1074/jbc.m109.000240

Varrin-Doyer, M., Vincent, P., Cavagna, S., Auvergnon, N., Noraz, N., Rogemond, V., et al. (2009). Phosphorylation of collapsin response mediator protein 2 on Tyr-479 regulates CXCL12-induced T lymphocyte migration. *J. Biol. Chem.* 284, 13265–13276. doi: 10.1074/jbc.M807664200

Vincent, P., Collette, Y., Marignier, R., Vuaillat, C., Rogemond, V., Davoust, N., et al. (2005). A role for the neuronal protein collapsin response mediator protein 2 in T lymphocyte polarization and migration. *J. Immunol.* 175, 7650–7660. doi: 10.4049/jimmunol.175.11.7650

Wakatsuki, S., Saitoh, F., and Araki, T. (2011). ZNRF1 promotes Wallerian degeneration by degrading AKT to induce GSK3B-dependent CRMP2 phosphorylation. *Nat. Cell Biol.* 13, 1415–1423. doi: 10.1038/ncb2373

Wang, L. H., and Strittmatter, S. M. (1996). A family of rat CRMP genes is differentially expressed in the nervous system. *J. Neurosci.* 16, 6197–6207. doi: 10.1523/JNEUROSCI.16-19-06197.1996

Wang, T., Wu, X., Yin, C., Klebe, D., Zhang, J. H., and Qin, X. (2013). CRMP-2 is involved in axon growth inhibition induced by RGMa *in vitro* and *in vivo*. *Mol. Neurobiol.* 47, 903–913. doi: 10.1007/s12035-012-8385-3

Wilson, S. M., Moutal, A., Melemedjian, O. K., Wang, Y., Ju, W., Francois-Moutal, L., et al. (2014). The functionalized amino acid (S)-Lacosamide subverts CRMP2-mediated tubulin polymerization to prevent constitutive and activity-dependent increase in neurite outgrowth. *Front. Cell. Neurosci.* 8:196. doi: 10.3389/fncel.2014.00196

Wilson, S. M., Xiong, W., Wang, Y., Ping, X., Head, J. D., Brittain, J. M., et al. (2012). Prevention of posttraumatic axon sprouting by blocking collapsin response mediator protein 2-mediated neurite outgrowth and tubulin polymerization. *Neuroscience* 210, 451–466. doi: 10.1016/j.neuroscience.2012.02.038

Wu, L. H., Lin, C., Lin, H. Y., Liu, Y. S., Wu, C. Y., Tsai, C. F., et al. (2016). Naringenin suppresses neuroinflammatory responses through inducing suppressor of cytokine signaling 3 expression. *Mol. Neurobiol.* 53, 1080–1091. doi: 10.1007/s12035-014-9042-9

Yamamoto, T., Setsu, T., Okuyama-Yamamoto, A., and Terashima, T. (2009). Histological study in the brain of the reelin/Dab1-compound mutant mouse. *Anat. Sci. Int.* 84, 200–209. doi: 10.1007/s12565-008-0009-7

Yamane, M., Yamashita, N., Hida, T., Kamiya, Y., Nakamura, F., Kolattukudy, P., et al. (2017). A functional coupling between CRMP1 and Nav1.7 for retrograde propagation of Semaphorin3A signaling. *J. Cell Sci.* 130, 1393–1403. doi: 10.1242/jcs.199737

Yamashita, N., and Goshima, Y. (2012). Collapsin response mediator proteins regulate neuronal development and plasticity by switching their phosphorylation status. *Mol. Neurobiol.* 45, 234–246. doi: 10.1007/s12035-012-8242-4

Yamashita, N., Mosinger, B., Roy, A., Miyazaki, M., Ugajin, K., Nakamura, F., et al. (2011). CRMP5 (collapsin response mediator protein 5) regulates dendritic development and synaptic plasticity in the cerebellar Purkinje cells. *J. Neurosci.* 31, 1773–1779. doi: 10.1523/JNEUROSCI.5337-10.2011

Yamashita, N., Ohshima, T., Nakamura, F., Kolattukudy, P., Honnorat, J., Mikoshiba, K., et al. (2012). Phosphorylation of CRMP2 (collapsin response mediator protein 2) is involved in proper dendritic field organization. *J. Neurosci.* 32, 1360–1365. doi: 10.1523/JNEUROSCI.5563-11.2012

Yamashita, N., Uchida, Y., Ohshima, T., Hirai, S., Nakamura, F., Taniguchi, M., et al. (2006). Collapsin response mediator protein 1 mediates reelin signaling in cortical neuronal migration. *J. Neurosci.* 26, 13357–13362. doi: 10.1523/JNEUROSCI.4276-06.2006

Yang, X., Zhang, X., Li, Y., Han, S., Howells, D. W., Li, S., et al. (2016). Conventional protein kinase Cβ-mediated phosphorylation inhibits collapsin response-mediated protein 2 proteolysis and alleviates ischemic injury in cultured cortical neurons and ischemic stroke-induced mice. *J. Neurochem.* 137, 446–459. doi: 10.1111/jnc.13538

Yoshimura, T., Kawano, Y., Arimura, N., Kawabata, S., Kikuchi, A., and Kaibuchi, K. (2005). GSK-3β regulates phosphorylation of CRMP-2 and neuronal polarity. *Cell* 120, 137–149. doi: 10.1016/j.cell.2004.11.012

Yu-Kemp, H. C., Kemp, J. P. Jr., and Brieher, W. M. (2017). CRMP-1 enhances EVL-mediated actin elongation to build lamellipodia and the actin cortex. *J. Cell Biol.* 216, 2463–2479. doi: 10.1083/jcb.201606084

Zhang, J., Zhao, B., Zhu, X., Li, J., Wu, F., Li, S., et al. (2018). Phosphorylation and SUMOylation of CRMP2 regulate the formation and maturation of dendritic spines. *Brain Res. Bull.* 139, 21–30. doi: 10.1016/j.brainresbull.2018.02.004

Zheng, Y., Sethi, R., Mangala, L. S., Taylor, C., Goldsmith, J., Wang, M., et al. (2018). Tuning microtubule dynamics to enhance cancer therapy by modulating FER-mediated CRMP2 phosphorylation. *Nat. Commun.* 9:476. doi: 10.1038/s41467-017-02811-7

Zhu, L. Q., Zheng, H. Y., Peng, C. X., Liu, D., Li, H. L., Wang, Q., et al. (2010). Protein phosphatase 2A facilitates axonogenesis by dephosphorylating CRMP2. *J. Neurosci.* 30, 3839–3848. doi: 10.1523/JNEUROSCI.5174-09.2010

Ziak, J., Weissova, R., Jeřábková, K., Janikova, M., Maimon, R., Petrasek, T., et al. (2020). CRMP2 mediates Sema3F-dependent axon pruning and dendritic spine remodeling. *EMBO Rep.* 21:e48512. doi: 10.15252/embr.201948512

Conflict of Interest: The authors declare that the research was conducted in the absence of any commercial or financial relationships that could be construed as a potential conflict of interest.

frontiers in Cellular Neuroscience

METHODS
published: 29 July 2020
doi: 10.3389/fncel.2020.00225

The Mouse *Levator Auris Longus* Muscle: An Amenable Model System to Study the Role of Postsynaptic Proteins to the Maintenance and Regeneration of the Neuromuscular Synapse

*Jorge Ojeda[1,2,3†], Francisca Bermedo-García[1†], Viviana Pérez[1], Jessica Mella[1], Patricia Hanna[1], Daniel Herzberg[4], Rocío Tejero[2], Mario López-Manzaneda[2], Lucia Tabares[2] and Juan Pablo Henríquez[1]**

[1]Neuromuscular Studies Laboratory (NeSt Lab), Department of Cell Biology, Faculty of Biological Sciences, Center for Advanced Microscopy (CMA BioBio), Universidad de Concepción, Concepción, Chile, [2]Department of Medical Physiology and Biophysics, School of Medicine, Universidad de Sevilla, Sevilla, Spain, [3]Developmental Neurobiology Unit, Biomedical Sciences Research Laboratory, Basic Sciences Department, Faculty of Medicine, Universidad Católica de la Santísima Concepción, Concepción, Chile, [4]Veterinary Sciences Clinic, Universidad de Concepción, Concepción, Chile

The neuromuscular junction (NMJ) is the peripheral synapse that controls the coordinated movement of many organisms. The NMJ is also an archetypical model to study synaptic morphology and function. As the NMJ is the primary target of neuromuscular diseases and traumatic injuries, the establishment of suitable models to study the contribution of specific postsynaptic muscle-derived proteins on NMJ maintenance and regeneration is a permanent need. Considering the unique experimental advantages of the *levator auris longus* (LAL) muscle, here we present a method allowing for efficient electroporation-mediated gene transfer and subsequent detailed studies of the morphology and function of the NMJ and muscle fibers. Also, we have standardized efficient facial nerve injury protocols to analyze LAL muscle NMJ degeneration and regeneration. Our results show that the expression of a control fluorescent protein does not alter either the muscle structural organization, the apposition of the pre- and post-synaptic domains, or the functional neurotransmission parameters of the LAL muscle NMJs; in turn, the overexpression of MuSK, a major regulator of postsynaptic assembly, induces the formation of ectopic acetylcholine receptor clusters. Our NMJ denervation experiments showed complete reinnervation of LAL muscle NMJs four weeks after facial nerve injury. Together, these experimental strategies in the LAL muscle constitute effective methods to combine protein expression with accurate analyses at the levels of structure, function, and regeneration of the NMJ.

Keywords: neuromuscular junction, presynaptic, postsynaptic, regeneration, electroporation, skeletal muscle

OPEN ACCESS

Edited by:
Thomas Fath,
Macquarie University, Australia

Reviewed by:
James N. Sleigh,
University College London, United Kingdom
Timothy Mosca,
Thomas Jefferson University, United States

****Correspondence:***
Juan Pablo Henríquez
jhenriquez@udec.cl

†These authors have contributed equally to this work

Specialty section:
This article was submitted to Cellular Neuropathology, a section of the journal Frontiers in Cellular Neuroscience

Received: *17 May 2020*
Accepted: *26 June 2020*
Published: *29 July 2020*

Citation:
Ojeda J, Bermedo-García F, Pérez V, Mella J, Hanna P, Herzberg D, Tejero R, López-Manzaneda M, Tabares L and Henríquez JP (2020) The Mouse Levator Auris Longus Muscle: An Amenable Model System to Study the Role of Postsynaptic Proteins to the Maintenance and Regeneration of the Neuromuscular Synapse. Front. Cell. Neurosci. 14:225. doi: 10.3389/fncel.2020.00225

INTRODUCTION

The vertebrate neuromuscular junction (NMJ) is a peripheral cholinergic synapse formed by a motor axon terminal, a specialized acetylcholine receptor (AChR)-enriched fraction of the muscle membrane, and terminal Schwann cells. The NMJ displays a high degree of subcellular specialization, large size, and easy experimental access, features that have significantly contributed to uncovering the principles of synaptic formation, growth, maturation, and maintenance *in vivo* (Sanes and Lichtman, 2001). Indeed, the ultrastructure of synaptic architecture and the principles of synaptic transmission were first characterized at the frog NMJ (Birks et al., 1960; Katz and Miledi, 1969; Katz, 1971).

To achieve its mature, complex shape, the NMJ undergoes drastic modifications during early postnatal development. At the muscle membrane, initial small "plaque"-like uniform AChR densities are sequentially transformed into bigger elaborate branches with a "pretzel"-like shape (Sanes and Lichtman, 2001; Shi et al., 2012). These morphological changes are closely associated with NMJ function. For instance, immature NMJs have lower amplitude evoked endplate potentials (EPPs), lower quantal content, and higher latency than mature NMJs (Bewick et al., 2004; Cano et al., 2013).

Severe motor pathologies and traumatic nerve injuries cause NMJ dysfunction (Moloney et al., 2014; Ko and Robitaille, 2015; Martineau et al., 2018). Upon NMJ denervation, the postsynaptic apparatus displays a remarkable maintenance ability, which, within a discrete time frame, allows successful functional regeneration (Sakuma et al., 2016). Even though muscle proteins, including local intracellular effectors and extracellular components, are thought to regulate the stability of AChR clusters after denervation (Bloch-Gallego, 2015), the identity and contribution of muscle-derived molecular mechanisms helping the maintenance of postsynaptic structures are still to be fully elucidated.

The *levator auris longus* (LAL) muscle offers unique experimental advantages to study the neuromuscular synapse. It is a superficially exposed muscle, which facilitates genetic modulation of post- and trans-synaptic proteins expression, drug delivery approaches, and *in vivo* time-lapse imaging to reinvestigate the same NMJs over time. The LAL is a mainly fast-twitch muscle that functions to move the pinna. It is constituted by flat and thin rostral and caudal portions, each having two to three muscle fiber layers, localized in the dorsal surface of the skull (Erzen et al., 2000; Murray et al., 2010a; Wright et al., 2011). It is innervated by a posterior auricular branch of the facial nerve, thus generating a well-described pattern of five different rostrals (R1–R5) and two caudal (C1–C2) innervation zones (Murray et al., 2008, 2010b). Together, these features have facilitated NMJ morphological studies (Angaut-Petit et al., 1987; Murray et al., 2008; Klooster et al., 2012). The LAL muscle has also been extensively employed for electrophysiological recording in *ex vivo* nerve/muscle preparations (Katz et al., 1996; Ruiz et al., 2010; Burke et al., 2018).

In this work, we extend the convenience of the LAL muscle through efficient electroporation-mediated gene transfer and integrative morpho-functional analysis of the NMJ. Also, we have standardized nerve injury protocols to analyze NMJ regeneration. Together, these experimental strategies represent accessible *in vivo* screening methods to analyze the contribution of muscle proteins on NMJ morphology, function and regeneration.

MATERIALS AND METHODS

Animals

Experimental procedures were approved by the Bioethics Committee at Universidad de Concepción, Chile, and followed the norms imposed by the Bioethics Committee of the National Commission for Scientific and Technological Research, Chile (CONICYT), as well as the guidelines of the European Council Directive for the Care of Laboratory Animals. Experimental procedures were conducted in P21 or adult male mice under sedation (2.5% Isofluorane with a 0.8–1 l/min oxygen mixture). Before LAL muscle dissection, animals were euthanized by an overdose of isofluorane or carbon dioxide.

In vivo Muscle Electroporation

LAL muscles from P21 or adult mice were electroporated following a method described for limb muscles, with minor modifications (DiFranco et al., 2009). The control DNA used through these studies was tdTomato-N1 (a gift from Michael Davidson, Nathan Shaner, and Roger Tsien; Addgene plasmid # 54642). To induce MuSK overexpression, we used the pBK-CMV-Δlac-rMuSK plasmid, which contains the exact coding sequence of rat MuSK (GenBank sequence accession number U34985, except for the 10 amino acid insert in the first splice site between E209 and V210; a kind gift of Dr. Jonathan B. Cohen, Harvard Medical School, MA, USA) fused to the myc tag sequence (rMuSK-myc; Bianchetta et al., 2005). We also used the MuSK-EGFP plasmid, which contains the full-length mouse MuSK coding sequence (a kind gift of Dr. William D. Phillips, University of Sydney, Camperdown, NSW, Australia; Ghazanfari et al., 2015). Plasmid DNAs were purified according to the Qiagen Maxiprep protocol following the instructions of the manufacturer. To facilitate the DNA plasmid access to the muscle surface, 10 μl of a 2 mg/ml solution of hyaluronidase (ref. H3884, Sigma-Aldrich) were applied under sedation by a subcutaneous injection using a Hamilton syringe (McMahon et al., 2001). After 1 h, mice were re-anesthetized and a 5–10 mm surgical skin incision was performed at the level of skull sagittal suture to expose the LAL muscles. Then, different amounts of total plasmid DNA coding for tdTomato or EGFP (controls), or rMuSK-myc or MuSK-EGFP in a final volume of 10 μl in 0.01 M PBS were injected just underneath the muscle fascia forming a bubble. The pBK-CMV-Δlac-rMuSK plasmid was co-electroporated along with the tdTomato-N1 plasmid in a 5:1 ratio. For the DNA electrotransfer procedure, two gold needle-type electrodes (Genetrodes, BTX Harvard Apparatus, Holliston, MA, USA) separated by 5 mm were positioned on the entire transversal length of the LAL muscle to deliver

five pulses of 100 V/cm of 20 ms duration at 1 Hz using an ECM 830 electroporator (BTX Harvard Apparatus). This procedure was repeated in the contralateral Hemi-LAL muscle. Finally, the skin was sutured using absorbable monofilament surgical suture (Ethicon Vicryl USP 6–0) and animals were monitored until their recovery.

Facial Nerve Injury

Facial nerve injuries were performed as described (Olmstead et al., 2015) with some modifications. Briefly, adult animals were anesthetized by isofluorane inhalation, as described above, and after shaving the right ear posterior region, a surgical 5 mm skin incision was performed to expose the facial nerve branches. The most dorsal branch of the facial nerve innervating the LAL muscles was carefully cleared avoiding direct manipulation. In the NMJ degeneration protocol, a section of 4 mm of the facial nerve branch was transected; in turn, for the reinnervation protocol, the facial nerve branch was crushed for 30 s using Dumont #5/45 forceps (Fine Science Tools). Control experiments only considered skin incision and facial nerve exposure. Finally, the skin was sutured using absorbable monofilament surgical suture (Ethicon Vicryl USP 6–0) and animals were monitored until their recovery.

Muscle Histology Analyses

At the indicated times after electroporation, mice were euthanized and the LAL muscles were dissected, fixed in 0.5% formaldehyde in 0.01 M PBS at 22°C for 90 min and embedded in optimal cutting temperature (OCT) compound (Sakura Fine Technical Company, Torrance, CA, USA). Samples were sectioned every 20 μm with a cryostat (Thermo Scientific Microm HM 525) and mounted on Vectabond (Vector Laboratories, Burlingame, CA, USA) coated slides. Muscle fiber morphology was analyzed through conventional hematoxylin/chromotrope staining (Woehlbier et al., 2016). Cryosections were also stained with an NADH reduced solution (Tris-buffer, pH 7.4, NADH reduced, nitro-blue tetrazolium; Sigma Aldrich, St. Louis, MO, USA) for 45 min, and fibers were classified into oxidative (dark blue) or non-oxidative (light blue). The identity of all muscle fibers contained within the Hemi-LAL muscles and the cross-sectional area (CSA) of >100 fibers per type in each Hemi-LAL were determined using the ImageJ software. To reveal the muscle membrane and nuclei, cryosections were stained with the wheat germ agglutinin lectin (WGA, Molecular Probes, Waltham, MA, USA (1 μg/ml) conjugated to Alexa488) plus DAPI (1 μg/ml), respectively, during 10 min (Woehlbier et al., 2016).

NMJ Staining, Imaging, and Analyses

Whole-mounted LAL muscles were fixed as described (Pérez-Garcia and Burden, 2012). After washing with 0.01 M PBS/0.5% v/v Triton X-100 for 2 h, samples were incubated with 0.1 M glycine in PBS for 30 min. Blocking was performed with 4% BSA dissolved in PBS/0.5% Triton X-100. Primary antibodies against neurofilaments (2H3, 1:300) plus synaptic vesicles (SV2, 1:200; both form the Developmental Studies Hybridoma Bank, DSHB, Department of Biology, University of Iowa, IA, USA) were incubated overnight in blocking solution (PBS/0.5% Triton X-100/4% BSA). After washing, samples were incubated with the secondary antibodies (Cy2 1:250; Donkey H + L, Jackson Immunoresearch Laboratories, West Grove, PA, USA) along with Alexa647- or Alexa488-conjugated α-bungarotoxin (αBTX, Molecular Probes; 1:500) overnight at 4°C, and subsequently mounted between two coverslips in DAKO fluorescence medium.

Images were acquired using an inverted Zeiss LSM 780 multiphoton or an LSM 700 laser scanning confocal microscope (CMA BioBio, Universidad de Concepción, Concepción, Chile). Confocal *z*-plane optical sections (1 μm) were captured using 25× (LD LCI Plan-Apochromat 25×/0.8 Imm Korr DIC M27), 40× (Plan-Apochromat 40×/1.3 Oil DIC M27), and 63× (Plan-Apochromat 63×/1.40 Oil DIC M27) objectives. Additionally, tilt-scan microscopy was employed to acquire the entire whole-mount LAL muscles. To adjust the fluorescence intensity in the deepest *z*-planes without varying the power of the laser scanning, the "auto *z* brightness correction" was used, which allows an automatic and linear interpolation of values amongst neighboring positions within the *z* stack. The electroporation efficiency was quantified as the ratio between fibers expressing tdTomato vs. the total fibers labeled with Alexa488-WGA. The postsynaptic morphometric analyses were performed as described (Bolliger et al., 2010; Jones et al., 2016; Woehlbier et al., 2016). At least 40–50 postsynaptic apparatuses from control or tdTomato-expressing fibers were counted per mice. To determine the NMJ innervation pattern, confocal images were analyzed as described (Jones et al., 2016). Briefly, the area of the pre-synaptic motor terminal within the NMJ region and the total AChR positive area of >45 NMJs per mice were calculated. Data are presented as the % of the apposition of postsynaptic AChR clusters by presynaptic motor axons.

Electrophysiological Intracellular Recording

LAL muscle *ex vivo* preparations containing an intact 5 mm facial nerve stump were transferred to the stage of an Olympus BX50WI upright microscope and continuously perfused with an external solution (in mM: 135 NaCl, 5 KCl, 1 $MgCl_2$, 12 $NaHCO_3$, 12 glucose, and 2 $CaCl_2$) at room temperature. First, the viability of the muscle preparation was evaluated by visual inspection under the microscope of muscle contraction after nerve stimulation at 2–15 V. Then, we evaluated action potentials in properly impaled muscle fibers having resting potentials between −50 and −70 mV. The recording electrode resistance was 15–25 MΩ. Evoked (EPP) and spontaneous miniature (mEPP) end-plate potentials were recorded and analyzed as described (Tejero et al., 2016). Briefly, the nerve was stimulated through square-wave pulses at the indicated frequencies using a suction electrode. A glass micropipette filled with 3 M KCl was connected to an intracellular recording amplifier (Neuro Data IR283, Cygnus technology, Southport, NC, USA) through a chloride silver wire and used to impale single muscle fibers near the motor nerve endings. Muscle contraction was prevented by including in the bath 3–4 mM μ-conotoxin GIIIB (Alomone Laboratories, Jerusalem, Israel), a specific blocker of muscular

voltage-gated sodium channels. The data were analyzed as previously described (Tejero et al., 2016, 2020). EPP amplitudes were normalized to −70 mV and corrected for nonlinear summation. All electrophysiological data are expressed as group mean values ± SEM, with *n* and *N* being the number of NMJs and the number of mice, respectively. All reported results are based on 23–24 fibers from at least three animals per condition.

Statistical Analyses

The statistical comparison was performed amongst data obtained from control and electroporated age-matched animals using Student's unpaired *t*-test, based on a normal distribution of the data. In facial nerve injury experiments, quantification of parameters obtained from control and experimental animals at different times were compared using one-way ANOVA. Results were considered statistically significant when the *p*-value was < 0.05.

RESULTS

Efficient Electroporation-Mediated Gene Transfer of LAL Muscles

The non-viral transfection by electroporation has proven to be an advantageous physical method to allow efficient gene transfer into muscle fibers *in vivo* (McMahon et al., 2001; Bloquel et al., 2004). Following this approach, gain and loss of function of specific genes have been employed to study skeletal muscle recovery in pathological contexts (Schertzer and Lynch, 2006; van der Pijl et al., 2016) and to address the contribution of muscle-derived proteins to the dynamic processes controlling NMJ morphology and function (Kong et al., 2004; Losen et al., 2005; Sadasivam et al., 2005; Punga et al., 2011; Chen et al., 2014; Wang et al., 2017). Based on this, we first standardized in LAL muscles an electroporation-mediated gene transfer protocol previously reported to be effective in the hind limb *flexor digitorum brevis* (FDB) muscle (DiFranco et al., 2009; **Figure 1A**). We chose to work with P21 mice as it coincides with the onset of plaque to the pretzel transition of the NMJ postsynaptic apparatus (Bolliger et al., 2010). A low magnification representative image reveals that a high proportion of rostral LAL muscle fibers express the tdTomato protein (**Figure 1B**). Transversal cryosections of the electroporated muscles were stained with the WGA lectin to reveal the sarcolemma, whereas nuclei were counterstained with DAPI (**Figures 1C,D**). This procedure allowed us to determine that the electroporation efficiency achieved an average of 66.7 ± 5.94% of total fibers (**Figure 1E**). It also allowed us to quantify the presence of central nuclei as a parameter of muscle regeneration after damage (**Figure 1D**). Quantification showed a similarly low percentage of fibers containing central nuclei in tdTomato-positive fibers (5.9 ± 2.7%) than in control non-electroporated fibers (3.2 ± 1.07%, non-significant, paired *t*-test; **Figure 1E**), revealing that the electroporation procedure did not result in muscle damage. To analyze if the electroporation procedure induced morphological defects in the LAL muscle, we performed histological analyses of LAL transversal cryosections. Our results show no gross differences in muscle fiber distribution or mononuclear cells infiltration (haematoxylin/chromotrope staining; **Figure 1F**). We also performed histochemical staining to reveal NADH-thioreductase activity to analyze potential changes in different muscle fiber-types after electroporation-mediated expression of tdTomato. Electroporated and control non-electroporated LAL muscles fibers are mostly fast-twitch (non-oxidative and intermediate; light and middle blue), whereas only a small proportion of fibers show an oxidative (dark blue) slow-twitch phenotype (**Figures 1G,H**). We did not find changes in the cross-sectional area (CSA) of both, oxidative and non-oxidative muscle fibers of electroporated compared to control LAL muscles (**Figures 1I,J**). Thus, our data show that an efficient electric field permeabilization procedure or the expression of a control protein does not affect LAL muscle morphology.

The *in vivo* Electroporation Procedure in the LAL Muscle Does not Affect Neuromuscular Transmission

Next, we aimed to determine if the neuromuscular synaptic function could be compromised by our procedure. First, we analyzed the NMJ innervation profile (**Figure 2A**). Low magnification of the LAL R5 region shows no gross differences in the innervation pattern of tdTomato-expressing fibers, compared to controls (**Figure 2A**). Next, NMJs were evaluated for evidence of denervation based on whether the endplate marked by AChR staining lacked an overlying nerve terminal, visualized by immunohistochemical detection of neurofilament plus synaptic vesicles proteins (**Figure 2B**). In our experimental conditions, NMJs looked fully innervated, as nerve terminal branches aligned precisely with the postsynaptic specialization in both tdTomato-expressing and control non-electroporated muscles (**Figures 2B,C**). Quantitative analyses confirmed our observations, as presynaptic staining apposes more than 60% of the postsynaptic domain in both muscles, an expected quantification for fully innervated NMJs (**Figure 2D**; Jones et al., 2016). Second, we analyzed neuromuscular communication in *ex vivo* nerve/muscle LAL preparations using electrophysiological intracellular recording. We examined the characteristics of short-term synaptic facilitation and depression by stimulating the facial nerve at a high frequency (100 Hz) for 1 s (**Figure 3A**). Under these conditions, efficient recycling and replacement of the readily releasable pool of synaptic vesicles are required during the stimulus train (Ruiz et al., 2011). We found that paired-pulse facilitation (PPF) ratio (control: 1.02 ± 0.02; tdTomato: 1.03 ± 0.04; $p > 0.05$ *t*-test; **Figure 3B**) and the depression index (control: 0.60 ± 0.03; tdTomato: 0.56 ± 0.04; $p > 0.05$ *t*-test; **Figure 3C**) were unaffected by the electroporation protocol or by the expression of tdTomato. Also, a low-frequency stimulation protocol (0.5 Hz; **Figure 3D**) showed no significant differences in the amplitudes of evoked EPPs in LAL muscle fibers of electroporated animals (46.12 ± 5.6 mV) compared to control non-electroporated ones (39.41 ± 3.41 mV; $p > 0.05$ *t*-test; **Figure 3E**). Similarly, the average amplitude of spontaneous mEPPs in electroporated fibers (1.545 ± 0.12 mV) was similar to controls (1.252 ± 0.09 mV; $p > 0.05$ *t*-test; **Figure 3F**). As the amplitude of EPPs depends on both, the number

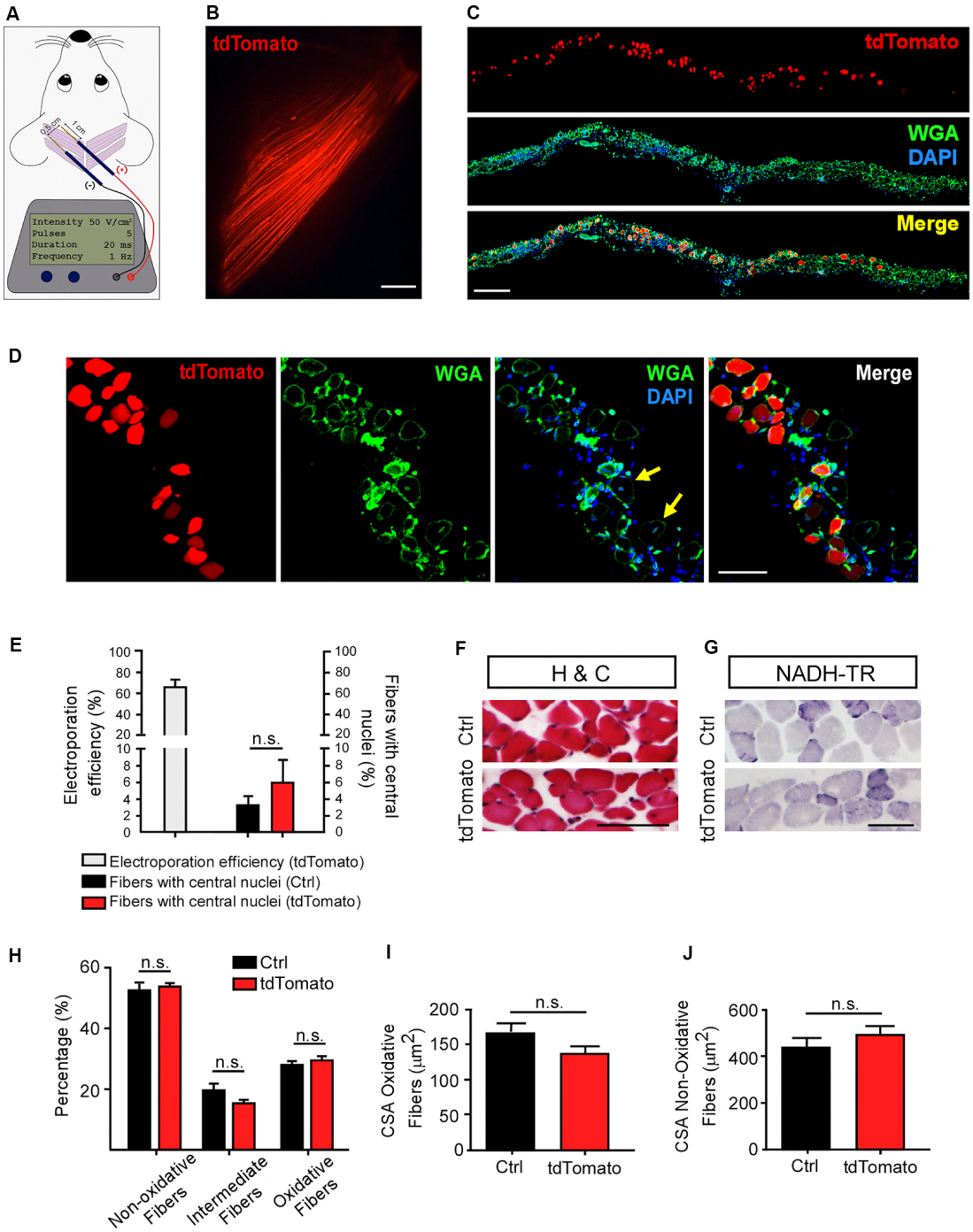

FIGURE 1 | Efficient electroporation-mediated gene transfer of Levator auris longus (LAL) muscles. LAL muscles from adult mice were electroporated *in vivo* with a plasmid coding for the tdTomato protein. Plasmid DNA was injected underneath the LAL muscle fascia and gold needle-type electrodes were positioned above the muscle to deliver five pulses of 100 V/cm^2 of 20 ms of duration at 1 Hz **(A)**. After 21 days, dissected whole-mounted muscles **(B)** were transversally sectioned and stained with Alexa488-WGA (green) and DAPI (blue) **(C)** to label the muscle membrane and nuclei, respectively. **(D)** Higher magnification images were used to quantify the efficiency of the procedure [as the percentage of tdTomato-expressing fibers from total fibers quantified based on wheat germ agglutinin (WGA) staining] **(E)** and the presence of central nuclei (arrowheads), as a parameter of muscle fiber damage/regeneration (E). **(F)** Transversal cryosections stained with Hematoxylin/Chromotrope revealed no significant alterations in muscle fiber histology or mononuclear cell infiltration. **(G)** NADH-TR histochemical activity detection was used to analyze non-oxidative (light and middle blue) and oxidative (dark blue) fibers. The proportion of these fiber types was quantified and expressed as a percentage of total fibers in the region of interest **(H)**. Also, the cross-sectional area (CSA) of oxidative **(I)** and non-oxidative **(J)** fibers was determined in >100 fibers per type in each Hemi-LAL. The results represent the mean ± SEM of N: three mice per group (control and electroporated). Scale bar 5 mm **(B)**, 200 μm **(C)**, 50 μm **(D)**, 50 μm **(F,G)**. $p > 0.05$, *t*-test; n.s.= non-significant.

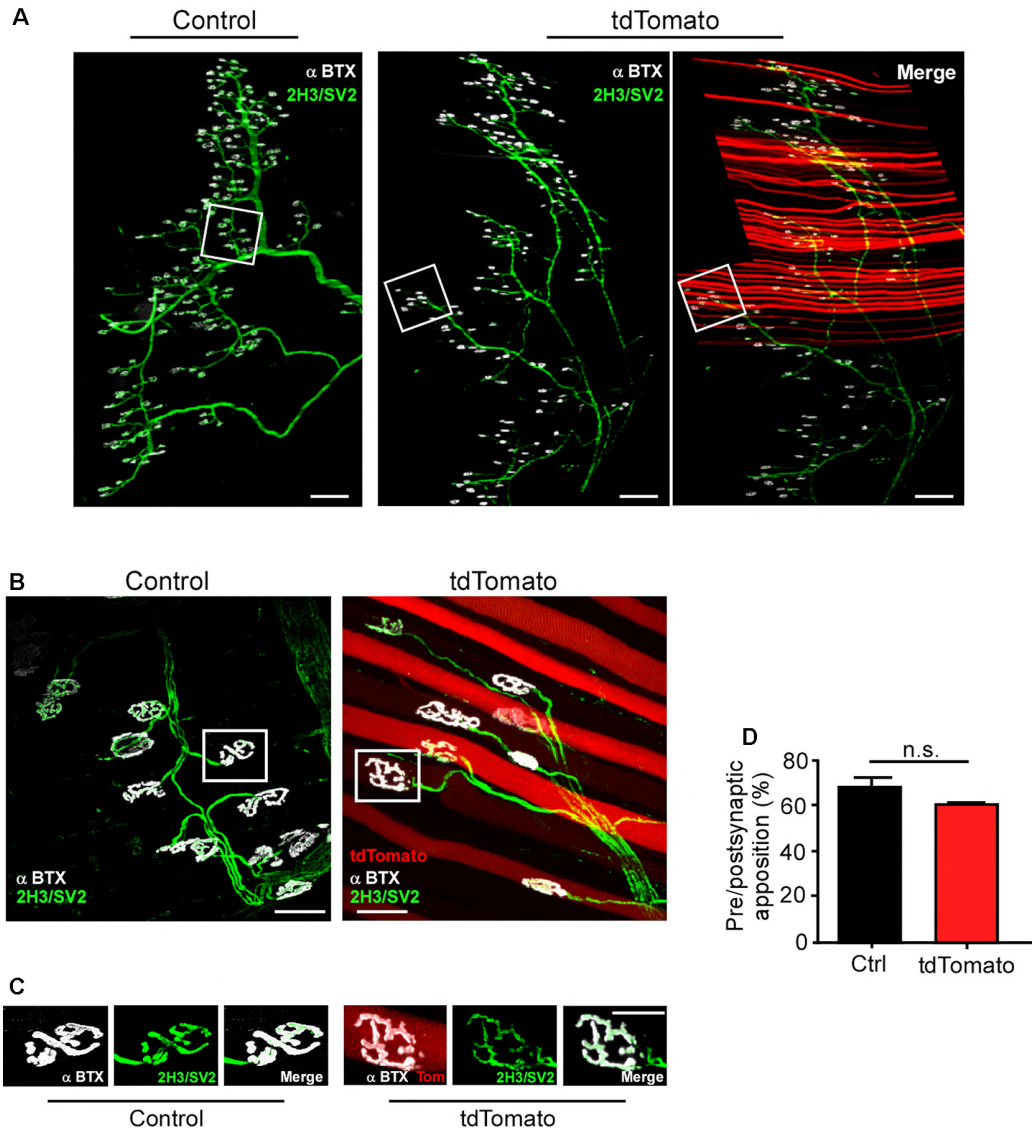

FIGURE 2 | The *in vivo* electroporation procedure in the LAL muscle does not affect neuromuscular junction (NMJ) innervation. LAL muscles from control adult mice and those expressing the tdTomato protein for 21 days were dissected and subjected to immunohistochemistry with the 2H3 (neurofilament) plus SV2 (synaptic vesicles) antibodies to reveal presynaptic motor terminals, along with Alexa647-BTX (white pseudocolor) to stain postsynaptic densities. **(A)** Low magnification images of whole-mount preparations show that the NMJ profile from the R5 region of right Hemi LAL muscles is maintained in tdTomato-expressing fibers, as compared to controls. **(B,C)** Higher magnification confocal images show that terminal motor axon branches contact postsynaptic apparatuses in control and electroporated muscle fibers. **(D)** Quantification of the apposition of postsynaptic acetylcholine receptor (AChR) pretzels by presynaptic motor axons. The plots correspond to >45 NMJs per mice. The bars represent the mean ± SEM of N: three mice per group (control and electroporated). Scale bar 200 μm **(A)**, 5 μm **(B,C)**. $p > 0.05$, *t*-test; n.s.= non-significant.

of released quanta and postsynaptic proteins (Del Castillo and Katz, 1954), we also calculated the quantal content during a 5-min period of continuous recording of each nerve terminal (**Figure 3G**). Our results indicate that the electroporation procedure does not affect the number of quanta released per action potential with values of 31.05 ± 1.56 and 28.62 ± 2.58 ($p > 0.05$ *t*-test) for control and td-Tomato expressing muscle fibers, respectively. Together, these data evidence that the electroporation of LAL muscles to overexpress the red fluorescent protein tdTomato does not affect the neuromuscular transmission.

Electroporation-Mediated Gene Transfer of tdTomato Does not Alter NMJ Post-synaptic Maturation

Next, we aimed to analyze the morphology of postsynaptic domains after electroporation-mediated gene transfer. Similar

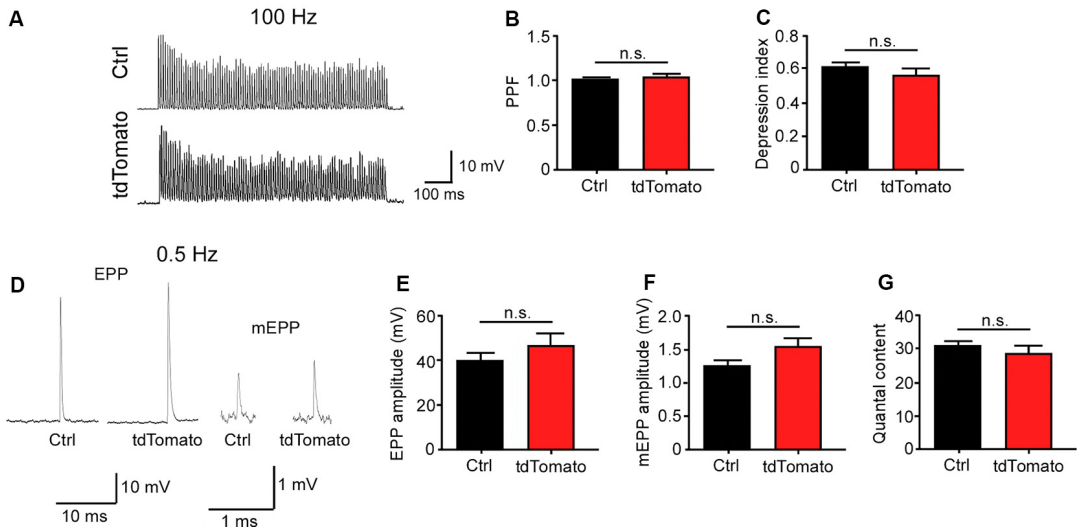

FIGURE 3 | Neuromuscular transmission is not altered after electroporation-mediated gene transfer of the LAL muscle. For functional studies, LAL muscles overexpressing the tdTomato protein at P14 were analyzed through electrophysiological intracellular recording at P21. Non-electroporated LAL muscles from age-matched mice were used as controls. After blocking muscle contraction, stimulation trains of 100 Hz during 1 s **(A)** showed no changes in synaptic plasticity, evidenced by paired-pulse facilitation (PPF) **(B)** and depression index **(C)** quantification in control and electroporated fibers. Plots represent the average ± SEM of N: 3, n: 24 (control and electroporated fibers). **(D)** Representative end plate potential (EPP) and miniature EPP (mEPP) traces after 0.5 Hz stimuli of NMJs from control and tdTomato-expressing fibers. Amplitudes of EPPs **(E)**, mEPPs **(F)**, and the quantal content **(G)** of control and electroporated fibers were quantified. Plots represent the average ± SEM of N: 3, n: 24 (control and electroporated fibers). $p > 0.05$, *t*-test; n.s.= non-significant.

pretzel-like postsynaptic morphologies were observed 10 and 21 days after muscle electroporation, compared to control non-electroporated fibers (**Figure 4A**). To quantitatively assess whether our procedure affects the NMJ structure, we analyzed the postsynaptic morphological transition occurring during NMJ maturation (Bolliger et al., 2010). As the most relevant morphological changes in the postsynaptic domain occur during early postnatal NMJ maturation (Sanes and Lichtman, 2001; Bolliger et al., 2010; Shi et al., 2012), the relative proportion of maturing postsynaptic shapes was quantified at P42, three weeks after electroporation. With that aim, AChR clusters were categorized into plaques (small uniformly distributed AChR clusters), perforated plaques (those containing internal poor-AChR regions), immature pretzels (exhibiting a peripheral opening), mature pretzels (complex highly branched shapes), and fragmented pretzels (more than four fragments; **Figure 4B**). As expected for P42 muscle fibers, we found no early plaque-like structures and a very small proportion of fragmented postsynaptic structures in control LAL fibers. Most structures corresponded to immature and mature pretzels (**Figure 4B**). Quantification shows that the electroporation protocol and the persistent expression of tdTomato did not alter the relative proportion of maturing NMJ structures, compared to control non-electroporated LAL muscles (**Figure 4B**). Also, quantification of other NMJ morphology parameters, such as the average area (tdTomato: 328.0 ± 11.13 μm^2; control: 355.6 ± 15.50 μm^2; $p > 0.05$ *t*-test; **Figure 4C**) or the perimeter (tdTomato: 141.7 ± 10.37 μm; control: 162.2 ± 7.99 μm; $p > 0.05$ *t*-test; **Figure 4D**) of postsynaptic apparatuses showed no differences, revealing that the maturation and stability of the NMJ postsynaptic domain are not affected by the electroporation procedure or by the expression of a control fluorescent protein.

Electroporation-Mediated Overexpression of the MuSK Receptor Results in Ectopic AChR Clustering

To further optimize our electroporation-mediated gene transfer procedure, we tried different concentrations and incubation times of hyaluronidase and combined them with varying amounts of total plasmid DNAs (data not shown). Visual inspection of the electroporation efficiency in transversal sections of LAL muscles stained with WGA at different times after electroporation (**Figure 5A**) showed that a 50% reduction in the time of hyaluronidase incubation (from 60–30 min) combined with a 10-fold reduction in the total DNA amount (from 80 to 8 μg) yielded high overexpression efficiencies. Quantification shows that, under these conditions, electroporation efficiency achieved an average of 77.2 ± 5.2; 69.5 ± 2.7; and 73.1 ± 4.3% ($p > 0.05$ *t*-test) of total fibers after 3, 7 and 14 days, respectively (**Figure 5B**). Using these optimal electroporation conditions, we conducted a functional validation of these standardized *in vivo* gene transfer conditions, which we aimed to modify the organization of the NMJ postsynaptic domain. To this aim, we used the pBK-CMV-Δlac-rMuSK plasmid (Bianchetta et al., 2005), which codes for a myc-tagged form of rat MuSK (rMuSK-myc), a muscle-specific tyrosine kinase receptor essential for NMJ assembly (DeChiara et al., 1996; Jing et al., 2009) and maintenance (Cantor et al., 2018). We also used a MuSK-EGFP plasmid, which contains the full-length mouse

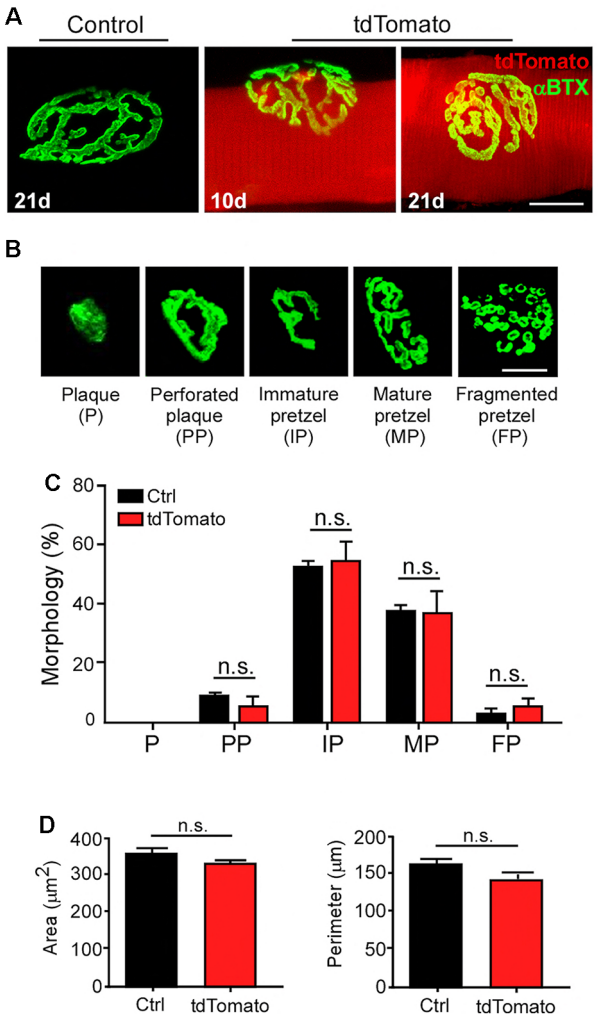

FIGURE 4 | Electroporation-mediated gene transfer of tdTomato does not alter NMJ postsynaptic maturation. LAL muscles from control adult mice and those expressing the tdTomato protein for 10 and 21 days were dissected and stained with Alexa488-BTX. **(A)** AChR pretzels on the surface of tdTomato-expressing fibers were similar to those on control non-electroporated fibers **(A)**. To analyze NMJ maturation, electroporated LAL muscles at P21 were analyzed at P42. Non-electroporated age-matched mice were used as controls. AChR clusters were categorized into plaques (P), perforated plaques (PP), immature pretzels (IP), mature pretzels (MP), and fragmented pretzels (FP; **B**, *upper panel*) and their relative abundance were plotted **(B**, *lower panel***)**. Postsynaptic area **(C)** and perimeter **(D)** were also determined. Plots represent the average ± SEM of N: 3, n: 130 (Control), and N:3, n: 149 (tdTomato-expressing fibers). Scale bar 50 μm **(A)**, 25 μm **(B)**. $p > 0.05$, *t*-test; n.s.= non-significant.

MuSK coding sequence fused to the EGFP protein (Ghazanfari et al., 2015; **Figure 5E**). We used the tdTomato plasmid as a tracer of co-electroporation with the plasmid coding for rMuSK-myc (**Figures 5C,D**). Control experiments confirmed the expression of rat MuSK-myc in transfected HEK293 cells and electroporated LAL muscles by Western blot using an anti-myc antibody (**Figure 5C**). Electroporated LAL muscles were stained to reveal postsynaptic AChR clusters and presynaptic motor axons 21 days after electroporation. Our findings show that electroporation-mediated overexpression of MuSK-myc resulted in the formation of aneural ectopic AChR clusters in most MuSK-expressing LAL muscle fibers (arrows in **Figure 5D**, *right panel*). Interestingly, ectopic AChR clusters distribute in discrete regions of the MuSK-overexpressing muscle fibers, thus resembling those assembled after MuSK overexpression by plasmid DNA microinjection *in vivo* (Sander et al., 2001). These AChR clusters are located hundreds of microns away from the innervation profile region (arrows in **Figure 5D**, *right panel*) and were completely absent in LAL muscle fibers overexpressing tdTomato only (**Figure 5D**, *left panel*). Similar results were obtained with the MuSK-EGFP plasmid. Transversal cryosections showed that overexpressed EGFP distributes intracellularly in synaptic and extrasynaptic regions of the muscle fibers, whereas MuSK-EGFP displayed a patched distribution along the sarcolemma and co-localizes with postsynaptic domains in synaptic regions (**Figure 5E**, *right bottom panels*). MuSK-EGFP overexpression also induced aneural ectopic AChR clustering in most electroporated LAL muscle fibers (**Figure 5E**, *left panels*). Overall, the standardization of electroporation-mediated gene transfer in the LAL muscle offers a valuable *in vivo* screening method to analyze the contribution of muscle proteins to NMJ morphology and function.

LAL Muscle as a Model for Degenerative and Regenerative Damage to the Nerve

One main condition to test the role of muscle-derived proteins is the process of NMJ regeneration. Therefore, as a first hint to explore the potential use of the LAL muscle as a model of NMJ regeneration, we refined a previously described procedure to accomplish facial nerve axotomy (Olmstead et al., 2015) and analyzed NMJ degeneration and regeneration. With this aim, we performed two procedures of nerve damage; to analyze NMJ degeneration, a 4 mm segment of the posterior auricular branch of the facial nerve was transected, whereas NMJ regeneration was evaluated after a 30 s crush injury of the same facial nerve branch (**Figure 6A**). LAL muscles were stained to reveal postsynaptic AChR clusters, presynaptic motor axons, and Schwann cells 7 and 30 days after nerve damage (**Figure 6B**). In both procedures, motor axons showed degeneration 7 days after facial nerve injury, leading to the denervation of the NMJ postsynaptic domains (**Figure 6B**). Also, terminal Schwann cells extended long projections away from the synaptic domains, as previously described in hind limb muscles (Reynolds and Woolf, 1992). Thirty days after facial nerve resection, postsynaptic AChR clusters suffered a transition from branched pretzel-like mature shapes to fragmented and blurry ones, whereas terminal Schwann cells still display long projections (**Figure 6B**). In turn, within a similar time frame after facial nerve crush, motor axons have regrown re-innervating the pretzel-like postsynaptic domains, whereas terminal Schwann cells retracted their projections (**Figure 6B**). Quantification of synaptic parameters shows a strong reduction of the nerve terminal area 7 days after both procedures of nerve injury. This value is recovered 30 days after nerve crush, although it does not reach control values (**Figure 6C**). Similarly, the area of postsynaptic AChR clusters is also decreased to a

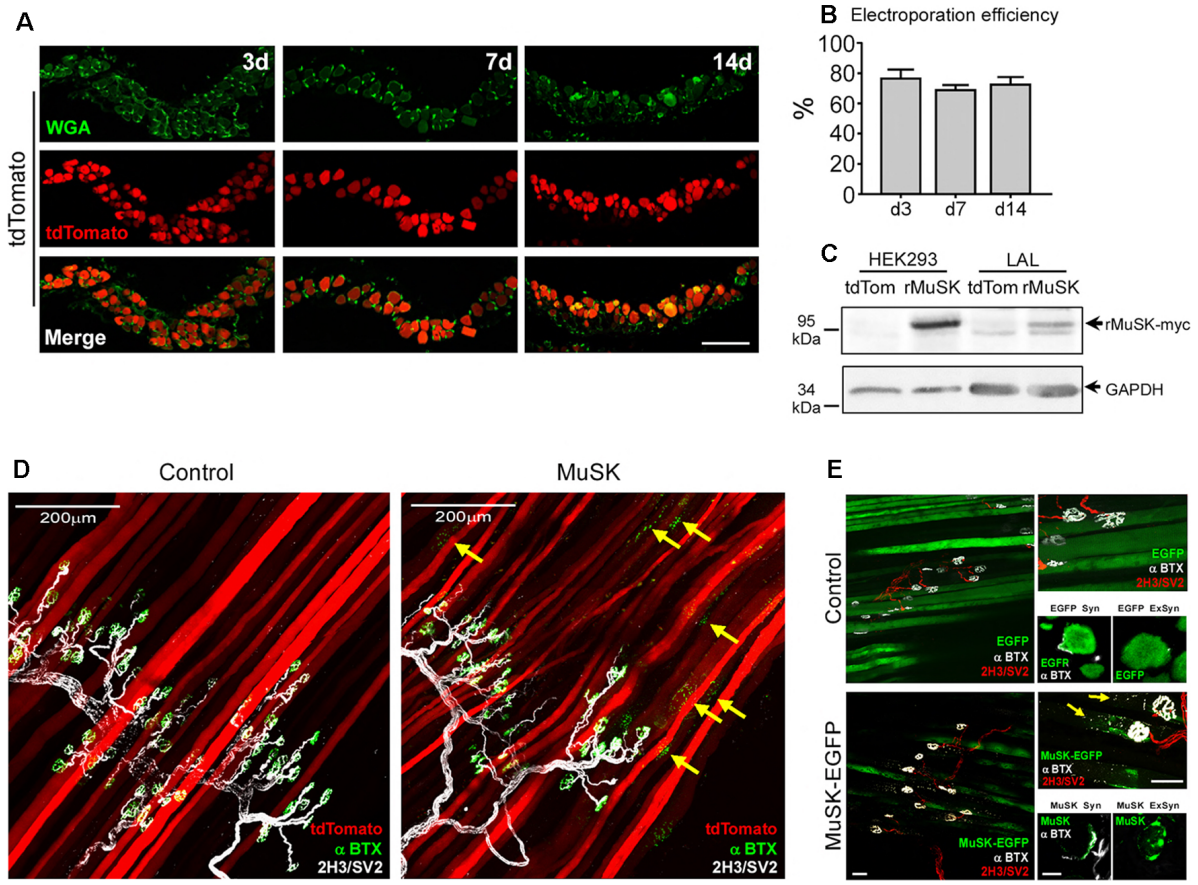

FIGURE 5 | Electroporation-mediated overexpression of the MuSK receptor results in ectopic AChR aggregation. LAL muscles were transversally sectioned and stained with WGA conjugated to Alexa488 (green) to label the muscle membrane at different times after electroporation **(A)**. **(B)** Quantification of electroporation efficiency at 3, 7, and 14 days after electroporation. To analyze the efficiency of our procedure to modulate postsynaptic organization at the NMJ, LAL muscles from adult mice were co-electroporated with plasmids coding for tdTomato and rMuSK-myc to overexpress a myc-tagged version of the rat MuSK receptor and tdTomato in a 5:1 (rMuSK-myc:tdTomato) proportion. Age-matched mice subjected to tdTomato electroporation only were used as controls. **(C)** Western blot using an anti-myc antibody was performed on protein extracts from HEK293 cells and LAL muscles electroporated with tdTomato and co-electroporated with tdTomato and rMuSK-myc. After 21 days, LAL muscles were dissected and subjected to immunohistochemistry with the 2H3 (neurofilament) plus SV2 (synaptic vesicles) antibodies to reveal presynaptic motor terminals (white pseudocolor) along with Alexa488-BTX to stain postsynaptic densities **(D)**. **(E)** LAL muscles were also electroporated with the MuSK-EGFP plasmid, which contains the full-length mouse MuSK coding sequence. We used a plasmid to express EGFP as control. After 14 days, LAL muscles were dissected and subjected to immunohistochemistry with the 2H3 (neurofilament) plus SV2 (synaptic vesicles) antibodies to reveal presynaptic motor terminals (red) along with Alexa647-BTX to stain postsynaptic densities (white pseudocolor). Images at the top of the right column are magnified images of the left panels. Images at the bottom of the right column show transversal cryosections of the same LAL muscles in synaptic (Syn) and extrasynaptic (ExSyn) regions of the muscle fiber. Arrows in panels **(D,E)** show AChR clusters in extrasynaptic regions of MuSK-overexpressing LAL fibers. Scale bar 100 μm **(A)**, 200 μm **(D)**, 50 μm **(E**, *left and right top panels*), 10 μm (*right bottom panels*).

similar extent 7 and 30 days after facial nerve cut and crush (**Figure 6D**). As a consequence, the overlap of pre/postsynaptic apposition decreases immediately after injury and returns to basal levels 30 days post nerve crush injury (**Figure 6E**). Even though the pre/postsynaptic apposition is significantly lower 30 days after injury, the overlap value (68.37 ± 1.351%) fits with complete NMJ reinnervation (Jones et al., 2016). As expected, pre/postsynaptic apposition does not exhibit any recovery 30 days after nerve cut (**Figure 6E**). Along with our previous results, the standardization of these two models of facial nerve injury allows for the study of proteins participating in the process of NMJ regeneration in the LAL muscle.

DISCUSSION

Several pathological conditions negatively affect NMJ integrity as a primary target. Compared to the central nervous system, the peripheral nervous system bears a higher regenerative ability; however, this process only occurs under permissive environmental conditions for a successful repair. One such crucial step is the stabilization of denervated muscle postsynaptic domains until they become re-innervated. Even though pretzel-like AChR clusters maintain their gross shape for several weeks after injury (Akaaboune et al., 1999), detailed analyses have demonstrated injury-dependent loss and gain of

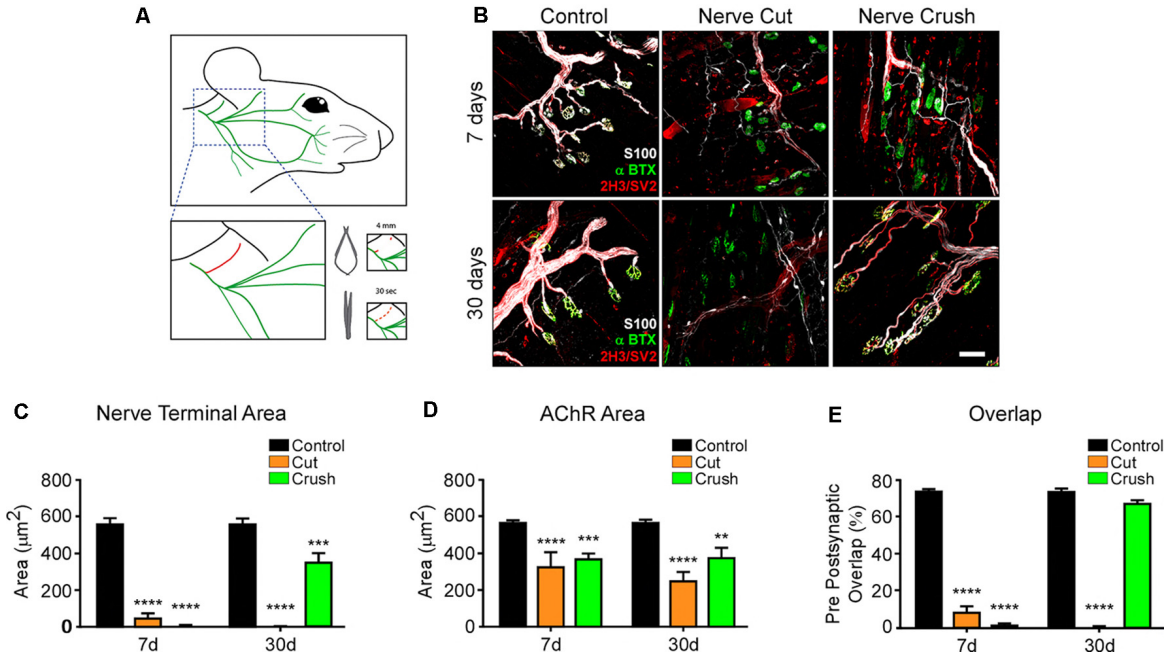

FIGURE 6 | LAL muscle after degenerative and regenerative nerve damage. To study NMJ regeneration in the LAL muscle, the posterior auricular branch of the facial nerve was subjected to two protocols of injury: a portion of approximately 4 mm was transected to induce NMJ degeneration, whereas the facial nerve was crushed for 30 s to accomplish NMJ regeneration **(A)**. To analyze NMJ behavior after nerve injury, LAL muscles in the different treatments were dissected 7 (upper panels) and 30 days (lower panels) after facial nerve damage. **(B)** AChRs were labeled with α-bungarotoxin (αBTX; green), motor axons were stained with antibodies against neurofilaments, 2H3, and synaptic vesicle proteins, SV2 (red), and Schwann cells were stained with the anti S100 antibody (white). The areas of the presynaptic motor terminal **(C)** and the postsynaptic AChR-rich domain **(D)** were measured. Quantification of the apposition of postsynaptic AChR pretzels by presynaptic motor axons **(E)**. Plots represent the average ± SEM of N: 4, n: 102 (Control, black bars), N: 3, n: 116 (7 days after crush, blue bars), and N: 3, n: 105 (30 days after crush, orange bars; $^{**}p < 0.01$; $^{***}p < 0.001$, $^{****}p < 0.0001$, one-way ANOVA). Scale bar 25 μm **(B)**.

AChRs in entire pretzel branches within postsynaptic regions, an effect that increases at longer denervation times (Kang et al., 2014). In this context, seeking for suitable models to analyze the contribution of muscle-derived molecules on postsynaptic NMJ stability for re-assembly is a permanent need. Our procedure constitutes a rapid, easily reproducible, and reliable screening method to modify the expression of candidate muscle-derived proteins in a time-dependent manner and to analyze their potential effect on NMJ behavior. In this regard, the LAL muscle offers unique experimental advantages for NMJ studies (Angaut-Petit et al., 1987; Erzen et al., 2000; Wright et al., 2011; Burke et al., 2018). It is a superficially and easily accessible muscle, which allows repeated *in vivo* manipulation and visualization, it is a flat and thin muscle, which facilitates the "*en face*" observation of NMJs in the optical plane of the microscopes in whole-mount preparations, and it allows nerve/muscle preparations for electrophysiological recording (Katz et al., 1996; Ruiz et al., 2010). Our studies also reveal the usefulness of this approach to analyze presynaptic morphology and apposition as well as the dynamic processes commanding NMJ maturation, including the neurotransmitter release dynamics and the consolidation of postsynaptic morphologies. Our findings demonstrate that the electroporation and the persistent expression of a control fluorescent protein in LAL muscle fibers during the transition from immature to mature NMJs do not modify neurotransmission parameters, further supporting the benefits of this procedure to characterize the effect of muscle-derived proteins on NMJ function.

How do muscle-derived proteins contribute to the stability of mature NMJs? Even though the original view stated dominant roles for motor neurons in NMJ formation, an increasing amount of evidence has highlighted the key contribution of skeletal muscle processes for embryonic NMJ assembly. For instance, an aneurally induced pre-pattern of AChR clusters guide motor axons for proper NMJ installation (Jing et al., 2009). Cumulative evidence also suggests that muscle proteins that act as main regulators of embryonic NMJ assembly are required for mature NMJ maintenance. These include proteins involved in the signaling triggered by agrin, a major motor neuron-derived organizer of the NMJ, such as the MuSK receptor (Bowen et al., 1998), its LRP4 co-receptor (Weatherbee et al., 2006), and the intracellular effectors Dok-7 (Okada et al., 2006), and rapsyn (Bruneau and Akaaboune, 2010). Auto-antibodies against MuSK and LRP4 cause Myasthenia gravis (Verschuuren et al., 2013; Plomp et al., 2015), whereas mutations affecting the function of each of these proteins are involved in Myasthenic Congenital Syndromes (Engel et al., 2015), thus demonstrating the requirement of these postsynaptic proteins for mature

NMJ maintenance. In this regard, *in vivo* gene transfer approaches have been efficiently employed to analyze the effect of muscle proteins on NMJ behavior (Kong et al., 2004; Sadasivam et al., 2005; Martínez-Martínez et al., 2007; Bruneau and Akaaboune, 2010; Punga et al., 2011; Chen et al., 2014; Gomez et al., 2016; Wang et al., 2017). For instance, electroporation-mediated modulation of rapsyn or Dok7 has allowed studies of its distribution at the mature NMJ and its effect on muscle response (Martínez-Martínez et al., 2007, 2009; Bruneau and Akaaboune, 2010; Gomez et al., 2016). Also, electrotransfer of a dsRNA sequence to silence MuSK expression in the *Soleus* muscle resulted in postsynaptic disruption (Kong et al., 2004). Interestingly, previous studies had shown that MuSK overexpression by plasmid microinjection in individual *Soleus* muscle fibers induced the formation of ectopic AChR clusters (Sander et al., 2001). By using electroporation-mediated gene transfer in LAL muscle fibers, here we have recapitulated these results by showing that most MuSK-expressing fibers display ectopic AChR clusters.

A key level for potential therapeutic interventions aimed at NMJ regeneration is to identify molecules and mechanisms that help AChR stability after denervation. Our study extends the usefulness of the LAL muscle to analyze NMJ regeneration. Following a facial nerve crush injury protocol, we observed axonal degeneration and muscle fiber reinnervation similar to that described in the hind limb *Tibialis anterior* muscle after sciatic nerve crush injury (Magill et al., 2007). In the context of NMJ regeneration, several muscle proteins that play essential roles in the embryonic assembly have demonstrated a potentially key role on helping NMJ maintenance, such as LRP4 (Barik et al., 2014), Dok-7 (Eguchi et al., 2016), and rapsyn (Kong et al., 2004; Martínez-Martínez et al., 2009). Indeed, overexpression of a low copy number of MuSK partially rescues the NMJ degeneration that takes place at pre-symptomatic stages of Amyotrophic Lateral Sclerosis animal models (Pérez-Garcia and Burden, 2012). Remarkably, these studies led to the discovery that antibody-mediated activation of endogenous MuSK has the same rescue effect (Cantor et al., 2018), opening a therapeutic alternative to prevent NMJ alterations in this and other pathological conditions resulting in neuromuscular synapse damage. It is also relevant to mention that successful NMJ regeneration is helped by signals derived from motor axon terminals and Schwann cells. For instance, nerve-released neurotrophic factors act as essential molecules to promote functional NMJ reinnervation (Bendella et al., 2018), whereas terminal Schwann cell-derived guidance molecules, such as CXCL12α, play essential roles in guiding motor axons to muscle fibers for functional repair (Negro et al., 2017). Also, recent findings reveal that local delivery of VEGF plus IGF-1, specifically at the distal site of sciatic nerve injury (i.e towards the NMJ), promoted functional reinnervation and muscle regeneration (Raimondo et al., 2019). These findings reveal that, regardless of the cellular origin of relevant trans-synaptic secreted proteins, electroporation of skeletal muscles as a common *in vivo* source of these molecules is a relevant therapeutic strategy to accomplish local beneficial effects on NMJ regeneration.

Therefore, in our view, protocols combining facial nerve injury and *in vivo* LAL muscle electroporation-mediated gene delivery are a reliable and fast strategy to investigate the potential role of muscle proteins on NMJ structure, function, and regeneration. Also, these methods can be used as a screening procedure before facing more complex and long-lasting approaches such as the generation of transgenic animal models.

DATA AVAILABILITY STATEMENT

The raw data supporting the conclusions of this article will be made available by the authors, without undue reservation.

ETHICS STATEMENT

The animal study was reviewed and approved by Bioethics Committee, Universidad de Concepción, Concepción, Chile.

AUTHOR CONTRIBUTIONS

JO, FB-G, LT, and JH contributed to the conception and design of the work. JO, FB-G, VP, JM, PH, DH, RT, and ML-M contributed experiments and data collection. JO, FB-G, LT, and JH contributed data analysis and interpretation. JO, LT, and JH wrote the manuscript. All authors contributed to the critical revision of the article and approve its final submitted version.

FUNDING

Our research has been supported by research grants Fondo Nacional de Desarrollo Científico y Tecnológico (FONDECYT) 1170614 and 1130321 to JH, 3190255 to VP, 3170464 to PH, and a grant from the Ministerio de Economia, Industria y Competitividad, Gobierno de España/FEDER (BFU2016-78934-P) to LT. JO, VP, FB-G, and JM are CONICYT fellows.

ACKNOWLEDGMENTS

We thank Daniel Sandoval and Jaime Teneb for their primary work. We dedicate this article to the memory of Cathy E. Krull, who very kindly and generously introduced us to the field of electroporation-mediated gene transfer.

REFERENCES

Akaaboune, M., Culican, S. M., Turney, S. G., and Lichtman, J. W. (1999). Rapid and reversible effects of activity on acetylcholine receptor density at the neuromuscular junction *in vivo*. *Science* 286, 503–507. doi: 10.1126/science.286.5439.503

Angaut-Petit, D., Molgo, J., Connold, A. L., and Faille, L. (1987). The levator auris longus muscle of the mouse: a convenient preparation for studies of short- and

long-term presynaptic effects of drugs or toxins. *Neurosci. Lett.* 82, 83–88. doi: 10.1016/0304-3940(87)90175-3

Barik, A., Lu, Y., Sathyamurthy, A., Bowman, A., Shen, C., Li, L., et al. (2014). LRP4 is critical for neuromuscular junction maintenance. *J. Neurosci.* 34, 13892–13905. doi: 10.1523/JNEUROSCI.1733-14.2014

Bendella, H., Rink, S., Grosheva, M., Sarikcioglu, L., Gordon, T., and Angelov, D. N. (2018). Putative roles of soluble trophic factors in facial nerve regeneration, target reinnervation, and recovery of vibrissal whisking. *Exp. Neurol.* 300, 100–110. doi: 10.1016/j.expneurol.2017.10.029

Bewick, G. S., Reid, B., Jawaid, S., Hatcher, T., and Shanley, L. (2004). Postnatal emergence of mature release properties in terminals of rat fast- and slow-twitch muscles. *Eur. J. Neurosci.* 19, 2967–2976. doi: 10.1111/j.0953-816x.2004.03418.x

Bianchetta, M. J., Betensky, R. A., and Cohen, J. B. (2005). Cell-surface MuSK self-association: a crucial role for the putative signal sequence. *Biochemistry* 44, 16229–16238. doi: 10.1021/bi051549j

Birks, R., Huxley, H. E., and Katz, B. (1960). The fine structure of the neuromuscular junction of the frog. *J. Physiol.* 150, 134–144. doi: 10.1113/jphysiol.1960.sp006378

Bloch-Gallego, E. (2015). Mechanisms controlling neuromuscular junction stability. *Cell. Mol. Life Sci.* 72, 1029–1043. doi: 10.1007/s00018-014-1768-z

Bloquel, C., Fabre, E., Bureau, M. F., and Scherman, D. (2004). Plasmid DNA electrotransfer for intracellular and secreted proteins expression: new methodological developments and applications. *J. Gene Med.* 6, S11–S23. doi: 10.1002/jgm.508

Bolliger, M. F., Zurlinden, A., Lüscher, D., Bütikofer, L., Shakhova, O., Francolini, M., et al. (2010). Specific proteolytic cleavage of agrin regulates maturation of the neuromuscular junction. *J. Cell Sci.* 123, 3944–3955. doi: 10.1242/jcs.072090

Bowen, D. C., Park, J. S., Bodine, S., Stark, J. L., Valenzuela, D. M., Stitt, T. N., et al. (1998). Localization and regulation of MuSK at the neuromuscular junction. *Dev. Biol.* 199, 309–319. doi: 10.1006/dbio.1998.8936

Bruneau, E. G., and Akaaboune, M. (2010). Dynamics of the rapsyn scaffolding protein at the neuromuscular junction of live mice. *J. Neurosci.* 30, 614–619. doi: 10.1523/jneurosci.4595-09.2010

Burke, S. R. A., Reed, E. J., Romer, S. H., and Voss, A. A. (2018). Levator auris longus preparation for examination of mammalian neuromuscular transmission under voltage clamp conditions. *J. Vis. Exp.* 135:57482. doi: 10.3791/57482

Cano, R., Torres-Benito, L., Tejero, R., Biea, A. I., Ruiz, R., Betz, W. J., et al. (2013). Structural and functional maturation of active zones in large synapses. *Mol. Neurobiol.* 47, 209–219. doi: 10.1007/s12035-012-8347-9

Cantor, S., Zhang, W., Delestree, N., Remedio, L., Mentis, G. Z., and Burden, S. J. (2018). Preserving neuromuscular synapses in ALS by stimulating MuSK with a therapeutic agonist antibody. *Elife* 7:e34375. doi: 10.7554/eLife.34375

Chen, Y., Ip, F. C., Shi, L., Zhang, Z., Tang, H., Ng, Y. P., et al. (2014). Coronin 6 regulates acetylcholine receptor clustering through modulating receptor anchorage to actin cytoskeleton. *J. Neurosci.* 34, 2413–2421. doi: 10.1523/jneurosci.3226-13.2014

DeChiara, T. M., Bowen, D. C., Valenzuela, D. M., Simmons, M. V., Poueymirou, W. T., Thomas, S., et al. (1996). The receptor tyrosine kinase MuSK is required for neuromuscular junction formation *in vivo*. *Cell* 85, 501–512. doi: 10.1016/s0092-8674(00)81251-9

Del Castillo, J., and Katz, B. (1954). Quantal components of the end-plate potential. *J. Physiol.* 124, 560–573. doi: 10.1113/jphysiol.1954.sp005129

DiFranco, M., Quinonez, M., Capote, J., and Vergara, J. (2009). DNA transfection of mammalian skeletal muscles using *in vivo* electroporation. *J. Vis. Exp.* 32:1520. doi: 10.3791/1520

Eguchi, T., Tezuka, T., Miyoshi, S., and Yamanashi, Y. (2016). Postnatal knockdown of dok-7 gene expression in mice causes structural defects in neuromuscular synapses and myasthenic pathology. *Genes Cells* 21, 670–676. doi: 10.1111/gtc.12370

Engel, A. G., Shen, X. M., Selcen, D., and Sine, S. M. (2015). Congenital myasthenic syndromes: pathogenesis, diagnosis, and treatment. *Lancet Neurol.* 14, 420–434. doi: 10.1016/S1474-4422(14)70201-7

Erzen, I., Cvetko, E., Obreza, S., and Angaut-Petit, D. (2000). Fiber types in the mouse levator auris longus muscle: a convenient preparation to study muscle and nerve plasticity. *J. Neurosci. Res.* 59, 692–697. doi: 10.1002/(sici)1097-4547(20000301)59:5<692::aid-jnr13>3.0.co;2-w

Ghazanfari, N., Linsao, E. L., Trajanovska, S., Morsch, M., Gregorevic, P., Liang, S. X., et al. (2015). Forced expression of muscle specific kinase slows postsynaptic acetylcholine receptor loss in a mouse model of MuSK myasthenia gravis. *Physiol. Rep.* 3:e12658. doi: 10.14814/phy2.12658

Gomez, A. M., Stevens, J. A., Mane-Damas, M., Molenaar, P., Duimel, H., Verheyen, F., et al. (2016). Silencing of Dok-7 in adult rat muscle increases susceptibility to passive transfer myasthenia gravis. *Am. J. Pathol.* 186, 2559–2568. doi: 10.1016/j.ajpath.2016.05.025

Jing, L., Lefebvre, J. L., Gordon, L. R., and Granato, M. (2009). Wnt signals organize synaptic prepattern and axon guidance through the zebrafish unplugged/MuSK receptor. *Neuron* 61, 721–733. doi: 10.1016/j.neuron.2008.12.025

Jones, R. A., Reich, C. D., Dissanayake, K. N., Kristmundsdottir, F., Findlater, G. S., Ribchester, R. R., et al. (2016). NMJ-morph reveals principal components of synaptic morphology influencing structure-function relationships at the neuromuscular junction. *Open Biol.* 6:160240. doi: 10.1098/rsob.160240

Kang, H., Tian, L., Mikesh, M., Lichtman, J. W., and Thompson, W. J. (2014). Terminal Schwann cells participate in neuromuscular synapse remodeling during reinnervation following nerve injury. *J. Neurosci.* 34, 6323–6333. doi: 10.1523/JNEUROSCI.4673-13.2014

Katz, B. (1971). Quantal mechanism of neural transmitter release. *Science* 173, 123–126. doi: 10.1126/science.173.3992.123

Katz, E., Ferro, P. A., Weisz, G., and Uchitel, O. D. (1996). Calcium channels involved in synaptic transmission at the mature and regenerating mouse neuromuscular junction. *J. Physiol.* 497, 687–697. doi: 10.1113/jphysiol.1996.sp021800

Katz, B., and Miledi, R. (1969). Spontaneous and evoked activity of motor nerve endings in calcium Ringer. *J. Physiol.* 203, 689–706. doi: 10.1113/jphysiol.1969.sp008887

Klooster, R., Plomp, J. J., Huijbers, M. G., Niks, E. H., Straasheijm, K. R., Detmers, F. J., et al. (2012). Muscle-specific kinase myasthenia gravis IgG4 autoantibodies cause severe neuromuscular junction dysfunction in mice. *Brain* 135, 1081–1101. doi: 10.1093/brain/aws025

Ko, C.-P., and Robitaille, R. (2015). Perisynaptic Schwann cells at the neuromuscular synapse: adaptable, multitasking glial cells. *Cold Spring Harb. Perspect. Biol.* 7:a020503. doi: 10.1101/cshperspect.a020503

Kong, X. C., Barzaghi, P., and Ruegg, M. A. (2004). Inhibition of synapse assembly in mammalian muscle *in vivo* by RNA interference. *EMBO Rep.* 5, 183–188. doi: 10.3410/f.1017505.203269

Losen, M., Stassen, M. H., Martínez-Martínez, P., Machiels, B. M., Duimel, H., Frederik, P., et al. (2005). Increased expression of rapsyn in muscles prevents acetylcholine receptor loss in experimental autoimmune myasthenia gravis. *Brain* 128, 2327–2337. doi: 10.1093/brain/awh612

Magill, C. K., Tong, A., Kawamura, D., Hayashi, A., Hunter, D. A., Parsadanian, A., et al. (2007). Reinnervation of the tibialis anterior following sciatic nerve crush injury: a confocal microscopic study in transgenic mice. *Exp. Neurol.* 207, 64–74. doi: 10.1016/j.expneurol.2007.05.028

Martineau, E., Di Polo, A., Vande Velde, C., and Robitaille, R. (2018). Dynamic neuromuscular remodeling precedes motor-unit loss in a mouse model of ALS. *Elife* 7:e41973. doi: 10.7554/eLife.41973

Martínez-Martínez, P., Losen, M., Duimel, H., Frederik, P., Spaans, F., Molenaar, P., et al. (2007). Overexpression of rapsyn in rat muscle increases acetylcholine receptor levels in chronic experimental autoimmune myasthenia gravis. *Am. J. Pathol.* 170, 644–657. doi: 10.2353/ajpath.2007.060676

Martínez-Martínez, P., Phernambucq, M., Steinbusch, L., Schaeffer, L., Berrih-Aknin, S., Duimel, H., et al. (2009). Silencing rapsyn *in vivo* decreases acetylcholine receptors and augments sodium channels and secondary postsynaptic membrane folding. *Neurobiol. Dis.* 35, 14–23. doi: 10.1016/j.nbd.2009.03.008

McMahon, J., Signori, E., Wells, K., Fazio, V., and Wells, D. (2001). Optimisation of electrotransfer of plasmid into skeletal muscle by pretreatment with hyaluronidase—increased expression with reduced muscle damage. *Gene Ther.* 8, 1264–1270. doi: 10.1038/sj.gt.3301522

Moloney, E. B., de Winter, F., and Verhaagen, J. (2014). ALS as a distal axonopathy: molecular mechanisms affecting neuromuscular junction stability in the

presymptomatic stages of the disease. *Front. Neurosci.* 8:252. doi: 10.3389/fnins.2014.00252

Murray, L. M., Comley, L. H., Thomson, D., Parkinson, N., Talbot, K., and Gillingwater, T. H. (2008). Selective vulnerability of motor neurons and dissociation of pre- and post-synaptic pathology at the neuromuscular junction in mouse models of spinal muscular atrophy. *Hum. Mol. Genet.* 17, 949–962. doi: 10.1093/hmg/ddm367

Murray, L. M., Gillingwater, T. H., and Parson, S. H. (2010a). Using mouse cranial muscles to investigate neuromuscular pathology *in vivo*. *Neuromuscul. Disord.* 20, 740–743. doi: 10.1016/j.nmd.2010.06.013

Murray, L. M., Talbot, K., and Gillingwater, T. (2010b). Neuromuscular synaptic vulnerability in motor neurone disease: amyotrophic lateral sclerosis and spinal muscular atrophy. *Neuropathol. Appl. Neurobiol.* 36, 133–156. doi: 10.1111/j.1365-2990.2010.01061.x

Negro, S., Lessi, F., Duregotti, E., Aretini, P., La Ferla, M., Franceschi, S., et al. (2017). CXCL12α/SDF-1 from perisynaptic Schwann cells promotes regeneration of injured motor axon terminals. *EMBO Mol. Med.* 9, 1000–1010. doi: 10.15252/emmm.201607257

Okada, K., Inoue, A., Okada, M., Murata, Y., Kakuta, S., Jigami, T., et al. (2006). The muscle protein Dok-7 Is essential for neuromuscular synaptogenesis. *Science* 312, 1802–1805. doi: 10.1126/science.1127142

Olmstead, D. N., Mesnard-Hoaglin, N. A., Batka, R. J., Haulcomb, M. M., Miller, W. M., and Jones, K. J. (2015). Facial nerve axotomy in mice: a model to study motoneuron response to injury. *J. Vis. Exp.* 96:e52382. doi: 10.3791/52382

Pérez-Garcia, M. J., and Burden, S. J. (2012). Increasing MuSK activity delays denervation and improves motor function in ALS mice. *Cell Rep.* 2, 497–502. doi: 10.1016/j.celrep.2012.08.004

Plomp, J. J., Morsch, M., Phillips, W. D., and Verschuuren, J. J. (2015). Electrophysiological analysis of neuromuscular synaptic function in myasthenia gravis patients and animal models. *Exp. Neurol.* 270, 41–54. doi: 10.1016/j.expneurol.2015.01.007

Punga, A. R., Maj, M., Lin, S., Meinen, S., and Ruegg, M. A. (2011). MuSK levels differ between adult skeletal muscles and influence postsynaptic plasticity. *Eur. J. Neurosci.* 33, 890–898. doi: 10.1111/j.1460-9568.2010.07569.x

Raimondo, T. M., Li, H., Kwee, B. J., Kinsley, S., Budina, E., Anderson, E. M., et al. (2019). Combined delivery of VEGF and IGF-1 promotes functional innervation in mice and improves muscle transplantation in rabbits. *Biomaterials* 216:119246. doi: 10.1016/j.biomaterials.2019.119246

Reynolds, M. L., and Woolf, C. J. (1992). Terminal Schwann cells elaborate extensive processes following denervation of the motor endplate. *J. Neurocytol.* 21, 50–66. doi: 10.1007/BF01206897

Ruiz, R., Cano, R., Casañas, J. J., Gaffield, M. A., Betz, W. J., and Tabares, L. (2011). Active zones and the readily releasable pool of synaptic vesicles at the neuromuscular junction of the mouse. *J. Neurosci.* 31, 2000–2008. doi: 10.1523/jneurosci.4663-10.2011

Ruiz, R., Casañas, J. J., Torres-Benito, L., Cano, R., and Tabares, L. (2010). Altered intracellular Ca2+ homeostasis in nerve terminals of severe spinal muscular atrophy mice. *J. Neurosci.* 30, 849–857. doi: 10.1523/JNEUROSCI.4496-09.2010

Sadasivam, G., Willmann, R., Lin, S., Erb-Vogtli, S., Kong, X. C., Ruegg, M. A., et al. (2005). Src-family kinases stabilize the neuromuscular synapse *in vivo via* protein interactions, phosphorylation and cytoskeletal linkage of acetylcholine receptors. *J. Neurosci.* 25, 10479–10493. doi: 10.1523/JNEUROSCI.2103-05.2005

Sakuma, M., Gorski, G., Sheu, S. H., Lee, S., Barrett, L. B., Singh, B., et al. (2016). Lack of motor recovery after prolonged denervation of the neuromuscular junction is not due to regenerative failure. *Eur. J. Neurosci.* 43, 451–462. doi: 10.1111/ejn.13059

Sander, A., Hesser, B. A., and Witzemann, V. (2001). MuSK induces *in vivo* acetylcholine receptor clusters in a ligand-independent manner. *J. Cell. Biol.* 155, 1287–1296. doi: 10.1083/jcb.200105034

Sanes, J. R., and Lichtman, J. W. (2001). Induction, assembly, maturation and maintenance of a postsynaptic apparatus. *Nat. Rev. Neurosci.* 2, 791–805. doi: 10.1038/35097557

Schertzer, J. D., and Lynch, G. S. (2006). Comparative evaluation of IGF-I gene transfer and IGF-I protein administration for enhancing skeletal muscle regeneration after injury. *Gene Ther.* 13, 1657–1664. doi: 10.1038/sj.gt.3302817

Shi, L., Fu, A. K. Y., and Ip, N. Y. (2012). Molecular mechanisms underlying maturation and maintenance of the vertebrate neuromuscular junction. *Trends Neurosci.* 35, 441–453. doi: 10.1016/j.tins.2012.04.005

Tejero, R., Balk, S., Franco-Espin, J., Ojeda, J., Hennlein, L., Drexl, H., et al. (2020). R-roscovitine improves motoneuron function in mouse models for spinal muscular atrophy. *iScience* 23:100826. doi: 10.1016/j.isci.2020.100826

Tejero, R., Lopez-Manzaneda, M., Arumugam, S., and Tabares, L. (2016). Synaptotagmin-2 and-1, linked to neurotransmission impairment and vulnerability in spinal muscular atrophy. *Hum. Mol. Genet.* 25, 4703–4716. doi: 10.1093/hmg/ddw297

van der Pijl, E. M., van Putten, M., Niks, E. H., Verschuuren, J. J., Aartsma-Rus, A., and Plomp, J. J. (2016). Characterization of neuromuscular synapse function abnormalities in multiple Duchenne muscular dystrophy mouse models. *Eur. J. Neurosci.* 43, 1623–1635. doi: 10.1111/ejn.13249

Verschuuren, J. J., Huijbers, M. G., Plomp, J. J., Niks, E. H., Molenaar, P. C., Martinez-Martinez, P., et al. (2013). Pathophysiology of myasthenia gravis with antibodies to the acetylcholine receptor, muscle-specific kinase and low-density lipoprotein receptor-related protein 4. *Autoimmun. Rev.* 12, 918–923. doi: 10.1016/j.autrev.2013.03.001

Wang, J., Song, F., and Loeb, J. A. (2017). Neuregulin1 fine-tunes pre-, post-, and perisynaptic neuromuscular junction development. *Dev. Dyn.* 246, 368–380. doi: 10.1002/dvdy.24494

Weatherbee, S. D., Anderson, K. V., and Niswander, L. A. (2006). LDL-receptor-related protein 4 is crucial for formation of the neuromuscular junction. *Development* 133, 4993–5000. doi: 10.1242/dev.02696

Woehlbier, U., Colombo, A., Saaranen, M. J., Pérez, V., Ojeda, J., Bustos, F. J., et al. (2016). ALS-linked protein disulfide isomerase variants cause motor dysfunction. *EMBO J.* 35, 845–865. doi: 10.15252/embj.201592224

Wright, M., Kim, A., and Son, Y. J. (2011). Subcutaneous administration of muscarinic antagonists and triple-immunostaining of the levator auris longus muscle in mice. *J. Vis. Exp.* 55:3124. doi: 10.3791/3124

Conflict of Interest: The authors declare that the research was conducted in the absence of any commercial or financial relationships that could be construed as a potential conflict of interest.

frontiers in Cellular Neuroscience

SYSTEMATIC REVIEW
published: 14 October 2020
doi: 10.3389/fncel.2020.00271

Neural Stimulation and Molecular Mechanisms of Plasticity and Regeneration: A Review

Matthew K. Hogan, Gillian F. Hamilton and Philip J. Horner*

Department of Neurosurgery, Center for Neuroregeneration, Houston Methodist Research Institute, Houston Methodist Hospital, Houston, TX, United States

Neural stimulation modulates the depolarization of neurons, thereby triggering activity-associated mechanisms of neuronal plasticity. Activity-associated mechanisms in turn play a major role in post-mitotic structure and function of adult neurons. Our understanding of the interactions between neuronal behavior, patterns of neural activity, and the surrounding environment is evolving at a rapid pace. Brain derived neurotrophic factor is a critical mediator of activity-associated plasticity, while multiple immediate early genes mediate plasticity of neurons following bouts of neural activity. New research has uncovered genetic mechanisms that govern the expression of DNA following changes in neural activity patterns, including RNAPII pause-release and activity-associated double stranded breaks. Discovery of novel mechanisms governing activity-associated plasticity of neurons hints at a layered and complex molecular control of neuronal response to depolarization. Importantly, patterns of depolarization in neurons are shown to be important mediators of genetic expression patterns and molecular responses. More research is needed to fully uncover the molecular response of different types of neurons-to-activity patterns; however, known responses might be leveraged to facilitate recovery after neural damage. Physical rehabilitation through passive or active exercise modulates neurotrophic factor expression in the brain and spinal cord and can initiate cortical plasticity commensurate with functional recovery. Rehabilitation likely relies on activity-associated mechanisms; however, it may be limited in its application. Electrical and magnetic stimulation direct specific activity patterns not accessible through passive or active exercise and work synergistically to improve standing, walking, and forelimb use after injury. Here, we review emerging concepts in the molecular mechanisms of activity-derived plasticity in order to highlight opportunities that could add value to therapeutic protocols for promoting recovery of function after trauma, disease, or age-related functional decline.

Keywords: neurostimulation, neuroplasticity, neuromodulation, plasticity, activity-dependent plasticity, regeneration, neurotrauma

OPEN ACCESS

Edited by:
Juan Pablo Henríquez, University of Concepcion, Chile

Reviewed by:
Xiaoming Jin, Indiana University, Purdue University Indianapolis, United States
Shaoyu Ge, Stony Brook University, United States

****Correspondence:***
Matthew K. Hogan
mkhogan@houstonmethodist.org

Specialty section:
This article was submitted to Cellular Neurophysiology, a section of the journal Frontiers in Cellular Neuroscience

Received: *31 March 2020*
Accepted: *31 July 2020*
Published: *14 October 2020*

Citation:
Hogan MK, Hamilton GF and Horner PJ (2020) Neural Stimulation and Molecular Mechanisms of Plasticity and Regeneration: A Review. Front. Cell. Neurosci. 14:271. doi: 10.3389/fncel.2020.00271

INTRODUCTION

Activity-associated plasticity refers to a form of functional and structural neuroplasticity that is driven by the depolarizing behavior of neurons, and it has been a focal area of research for the past several decades. Much of our current understanding about activity-associated plasticity has been demonstrated or discovered in experiments targeting memory, learning, and/or

development (Spitzer, 2006; Feldman, 2012; Minatohara et al., 2016) Within such contexts, researchers have uncovered fundamental mechanisms governing activity-associated plasticity, including long-term depression (LTD) (Ahn et al., 1999), long-term potentiation (LTP) (Kandel, 2001), and activity-associated development of corticospinal circuitry (Martin, 2005). Still, our understanding continues to grow. Recent research has revealed a vast array of immediate early genes (IEGs), epigenetic modifiers, and even new mechanisms for transcriptional and translational regulation associated with neuronal activity (Guzowski et al., 2005; Karpova, 2014; Chen et al., 2015). Transcriptional pause-release phenomena, enhancer ribonucleic acid (RNA), and neural activity induced double-strand DNA breaks (DSBs) are just a few examples of transcriptional mechanisms that may be regulated by neural activity. Of note, DSBs can form in response to neural activity in the promoters of a subset of IEGs and can serve to enhance transcription by removing topological constraints through DNA repair of the breaks. The goal of this review is to consider these mechanisms in the context of various neural activity types, such as neuronal subtypes and their requisite receptors, the type of network in which a neuron is connected, and the pattern or duration of activity. These variables fundamentally define the differential activity-associated responses in a neuron. We recognize that in addition to those we present here, many other existing factors influence neuronal responses to changing levels of activity. For example, it is clear that metabolic and glial responses to neural activity are crucial factors (Fields and Nelson, 1992; Fields, 2008; Allaman et al., 2011; Schafer et al., 2012; Sakry et al., 2014; Jolivet et al., 2015; Kondiles and Horner, 2018); however, they are ultimately beyond the scope of this review. In addition, neuronal activity has been shown to drive neurogenesis, progenitor migration, and integration during development and in the adult hippocampus and olfactory bulb. For the purpose of this review, we focus on synaptic and network levels of plasticity rather than activity induced neurogenesis and myelination, as this topic has been well-discussed (Cao et al., 2004; Ge et al., 2007; Ma et al., 2009; Young et al., 2011; Fields, 2015; Kondiles and Horner, 2018).

Given the increasingly mechanistic understanding of activity-associated plasticity, it becomes clear that a review of emerging mechanisms is timely and has the potential to define new opportunities for research, collaboration, and pathways for application. However, the reader is urged to consider developmental stage, neuronal subtype, environment, and mechanism of activity in applying the concepts considered here. For example, neural subtypes express disparate receptor populations and will thus differentially integrate environmental signals. Therefore, how neurons absorb information at the cellular and circuit level is of critical importance when attempting to leverage activity-associated plasticity mechanisms in the design of experiments or applications since such experiments and applications may not be universal in outcome and application. Modification of neural activity, whether it be through chemical, electrical, magnetic, or some other means, may have unintended consequences through non-biological alteration of the microenvironment or secondary effects on the cellular or tissue target itself. Less considered aspects of activity-associated plasticity such as the duration and pattern of neuronal depolarization may play a critical role in the transcriptional profile of a neuron. Context is also critically important to consider. The environment, developmental stage, and/or presence of an injury likely alters the mechanism of activity-associated plasticity and certainly impacts the cellular response. The tools used to manipulate neural plasticity are almost as unique as the neuronal circuits they target and must be carefully considered alongside the environmental milieu. Hence, this review will cover relevant mechanisms of activity-associated plasticity and potential considerations for harnessing them to promote regeneration and restoration of function. Neural activity can mediate plastic responses through several intrinsic and extrinsic vectors. Additionally, by manipulating activity patterns, it may be possible to repair a degenerated or damaged brain or spinal cord (**Figure 1**). We will: (1) consider the differences between exogenous and endogenous modulation of neural activity; (2) provide a brief overview of mechanisms of neuronal activity-associated plasticity, such as brain derived neurotrophic factor (BDNF) and its receptors, trophic modifiers, IEGs, epigenetics, and genetic regulation; (3) present research demonstrating robust transcriptional alterations to changes in intrinsic neuronal activity patterns; (4) review potential therapeutic methods to leverage these mechanisms to promote recovery; and (5) explore how different types of rehabilitation and stimulation differentially affect these mechanisms and potentially recovery.

EXOGENOUS VS. ENDOGENOUS MODULATION OF NEURAL ACTIVITY

The distinction between changes in neural activity initiated by exogenous stimulation through an electrode, magnetic coil, or some such device compared with those brought on by behavioral activity or endogenous stimuli is a crucial one (Linderoth and Foreman, 1999; Stagg and Nitsche, 2011; Young et al., 2011; Kravitz and Bonci, 2013). Endogenous stimulation induced by physical activity or sensory stimulation initiates neural activity through physiological changes in local ion gradients caused by synaptic activity or environmental sensing receptors. Exogenous stimulation causes local changes in ion gradients in a non-physiological and larger scale mode when applied magnetically or electrically. While this type of stimulation arguably initiates normal depolarization of a neuron, it may also affect other systems and cause non-physiologic responses. Although the end result can be similar, the question remains as to whether exogenous stimulation is truly synonymous with endogenous or natural activation of neurons given that exogenous stimulation methods may indirectly manipulate local ion gradients and initiate other changes not demonstrated through natural activation of neural pathways. Still, research has shown that exogenous stimulation can induce spike-timing-dependent plasticity through closed loop stimulation coincident with voluntary behavior or endogenous stimulation in rats (Rebesco et al., 2010) and non-human primates (Zanos et al.,

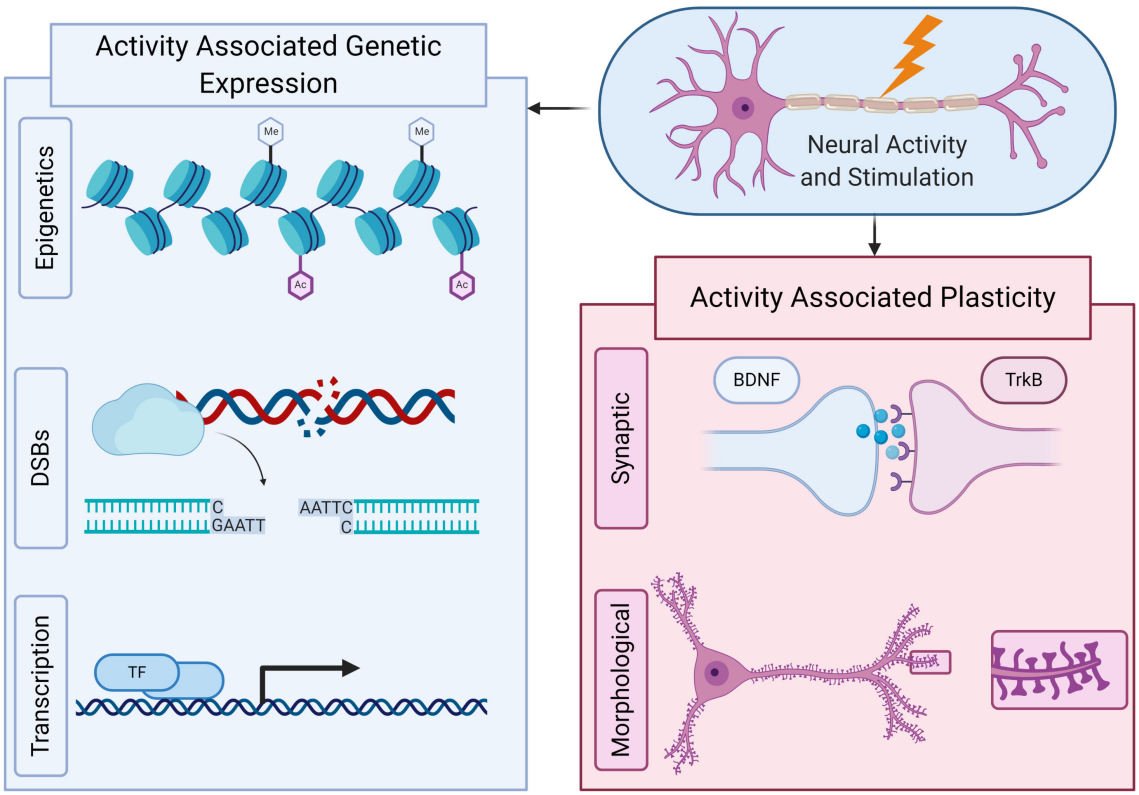

FIGURE 1 | Neural activity can have broad effects on the presentation of neurons, both through altered genetic expression and changes to its structure and function. Genetically, neural activity and stimulation can cause epigenetic changes that alter the accessibility of specific genes to genetic transcription. Also, the can induce double stranded DNA breaks (DSBs) at specific sites of the genome, which can result in more stable and enhanced transcription and ultimately, through a wide variety of mechanisms including transcription factors and IEGs, can rapidly induce transcriptional changes that alter a neuron's overall genetic expression. Neural activity and stimulation can ultimately cause plasticity changes, both morphological and synaptic, through such transcriptional changes as well as in response to neurotransmitters and other signaling mechanisms.

2011). Thus, tools to manipulate neural activity can impact the plastic rewiring of neural circuits. Importantly, altered activity patterns can induce strengthening or weakening of connections between two neural circuits independent of voluntary action, as demonstrated by activity-dependent strengthening or depression between sites in the sensorimotor cortex of awake behaving primates via paired stimulation (Seeman et al., 2017). A host of tools have been developed to manipulate neural activity, and many have relevance in a clinical context. Notably, neural activity modulating therapies have emerged with varying degrees of success (Mailis-Gagnon et al., 2004; Williams et al., 2010; Harkema et al., 2011; Sayenko et al., 2019).

Furthermore, there is a considerable nuance in activity-associated plasticity, particularly in the context of extrinsic factors, such as injury and the environment. While much is known about activity-associated modifiers in specific frameworks (e.g., learning, memory, and principles of Hebbian plasticity), exciting research has surfaced that illustrates the importance of neuronal cell type (Dehorter et al., 2015) and temporal firing patterns (Fields et al., 2005; Lee et al., 2017; Tyssowski et al., 2018) on activity-associated responses relevant to regeneration. After spinal cord injury (SCI), the spinal cord environment is largely changed; thus, results from healthy spinal cord experiments may not be predictive of activity-evoked plasticity effects in models that exhibit gliosis, neuronal atrophy, inflammation and altered channel distribution or function. For example, following injury, gamma-aminobutyric acid (GABA)-ergic neurons reduce their expression of the membrane-bound potassium-chloride co-transporter 2 (KCC2), which shuttles chloride outside of the cell. This imbalance, which is not present in the healthy spinal cord, causes a shift in membrane polarization, resulting in normally inhibitory GABAergic cells becoming excitatory. Interestingly, this shift after injury is a recapitulation of development where NKCC1 cotransporters appear earlier than KCC2 cotransporters, allowing preferential flow of chloride into GABAergic neurons, and in this developmental state GABAergic neurons exhibit excitatory behavior (Medina et al., 2014). KCC2 reduction has been shown to occur within 24 h of injury and is associated with maladaptive plasticity in chronic SCI (Grau and Huang, 2018). This suggests that injury can alter the excitatory/inhibitory balance through this conversion and disrupt normal circuit function (Huang et al., 2016). In addition, injury to the central nervous system (CNS) can differentially affect how BDNF regulates KCC2 expression in spinally transected and

intact rats. For instance, BDNF normally downregulates KCC2, producing an increase in central sensitization. In contrast, following transection injury, BDNF causes an increase in membrane bound KCC2, thereby restoring the inhibitory action of GABAergic neurons, leveling the excitatory/inhibitory balance and decreasing central sensitization (Huang et al., 2017). The variability in pathological states of neural circuitry as well as the unique mechanisms of unique modes of neuromodulation are important considerations for not only the interpretation of current literature, but also a challenge to the design of future, mechanistic studies.

MECHANISMS OF NEURONAL ACTIVITY-ASSOCIATED PLASTICITY

Activity-associated plasticity has long been linked with development; however, such mechanisms may also be relevant in the adult nervous system. Post-mitotic neurons in the brain and spinal cord, long thought to be generally stable in structure and nature, have since been proven to adapt significantly in response to neuronal activity, exhibiting changes in morphological properties, gene expression, and synaptic strength. Further, neuronal firing behavior has been shown to influence a host of mechanisms from synaptic plasticity (Davis, 2006) to dendritic arborization (Kellner et al., 2014) and even to neuronal regeneration (Elzinga et al., 2015; Chan et al., 2016). Such mechanisms are naturally governed by the intrinsic signaling of molecular factors that have been, and continue to be, increasingly illuminated over the past several decades. A host of intrinsic and extrinsic factors exhibit direct activity-associated expression changes and have broad effects on neuronal expression, such as BDNF, neuronal PAS domain protein 4 (Npas4), and many others. Recent literature describes neuronal activity-associated gene expression control mechanisms, including a potential role for activity induced DSBs and RNA pause-release, alluding to the depth and breadth of complexity of activity-associated gene expression (Madabhushi and Kim, 2018). A full understanding of the ways in which neuronal activity influences gene expression may prove critical to developing potential neuronal activity modulation therapies. We here highlight some well-documented and some newly-discovered fundamental mechanisms for intrinsic neural control of molecular behavior and signaling in response to neural activity.

BDNF and Neuronal Plasticity

BDNF and its receptor2, TrkB, have been widely studied in both the CNS and the peripheral nervous system (PNS) (Nagappan and Lu, 2005; Nagahara and Tuszynski, 2011). BDNF is a powerful neurotrophic factor known to induce plastic changes that regulate neuronal growth, excitability, and even regeneration (Jin et al., 2002; Garraway and Huie, 2016). A major mechanism of action for BDNF is via the binding of TrkB. This binding initiates a signaling cascade that regulates activity-associated dendritic plasticity in mice (Lai et al., 2012) as well as local production of proteins associated with synapse formation (Lu et al., 2008). Dendritic TrkB is upregulated in an activity-associated manner and inserted specifically at targeted dendrites, explaining how a diffusible molecule (e.g., BDNF) can initiate local changes in synaptic plasticity (Tongiorgi et al., 1997; Nagappan and Lu, 2005). Importantly, field electric stimulation has been shown to influence the trafficking of TrkB from the intracellular pool to the membrane of neuronal processes in cultured hippocampal neurons (Du et al., 2000).

BDNF is one of a few neurotrophic factors that exhibit activity-associated behavior, with activity-associated mechanisms governing BDNF transcription, dendritic targeting, and trafficking of BDNF protein, and messenger RNA (mRNA) release and conversion of BDNF to a mature form (Jin et al., 2002; Zhou et al., 2006; Im et al., 2010; Bading, 2013; Palomer et al., 2016). BDNF is widely implicated as a major driver of neuronal plasticity that directly contributes to learning. For example, TrkB signaling is required for spatial memory formation in mice (Lai et al., 2012), BDNF signaling contributes to the conversion of early to late phase long-term memory (Lu et al., 2008), BDNF signaling facilitates cocaine-seeking addictive behavior in mice (Im et al., 2010), and BDNF administration has even been implicated in functional recovery after stroke (Berretta et al., 2014) and SCI (Ghosh et al., 2018) in rodents.

Critical reasons for considering BDNF and its effects under the umbrella of neural stimulation are: (1) BDNF is a potent regulator of neural plasticity, including downstream enhancement/modulation of synaptic plasticity (Karpova, 2014), cell survival, and morphological properties of neurons (Zagrebelsky and Korte, 2014) and (2) BDNF activity is associated with levels of neural activity. Synaptic plasticity is largely regulated by, and sometimes dependent on, BDNF signaling (Lu et al., 2008). In fact, BDNF is thought to be synthesized in dense core vesicles and secreted at the synapse in response to neuronal activity. Importantly, new evidence tracking BDNF tagged with quantum dots in hippocampal cultures suggests a mechanism for activity-associated release of BDNF from endocytosed vesicles in the post-synaptic dendrite (Wong et al., 2015), indicating multiple sources and mechanisms exist to regulate activity-associated release of BDNF at synapses. *In vitro* experiments using mouse hippocampal cultures at different developmental time-points highlight the importance of neuronal activity on BDNF's structural effects on neurons. In loss-of-function experiments, blocking endogenous BDNF resulted in hippocampal neurons with less dendritic complexity and longer dendritic spines with thinner heads (Kellner et al., 2014). Exogenous application of BDNF in culture did not significantly alter dendritic structure or density as reported in *in vivo* experiments (Ji et al., 2010); however, cultures with reduced levels of spontaneous activity were responsive to exogenous BDNF and exhibited increased dendritic density, indicating that levels of neural activity may play an important role in the neuronal response to BDNF (Kellner et al., 2014). Overall, these studies show that BDNF regulation is quite complex, and that the effects of BDNF include modulation of synaptic and dendritic structure as well as network plasticity; but, they are ultimately context and activity specific.

Observations on the effects, control, and pharmacological application of BDNF in disease not only have led to an appreciation of its importance, but have also raised questions

about the mechanisms whereby levels of BDNF are modulated in the spinal cord. In patients with incomplete SCI, a graded-intensity, locomotor exercise regimen increased serum levels of BDNF. Still, said levels were related to the intensity of the locomotor activity rather than the activity itself (Leech and Hornby, 2017). It remains unclear in injury models to what extent such recovery is dependent on neural activity-associated plasticity vs. metabolic mechanisms. Rodent work indicates that voluntary wheel running increased the expression of several downstream effectors for the action of BDNF on synaptic plasticity [e.g., synapsin I and growth-associated protein (GAP-43) mRNA] (Gómez-Pinilla et al., 2002). Further, voluntary wheel running increased production of the ketone body β-hydroxybutyrate in the liver, which is both an energy source used in the brain and an inhibitor of class 1 histone deacetylases (HDACs) (Sleiman et al., 2016). HDACs cause the deacetylation of histones, resulting in less accessible and more tightly bound DNA. HDAC inhibition increases levels of synaptic plasticity genes, including cAMP response element-binding protein (CREB), BDNF, and calmodulin-dependent kinase II (CaMKII) (Guan et al., 2009; Koppel and Timmusk, 2013). Thus, production of this ketone could explain some of the beneficial effects of exercise. In fact, application of β-hydroxybutyrate to cultured cortical neurons, hippocampal slices, and via *in vivo* intraventricular injection all resulted in elevated expression of BDNF transcripts (Sleiman et al., 2016). Therefore, exercise-associated BDNF production may not directly rely on intrinsic firing of neurons. Rather, it may be a passive result of metabolite production.

BDNF appears to be a potent regulator of neural plasticity; however, some studies have tempered enthusiasm for a potential BDNF panacea-type therapy to injury and disease due to its possible pronociceptive effects, particularly following CNS trauma (Garraway and Huie, 2016). For instance, Grau and Huang (2018) have demonstrated that BDNF is necessary and sufficient to enable spinal learning of a shock withdrawal response in a thoracic transection model in rats. Yet, BDNF also appears to play a critical role in the formation of neuropathic pain after injury (Smith, 2014; Garraway and Huie, 2016). Given the broadly acting nature of BDNF (Karpova, 2014) and that its effects are context dependent (Xiao et al., 2009), it seems logical to conclude that other activity-associated mechanisms may play a role in regulating neural behavior and in modulating the effects of BDNF itself.

Trophic Modifiers of Neuronal Complexity and Excitability

Aside from BDNF, other trophic factors are modulated or released in an activity-dependent manner. For instance, neuritin mRNA was initially identified as having activity-associated transcription and purified neuritin and was later revealed as a modulator of neurite outgrowth and arborization in embryonic hippocampal and cortical mouse neurons (Naeve et al., 1997). Subsequent studies have demonstrated that neuritin induces neuritogenesis and that it plays a role in the maturation and stability of synapses while also increasing neurotransmitter release in cortical neurons (Yao et al., 2018). Neuritin activity can also be mediated through nuclear factor of activated T-cells cytoplasmic 4 (NFATc4) and calcineurin (CaN). Neuritin induces neurite morphological changes through calcium signaling by upregulating L-type voltage gated calcium channels (Zhao et al., 2018). Additionally, the trophic factor fibroblast growth factor (FGF) appears to mediate the activity-dependent neurite morphological effects of neuritin. Inhibition of the FGF receptor attenuates the effects of neuritin on neurite arborization and complexity, indicating that other trophic factors play a role in activity-associated effects, albeit indirectly (Shimada et al., 2016). Neuritin and FGF are not the only identified trophic factors associated with neuronal activity. Isoforms of the *homer1* gene were found to express activity dependent expression and Homer1a, a product of the *homer1a* IEG, was found to modulate pre- and post- synaptic remodeling in glutamatergic neurons in a biphasic activity induced manner (Xiao et al., 2000; Inoue et al., 2007). Further, other products of the *homer1* gene, Homer 1b/c, are spinal synaptic scaffolding proteins in the post-synaptic density of excitatory synapses. Indeed, work from Yao et al. demonstrates that Homer 1b/c not only regulates CREB phosphorylation and c-fos activation in the spinal dorsal horn, but that it may play a role in the formation of chronic pain following spinal injury (Yao et al., 2014).

Neural Activity and IEGs

IEGs are genes that exhibit a rapid and transient change in expression in response to a variety of extracellular stimuli in a protein synthesis independent manner. In the context of neural activity, IEGs are a proposed mechanism for rapid, functional translation of altered depolarization behavior (Flavell and Greenberg, 2008). A host of genes have been identified as IEGs and are upregulated/downregulated in response to changes in neural activity at early time points after stimulus administration (Carulli et al., 2011). In some cases, IEG responses mediate transcriptional factors, including growth arrest and DNA damage inducible β (Gadd45β), Npas4, early growth response 4 (Egr4), nuclear receptor subfamily 4 group a member 1 (Nr4a1), Fos, and many others (Spiegel et al., 2014). IEGs exhibit transcriptional changes immediately following an altered period of activity and the full time-course of this response can range from hours to days (Morgan and Curran, 1989). For instance, increased transcription of c-fos occurs within 5 min of induction (Sheng and Greenberg, 1990). Recently, it was demonstrated that some IEGs exhibit control mechanisms that are not directly dependent on neural activity (Okuno, 2011; Bahrami and Drabløs, 2016). While Arc expression is normally tightly associated with neural activity initiated through behavior or sensation, it has been shown that Arc is decoupled from activity patterns in novel recognition paradigms. For example, control mice placed in a novel environment exhibit increased Arc expression in their hippocampi. However, Arc levels are reduced following lesions to the fornix (Fletcher et al., 2006) and following repeated environmental exposure (Guzowski et al., 2006). Fornix lesions did not impact overall activity levels in the hippocampus and overall hippocampal electrophysiology remained unchanged throughout the study. This indicates that there is a secondary

regulator of Arc expression in the hippocampus beyond neural activity alone. Both the target responsiveness to an IEG and the environment of the circuit and organism are critical considerations for manipulating IEG expression to promote activity-dependent plasticity in a clinical context.

IEGs have been identified as a potential primary mechanism for modulating and maintaining neural connectivity, and they may have mechanisms for neuron-to-neuron signaling in an activity-associated manner. Arc protein has recently been shown to form a structure reminiscent of a Gag capsid. This capsid-like structure is secreted from neural cells and can inject mRNA into recipient cells, which can then exhibit activity-associated translation (Pastuzyn et al., 2018). This striking example of neuron-to-neuron signaling highlights the importance of considering activity-associated signaling at the circuit level since modulation of activity in a single neuron can initiate changes in transcription and translation in other neurons. The full extent to which this extrinsic signaling is relevant remains unknown. Therefore, future research must explore this further to better understand how neuron-to-neuron signaling mediates plasticity following bouts of depolarizing activity.

Activity-Associated Plasticity in Epigenetics and Gene Expression

How environmental stimuli cause lasting adaptive changes (i.e., the formation of memory) has been an area of study since Flexner et al. first established that new protein synthesis was necessary for the formation of adaptive behavior, namely memory, in a short window following an environmental stimulus (Flexner et al., 1963). Specifically, bilateral injections of puromycin, a protein synthesis inhibitor, into the hippocampi and adjacent temporal cortices of mice abrogated conversion of memory from short- to long-term in a simple maze learning paradigm, indicating that a protein was necessary for the formation of long-term memory in mice. The model of transcription and translation at the time did not include a mechanistic explanation for the formation of adaptive behavior in response to environmental stimuli. This led researchers to investigate how exactly adaptive behaviors are formed. The eventual discovery of transcription factors and promoter regulatory elements explained how gene expression might vary following exposure to external stimuli. Particularly, in neural activity coupled gene expression, serum factors, and upstream non-coding promoter regulatory elements were both found to produce rapid changes in transcription following bouts of neural activity. For instance, calcium induction through voltage gated channels was found to be the driving event for induction of *c-fos* expression in neurons (Morgan and Curran, 1986). Such expression required a particular sequence upstream of the promoter (Sheng et al., 1988), which was bound by CREB. CREB was eventually discovered to be a transcription factor that stabilized expression of *c-fos* when phosphorylated by calmodulin dependent kinase (Sheng et al., 1991). Together, these discoveries describe a mechanism whereby external stimuli such as neural depolarization can cause changes that initiate a signaling cascade capable of altering transcription factors, which may then affect a transcriptional response by binding to transcriptional regulatory elements and stabilizing or inhibiting transcription. Still, such observations do not describe how lasting gene expression changes could occur in response to environmental stimuli. With demonstrations that histone methylation causes conformational chromatin changes, which decrease gene expression at the site of methylation (Rea et al., 2000) and that acetylation results in looser chromatin structures with enhanced transcription at the site of acetylation (Brownell et al., 1996), researchers discovered mechanisms whereby environmental influences could affect stable changes to gene expression. Epigenetic modifiers were linked to neural activity (Qiu and Ghosh, 2008) and have since been considered critical in describing activity-associated changes in neural cells (Carulli et al., 2011; Ciccarelli and Giustetto, 2014; Karpova, 2014). Through epigenetic modifications, environmental triggering of signaling cascades, and transcription factor binding to promoter regulatory elements, it is clear that neural activity patterns can cause both temporary and stable changes to neural transcription.

In addition to transcription factors binding to regulatory elements, novel mechanisms for transcriptional regulation have been uncovered. Gariglio et al. found an unanticipated clustering of RNA polymerase II (RNAPII) at the 5′ end of the β-globin genes in mature erythrocytes in transcriptional run-off assays, which they posited may constitute a rate-limiting step to transcription (Gariglio et al., 1981). Initially identified in metazoan model systems, researchers have uncovered a mechanism of RNAPII pause-release that is widespread and that not only regulates rates of transcription, but also is subject itself to regulation (Adelman and Lis, 2012; Jonkers and Lis, 2015). Chromatin immunoprecipitation sequencing (ChIP-seq) revealed RNAPII binding at promoters of various IEGs under basal conditions (Kim et al., 2010). Researchers have directly identified transcriptional pause-release regulation of c-fos and Arc, and it is likely that activity-associated signaling pathways regulate this pause-release phenomena (Kim et al., 2010; Schaukowitch et al., 2014; Joo et al., 2016). Continually, it has been posited that enhancer RNA may be recruited to IEG promoters and initiate RNAPII unpausing in an activity-associated manner (Madabhushi and Kim, 2018). Recent studies have revealed that pausing of RNAPII positively correlated with tri-methylation of the 27th lysine residue at histone 3 (H3K27me3) in developing mouse cortical neurons (Liu et al., 2017), indicating a role of pausing in fate selection and expression during development. Enhancer RNA (eRNA) have been shown to trigger transition of RNAPII from a paused to active state by facilitating release of the negative elongation factor (NELF) complex from target promoters following IEG activation (Schaukowitch et al., 2014). RNA pause-release may thus be a key transcriptional regulator of neural activity-associated gene expression and may describe yet another method whereby neural depolarization causes changes in gene expression.

Beyond pause-release, the discovery of neural activity-induced DSBs indicates a startling potential mechanism for regulating transcription (Madabhushi et al., 2015). DSBs are generally thought to be a destabilizing and cytotoxic event. Neural activity has been found to cause DSBs both *in vitro* (Crowe et al., 2006)

and *in vivo* (Suberbielle et al., 2013); and, neural activity-induced DSBs may be used as a method to regulate activity-associated transcription (Madabhushi and Kim, 2018). Researchers have demonstrated that neural activity-induced DSBs form within the promoters of several IEGs (e.g., Fos, Npas4, and Egr1) and that said DSBs are sufficient to enhance transcription (Bunch et al., 2015; Madabhushi et al., 2015). Neural activity-induced DSBs are generated by topoisomerase IIβ and are stabilized rather than rapidly repaired. Normally, topoisomerases cause transient breaks in DNA to relieve strain caused by DNA processing activity. They rapidly repair DSBs, allowing the breaks to avoid detection by DNA damage response pathways. In contrast, neural activity-induced DSBs are longer lasting and are somehow stabilized, though the mechanisms remain unclear. Activity-induced stable DSBs are then detected by DNA damage repair pathways, which can result in enhanced transcription (Madabhushi et al., 2015). Recently, a member of the growth and arrest DNA damage family, growth arrest and DNA damage inducible gamma (GaDD45y), was identified as mediating fear memory consolidation in mice through binding at DSBs in the promoter regions of several plasticity related IEGs (Li et al., 2019). More research is needed to fully understand how DSBs form and whether different types of activity may influence their activity. Still, these startling observations hint at yet another mechanism in the complex and layered activity-associated regulation of neural plasticity.

Temporal Patterns of Activity and Gene Expression

The wealth of transcriptional and translational regulatory mechanisms sensitive to neural activity describe a layered and complex system. Clearly, activity-associated plasticity occurs. Newly discovered mechanisms indicate that the pattern and length of neural activity trains produce distinct changes in transcription. Further, they hint at a potentially subtle and temporally regulated interaction between activity and transcriptional and translational response. Indeed, patterns of neural depolarization and the duration of a depolarization train may initiate unique transcriptional responses. Enticing new research in mouse DRG neurons examined genes regulated by activity patterns and timing (Lee et al., 2017). While previously identified activity-associated master regulators such as BDNF, EGR4, Gadd45b, Npas4, and Nr4a1 were generally found to be differentially controlled by stimuli, independent of pattern or time, a host of novel RNA transcripts whose levels depended explicitly on temporal patterns of activity in mouse DRG neurons were determined (Lee et al., 2017). Pathway analysis of the observed transcripts revealed different patterns and total durations of stimulation can induce activity-associated changes in NGF and Rac signaling, important modulators of neurite outgrowth. Electrical stimulation of mouse DRG neurons using different patterns, but the same total number of electrical pulses at 10 Hz, revealed network changes in gene expression dependent on patterned stimulation (Lee et al., 2017). Excitingly, many of the novel transcripts exhibited changes in transcription levels when DRG neurons were paced with different patterns of stimulus, thus classifying them as activity-associated and suggesting their actions affect neuronal plasticity and growth. The observation that patterned activity can alter gene expression, while preliminary, has vast implications on neuronal response to stimulation. If patterns of activity have broadly differential effects on neuronal transcripts, then the implications for clinical stimulators would be profound. Driving specific patterns of activity in targeted brain and spinal circuitry may thus be a way to control transcriptional response and cause desirable expression changes to promote recovery following CNS trauma. Work by Tyssowski et al. (2018) further supports the hypothesis that there are temporal signatures of neural response to activity and that sustained vs. brief depolarizations result in large differentials in RNA transcripts. By manipulating the duration, but not frequency, of neuronal activity, Tyssowski et al. identified three functionally distinct transcriptional patterns dependent on unique regulatory pathways comprising exclusive waves of transcription that occur in response to patterned neural activity. These examples are the first to show not only the importance of duration and temporal pattern of neuronal activity on transcriptional output, but also how neural firing patterns may cause large changes in neuronal transcription. It has yet to be determined whether frequency of stimulation may play a role, or whether these effects are restricted to mouse DRG neurons and mouse and rat cortical neurons. Still, these observations may prove critical when considering how to modulate neuronal activity to enhance recovery. In particular, stimulation regimes for exciting the brain or spinal cord through optogenetic, electrical, or magnetic stimulation are often static and periodic in nature.

It is critical to examine how dosing and pattern play a role when stimulating the brain and spinal cord. Work by Taccola et al. demonstrates that locomotive central pattern generators in the rat spinal cord are optimally activated by noisy dorsal root stimulation patterns (Taccola, 2011). Such an observation may have implications for existing clinical spinal stimulators given that introduction of randomness could improve the efficacy with which central pattern generators are recruited during spinal neuromodulation. Still, this begs the question of whether overstimulation or random stimulation may induce negative effects. After spinal injury, there is a known excitatory inhibitory imbalance that drives additional activity for prolonged periods, and thus may encourage the onset of spasticity and neuropathic pain through inadvertent maladaptive plasticity (Lavrov et al., 2008; Ferguson et al., 2012; Grau et al., 2017). Therefore, it is crucial to minimize the risks of stimulation induced maladaptive plasticity through optimal dosing and careful targeting of select circuits to minimize secondary effects while maximizing the benefits. While random stimulation paradigms may more effectively enhance recruitment of motor associated dorsal roots, it remains to be determined whether such paradigms may also more effectively enhance maladaptive plasticity (Lavrov et al., 2008).

Given the observation that pattern and duration of neural activity can each greatly alter the functional transcripts of a neuron, it seems clear that stimulation paradigms must be more closely considered. It is no surprise that most reported *in vivo*

CNS stimulation paradigms have been static in nature. *In vivo* injury and stimulation experiments are already costly, difficult, and complex enough without the addition of stimulation regime variables, such as pattern and duration. It seems imperative that future research includes a characterization, whenever possible, of the activity dependent transcriptional changes relevant to injured circuitry and the response of the damaged nervous system to changes in neural activity. Given the cost, time, and importance associated with neural injury and neuromodulation studies, the field would greatly benefit from shared resources such as a tissue repository or transcriptional database to enhance our ability to leverage activity associated mechanisms to initiate recovery.

LEVERAGING NEURONAL ACTIVITY-ASSOCIATED MECHANISMS TO PROMOTE RECOVERY

Neuronal activity-associated plasticity mechanisms play an important role in recovery following damage to the PNS and/or CNS through trauma, stroke, and neuroregenerative disease. Given the array of methods currently in use or being developed for manipulating neuronal activity following injury, it may be relevant to consider our understanding of activity-associated plasticity in the context of potential clinical applications. Following damage to the nervous system, some evidence suggests that regrowth and reconnection of axons occurs in the PNS, while very limited evidence indicates that such plasticity occurs in the CNS (Liu et al., 2011). The success of physical rehabilitation, electrical stimulation, and other therapeutic strategies to mitigate CNS and PNS damage from trauma, stroke, or neurodegenerative disease indicates a possible role of activity-associated plasticity in recovery following damage. Here, we present some of the clinical and potentially translatable methods to manipulate neuronal activity, and we highlight potentially relevant considerations (**Figure 2**).

Passive and Active Exercise Are Effective Tools for Initiating Recovery After SCI

Two common rehabilitation tools are (1) passive exercise, which requires no controlled physical effort, and (2) active exercise, which involves subjects performing assisted or unassisted movements using volitional control. After spinal injury, a lack of supraspinal input can enhance sensory control of spinal circuitry. Stretching of a skeletal muscle activates the H reflex through group Ia afferents, which can lead to changes in sensory driven reflexes (Skinner et al., 1996; Gazula et al., 2004). Repetitive passive conditioning of limbs after spinal injury has been shown to "normalize" reflex responses in absence of supraspinal input in both rodents (Skinner et al., 1996) and humans (Rösche et al., 1997; Kiser et al., 2005). This can reduce spasticity and habituation of somatosensory reflexes. However, continued passive conditioning is necessary to maintain such effects, at least in humans. Passive bicycling in spinally transected rats led to an upregulation of neural activity-associated proteins, BDNF, and adenylate cyclase 1 (ADCY1) in the somatosensory cortex, and said upregulation was accompanied by an increased tactile response in the denervated limb (Graziano et al., 2013). This indicates that, at least in rats, passive exercise can facilitate cortical plasticity through activity-associated mechanisms, though the degree to which passive exercise alone leverages permanent cortical changes in humans remains unclear. Other studies have demonstrated that active exercise also produces neuronal plasticity, which can lead to functional recovery in both humans (Jurkiewicz et al., 2007) and rats (Kao et al., 2011). Many active exercise-associated functional plasticity studies have exhibited a task-dependent and/or task-specific plasticity that is associated with particular movements, indicating that movement-associated circuitry should be targeted in rehabilitation therapy (Lynskey et al., 2008). For example, one case report revealed that a person with cervical injury who received bimanual somatosensory stimulation in combination with massed practice (repetitive task oriented training) manifested enhanced sensation, grip force, and performance of task-specific hand skills, such as writing, page turning, lifting of a small object, manipulating checkers etc., which coincided with a reorganization of the cortical map (Hoffman and Field-Fote, 2007). Such cortical rewiring suggests active exercise can initiate a type of synaptic plasticity that is driven by activity-associated mechanisms. The improvement of task-specific movements and enhanced sensation through passive and active exercise following disruption of the CNS indicate plasticity plays a role, possibly through activity-associated mechanisms, in the restoration of motor function following injury. In passive exercise regimens, such as on a fixed bike, functional recovery is dependent on continued input. It is believed that load sensing sensory afferents cause plastic changes to occur in central pattern generators located in the spinal cord (Dietz and Harkema, 2004). Alternatively, active exercise (i.e., voluntary or assisted standing/walking, treadmill training, and forelimb reaching) can produce reorganization of cortical and spinal circuitry, resulting in improved motor function. Yet, the degree to which such plasticity is sensory load-dependent or can be mediated by other forms of propriospinal input remains unknown (Lynskey et al., 2008).

Clearly, exercise can initiate plastic changes in the CNS, but through what activity-associated mechanisms is this achieved? A myriad of reports haven examined the benefits of exercise on the brain. The hippocampus in particular has been proven to exhibit significant and long-lasting changes in response to increased levels of physical activity (Rendeiro and Rhodes, 2018). BDNF levels increase in the rat brain following bouts of elevated physical activity (Marais et al., 2009; Rasmussen et al., 2009). These increased levels are thought to occur, in part, due to muscle derived factors such as PGC-1α and its downstream protein FNDC5, both of which were found to be elevated in the hippocampus of exercising mice (Rendeiro and Rhodes, 2018). Circulating FNDC5 is believed to cross the blood brain barrier and directly modulate hippocampal gene expression. Therefore, a factor released from skeletal muscle during exercise can effect changes in the brain. Interestingly, neural activity can also effect changes in skeletal muscle by initiating transcriptional changes in the muscle through HDAC4 signaling at the neuromuscular junction (NMJ) (Cohen et al., 2007). HDAC4 is normally

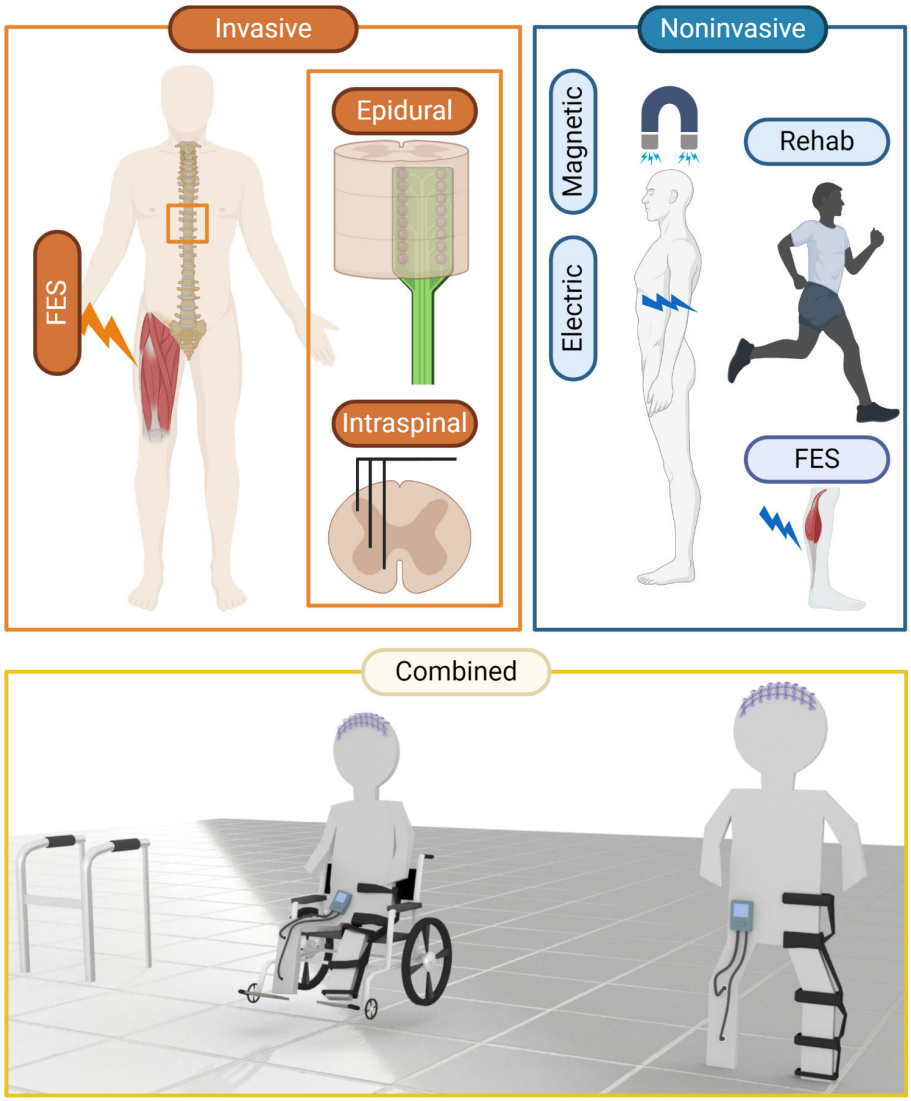

FIGURE 2 | Clinical means to alter neural activity have been employed with a view to restore or improve function after insult. Invasive techniques, typically involving surgical placement of electrodes to control muscle or neural activation have been used for pain management and functional restoration after neural trauma or stroke. Non-invasive techniques, such as TES, TMS, FES, and rehabilitation are more clinically palatable, though non-invasiveness is generally correlated with a decrease in precision. An exciting area is emerging where techniques are being combined with greater effect. Invasive and non-invasive means to record and manipulate neural activity are being combined to "close the loop" and restore previously intractable function.

localized at the NMJ; however, following reduced neural input through denervation, HDAC4 is released and exhibits activity dependent transcription in the muscle. Consequently, there are bidirectional control mechanisms whereby neural activity can initiate transcriptional changes in the muscle and altered muscle activity can influence transcription in the brain. Stimulation, particularly in the spine, can initiate motor responses and thus cause changes to the neuromuscular axis. Therefore, it is critical to consider the broad physiological responses initiated by spinal stimulation or physical activity. Such changes initiated by physical activity are not limited to effects induced by the muscle alone. Exercise also causes changes in peripheral organs, which may in turn produce paracrine factors capable of initiating transcriptional changes in the CNS. Recently identified metabolic factors such as β-hydroxybutyrate may contribute to changes in BDNF expression in the hippocampus, possibly describing a mechanism where exercise influences learning, memory, and mood (Chen et al., 2011; Sleiman et al., 2016). Importantly, serum levels of BDNF in humans with spinal injury have been positively correlated with exercise intensity (Leech and Hornby, 2017). These observations argue for a potentially metabolic mechanism for BDNF release and activity, and this may be the case particularly in facilitating supraspinal plasticity. There are a host of ways in which exercise and activity influence neural

plasticity in the brain and spinal cord, both in the long- and short-term. Bouts of physical activity can transiently enhance blood brain barrier permeability, serum levels of BDNF and VEGF, neuronal IGF-1 uptake, and VEGF expression in the hippocampus as well as initiate long term cardiovascular changes and neuroplastic rewiring (Stimpson et al., 2018).

The observation that BDNF and other neurotrophin levels are locally modulated by neural activity is further supported by changes in neurotrophin levels at the spinal level following different exercise regimens. For example, Côté et al. (2011) examined how passive cycling and treadmill stepping rehabilitation may contribute to activity-associated plasticity after complete thoracic spinal trans-section in rats. They found that both stepping and cycling promoted increased levels of BDNF, neurotrophin-3 (NT-3), and neurotrophin-4 (NT-4) at the lumbar enlargement of SCI rats. The increased levels were positively correlated with recovery of spinal H-reflex responses. Further, the researchers demonstrated that while both exercise regimens promoted enhanced levels of glial derived neurotrophic factor (GDNF) rostral to the injury site, only step-training promoted elevated levels of GDNF at the lumbar enlargement, indicating that sensory feedback may play a critical role in spinal neurotrophic expression. This experiment provides significant evidence that different physical movements may involve unique spinal networks. Further, spinal network activity may contribute to unique molecular changes post-injury that may be relevant in the selection of rehabilitation regimens.

One major barrier in developing effective rehabilitation exercises to promote functional improvement stems from limited control of neural circuitry following CNS injury. Numerous efferent fibers and interneuron circuits that could be manipulated to provide beneficial plastic changes may exist; however, it is also possible that said fibers and circuits are not accessible through exercise. There are means to manipulate neural circuitry purely through exercise and movement-based therapy (e.g., stretch receptor activation and supraspinal/cortical activation through voluntary intent and propriospinal activation); however, the types and patterns of activation are limited to physiological responses under fixed conditions. A further barrier is the degree to which voluntary control is possible after damage. In active exercise, the ability to exert supraspinal control is important and limitations in volitional control minimize the abundance and types of neurons that can be activated. Still, physical rehabilitation remains the most effective and only accepted therapy following damage to the CNS and PNS.

Electrical Stimulation of the CNS and PNS

Given the limits of rehabilitation, researchers have explored techniques to actively manipulate neural activity within the spinal cord. Direct application of an electric current via penetrating or non-penetrating electrodes can alter activity patterns of neural circuits in the brain and spinal cord. Electrical stimulation may be leveraged following CNS injury to enhance basal excitability of spared circuitry, thereby facilitating supraspinal control or directly activating disconnected networks to initiate activity-associated rewiring or regeneration. Intraspinal microstimulation (ISMS) and dorsal epidural spinal stimulation (ES) are two methods for electrically altering activity in the spinal cord following injury in order to enhance recovery or manage pain. Both ISMS and ES have been applied following cervical injury in rats, and each have proven to be advantageous. Work from the Moritz and Horner laboratories demonstrates beneficial application of ISMS following cervical hemicontusion injury in rats as measured by improvement in a skilled forelimb reaching task following application of cervical stimulation (Sunshine et al., 2013; Mondello et al., 2014). ISMS stimulation of forelimb motor associated motor pools resulted in persistent enhancement of digit extension, pronation, and supination of the wrist during a forelimb reaching task. These effects persisted for hours following cessation of ISMS stimulation (Kasten et al., 2013). Further, cervical ES was beneficial in a cervical crush injury in rats as it reduced aberrant co-activation of antagonistic muscle groups (Alam et al., 2017). After a unilateral pyramidotomy in rats, penetrating electrical stimulation to the forelimb area of the contralateral motor cortex or contralateral medullary pyramid produced increased axon sprouting to the side of the cord ipsilateral to the injury and improved motor function that was still present thirty days after therapeutic electrical stimulation had been halted (Brus-Ramer et al., 2007; Carmel et al., 2010). Electrical stimulation may not only improve plasticity and sprouting, but also affect connectivity and pruning of developing tracts. Stimulation of the medullary pyramid in cats during development maintained connections that might otherwise be pruned and hold the potential to promote sprouting of descending tracts (Salimi and Martin, 2004). New connections are formed spontaneously after midthoracic partial dorsal hemisection, but subsequently lost if they do not connect with intact neurons such as long propriospinal neurons that bridge the lesion site after injury (Bareyre et al., 2004). Thus, electrical stimulation may be critical for maintaining and improving spared spinal circuitry after injury.

In terms of spinal stimulation after SCI, ISMS and ES each have their own advantages; however, they also have drawbacks that limit their therapeutic potential. ISMS allows for relative precision compared to other spinal stimulation paradigms, as intraspinal wires can be guided to specific locations and tested for discrete activity of pools of interest. Given this, ISMS approaches can elicit more controlled modulation of activity in the spinal cord when compared with ES. Importantly, it is not currently feasible to target specific motor pools via dorsal ES. In fact, it is likely that ES preferentially activates central pattern generator circuitry, which limits its therapeutic potential (Bareyre et al., 2004; Taccola et al., 2017) Conversely, scarring and functional stability are major barriers for clinical translation of intraparenchymal stimulation techniques, whereas ES has been widely applied in the clinic with favorable outcomes (Stidd et al., 2014).

Geometric location may be a primary concern when considering ES approaches. Given that sensory and propriospinal afferents are generally located on the dorsal aspect of the cord, while the majority of motor associated circuitry is situated in the ventral region, targeting the ventral surface could allow for more select activation without recruitment of central pattern generators. The ventral surgical approach is commonly applied

in humans; however, given the challenge of accessing the ventral epidural space in rodents, ventral epidural spinal stimulation (VSS) has not been extensively studied. Still, an analysis of motor responses in the cervical spine in monkeys revealed that stimulation applied from the ventral and dorsal surfaces evoked muscle responses through different spinal circuitry (Sharpe and Jackson, 2014). Therefore, there is a rationale for exploring geometric placement of epidural electrodes in order to manipulate unique circuits in the spinal cord.

Given the potential for failure and the invasive nature of implantable stimulators, researchers have examined other avenues to therapeutically manipulate neural activity. Techniques such as magnetic stimulation and transcutaneous electrical stimulation are being examined to determine whether less invasive and chronically stable forms of stimulation may facilitate recovery, particularly after SCI, traumatic brain injury, and stroke (Rossini et al., 1994; Hummel and Cohen, 2006; O'Connell et al., 2018).

The idea of non-invasively manipulating neural activity is not a new one. Functional electrical stimulation (FES), a technique of directly stimulating affected musculature, has been leveraged both through implants and via transcutaneous electrodes to facilitate movement and improve function for over five decades. In a meta-analysis of studies applying FES after stroke in humans, FES was found to provide improvement over no intervention and rehabilitative training alone (Howlett et al., 2015). Non-invasive FES is applied through coupled transdermal electrodes placed on the skin that depolarize local motor neurons and facilitate neuromuscular activation and muscle contractions (Peckham and Knutson, 2005). Still, FES is limited in terms of which neurons can be manipulated by stimulation. FES directly activates motor neurons, initiating contractions and ultimately stimulating stretch receptors, thus triggering changes in sensory feedback. This activation is unidirectional, beginning at the motor level and facilitating activity of peripheral nerves, while not directly engaging spinal circuits of motor control. This limitation may represent a ceiling on the potential for FES as a therapy. Still, means of engaging supraspinal and motor associated spinal circuits coincident with FES stimulation exist. Coupling non-invasive EEG recordings with surface stimulating electrodes may provide a means to non-surgically allow "thought-control" of functional movements. This concept has been successfully applied to facilitate task specific movements such as grasping of a cylinder in subjects with tetraplegia (Pfurtscheller et al., 2003). Though closed-loop FES may provide a means to facilitate recruitment of supraspinal and descending motor associated circuits, such techniques are limited in terms of recruiting disconnected circuitry at the spinal and even supraspinal level.

Given this, non-invasive means of applying current directly to the brain and spinal cord have been examined. Transcutaneous electrical stimulation (TES) involves the application of transdermal electrodes above the brain or spinal cord and has been shown to evoke functional activation of motor associated circuitry (Gerasimenko Y. et al., 2015). A major hypothesis behind many TES therapies is that central pattern generator circuits exist in humans and can be accessed when excitability of spinal circuits is raised above a certain level. When a neuromodulatory stimulus is applied, TES can facilitate supraspinal control of muscle activity in humans with motor complete injury and allow strengthening of connections to initiate or improve voluntary control, which would otherwise be impossible (Gerasimenko Y. P. et al., 2015). This motor engagement can lead to functional movements and can even allow for improved postural control (Rath et al., 2018) and voluntary standing without trainer assistance in humans with chronic motor and sensory complete paralysis (Sayenko et al., 2019). Clearly TES can facilitate recruitment of circuits at the spinal level, though a major application barrier is a lack of specificity in terms of circuit engagement. It remains to be shown whether TES can reach deep areas of the brain and spinal cord directly. Regardless, such stimulation will necessarily be non-specific. Further, success of TES is thought to be dependent on spinally encoded circuits and may not extend to more eloquent motor movements outside of stepping and standing. Strategies to raise levels of spinal excitability can lead to spasticity and pain and, as such, more research is needed to understand how TES may be applied safely to improve outcomes after injury.

Transcranial magnetic stimulation (TMS) is another way to non-invasively manipulate activity of neural circuits. It involves generating a magnetic field that creates an electric current to activate neural structures. Since magnetic fields can pass through tissues more readily than electric fields with less interference, they can be used to generate electric currents in deeper brain layers than TES (Walsh and Pascual-Leone, 2003). Resultantly, TMS has been explored in the treatment of depression (Philip et al., 2018), addiction (Diana et al., 2017), migraine headaches (Fischell et al., 2017), traumatic brain injury (Neville et al., 2015), and others. Despite the name, TMS can also be applied to the spine. A study involving twelve human participants with reoccurring neck pain revealed that cervical manipulation of the spine with single and paired TMS pulses resulted in altered corticomotor processing and control of two upper limb muscles, the abductor pollicis brevis and extensor indices proprios (Taylor and Murphy, 2008). Still, the mechanism of action of such therapies is not well-understood. This is in part due to the difficulty of determining exactly which structures and circuits are activated by TMS. *In vitro* studies of cultured rat hippocampal neurons revealed that sensitivity to TMS induction was dependent on the shape and superstructure of neural cultures (Rotem and Moses, 2008). The complicated physics of TMS and our general limited understanding of specifically what may be activated by TMS limits the therapeutic potential of this strategy. Still, the possibility to somewhat selectively activate deeper structures of the brain and spinal cord may be an important component of future therapies.

Indeed, given the importance of selective activation of neural circuitry, novel strategies involving transgenic manipulation of neurons may one day play a therapeutic role. Optogenetics for instance, a technique where a modified algae derived opsin can be genetically engineered into a neuron, allows for wavelength specific activation or inhibition of neurons (Yizhar et al., 2016). Genetic engineering strategies allow local control of specific neural populations through promoter specific

transfection and local delivery of an engineered virus. Such strategies have produced techniques that alter neural activity through application of not only light, but also administration of magnetic fields or delivery of generally inert designer drugs (Wheeler et al., 2016; Gomez et al., 2017). While admittedly, such techniques are mostly limited in clinical application, the enhanced targeting of such strategies as well as the ability to selectively initiate changes in specific neural circuits with a high degree of temporal precision will undoubtedly prove a critical resource for uncovering the role of activity-associated plasticity mechanisms at the circuit and cellular level.

CONCLUSION

Molecular responses to activity-associated plasticity are driven by a layered and complex system. The mechanisms and outcome of extrinsic or intrinsic changes in activity are context dependent with much to be considered, particularly with regards to the post-injury environment. IEGs drive rapid and transient neuronal responses, which can initiate unique transcription programs following changes in neural activity patterns. The genetic control mechanisms dictating neuronal responses to depolarization patterns result in neural activity pattern-specific genetic expression programs that are circuit and situation specific. While tools to manipulate neural activity have existed for decades, the interplay between neural activity and behavior highlights the importance and potential clinical relevance of new methods to affect both factors synergistically. Given the complexity of interactions, the apparent fluid nature governing cellular responses to changing activity patterns, and the conflicting reported results, more studies are needed to fully realize the clinical applications of activity-associated plasticity. Still, a surge of new tools has led to an impressive growth in our understanding of wide-ranging activity-associated mechanisms and equally driven excitement for the promise of clinical application. Indeed, the partial success of several brain, spine, and peripheral stimulation therapies following trauma or disease hints at the true potential of leveraging activity-associated mechanisms to combat CNS damage. This broad review of activity dependent plasticity, however, reveals the largely siloed nature of laboratories focused on cellular and molecular mechanisms of plasticity and that of research focused on the physiological and functional impact of neuromodulation. Exciting opportunities exist at the intersection of these disciplines that will require tool, model, and conceptual collaborations. Seminal discoveries await that will help us uncover the full extent to which neural activity may be leveraged to provide recovery after CNS injury, degenerative disease, and age-related decline.

DATA AVAILABILITY STATEMENT

The raw data supporting the conclusions of this article will be made available by the authors, without undue reservation.

AUTHOR CONTRIBUTIONS

MH prepared the manuscript with contributions from PH and GH. PH, GH, and MH collected references and materials to present in the review article, and edited the document for correctness and grammar. MH collected and interpreted all data presented in this manuscript, and prepared all drawings and illustrations. All authors contributed to the article and approved the submitted version.

FUNDING

This work was funded by a generous grant provided by the Wings for Life Foundation (PH) and the Craig H. Neilsen Foundation (PH). The authors would like to thank the Morton Cure Paralysis Fund (grant number 599274) and Craig H. Neilsen foundation for funding of the post-doctoral fellowship of MH during the completion of this work.

REFERENCES

Adelman, K., and Lis, J. T. (2012). Promoter-proximal pausing of RNA polymerase II: emerging roles in metazoans. *Nat. Rev. Genet.* 13, 720–731. doi: 10.1038/nrg3293

Ahn, S., Ginty, D. D., and Linden, D. J. (1999). A late phase of cerebellar long-term depression requires activation of CaMKIV and CREB. *Neuron* 23, 559–568. doi: 10.1016/S0896-6273(00)80808-9

Alam, M., Garcia-Alias, G., Jin, B., Keyes, J., Zhong, H., Roy, R. R., et al. (2017). Electrical neuromodulation of the cervical spinal cord facilitates forelimb skilled function recovery in spinal cord injured rats. *Exp. Neurol.* 291, 141–150. doi: 10.1016/j.expneurol.2017.02.006

Allaman, I., Bélanger, M., and Magistretti, P. J. (2011). Astrocyte–neuron metabolic relationships: for better and for worse. *Trends Neurosci.* 34, 76–87. doi: 10.1016/j.tins.2010.12.001

Bading, H. (2013). Nuclear calcium signalling in the regulation of brain function. *Nat. Rev. Neurosci.* 14, 593–608. doi: 10.1038/nrn3531

Bahrami, S., and Drabløs, F. (2016). Gene regulation in the immediate-early response process. *Adv. Biol. Regul.* 62, 37–49. doi: 10.1016/j.jbior.2016.05.001

Bareyre, F. M., Kerschensteiner, M., Raineteau, O., Mettenleiter, T. C., Weinmann, O., and Schwab, M. E. (2004). The injured spinal cord spontaneously forms a new intraspinal circuit in adult rats. *Nat. Neurosci.* 7, 269–277. doi: 10.1038/nn1195

Berretta, A., Tzeng, Y.-C., and Clarkson, A. N. (2014). Post-stroke recovery: the role of activity-dependent release of brain-derived neurotrophic factor. *Expert Rev. Neurother.* 14, 1335–1344. doi: 10.1586/14737175.2014.969242

Brownell, J. E., Zhou, J., Ranalli, T., Kobayashi, R., Edmondson, D. G., Roth, S. Y., et al. (1996). Tetrahymena histone acetyltransferase A: a homolog to yeast Gcn5p linking histone acetylation to gene activation. *Cell* 84, 843–851. doi: 10.1016/S0092-8674(00)81063-6

Brus-Ramer, M., Carmel, J. B., Chakrabarty, S., and Martin, J. H. (2007). Electrical stimulation of spared corticospinal axons augments connections with ipsilateral spinal motor circuits after injury. *J. Neurosci.* 27, 13793–13801. doi: 10.1523/JNEUROSCI.3489-07.2007

Bunch, H., Lawney, B. P., Lin, Y.-F., Asaithamby, A., Murshid, A., Wang, Y. E., et al. (2015). Transcriptional elongation requires DNA break-induced signalling. *Nat. Commun.* 6:10191. doi: 10.1038/ncomms10191

Côté, M.-P., Azzam, G. A., Lemay, M. A., Zhukareva, V., and Houlé, J. D. (2011). Activity-dependent increase in neurotrophic factors is associated with an enhanced modulation of spinal reflexes after spinal cord injury. *J. Neurotrauma* 28, 299–309. doi: 10.1089/neu.2010.1594

Cao, L., Jiao, X., Zuzga, D. S., Liu, Y., Fong, D. M., Young, D., et al. (2004). VEGF links hippocampal activity with neurogenesis, learning and memory. *Nat. Genet.* 36, 827–835. doi: 10.1038/ng1395

Carmel, J. B., Berrol, L. J., Brus-Ramer, M., and Martin, J. H. (2010). Chronic electrical stimulation of the intact corticospinal system after unilateral injury restores skilled locomotor control and promotes spinal axon outgrowth. *J. Neurosci.* 30, 10918–10926. doi: 10.1523/JNEUROSCI.1435-10.2010

Carulli, D., Foscarin, S., and Rossi, F. (2011). Activity-dependent plasticity and gene expression modifications in the adult CNS. *Front. Mol. Neurosci.* 4:50. doi: 10.3389/fnmol.2011.00050

Chan, K. M., Curran, M., and Gordon, T. (2016). The use of brief post-surgical low frequency electrical stimulation to enhance nerve regeneration in clinical practice. *J. Physiol.* 594, 3553–3559. doi: 10.1113/JP270892

Chen, J. L., Lin, W. C., Cha, J. W., So, P. T., Kubota, Y., and Nedivi, E. (2011). Structural basis for the role of inhibition in facilitating adult brain plasticity. *Nat. Neurosci.* 14, 587–594. doi: 10.1038/nn.2799

Chen, K., Chen, Z., Wu, D., Zhang, L., Lin, X., Su, J., et al. (2015). Broad H3K4me3 is associated with increased transcription elongation and enhancer activity at tumor-suppressor genes. *Nat. Genet.* 47, 1149–1157. doi: 10.1038/ng.3385

Ciccarelli, A., and Giustetto, M. (2014). Role of ERK signaling in activity-dependent modifications of histone proteins. *Neuropharmacology* 80, 34–44. doi: 10.1016/j.neuropharm.2014.01.039

Cohen, T. J., Waddell, D. S., Barrientos, T., Lu, Z., Feng, G., Cox, G. A., et al. (2007). The histone deacetylase HDAC4 connects neural activity to muscle transcriptional reprogramming. *J. Biol. Chem.* 282, 33752–33759. doi: 10.1074/jbc.M706268200

Crowe, S. L., Movsesyan, V. A., Jorgensen, T. J., and Kondratyev, A. (2006). Rapid phosphorylation of histone H2A. X following ionotropic glutamate receptor activation. *Eur. J. Neurosci.* 23, 2351–2361. doi: 10.1111/j.1460-9568.2006.04768.x

Davis, G. W. (2006). Homeostatic control of neural activity: from phenomenology to molecular design. *Annu. Rev. Neurosci.* 29, 307–323. doi: 10.1146/annurev.neuro.28.061604.135751

Dehorter, N., Ciceri, G., Bartolini, G., Lim, L., del Pino, I., and Marín, O. (2015). Tuning of fast-spiking interneuron properties by an activity-dependent transcriptional switch. *Science* 349, 1216–1220. doi: 10.1126/science.aab3415

Diana, M., Raij, T., Melis, M., Nummenmaa, A., Leggio, L., and Bonci, A. (2017). Rehabilitating the addicted brain with transcranial magnetic stimulation. *Nat. Rev. Neurosci.* 18, 685–693. doi: 10.1038/nrn.2017.113

Dietz, V., and Harkema, S. J. (2004). Locomotor activity in spinal cord-injured persons. *J. Appl. Physiol.* 96, 1954–1960. doi: 10.1152/japplphysiol.00942.2003

Du, J., Feng, L., Yang, F., and Lu, B. (2000). Activity-and Ca2+-dependent modulation of surface expression of brain-derived neurotrophic factor receptors in hippocampal neurons. *J. Cell Biol.* 150, 1423–1434. doi: 10.1083/jcb.150.6.1423

Elzinga, K., Tyreman, N., Ladak, A., Savaryn, B., Olson, J., and Gordon, T. (2015). Brief electrical stimulation improves nerve regeneration after delayed repair in sprague dawley rats. *Exp. Neurol.* 269, 142–153. doi: 10.1016/j.expneurol.2015.03.022

Feldman, D. E. (2012). The spike-timing dependence of plasticity. *Neuron* 75, 556–571. doi: 10.1016/j.neuron.2012.08.001

Ferguson, A. R., Huie, J. R., Crown, E. D., Baumbauer, K. M., Hook, M. A., Garraway, S. M., et al. (2012). Maladaptive spinal plasticity opposes spinal learning and recovery in spinal cord injury. *Front. Physiol.* 3:399. doi: 10.3389/fphys.2012.00399

Fields, R. D. (2008). Oligodendrocytes changing the rules: action potentials in glia and oligodendrocytes controlling action potentials. *Neurosci.* 14, 540–543. doi: 10.1177/1073858408320294

Fields, R. D. (2015). A new mechanism of nervous system plasticity: activity-dependent myelination. *Nat. Rev. Neurosci.* 16, 756–767. doi: 10.1038/nrn4023

Fields, R. D., Lee, P. R., and Cohen, J. E. (2005). Temporal integration of intracellular Ca2+ signaling networks in regulating gene expression by action potentials. *Cell Calcium* 37, 433–442. doi: 10.1016/j.ceca.2005.01.011

Fields, R. D., and Nelson, P. G. (1992). A role for glial cells in activity-dependent development of the vertebrate nervous system. *Int. Rev. Neurobiol.* 34, 133–214. doi: 10.1016/S0074-7742(08)60098-7

Fischell, R. E., Fischell, D. R., Fredrick, J. P., and Woods, S. P. (2017). U.S. Patent No. 9,561,384. Washington, DC: U.S. Patent and Trademark Office.

Flavell, S. W., and Greenberg, M. E. (2008). Signaling mechanisms linking neuronal activity to gene expression and plasticity of the nervous system. *Annu. Rev. Neurosci.* 31, 563–590. doi: 10.1146/annurev.neuro.31.060407.125631

Fletcher, B. R., Calhoun, M. E., Rapp, P. R., and Shapiro, M. L. (2006). Fornix lesions decouple the induction of hippocampal arc transcription from behavior but not plasticity. *J. Neurosci.* 26, 1507–1515. doi: 10.1523/JNEUROSCI.4441-05.2006

Flexner, J. B., Flexner, L. B., and Stellar, E. (1963). Memory in mice as affected by intracerebral puromycin. *Science* 141, 57–59. doi: 10.1126/science.141.3575.57

Gariglio, P., Bellard, M., and Chambon, P. (1981). Clustering of RNA polymerase B molecules in the 5′ moiety of the adult β-globin gene of hen erythrocytes. *Nucleic Acids Res.* 9, 2589–2598. doi: 10.1093/nar/9.11.2589

Garraway, S. M., and Huie, J. R. (2016). Spinal plasticity and behavior: BDNF-induced neuromodulation in uninjured and injured spinal cord. *Neural Plast.* 2016:9857201. doi: 10.1155/2016/9857201

Gazula, V., Roberts, M., Luzzio, C., Jawad, A. F., and Kalb, R. G. (2004). Effects of limb exercise after spinal cord injury on motor neuron dendrite structure. *J. Comp. Neurol.* 476, 130–145. doi: 10.1002/cne.20204

Ge, S., Pradhan, D. A., Ming, G., and Song, H. (2007). GABA sets the tempo for activity-dependent adult neurogenesis. *Trends Neurosci.* 30, 1–8. doi: 10.1016/j.tins.2006.11.001

Gerasimenko, Y., Gorodnichev, R., Moshonkina, T., Sayenko, D., Gad, P., and Edgerton, V. R. (2015). Transcutaneous electrical spinal-cord stimulation in humans. *Ann. Phys. Rehabil. Med.* 58, 225–231. doi: 10.1016/j.rehab.2015.05.003

Gerasimenko, Y. P., Lu, D. C., Modaber, M., Zdunowski, S., Gad, P., Sayenko, D. G., et al. (2015). Noninvasive reactivation of motor descending control after paralysis. *J. Neurotrauma* 32, 1968–1980. doi: 10.1089/neu.2015.4008

Ghosh, B., Wang, Z., Nong, J., Urban, M. W., Zhang, Z., Trovillion, V. A., et al. (2018). Local BDNF delivery to the injured cervical spinal cord using an engineered hydrogel enhances diaphragmatic respiratory function. *J. Neurosci.* 38, 5982–5995. doi: 10.1523/JNEUROSCI.3084-17.2018

Gomez, J. L., Bonaventura, J., Lesniak, W., Mathews, W. B., Sysa-Shah, P., Rodriguez, L. A., et al. (2017). Chemogenetics revealed: DREADD occupancy and activation via converted clozapine. *Science* 357, 503–507. doi: 10.1126/science.aan2475

Gómez-Pinilla, F., Ying, Z., Roy, R. R., Molteni, R., and Edgerton, V. R. (2002). Voluntary exercise induces a BDNF-mediated mechanism that promotes neuroplasticity. *J. Neurophysiol.* 88, 2187–2195. doi: 10.1152/jn.00152.2002

Grau, J. W., and Huang, Y.-J. (2018). Metaplasticity within the spinal cord: Evidence brain-derived neurotrophic factor (BDNF), tumor necrosis factor (TNF), and alterations in GABA function (ionic plasticity) modulate pain and the capacity to learn. *Neurobiol. Learn. Mem.* 154, 121–135. doi: 10.1016/j.nlm.2018.04.007

Grau, J. W., Huang, Y.-J., Turtle, J. D., Strain, M. M., Miranda, R. C., Garraway, S. M., et al. (2017). When pain hurts: nociceptive stimulation induces a state of maladaptive plasticity and impairs recovery after spinal cord injury. *J. Neurotrauma* 34, 1873–1890. doi: 10.1089/neu.2016.4626

Graziano, A., Foffani, G., Knudsen, E. B., Shumsky, J., and Moxon, K. A. (2013). Passive exercise of the hind limbs after complete thoracic transection of the spinal cord promotes cortical reorganization. *PLoS ONE* 8:e54350. doi: 10.1371/journal.pone.0054350

Guan, J.-S., Haggarty, S. J., Giacometti, E., Dannenberg, J.-H., Joseph, N., Gao, J., et al. (2009). HDAC2 negatively regulates memory formation and synaptic plasticity. *Nature* 459, 55–60. doi: 10.1038/nature07925

Guzowski, J. F., Miyashita, T., Chawla, M. K., Sanderson, J., Maes, L. I., Houston, F. P., et al. (2006). Recent behavioral history modifies coupling between cell activity and arc gene transcription in hippocampal CA1 neurons. *Proc. Natl. Acad. Sci.* 103, 1077–1082. doi: 10.1073/pnas.0505519103

Guzowski, J. F., Timlin, J. A., Roysam, B., McNaughton, B. L., Worley, P. F., and Barnes, C. A. (2005). Mapping behaviorally relevant neural circuits with immediate-early gene expression. *Curr. Opin. Neurobiol.* 15, 599–606. doi: 10.1016/j.conb.2005.08.018

Harkema, S., Gerasimenko, Y., Hodes, J., Burdick, J., Angeli, C., Chen, Y., et al. (2011). Effect of epidural stimulation of the lumbosacral spinal cord on voluntary movement, standing, and assisted stepping after motor complete paraplegia: a case study. *Lancet* 377, 1938–1947. doi: 10.1016/S0140-6736(11)60547-3

Hoffman, L. R., and Field-Fote, E. C. (2007). Cortical reorganization following bimanual training and somatosensory stimulation in cervical spinal cord injury: a case report. *Phys. Ther.* 87, 208–223. doi: 10.2522/ptj.20050365

Howlett, O. A., Lannin, N. A., Ada, L., and McKinstry, C. (2015). Functional electrical stimulation improves activity after stroke: a systematic review with meta-analysis. *Arch. Phys. Med. Rehabil.* 96, 934–943. doi: 10.1016/j.apmr.2015.01.013

Huang, Y.-J., Lee, K. H., and Grau, J. W. (2017). Complete spinal cord injury (SCI) transforms how brain derived neurotrophic factor (BDNF) affects nociceptive sensitization. *Exp. Neurol.* 288, 38–50. doi: 10.1016/j.expneurol.2016.11.001

Huang, Y.-J., Lee, K. H., Murphy, L., Garraway, S. M., and Grau, J. W. (2016). Acute spinal cord injury (SCI) transforms how GABA affects nociceptive sensitization. *Exp. Neurol.* 285, 82–95. doi: 10.1016/j.expneurol.2016.09.005

Hummel, F. C., and Cohen, L. G. (2006). Non-invasive brain stimulation: a new strategy to improve neurorehabilitation after stroke? *Lancet Neurol.* 5, 708–712. doi: 10.1016/S1474-4422(06)70525-7

Im, H.-I., Hollander, J. A., Bali, P., and Kenny, P. J. (2010). MeCP2 controls BDNF expression and cocaine intake through homeostatic interactions with microRNA-212. *Nat. Neurosci.* 13, 1120–1127. doi: 10.1038/nn.2615

Inoue, Y., Udo, H., Inokuchi, K., and Sugiyama, H. (2007). Homer1a regulates the activity-induced remodeling of synaptic structures in cultured hippocampal neurons. *Neuroscience* 150, 841–852. doi: 10.1016/j.neuroscience.2007.09.081

Ji, Y., Lu, Y., Yang, F., Shen, W., Tang, T. T.-T., Feng, L., et al. (2010). Acute and gradual increases in BDNF concentration elicit distinct signaling and functions in neurons. *Nat. Neurosci.* 13, 302–309. doi: 10.1038/nn.2505

Jin, Y., Fischer, I., Tessler, A., and Houle, J. D. (2002). Transplants of fibroblasts genetically modified to express BDNF promote axonal regeneration from supraspinal neurons following chronic spinal cord injury. *Exp. Neurol.* 177, 265–275. doi: 10.1006/exnr.2002.7980

Jolivet, R., Coggan, J. S., Allaman, I., and Magistretti, P. J. (2015). Multi-timescale modeling of activity-dependent metabolic coupling in the neuron-glia-vasculature ensemble. *PLoS Comput. Biol.* 11:e1004036. doi: 10.1371/journal.pcbi.1004036

Jonkers, I., and Lis, J. T. (2015). Getting up to speed with transcription elongation by RNA polymerase II. *Nat. Rev. Mol. Cell Biol.* 16, 167–177. doi: 10.1038/nrm3953

Joo, J.-Y., Schaukowitch, K., Farbiak, L., Kilaru, G., and Kim, T.-K. (2016). Stimulus-specific combinatorial functionality of neuronal c-fos enhancers. *Nat. Neurosci.* 19, 75–83. doi: 10.1038/nn.4170

Jurkiewicz, M. T., Mikulis, D. J., McIlroy, W. E., Fehlings, M. G., and Verrier, M. C. (2007). Sensorimotor cortical plasticity during recovery following spinal cord injury: a longitudinal fMRI study. *Neurorehabil. Neural Repair* 21, 527–538. doi: 10.1177/1545968307301872

Kandel, E. R. (2001). The molecular biology of memory storage: a dialogue between genes and synapses. *Science* 294, 1030–1038. doi: 10.1126/science.1067020

Kao, T., Shumsky, J. S., Knudsen, E. B., Murray, M., and Moxon, K. A. (2011). Functional role of exercise-induced cortical organization of sensorimotor cortex after spinal transection. *J. Neurophysiol.* 106, 2662–2674. doi: 10.1152/jn.01017.2010

Karpova, N. N. (2014). Role of BDNF epigenetics in activity-dependent neuronal plasticity. *Neuropharmacology* 76, 709–718. doi: 10.1016/j.neuropharm.2013.04.002

Kasten, M. R., Sunshine, M. D., Secrist, E. S., Horner, P. J., and Moritz, C. T. (2013). Therapeutic intraspinal microstimulation improves forelimb function after cervical contusion injury. *J. Neural Eng.* 10:44001. doi: 10.1088/1741-2560/10/4/044001

Kellner, Y., Gödecke, N., Dierkes, T., Thieme, N., Zagrebelsky, M., and Korte, M. K. (2014). The BDNF effects on dendritic spines of mature hippocampal neurons depend on neuronal activity. *Front. Synaptic Neurosci.* 6:5. doi: 10.3389/fnsyn.2014.00005

Kim, T.-K., Hemberg, M., Gray, J. M., Costa, A. M., Bear, D. M., Wu, J., et al. (2010). Widespread transcription at neuronal activity-regulated enhancers. *Nature* 465, 182–187. doi: 10.1038/nature09033

Kiser, T. S., Reese, N. B., Maresh, T., Hearn, S., Yates, C., Skinner, R., et al. (2005). Use of a motorized bicycle exercise trainer to normalize frequency-dependent habituation of the H-reflex in spinal cord injury. *J. Spinal Cord Med.* 28, 241–245. doi: 10.1080/10790268.2005.11753818

Kondiles, B. R., and Horner, P. J. (2018). Myelin plasticity, neural activity, and traumatic neural injury. *Dev. Neurobiol.* 78, 108–122. doi: 10.1002/dneu.22540

Koppel, I., and Timmusk, T. (2013). Differential regulation of Bdnf expression in cortical neurons by class-selective histone deacetylase inhibitors. *Neuropharmacology* 75, 106–115. doi: 10.1016/j.neuropharm.2013.07.015

Kravitz, A., and Bonci, A. (2013). Optogenetics, physiology, and emotions. *Front. Behav. Neurosci.* 7:169. doi: 10.3389/fnbeh.2013.00169

Lai, K.-O., Wong, A. S. L., Cheung, M.-C., Xu, P., Liang, Z., Lok, K.-C., et al. (2012). TrkB phosphorylation by Cdk5 is required for activity-dependent structural plasticity and spatial memory. *Nat. Neurosci.* 15, 1506–1515. doi: 10.1038/nn.3237

Lavrov, I., Dy, C. J., Fong, A. J., Gerasimenko, Y., Courtine, G., Zhong, H., et al. (2008). Epidural stimulation induced modulation of spinal locomotor networks in adult spinal rats. *J. Neurosci.* 28, 6022–6029. doi: 10.1523/JNEUROSCI.0080-08.2008

Lee, P. R., Cohen, J. E., Iacobas, D. A., Iacobas, S., and Fields, R. D. (2017). Gene networks activated by specific patterns of action potentials in dorsal root ganglia neurons. *Sci. Rep.* 7:43765. doi: 10.1038/srep43765

Leech, K. A., and Hornby, T. G. (2017). High-intensity locomotor exercise increases brain-derived neurotrophic factor in individuals with incomplete spinal cord injury. *J. Neurotrauma* 34, 1240–1248. doi: 10.1089/neu.2016.4532

Li, X., Marshall, P. R., Leighton, L. J., Zajaczkowski, E. L., Wang, Z., Madugalle, S. U., et al. (2019). The DNA repair-associated protein Gadd45γ regulates the temporal coding of immediate early gene expression within the prelimbic prefrontal cortex and is required for the consolidation of associative fear memory. *J. Neurosci.* 39, 970–983. doi: 10.1523/JNEUROSCI.2024-18.2018

Linderoth, B., and Foreman, R. D. (1999). Physiology of spinal cord stimulation: review and update. *Neuromudulation* 2, 150–164. doi: 10.1046/j.1525-1403.1999.00150.x

Liu, J., Wu, X., Zhang, H., Pfeifer, G. P., and Lu, Q. (2017). Dynamics of RNA polymerase II pausing and bivalent histone H3 methylation during neuronal differentiation in brain development. *Cell Rep.* 20, 1307–1318. doi: 10.1016/j.celrep.2017.07.046

Liu, K., Tedeschi, A., Park, K. K., and He, Z. (2011). Neuronal intrinsic mechanisms of axon regeneration. *Annu. Rev. Neurosci.* 34, 131–152. doi: 10.1146/annurev-neuro-061010-113723

Lu, Y., Christian, K., and Lu, B. (2008). BDNF: a key regulator for protein synthesis-dependent LTP and long-term memory? *Neurobiol. Learn. Mem.* 89, 312–323. doi: 10.1016/j.nlm.2007.08.018

Lynskey, J. V., Belanger, A., and Jung, R. (2008). Activity-dependent plasticity in spinal cord injury. *J. Rehabil. Res. Dev.* 45, 229–40. doi: 10.1682/JRRD.2007.03.0047

Ma, D. K., Jang, M.-H., Guo, J. U., Kitabatake, Y., Chang, M., Pow-Anpongkul, N., et al. (2009). Neuronal activity–induced Gadd45b promotes epigenetic DNA demethylation and adult neurogenesis. *Science* 323, 1074–1077. doi: 10.1126/science.1166859

Madabhushi, R., Gao, F., Pfenning, A. R., Pan, L., Yamakawa, S., Seo, J., et al. (2015). Activity-induced DNA breaks govern the expression of neuronal early-response genes. *Cell* 161, 1592–1605. doi: 10.1016/j.cell.2015.05.032

Madabhushi, R., and Kim, T.-K. (2018). Emerging themes in neuronal activity-dependent gene expression. *Mol. Cell. Neurosci.* 87, 27–34. doi: 10.1016/j.mcn.2017.11.009

Mailis-Gagnon, A., Furlan, A. D., Sandoval, J. A., and Taylor, R. S. (2004). Spinal cord stimulation for chronic pain. *Cochrane Database Syst Rev. Rev.* 3, 1454–1858. doi: 10.1002/14651858.CD003783.pub2

Marais, L., Stein, D. J., and Daniels, W. M. U. (2009). Exercise increases BDNF levels in the striatum and decreases depressive-like behavior in chronically stressed rats. *Metab. Brain Dis.* 24, 587–597. doi: 10.1007/s11011-009-9157-2

Martin, J. H. (2005). The corticospinal system: from development to motor control. *Neurosci.* 11, 161–173. doi: 10.1177/1073858404270843

Medina, I., Friedel, P., Rivera, C., Kahle, K. T., Kourdougli, N., Uvarov, P., et al. (2014). Current view on the functional regulation of the neuronal K+-Cl– cotransporter KCC2. *Front. Cell. Neurosci.* 8:27. doi: 10.3389/fncel.2014.00027

Minatohara, K., Akiyoshi, M., and Okuno, H. (2016). Role of immediate-early genes in synaptic plasticity and neuronal ensembles underlying the memory trace. *Front. Mol. Neurosci.* 8:78. doi: 10.3389/fnmol.2015.00078

Mondello, S. E., Kasten, M. R., Horner, P. J., and Moritz, C. T. (2014). Therapeutic intraspinal stimulation to generate activity and promote long-term recovery. *Front. Neurosci.* 8:21. doi: 10.3389/fnins.2014.00021

Morgan, J. I., and Curran, T. (1986). Role of ion flux in the control of c-fos expression. *Nature* 322, 552–555. doi: 10.1038/322552a0

Morgan, J. I., and Curran, T. (1989). Stimulus-transcription coupling in neurons: role of cellular immediate-early genes. *Trends Neurosci.* 12, 459–462. doi: 10.1016/0166-2236(89)90096-9

Naeve, G. S., Ramakrishnan, M., Kramer, R., Hevroni, D., Citri, Y., and Theill, L. E. (1997). Neuritin: a gene induced by neural activity and neurotrophins that promotes neuritogenesis. *Proc. Natl. Acad. Sci. U.S.A.* 94, 2648–2653. doi: 10.1073/pnas.94.6.2648

Nagahara, A. H., and Tuszynski, M. H. (2011). Potential therapeutic uses of BDNF in neurological and psychiatric disorders. *Nat. Rev. Drug Discov.* 10, 209–219. doi: 10.1038/nrd3366

Nagappan, G., and Lu, B. (2005). Activity-dependent modulation of the BDNF receptor TrkB: mechanisms and implications. *Trends Neurosci.* 28, 464–471. doi: 10.1016/j.tins.2005.07.003

Neville, I. S., Hayashi, C. Y., El Hajj, S. A., Zaninotto, A. L. C., Sabino, J. P., Sousa, L. M., et al. (2015). Repetitive transcranial magnetic stimulation (rTMS) for the cognitive rehabilitation of traumatic brain injury (TBI) victims: study protocol for a randomized controlled trial. *Trials* 16:440. doi: 10.1186/s13063-015-0944-2

O'Connell, N. E., Marston, L., Spencer, S., DeSouza, L. H., and Wand, B. M. (2018). Non-invasive brain stimulation techniques for chronic pain. *Cochrane Database Syst Rev.* 8:CD008208. doi: 10.1002/14651858.CD008208.pub5

Okuno, H. (2011). Regulation and function of immediate-early genes in the brain: beyond neuronal activity markers. *Neurosci. Res.* 69, 175–186. doi: 10.1016/j.neures.2010.12.007

Palomer, E., Carretero, J., Benvegnu, S., Dotti, C. G., and Martin, M. G. (2016). Neuronal activity controls Bdnf expression via polycomb de-repression and CREB/CBP/JMJD3 activation in mature neurons. *Nat. Commun.* 7:11081. doi: 10.1038/ncomms11081

Pastuzyn, E. D., Day, C. E., Kearns, R. B., Kyrke-Smith, M., Taibi, A. V., McCormick, J., et al. (2018). The neuronal gene Arc encodes a repurposed retrotransposon Gag protein that mediates intercellular RNA transfer. *Cell* 172, 275–288. doi: 10.1016/j.cell.2017.12.024

Peckham, P. H., and Knutson, J. S. (2005). Functional electrical stimulation for neuromuscular applications. *Annu. Rev. Biomed. Eng.* 7, 327–360. doi: 10.1146/annurev.bioeng.6.040803.140103

Pfurtscheller, G., Müller, G. R., Pfurtscheller, J., Gerner, H. J., and Rupp, R. (2003). 'Thought'–control of functional electrical stimulation to restore hand grasp in a patient with tetraplegia. *Neurosci. Lett.* 351, 33–36. doi: 10.1016/S0304-3940(03)00947-9

Philip, N. S., Barredo, J., Aiken, E., and Carpenter, L. L. (2018). Neuroimaging mechanisms of therapeutic transcranial magnetic stimulation for major depressive disorder. *Biol. Psychiatry Cogn. Neurosci. Neuroimaging* 3, 211–222. doi: 10.1016/j.bpsc.2017.10.007

Qiu, Z., and Ghosh, A. (2008). A calcium-dependent switch in a CREST-BRG1 complex regulates activity-dependent gene expression. *Neuron* 60, 775–787. doi: 10.1016/j.neuron.2008.09.040

Rasmussen, P., Brassard, P., Adser, H., Pedersen, M. V., Leick, L., Hart, E., et al. (2009). Evidence for a release of brain-derived neurotrophic factor from the brain during exercise. *Exp. Physiol.* 94, 1062–1069. doi: 10.1113/expphysiol.2009.048512

Rath, M., Vette, A. H., Ramasubramaniam, S., Li, K., Burdick, J., Edgerton, V. R., et al. (2018). Trunk stability enabled by noninvasive spinal electrical stimulation after spinal cord injury. *J. Neurotrauma* 35, 2540–2553. doi: 10.1089/neu.2017.5584

Rea, S., Eisenhaber, F., O'carroll, D., Strahl, B. D., Sun, Z.-W., Schmid, M., et al. (2000). Regulation of chromatin structure by site-specific histone H3 methyltransferases. *Nature* 406, 593–599. doi: 10.1038/35020506

Rebesco, J. M., Stevenson, I. H., Koerding, K., Solla, S. A., and Miller, L. E. (2010). Rewiring neural interactions by micro-stimulation. *Front. Syst. Neurosci.* 4:39. doi: 10.3389/fnsys.2010.00039

Rendeiro, C., and Rhodes, J. S. (2018). A new perspective of the hippocampus in the origin of exercise–brain interactions. *Brain Struct. Funct.* 223, 2527–2545. doi: 10.1007/s00429-018-1665-6

Rösche, J., Paulus, C., Maisch, U., Kaspar, A., Mauch, E., and Kornhuber, H. H. (1997). The effects of therapy on spasticity utilizing a motorized exercise-cycle. *Spinal Cord* 35, 176–178. doi: 10.1038/sj.sc.3100376

Rossini, P. M., Barker, A. T., Berardelli, A., Caramia, M. D., Caruso, G., Cracco, R. Q., et al. (1994). Non-invasive electrical and magnetic stimulation of the brain, spinal cord and roots: basic principles and procedures for routine clinical application. Report of an IFCN committee. *Electroencephalogr. Clin. Neurophysiol.* 91, 79–92. doi: 10.1016/0013-4694(94)90029-9

Rotem, A., and Moses, E. (2008). Magnetic stimulation of one-dimensional neuronal cultures. *Biophys. J.* 94, 5065–5078. doi: 10.1529/biophysj.107.125708

Sakry, D., Neitz, A., Singh, J., Frischknecht, R., Marongiu, D., Biname, F., et al. (2014). Oligodendrocyte precursor cells modulate the neuronal network by activity-dependent ectodomain cleavage of glial NG2. *PLoS Biol.* 12:e1001993. doi: 10.1371/journal.pbio.1001993

Salimi, I., and Martin, J. H. (2004). Rescuing transient corticospinal terminations and promoting growth with corticospinal stimulation in kittens. *J. Neurosci.* 24, 4952–4961. doi: 10.1523/JNEUROSCI.0004-04.2004

Sayenko, D. G., Rath, M., Ferguson, A. R., Burdick, J. W., Havton, L. A., Edgerton, V. R., et al. (2019). Self-assisted standing enabled by non-invasive spinal stimulation after spinal cord injury. *J. Neurotrauma* 36, 1435–1450. doi: 10.1089/neu.2018.5956

Schafer, D. P., Lehrman, E. K., Kautzman, A. G., Koyama, R., Mardinly, A. R., Yamasaki, R., et al. (2012). Microglia sculpt postnatal neural circuits in an activity and complement-dependent manner. *Neuron* 74, 691–705. doi: 10.1016/j.neuron.2012.03.026

Schaukowitch, K., Joo, J.-Y., Liu, X., Watts, J. K., Martinez, C., and Kim, T.-K. (2014). Enhancer RNA facilitates NELF release from immediate early genes. *Mol. Cell* 56, 29–42. doi: 10.1016/j.molcel.2014.08.023

Seeman, S. C., Mogen, B. J., Fetz, E. E., and Perlmutter, S. I. (2017). Paired stimulation for spike-timing-dependent plasticity in primate sensorimotor cortex. *J. Neurosci.* 37, 1935–1949. doi: 10.1523/JNEUROSCI.2046-16.2017

Sharpe, A. N., and Jackson, A. (2014). Upper-limb muscle responses to epidural, subdural and intraspinal stimulation of the cervical spinal cord. *J. Neural Eng.* 11:16005. doi: 10.1088/1741-2560/11/1/016005

Sheng, M., Dougan, S. T., McFadden, G., and Greenberg, M. E. (1988). Calcium and growth factor pathways of c-fos transcriptional activation require distinct upstream regulatory sequences. *Mol. Cell. Biol.* 8, 2787–2796. doi: 10.1128/MCB.8.7.2787

Sheng, M., and Greenberg, M. E. (1990). The regulation and function of c-fos and other immediate early genes in the nervous system. *Neuron* 4, 477–485. doi: 10.1016/0896-6273(90)90106-P

Sheng, M., Thompson, M. A., and Greenberg, M. E. (1991). CREB: a Ca (2+)-regulated transcription factor phosphorylated by calmodulin-dependent kinases. *Science* 252, 1427–1430. doi: 10.1126/science.1646483

Shimada, T., Yoshida, T., and Yamagata, K. (2016). Neuritin mediates activity-dependent axonal branch formation in part via FGF signaling. *J. Neurosci.* 36, 4534–4548. doi: 10.1523/JNEUROSCI.1715-15.2016

Skinner, R. D., Houle, J. D., Reese, N. B., Berry, C. L., and Garcia-Rill, E. (1996). Effects of exercise and fetal spinal cord implants on the H-reflex in chronically spinalized adult rats. *Brain Res.* 729, 127–131. doi: 10.1016/0006-8993(96)00556-2

Sleiman, S. F., Henry, J., Al-Haddad, R., El Hayek, L., Haidar, E. A., Stringer, T., et al. (2016). Exercise promotes the expression of brain derived neurotrophic factor (BDNF) through the action of the ketone body β-hydroxybutyrate. *Elife* 5:e15092. doi: 10.7554/eLife.15092.012

Smith, P. A. (2014). BDNF: no gain without pain? *Neuroscience* 283, 107–123. doi: 10.1016/j.neuroscience.2014.05.044

Spiegel, I., Mardinly, A. R., Gabel, H. W., Bazinet, J. E., Couch, C. H., Tzeng, C. P., et al. (2014). Npas4 regulates excitatory-inhibitory balance within neural circuits through cell-type-specific gene programs. *Cell* 157, 1216–1229. doi: 10.1016/j.cell.2014.03.058

Spitzer, N. C. (2006). Electrical activity in early neuronal development. *Nature* 444, 707–712. doi: 10.1038/nature05300

Stagg, C. J., and Nitsche, M. A. (2011). Physiological basis of transcranial direct current stimulation. *Neuroscientist* 17, 37–53. doi: 10.1177/1073858410386614

Stidd, D. A., Rivero, S., and Weinand, M. E. (2014). Spinal cord stimulation with implanted epidural paddle lead relieves chronic axial low back pain. *J. Pain Res.* 7, 465–470. doi: 10.2147/JPR.S66414

Stimpson, N. J., Davison, G., and Javadi, A.-H. (2018). Joggin'the noggin: towards a physiological understanding of exercise-induced cognitive benefits. *Neurosci. Biobehav. Rev.* 88, 177–186. doi: 10.1016/j.neubiorev.2018.03.018

Suberbielle, E., Sanchez, P. E., Kravitz, A. V., Wang, X., Ho, K., Eilertson, K., et al. (2013). Physiologic brain activity causes DNA double-strand breaks in neurons, with exacerbation by amyloid-β. *Nat. Neurosci.* 16, 613–621. doi: 10.1038/nn.3356

Sunshine, M. D., Cho, F. S., Lockwood, D. R., Fechko, A. S., Kasten, M. R., and Moritz, C. T. (2013). Cervical intraspinal microstimulation evokes robust forelimb movements before and after injury. *J. Neural Eng.* 10:36001. doi: 10.1088/1741-2560/10/3/036001

Taccola, G. (2011). The locomotor central pattern generator of the rat spinal cord in vitro is optimally activated by noisy dorsal root waveforms. *J. Neurophysiol.* 106, 872–884. doi: 10.1152/jn.00170.2011

Taccola, G., Sayenko, D., Gad, P., Gerasimenko, Y., and Edgerton, V. R. (2017). And yet it moves: Recovery of volitional control after spinal cord injury. *Prog Neurobiol.* 160:64–81. doi: 10.1016/j.pneurobio.2017.10.004

Taylor, H. H., and Murphy, B. (2008). Altered sensorimotor integration with cervical spine manipulation. *J. Manipulative Physiol. Ther.* 31, 115–126. doi: 10.1016/j.jmpt.2007.12.011

Tongiorgi, E., Righi, M., and Cattaneo, A. (1997). Activity-dependent dendritic targeting of BDNF and TrkB mRNAs in hippocampal neurons. *J. Neurosci.* 17, 9492–9505. doi: 10.1523/JNEUROSCI.17-24-09492.1997

Tyssowski, K. M., DeStefino, N. R., Cho, J.-H., Dunn, C. J., Poston, R. G., Carty, C. E., et al. (2018). Different neuronal activity patterns induce different gene expression programs. *Neuron* 98, 530–546. doi: 10.1016/j.neuron.2018.04.001

Walsh, V., and Pascual-Leone, A. (2003). *Transcranial Magnetic Stimulation: A Neurochronometrics of Mind*. Cambridge, MA: MIT press. doi: 10.7551/mitpress/6896.001.0001

Wheeler, M. A., Smith, C. J., Ottolini, M., Barker, B. S., Purohit, A. M., Grippo, R. M., et al. (2016). Genetically targeted magnetic control of the nervous system. *Nat. Neurosci.* 19, 756–761. doi: 10.1038/nn.4265

Williams, A., Gill, S., Varma, T., Jenkinson, C., Quinn, N., Mitchell, R., et al. (2010). Deep brain stimulation plus best medical therapy versus best medical therapy alone for advanced parkinson's disease (PD SURG trial): a randomised, open-label trial. *Lancet Neurol.* 9, 581–591. doi: 10.1016/S1474-4422(10)70093-4

Wong, Y.-H., Lee, C.-M., Xie, W., Cui, B., and Poo, M. (2015). Activity-dependent BDNF release via endocytic pathways is regulated by synaptotagmin-6 and complexin. *Proc. Natl. Acad. Sci. U.S.A.* 112, E4475–E4484. doi: 10.1073/pnas.1511830112

Xiao, B., Tu, J. C., and Worley, P. F. (2000). Homer: a link between neural activity and glutamate receptor function. *Curr. Opin. Neurobiol.* 10, 370–374. doi: 10.1016/S0959-4388(00)00087-8

Xiao, J., Wong, A. W., Willingham, M. M., Kaasinen, S. K., Hendry, I. A., Howitt, J., et al. (2009). BDNF exerts contrasting effects on peripheral myelination of NGF-dependent and BDNF-dependent DRG neurons. *J. Neurosci.* 29, 4016–4022. doi: 10.1523/JNEUROSCI.3811-08.2009

Yao, J., Zhao, Q., Lu, J., and Mei, Y. (2018). Functions and the related signaling pathways of the neurotrophic factor neuritin. *Acta Pharmacol. Sin.* 39, 1414–1420. doi: 10.1038/aps.2017.197

Yao, Y.-X., Zhang, Y.-F., Yang, Y., Guo, S.-H., Jiang, Z., and Zhao, Z.-Q. (2014). Spinal synaptic scaffolding protein Homer 1b/c regulates CREB phosphorylation and c-fos activation induced by inflammatory pain in rats. *Neurosci. Lett.* 559, 88–93. doi: 10.1016/j.neulet.2013.11.049

Yizhar, O., Fenno, L. E., Davidson, T. J., Mogri, M., and Deisseroth, K. (2016). Optogenetics in Neural Systems. *Neuron* 71, 9–34. doi: 10.1016/j.neuron.2011.06.004

Young, S. Z., Taylor, M. M., and Bordey, A. (2011). Neurotransmitters couple brain activity to subventricular zone neurogenesis. *Eur. J. Neurosci.* 33, 1123–1132. doi: 10.1111/j.1460-9568.2011.07611.x

Zagrebelsky, M., and Korte, M. (2014). Form follows function: BDNF and its involvement in sculpting the function and structure of synapses. *Neuropharmacology* 76, 628–638. doi: 10.1016/j.neuropharm.2013.05.029

Zanos, S., Richardson, A. G., Shupe, L., Miles, F. P., and Fetz, E. E. (2011). The Neurochip-2: an autonomous head-fixed computer for recording and stimulating in freely behaving monkeys. *IEEE Trans. Neural Syst. Rehabil. Eng.* 19, 427–435. doi: 10.1109/TNSRE.2011.2158007

Zhao, Q., Lu, J., Li, Z., and Mei, Y. (2018). Neuritin promotes neurite and spine growth in rat cerebellar granule cells via L-type calcium channel-mediated calcium influx. *J. Neurochem.* 147, 40–57. doi: 10.1111/jnc.14535

Zhou, Z., Hong, E. J., Cohen, S., Zhao, W., Ho, H. H., Schmidt, L., et al. (2006). Brain-specific phosphorylation of MeCP2 regulates activity-dependent Bdnf transcription, dendritic growth, and spine maturation. *Neuron* 52, 255–269. doi: 10.1016/j.neuron.2006.09.037

Conflict of Interest: The authors declare that the research was conducted in the absence of any commercial or financial relationships that could be construed as a potential conflict of interest.

Advantages of publishing in Frontiers

OPEN ACCESS
Articles are free to read for greatest visibility and readership

FAST PUBLICATION
Around 90 days from submission to decision

HIGH QUALITY PEER-REVIEW
Rigorous, collaborative, and constructive peer-review

TRANSPARENT PEER-REVIEW
Editors and reviewers acknowledged by name on published articles

Frontiers
Avenue du Tribunal-Fédéral 34
1005 Lausanne | Switzerland

Visit us: www.frontiersin.org
Contact us: frontiersin.org/about/contact

REPRODUCIBILITY OF RESEARCH
Support open data and methods to enhance research reproducibility

DIGITAL PUBLISHING
Articles designed for optimal readership across devices

FOLLOW US
@frontiersin

IMPACT METRICS
Advanced article metrics track visibility across digital media

EXTENSIVE PROMOTION
Marketing and promotion of impactful research

LOOP RESEARCH NETWORK
Our network increases your article's readership